

# Nanofabrication for Nanophotonics

Younghwan Yang, Youngsun Jeon, Zhaogang Dong, Joel K. W. Yang, Mahsa Haddadi Moghaddam, Dai-Sik Kim, Dong Kyo Oh, Jihae Lee, Mario Hentschel, Harald Giessen, Dohyun Kang, Gyeongtae Kim, Takuo Tanaka, Yang Zhao, Johannes Bürger, Stefan A. Maier, Haoran Ren, Wooik Jung, Mansoo Choi, Gwangmin Bae, Haomin Chen, Seokwoo Jeon, Jaekyung Kim, Eunji Lee, Hyunjung Kang, Yujin Park, Dang Du Nguyen, Inki Kim, Pablo Cencillo-Abad, Debashis Chanda, Xinxin Jing, Na Liu, Irina V. Martynenko, Tim Liedl, Yuna Kwak, Jwa-Min Nam, Sang-Min Park, Teri W. Odom, Hye-Eun Lee, Ryeong Myeong Kim, Ki Tae Nam, Hyunah Kwon, Hyeon-Ho Jeong, Peer Fischer, Jiwon Yoon, Shin-Hyun Kim, Sangmin Shim, Dasol Lee, Luis A. Pérez, Xiaoyu Qi, Agustin Mihi, Hohyun Keum, Moonsub Shim, Seok Kim, Hanhwi Jang, Yeon Sik Jung, Christian Rossner, Tobias A.F. König, Andreas Fery, Zhiwei Li, Koray Aydin, Chad A. Mirkin, Junhwa Seong, Nara Jeon, Zhiyun Xu, Tian Gu, Juejun Hu, Hyounghan Kwon, Hojoong Jung, Hossein Aljani, Igor Aharonovich, Joohoon Kim, and Junsuk Rho\*



Cite This: <https://doi.org/10.1021/acsnano.4c10964>



Read Online

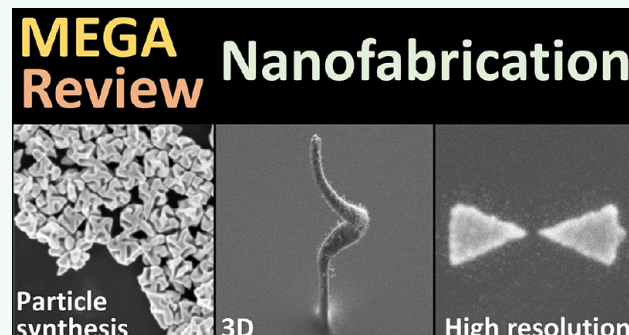
ACCESS |

Metrics & More

Article Recommendations

**ABSTRACT:** Nanofabrication, a pivotal technology at the intersection of nanoscale engineering and high-resolution patterning, has substantially advanced over recent decades. This technology enables the creation of nanopatterns on substrates crucial for developing nanophotonic devices and other applications in diverse fields including electronics and biosciences. Here, this mega-review comprehensively explores various facets of nanofabrication focusing on its application in nanophotonics. It delves into high-resolution techniques like focused ion beam and electron beam lithography, methods for 3D complex structure fabrication, scalable manufacturing approaches, and material compatibility considerations. Special attention is given to emerging trends such as the utilization of two-photon lithography for 3D structures and advanced materials like phase change substances and 2D materials with excitonic properties. By highlighting these advancements, the review aims to provide insights into the ongoing evolution of nanofabrication, encouraging further research and application in creating functional nanostructures. This work encapsulates critical developments and future perspectives, offering a detailed narrative on the state-of-the-art in nanofabrication tailored for both new researchers and seasoned experts in the field.

**KEYWORDS:** Nanofabrication, Nanomanufacturing, Metaphotonics, Top-down fabrication, Bottom-up fabrication, Metasurfaces, Metamaterials, Additive manufacturing, Scalable manufacturing, High-resolution lithography



## 1. INTRODUCTION

Younghwan Yang, Youngsun Jeon, and Junsuk Rho

Nanofabrication refers to the process of creating extremely small structures and devices at the nanoscale.<sup>1–5</sup> Over the past decades, collaborative research efforts spanning physics, chemistry, and interdisciplinary domains have led to the birth of various fabrication methods. As a result, it was possible to deposit films using chemical reactions, pattern using photoreactive polymers, or create high-resolution beams.

These technologies have been further developed and can be commercialized with high resolution, such as photolithog-

Received: August 10, 2024

Revised: February 13, 2025

Accepted: February 13, 2025

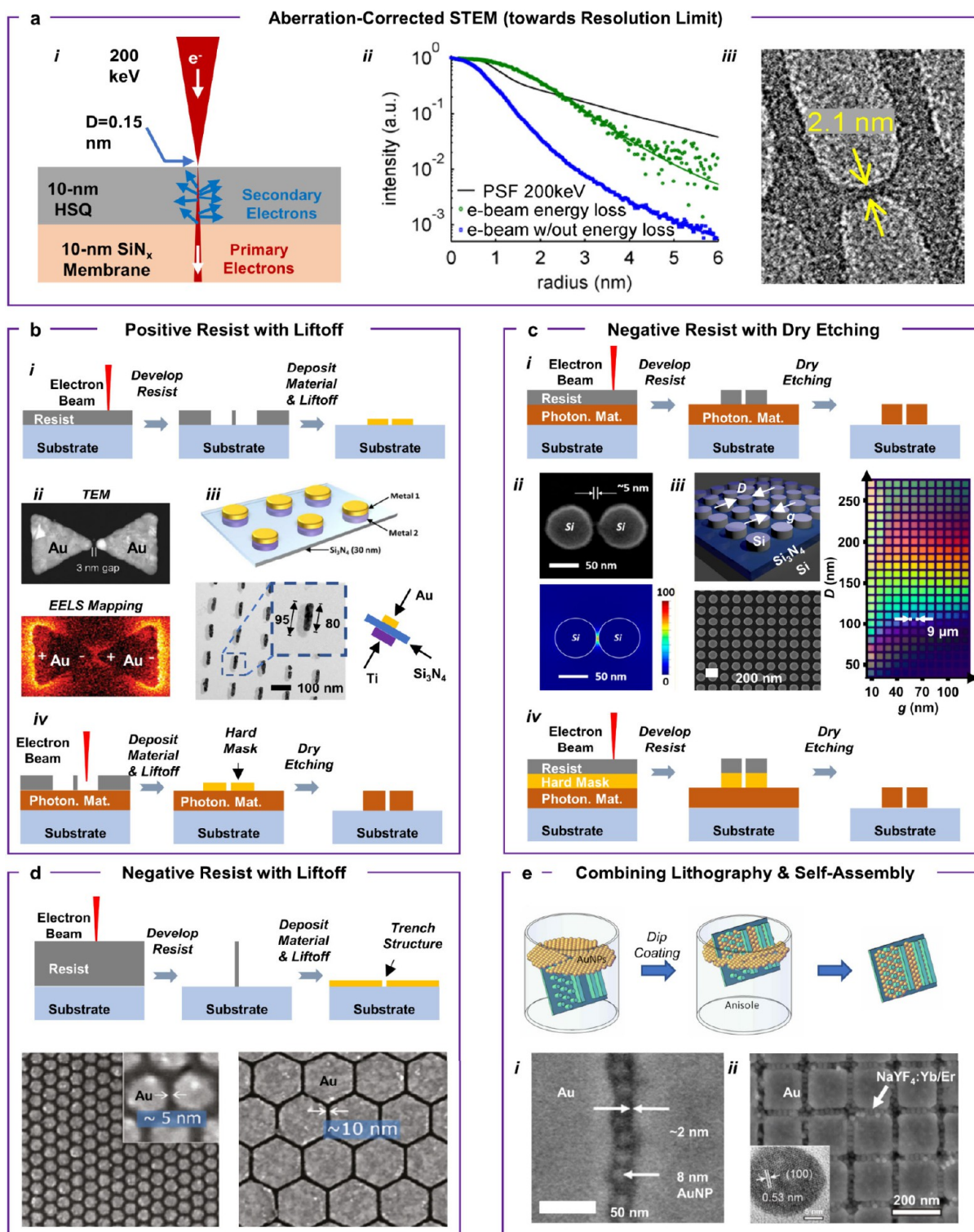


**Figure 1.** High-resolution electron-beam lithography technologies for nanophotonics. (a) Pushing toward the nanofabrication limit via the aberration-corrected scanning transmission electron microscope (STEM) setup.<sup>92</sup> Panel I shows that the diameter of the focused electron beam is around 0.15 nm when the electron acceleration voltage is 200 keV. The testing sample is 10 nm hydrogen silsesquioxane (HSQ) resist as spin coated onto 10 nm SiN<sub>x</sub> membrane, where the figure illustrates the trajectories of the primary electrons and secondary electrons. Panel II (black line) presents the point spread function (PSF) of the electron dosage with respect to radius. Panel III shows the reliable fabrication resolution limit of 2.1 nm when the HSQ resist is developed with the NaOH: NaCl salty solution. Adapted with permission from ref 92. Copyright 2013 ACS. (b) Fabrication of nanophotonic cavities via the positive resist, such as poly(methyl methacrylate) (PMMA) or ZEP, with the lift-off process. After the development process, the resist region being exposed by electron beams will be washed away. Followed by the metal evaporation process and liftoff, metallic nanostructures with localized plasmonic resonance can be fabricated. Panel II presents the fabricated plasmonic Au dimer with a gap size of 3 nm, where the corresponding EELS map shows the plasmonic mode pattern in high resolution.<sup>102</sup> Panel III shows the direct patterning of self-aligned metallic nanostructures with two different metals, such as Au and Ti, on top and bottom sides of the thin Si<sub>3</sub>N<sub>4</sub> membrane.<sup>127</sup> Panel IV presents the fabrication of hard mask for dry

Figure 1. continued

etching, via positive resist with liftoff process. Adapted with permission from ref 102. Copyright 2013 ACS. Adapted with permission from ref 127. Copyright 2014 IOP Publishing. (c) Fabrication of nanophotonic cavities via the negative resist, such as HSQ, with the dry etching process. The typical photonic materials, such as silicon, TiO<sub>2</sub>, GaN, are grown or deposited onto the designed substrate. Panel II shows that this approach is able to fabricate silicon nanostructures with 5 nm gap size for interband plasmonics at ultraviolet (UV) regime.<sup>112</sup> Panel III presents the fabricated silicon nanostructures with dielectric Mie resonance in the visible regime for the full color palette with the high color saturation.<sup>113</sup> Panel IV presents the fabrication process to pattern the hard mask via negative resist via dry etching and subsequently to the photonic materials. Adapted with permission from ref 112. Copyright 2019 ACS Publication. Adapted with permission from ref 113. Copyright 2017 ACS. (d) Fabrication of nanophotonic cavities via the negative resist, such as HSQ, with the liftoff process to fabricate the nanoscale trenches. The fabricated Au nanotrenches have gaps down to 5 nm to show the strong localized plasmon resonance.<sup>121</sup> Adapted with permission from ref 121. Copyright 2011 ACS. (e) Hybrid nanofabrication method via combining top-down lithography and directed self-assembly process to fabricate sub-5 nm gaps. Via dip coating 8 nm Au nanoparticles (AuNPs) with the oleylamine ligand in hexane solvent<sup>123</sup> onto the template stripped Au nanotrenches, 2 nm double gaps can be fabricated in a reliable manner as shown in Panel I.<sup>124</sup> In addition, Panel II shows that this approach is able to deposit the functional materials onto it, such as upconversion nanoparticles.<sup>126</sup> Adapted with permission from ref 123. Copyright 2012 ACS Publication. Adapted with permission from ref 124. Copyright 2015 ACS Publication. Adapted with permission from ref 126. Copyright 2021 ACS.

raphy, chemical vapor deposition (CVD), and focused ion beam (FIB). Currently, thanks to cutting-edge nanofabrication, a variety of nanostructures can be realized and utilized across numerous fields.

One of the examples is nanophotonics.<sup>6–10</sup> By controlling geometrical parameters or types of materials such as metals,<sup>11–17</sup> dielectrics,<sup>18–21</sup> and polymers,<sup>22–25</sup> fundamental optical properties like surface plasmon polariton,<sup>26,27</sup> phase delay,<sup>28</sup> and resonance<sup>29–32</sup> can be manipulated. As a result of light-matter interaction, applications like metalens,<sup>33–37</sup> metahologram,<sup>38–49</sup> and color filters<sup>50–56</sup> can be realized. Hence, nanofabrication stands as an essential tool in the field of nanophotonics, facilitating the translation of theoretical designs into practical applications. Furthermore, nanofabrication offers potential applications in diverse fields such as electronics,<sup>57,58</sup> biosciences,<sup>59–63</sup> and beyond. As nanofabrication can enrich our lives in various fields, the development of nanofabrication is necessary. For example, in nanophotonics, by increasing the resolution and geometric flexibility through the advancement of nanofabrication, nanostructures can be controlled in units of several nanometers. This allows us to precisely control the optical properties of the device. As a result, the optimized free-form structure can be controlled freely. This can improve the performance of the device and produce compact devices, which play an important role in promoting research and application in nanophotonics. Therefore, nanofabrication is indispensable in the development of nanophotonics.<sup>64–67</sup>

Thus far, in terms of resolution, high-resolution patterning has been achieved using ArF immersion lithography,<sup>68</sup> which combines a 193 nm wavelength light source with liquid immersion, and electron beam lithography (EBL)<sup>69,70</sup> employing extremely high-resolution electron beams. In terms of scalability, large-area nanopatterns have been realized through nanoimprint lithography (NIL),<sup>71–73</sup> which utilizes soft molds to transfer nanopatterns, and colloidal lithography,<sup>74–76</sup> which arranges hexagonally closed-packed nanostructures based on self-assembly. In addition, it has become possible to create complex shapes through direct laser writing,<sup>77,78</sup> which produces complex shapes using photoresponsive materials and lasers, or aerosol jets,<sup>79,80</sup> which produces three-dimensional (3D) metal nanostructures using prepatterned substrates. By combining the characteristics of advanced nanofabrication, it is possible to overcome existing limitations by combining the high resolution of EBL and the low-cost and high throughput of NIL.<sup>81,82</sup> As in the previous examples,

nanofabrication is being developed to increase resolution, scalability and realizing complex structures while overcoming existing challenges. However, the desire for a higher level of performance still requires defect-free finer patterns or more complex 3D structures. Also, there are numerous issues to be solved such as scalability, price, and complementary metal-oxide semiconductor (CMOS) compatibility for commercialization in the growing nano market. The goal of this mega-review is to highlight various nanofabrication that go beyond existing limitations in fabricating nanophotonics applications. Furthermore, insights can be gained from the perspective of nanofabrication to advance the future.

Herein, we will introduce trends and applications of nanofabrication. This mega-review first focuses on high-resolution nanolithography (Sections 2–6, 17–19). Then, we will continue with nanofabrication which specializes in 3D complex shapes (Sections 7–12, 20–23) and scalability (Sections 13–16, 24–29). Finally, we will describe an overview and applications in terms of compatible materials (Sections 30–32).

## 2. HIGH-RESOLUTION ELECTRON BEAM LITHOGRAPHY

Zhaogang Dong and Joel K. W. Yang

High-resolution electron-beam lithography provides a versatile and rapid prototyping approach to fabricate the designed optical cavities in nanophotonics. Due to its ability to pattern fine details down to few nanometer dimensions, one can produce photonic structures with varying geometries corresponding to a myriad of resonant structures, such as localized plasmon resonances,<sup>83</sup> dielectric Mie resonances,<sup>84</sup> anapole,<sup>85</sup> toroidal resonances,<sup>86,87</sup> Fano resonances,<sup>88</sup> and bound-states-in-the-continuum (BIC).<sup>89–91</sup>

In electron-beam lithography, a focused beam of electrons acts as the tip of a “pen” and is electrostatically deflected by computer control to write patterns in the form of chemical changes in a suitable resist material. As the electrons are accelerated to 10s or ~100 kV under high vacuum conditions, their effective wavelengths are orders of magnitude smaller than the photons used in photolithography. Hence, the sub-10 nm resolution limit in electron-beam lithography is limited by aberrations of the electron optics, Coulombic repulsion of electrons, and electron scattering in the resist, instead of the wave-nature diffraction limit of the electron.

Figure 1a presents the research efforts toward pushing the ultimate fabrication limit, where the focused electron beam size

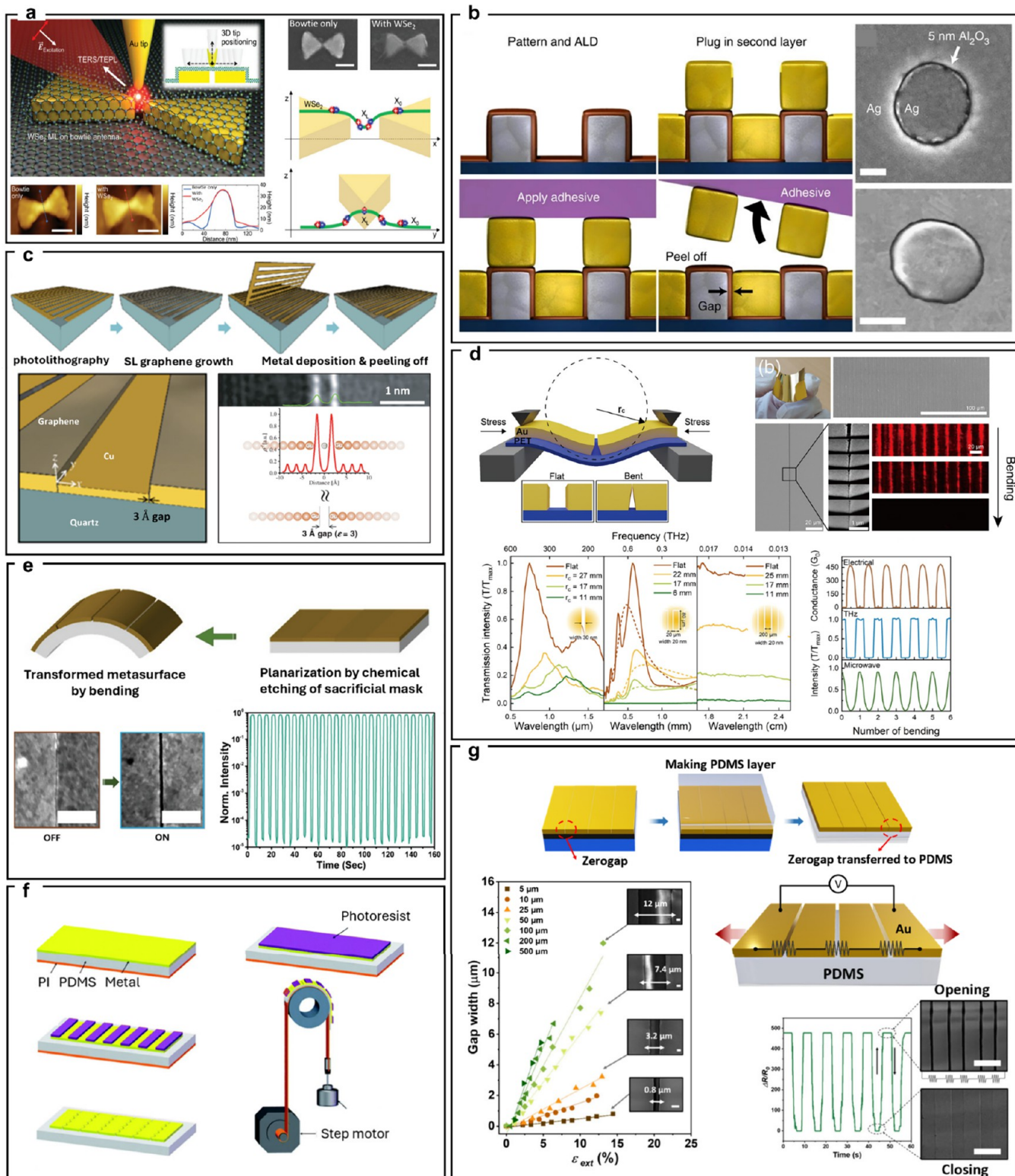


**Figure 2. Nanogap lithography.** (a) Triple-sharp-tips structure for local excitation of excitons of the WSe<sub>2</sub>ML. AFM and SEM images of the bowtie nanoantenna and schematic of the sharply curved WSe<sub>2</sub> crystal at the nanogap.<sup>129</sup> Adapted with permission from ref 129. Copyright 2014 Wiley-VCH. (b) Fabrication process and SEM image of nanogap with atomic layer lithography.<sup>130</sup> Adapted with permission from ref 130. Copyright 2014 Wiley-VCH. (c) Schematic representation of the fabrication of vertically aligned graphene spacers in a Cu-SLG-Cu composite material and TEM cross-sectional image of two van der Waals gaps. The red curve shows the inverse charge density of the valence electrons.<sup>143</sup> Adapted with permission from ref 143. Copyright 2015 American Physical Society. (d) Schematic and SEM images of the closing mechanism of nano trenches, transmission intensities for various bending radii measured in the visible-NIR, terahertz and microwave range and modulation of the electrical conductivity.<sup>151</sup> Adapted with permission from ref 151. Copyright 2021 ACS. (e) Schematic description of the bending of a "Zerogap", and SEM image of the cycle of "OFF" and "ON" states.<sup>132</sup> Adapted with permission from ref 132. Copyright 2021 Wiley-VCH. (f) Photolithographically supported nano crack pattern process.<sup>152</sup> Adapted with permission from

Figure 2. continued

ref 152. Copyright 2021 Royal Society Chemistry. (g) schematic representation of the transfer of the 'Zerogap' to the flexible substrate and SEM data of the gap width as a function of the external strain for different periodicities, with opening and closing cycles.<sup>153</sup> Adapted with permission from ref 153. Copyright 2024 ACS.

can be pushed down to 0.15 nm via aberration correction by electron optics in a scanning transmission electron microscope (STEM) setup with an acceleration voltage of 200 keV.<sup>92</sup> The actual resolution in the patterned resist is determined by several factors, such as beam diameter, primary/secondary electron scattering (see Panel I for illustration), Coulombic repulsion in the electron path and the use of high contrast resist development processes, e.g., NaOH/NaCl salty developer for hydrogen silsesquioxane (HSQ) resist<sup>93</sup> and cold developer for PMMA resist.<sup>94</sup> As a result, the actual patterned resist resolution is larger than the electron beam size. For instance, Panel II (black line) presents the point spread function (PSF) of the exposure dosage with respect to radius, and Panel III shows the minimum feature size of 2.1 nm when the HSQ resist is developed with the salty solution (1% weight NaOH + 4% weight NaCl).<sup>92</sup>

For the research work in the field of fabricating nanophotonic cavities, there are four major approaches. The first approach is to pattern the positive resist, such as poly(methyl methacrylate) (PMMA) or ZEP, with the liftoff process. After the development process, the resist region being exposed by electron beams will be washed away. After that, it is followed by the material evaporation and liftoff process, where metallic nanostructures with localized plasmonic resonance<sup>95–100</sup> or dielectric nanoantennas (e.g., TiO<sub>2</sub>) with Mie resonance<sup>101</sup> can be fabricated. Panel II in Figure 1b presents the fabricated plasmonic Au dimer with a gap size of 3 nm on a thin SiN<sub>x</sub> membrane, where the corresponding electron energy loss spectroscopy (EELS) map shows the plasmonic mode pattern in high resolution.<sup>102</sup> Moreover, Panel III in Figure 1b shows the direct patterning of self-aligned metallic nanostructures with two different metals, such as Au and Ti, on the two sides of the thin Si<sub>3</sub>N<sub>4</sub> membrane. In addition, Panel IV shows that this liftoff approach can be used to pattern the hard masks (e.g., Cr and Pd), for etching the photonic materials. This approach can be used to fabricate phase change optical nanoantennas for the tunable color pixels,<sup>103</sup> and hybrid on-chip optical nanoantennas.<sup>104</sup>

The second major lithography approach is to fabricate nanophotonic cavities via the negative resist, such as HSQ, with the dry etching process. The photonic materials, such as silicon,<sup>105,106</sup> TiO<sub>2</sub>, GaN,<sup>107</sup> Si<sub>3</sub>N<sub>4</sub>,<sup>108</sup> diamond,<sup>109</sup> or phase change materials (e.g., antimony sulfide,<sup>103,110</sup> germanium–antimony–tellurium<sup>111</sup>), are grown or deposited onto the designed substrates. Panel II in Figure 1c shows that silicon nanostructures with 5 nm gap size can be fabricated for investigating interband plasmonics at ultraviolet (UV) regime, where the hot spot at the nanogap region is shown by the simulation results.<sup>112</sup> In addition, Panel III in Figure 1c presents that patterning silicon nanostructures with dielectric Mie resonance in the visible regime is able to show the full color palette with the high color saturation.<sup>113</sup> In fact, this approach is extremely widely used in the patterning of dielectric metasurface nanocavities for various applications, such as metalens,<sup>114</sup> miniaturized spectrometers,<sup>115</sup> metasurface holograms,<sup>105,106</sup> near-/mid-infrared detectors,<sup>116</sup> Rashba photonic crystal cavity,<sup>117</sup> optical nanoantennas for fluores-

cence enhancements,<sup>118,119</sup> and tunable color pixels.<sup>120</sup> Moreover, as illustrated in Panel IV, for some photonic materials, we need to pattern the hard masks first based on the negative resist.

The third major lithography approach is to fabricate nanophotonic cavities via the negative resist, such as HSQ, with the sonication liftoff process to fabricate the nanoscale trenches as illustrated in Figure 1d. The SEM images present the fabricated Au nanotrenches with gaps down to 5 nm to show the strong localized plasmon resonance.<sup>121</sup> Since hydrogen fluoride (HF) acid is normally used to etch away HSQ, sonication in HF solution imposes the potential experiment danger. One improved way is to spin coat the positive PMMA resist first and followed by the negative HSQ resist, which is then used as a mask to etch PMMA with inductive coupled plasma (ICP) based on O<sub>2</sub> gas.<sup>122</sup> After that, the metal layer could be then evaporated onto the sample and followed with a lift off process in the organic N-Methyl-2-pyrrolidone (NMP) solvent.<sup>122</sup>

The fourth category lies in the hybrid nanofabrication method via combining top-down lithography and directed self-assembly process<sup>123</sup> to fabricate sub-5 nm gaps, as shown in Figure 1e. Panel I shows that via dip coating 8 nm Au nanoparticles (AuNPs) with the oleylamine ligand in hexane solvent onto the template stripped Au nanotrenches, 2 nm double gaps can be fabricated in a reliable manner.<sup>124</sup> This approach is also used to achieve the nanoparticle fusing with sub-1 nm gaps.<sup>125</sup> Moreover, this hybrid approach is also can be used to deposit functional materials onto the optical nanoantennas onto it, such as upconversion nanoparticles.<sup>126</sup>

### 3. NANOGAP LITHOGRAPHY

Mahsa Haddadi Moghaddam and Dai-Sik Kim

Inevitably, the development of nanophotonics has parallel advances in nanofabrication techniques. Leading lithography methods, including extreme-UV (EUV) photolithography, EBL and FIB, achieve impressive resolutions of 3–5 nm.<sup>102,128</sup> In these techniques, energetic particles are used to change the material properties of a PR or to etch the target material directly. However, a significant drawback of these techniques is their high cost combined with their limited ability to create patterns smaller than 10 nm across the entire wafer, a critical requirement for modern semiconductor manufacturing. As the demand for smaller and more intricate patterns increases in various technological applications, there is an urgent need for more cost-effective and scalable nanofabrication methods to meet these requirements.

Here, we provide an overview of established methods to fabricate gaps below 10 nm and explore different strategies to push the boundaries into the subto-zero nanometer range. Conventional techniques such as tip-based,<sup>129</sup> atomic layer lithography,<sup>130</sup> break junctions,<sup>131</sup> as well as crack lithography<sup>132–134</sup> are discussed, with a focus on spacer-based methods that enable vertically aligned metal–insulator–metal (MIM) structures. These techniques enable creation of in-plane MIM configurations with gap widths as small as 0.3 nm,

while cracks and break junctions provide routes to reach the zero-nanometer threshold.

A tip-based approach, using feedback control between the tip probe and the substrate surface, provides exceptional precision in the fabrication of sub- to zero-nanometer metallic voids. This technique utilizes the lightning rod effect, which concentrates free charges into the sharp probe tip when it is aligned with incident electromagnetic waves (Figure 2a).<sup>129</sup> The capacitance gap enhances the localization of the electric field intensity by funneling the electric field into the gap.<sup>135</sup> Various geometries such as blunt metal-coated probes,<sup>136</sup> probes that mimic a split-ring resonator,<sup>136</sup> and probes attached to gold particles<sup>137</sup> have been shown to be effective. Feedback mechanisms regulate the gap distances in atomic force microscopy (AFM) and scanning tunneling microscopy (STM). STM makes it possible to measure the tunnel current depending on the slit distance, which allows control in the range of a few tens of picometers. AFM, on the other hand, relies on the deflection of light from the cantilever to measure distance and offers versatility for samples with larger height differences and operates under ambient conditions. However, the tip-based approach, which requires careful attention and out-of-plane-oriented point gaps is impractical for mass production and device applications.

Thanks to advances in fabrication techniques, it is now possible to produce lithographically predetermined few nanometer gaps using dielectric spacers. In these spacer-based methods, this dielectric prevents unintentional connection between metallic layers, facilitating the fabrication of gaps over a large area with high throughput. Precise control of dielectric layer deposition with an accuracy of ~1 nm enables careful adjustment of the gap width. Chen and Park et al. have shown that it is possible to create in-plane stacked MIM gap structures using atomic layer deposition (ALD) for gap-filling dielectric deposition, achieving isotropic layer deposition with an accuracy of ~1 nm (Figure 2b).<sup>130</sup> In atomic layer lithography, a desired metallic structure is initially patterned through electron beam lithography or standard photolithography. The entire wafer is then coated with aluminum oxide by ALD, which also encloses the sidewalls of the original metal pattern. A second layer of metal is then deposited, forming a metal–insulator–metal gap aligned vertically on the side wall. To expose the gaps, the excess metal is removed using a peeling process. The shape and size of the gap is determined by the circumference of the first metallic pattern and thickness of the spacer, respectively, so that practically unlimited metallic gaps from a few tens to one nanometer and different operating wavelengths from the visible range<sup>138</sup> to IR, terahertz<sup>139–141</sup> and microwaves<sup>142</sup> can be achieved. Variations of this method, in which ALD is replaced by other coating processes, such as the use of CVD make it possible to achieve ultimate gap widths, even down to a thickness of just one atom (0.3 nm) using graphene as a spacer (Ångstrom Lithography, Figure 2c).<sup>143</sup> Terahertz waves through these high aspect ratio gaps, achieving a remarkable 97% reduction in transmission, enabled tunneling electrons in the van der Waals gaps. This promotes an improved interplay between classical optics and quantum tunneling. Other planarization techniques for this method include chemical etching of a sacrificial layer,<sup>71</sup> ion milling,<sup>144</sup> self-assembled monolayers (SAM)<sup>145</sup>, and more.

Despite their precision, in the case of metal gaps with spacers, there is a restriction that the dielectric spacers occupy the “hot spot”, i.e., the area with the strongest amplification of

the electromagnetic field, which hinders efficient coupling with target systems. Tripathi et al. solved this problem by using the target material itself as a spacer,<sup>146</sup> while Jeong et al. demonstrated a method to effectively reach the hotspots in spacer-based nanogaps with a high width-to-height aspect ratio by wet etching the dielectric. Liquid water or similar molecules can efficiently couple within 10 nm wide metallic trenches, which is achieved by etching and dilution processes.<sup>147</sup> Notably, these gaps can be further reduced by utilizing the thermal modulation inherent in the metallic nanostructure. This provides an additional opportunity to improve the functionality of nanostructures, as the thermal expansion of metals can be used for the controlled modulation of a nano-optical device.<sup>148</sup> These techniques offer versatile options for creating precise metallic gaps for applications in different wavelength ranges, from terahertz to microwaves.

Creating nanogaps from “zero nanometers”, rather than shrinking them from a few nanometers, allows the formation of junctions to be observed in real time, as indicated by jumps in resistance across the wire. In the method of mechanically controllable break junctions (MCBJs), the structure is bent to elongate the metal wire, allowing sub-Ångstrom precision in gap control.<sup>148</sup> MCBJ-based bowtie antennas by Liable et al.<sup>149</sup> and plasmonic nanogap structures by Ward et al.<sup>150</sup> demonstrate precise monitoring and control of gaps with applications in photon-induced tunneling, optical rectification, and surface-enhanced Raman spectroscopy (SERS). While MCBJs are effective for point gaps, due to the randomness of the gaps, they are less suitable for extended structures such as slits or slot antennas, which are crucial for the study of light-matter interactions and optical applications.

In a study by Nam et al. the generation of patternable nanoholes by controlled cracking in a stress-controlled silicon nitride layer was demonstrated.<sup>134</sup> This technique was extended to a thin, top-coated metal film, where the authors successfully produced a 10 nm wide slot over on a 15 nm thick titanium film.<sup>25</sup> In a subsequent study, Dubois et al. embedded a prestressed bridge of titanium nitride under a gold pattern and induced a localized crack by detaching the bridge structure.<sup>26</sup> A disadvantage of these methods is that, despite achieving gap widths of less than 3 nm, which are applicable at the wafer level, the cracks formed are irreversible and prevent a return to the “zero nanometer” limit. An innovative approach to overcome the above limitations is to fabricate metal gaps on a flexible substrate that allows the reduction or “healing” of the gap. Kim et al. defined the gap by depositing a spacer using ALD on a polyethylene terephthalate (PET) substrate and then wet etching the dielectric filling the gap (Figure 2d).<sup>151</sup> This “healable gap” can be fabricated on the wafer scale without significant restrictions on gap size. The internal bending of the substrate causes the gaps to close, narrowing from 20 to 0 nm. This triggers an instant topological transformation due to the partial contact between the two metallic layers, leading to an abrupt change in metamaterial functions, including resonance, chirality, and polarization selectivity, especially at terahertz and microwave frequencies.

Das et al. used a different philosophy, using lithographically defined, sequential deposition of metal films *without spacers*, allowing zero nanometer gaps or “Zerogaps”, and gradually increasing it to several hundred nanometers by external bending (Figure 2e).<sup>132</sup> This property leads to a remarkably high modulation depth between the “OFF” and “ON” states of the transmitted microwaves, which is related to the minimum

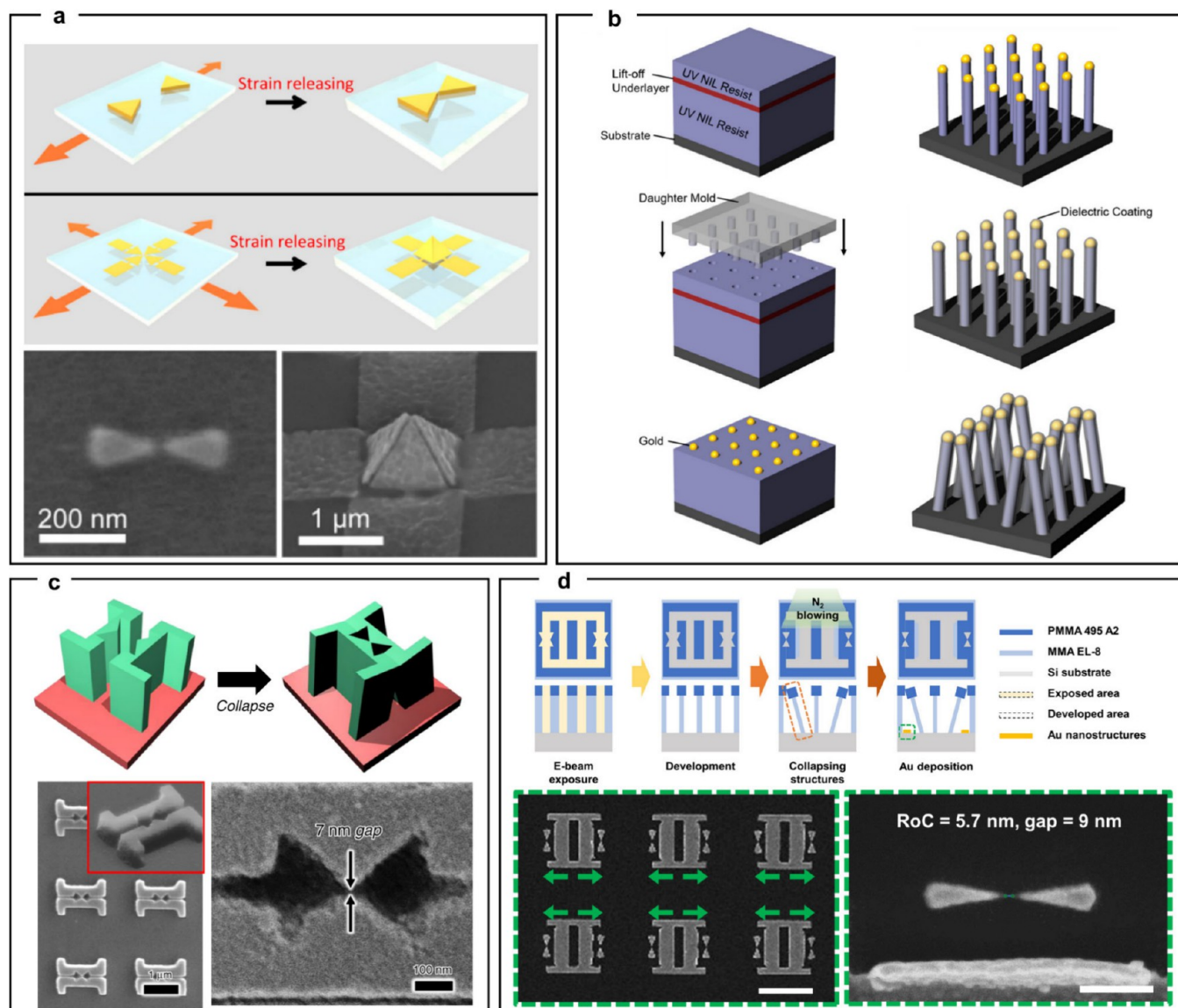


**Figure 3. Mechanical-force-assisted electron-beam lithography.** (a) Schematic of plasmonic nanostructures with subnm nanogaps and the 3-dimensional kirigami fabrication on prestrained elastomer and respective SEM images.<sup>157</sup> Adapted with permission from ref 157. Copyright 2019 ACS. (b) Schematic of collapsing nanofingers using nanoimprint lithography (NIL) and atomic layer deposition (ALD).<sup>160</sup> Adapted with permission from ref 160. Copyright 2017 Wiley-VCH. (c) Schematic of capillary-force-induced collapse lithography and SEM images of bowtie-shape plasmonic structures with 7 nm gap.<sup>161</sup> Adapted with permission under a Creative Common CC BY License from ref 161. Copyright 2020 Springer Nature. (d) Schematics and SEM images of cascaded domino lithography and guided domino lithography.<sup>163</sup> Adapted with permission under a Creative Common CC BY License from ref 163. Copyright 2014 De-Gruyter.

and maximum gap width, respectively, even after numerous cycles of repeated modulations. Liu et al. used a photo-lithography-assisted method to generate nanocracks in a thin metal film on a flexible substrate (Figure 2f).<sup>152</sup> Careful bending was used to selectively form cracks in areas where there was no PR. The result was an array of long metallic slits that can be replicated multiple times to create additional gaps (pattern-and-pool method). Haddadi et al. present a novel stretchable crack-based sensor, which has 3–5 nm wide gaps lithographically arranged along periodic lines (Figure 2g).<sup>153</sup> By transferring “Zerogap” samples to polydimethylsiloxane (PDMS), they achieved versatility in strain sensing with customizable periodicities of the gaps. Under external strain, the gaps widen, leading to increased electrical resistance without the need for conventional cracking processes. The

sensor shows a linear correlation between the periodicity and the gap widening under external strain. Microwave spectroscopy on the sample reveals strain-dependent gap behavior as evidenced by the sensitivity of the transmission spectra, which is consistent with the gap width over different periodicities at 15 GHz. This review provided a comprehensive overview of the types and properties of sub-10 nm metal gaps, including spacer-based gaps, cracks, fractures, tip-based gaps, and Zerogaps, considering the minimum achievable gap widths and the feasibility of large-scale fabrication.

These advanced nanofabrication techniques have the potential to revolutionize the industry by enabling ultrafast quantum tunneling devices on wafer scale for the next generation processors, nanophotonic sensors for health monitoring, wearable medical sensors for real-time health

monitoring, and hyper-realistic and energy-efficient screens beyond OLED or microLED. Additionally, controlling terahertz waves could enable faster wireless communication and energy harvesting devices, powering small electronic devices indefinitely. Even though much of the work is still taking place in laboratories, these innovations could soon transform various sectors.

#### 4. MECHANICAL-FORCE-ASSISTED ELECTRON-BEAM LITHOGRAPHY

Dong Kyo Oh, Jihae Lee, and Junsuk Rho

EBL has been widely used to realize plasmonic nanoantennas because of its sub-10 nm resolution, but the resolution is limited by the proximity effect of the electron beam.<sup>102,154</sup> To realize single-digit-nanometer resolution of nanostructures, numerous methods have been introduced such as geometrical design correction and electrical or thermal modulation, which still demand labor and external sources.<sup>155,156</sup> In this section, we focus on mechanically driven techniques with the EBL process for the more manageable extreme resolution under sub-10 nm of nanostructures.

The mechanical strain of an elastomer substrate has achieved sub-10 nm resolution nanostructures.<sup>157</sup> After transferring Au bowtie nanostructures on a prestrain PDMS substrate, the nanogap size between bowtie nanostructures can be narrowed by releasing the restrained PDMS substrate (Figure 3a). Moreover, the prestrain degree of the PDMS substrate can tune final nanogap sizes after releasing it, which proposes mechanically variable nanogaps of bowtie nanoantennas. While the initial nanogap size of bowtie nanostructures is 108 nm, a final nanogap size can of 5 nm under the condition of 60% prestrained PDMS substrate can be achieved. As the nanogap size is modulated by strain, peak wavelengths also change from 927 nm at prestrain of 0% to 810 nm at prestrain of 60%. Additionally, 3-dimensional nanostructures also can be produced by restoring 2-dimensional Au nanostructures on the prestrained PDMS substrate, like nanokirigami, which is unable to be produced by conventional nanofabrication. On the other hand, the strain can be directly used to control nanogaps in real time.<sup>158</sup> By using the deformation of the PDMS, which means compression occurs in the orthogonal direction as the strain is applied in one direction from volumetric statics, the nanogap can be increased or decreased on the PDMS substrate. By stretching the PDMS by 25%, the initial nanogap size is also reduced by 25%, which achieves a single-digit nanogap.

Furthermore, achieving extreme resolution has been made possible through the collapse of nanostructures. Using the unstable equilibrium of nanostructures with a high-aspect-ratio such as nanowires, precise collapse of the nanostructures by external force has been derived.<sup>159</sup> After fabricating a Si nanofinger master mold with 70 nm diameter and 650 nm height by EBL and an etching process, polymer nanofingers are transferred by UV NIL as-is. Following a uniform deposition of 1 nm-thick tetrahedral amorphous carbon (ta-C) on the surface of nanofingers with 50 nm-thick Ag caps, the high-aspect-ratio nanofingers collapse toward adjacent nanofingers via capillary force due to a solvent drying process to form a couple of nanofingers, which causes a uniform and large-area fabrication of 2 nm nanogap plasmonic structures. The nanofingers with extremely narrow nanogaps have shown increased scattering intensity compared with nanofingers without gaps and with silica coatings. In addition, the gap

plasmonic nanofingers have also been applied to enhancing the SERS signal at 532 nm wavelength excitation, which enables single-molecule label-free SERS detection. Moreover, by varying coating materials, the plasmonic properties of nanofingers are tailored<sup>160</sup> (Figure 3b). After the fabrication of 60 nm diameter and 350 nm height nanofingers with Au nanocaps, the ALD process of various dielectric materials such as TiO<sub>2</sub>, WO<sub>3</sub>, and SiO<sub>2</sub> has been applied to the nanofingers. By controlling the thicknesses and refractive indices of coating materials, positions of absorption peaks have been changed from 530 to 680 nm, respectively.

Capillary-force-induced collapse lithography (CCL) is another method for producing sub-10 nm gaps by collapsing nanostructures with capillary force.<sup>161</sup> As shown in Figure 3c, electron beam PR nanopillars fabricated by EBL are collapsed, producing sub-10 nm gaps. CCL utilizes both the cohesion and collapse effect to control the precise collapse. The cohesion process between adjacent nanopillars is induced by the capillary force, while the collapse process is mainly controlled by geometries of nanopillars. The CCL process is conducted by experimentally adjusting the development time, electron beam dose, and geometries of nanopillars. When two opposing nanopillars patterned with half of the bowtie-shape collapse, a whole bowtie-shape is fabricated. For efficient collapse, supporting nanostructures are positioned behind the nanopillars. A 10 nm-thick Au film is deposited on the collapsed PR nanopillars to realize plasmonic sub-10 nm structures, where the electric field is localized by plasmonic effects. Various plasmonic structures such as bowtie- and flower-shapes with sub-10 nm gaps are fabricated through the CCL method.

While sub-10 nm gaps can be fabricated using previous methods, realizing sharp tips with a sub-nm radius of curvature (ROC) has been challenging due to the proximity effect of EBL. Cascade domino lithography (CDL) has been proposed to simultaneously produce sub-10 nm gaps and sharp tips.<sup>162</sup> CDL involves the collapse of PR nanostructures resembling dominos, leading to a sharp edge. A bilayer PR consisting of PMMA and methyl methacrylate (MMA) with different solubilities is utilized to make unstable T-shape nanostructures through overdevelopment. T-shaped nanostructures have surface tension between the PR and substrate due to the inevitably remaining liquids such as developer and rinse liquids. The isolated T-shaped nanostructure falls against the adjacent wall when the nitrogen gas is blown directly. A sharp edge is produced as the structure collapses. Additionally, T-shape nanostructures with an asymmetric rectangle enable precise directional control for collapsing. Through the process, subnm ROC and single-digit nanogap arrays are experimentally produced. The electric field is strongly concentrated at hotspots of sharp tip bowtie nanoantennas fabricated by CDL, which makes them valuable for research in SERS<sup>162</sup> and the localized exciton of 2-dimensional transition dichalcogenides.<sup>129</sup>

Furthermore, the advanced method, guided domino lithography (GDL), has been suggested to control the collapsing direction of CDL.<sup>163</sup> Through the GDL process, nanostructures collapse in both directions, producing uniform arrays of sharp tip nanoantennas (Figure 3d). Similar to CDL, a bilayer PR composed of PMMA and MMA is developed to make T-shaped nanostructures. However, slightly different shaped nanostructures are used to control the collapsing direction. While CDL allows T-shape nanostructures to collapse randomly to the right or left, the modified

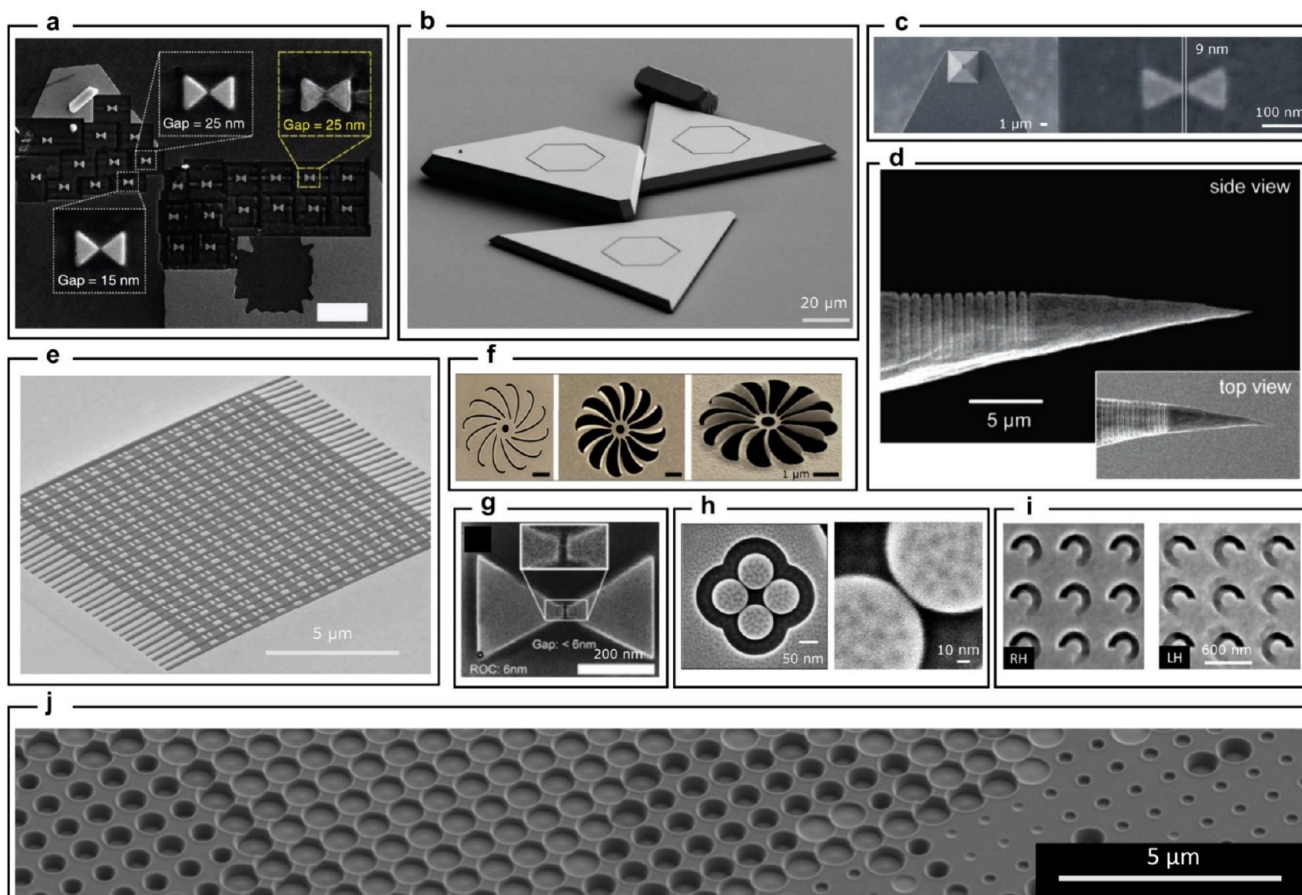


**Figure 4.** FIB structuring in nanophotonic and plasmonic systems (for details see main text). (a) Bowtie nanoantennas milled from single-crystalline gold platelets and an evaporated gold film.<sup>171</sup> Adapted with permission from ref 171. Copyright 2010 Springer Nature. (b) Grooves milled into single-crystalline gold platelets.<sup>172</sup> Adapted with permission from ref 172. Copyright 2020 AAAS. (c) A gold bowtie antenna fabricated on the tip of an AFM probe.<sup>173</sup> Adapted with permission from ref 173. Copyright 2015 Wiley-VCH. (d) Gold nanotip with FIB-structured grating.<sup>175</sup> Adapted with permission from ref 175. Copyright 2007 ACS. (e) Plasmonic nanostructures fabricated on a TEM membrane.<sup>181</sup> Adapted with permission under a Creative Common CC BY License from ref 181. Copyright 2023 Springer Nature. (f) Nanokirigami made by FIB structuring of a gold-plated TEM membrane.<sup>182</sup> Adapted with permission from ref 182. Copyright 2018 AAAS. (g) Gold bowtie antenna structured with helium ions.<sup>186</sup> Adapted with permission from ref 186. Copyright 2014 ACS. (h) Plasmonic tetramer structured into a gold flake with helium ions.<sup>187</sup> Adapted with permission under a Creative Common CC BY License from ref 187. Copyright 2021 Beilstein Institut. (i) Nanocrescents with varying depth.<sup>189</sup> Adapted with permission from ref 189. Copyright 2019 ACS. (j) So-called Mie voids of varying diameter and depth structured with FIB into silicon.<sup>190</sup> Adapted with permission under a Creative Common CC BY License from ref 190. Copyright 2023 Springer Nature.

nanostructures of GDL collapse bidirectionally within one array. Subsequently, a 60 nm-thick layer of Au is deposited and two plasmonic sharp tip bowties are fabricated. GDL increases the total exposed area of unit nanostructures under the same dose condition, resulting in more unstable T-shaped nanostructures. Thus, uniform nanoantenna arrays can be fabricated by collapsing them with a slight blowing of nitrogen gas. GDL allows for achieving bowtie arrays having sub-10 nm gaps and subnm ROC with high yields.

## 5. HIGH-RESOLUTION FOCUSED ION BEAM

*Mario Hentschel and Harald Giessen*

Ion beam lithography has been established as an important addition to the nanofabrication toolkit, while originally mainly used in sample preparation for transmission electron microscopy (TEM).<sup>164,165</sup> Despite the apparent limitations in resolution and throughput, FIB-based techniques for nanophotonics have true benefits compared to traditional lithographic techniques, such as EBL. FIB can work on unusual

substrates, is resist-free and is an intrinsic gray scale technique. These features are so powerful that significant efforts have been invested in FIB techniques, from an instrumentation standpoint but also from the process-related viewpoint.<sup>166,167</sup> The first trend led to the development of novel FIB columns using heavier ions such as gold or noble gases such as helium, which have enabled higher milling rates and extremely high resolution, respectively.<sup>168</sup> Moreover, the resist-free process allows to structure, e.g., AFM tips and TEM membranes, as well as materials prone to contamination and degradation, which are not compatible with resist-based techniques. The intrinsic gray scale capabilities, simply related to the deposited dose or number of ions, even allows to structure surface topography and 2.5D shapes into materials of interest.

Figure 4 depicts examples from the literature, trying to give an impression of the different areas in which FIB techniques can make a real impact.<sup>167,169</sup> In plasmonics, chemically grown single-crystalline gold platelets have attracted considerable attention due to reduced internal and surface scattering,

making them ideal candidates for low-loss applications.<sup>170</sup> The limited size of the platelets as well as possible contamination of the surface by resists makes FIB the ideal structuring technique. Figure 4a shows so-called bowtie antennas fabricated from a single-crystalline platelet (left).<sup>171</sup> The milling results using the platelets as the starting material are of excellent quality, also demonstrated by superior optical properties in the experiment as well as the reference bowtie antennas which have been structured from an evaporated gold film (right). This easy mix-and-match of different materials on the same substrate is another added benefit of FIB techniques. In another experiment, the authors study the propagation and time dynamics of complex plasmonic skyrmions with the help of two-photon photoemission photoelectron electron microscopy (2PEE-PEEM).<sup>172</sup> In order to observe these dynamics, ultrasmooth gold surfaces are needed, as they are mostly only observed on single-crystalline gold platelets. For the excitation of the plasmonic surface waves, grooves are structured with FIB into these flakes. The direct FIB structuring approach prevents contamination of the surface which might be caused by a resist based process. Moreover, the authors used gold ions in the milling process (Raith Velion), which are now available as an alternative to gallium ions and thus preclude any possible gallium contamination of the gold platelets.

Another important application of FIB structuring lies with unusual substrates, for example, the tip of an AFM probe. Any resist based process will be extremely difficult if not impossible due to the extremely small “substrate” size. FIB is truly an enabling technology here. Figure 4c shows a gold bowtie antenna fabricated on an AFM probe via direct milling.<sup>173</sup> The structure quality is very high, reaching a gap size on the order of 10 nm, which is crucial for plasmonic near field enhancement. Such structures have proven to work well in single-emitter scanning near-field optical microscopy, observing locally enhanced photoluminescence.<sup>174</sup> A tapered gold tip can focus propagating surface plasmon waves at the tip apex and thus function as a nanoscale light source, as shown in panel d.<sup>175</sup> In order to excite the wave efficiently, a grating coupler is needed, which can be directly milled via FIB into the gold tip. In both cases the small surface area as well as the topography of the substrates are incompatible with standard resist-based processes, an issue that can be straightforwardly solved with FIB.

In many nanophotonic applications, TEM membranes are used as substrates for devices. The reasons can be multifold. In some cases, the fabricated devices will exhibit mechanical tuneability or deformability;<sup>176,177</sup> in other cases, a finite transmission for photons or electrons through the substrate is required. The challenge lies with the fragile membranes, often having thicknesses below 50 nm at sizes of hundreds of microns square. Resist-based lithography has been applied here, yet direct milling is a powerful alternative.<sup>178–180</sup> Figure 4e depicts a photonic metamaterial analogue of a continuous time crystal.<sup>181</sup> Here, plasmonic resonators are structured into a gold film evaporated onto a silicon nitride membrane. One key feature of the final device is its ability to deform, as the individual silicon nitride stripes cut from the continuous membrane can bend. Apart from the fragile membrane, the two different materials and in particular the required different milling depth into the silicon nitride make the structure incompatible with standard resist-based etching. Panel f shows another beautiful example of the power of FIB structuring.<sup>182</sup>

Here, the authors drew inspiration from kirigami, the art of paper folding. After evaporating a gold film onto a TEM membrane, outlines were cut using FIB. Afterward, a small but homogeneous ion dose applied on the entire structure causes strain in the film, deforming it. According to the cuts made, the structure will bend, resulting in a truly 3D shape—just as in paper kirigami. The authors could also demonstrate plasmonic properties of such structures, for example very strong circular dichroisms, resulting from the truly 3D structures.

As mentioned already, FIB instrumentation has developed significantly in recent years, leading to a steep increase in the number of available ion species.<sup>168</sup> To first order, lighter ions will result in the highest possible resolution. The development of gas sources has enabled, e.g., the milling with helium ions (Zeiss Orion NanoFab).<sup>183–185</sup> Figure 4g depicts a gold bowtie antenna structured with helium ions.<sup>186</sup> The shape fidelity is extremely high, edges show ROC of around 6 nm and gap sizes smaller than 6 nm, still maintaining large aspect ratio in thickness and width. While this technique has little throughput due to the small milling rates observed, the resolution is unparalleled. Panel h depicts another highest resolution structure. The plasmonic tetramer is milled with helium ions into a 40 nm thick gold flake, resulting in gaps below 5 nm between the individual elements.<sup>187</sup> The authors of this work also provide results of a combined ansatz in which standard gallium ion milling is used for the smaller resolution structures and helium ions for final sculpting and the definition of the highest resolution section. In all the cases, the correct milling strategy and the optimization of the process is key for the final result and is being implemented as the Python toolbox FIB-o-mat for automated pattern creation and optimization, providing full flexibility to accomplish demanding patterning tasks.

For some applications, the ability to structure with varying depth into the material of interest is crucial. Gray-scale processes based on RIE and EBL are being used, yet are notoriously difficult and cannot be easily adapted to every material class.<sup>188</sup> FIB intrinsically offers gray scale structuring due to its direct milling approach and is thus a great alternative fabrication route. One example shown in Figure 4i is related to chirality, which has attracted considerable attention in the nanophotonics community. As chirality is a truly 3D property, the structures need to be 3D, rendering them challenging for EBL, requiring multilayered exposures. Figure 4i depicts chiral crescent-shaped structures milled with FIB into a gold film.<sup>189</sup> A variation in dose over the circumference of the crescent allows to vary its depth, thus rendering it truly 3D. Consequently, the structures do exhibit strong circular dichroism. Panel j displays another structure utilizing elements of varying depth on the same substrate.<sup>190</sup> Voids in high-index dielectrics have been shown to support localized resonant modes, so-called Mie void modes. These Mie voids show brilliant and naturalistic colors, making them ideal for nanoscale color printing. As the spectral position of the resonances and thus the color depends on their diameter and depth, both parameters can be used for best color and saturation match. The SEM images depicts a section of a nanoscale color print with varying void size and depth, realized with direct FIB milling into silicon.

Overall, FIB nanostructuring offers intriguing additional possibilities and options compared to traditional resist based techniques, yet in many cases FIB cannot replace these. Electron-beam lithography, for example, offers very high

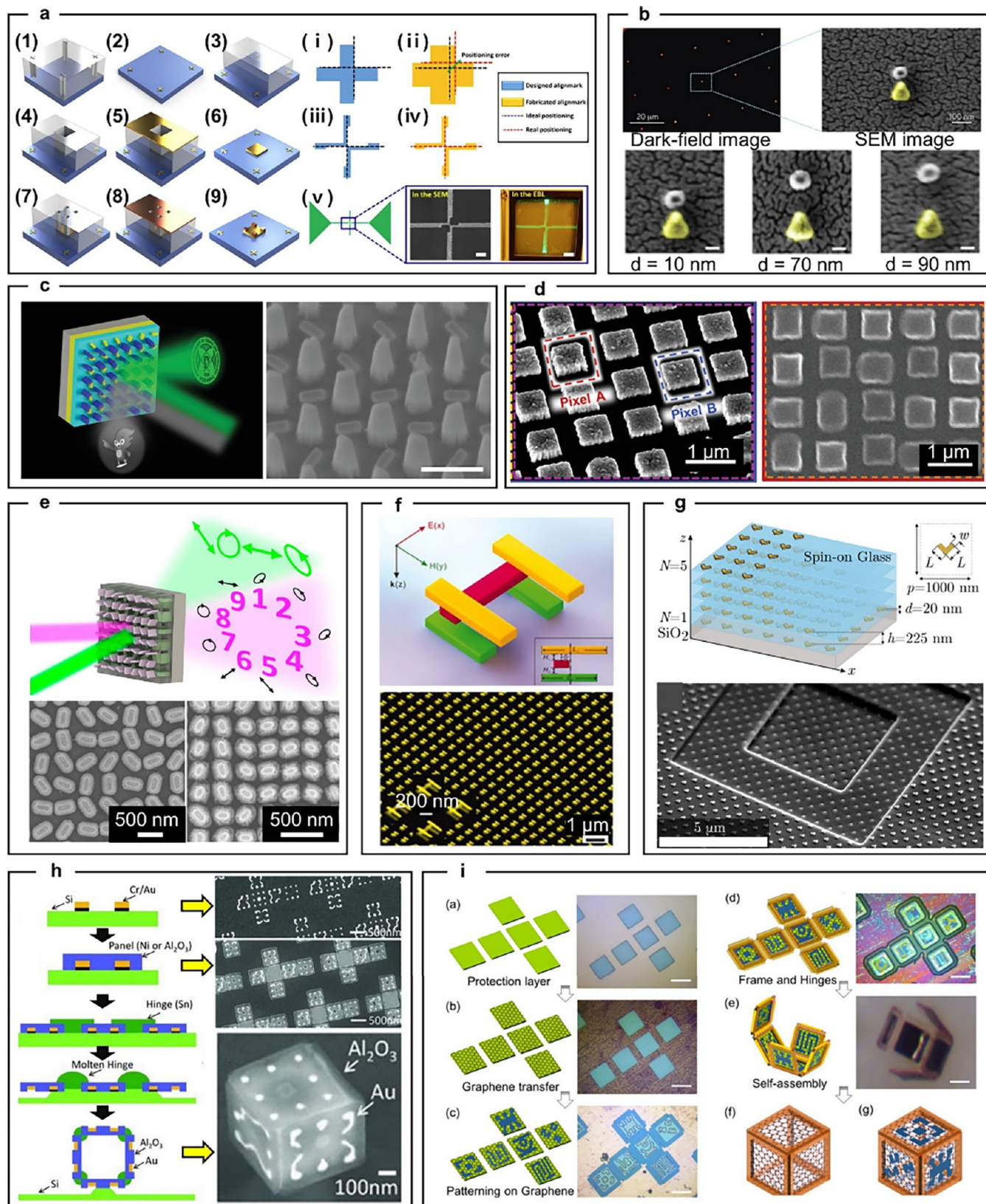


Figure 5. Layer-by-layer process with EBL. (a) The left image illustrates a flowchart delineating the optimized layer-by-layer EBL process aimed at achieving high alignment accuracy. On the right, blue color denotes designed marks, while yellow color signifies fabricated marks. This demonstrates that despite proximity effects, precise alignment is attainable. Below, the SEM image further elucidates this.<sup>204</sup> Adapted with permission under a Creative Common CC BY License from ref 204. Copyright 2017 Springer Nature. (b) The top image depicts a dark-field image of the aligned palladium nanoparticle and gold antenna, alongside an SEM image. The bottom image shows SEM images with gap variations ranging from 10 to 90 nm.<sup>205</sup> Adapted with permission from ref 205. Copyright 2011 Springer Nature. (c) The left image shows a schematic of a wavelength multiplexing metahologram in the visible and NIR, fabricated by layer-by-layer EBL. The right image displays an

Figure 5. continued

SEM image of the fabricated structure.<sup>207</sup> Adapted with permission from ref 207. Copyright 2021 Wiley-VCH. (d) The left image displays an SEM image of a 3D master mold, fabricated by layer-by-layer EBL. The right image shows an SEM image of replicated 3D nanopatterns.<sup>210</sup> Adapted with permission under a Creative Common CC BY License from ref 210. Copyright 2023 Wiley-VCH. (e) The top image shows a schematic of wavelength multiplexing metaholograms in the visible and UV region. The bottom images depict SEM images of the first layer and second layer, each optimized for the visible and UV regions, respectively.<sup>211</sup> Adapted with permission under a Creative Common CC BY License from ref 211. Copyright 2022 ACS. (f) The top images illustrate a schematic of a 3D plasmonic ruler, fabricated by layer-by-layer EBL. The bottom image shows an SEM image of the fabricated structure.<sup>212</sup> Adapted with permission from ref 212. Copyright 2011 AAAS. (g) The top image illustrates a schematic of proposed 5-layer stacked metasurfaces for backward phase-matched SHG. The bottom image shows an SEM image of the fabricated structure.<sup>213</sup> Adapted with permission from ref 213. Copyright 2014 American Physical Society. (h) Nanoscale self-folding of multilayered thin films through origami-inspired techniques, demonstrating the transformation of planar designs into optically active cubic structures via electron-beam lithography and plasma etching.<sup>215</sup> Adapted with permission from ref 215. Copyright 2011 Wiley-VCH. (i) Self-assembled 3D graphene-based polyhedrons illustrating volumetric light confinement achieved through plasmonic hybridization, leading to enhanced field localization and novel optical functionalities.<sup>216</sup> Adapted with permission from ref 216. Copyright 2019 ACS.

throughput, resolution, and reliability. If structures can be made with more standard lift-off or dry etching based techniques, optical or EBL is an excellent choice, also in terms of technology readiness. Many nanophotonic applications require true large area fabrication on the order of centimeter square, which at this point seem infeasible for FIB techniques. However, one should mention that smart ideas and combination of FIB-milling with electron-beam lithography can be very useful.<sup>191</sup> Also, further advances in instrumentation might push FIB to new working ranges.<sup>192</sup> Section 7 of this review discusses a sketch and peel approach in which FIB is used to define the outlines of structures, vastly improving fabrication speed.<sup>193</sup> Additionally, modern instrumentation allows to combine FIB with other techniques, such as overlay processes with EBL,<sup>194–196</sup> benefiting from the respective strength of the two techniques.

## 6. 3D NANOPHOTONICS WITH ELECTRON BEAM LITHOGRAPHY

Gyeongtae Kim, Dohyun Kang, and Junsuk Rho

EBL has been widely researched due to the growing demand for elaborate nanopatterning techniques, such as quantum emitters, photonic crystals, cavities, and antennas. Unlike commonly used sources in lithography such as argon fluoride (ArF) and krypton fluoride (KrF) lithography, which utilize UV wavelengths, EBL offers a significant resolution advantage due to the distinction between photons and electrons. While diffraction limits the resolution of ArF and KrF lithography to several hundred nanometers, it is not a limiting factor in EBL, thanks to the remarkably small electron wavelength, measuring approximately 4 picometers at 100 keV electrons.<sup>197–199</sup> Notably, TEM has achieved resolutions as fine as 0.1 nm, underscoring the superior capabilities of electron beam.<sup>200</sup> However, considering interactions between electrons and photoresist (PR) during exposure, EBL can achieve sub-10 nm resolution. For instance, poly(methyl methacrylate) (PMMA), commonly used as a positive PR, has achieved sub-10 nm resolution with 3–5 nm wide lines by Vieu et al.<sup>201</sup> To fabricate this sub 10 nm structures, intermolecular forces, hindering the dissolution of PR by the developer, have been solved by ultrasonic agitation. Moreover, other groups have achieved sub-10 nm resolution with negative PR, hydrogen silsesquioxane (HSQ).<sup>202</sup> A proximity effect caused by backscattered electrons is another factor influencing EBL resolution. Sub-1 nm nanogaps have been demonstrated by

minimizing backscattered electrons using thin film substrates under 100 nm thickness.<sup>203</sup>

Recently, achieving high resolution in layer-by-layer EBL processes has garnered attention as their capability to expand design freedom to out-of-plane. Layer-by-layer EBL, as its name implies, is a process capable of realizing multiple layers on the same substrate, incorporating diverse materials, varying heights, and stacking the structures. In this process, two alignment marks can align fabricated areas precisely at their center relative to each other. The alignment error is a critical factor that significantly influences sample performance, with two primary factors contributing to alignment error: the sample stage and alignment marks. Yoon et al. have achieved sub-20 nm alignment accuracy by optimizing these factors.<sup>204</sup> The sample stage error occurs when the stage moves according to alignment marks, but identical alignment marks consistently induce the same stage error. Therefore, fabricating alignment marks separately first, as shown in Figure 5a, solves the stage error issue. Additionally, the alignment mark errors due to the proximity effect, leading to marker enlargement and the rounded edges, were addressed by designing optimized markers considering this effect, as depicted in Figure 5a, ultimately achieving sub-20 nm alignment accuracy.

Layer-by-layer EBL processes have been implanted for realizing versatile metasurface performance. For example, Liu et al. have demonstrated a hydrogen gas sensor by aligning a single palladium nanoparticle and a gold nanoantenna with minimum gaps of 10 nm (Figure 5b).<sup>205</sup> In response to hydrogen exposure, the optical properties of palladium metasurfaces change rapidly, albeit with a broad spectrum. Therefore, through layer-by-layer EBL, aligning gold with gaps ranging from 10 to 90 nm results in significant peak enhancement and narrow bands. Furthermore, layer-by-layer EBL have been used to design metaholograms with multiplexing performances. Achieving multiplexing, such as wavelength, polarization, angle, and orbital angular momentum multiplexing, is crucial.<sup>206</sup> Generally, additional components and design methods are needed, complicating the system. With a single metasurface, wavelength multiplexing metaholograms have been demonstrated in the visible and near-infrared (NIR) by aligning specifically optimized structures for each spectral range (Figure 5c).<sup>207</sup> Optimized structures for each wavelength were uniformly arranged with a pitch of 600 nm and an aligning error of sub-20 nm.

Layer-by-layer EBL not only enables fabrication on the same plane but also fabricates three-dimensional nanostructures. In comparison, other 3D nanofabrication techniques such as two-

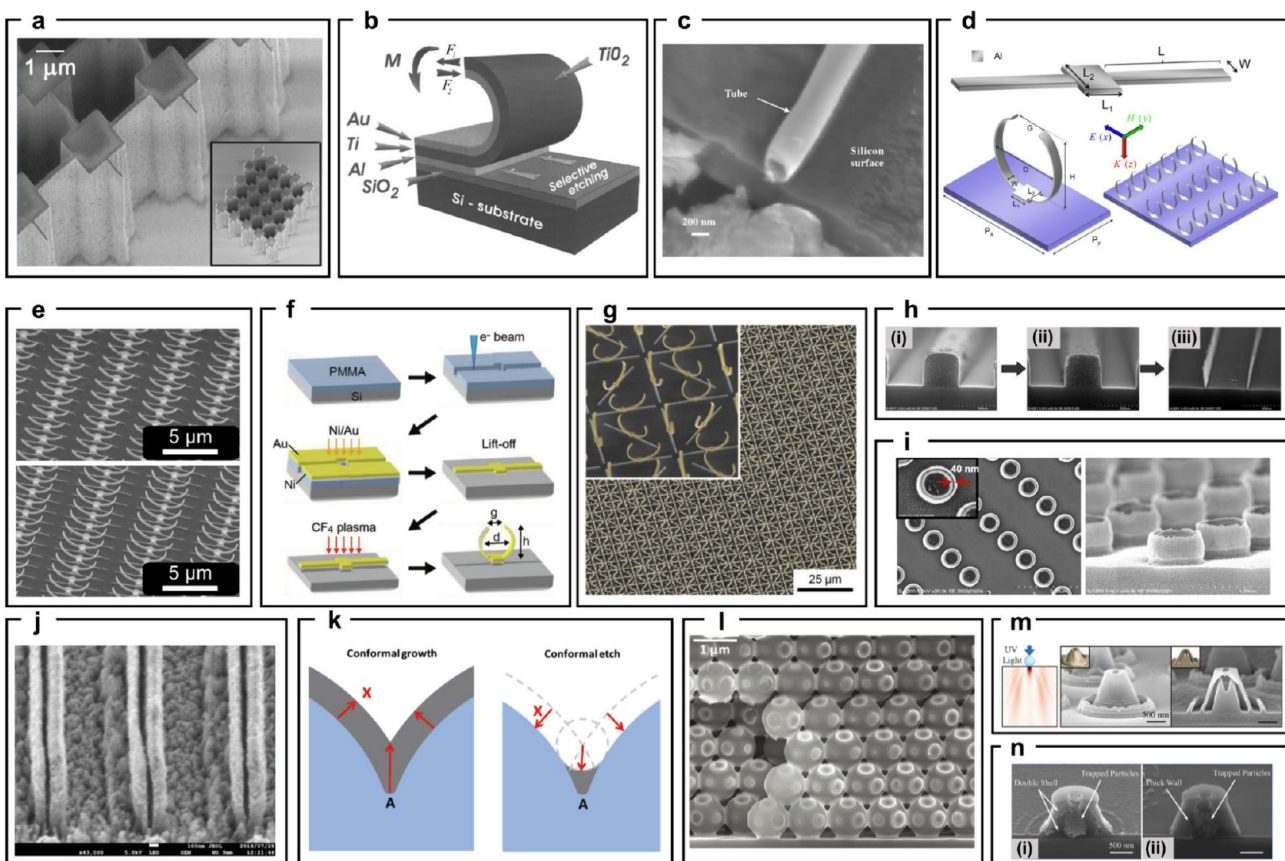


**Figure 6. 3D lithography.** (a) SEM image of  $2 \times 2 \mu\text{m}^2$  pillars etched into a  $10 \mu\text{m}$  thick SU-8 layer using a 1 MeV proton beam. Each pillar is connected by high-aspect ratio walls, measuring 60 and 120 nm in width.<sup>217</sup> Adapted with permission from ref 217. Copyright 2003 American Institute of Physics. (b) Schematic of the tube formation process using Au/Ti/Al thin films on an oxidized silicon substrate. The Au/Ti bilayer forms a tube during the selective etching of the sacrificial Al layer.<sup>220</sup> Adapted with permission from ref 220. Copyright 2005 IOP Publishing. (c) Cross-sectional SEM image of a 250 nm internal diameter Au/Ti nanotube formed on a silicon substrate.<sup>220</sup> Adapted with permission from ref 220. Copyright 2005 IOP Publishing. (d) Schematic diagram showing aluminum 3D SRRs before and after being released from the substrate by a dry etching method.<sup>231</sup> Adapted with permission under a Creative Common CC BY License from ref 231. Copyright 2012 Optica. (e) Oblique view SEM images with a tilting angle of 40 degrees for the 3D SRRs.<sup>231</sup> Adapted with permission under a Creative Common CC BY License from ref 231. Copyright 2012 Optica. (f) The fabrication process of a 3D SRR, including spin-coating resist, EBL, Ni/Au (10/60 nm) deposition, lift-off, CF<sub>4</sub> plasma dry-etching, and self-folding, in sequence.<sup>222</sup> Adapted with permission from ref 222. Copyright 2015 Wiley-VCH. (g) SEM image of the fabricated isotropic metamaterial consisting of 4-fold symmetric 3D SRRs over a total sample area of  $4 \times 4 \text{ mm}^2$ . The inset shows a magnified image.<sup>222</sup> Adapted with permission from ref 222. Copyright 2015 Wiley-VCH. (h) Cross-sectional SEM images of a nanopattern on a substrate: (h.1) after 30 cycles of the surface sol-gel process, (h.2) after CHF<sub>3</sub> plasma etching to remove the topmost portion of the silica layer, and (h.3) after oxygen plasma etching.<sup>223</sup> Adapted with permission from ref 223. Copyright 2006 American Chemical Society. (i) Au double nanopillars (DNP) with a hollow nanogap after the removal of the template and polymer layer (left), and top view of Au DNP arrays with a nanogap width of 40 nm.<sup>224</sup> Adapted with permission from ref 224. Copyright 2011 ACS. (j) SEM image of a vertically oriented metal-insulator-metal (MIM) structure with a 25 nm channel sandwiched between two gold fins made on a glass substrate.<sup>225</sup> Adapted with permission from ref 225. Copyright 2019 ACS. (k) Schematic of the conformal growth (left) and conformal etching (right) processes. Despite the deposition and etching being conducted with the same material thickness, some material remains in areas with a small negative radius of curvature.<sup>228</sup> Adapted with permission from ref 228. Copyright 2009 ACS. (l) Cross-section SEM image of the metadielectric photonic crystal composed of discrete tungsten ring particles.<sup>228</sup> Adapted with permission from ref 228. Copyright 2009 ACS. (m) Fabrication process of hollow 3D nanostructures using light scattering from a colloidal nanoparticle, and SEM images of the fabricated hollow 3D nanostructure and its cross-sectional view.<sup>229</sup> Adapted with permission from ref 229. Copyright 2013 ACS. (n) Micrographs of particle-trapping nanovolcanoes. Silica particles, 50 nm in diameter, are trapped in double-shelled (left) and thick-walled nanovolcanoes (right).<sup>229</sup> Adapted with permission from ref 229. Copyright 2013 ACS.

photon lithography, holographic lithography, and phase-mask lithography have limitations in materials, resolution, or structure.<sup>208,209</sup> However, layer-by-layer EBL offers the flexibility to select diverse materials according to preference, enabling the attainment of ultrahigh resolution with arbitrary structures. For example, humidity-responsive 3D metasurfaces for full-color displays have validated using poly(vinyl alcohol) (PVA) and silver nanoparticles by layer-by-layer EBL, as well as NIL (Figure 5d).<sup>210</sup> Two nanostructures with heights of 100

and 250 nm were accurately arranged by layer-by-layer EBL and replicated with the NIL process. The structures represented by blue and cyan colors each, with residual layers represented by magenta, enable full-color displays. Furthermore, layer-by-layer EBL has enabled the achievement of multiplexing metaholograms in both the visible and ultraviolet (UV) regions.<sup>211</sup> Similar to visible and NIR metasurfaces, specifically optimized structures for each spectral range were arranged, albeit in separate layers. While the pitch could be the

same for visible and NIR metasurfaces, around 600 nm, it differed for visible and UV metasurfaces, with optimized pitches of 500 and 280 nm, respectively. By utilizing a separating layer, spin-on glass (SOG), polarization-dependent vectorial metaholograms have been successfully demonstrated, as depicted in **Figure 5e**.

Furthermore, more than two layers can be fabricated using layer-by-layer EBL. Liu et al. have demonstrated plasmon rulers to gauge nanoscale distances akin to chemical or biological entities with 3D stacked metasurfaces through layer-by-layer EBL.<sup>212</sup> Strong coupling between a single nanorod (red one in **Figure 5f**) and two nanorod pairs (yellow one and green one in **Figure 5f**) leads to the activation of two sharp quadrupolar resonances within the broad dipolar resonance spectrum, supporting high-resolution plasmon spectroscopy. Additionally, 5-layers stacked metasurfaces for backward phase-matched second harmonic generation (SHG) have been demonstrated using layer-by-layer EBL (**Figure 5g**).<sup>213</sup> The phase-matched SHG signal scales superlinearly according to the number of layers.

Recent advancements in origami-inspired nanofabrication techniques present exciting opportunities for achieving complex 3D nanostructures with enhanced optical and mechanical functionalities.<sup>214</sup> For instance, Cho et al. demonstrated nanoscale self-folding approaches leveraging differential stresses within multilayered thin films, enabling the creation of optically active cubic structures with precise nanoscale features.<sup>215</sup> These methods utilize electron-beam lithography to pattern planar designs, followed by plasma etching to release and fold the structures into 3D configurations (**Figure 5h**). Similarly, Joung et al. introduced self-assembled graphene-based 3D polyhedrons capable of volumetric light confinement through plasmonic hybridization, showcasing the potential for high field enhancement and novel optical behaviors that exceed those of conventional 2D materials<sup>216</sup> (**Figure 5i**). Integrating these approaches with existing electron-beam lithography techniques could unlock new pathways for producing multifunctional nanophotonic devices, bridging the gap between nanoscale fabrication precision and the scalability of 3D architectures.

## 7. 3D NANOFABRICATION WITH FOCUSED BEAM SCANNING

Takuo Tanaka

Due to the ultrashort wavelength of the extreme ultraviolet light source and the high numerical aperture (NA) of the optical system, the minimum line width achievable for semiconductor devices has reached the single nanometer scale. However, as the device structure is limited to two-dimensional patterns or simple stacks of these 2D patterns, fabricating 3D nanometer-scale structures remains a significant challenge. This limitation underscores a pressing need for new fabrication technologies that can create arbitrary 3D nanostructures, which are crucial for advancing the development of volumetric optical metamaterials.

Top-down techniques employing focused beam scanning, such as laser, electron, and ion beams, have been extensively explored and developed. These techniques involve 3D focusing and scanning of beams to alter material properties, including solubility to developers or hardness. Within the realm of beam scanning lithography, J. A. Kan et al. have advocated for the use of a proton beam.<sup>217</sup> The interaction probability between protons and electrons in materials is significantly higher than

that of nuclear scattering. However, due to the significant mass discrepancy between protons and electrons, this interaction remains minimal, allowing for deeper proton beam penetration into materials. Leveraging this property, the technique has been applied to achieve sub-100 nm lithography with high aspect ratios. The technique has been demonstrated in two forms: positive-tone lithography using PMMA as a resist, and negative-tone lithography with SU-8. An example provided, **Figure 6a**, depicts a scanning electron micrograph of  $2 \times 2 \mu\text{m}^2$  pillars interconnected by high aspect ratio walls, measuring 60 and 120 nm in width and 10  $\mu\text{m}$  in height, created using a 1 MeV proton beam.

While direct beam lithography offers the advantage of fabricating arbitrary 3D structures, its application in mass or large-area production of minuscule 3D structures is hindered by low throughput. To address this challenge, the direct beam scanning technique has been utilized solely for creating templates for the final structures, followed by the adoption of mass-production techniques such as thin film deposition. D. B. Burckel et al. introduced the self-aligned membrane projection lithography technique.<sup>218</sup> This method involves depositing layers of polyimide and PMMA on a silicon substrate, followed by patterning split-ring resonators (SRRs) using electron-beam lithography on the PMMA layer. After developing the PMMA pattern with methyl isobutyl ketone (MIBK), the polyimide layer and silicon substrate beneath the PMMA are isotropically dissolved to create hemispherical holes. Subsequently, Ti/Au thin films are obliquely deposited through the shaped slits in the PMMA using electron-beam evaporation at a 45° angle, with three instances of 120° in-plane rotation after each evaporation. While each PMMA film pattern is drawn individually using electron-beam lithography, the metal thin film deposition simultaneously forms all patterns on the substrate. This group also developed a similar technique for forming split-ring resonator patterns on the vertical walls of cubic holes in SU-8, fabricated via contact photolithography.<sup>219</sup>

Y. V. Nastaushev et al. introduced a technique for the self-organized formation of micro- and nanotubes using strained metal bilayers.<sup>220</sup> Their process involved the deposition of three metal thin films—aluminum (Al), titanium (Ti), and gold (Au)—on an oxidized silicon substrate. Initially, a 20 nm thick Al film was deposited using electron beam sputtering, followed by the deposition of Ti and Au thin films. The Al film served as a sacrificial layer, later etched away using a KOH-based etchant. The proposed method and its experimental results are depicted in **Figure 6b** and c. During the etching process, the Ti layer undergoes oxidation to form  $\text{TiO}_2$ . The research team experimented with several metals (Ni, Ti, Au, Ge, and Al) and their combinations, concluding that the Au/Ti bilayer exhibited the most favorable properties for tube formation. These structures function as what is termed Swiss-roll resonant units. Employing a similar technique, Y. Mei et al. successfully formed an integrated microtube array and conducted studies on the photoluminescence spectrum of  $\text{SiO}/\text{SiO}_2$  microtubes.<sup>221</sup> C. C. Chen et al. has developed a metal stress-driven self-folding method that combines the inherent self-folding phenomena, resulting from the residual stress in metal thin films, with two-dimensional electron beam patterning. This technique, depicted in **Figure 6d**, starts with using EBL to pattern self-standing 3D SRRs as a two-dimensional pattern on the substrate surface. Following this, an isotropic dry-etching process releases the 2D metal patterns from the substrate,

except at the structure's center part. Due to the residual stress in the metal thin films, the released metal ribbons fold, self-organizing into 3D SRR structures. This method has successfully produced 3D SRR structures, as depicted in Figure 6e.<sup>222</sup> To enhance the technique, a bimetal structure incorporating nickel (Ni) and Au was introduced, significantly improving the control over the tailored structural parameters of 3D SRRs, such as curvature radius and gap distance. The process for fabricating a 3D gold SRR array is illustrated in Figure 6f. Using this 3D SRR array structure, shown in Figure 6g, magnetic responses to incident terahertz (THz) waves and isotropic optical properties were observed, despite the strong anisotropic property of the individual 3D SRRs.

S. Fujikawa et al. have developed a novel 3D fabrication technique that ingeniously integrates top-down and bottom-up approaches.<sup>223</sup> Illustrated in Figure 6h, the process begins with the creation of a surface relief structure on PR via photolithography, serving as a template. This template's surface is then coated with a silica nanolayer through a sol-gel process, as depicted in Figure 6h(i). The topmost portion of the silica layer undergoes etching using a RIE technique with CHF<sub>3</sub> plasma, detailed in Figure 6h(ii). Following the removal of the PR template, silica walls under 20 nm in width are achieved on the Si substrate, shown in Figure 6h(iii). This method uniquely allows for precise control over the silica wall's line width—originating from the silica layer's thickness—through the adjustment of sol-gel cycle repetitions, thus facilitating the desired wall width adjustment. In 2011, W. Kubo et al. leveraged this technique to construct metal double nanopillars featuring nanogap structures, as demonstrated in Figure 6i.<sup>224</sup> This was accomplished using a layer-by-layer polymer coating technique and magnetron sputtering of an Au layer onto a polymer pillar template, resulting in an array of double nanopillars. Utilizing a similar approach, D. Su et al. crafted a high-aspect ratio Au double fin array structure on a glass substrate, showcased in Figure 6j.<sup>225</sup> This structure was subsequently applied in the development of a plasmonic gas sensor, underscoring the technique's versatility and potential for diverse applications.

J. Shen et al. pioneered the DNA modular epitaxy technique to construct 3D nanostructures.<sup>226</sup> This approach employs a seed-mediated growth technique to form 3D DNA modules, which are then assembled on a flat DNA brick crystal substrate. These 3D DNA modules are stabilized with Ni<sup>2+</sup> ions to prevent the collapse of DNA features. This stabilized 3D DNA structure serves as a mask pattern for the reactive ion-etching (RIE) of the underlying Si substrate. A single-run RIE process yields ultrascaled Si nanostructures with a pitch and critical dimension of  $16.2 \pm 0.6$  nm and  $7.2 \pm 1.0$  nm, respectively. These dimensions are 50% smaller than those achieved through quadruple patterning or EUV lithography.

E. Berganza et al. also introduced a 3D nanolithography technique, utilizing lipid dip-pen nanolithography (L-DPN) and a bovine serum albumin (BSA)-coated substrate.<sup>227</sup> The chemical modification of the substrate surface with BSA molecules enables the anchoring of phospholipid molecules without undesired spreading during and after L-DPN. This method allows for the formation of 3D scaffolds through layer-by-layer L-DPN, with physical vapor deposition (PVD) applied to metallize the surface of the 3D scaffold template. X. Yu et al. proposed a different 3D templating technique, leveraging a 3D template created by self-assembled micrometer-scale colloidal particles, complemented with conformal coating and etching

techniques.<sup>228</sup> The uniqueness of this method lies in the fact that conformal etching does not inversely replicate the conformal material deposition at locations with negative surface curvature, leaving some material in areas of negative curvature, as illustrated in Figure 6k. Figure 6l showcases a fabricated 3D metallocodielectric photonic crystal consisting of discrete tungsten ring particles, 88 nm in thickness and 328 nm in diameter, demonstrating the technique's potential for creating intricate 3D nanostructures.

The method known as "particle lithography," which employs self-assembled micro/nano particles as a shadow mask, is detailed in a separate section. In contrast to particle lithography, X. A. Zhang et al. have showcased a technique utilizing the scattered light pattern from dielectric colloidal particles to fabricate 3D hollow nanostructures, termed "nano volcano" by the authors.<sup>229</sup> This process involves assembling a dielectric Mie particle on the PR layer of a substrate and then illuminating it with a linearly polarized 325 nm laser. The particle scatters the incident light, and the near-field scattering pattern is captured by the underlying PR, resulting in the formation of 3D hollow structures. An example of such fabricated structures is presented in Figure 6m. As a practical application of these 3D structures, the accumulation of 50 nm silica particles within the nanovolcano structures was demonstrated. This capability is anticipated to have potential applications in drug delivery. Furthermore, X. A. Zhang et al. have advanced this technique by employing two laser beams to create more complex structures.<sup>230</sup> This expansion of the original method allows for greater versatility in the design and functionality of the nanostructures produced, opening new avenues for research and application in nanotechnology fields.

## 8. 3D NANOLITHOGRAPHY

Yang Zhao

3D nanolithography is a critical step in creating nanostructures essential for nanophotonic and nano-optic devices, as well as functional nanomaterials. These devices and materials find extensive applications in communications, computing, sensing, and imaging. However, 3D nanolithography does not operate in isolation. To create a functional nanodevice or nanomaterial, specific materials often need to be deposited within the defined 3D nanostructures or the 3D nanostructures need to be transferred. Consequently, 3D nanolithography is typically accompanied by effective metallization or etching processes to yield functional nanodevices. To realize these devices, three primary approaches to 3D nanolithography are often employed: the layer-by-layer fabrication approach, the direct writing approach (either by cross-linking or deposition), and the templated approach.

The multilayer fabrication approach is commonly used to create optical metamaterials.<sup>232,233</sup> Due to the challenges of constructing 3D periodic nanostructures, many designs have adopted 2D counterparts, metasurfaces.<sup>234</sup> Although single-layer metasurfaces can achieve a broad range of functionalities, certain functionalities, such as broadband applications, require 3D nanostructures. As a result, discretizing 3D nanostructures into layered 2D nanostructures has become one straightforward solution.<sup>235</sup> Nevertheless, this approach presents challenges related to the precision in stacking and the introduction of errors, particularly in the third dimension.

The multilayer fabrication process constructs 3D nanostructures by repeating 2D lithography processes, which include conventional electron beam lithography followed by reactive

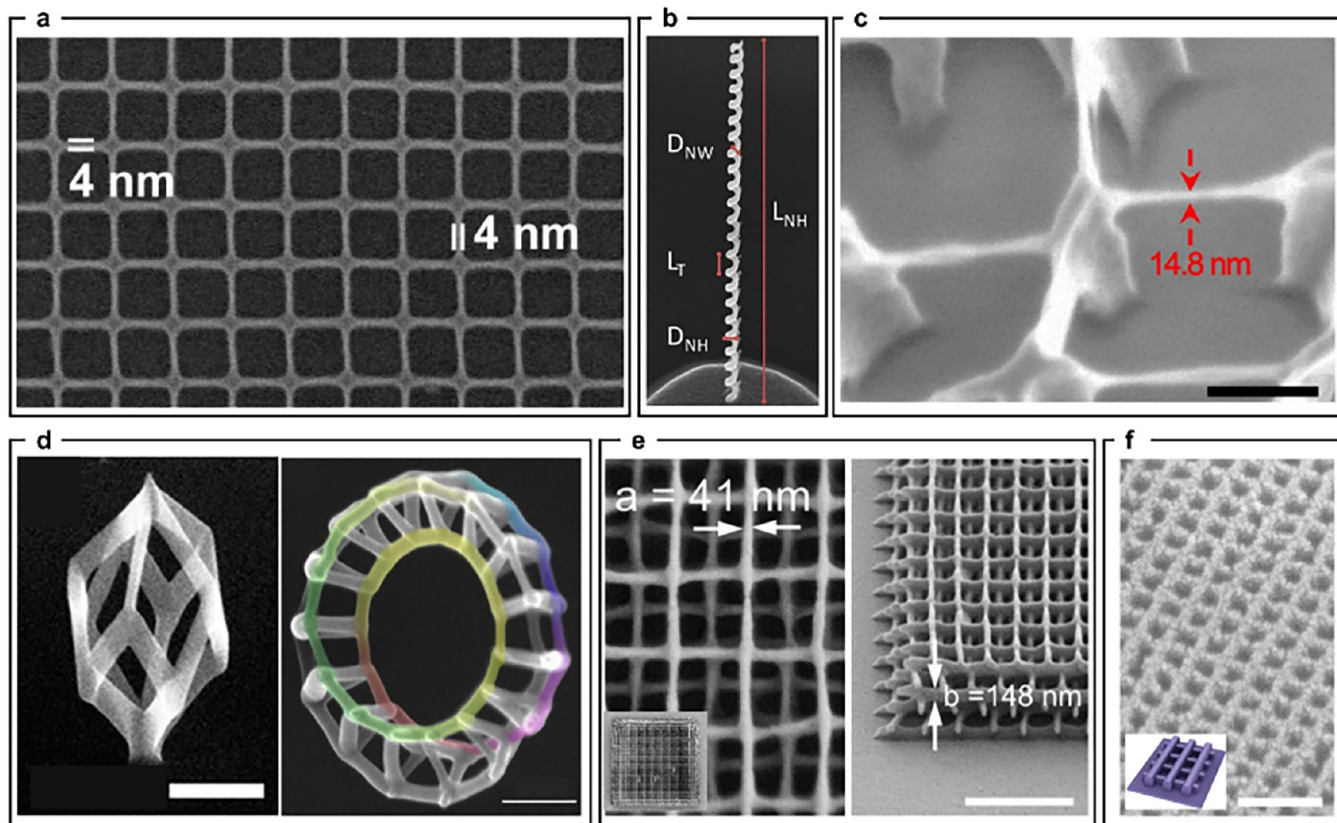


**Figure 7. 3D Nanolithography.** Scanning electron microscopy images of (a) A large area grid with line widths as small as 4 nm and an aspect ratio of  $\sim 6$ , written using a low-molecular-mass precursor resist and a commercial 100 kV e-beam.<sup>239</sup> Adapted with permission from ref 239. Copyright 2022 ACS. (b) A nanohelix with a nanowire diameter (DNW) of 50 nm, nanohelix diameter (DNH) of 100 nm, turn length (LT) of 200 nm, and nanohelix length (LNH) of 23 turns, fabricated using focused helium ion on a curved substrate.<sup>245</sup> Adapted with permission under a Creative Common CC BY License from ref 245. Copyright 2019 ACS. (c) A nanobridge with a resolution of  $\sim 15$  nm fabricated using a voltage-gated approach, scale bar = 200 nm.<sup>242</sup> Adapted with permission under a Creative Common CC BY License from ref 242. Copyright 2021 Springer Nature. (d) A modified icosahedron nanostructure (left) and a Möbius strip (right) with triangular cross-section and individual wire dimensions around 25 nm, fabricated using FEBIP. The icosahedron nanostructure has a PtCx composition. Scale bar= 200 nm.<sup>250</sup> Adapted with permission from ref 250. Copyright 2016 ACS. (e) A woodpile structure made with light and matter coconfined multiphoton lithography, scale bar = 1  $\mu$ m.<sup>257</sup> Adapted with permission from ref 257. Copyright 2024 Springer Nature. (f) A 3D woodpile structure with a vertical critical dimension of 2 nm, transferred using a DNA molecular mask onto a silicon substrate, scale bar = 100 nm.<sup>226</sup> Adapted with permission from ref 226. Copyright 2021 Springer Nature.

ion etching, metallization, lift-off, and planarization processes. These processes are not necessarily conducted sequentially. For instance, a commonly adopted method starts by defining 2D nanostructures through electron beam lithography, followed by metallization and lift-off. Subsequently, a solidifiable spin-on dielectric spacer<sup>236,237</sup> is used to even out the nanostructures within the layer before patterning the next layer. Alternatively, negative nanostructures can be defined by electron beam lithography and reactive ion etching, where the depth of the negative nanostructures matches the metallization, resulting in a planarized surface after the lift-off process.<sup>235</sup> Both approaches highlight the multilayer process's limitations regarding the number of layers that can be built due to the accumulation of errors. Although achieving precise alignment across layers is challenging, misalignment can be mitigated or even considered negligible if the design addresses the layer spacing relative to the in-plane periodicity, often in the context of optical metasurfaces.<sup>238</sup>

The resolution of multilayer 3D nanolithography is constrained by the current capabilities of state-of-the-art electron beam lithography within the 2D plane. This limitation is primarily due to electron beam aberration, beam diameter, and

electron scattering within the resist. To date, a resolution of 4 nm has been achieved using commercial electron beam lithography with a low-molecular-mass single-source precursor resist (Figure 7a).<sup>239</sup>

In addition to the traditional planner electron beam patterning used in the multilayer approach, which produces discretized 3D nanostructures, electron beam lithography has also demonstrated the capability to create continuous 3D nanostructures. These structures can be achieved through several innovative methods: fabricating on a nonplanar substrate,<sup>240</sup> utilizing postlithography self-rolled-up membrane technologies,<sup>241</sup> or employing voltage-regulated electron beam with genetically engineered resist.<sup>242</sup>

Fabricating on a nonplanar substrate relies on using an evaporated dry resist or ice resist for the electron beam, achieving resolutions as fine as 10 nm.<sup>240</sup> This process, however, is constrained by the limitations of the evaporating tool for dry resists or by the operational temperature for organic ice or water ice resists.<sup>243,244</sup> Due to its potential for high spatial resolution, this approach can be an alternative to FIB milling on nonplanar substrates. Nevertheless, the use of an electron beam on nonplanar substrates often results in a

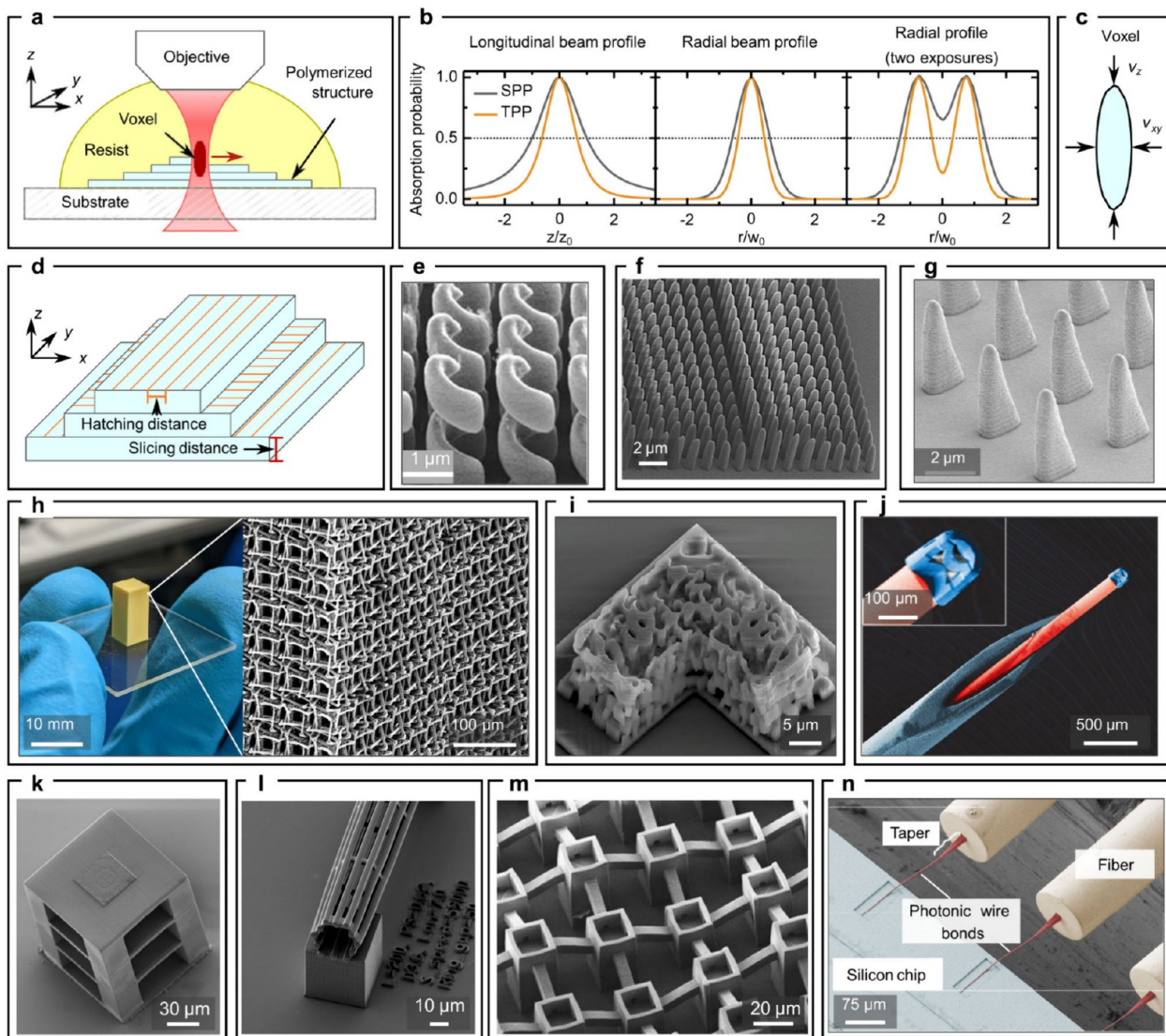


**Figure 8. Theory and applications of 3D nanoprinting.** (a) A 3D nanoprinting system. (b) Polymerization occurs where the intensity surpasses a threshold (dashed line). Two-photon polymerization (TPP, orange) suppresses polymerization in the out-of-focus regions, while single-photon polymerization (SPP, gray) can lead to artifacts from several below-threshold exposures (right panel). A Gaussian beam with beam waist  $w_0$  and Rayleigh length  $z_R$  was assumed. (c) Shape of a voxel. (d) Sketch indicating hatching and slicing distance. Fabricating in three dimensions unlocks various applications, such as metasurfaces with nontrivial unit cells, like (e) helices,<sup>275</sup> Adapted with permission from ref 275. Copyright 2009 AAAS. (f) Multiheight nanopillars and (g) nanofins.<sup>287</sup> Adapted with permission from ref 287. Copyright 2022 AAAS. (h) Parallelizing fabrication using multifocal arrays enables centimeter-scale metamaterials.<sup>272</sup> Adapted with permission under a Creative Common CC BY License from ref 272. Copyright 2024 Springer Nature. (i) The full freedom of 3D fabrication is exploited in inverse-designed volume elements.<sup>288</sup> Adapted with permission under a Creative Common CC BY License from ref 288. Copyright 2023 Springer Nature. Multilayer structures allow implementing (j) compound metalenses,<sup>291</sup> Adapted with permission from ref 291. Copyright 2016 Springer Nature. Or (k) diffractive neural networks.<sup>297</sup> Adapted with permission under a Creative Common CC BY License from ref 297. Copyright 2022 Springer Nature. (l) Moreover, novel on-chip hollow-core waveguides can be realized.<sup>298</sup> Adapted with permission under a Creative Common CC BY License from ref 298. Copyright 2021 Optica. (m) Among biomedical applications, scaffolds for directed cell growth have attracted particular interest.<sup>303</sup> Adapted with permission from ref 303. Copyright 2019 Wiley-VCH. Lastly, fabrication directly onto fiber-end faces (j), or onto existing photonic chips (n) is achievable.<sup>309</sup> Adapted with permission under a Creative Common CC BY License from ref 309. Copyright 2020 Springer Nature.

limited aspect ratio for the nanostructure. FIB offers an alternative for fabricating 3D nanostructures on nonplanar substrates.<sup>245</sup> While FIB using gallium ions typically achieves a spatial resolution in the tens of nanometers range, using helium or neon<sup>246,247</sup> ions can significantly enhance the resolution to around 1 nm, depending on the substrate type.<sup>248</sup> For example, when combined with a precursor gas, helium ion beams have been used to directly write 3D helical nanostructures with a high aspect ratio, reaching up to 65 (Figure 7b).<sup>245</sup>

Another approach to achieving 3D helical or coil nanostructures with high aspect ratios involves self-rolled-up technology.<sup>249</sup> This method combines electron beam lithography with a strain-induced roll-up of substrate membranes to create helical or coil nanostructures. The radius and number of turns in these nanostructures can be precisely controlled by adjusting the lattice mismatch of the epitaxially grown films. Notably, these films are not restricted to semiconductors; they can be composed of dielectrics and/or metals,<sup>241</sup> providing a

versatile method for creating 3D nanostructures with rotational features.

The previously discussed 3D nanolithography methods lack the ability to precisely control arbitrary shapes. To fabricate such intricate 3D nanostructures, direct-writing approaches are often employed. One notable method combines a voltage-regulated electron beam with genetically engineered resists.<sup>242</sup> By adjusting the electron beam accelerating voltage, the exposure depth can be controlled to directly write the desired 3D nanostructure. A low molecular-weight resist is typically preferred for achieving high spatial resolution, although it may lack structural integrity. To address this, lab-made recombinant spider silk proteins can be used as the resist. These proteins offer a well-defined molecular weight that balances the structural integrity and spatial resolution of the fabricated nanostructure. This method has achieved resolutions below 15 nm (Figure 7c).<sup>242</sup> Furthermore, genetic modifications of the resist can introduce additional functionalities throughout the depth of the 3D nanostructure.

Beyond cross-linking resists, an electron beam can also deposit 3D nanostructures using a gas precursor, a process known as focused electron-beam-induced processing.<sup>250,251</sup> This method relies on the local dissociation of gas precursor molecules due to electron-molecule interactions facilitated by electron multiscattering. Precise control over the electron density and gas precursor pressure, along with their synchronization, is essential for forming high-resolution nanostructures. Focused electron-beam-induced processing can create arbitrarily shaped 3D nanostructures with critical dimensions ranging from 20 to 50 nm (Figure 7d).<sup>250</sup> Although the as-deposited nanostructures may contain carbon, this can be removed with a synchronized pulsed laser.<sup>252</sup> To date, focused electron-beam-induced processing has successfully deposited 3D nanostructures in various materials, including gold, copper, platinum, and silicon, among more than ten different solids.<sup>253</sup> However, similar to the other electron beam technologies, focused electron-beam-induced processing is limited by speed and throughput due to its single electron source and point-by-point writing process.

In the above-mentioned approaches, electron beams are primarily used to cross-link materials and define nanostructures. However, photons are also widely employed for fabricating arbitrary 3D micro- and nanostructures. While multiphoton<sup>254</sup> lithography has a dedicated section in this review, we will only comment on its capacity to create 3D nanostructures here. Photon sources are typically constrained by the diffraction limit, preventing them from achieving voxel sizes below this limit without postexposure modifications. Although reducing the excitation wavelength theoretically decreases the critical dimension, it requires an optimal multiphoton resist at that specific wavelength.<sup>255</sup> To further shrink the critical dimensions and improve lateral resolution beyond the diffraction limit, challenges related to the diffusion and accumulation of free radicals must be addressed. Light confinement and matter confinement can help overcome these issues. Light confinement involves photon inhibition using a donut beam inspired by stimulated emission depletion (STED) microscopy, while matter confinement uses chemical quenchers within the resist to narrow the free radical distribution.<sup>256</sup> Recent developments in multiphoton lithography have demonstrated a light and matter coconfined approach, achieving a 3D woodpile structure with a critical dimension of 30 nm and a lateral resolution of 100 nm (Figure

7e).<sup>257</sup> For these complex 3D nanostructures, surface functionalization followed by electroless deposition of gold or silver can create functional nanophotonic devices.<sup>258</sup>

Another versatile approach for creating 3D nanostructures involves using DNA as a template<sup>259,260</sup> for lithography, enabling pattern transfer. Recent advancements in this direction utilize DNA bricks as the foundational elements, scaling up with seed-mediated growth of 3D DNA modules. These nanostructures are stabilized with Ni<sup>2+</sup>, and the DNA 3D mask is transferred onto a substrate, such as silicon, through one-step reactive ion etching (Figure 7f).<sup>226</sup> This technique has achieved lateral critical dimensions of 7 nm and vertical critical dimensions as low as 2 nm.

We have reviewed a range of 3D nanolithography methods capable of achieving critical dimensions from 50 nm down to 2 nm. These techniques support pattern transfer, allowing for the fabrication of 3D nanostructures in a variety of materials beyond the resist/air contrast. This versatility enables the integration of metals, semiconductors, and other genetically functionalized materials, thereby enhancing the functionalities and applications of the resulting nanophotonic devices.

## 9. DIRECT LASER PRINTING

Johannes Bürger, Stefan A. Maier, and Haoran Ren

3D laser nanoprinting via two-photon polymerization, introduced in 1997<sup>261</sup> and commercialized by Nanoscribe GmbH in 2007, is one of the few widely available methods capable of fabricating 3D photonic structures. With feature sizes down to hundreds of nanometers and sample footprints up to several centimeters, it has become a mature technology offered by at least 9 companies.<sup>262</sup> Three advantages set it apart from other lithographic techniques: (1) the ability to create 3D structures in a single processing step, (2) short manufacturing times allowing fabrication of large-scale structures, and (3) cost-effective prototyping without the need for high temperatures, harsh chemicals or cleanroom conditions.

As illustrated in Figure 8a, 3D nanoprinting works by scanning a focused laser beam through a positive PR containing monomers and a small concentration of a photoinitiator. The photoinitiator starts a polymerization reaction in the focal volume resulting in the formation of a polymerized voxel—the fundamental building block of the process. 3D structures are then built up layer by layer by raster scanning the laser focus through the PR, similar to a conventional 3D printer. Galvanometric mirrors typically handle *xy* displacements (scanning speeds: 10–1000 mm/s) and a piezo stage manages *z* displacements. Adjacent layers are spaced by the slicing distance and individual lines within one layer by the hatching distance (tens to hundreds of nanometers), resulting in surface roughness of down to  $\leq 5$  nm.<sup>263</sup> After exposure, unpolymerized resist is removed by a solvent, yielding structures with a refractive index between 1.5 and 1.7. Furthermore, materials like conductive or biocompatible polymers, metals (via photoreduction of metal salts), high-*n* glasses (via molecular glass resists), and composite materials consisting of multiple dye- or quantum-dot infused polymeric resists can be used.<sup>264</sup>

Maybe unexpectedly, the achievable feature size in 3D nanoprinting is not limited by diffraction. This is because a certain threshold intensity must be reached for a voxel to form (Figure 8b). Due to this chemical nonlinearity, operating near the threshold principally allows for the realization of arbitrarily

small features.<sup>265</sup> For example, suspended wires with a record width of 23 nm<sup>266</sup> have been demonstrated. However, these small voxel sizes come at the cost of decreased mechanical stability and higher susceptibility to laser power fluctuations because the degree of cross-linking in the polymer is low near threshold.<sup>267</sup> More complex structures require minimal lateral voxel sizes of at least 200 nm.<sup>268</sup> Since the focal volume is elongated along the axial direction  $v_z$ , the shape of the voxel is ellipsoidal with an aspect ratio  $A = v_z/v_{xy}$  of typically around 3.5.<sup>268</sup> (Figure 8c).

The key advantage of using two-photon absorption is a more technical aspect: once the photoinitiator is activated, it remains in this state for prolonged times if the threshold concentration is not yet reached, resulting in a buildup of active photoinitiator along the beam path.<sup>267</sup> This memory effect is especially detrimental in single-photon polymerization as 100 out-of-focus exposures with 1% of the threshold intensity would already be enough to create unwanted artifacts, while two-photon polymerization can withstand 10,000 of such exposures.<sup>269</sup> Due to this memory effect, the achievable lateral and axial resolution is still constrained by Abbe's diffraction limit for a two-photon process:<sup>267</sup>

$$\begin{aligned} d_{\text{lateral}} &= \frac{\lambda}{2\sqrt{2}\text{NA}} = 197 \text{ nm}, \\ d_{\text{axial}} &\approx \frac{\lambda A}{2\sqrt{2}\text{NA}} = 689 \text{ nm} \end{aligned} \quad (1)$$

assuming  $A = 3.5$ ,  $\lambda = 780 \text{ nm}$ , and  $\text{NA} = 1.4$ . Experimentally,  $d_{\text{lateral}} = 375 \text{ nm}$  and  $d_{\text{axial}} = 509 \text{ nm}$  have been demonstrated with similar parameters.<sup>270</sup> Further improvements in the resolution can be achieved by shrinking the polymer structures in a heat treatment allowing up to a 5-fold reduction in side lengths.<sup>271</sup> Overall, 3D nanoprinting currently offers the best combination of high printing speed (voxels/s) and high resolution within the group of 3D additive manufacturing techniques<sup>272</sup> (see up-to-date ranking at <https://3dprintingspeed.aph.kit.edu/>).

Like planar fabrication methods, 3D nanoprinting can realize flat optical structures such as metasurfaces of a single height,<sup>273</sup> or on-chip waveguides.<sup>274</sup> However, the main advantage of 3D nanoprinting lies in two key categories: the creation of truly 3D architectures and the fabrication onto existing optical components.

Looking at the first category, 3D nanoprinting has enabled new applications in 3D optical metamaterials, including the first realization of helical unit cells acting as broadband circular polarizers (Figure 8e, helix radius: 500 nm, helix pitch: 1.8  $\mu\text{m}$ , total height: 5  $\mu\text{m}$ ,  $\lambda = 3.5\text{--}7.5 \mu\text{m}$ ).<sup>275</sup> Unlike planar chiral structures, such a polarizer can block the polarization of a certain handedness regardless of whether the beam is incident from the front or back side of the material.<sup>276</sup> Related realizations include chiral mechanical metamaterials,<sup>277</sup> chiral metalenses,<sup>278</sup> and chiral microparticles.<sup>279</sup> Furthermore, woodpile photonic crystals are well-known 3D nanoprinted metamaterials and are often used as a benchmark for printer development.<sup>280</sup> In 2004, the first 3D nanoprinted woodpile structure with stopbands at telecommunication wavelengths was demonstrated, followed by a realization in the visible spectrum (lattice spacing: 600 nm, lateral rod diameter: 100 nm).<sup>281</sup> Additionally, 3D nanoprinting is well suited for the realization of the intricate unit cells of mechanical metamaterials (Figure 8h). Such materials benefit from a

high resolution on the (sub)micrometer scale and the ability to realize macroscopic samples on the order of several mm.<sup>272</sup> 3D nanoprinted mechanical metamaterials have been used to emulate phononic properties of condensed matter systems,<sup>272</sup> or for mechanical engineering<sup>277</sup> and acoustics.<sup>282</sup>

In contrast, photolithography faces difficulties even with the simpler two-dimensional metasurfaces once multiple height levels are involved, each requiring an additional processing step.<sup>283</sup> Instead, 3D nanoprinting allows the fabrication of metasurfaces with arbitrary height levels in a single step, thereby increasing the size of the available unit cell library severalfold (Figure 8f). This larger parameter space simplifies the design of metasurfaces that can control phase, amplitude, and polarization of light independently at each pixel and wavelength. Realized examples include complex-amplitude OAM-multiplexing holograms,<sup>25</sup> achromatic metalenses,<sup>284</sup> metalenses for chiral imaging,<sup>285</sup> and vector beam generators.<sup>286</sup> Furthermore, more complex unit cells can be realized where the cross-section changes with height, such as nanofin metasurfaces (Figure 8g,  $\lambda = 2\text{--}10 \mu\text{m}$ ).<sup>287</sup>

At higher complexity, the large parameter space of 3D nanoprinting is used for inverse-designed metamaterials without periodic patterns. Examples include a 6-layer multispectral polarimetric sorting device<sup>288</sup> (Figure 8i,  $\lambda = 3\text{--}6 \mu\text{m}$ ), a 3-layer metamaterial for angular multiplexing of optical fiber modes ( $\lambda = 1030 \text{ nm}$ ),<sup>289</sup> and a high NA aberration-corrected lens (NA: 0.85,  $\lambda = 980 \text{ nm}$ , diameter: 25  $\mu\text{m}$ , focusing efficiency: 73%).<sup>290</sup>

Similarly, 3D nanoprinting enables a straightforward path to implement other multilayer structures. A prime example is the triplet refractive lens system shown in Figure 8j which corrects for the same aberrations as typical high-quality microscope objectives.<sup>291</sup> Furthermore, stacked achromatic metalenses have been demonstrated consisting of two layers<sup>292</sup> (NA: 0.35,  $\lambda = 1000\text{--}1800 \text{ nm}$ , focusing efficiency: 27%), as well as an improved 3-layer version operating at visible wavelengths (NA: 0.7,  $\lambda = 400\text{--}800 \text{ nm}$ , focusing efficiency: 42%).<sup>293</sup>

3D photonic architectures are also of interest for realizing the high interconnection density required for photonic neural networks and optical computing.<sup>294</sup> While planar structures require large surface areas,<sup>294</sup> 3D neural networks can distribute the neurons across multiple layers in an  $N \times N \times N$  layout, potentially exceeding the high component density in electronic chips, where such architectures are limited by thermal constraints.<sup>295</sup> Initial efforts include 3D nanoprinted networks with dendrite-like connections<sup>296</sup> and a 4-layer diffractive neural network (Figure 8k).<sup>297</sup>

Another crucial application is the implementation of complex waveguide structures including the recently demonstrated "light cages" (Figure 8l)<sup>298</sup> and "microgap waveguides"<sup>299</sup> with side-wise accessible hollow cores, which accelerate analyte exchange in biochemical sensing compared to conventional glass fibers.<sup>300</sup> Furthermore, 3D nanoprinting is of interest for the implementation of twisted waveguides,<sup>274</sup> such as a recent demonstration of twisted hollow-core waveguides with a record twist period of 90  $\mu\text{m}$ ,<sup>301</sup> far shorter than the 10 mm seen in glass-based fibers.<sup>302</sup> This enables smaller devices using twisted waveguides, e.g., for circular polarization filtering, generation of orbital angular momentum beams, or twist sensing.

Lastly, biocompatible PRs open the door to a wide array of biomedical applications, from 3D scaffolds directing cell growth for culturing of neuronal networks (Figure 8m)<sup>303</sup> to

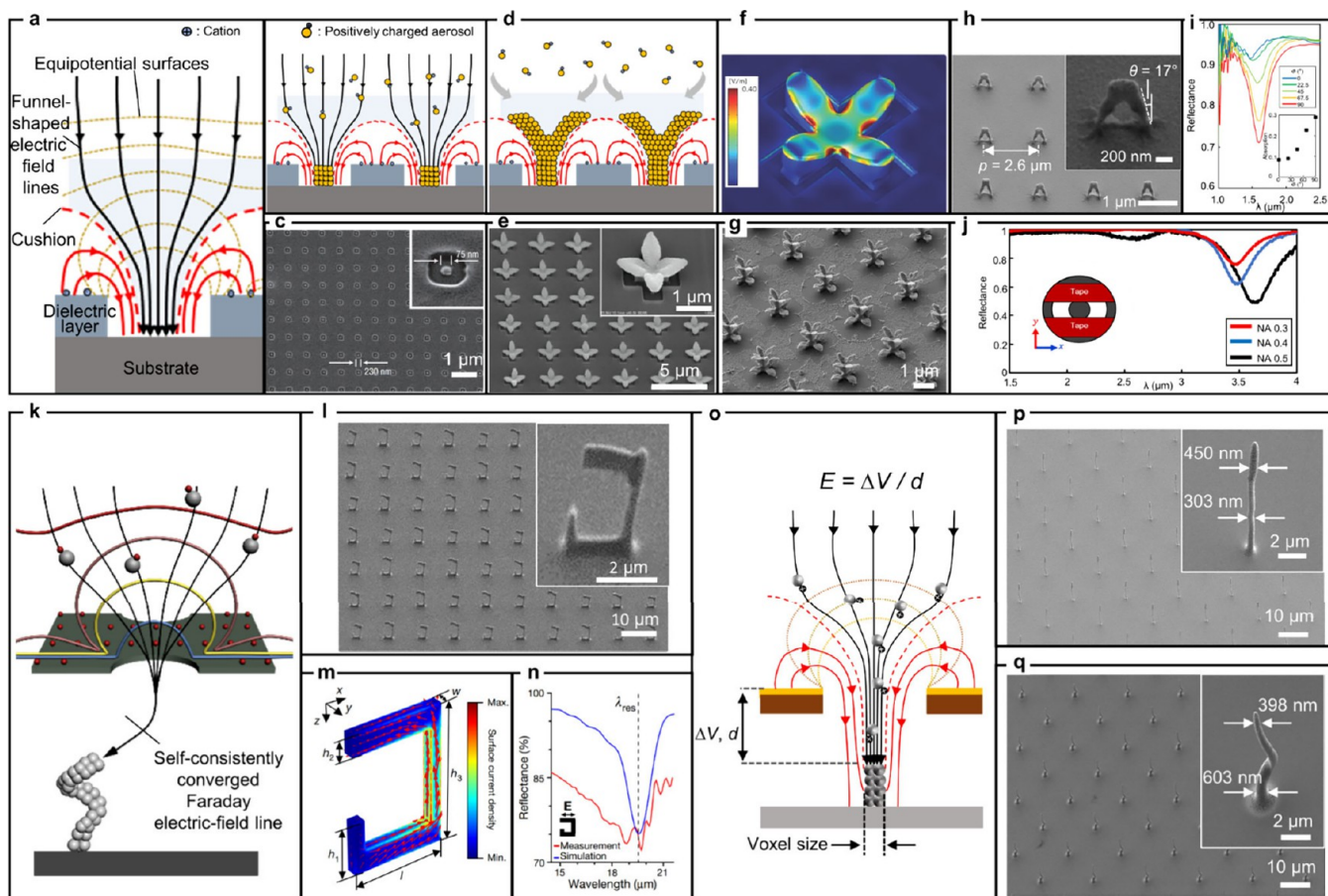


**Figure 9.** Aerosol printing process. (a) A dielectric layer prepatterned conductive Si substrate is negatively biased, leading to the accumulation of introduced cations on the dielectric layer and the generation of cushion regions (red dashed lines). Electric field lines (black solid lines) are transformed into funnel-shaped electric field lines due to the accumulated cations.<sup>324</sup> Adapted with permission from ref 324. Copyright 2021 ACS. (b) Positively charged aerosols introduced follow the electric field lines, enabling printing at the center of the dielectric layer openings.<sup>324</sup> Adapted with permission from ref 324. Copyright 2021 ACS. (c) 75 nm diameter of Ag nanodot array from 230 nm hole dielectric layer apertures.<sup>323</sup> Adapted with permission from ref 323. Copyright 2006 Springer Nature. (d) Continuous printing of charged aerosols results in the fabrication of 3D nanostructures following the shape of the funnel-shaped electric field lines/cushions. The aerosol 3D nanoprinting process is depicted in the order of (a), (b), and (d).<sup>324</sup> Adapted with permission from ref 324. Copyright 2021 ACS. (e) An array of printed flower-shaped Cu 3D nanostructures from cross-patterned dielectric layer.<sup>331</sup> Adapted with permission from ref 331. Copyright 2011 ACS. (f) Simulation result show electric field strength from the 4-petal flower-shaped 3D nanostructure.<sup>332</sup> Adapted with permission from ref 332. Copyright 2014 Wiley-VCH. (g) Vertically stacked 4-petal flower-shaped Cu 3D nanostructure.<sup>336</sup> Adapted with permission from ref 336. Copyright 2016 IOP Publishing. (h)  $\pi$ -shaped plasmonic Au 3D nanostructures resulted from controlling the cushion shapes.<sup>334</sup> Adapted with permission from ref 334. Copyright 2024 ACS. (i) Reflectance spectra measured data from the structure in (h).<sup>334</sup> The graph displays the reflectance spectra, which vary in response to the angle of incident linearly polarized light.  $\Phi$  presents polarization axis angle. Adapted with permission from ref 334. Copyright 2024 ACS. (j) Reflectance spectra depending on NAs of objective lenses. The  $\pi$ -shaped plasmonic Au 3D nanostructure has azimuthal angle sensitive optical responses.<sup>334</sup> Adapted with permission from ref 334. Copyright 2024 ACS. (k) Schematic showing aerosol 3D nanoprinting principle using the floating mask. The sharp tip of growing structure prolongs the funnel-shaped electric field lines to the tip with self-consist manner.<sup>79</sup> (l) An array of printed vSRR structure from (k).<sup>79</sup> Adapted with permission from ref 79. Copyright 2021 Springer Nature. (m) Simulated surface currents of vSRR structure, which induce a magnetic dipole.<sup>79</sup> Adapted with permission from ref 79. Copyright 2021 Springer Nature. (n) Simulated (blue line) and measured reflectance data (red line).<sup>79</sup> The magnetic dipole peak appears at the wavelength of 19.8  $\mu\text{m}$  under linearly polarized light. Adapted with permission from ref 79. Copyright 2021 Springer Nature. (o) Schematic shows electrified mask employed aerosol 3D nanoprinting technique.<sup>340</sup> Adapted with permission from ref 340. Copyright 2022 ELSEVIER. (p) Multivoxel sized vertical nanopillars printed from (o).<sup>340</sup> Adapted with permission from ref 340. Copyright 2022 ELSEVIER. (q) 3D nanohelices with continuously decreasing voxel size from the bottom to the top.<sup>340</sup> Adapted with permission from ref 340. Copyright 2022 ELSEVIER.

microfluidic organ-on-a-chip devices<sup>304</sup> and microneedles for drug delivery.<sup>305</sup>

Coming to the second application category, 3D nanoprinting allows fabrication onto existing structures, which can be challenging in a standard photolithography process. One example is the fabrication directly onto the end face of optical fibers equipping them with diffractive<sup>290</sup> or refractive lenses,<sup>291</sup>

metasurfaces for vector or OAM beam generation,<sup>286</sup> holographic metasurfaces,<sup>306</sup> diffractive and refractive free-form optics,<sup>307</sup> or total internal reflection optics for off-axis focusing in endoscopes.<sup>308</sup> Commercially, 3D nanoprinting enables interconnection of multiple photonic chiplets by photonic wire bonding (Figure 8n),<sup>309,310</sup> and mode conversion in on-chip waveguides using free-form tapers.<sup>311</sup> Lastly, 3D nanoprinted

refractive microlenses are of industrial interest for integration directly onto light emitters or sensors.<sup>312</sup>

Implementing 3D nanoprinted structures faces certain challenges not commonly encountered in planar lithography. For example, in multiheight metasurfaces shorter meta-atoms may experience a “shadowing effect” from taller neighbors altering their optical response. This can be mitigated by minimizing height differences or simulating the response of the complete metasurface with large-area algorithms.<sup>290,313</sup> Furthermore, it is challenging to scale 3D nanoprinted metasurfaces from the NIR to the visible spectrum, as subwavelength unit cell sizes are required to suppress loss to higher-order grating modes, though the resulting amplitude modulation can be intentionally leveraged for complex-amplitude metasurfaces.<sup>285</sup>

Lastly, mechanical stability must be considered as capillary forces act on adjacent elements of the structure while the developer evaporates during the final fabrication step.<sup>314</sup> Insufficient polymer cross-linking or too narrow geometries can result in structural collapse. Solutions include using higher laser powers, smaller hatching and slicing distances, low-surface-tension solvents (e.g., Methoxy-nonafluorobutane), or critical point drying.<sup>315</sup> Such structural collapse is particularly pronounced for metasurfaces, where the cross-section of each nanopillar is often smaller than  $1\text{ }\mu\text{m}^2$ . Therefore, the maximal feasible height of 3D nanoprinted metasurfaces currently stands at  $11\text{ }\mu\text{m}$  (pillar cross-section:  $550\text{ nm} \times 1600\text{ nm}$ ).<sup>286</sup> Ultrahigh aspect ratio structures such as light cages even require strand diameters in the micrometer range.<sup>298</sup>

To make mass-scale 3D nanoprinting economically viable, manufacturing costs need to be lowered - considering investments of several hundred thousand euros for a machine fabricating in a field-of-view of a few hundred micrometers. Two main approaches have been explored. First, fabrication can be parallelized using multifocal arrays with a recent demonstration using 2000 individually addressable focal spots generated via a digital micromirror device (DMD), achieving printing speeds of  $2 \times 10^6$  voxels/s.<sup>316</sup> Even higher printing speeds of  $1.4 \times 10^8$  voxels/s were demonstrated using a diffractive optical element generating 49 aberration-corrected foci in combination with a high scanning speed of 1000 mm/s (Figure 8h).<sup>272</sup>

A second target is the expensive femtosecond laser. Here, a novel approach uses two-step rather than two-photon absorption, increasing the likelihood of the nonlinear process while maintaining the square dependence on intensity.<sup>256</sup> This enables the use of significantly cheaper continuous-wave (CW) lasers (405 nm laser diode, power: 0.1 mW).

Another strategy to increase writing speed and reduce cost is light-sheet 3D microprinting.<sup>317</sup> Here, one CW laser illuminates a single layer of the PR, while a second CW laser of a different color projects an intensity pattern onto this layer. The used two-step photoinitiator acts as an “AND gate” resulting in the polymerization of a whole layer at once. With this technique printing speeds of  $7 \times 10^6$  voxels/s were reached (voxel size:  $500\text{ nm} \times 2200\text{ nm}$ ).

Lastly, increases in resolution to subdiffraction levels have been pioneered about a decade ago using stimulated-emission depletion (STED), where a depletion beam returns excited photoinitiator molecules to their ground state at the edges of the laser focus. STED 3D nanoprinting has achieved single suspended nanowires with features as small as 9 nm and a lateral resolution of 52 nm,<sup>318</sup> while 3D woodpile structures

reached feature sizes of 125/175 nm with a resolution of 275/290 nm in the lateral and axial directions, respectively.<sup>270</sup> As a further advantage, this method allows to use higher laser powers, reducing sensitivity to laser power fluctuations.<sup>319</sup> Additionally, beam engineering involving a radially polarized beam can be used to tune the aspect ratio of the voxel, resulting in a decrease of its volume by 71%.<sup>320</sup>

Combining all these approaches could significantly reduce fabrication costs and achievable feature sizes, opening avenues for various industrial and research applications such as integrated optical components for telecommunication or consumer devices, point-of-care diagnostics, chemical analysis, biomedical engineering, or material science. Looking further ahead, advances in 3D nanoprinting could lead to a new era of 3D photonic architectures, affecting applications as far as optical neural networks,<sup>321</sup> or optical analog computing.<sup>322</sup>

## 10. AEROSOL PRINTING

*Wook Jung and Mansoo Choi*

The aerosol 3D nanoprinting technique offers significant advantages in the field of nanophotonics. Its practical capability for parallel printing of periodically arranged complex shapes of 3D nanostructures in atmospheric conditions makes it a powerful 3D nanoprinting tool for diverse photonics applications. Furthermore, owing to the direct printing of subwavelength scale metallic 3D nanostructures, fabricated 3D nanostructures interact with light without requiring post-processing of the structures.

Aerosol 3D nanoprinting relies on self-focusing electric field lines to guide and print charged aerosols at desired position. In this process, generating funnel-shaped electric field lines that focused as a nanoscale bundle is essential. The formation of these funnel-shaped electric field lines begins by fabricating a dielectric layer prepattered Si substrate from photo- or electron beam lithography. By applying a negative electric potential to the conductive Si substrate, introduced cations accumulate on the dielectric layer, giving rise to localized repelling electric field regions termed the cushion.<sup>323</sup> This repelling cushion distorts the local electrostatic environment, leading to focusing electric field lines directed to the center region of the opened area of Si substrate (Figure 9a). Soon after the arrival of positively charged aerosols, they are printed only in the center region on Si substrate following along the focusing electric field lines (Figure 9b), thereby enabling nanoscale printing of charged aerosols under atmosphere.<sup>324</sup>

Kim et al.<sup>324</sup> first demonstrated the principle of the aerosol 3D nanoprinting technique. Figure 9c shows an array of 75 nm resolution dots printed at the center of 230 nm circular dielectric apertures with 10 nm-sized Ag charged aerosols. As shown in Figure 9c, an array of dots, with a resolution of 75 nm, was printed at the center of 230 nm circular dielectric apertures using 10 nm-sized Ag charged aerosols. This outcome corresponds to Figure 9b, depicting the early stage of the charged aerosol printing. By comparing the printing results using the substrate with or without cations, they proved the charged aerosol focusing effect induced by local electric field modification. Prior to delivering the aerosols toward the substrate, a corona discharger<sup>325</sup> was employed to supply sufficient cations onto the dielectric layer, thereby forming the funnel-shaped electric field lines for high-resolution aerosol printing. Such an experimental technique is commonly employed for printing aerosols generated from electro-

spray,<sup>326,327</sup> and evaporation and condensation,<sup>324</sup> which may not supply adequate cations.

Since then, spark discharging<sup>328–330</sup> has become a preferred method for generating metallic charged aerosols due to their capability to produce aerosols of a few nanometers in size with narrow size distribution and sufficient cations. This has advantages for printing densified 3D nanostructures and establishing the electrostatic conditions required for nanoscale electric field line funnels. Even though charged aerosols and cations from the spark discharger are simultaneously introduced into the 3D nanoprinting chamber, cations with faster mobility<sup>325</sup> reach the vicinity of the negatively biased substrate before the aerosols do, thus accumulating on the dielectric layer and generating focusing electric field lines before charged aerosols approach.<sup>331</sup>

The continued printing of charged aerosols under the given electric field, as illustrated in Figure 9b, results in the formation of 3D nanostructures. As shown in Figure 9d, incoming charged aerosols are continuously deposited within the electric field lines touching the Si surface. The geometries of the printed 3D nanostructure can be controlled by manipulating the shape and distance of patterns in the dielectric layer,<sup>331–333</sup> along with adjusting the surface charge density induced by the accumulation of cations and applied electric potential to the substrate.<sup>334</sup> These factors play a crucial role in shaping the electric field line funnel and cushion, ultimately determining the final form of the 3D nanostructures.<sup>324</sup>

An array of four-petal flower-shaped Cu 3D nanostructure (Figure 9e) is printed using a cross patterned dielectric layer,<sup>331</sup> visually depicting the funnel-shaped electric field lines in Figure 9d. These structures exhibit localized surface plasmons between neighboring petals, leading to a significant enhancement of surface-enhanced Raman spectroscopy (SERS) signals, enabling single molecule detection<sup>331,332</sup> (Figure 9f). Additionally, by utilizing a multipin spark discharger, we expanded the printing area, demonstrating flower-shaped Ag 3D nanostructures over a 25 cm<sup>2</sup> substrate.<sup>335</sup>

Our technique offers scalability, as the funnel-shaped electric field line bundles can be efficiently formed across any substrate size. By supplying charged aerosols to substrates with these field line bundles, our method allows for precise and uniform 3D nanostructure printing, regardless of the area being printed. This scalability is particularly beneficial for larger-scale production, overcoming the area limitations seen in other printing techniques.

Figure 9g demonstrates the stacking of flower-shaped 3D nanostructures.<sup>336</sup> After printing the first layer of the structures, the dielectric layer is removed, followed by patterning of a second layer above the existing flower-shaped 3D nanostructures. Subsequently, charged aerosol printing process fabricates the second layer of 3D nanostructures. FE-SEM image shows vertically stacked flower-shaped 3D nanostructures after removal of the dielectric layer. Those vertically stacked 3D nanostructures exhibit intensified Raman peaks, displaying relative enhancement factors approximately 5 times than monolayer 3D nanostructures.

By patterning the dielectric layer with an array of hole pairs with 2.6 μm periods, the asymmetric surface area between holes causes disparities in cushion size (or repelling force from accumulated cations) because of repelling Coulomb force from accumulated cations.<sup>334</sup> This results in incoming electric funnels to slant toward each hole in hole pair. As a result,

16°-angled pillars are printed and connected with floating nanorod parallel to the substrate. Figure 9h shows the π-shaped plasmonic structures from printing of Au charged aerosols after removing the dielectric layer.<sup>334</sup> In this printing process, it is crucial to control the surface charge density of the dielectric layer, considering the ratio of surface area of dielectric layer resulting from spacing the dielectric layer between the holes. This regulation can be achieved by adjusting the applied electric potential to the substrate, which also allows for the controlling tilt angle of the structure under different periodic conditions. Notably, this technique enables the fabrication of complex 3D nanostructures at a remarkably low cost, making it suitable for mass production. The geometrical configuration of π-shaped plasmonic structures facilitates the dual-resonance mode within a single structures. The dual-resonance mode encompasses polarization-sensitive localized surface plasmon resonances (Figure 9i) and azimuthal-angle sensitive quasi-bound states in the continuum (Figure 9j). These optical characteristics offer a promising application of angle-resolved polarimetry.

The prepatterned substrate serves as a foundation for printing of diverse 3D nanostructures, yet its fixed electrostatic field limits the geometries of the structures. By replacing the dielectric layer with a dielectric stencil mask, known as a focusing mask, it is possible to achieve the same focusing of charged aerosols and printing of 3D nanostructures, eliminating the need for substrate surface modification.<sup>326</sup> The mask can be floated to allow direct printing of charged aerosols on the substrate.<sup>337</sup> The stationary floating mask is positioned above the negatively biased substrate, with a piezoelectric 3D nanostage enabling translation of the substrate in three dimensions. The formation of focusing electric field lines is facilitated by the accumulation of cations around the apertures in the floating dielectric mask. This configuration combining nanoscale movement of the substrate in three dimensions provides nanoscale-focused charged aerosol jets directing to the moving substrate, enabling 3D shape controllability of the desired structures. During the printing process of 3D nanostructures, the sharp tips of the metallic nanostructures converge electric field lines in between the mask and the substrate, inducing their self-focusing. These self-focused electric field lines guide charged aerosols to the tips, even when moving in 3D space, thus enabling the real 3D nanoprinting that can realize complex 3D nanostructures in a parallel fashion under atmospheric conditions (Figure 9k).<sup>338</sup> For instance, Figure 9l displays vertical SRRs (vSRRs),<sup>339</sup> exhibiting a magnetic dipole resonance under linearly polarized incident light. Numerical simulation has demonstrated that the magnetic dipole resonance is triggered by magnetic current density (Figure 9m). Measured reflectance spectra showed a resonant wavelength of 19.8 μm, consistent with simulation results (Figure 9n). To verify the reproducibility, multiple experiments were conducted to print 3D nanostructures and measure their dimensions, including size, length, and angle. The minimal variations in these parameters confirm the high reproducibility of the technique, which is beneficial for nanophotonics applications that require precise control over structure shapes for consistent optical performance.

In recent advancements, aerosol 3D nanoprinting has been technically progressed by adopting an electrified mask, replacing the dielectric floating mask.<sup>337,340</sup> This electrified mask consists of a metal-coated dielectric layer onto which an electric potential is applied. In this approach, the difference in

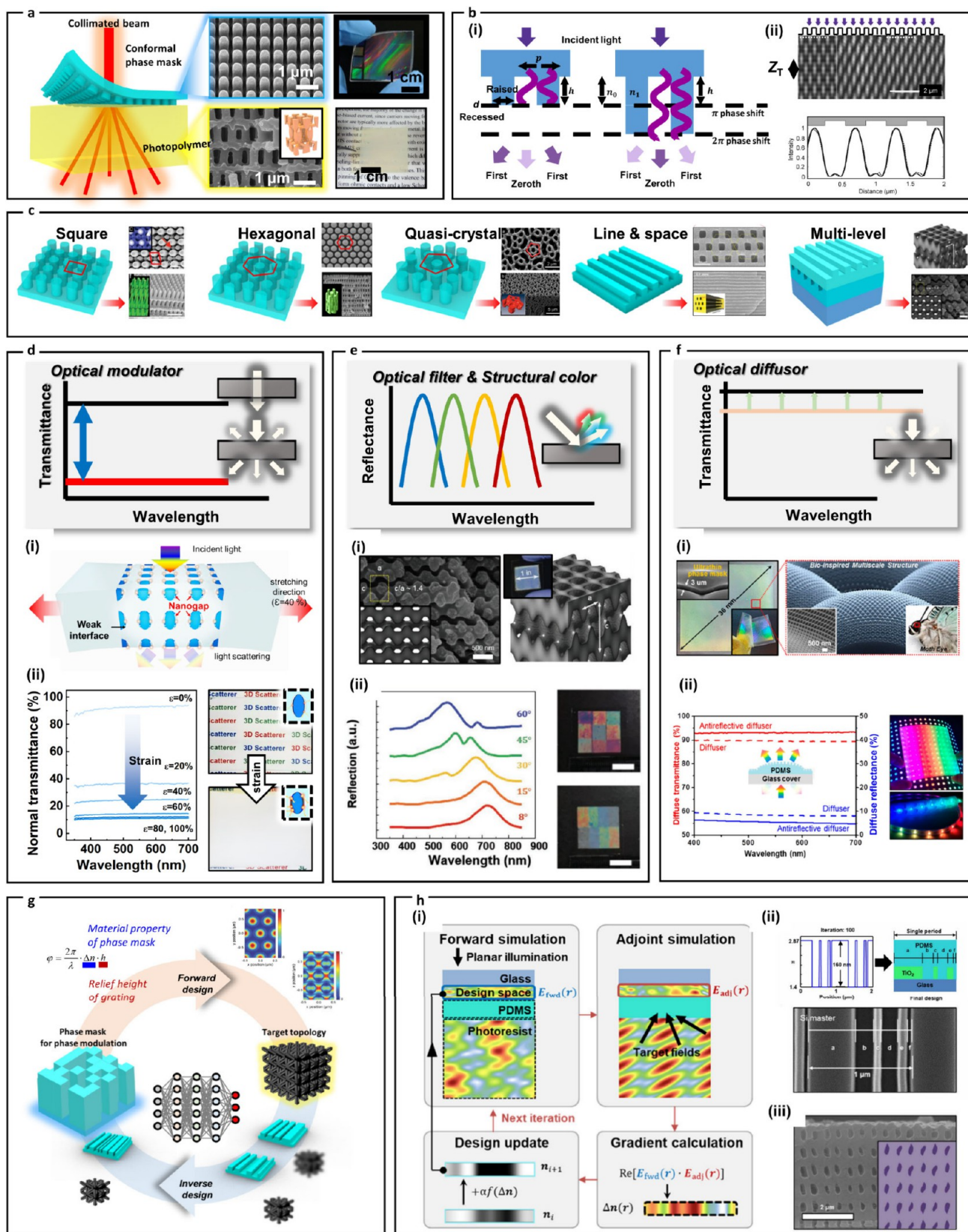


**Figure 10. PnP for nanophotonics.** (a) Schematic of the PnP process and SEM and digital images of the conformal phase mask and 3D nanostructures obtained by PnP.<sup>374</sup> Adapted with permission from ref 374. Copyright 2012 Springer Nature. (b) Concept images of (b.i) a binary phase mask illustrating  $\pi$  phase shift condition for maximized diffraction efficiency<sup>352</sup> and (b.ii) the Talbot effect.<sup>347</sup> Adapted with permission from ref 352. Copyright 2014 Wiley-VCH. Adapted with permission from ref 347. Copyright 2007 ACS. (c) Type of binary phase masks and resultant 3D topologies using PnP.<sup>343,346,353,354,356</sup> Adapted with permission under a Creative Common CC BY License from ref 343. Copyright 2004 National Academy of Sciences. Adapted with permission from ref 346. Copyright 2021 Springer. Adapted with

Figure 10. continued

permission from ref 353. Copyright 2008 ACS. Adapted with permission from ref 354. Copyright 2019 Wiley-VCH. Adapted with permission from ref 356. Copyright 2022 AAAS. (d) Optical modulator achieved by PnP.<sup>379</sup> (d.i) Schematic illustration of mechanical scatters using 3D nanocomposites. (d.ii) Spectra of normal transmittance of the 3D scatters loaded with different lateral tensile strains and digital image of the 3D scatter before and after applying lateral strain. Adapted with permission from ref 379. Copyright 2020 Wiley-VCH. (e) Concept of optical filter realizing structural color using PnP.<sup>354</sup> (e.i) Cross-sectional SEM image and simulated image of the 3D woodpile photonic crystal formed by PnP (inset: digital image of an inch-scale photonic crystal film). (e.ii) Reflection spectra of the woodpile photonic crystals at incident light angle, and digital images of inch-scale pixelated multicolor patterns. Adapted with permission from ref 354. Copyright 2019 Wiley-VCH. (f) Application of optical diffusor applying PnP on the nonflat surface.<sup>379</sup> (f.i) Digital and SEM image of the hierarchical antireflective film obtained by PnP on curved surfaces. (f.ii) Left: Diffuse transmittance and reflectance spectra of the antireflective diffusor in the visible range, Right: Digital images of the diffusion sheet on the LED arrays showing antireflective diffuser film. Adapted with permission from ref 379. Copyright 2022 ACS. (g) Schematic illustration of forward and inverse design diffraction of PnP process.<sup>380</sup> Adapted with permission from ref 380. Copyright 2016 ACS. (h) Realization of target topology using an Adjoint method,<sup>355</sup> (h.i) One iteration of the Adjoint simulation to obtain optimized phase mask design for target topology, (h.ii) Geometry of the nontrivial phase mask, consisting of TiO<sub>2</sub> and PDMS layers, obtained by Adjoint simulation, (h.iii) Resultant cross-sectional SEM image of the square nanochannel array (inset: simulated image obtained by FDTD). Adapted with permission under a Creative Common CC BY License from ref 355. Copyright 2022 AAAS.

electric potential between the electrified mask and the substrate ( $\Delta V$ ) allows for precise adjustment of the diameter of funnel-shaped focusing electric field lines and, consequently, the diameter of charged aerosol jets (Figure 9o). This level of control enables manipulation of voxel sizes of 3D nanostructures during printing process by regulating the electric field strength ( $E = \Delta V/d$ , where  $d$  presents the z-axis distance between the mask and the substrate) without the need of providing exact amount of ions. As demonstrated in Figure 9p, multivoxel-sized vertical nanopillars with diameters of 300 and 450 nm are achieved by decreasing  $E$  from 50 V/ $\mu\text{m}$  to 25 V/ $\mu\text{m}$ . Furthermore, continuous increase of  $E$  from 20 V/ $\mu\text{m}$  to 36.4 V/ $\mu\text{m}$  results in dynamic voxel size variations in 3D nanohelices, as shown in Figure 9q. The voxel size manipulation of 3D nanostructure can be employed for optimizations of plasmonic responses in nanophotonic device design.<sup>341,342</sup>

Future development of our aerosol 3D nanoprinting techniques aims at downscaling and upscaling the process while maintaining precise control over electric field configurations. These advancements may enable the exploration of uncovered applications in nanophotonics.

## 11. PROXIMITY-FIELD NANOPATTERNING

Gwangmin Bae, Haomin Chen, and Seokwoo Jeon

Proximity-field nanopatterning (PnP) that generates 3D interference patterns provides an unconventional and facile route for rapid fabrication of intricate periodic 3D nanostructures. With a single exposure step for only nanoseconds to seconds, highly ordered structures can be fabricated in inch scales with a resolution of  $\sim$ 100 nm.<sup>343–345</sup> In PnP, there are three main elements: a single collimated beam, an elastomeric transparent phase mask with surface gratings, and photo-polymer that can record the holographic pattern generated by the mask and transform it into material structures (Figure 10a).<sup>346,347</sup> Thanks to its softness, the phase mask can spontaneously form a conformal contact with PRs.<sup>348</sup> Compared to other 3D nanofabrication technologies, PnP features a simple optic setup, rapid and large-scale fabrication with high resolution and superior reproducibility. The conformal contact between the phase mask and PRs allows nanometer precision alignment in the out-of-plane direction, which is robust against environmental factors such as vibrations.<sup>346</sup> Meanwhile, the coherence requirement of the

light source is greatly relaxed, enabling the formation of 3D patterns even when using a UV lamp as the source.<sup>349,350</sup>

When a collimated beam is incident to the phase mask, the diffracted beams by the gratings interfere and generate 3D patterns periodically recurring along the axis of light propagation, which is known as the Talbot effect or self-imaging effect.<sup>351</sup> The pattern geometry is determined by phase mask parameters including relief diameter ( $d$ ), period ( $p$ ), relief depth ( $h$ ), and refractive index ( $n$ ). As shown in Figure 10b(i), incident light passing through the phase mask's raised and recessed areas undergoes a phase shift due to variations in optical path lengths.<sup>352</sup> Maximum patterning contrast can be achieved when this phase shift equals an odd multiple of  $\pi$ , rendering suppression of the zeroth order diffraction. The pattern typically displays constructive and destructive interference close to the grating's raised and recess, recurring along the direction of light propagation at a distance defined by

$$Z_T = \frac{\lambda}{1 - (1 - \lambda^2/p^2)^{0.5}} \approx \frac{2p^2}{\lambda} \quad (\text{when } \lambda/p \text{ is small}) \quad (2)$$

where  $Z_T$  and  $\lambda$  are Talbot distance and the incident wavelength, respectively (Figure 10b(ii)).

Since 2004 when PnP was demonstrated for 3D patterning for the first time,<sup>343</sup> the development of PnP in the phase mask design and the patterning strategies have brought about a series of lattices including body-centered tetragonal (BCT),<sup>343</sup> hexagonal closed packed (HCP),<sup>344</sup> quasi-crystal,<sup>353</sup> diamond,<sup>354</sup> and oblique 3D nanostructures,<sup>355</sup> along with tunable periodicity or density gradience (Figure 10c).<sup>350,356,357</sup> With such structural diversities, PnP has provided a platform to shed light on how the structural factors influence the mass transport dynamics in sensors,<sup>358–361</sup> the electron/ion kinetics in energy storage devices,<sup>346,357,362–368</sup> and the load-transfer behavior in mechanical structural materials.<sup>346,359,361,366,369–374</sup> There are several review papers elaborating on the overall principles of PnP<sup>346</sup> and summarizing the application of PnP for sensors,<sup>359,362</sup> energy storage devices,<sup>375</sup> and structural materials.<sup>372</sup> While these advancements impact multiple fields, PnP holds particular promise in controlling how the light across UV, visible, and NIR wavelengths interacts with materials because of the fabricated periodic structures with feature sizes and perio-

dencies ranging from hundreds of nanometers to microns.<sup>376</sup> Importantly, these structures can be endowed with a variety of materials possessing specifically designed optical properties, thanks to the material conversion techniques that are compatible with PnP.<sup>362,377</sup> Here, we scrutinize the unique opportunities provided by PnP in developing nanophotonic materials that regulate light, which opens up a wide array of applications in this field including optical modulators, filters, and diffusers.

First, optical modulators play a crucial role in nanophotonics, as they can dynamically alter their optical properties in response to mechanical strains.<sup>376</sup> A crucial requirement for these devices is the capability to maintain an initial homogeneity in  $n$  and to induce significant  $n$  mismatches upon external strains, thereby controlling light transmission efficiently. PnP fulfills these requirements by enabling the fabrication of nanostructures with tailororable  $n$ . For example, the study by Cho et al. fabricated 3D structures with ordered pores in a period of 600 nm.<sup>378</sup> Through material conversion, a nanocomposite composed of two interconnected PDMS networks, sandwiching a thin layer of alumina, was prepared. The seamless contact of the three phases endowed the nanocomposite with a high transmittance of ~90% for visible light. When strains were loaded, numerous air gaps were generated as the sites for multiple light scattering due to their much lower  $n$  (~1.0) than that of the matrix materials (~1.4 for PDMS). Thus, the transmittance decreased dramatically by 74% upon strain, while diffused transmittance and reflectance were increased (Figure 10d(i)). Following this, Chen et al. took a step further.<sup>379</sup> By replacing the alumina with silicon oxide ( $n \sim 1.4$ ) and inducing strain localization, the homogeneity of the  $n$  in the unstrained state was enhanced and the generation of air gaps upon strains was facilitated, giving rise to improved contrast of 82% (Figure 10d(ii)). The PnP-produced ordered 3D nanostructures here offered three key advantages for developing an advanced optical modulator: (i) enabled multiple light scattering for maximum transmission modulation, (ii) prevented air gaps from merging, maintaining the scattering sites, and (iii) ensured uniform optical properties across the modulator.

Moreover, considering its rapid fabrication of periodic 3D nanostructures, PnP is exceptionally powerful in realizing large-area optical filters that realize selective control of light over different wavelength. Photonic crystals, which are specially engineered materials with a periodic arrangement of dielectric or semiconductor components, possess photonic band structure that manipulates the flow of light in a manner analogous to how electronic crystals control the flow of electrons. These materials have a unique ability to control and manipulate the propagation of light waves, such as filtering specific wavelengths or guiding light in desired directions. However, challenges remain in quickly producing photonic crystals with high spatial resolution. PnP is a good candidate to efficiently produce photonic crystals in a large area for optical applications. In the work by Nam et al., large-scale full-color woodpile photonic crystals were fabricated to realize a wide range of structural colors (Figure 10e).<sup>354</sup> They proposed a multilevel phase mask consisting of two orthogonal line-and-space phase masks and a spacer to produce large-scale woodpile topologies (~1 in.<sup>2</sup>) by a single exposure step. Fabricated 3D nanostructures using multilevel phase mask exhibited woodpile symmetry with 300 nm of planar periodicity and 716 nm of vertical periodicity, confirming

high correspondence of aspect ratio of ideal woodpile symmetry ( $c/a \sim 1.4$ ) (Figure 10e(i)). When compared to alternative methods used to manufacture woodpile photonic crystals with submicron periodicity, it is evident that PnP offers benefits in terms of both processing time (~tens of seconds) and production area (~few inches). The reflectance spectra of the inch-scale photonic crystals demonstrated that structural colors can be tailored by adjusting the incident light angle, and pixelated multicolor patterns were exhibited in a large area by adjusting the exposure dose (Figure 10e(ii)).

Lastly, PnP not limited to flat substrates has been demonstrated to pattern on curved substrate to realize antireflective diffusors based on hierarchical nanostructures mimicking the moth-eye topologies (Figure 10f).<sup>380</sup> Multiscale hierarchical structures can be produced using an ultrathin phase mask (~3  $\mu\text{m}$ ) that conformally contacts a nonflat substrate with a low radius of curvature (~28  $\mu\text{m}$ ). PnP enables large-area production (~16 in.<sup>2</sup>) of the hierarchical topology which perfectly mimics moth-eye structures in a single exposure step (Figure 10f(i)). Fabricated hierarchical nanosheet exhibited improved diffuse transmittance and correspondingly reduced diffuse reflection over the visible light range compared to conventional antireflective films without hierarchical topology (Figure 10f(ii)). Bioinspired hierarchical topology and large-area production technique can be applied in various optoelectronic applications, including light trapping for solar cells, projection screens, and diffuser sheets for light emitting diodes (LEDs).

Recently, there has been an effort to expand the range of topological diversity achievable through PnP using computing algorithms.<sup>381</sup> Traditionally, the selection of phase mask geometries for the fabrication of 3D nanostructures preceded, which progressed toward realizing the resulting 3D nanostructure topology through optical analysis (referred to as forward design in Figure 10g). However, current research approaches this from the opposite direction, utilizing computing algorithms to first select the optimal 3D nanostructures for a given research area and then inversely calculate the phase mask geometries needed for nanostructure fabrication (referred to as inverse design in Figure 10g). For example, Nam et al. investigated a new type of design platform for developing nontrivial topology and motifs in 2D lattices.<sup>355</sup> They proposed an adjoint method for PnP to calculate the geometries of the phase mask, allowing the target topology and motifs to be realized in 2D space. The adjoint method is an efficient design tool used to calculate the gradients of functions with respect to the optical parameters and to derive optimal data fulfilling the objective.<sup>382,383</sup> As a proof of concept, a square array nanopattern was set as a target topology, which had been hard to realize using normal incident light exposure. A new type of phase mask consisting of TiO<sub>2</sub> ( $n \sim 2.87$ ) and PDMS ( $n \sim 1.40$ ) was selected to maximize the difference in  $n$  and conformally contact to PR. By virtue of the symmetry of Maxwell's equations, a gradient of the figure of merit (FoM) function can be obtained by only two simulations, and the phase mask geometry which realizes the target interference in the design space is calculated by following the optimized gradient direction of the FoM (Figure 10h(i)). After iterations, the optimized geometry of the binary phase mask consisting of TiO<sub>2</sub> and PDMS was derived (Figure 10h(ii)), and the square array of the 2D lattices can be realized using the optimized phase mask without changing the angle of the incident light (Figure 10h(iii)).

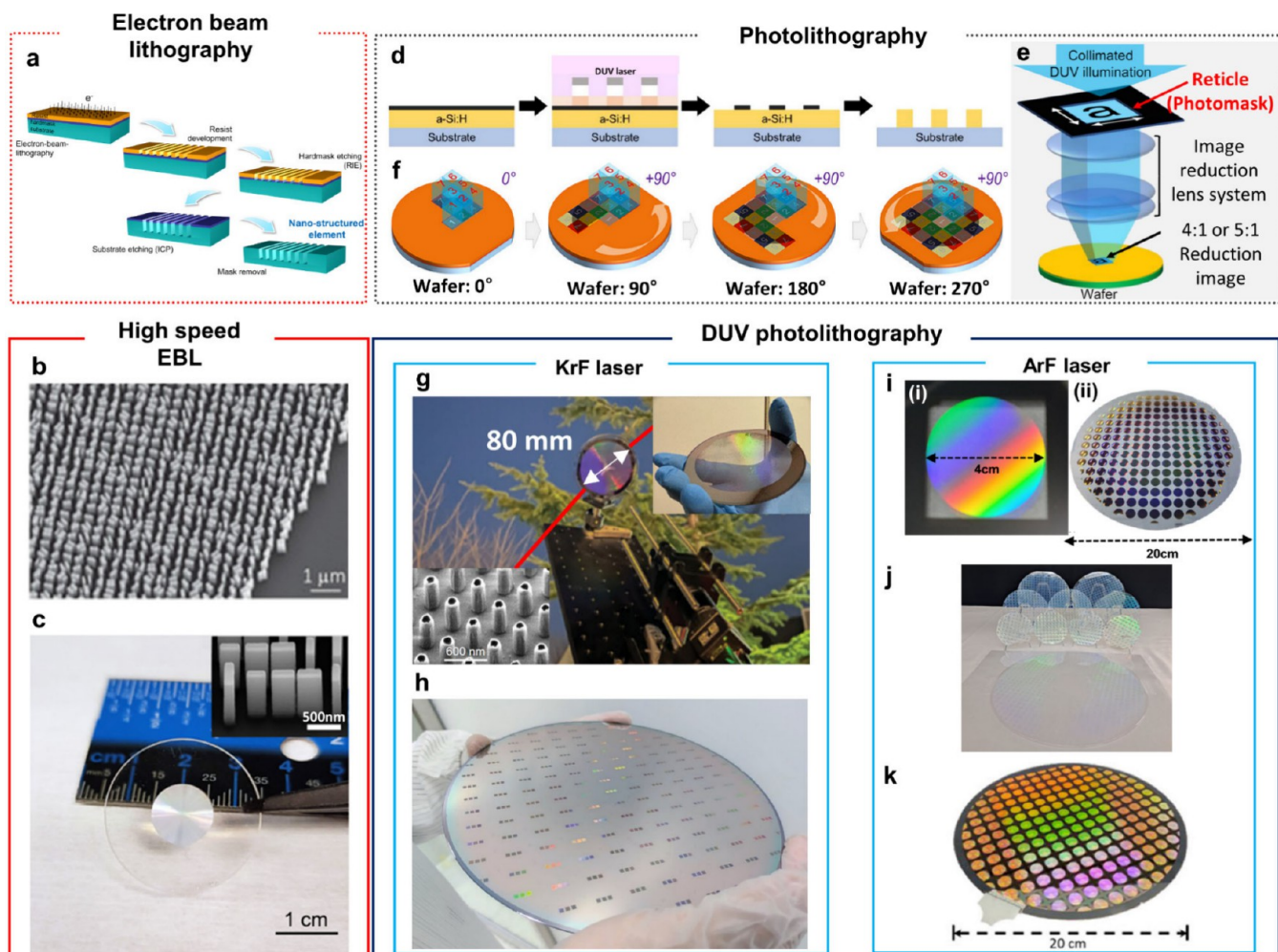


**Figure 11. Large-area lithography.** (a) Schematic of the fabrication process based on the EBL.<sup>390</sup> Adapted with permission from ref 390. Copyright 2023 SPIE-Publications. (b) SEM image of the fabricated  $\text{TiO}_2$  nanofins.<sup>391</sup> Adapted with permission License from ref 391. Copyright 2021 AAAS. (c) A 1 cm-diameter RGB achromatic metalens fabricated using high-speed EBL,<sup>392</sup> scale bar: 1 cm. (Upper inset) The SEM image of the nanostructures, scale bar: 500 nm. Adapted with permission under a Creative Common CC BY License from ref 392. Copyright 2022 Springer Nature. (d) Schematic of the manufacturing process based on the DUV photolithography.<sup>400</sup> Adapted with permission from ref 400. Copyright 2024 Wiley-VCH. (e) Drawing of DUV photolithography system. A DUV beam is incident on a reticle which has the desired pattern and demagnified by image reduction lenses or immersion system for higher resolution.<sup>401</sup> Adapted with permission from ref 401. Copyright 2024 ACS. (f) Diagram of large area metalens by rotating and aligning the reticle set.<sup>401</sup> Adapted with permission from ref 401. Copyright 2024 ACS. (g) A 80 mm large area metalens working as the objective and focusing lens for the telescope.<sup>402</sup> (Upper inset) A photograph of the fabricated wafer-scale metalens. (Lower inset) The SEM image of meta-atoms, scale bar: 600 nm. Adapted with permission from ref 402. Copyright 2023 ACS. (h) Mass manufactured metalens on 8-in. wafer for full-duplex metabroadcasting communication system network.<sup>403</sup> Adapted with permission from ref 403. Copyright 2022 Wiley-VCH. Adapted with permission from ref 81. Copyright 2023 Springer Nature. (i). (i.i) Photograph of 4 cm reticle fabricated using high-speed EBL. (i.ii) Mass manufactured 1 cm  $\text{ZrO}_2$  atomic layer–polymer hybrid metaleenses on 8-in. wafer operating in the UV region.<sup>33</sup> Adapted with permission from ref 33. Copyright 2024 ELSEVIER. (j) Mass manufactured 1 cm  $\text{TiO}_2$  atomic layer–polymer hybrid metaleenses on 12-in. wafer operating in the visible region.<sup>81</sup> Adapted with permission from ref 81. Copyright 2023 Springer Nature. (k) Mass manufactured 1 cm polarization-independent metaleenses on 8-in. wafer operating in the NIR region.<sup>400</sup> Adapted with permission from ref 400. Copyright 2024 Wiley-VCH.

This advancement in PnP, particularly through inverse design and computational methods, opens the door to a myriad of potential applications in nanophotonics. For example, by introducing asymmetry to the periodicity, structures can be engineered to exhibit directional optical responses. The fabrication of 3D chiral structures could pave the way for new types of optical modulators that can regulate not only the transmittance but also the polarization of light. Additionally, engineering a large scale diamond topology could allow for the realization of complete photonic band gaps, offering unprecedented control over light propagation and

confinement. These advancements highlight the promising future of PnP in 3D nanofabrication, positioning it as a versatile tool capable of empowering structural studies and practical applications across various scenarios, thanks to its ability to combine high design freedom with the benefits of mass production and rapid fabrication. Although the current topology and motifs of the target 3D nanostructures are restricted in 2D space, adjusting other calculation tools and introducing multilevel phase modulations could expand the range of producible 3D topologies, thereby simultaneously achieving high design freedom and mass-producibility. In

short, PnP is a promising candidate for 3D nanofabrication that can empower the structural study and practical use in a variety of application scenarios thanks to its versatility in mass production, fabrication speed, and structural diversity.

## 12. LARGE-SCALE LITHOGRAPHY

*Jaekyung Kim, Eunji Lee, and Junsuk Rho*

Large-scale lithography is essential for commercialization as it enables mass production and large size manufacturing, making it ideal for integration into various devices and systems. To effectively use metasurfaces with advanced functionalities in actual devices, ensuring high resolution is also crucial.<sup>384</sup> Fabrication resolution is related to the ability to precisely construct subwavelength meta-atoms, which are the fundamental building blocks of metasurfaces.<sup>385–387</sup> While conventional EBL can achieve the required resolution, it is limited by low throughput and difficulty in scaling up due to its slow speed and high cost. As a result, the production of metasurfaces is constrained to dimensions within a few millimeters.<sup>293</sup> This bottleneck has restricted the practical application and scalability of metasurface-based devices. Significant efforts have been made to develop alternative lithography techniques that can overcome these existing limitations.<sup>388,389</sup> Among these techniques the development of high-speed EBL and deep UV (DUV) photolithography has especially facilitated the transition of metasurfaces from laboratory innovations to mainstream optical devices, unlocking their full potential for a wide range of applications.

The conventional EBL process involves resist exposure, development, hard mask etching, target material etching, and mask removal<sup>390</sup> (Figure 11a). Although electron beam lithography offers high resolution, its low beam current leads to prolonged patterning times limiting its applicability in fabricating large-area metasurfaces. To address this issue, high-speed EBL with a beam current ( $\sim$ nA) higher than that of conventional EBL ( $\sim$ pA) has been used to fabricate large-area metasurfaces on mm and cm scales.<sup>391,392</sup> Utilizing higher currents increases electron beam energy and charge density, facilitating faster modification of resist and enhancing pattern generation speed.<sup>393</sup> However, higher currents can reduce resolution due to electron beam scattering and thermal effects,<sup>394</sup> making it essential to optimize the current to achieve the resolution suitable for the pattern size.<sup>395</sup> For example, using high-speed EBL, researchers fabricated a 2 mm diameter RGB achromatic metalens composed of TiO<sub>2</sub> nanofins<sup>391</sup> (Figure 11b). The fabrication process involved standard steps similar to conventional EBL processes, including resist exposure, development, TiO<sub>2</sub> film deposition using ALD, removal of excessively grown TiO<sub>2</sub> layer via RIE, and lift-off of the remaining resist. To overcome the computational limitations of forward design for large-area metasurfaces, the adjoint method, an inverse design approach, has been proposed. Using this approach, a 1 cm diameter RGB achromatic metalens with a resolution of 10 nm has been fabricated<sup>392</sup> (Figure 11c). While high-speed EBL allows the fabrication of large-area metasurfaces, its reliance on direct writing has limited mass production.

To further address scalability, researchers are exploring DUV photolithography. This leverages advancements in excimer laser technology to overcome the resolution constraints of conventional photolithography and fabrication speed of EBL. Conventional photolithography resolution has been limited by the Rayleigh criterion, which states that resolution is

proportional to half of the source wavelength.<sup>396</sup> However, advancements in excimer laser technology, leveraging shorter wavelength sources like KrF<sup>397</sup> and ArF<sup>398,399</sup> have enabled more precise patterning processes. This method allows for rapid patterning through a single exposure, employing light exposure patterning rather than direct writing like EBL. This method employs light exposure patterning through a single exposure, which enables more rapid patterning compared to the direct writing like EBL. These improvements in speed and precision have been achieved while maintaining a fabrication process that closely resembles traditional photolithography methods<sup>400</sup> (Figure 11d). The DUV photolithography process involves hard mask deposition on the target material, spin-coating the PR, and transferring the reticle pattern using an excimer laser. This is followed by development to serve as an etch mask for the hard mask, hard mask etching, residual PR removal and finally target material etching to achieve the desired pattern. In this process, the reticle pattern plays a key role as it directly dictates the resolution of the final pattern. The reticle is typically fabricated using high-speed EBL to achieve the required resolution. To achieve higher resolution, advanced lithography techniques such as immersion lithography or reduction lithography are employed<sup>401</sup> (Figure 11e). Immersion lithography replaces air with higher  $n$  materials such as water or oil, while reduction lithography uses advanced lens systems. Despite some drawbacks related to cost and contamination risks, the trade-offs are justified by the substantial improvements in fabrication precision. By applying reticle-based process, the larger metasurfaces up to 100 mm in diameter have been achieved by rotating the reticle set<sup>401</sup> (Figure 11f). After loading the wafer at 0 degrees, the reticle set of 1–7 is exposed. Then, the wafer is rotated by 90 deg and the reticle set of 2–7 is exposed, excluding the center reticle 1. This process is repeated by rotating the wafer 180 and 270 deg to create an expanded size metalens. Despite conducting several exposures, the alignment marks have allowed for an alignment error to be under 45 nm. Automating the alignment and exposure reduces the processing time to less than 20 min per wafer. This is about 450 times faster than the time it takes to produce the same size with typical high-speed EBL, bringing it closer to commercialization.

The 248 nm KrF laser photolithography can be applied to both large area and mass production based on the above scheme. An 80 nm diameter metasurface for a telescope has been proposed using the rotating reticle method<sup>402</sup> (Figure 11g). Despite this large fabrication process, alignment error was kept to less than 1  $\mu$ m, resulting in diffraction-limited focal spot sizes and over 80% peak focusing efficiency at 1450 nm. Additionally, for mass production, it can be performed by repeatedly exposing and progressively stepping on the wafer<sup>403</sup> (Figure 11h). Here 2 mm by 2 mm beam-steering metasurfaces based devices for optical wireless broadcasting communication links have been fabricated on an 8-in. wafer. However, KrF laser photolithography has mostly been used in the NIR due to its relatively large diffraction limit size. Although it has been extended to the visible, it requires a more precise process to further expand its application range to the UV region. To achieve high NA for the metalens and high-performance wavefront shaping, reducing the gap between meta-atoms is necessary. Therefore, research is actively underway to apply an ArF excimer laser to increase resolution and enable mass production. By using this method to create master molds for NIL, recent studies are increasingly focusing on using different

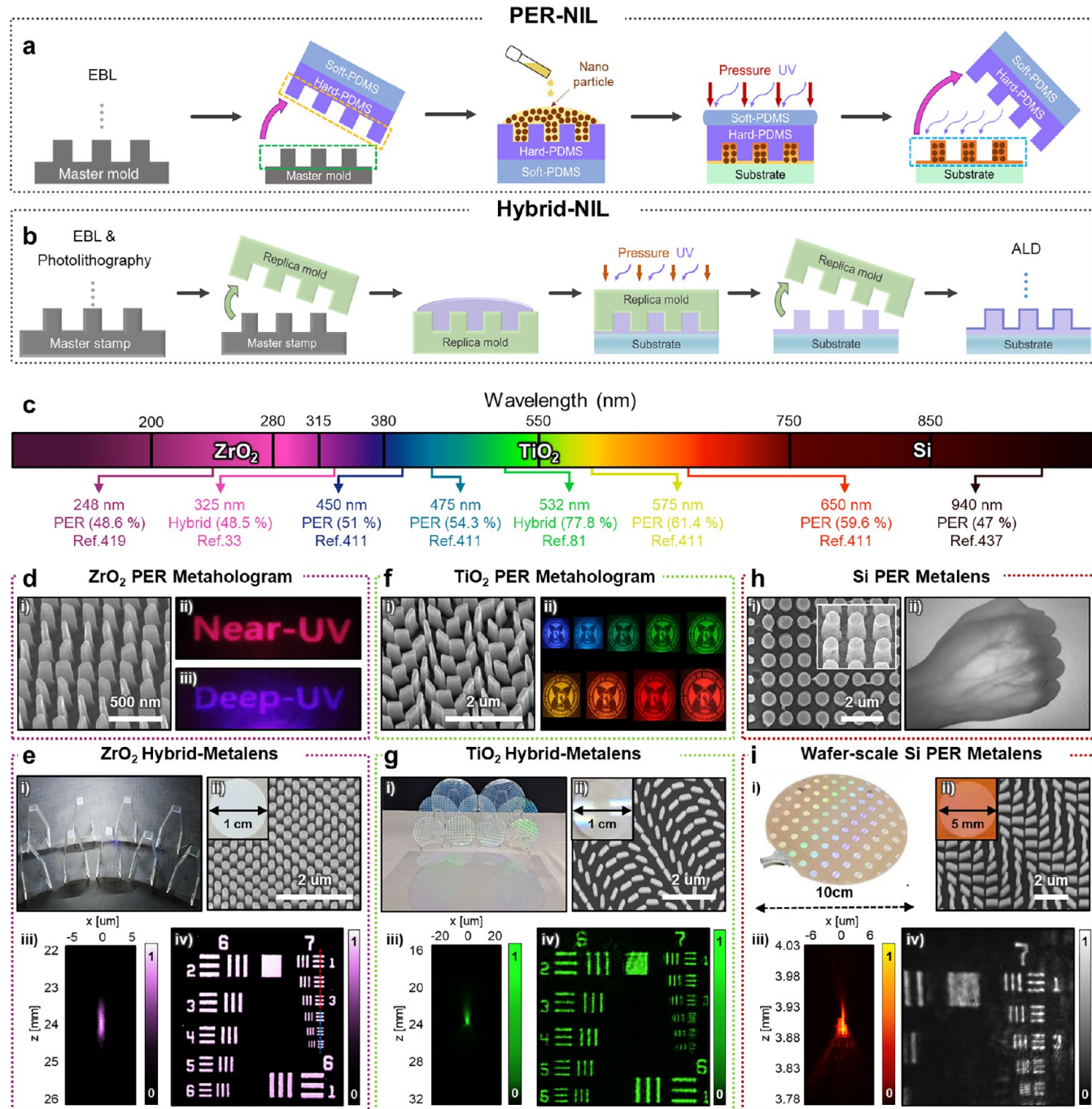


**Figure 12.** Nanoimprinting technology for fabrication of high- $n$  metasurfaces. (a) Schematic of procedure of particle-embedded-resin based nanoimprint lithography (PER-NIL). (b) Schematic of procedure of hybrid atomic layer deposition (ALD)-NIL (hybrid-NIL). (c) Reported measured efficiency depending on the working wavelength. (d) (d.i) Scanning electron microscopy (SEM) image of fabricated metaholos through ZrO<sub>2</sub> PER-NIL. Measured image of the holograms designed for (d.ii)  $\lambda = 325$  nm and (d.iii)  $\lambda = 248$  nm.<sup>419</sup> Adapted with permission under a Creative Common CC BY License from ref 419. Copyright 2024 Springer Nature. (e) (e.i) Image of manufactured 1 cm UV metalenses on 4-, 6-, and 8-in. wafer. (e.ii) SEM image of the fabricated 1 cm UV metalens through ZrO<sub>2</sub> hybrid-NIL. Inset: Photograph of the fabricated 1 cm metalens. (e.iii) Experimental intensity distributions in the  $x$ - $z$  plane and (e.iv) captured images of a negative 1951 USAF resolution target with the fabricated 1 cm UV metalens at a wavelength of 325 nm.<sup>33</sup> Adapted with permission from ref 33. Copyright 2024 Science Direct. (f) (f.i) SEM image of fabricated metaholos through TiO<sub>2</sub> PER-NIL. (f.ii) Measured images of the holograms with wavelengths ranging from 450 to 650 nm.<sup>411</sup> Adapted with permission from ref 411. Copyright 2022 Wiley-VCH. (g) (g.i) Image of manufactured 1 cm metalenses on 4-, 6-, 8-, and 12-in. wafer. (g.ii) SEM image of the fabricated 1 cm metalens through TiO<sub>2</sub> hybrid-NIL. Inset: Photograph of the fabricated 1 cm metalens. (g.iii) Experimental intensity distributions in the  $x$ - $z$  plane and (g.iv) captured images of a negative 1951 USAF resolution target with the fabricated 1 cm UV metalens at a wavelength of 532 nm.<sup>81</sup> Adapted with permission from ref 81. Copyright 2023 Springer Nature. (h) (h.i) SEM image of fabricated NIR metalenses through Si PER-NIL. Inset: Magnified image of the SEM image. (h.ii) Captured image of the veins underneath the human hand using NIR metalens based camera.<sup>437</sup> Adapted with permission from ref 437. Copyright 2020 ACS. (i) (i.i) Image of fabricated 5 mm metalenses on a 4-in wafer. (i.ii) SEM image of the fabricated metalens through Si PER-NIL. Inset: Photograph of the fabricated 5 mm metalens. (i.iii) Experimental intensity

Figure 12. continued

distributions in the  $x$ - $z$  plane and (i.iv) captured images of a negative 1951 USAF resolution target with the fabricated 5 mm metalens at a wavelength of 940 nm.<sup>82</sup> Adapted with permission from ref 82. Copyright 2024 Wiley-VCH.

materials tailored to specific operating wavelengths. In the UV region, 1 cm<sup>33</sup> scale metalenses composed of high-index zirconium dioxide ( $ZrO_2$ ) atomic layer–polymer hybrid structures have been mass-produced on 8" wafer (Figure 11i).<sup>33</sup> First, a 4 cm reticle has been fabricated using high-speed EBL for mass production of UV metalens (Figure 11i-(i)). Subsequently, an ArF immersion scanner has been utilized to achieve a high resolution of 40 nm scale and NIL has been utilized to reduce the wafer-scale production costs (Figure 11i-(ii)). Additionally, to compensate for the efficiency reduction caused by the low  $n$  of the NIL resin, high-index  $ZrO_2$  atomic layer in UV region has been coated to make strong light confinement. In the visible region, 1 cm scale high-index  $TiO_2$  atomic layer–polymer hybrid metalenses have been fabricated, with hundreds of them on a single 12" wafer<sup>81</sup> (Figure 11j). The ArF immersion scanner and NIL have been utilized exactly the same way as in Figure 11i. Additionally, high-index  $TiO_2$  atomic layer in visible region has been coated on the resin-based nanostructures for realizing strong light confinement. In NIR region, 1 cm polarization-independent metalenses composed of hydrogenated amorphous silicon (a-Si:H) cylinders have been mass-produced on 8" wafer<sup>400</sup> (Figure 11k). ArF dry scanner has been utilized instead of immersion scanner to save fabrication costs, and since metalenses operate in the NIR region, the resolution of the ArF dry scanner was sufficient to make nanoscale cylinders. Furthermore, a-Si:H with high  $n$  and low extinction coefficient has been adopted to achieve high-performance metalens in the NIR region.

To summarize, high-speed EBL has been introduced to overcome the limitation of conventional EBL for large-area fabrication. However, due to the challenges of EBL in mass production, DUV photolithography has been applied to achieve mass production. This enables faster production, lower costs, and improved process stability, enhancing the potential for large-scale manufacturing of metasurface-based optical devices while maximizing economic benefits. Furthermore, the high compatibility with CMOS technology facilitates the integration of metasurfaces with semiconductor devices, enabling the large-scale integration of optoelectronic devices. As a result, these devices can be applied in high-performance optical systems such as virtual reality (VR) and augmented reality (AR) devices, smartphone camera modules, and LiDAR systems. However, managing defects is critical because they directly impact device performance and production costs, with acceptable defect levels varying depending on the intended application. As the fabrication area increases, variations in process conditions can introduce defects.<sup>399</sup> Optimizing both the metasurface design and fabrication parameters is essential to minimize defects and ensure uniform performance. Evaluating defects through efficiency testing and yield analysis associated efficiency losses in large-area metasurfaces, can be determined by measuring the efficiency of each fabricated metasurface and comparing it to theoretical and average values.<sup>33</sup> Despite significant progress in mass-producing metasurfaces, especially in the UV and shorter wavelength regions, further resolution improvements may require sources with even shorter wavelengths, such as EUV lithography.<sup>404</sup>

These approaches not only increase the commercial adaptability but also commitment to overcoming the inherent limitations of traditional photolithography, setting the stage for the next generation of optical device manufacturing. To advance commercialization further, research will be required to combine various other fabrication techniques such as roll-to-roll nanoimprint lithography<sup>405</sup> to further reduce the cost of large-area fabrication and mass production.

### 13. NANOIMPRINT LITHOGRAPHY WITH HIGH-REFRACTIVE-INDEX RESIN

Hyunjung Kang, Yujin Park, and Junsuk Rho

EBL has been employed to fabricate metasurfaces with higher resolution compared to i-line stepper lithography and KrF stepper lithography. However, EBL is costly and time-consuming, hindering the mass production of metasurfaces at the wafer scale. To address these challenges, NIL has emerged as a low-cost and one-step fabrication technique: nanostructures are transferred onto imprint resin using a replica mold made from a master mold. Regardless of their massive producibility, conventional imprint resin, with its low  $n$  ( $\sim 1.5$ ), is unsuitable for designing meta-atoms as it lacks the capability to effectively modulate light. To enhance the effective  $n$ , various methods including dispersing nanoparticles into the typical resin<sup>406–409</sup> and depositing high- $n$  film onto printed structures<sup>33,81</sup> have been introduced.

By dispersing nanoparticles into the resin, a particle-embedded resin (PER), with high  $n$ , has been developed (Figure 12a).<sup>38,407,408,410,411</sup> PER-based NIL (PER-NIL) process is as follows: a reusable master mold is made using EBL, followed by pouring PDMS onto it to form a replica mold. PER is spin-coated onto the replica mold and then placed onto a target substrate, where it is directly imprinted under exposure to UV radiation (or heat) and pressure. PER-NIL does not require secondary operations such as etching, enabling the low-cost and high-throughput fabrication of the metasurfaces. Cost analysis shows that producing a single sample costs approximately 1.37 USD, confirming its low-cost nature.<sup>38,407,408,410,411</sup> High-index atomic layer–polymer hybrid metasurfaces have been formed by coating a thin film through ALD onto imprinted polymer meta-atoms, known as hybrid-NIL<sup>81</sup> (Figure 12b). The thin film enhances light confinement, increasing the effective  $n$  and consequently improving optical efficiency. On the other hand, the hybrid-NIL process is as follows: a wafer-scale master mold is fabricated by photolithography and high-speed EBL owing to the large fabricated area. Photolithography using an ArF immersion scanner with a wavelength of 193 nm has been employed to create the master mold with high resolution ( $\sim 40$  nm). Then, NIL is used to replicate the wafer-scale master mold at an extremely low cost, followed by coating with a thin film using ALD, enabling mass production of scalable metasurfaces. This method demonstrates that, for a 4-in. wafer, only 3 defects occur out of 68 transferred 1 cm metalenses, and it also proves repeatability across 20 cycles, validating the potential for large-scale metasurface mass production. PER- and hybrid-NIL have demonstrated high efficiency in optical properties, indicating

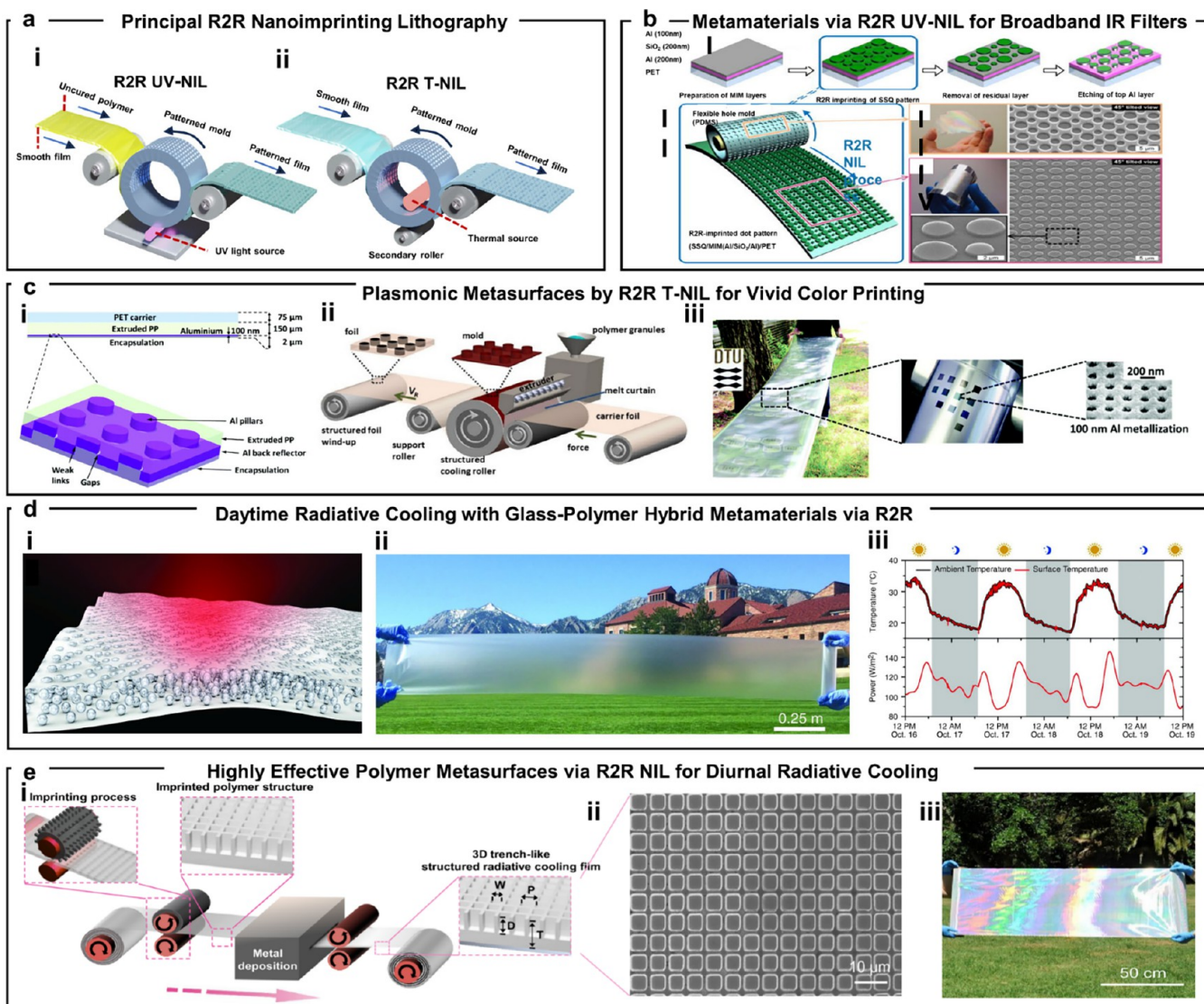


**Figure 13.** Scalable metasurfaces with R2R nanoimprint technology for nanophotonics. (a) Two main R2R NIL techniques are photolithography and thermal imprinting. Panel i demonstrates photolithography applied to an uncured photopolymer on a substrate, which cures and patterns upon UV light exposure on a drum mold and then detaches as a patterned film. Panel ii shows substrate heating above its glass transition temperature with a patterned drum using R2R T-NIL technique. During the heating, pressure from a secondary roller molds the softened material to the drum's pattern, and then the web cools and detaches. (b) R2R UV-NIL uses a flexible stamp to pattern dot patterns on MIM-stacked polymer films for broadband IR filters. Panel i illustrates the fabrication process, starting with sputter-coating the MIM stack on a large PET substrate. Then, a UV-curable SSQ layer was added and patterned with R2R NIL, as shown in Panel ii. Panel iii presents a large, flexible mold with 600 nm deep hole patterns made by stamping a 4-in. silicon master onto a PDMS pad. Panel iv displays successful SSQ patterning at speeds up to 1 m/min and the precise etching of an Al disk array on the MIM-coated PET substrate.<sup>454</sup> Adapted with permission from ref 454. Copyright 2012 AIP Publication. (c) Scalable plasmonic color metasurface created using high-speed R2R extrusion coating. Panel i depicts a schematic of layers where nanopits in transparent PP on PET foil, filled with Al, produce nanopillars with nanometer gaps to the back reflector, enabling color visibility through the foil. Panel ii indicates the R2R T-NIL process: polymer melt is extruded, pressed between structured and silicone rolls to form patterns on the film, and then wound onto a roll. As illustrated in Panel iii, a 45 cm wide metalized foil shows scalability achieved by varying pit sizes and spacing.<sup>456</sup> Adapted with permission from ref 456. Copyright 2017 RSC Publishing. (d) Glass–polymer hybrid metamaterial for daytime cooling. Panel i presents a polymer-based hybrid metamaterial with dispersed SiO<sub>2</sub> microspheres for large-scale radiative cooling. The microspheres interact strongly with IR light, enhancing emissivity across the atmosphere while maintaining solar transparency. Panel ii depicts a photograph of the 300 mm-wide hybrid metamaterial thin film, fabricated via R2R manufacturing at a speed of 5 m/min. The scalable hybrid metamaterial demonstrated 93 W/m<sup>2</sup> cooling power in a three-day test under direct sunlight in Panel iii. Additionally, it exceeded 110 W/m<sup>2</sup> in a continuous 72h day-and-night test.<sup>458</sup> Adapted with permission from ref 458. Copyright 2017 AAAS. (e) A metasurface featuring 3D trench structures for radiative cooling was generated using R2R photomanufacturing. Panel i schematically shows key manufacturing steps, starting with mold fabrication using laser 3D nanoprinting. Then, the mold is used for R2R photoimprinting onto a PET film. A SEM image showing uniform trench structures with matrix symmetry and a depth of approximately 2.5 µm as displayed in Panel ii. Step 2 involves applying a 100 nm-thick silver layer to the polymer film's back, showcasing the R2R process's efficiency and cost-effectiveness in Panel iii.<sup>462</sup> Adapted with permission under a Creative Common CC BY License from ref 462. Copyright 2023 Springer Nature.

significant potential for large-scale production of metasurfaces across a broad spectrum from UV to infrared (IR) wavelengths.

UV metasurfaces feature nanostructures designed to finely manipulate short-wavelength light, leading to advancements in various applications such as sensors,<sup>412,412</sup> holograms,<sup>211,413</sup> and lenses.<sup>414,415</sup> However, UV metasurfaces have long faced challenges due to the lack of materials with low loss in the UV region. To address this, dielectrics with wide bandgap such as tantalum pentoxide<sup>416</sup> ( $Ta_2O_5$ ), hafnium oxide<sup>417</sup> ( $HfO_2$ ), and niobium pentoxide<sup>418</sup> ( $Nb_2O_5$ ) have been primarily utilized. Yet, processing these materials has required high-resolution and high-cost techniques such as EBL, prompting the introduction of NIL. To enhance the effective  $n$  of typical imprint resin in the UV region, PER- and hybrid-NIL, utilizing  $ZrO_2$  with a high  $n$  (~2.3) and low extinction coefficient (~0.0), have been introduced.<sup>33,419,420</sup> They exhibit high-efficiency UV metasurfaces operating in the region of 248 to 325 nm. Following, a cost-effective one-step printable platform utilizing  $ZrO_2$  PER, where  $ZrO_2$  nanoparticles are mixed with UV-curable imprint resin, has been demonstrated<sup>419</sup> (Figure 12c.i). This was proved by exhibiting a metahologram with a conversion efficiency of 72.3% at near-UV (325 nm) and 48.6% at deep-UV (248 nm) (Figure 12c.ii,iii). However, the  $ZrO_2$  PER-NIL method still faces limitations in terms of small patterning area and challenges in mass production. To overcome these limitations, the use of  $ZrO_2$  hybrid-NIL has been introduced, resulting in an array pattern of a 1 cm UV metalens on an 8-in. wafer<sup>33</sup> (Figure 12d,i,ii). By depositing a 15 nm  $ZrO_2$  film onto the existing imprint resin using ALD, a 1 cm UV metalens with a focal efficiency of 48.5% at 325 nm has been achieved. Additionally, the clear focusing ability of the metalens has been demonstrated (Figure 12d.iii,iv). The red and blue vertical dotted lines in Figure 12d.iv illustrate the resolving capabilities of the imaging target.

The development of visible metasurfaces is crucial for achieving the miniaturization of optical devices, such as augmented reality (AR), virtual reality (VR), and wearable devices. To design efficient metasurfaces, optical materials must possess a high  $n$  and a near-zero extinction coefficient across the entire visible region. This is particularly desirable for functional metasurfaces like achromatic metalenses<sup>292,421</sup> and vibrant structural color.<sup>422</sup> Visible-transparent optical materials such as hydrogenated amorphous silicon<sup>207,423</sup> (a-Si:H) and gallium nitride<sup>424,425</sup> (GaN) have been proven for efficient metasurfaces. In this section, titanium dioxide ( $TiO_2$ ), characterized by a high  $n$  (~2.7) and low extinction coefficient (~0.0) in the visible region, has been incorporated into PER-NIL<sup>38,407,408,410,411</sup> and hybrid-NIL<sup>81</sup> for the creation of high-efficiency metasurfaces. The  $n$  of  $TiO_2$  PER, where  $TiO_2$  nanoparticles are dispersed in UV-curable (or thermally curable) resin, is approximately 1.9, indicating a rise of about 0.4 compared to the typical imprint resin. This property has led to extensive research across various applications, including 3D imaging,<sup>426</sup> metalens,<sup>410</sup> and nanoprinting.<sup>406</sup> Specifically,  $TiO_2$  PER-based metaholograms achieve an average conversion efficiency of 62.4% in the range from 450 to 650 nm, with a maximum of 90.6% at 532 nm<sup>64,411</sup> (Figure 12e.i,ii). Although the  $TiO_2$  PER-NIL method has demonstrated the potential for commercialization of metasurfaces through its broadband characteristics and high-performance functionalities, the size of the metasurfaces still remains at the microscale. To achieve mass production, the  $TiO_2$  hybrid-NIL method has

been introduced<sup>81</sup> (Figure 12f.i). By depositing a 23 nm  $TiO_2$  thin film onto the existing imprint resin using ALD, 1 cm metalenses on a 12-in. wafer have been demonstrated (Figure 12f.ii). It exhibits  $n$  of approximately 2.5 and achieves a performance of around 78% conversion efficiency at 532 nm. Additionally, the intensity profile of the focal spot on the  $xz$  plane has been measured at 532 nm, evaluating the performance of the fabricated metalens (Figure 12f.iii). Imaging a negative 1951 USAF target has confirmed the imaging capabilities, successfully resolving elements #5 and #6 from group 7 at 532 nm (Figure 12f.iv). This performance highlights its potential toward the scalable manufacturing of metophotonic devices.

IR metasurfaces have been utilized to manipulate light across a wavelength range of 0.8 to 15  $\mu\text{m}$  for various applications like imaging<sup>402,427</sup> and biosensing.<sup>397,428,429</sup> To facilitate the development of these nanodevices, IR metasurfaces have been constructed using a variety of IR-transparent materials, including poly-Si,<sup>430</sup> germanium<sup>431,432</sup> (Ge), lead telluride<sup>433,434</sup> (PbTe) and gallium antimonide<sup>435,436</sup> (GaSb). Given that Si-type dielectrics typically exhibit  $n$  around 3.5, Si PER, synthesized by dispersing Si nanoparticles in a thermally curable resin, has been proposed to achieve high-efficiency IR metasurfaces.<sup>72</sup> By utilizing Si PER with a high  $n$  of 2.2, a 4 mm-diameter metalens has been realized, achieving a focusing efficiency of 47% at  $\lambda = 940 \text{ nm}$ <sup>437</sup> (Figure 12g.i). Furthermore, a compact NIR camera employing the Si PER metalens has been successfully demonstrated for imaging veins underneath the skin, confirming its applicability for biomedical imaging (Figure 12g.ii). Recently, the fabrication of a wafer-scale metalens array using Si PER-NIL has been demonstrated, allowing for the production of large-area metalenses in significant quantities. Polarization-dependent 5 mm-diameter metalenses utilizing Si PER have been manufactured on a 4-in. glass wafer<sup>82</sup> (Figure 12h.i,ii). The intensity profile along the optical axis near the focal length has been measured (Figure 12h.iii). Although the imaging quality is not perfect, the 1951 USAF resolution test target has been well resolved (Figure 12h.iv). Based on the progress shown in this section, PER- and hybrid-NIL have demonstrated the potential for commercialization beyond nanoengineering of metasurfaces. These techniques simplify the production of large-area metasurfaces, paving the way for scalable manufacturing with enhanced efficiency across diverse optical applications.

## 14. ROLL-TO-ROLL PRINTING

Dang Du Nguyen and Inki Kim

Roll-to-roll NIL (R2R NIL) offers a viable method for the continuous high-speed patterning of nanoscale features across wide areas on flexible substrates.<sup>438,439</sup> It facilitates cost-effective production while significantly enhancing throughput. In addition, this method overcomes the shortcomings of the traditional NIL by ensuring uniform pressure and successfully demolding large-area imprints. This technique can generate structures across various nanometer, micrometer, and centimeter scales.<sup>440,441</sup> This versatility allows for the production of photonic resonant structures with diverse geometries, catering to wide applications, including photonic integrated circuits,<sup>442</sup> nanophotonic sensors,<sup>443</sup> flexible electronics,<sup>444</sup> and solar cells.<sup>445</sup>

The two principal techniques used in R2R NIL are photolithography and thermal imprinting (Figure 13a). Photolithography involves applying an uncured photopolymer

onto a smooth substrate. The photopolymer-coated substrate was wrapped around a drum mold and cured upon UV light exposure. The cured polymer adheres to the backing to yield a patterned film that is subsequently detached from the mold (see Panel i for an illustration). In R2R thermal NIL (R2R T-NIL), the temperature of the substrate is raised beyond its glass transition temperature by heating at patterned drum. Concurrently, a secondary roller exerts pressure on the reverse side of the substrate, enabling the softened material to conform to the patterned surface of the drum mold. Subsequently, the web is cooled and disengaged from the drum, as depicted in Panel ii. R2R NIL employs roller stamps in lieu of traditional flat and rigid stamps, facilitating continuous imprinting with uniformity and conformal pressure, improved resist movement, seamless pattern transfer, and increased throughput.<sup>446</sup> An R2R UV-NIL process, operating at room temperature, presents key advantages over R2R T-NIL by avoiding high-temperature imprinting and reducing thermal expansion between the mold, substrate, and resist.<sup>447</sup> Moreover, using a less viscous liquid PR in the imprinting process enables operation at lower pressures than those required for T-NIL processes.<sup>448,449</sup> The reduced viscosity of the resist accelerates the filling of the mold cavity while eliminating the temperature cycle, thereby improving the process efficiency.<sup>448</sup> Nevertheless, UV-NIL resins are costly due to their complex components, including specific monomers and solvents that lower viscosity. Furthermore, they require meticulous handling and volatile organic compound (VOC) treatment equipment. Therefore, T-NIL is more cost-effective than UV-NIL and is an eco-friendly procedure that avoids the use of VOC chemicals. Both R2R UV and T-NIL enable continuous large-scale production. Their choice depends on application requirements, such as material properties, patterned mold fabrication, processing speed, pressure, and heat sensitivity.<sup>447,450</sup>

Despite various fabrication techniques, a universally applicable, scalable, and efficient manufacturing approach for integrating large-scale optical metasurfaces into device-level applications is yet to be developed thoroughly. This section summarizes recent advancements in different meta-devices that utilize R2R NIL methods. The MIM configuration with subwavelength patterning induces surface plasmon polaritons (SPP) in metamaterials at metal–dielectric interfaces. However, conventional fabrication of large-area MIM structures using photo-, or electron beam lithography has limited scalability, throughput, and cost-effectiveness for practical use.<sup>451–453</sup> An R2R NIL for patterning dot patterns on MIM stacked polymer films utilizing a flexible stamp has been developed to surmount these issues.<sup>454</sup> Panel i in Figure 13b depicts the comprehensive fabrication process. Initially, an Al/SiO<sub>2</sub>/Al MIM stack was sputter-coated onto a large PET substrate. A UV-curable epoxy-silsesquioxane (SSQ)<sup>455</sup> layer was then applied to the substrate, followed by an R2R NIL to pattern the cured SSQ (Panel ii in Figure 13b). Panel iii shows a flexible mold featuring 600 nm depth hole patterns over a wide area, which was fabricated by stamping a 4-in. silicon pillar master onto a PDMS pad. Furthermore, Panel IV shows the successful SSQ patterning at speeds of up to 1 m/min and subsequent etching, creating an array of Al disks on a layered PET surface with metallic and insulating coatings. The created metamaterial structure demonstrates broadband IR filtering capabilities owing to multiple resonance dips, potentially facilitating the cost-effective and rapid fabrication of diverse metamaterials on scalable and flexible substrates.

Plasmonic color metasurfaces have achieved vivid colors with nanostructures and metalized surfaces. However, scaling to large areas is challenging because of the precise metal thickness requirements. Murthy et al. demonstrated a scalable plasmonic color metasurface amenable to high-speed R2R extrusion coating at 10 m/min<sup>456</sup> by fortifying the resilience of plasmonic color printing for large-scale production. Figure 13c depicts the layer design schematic, where nanopits in transparent polypropylene (PP) atop a PET sheet are filled with a continuous Al coating. This process forms Al nanopillars with a few nanometers wide gaps and the Al back reflector, which makes colors visible via the transparent foil (see Panel i for an illustration). As shown in Panel ii, the 3D drawing illustrates the R2R T-NIL extrusion coating process. A polymer melt is extruded through a die and bonded to a support sheet through compression between a patterned cooling roller and a silicone rubber pressure roller, replicating the cooling roll structure onto the thermoplastic film before solidification. Subsequently, the structured foil is wrapped around the winding roll. To illustrate the scalability of the plasmonic color metasurface, Panel iii in Figure 13c presents a 45 cm wide metalized and encapsulated foil. The inset displays an enlarged view of the DTU logo printed on the foil using pit diameter and pitch length variations. This study expand the scope of plasmonic metasurface applications, including memory storage, surface-enhanced Raman scattering, biosensing, and flexible display technologies.

Combining random optical metamaterials using polymer photonics can provide efficient daytime radiative cooling. The collective excitation of electromagnetic resonators in a random metamaterial enhances the extinction and optical path length, yielding near-perfect absorption at resonance.<sup>457</sup> This underscores the potential of employing random optical resonators in metamaterials for effective thermal radiation cooling, provided complete absorption through the atmospheric transmittance range is achievable. Zhai et al. investigated effective day and nighttime radiative cooling employing a randomized glass–polymer hybrid metamaterial incorporating resonant silicon dioxide (SiO<sub>2</sub>) microspheres, as shown in Figure 13d (Panel i).<sup>458</sup> Despite being fully transparent to the solar spectrum, the metamaterial exhibits an IR emissivity exceeding 0.93 throughout the atmospheric window. Utilizing a polymer for radiative cooling offers advantages such as being lightweight and easy to laminate on curved surfaces. It can tolerate slight variations in the microsphere size and shape with minimal impact on performance. A vital benefit of a glass–polymer hybrid metamaterial is its potential for cost-effective and scalable fabrication. Panel ii shows the production of a 300 mm-wide, 50-μm-thick hybrid metamaterial film at a speed of 5 m/min. The SiO<sub>2</sub> microsphere concentration was adjusted using gravimetric feeders. This resulted in a film with evenly spread microspheres and a minimal concentration variation below 0.4%. An average radiative cooling power of 93 W/m<sup>2</sup> was obtained over a three-day period under direct sunlight to assess the effectiveness of the scalable hybrid metamaterial for radiative cooling. Additionally, over a continuous 72h day-and-night test, the average cooling power exceeded 110 W/m<sup>2</sup> (see Panel iii in Figure 13d). While integrating randomly distributed particles can enhance spectral controllability, attaining precise control over the spectrum is challenging.

Metasurfaces with periodic structures have demonstrated outstanding spectral breadth and selectivity for daytime radiative cooling.<sup>459,460</sup> However, most only exhibit this quality

on rigid and thick substrates, limiting their adaptability to various shapes.<sup>460</sup> Additionally, fabrication challenges of these micro/nanostructures restrict them to small areas, rendering them impractical for widespread application. Recently, a metasurface enabled by periodically arranged 3D trench-like structures within a thin polymer layer for enhanced radiative cooling was achieved via R2R photomanufacturing technology.<sup>461,462</sup> The essential manufacturing steps are schematically illustrated in Panel i of Figure 13e, including initial mold fabrication with specific structural parameters using a 3D laser nanoprinting technique. Then, the mold facilitated the R2R photoimprinting of the structures onto a PET film. Panel ii shows a top-view SEM image of a uniform, large-area trench structure with matrix symmetry and a depth of approximately 2.5 μm. In the second step, a 100 nm-thick silver layer was applied to the reverse side of the imprinted polymer film, demonstrating the R2R process's efficiency and cost-effectiveness, as shown in Panel iii. The 50-μm PMRC film absorbs and emits heat omnidirectionally (96.1%) while maintaining low solar absorption (4.8%) and high stability. It provides 129.8 W m<sup>-2</sup> of cooling and lowers temperatures by 7 °C during midday under a clear sky. The large-scale R2R-produced PMRC film is an affordable, flexible option for wide-ranging cooling needs. It easily applies to any surface without energy use. This study suggests a method for mass-producing radiative cooling material with arrayed photonic structures.

Despite the benefits of R2R NIL, conducting a continuous process presents challenges that require integrated solutions for various interconnected issues. The primary challenge lies in fabricating flexible molds, which are essential for the continuous implementation of R2R NIL for nanostructures. Molds for R2R NIL must conform to roller surfaces and have the requisite modulus and strength for imprinting onto other materials. Low surface energy is crucial for effective mold release. Furthermore, roller mold durability is necessary for consistent and stable mass production. Additionally, material selection for R2R NIL molds is critical to address mold sticking and thermal expansion mismatch in T-NIL, and for lifespan extension. In contrast, resist materials must have excellent coating properties and low viscosity.<sup>446,463</sup> Imprint replicas can be created by polymer casting using nonsticking materials such as PDMS or ethylene-tetrafluoroethylene, as demonstrated by several research groups.<sup>446,449,464</sup> Ye et al.<sup>465</sup> emphasized that PDMS polymer molds are favored in UV roller imprinting because of their affordability, nonstickiness, elasticity, and ease of production over metal molds. Furthermore, the continuous R2R NIL process requires an integrated resistance coating mechanism to manage substrate feeding during imprinting. This challenge necessitates a complex mechanism and strict uniformity control.<sup>446</sup> Studies on various resins and their properties aim to enhance R2R NIL process efficiency.<sup>466,467</sup> The application of airbrush technology for the conformal coating of SSQ resin exemplifies an effective method to obtain thin-film coatings with minimal residual layer thickness (RLT).<sup>468</sup> RLT is key for R2R NIL efficiency, as it determines resin waste; adjusting resin concentration and airbrushing pressure simplifies film thickness and RLT control. Moreover, Donie et al. tackled existing R2R UV-NIL challenges, such as slow printing speeds, limited material choices, energy-intensive use, and lengthy procedures that limit additive micro/nanopatterning through wetting control.<sup>469</sup> They developed a cost-effective, scalable additive metamaterial manufacturing method, called topochemical

wetting control for metamaterial printing. This method leverages the PDMS stamp surface chemistry and selective wetting to imprint hydrophilic cells with hydrophobic surroundings and fabricate Ag nanopatterns down to 83 nm in a single step. At speeds of up to 12 m/min, this platform quickly generates complex patterns from various materials, precisely controlling the structure height, thickness, and multilayer structures on many substrates, including thin and free-standing sheets. The high speed of this process enables it to rival traditional roll-based printing, offering an efficient alternative for the fabrication of R2R metamaterials.

Recently, concerns were raised in the large-scale manufacturing of dielectric metasurfaces for exciting applications, such as color printing,<sup>470,471</sup> metahologram,<sup>207,472</sup> and biosensors.<sup>473–477</sup> Indeed, efficient dielectric metasurfaces necessitate using materials characterized by high refractive indices and minimal extinction coefficients. Generally, the *n* of the resins employed in NIL is insufficient for metasurface applications, prompting investigations into developing highly functional metasurfaces that leverage the high yield of NIL.<sup>410,478</sup> Typically, dielectric metasurfaces are fabricated by high-resolution EBL,<sup>479,480</sup> limiting their scalability. Concurrently, mask-based techniques, including deep UV lithography and NIL<sup>81,419</sup> enable high-throughput metasurface fabrication. However, they are limited by the size restrictions of wafer-based methods. Utilizing R2R systems for NIL can boost mass production and cost-effectiveness, enabling the creation of large-area dielectric metasurfaces<sup>481</sup> for applications in virtual reality devices<sup>81</sup> and autonomous vehicle distance sensors. To leverage R2R technology effectively, overcoming two key challenges is crucial: extending patterns over large film surfaces and adjusting metasurface designs for R2R manufacturing optimization.

Defects present a significant challenge in R2R NIL due to the process's high-speed and large-scale production. The acceptable density of defects varies depending on the application. Using UV-NIL, a 300 mm diameter wafer can be imprinted with a filling time as brief as 1 s, achieving a defect density as low as approximately 0.1 defects per cm<sup>2</sup> and a resolution exceeding 10 nm.<sup>483</sup> Nevertheless, defects caused by air bubbles are commonly observed within fabricated patterns, particularly in applications involving large-area production.<sup>484</sup> To mitigate these defects, vacuum processing has been employed; however, it is often associated with increased costs and extended processing times. Defect risks increase with mold depressions or droplet-applied resist instead of through spin coating as this method more readily traps air,<sup>485</sup> necessitating vacuum imprinting to prevent air bubble entrapment.<sup>486</sup> However, vacuum chambers are challenging in continuous web-feed systems, then Hiroshima et al. proposed using pentafluoropropane as an ambient medium to address bubble defects.<sup>487–489</sup> Additionally, various other strategies have been investigated to address bubble issues, such as step-and-flash NIL and R2R NIL.<sup>435</sup> Step-and-flash NIL technology effectively lowers defect rates by minimizing the imprint area.<sup>490</sup> Besides, the R2R NIL process ensures bubble-free operation with line contact between mold and substrate, while providing high throughput through continuous imprinting. Notably, Ok, J. G. et al. demonstrated how R2R NIL can be used to fabricate large-area flexible metamaterial films with tolerable defect levels that still meet the functional requirements for broadband infrared filtering applications.<sup>451</sup> For solar cells, defect densities from UV-NIL

are acceptable up to a certain threshold, as these applications can tolerate minor imperfections without severely impacting performance.<sup>491</sup> Although it does not specify a defect threshold, Choi et al. demonstrated T-NIL for the fabrication of photonic crystal slabs with emphasis on achieving low defect densities necessary for photonic integrated circuit application.<sup>492</sup> Additionally, improved pressing mechanisms in large-area R2R NIL systems have further reduced patterning defects by achieving uniform contact pressure across the rollers, even in large-scale production environments. These innovations reduce pressure deviations, leading to more consistent and high-quality imprints.<sup>493</sup> In addition, recent advancements focusing on improving resist flow and pattern transfer uniformity have been instrumental in minimizing defect levels in these processes.<sup>436</sup>

Reliability and reproducibility in R2R NIL are impacted by several factors, including mold durability, resist uniformity, and the precise control of web tension and pressure during the imprinting process.<sup>435</sup> The reliability improvements can be achieved through enhanced web alignment systems and more resilient roller molds, such as those made from PDMS, which exhibit good nonstick properties and elasticity.<sup>463</sup> Moreover, advances in RLT control through web tensioning have been shown to enhance the reproducibility of patterns by minimizing inconsistencies in the layer height, a critical factor for many applications.<sup>494</sup> Recent study has introduced method called topochemical wetting control, which allows for the rapid production of complex nanostructures, ensuring consistent and reproducible output.<sup>469,495</sup>

Cost-effectiveness in R2R NIL is a critical factor for its industrial adoption, particularly for large-scale applications such as photovoltaics, optoelectronics, and functional surface production. Several factors influence the economic viability of this technique, and recent research has provided insights into how these challenges can be addressed. First, R2R NIL offers significant cost advantages over traditional nanolithography methods due to its high throughput and ability to pattern large areas in a continuous manner. This capability makes it an attractive option for industries requiring mass production of nanoscale structures.<sup>436</sup> However, the process faces challenges such as uneven resin filling, which can lead to defects and reduced production efficiency. To address this, optimization of UV-resin filling and process parameters has been proposed, significantly enhancing the precision and speed of pattern replication.<sup>496</sup> R2R NIL has demonstrated cost reductions in the production of optical components, such as Fresnel lenses used in microconcentrator photovoltaic systems.<sup>497</sup> By utilizing UV-curable resins and improving the replication fidelity of nanostructures, the process has shown to increase optical efficiency while minimizing material and operational costs. To further improve cost efficiency, fine-tuning the imprinting parameters, such as resin viscosity, imprinting speed, and web tension, can reduce defects and improve production efficiency, lowering overall costs. Second, the development of low-cost UV-curable resins with enhanced properties can further reduce the expense of consumables while maintaining high-quality output. Third, increasing the speed of production through advancements in mold materials and pattern transfer technologies allows for greater economies of scale. In conclusion, R2R NIL holds substantial potential for cost-effective mass production of nanoscale structures. By optimizing process parameters, enhancing material properties, and scaling up production, the overall cost-effectiveness of this

technique can be significantly improved, making it a highly competitive option for industrial applications.

## 15. PHYSICAL VAPOR DEPOSITION ASSISTED PLASMONIC SELF-ASSEMBLY

Pablo Cencillo-Abad and Debasish Chanda

Crafting stained-glass windows for cathedrals and monasteries, medieval artisans pursued a dual mission: to educate and uplift the faithful.<sup>498</sup> The colorful light emanating from these windows, a result of embedding metallic nanoparticles into the glass, showcases a remarkable scientific phenomenon: plasmonic resonance.<sup>499</sup> When light impinges on a metallic nanoparticle, it can cause the electrons in the metal to move collectively, creating intense localized electric fields near the surface. This collective oscillation of free electrons within the metallic nanostructures is known as a surface plasmon resonance.<sup>500</sup> Critically, the interaction between light and these free electrons is highly dependent on the size, shape, and arrangement of the metallic resonators.<sup>501</sup> Thus, manipulating the geometrical parameters, one can control the light-matter interaction at the nanoscale.<sup>502</sup> While the artisans of the medieval era lacked a scientific understanding of plasmonic resonances, their work remains a testament to the ingenuity of mankind and the quest to control nature for practical purposes. Inspired by these millennia-old achievements, the widespread adoption and development of nanofabrication techniques in the early 2000s fueled the burgeoning of research in the field of plasmonics, uncovering deeper insights into its mechanisms and revealing new potential applications.<sup>502–506</sup>

Over the last decades, researchers have shown how plasmonic structures hold immense potential across a multitude of fields due to their unique light-manipulating properties.<sup>507</sup> For instance, in biosensing applications, they enable highly sensitive detection methods by amplifying weak biomolecular signals, paving the path for advancements in medical diagnostics and drug discovery.<sup>508–512</sup> In solar cells, plasmonic structures enhance light trapping and absorption, leading to improved energy conversion efficiency and the development of more cost-effective photovoltaic systems.<sup>513–521</sup> Moreover, in the realm of metamaterials, these structures facilitate the creation of artificial materials with exotic properties not found in nature, such as negative refraction,<sup>522–526</sup> opening avenues for innovations in telecommunications, imaging, and beyond.<sup>527–532</sup> Nevertheless, while research has demonstrated the remarkable capabilities of these structures, their commercial application has been hindered by the limitations of conventional fabrication techniques. With the groundwork of fundamental research laid in recent years, researchers are now tasked with realizing the potential by offering solutions for real-world challenges that can be integrated into industrial fabrication processes.<sup>533</sup> Current methods, however, often involve complex and time-intensive processes, leading to increased costs and limited scalability. As a result, the practical application of plasmonic structures still far away from reality unless there is advancement in large-scale fabrication techniques.<sup>534</sup>

While lab-made nanostructures have shown immense promise, large-scale fabrication is crucial to bridge the gap from proof-of-principle to real-world application. The shift in paradigm should result in integration into existing infrastructure, accelerating innovation and turning plasmonics into an enabling technology of the 21st century. Here, PVD techniques emerge as a powerful approach for self-assembly

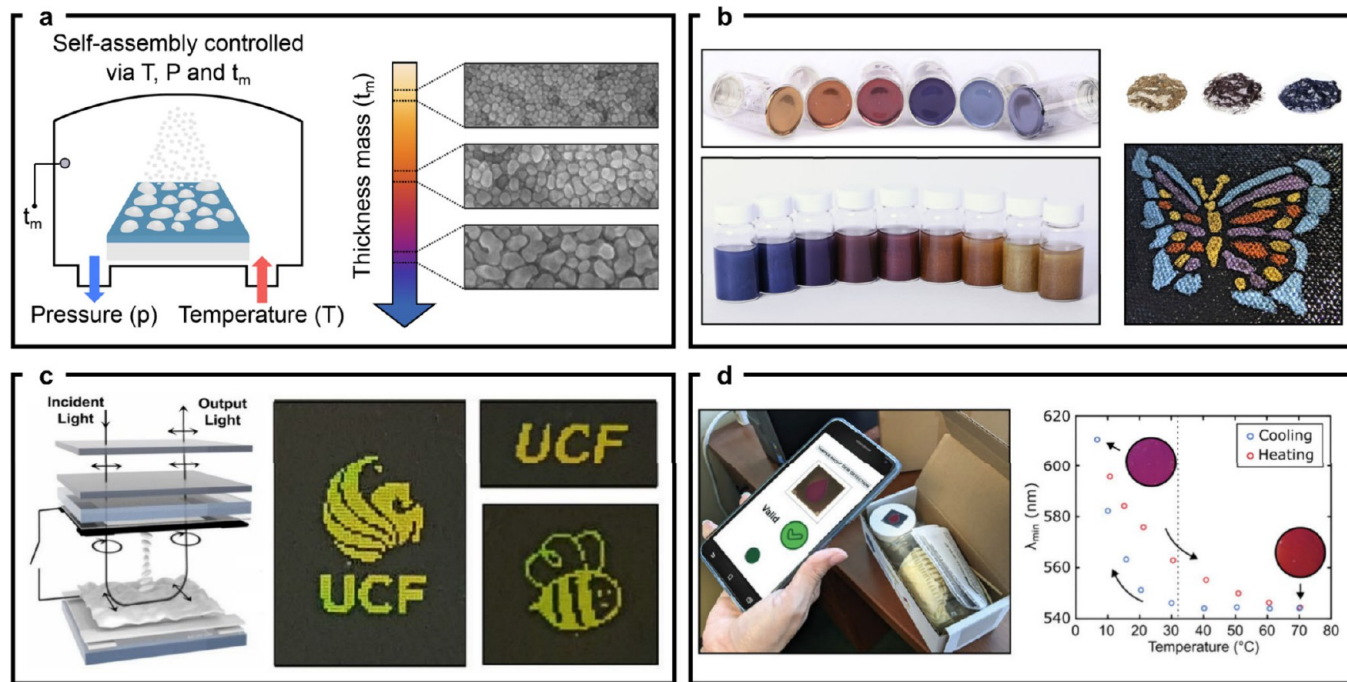


**Figure 14. PVD based controlled self-assembly for large scale plasmonic nanostructures.** (a) In the Volmer–Weber growth mode, the size of nanoislands can be controlled by adjusting pressure, temperature, and material properties. (b) Integration of plasmonic nanostructures with liquid crystals can yield high-resolution, low power reflective displays capable of programmable video and image output.<sup>545</sup> Adapted with permission under a Creative Common CC BY License from ref 545. Copyright 2020 National Academy of Science. (c) Production of plasmonic nanostructures in transferrable flakes yields paints applicable to any surface, providing a versatile solution for large-scale applications.<sup>548</sup> Adapted with permission from ref 548. Copyright 2023 AAAS. (d) Hybridization of plasmonic nanostructures with active polymers enables self-powered sensing capabilities accessible via a smartphone application.<sup>551</sup> Adapted with permission from ref 551. Copyright 2023 Wiley-VCH.

nanofabrication of large-scale plasmonic structures. PVD encompasses a range of well-established thin-film deposition methods that provide precise control over material properties, composition, and structure, along with excellent uniformity across large areas.<sup>535</sup> Routinely employed in industries such as electronics, semiconductors, and optics, these techniques are particularly valuable for plasmonic structures, where thickness and morphology significantly impact performance.<sup>536</sup> In particular, three techniques are well-suited for this purpose: resistive evaporation, electron beam evaporation, and sputtering. Resistive evaporation is a simple and cost-effective method; however, it is limited to materials with low melting points. On the other hand, electron beam evaporation offers a higher deposition rate and can handle a wider range of materials. Finally, sputtering provides excellent film uniformity and control and is suitable for high-melting-point materials, but it is a slower process compared to the other two techniques.<sup>537</sup> Nevertheless, while PVD excels at large-area thin-film deposition, creating patterned plasmonic nanostructures requires additional steps such as lithography (electron beam, laser, or UV), etching, or dewetting, that add complexity and reduce the high-throughput advantage of PVD.<sup>121,538,539</sup> To achieve cost-effective mass production of patterned plasmonic structures, alternative methods are needed. Some promising approaches include nanotemplating, nanoimprinting, colloidal self-assembly, and glancing angle deposition.<sup>540–544</sup> These techniques offer the potential for large-scale fabrication of complex nanostructures but may have limitations in terms of material compatibility, cost, or scalability.

Recently, researchers have demonstrated a self-assembly lithography-free method for creating nanoplasmonic arrays for functional coatings.<sup>545</sup> This method overcomes limitations associated with conventional nanofabrication techniques, such as high cost and low throughput, making it attractive for large-scale production. The technique relies on the Volmer–Weber growth mode to achieve self-assembly of metal nanoislands on a dielectric substrate using an electron beam evaporator in a large-scale, highly versatile, and reproducible manner. In Volmer–Weber growth, deposited atoms cluster into islands instead of forming a continuous film at the initial stages. Hence, by carefully controlling factors like pressure, temperature, and rate of evaporation, all macroscopic parameters, researchers can manipulate the size and spacing of these nanoislands to create different nanostructures, Figure 14a. Interestingly, this approach can be generalized to many different metals, making it a promising strategy for producing a wider range of plasmonic nanostructures for various photonic applications in the visible, ultraviolet and IR spectral ranges. Furthermore, leveraging these strengths, PVD's compatibility with roll-to-roll processing allows for continuous deposition of plasmonic films onto flexible substrates, an approach particularly attractive for high-throughput production of plasmonic devices on a commercially viable scale.<sup>234</sup>

Following the legacy of medieval artisans, scientists are now exploiting self-assembled plasmonic nanostructures to generate color, departing from traditional chemical colorants and highlighting the vast potential of plasmonics to offer practical solutions beyond laboratory settings.<sup>546,547</sup> This paradigm shift extends to various applications, including, among others,

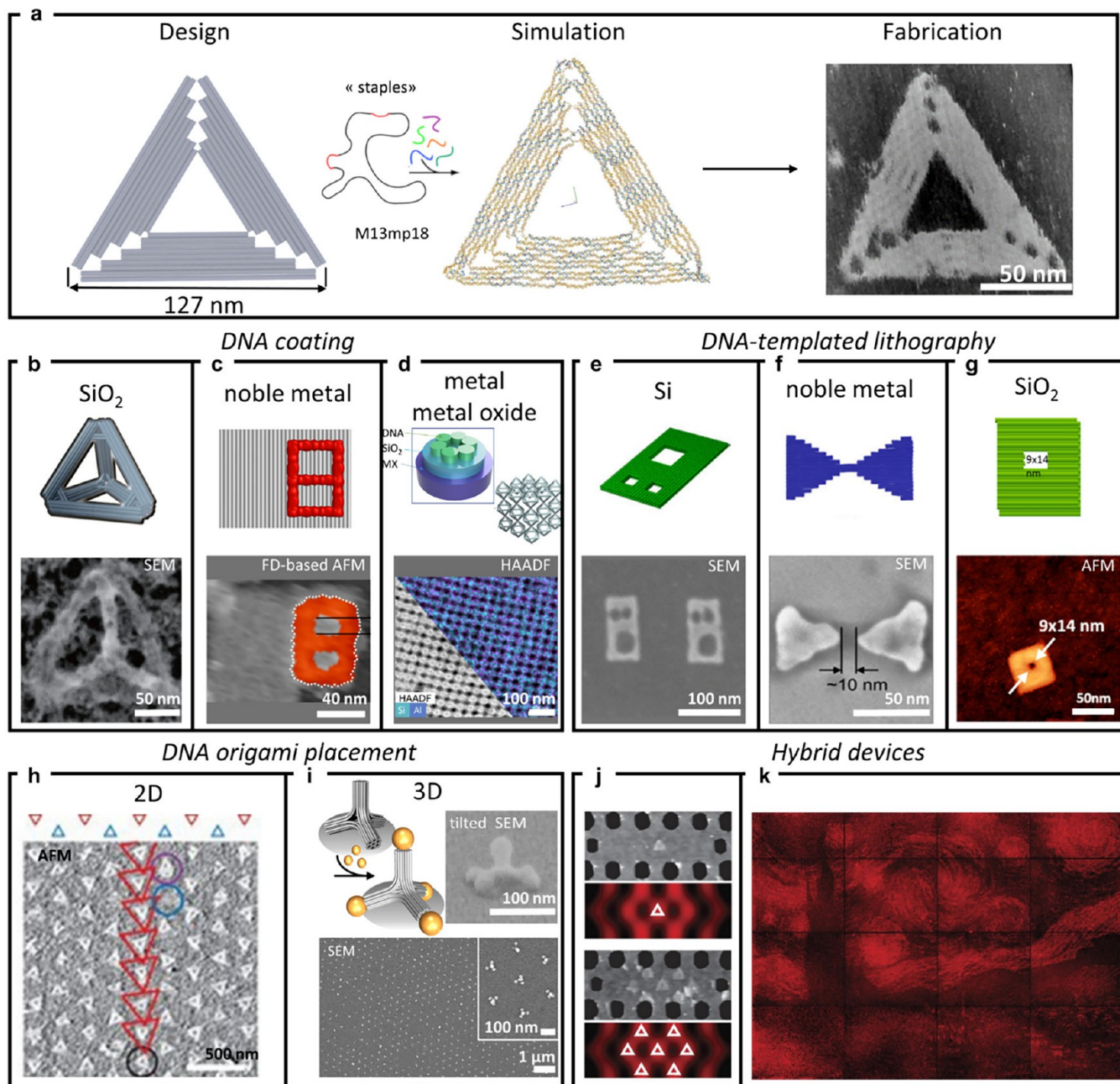


**Figure 15.** DNA origami for precise nanopatterning. (a) Schematic illustration of the DNA origami fabrication process. Typically, a DNA origami structure (here a triangle<sup>259</sup>) is designed *in silico*,<sup>619,620</sup> then its relaxed configuration can be simulated with software (here oxView,<sup>621</sup> various other packages are available<sup>622</sup>). After folding in buffer containing MgCl<sub>2</sub>, the object can be characterized by liquid mode AFM or other means like TEM or SEM (b–g) DNA origami shape transfer into inorganic materials. (b) Fabrication of hybrid DNA-SiO<sub>2</sub> nanostructures by silicification of DNA through mixing DNA framework with prehydrolyzed tetraethylorthosilicate (TEOS).<sup>591</sup> Adapted with permission from ref 591. Copyright 2018, Springer Nature. (c) Fabrication of hybrid DNA-gold nanostructures by site-selective metallization of DNA origami.<sup>594</sup> The panel shows force-distance AFM image (FD-AFM). Adapted with permission under a Creative Common CC BY License from ref 594. Copyright 2019 Springer Nature. (d) Fabrication of hybrid DNA-SiO<sub>2</sub>-Al<sub>2</sub>O<sub>3</sub> lattices by silicification and via vapor infiltration technique.<sup>593</sup> The panel shows TEM cross-sectional high-angle annular dark-field (HAADF) imaging and energy dispersive spectrometry (EDS)map of SiO<sub>2</sub> (blue) coated with Al<sub>2</sub>O<sub>3</sub> (purple). Adapted with permission from ref 593. Copyright 2024 AAAS. (e) Fabrication of Si nanostructures using DNA origami as the etch mask.<sup>600</sup> Adapted with permission from ref 600. Copyright 2020 ACS. (f) Fabrication of Au nanostructures using DNA origami as the deposition mask.<sup>598</sup> Adapted with permission under a Creative Common CC BY License from ref 598. Copyright 2018 AAAS. (g) Fabrication of SiO<sub>2</sub> nanostructures using metallized DNA origami as the etch mask.<sup>602</sup> Adapted with permission from ref 602. Copyright 2013 Springer Nature. (h), (i) Directed-assembly of DNA nanostructures into lithography patterns. (h) AFM image of assembled DNA triangles on SiO<sub>2</sub>.<sup>604</sup> Adapted with permission from ref 604. Copyright 2009 Springer Nature. (i) SEM image of assembly of hybrid gold nanoparticles-SiO<sub>2</sub>-DNA nanostructures on SiO<sub>2</sub>.<sup>606</sup> Adapted with permission from ref 606. Copyright 2023 Springer Nature. (j), (k) DNA origami-programmed optical devices. (j) AFM of DNA origami triangles used to position fluorophores within lithographically patterned photonic crystal cavities (PCCs).<sup>611</sup> AFM and schematics show one or seven origami placed in distinct antinodes of a single PCC. Adapted with permission from ref 611. Copyright 2016 Springer Nature. (k) Van Gogh's The

Figure 15. continued

Starry Night approximated with 65,536 PCCs each having from zero to seven binding sites.<sup>611</sup> Adapted with permission from ref 611. Copyright 2016 Springer Nature.

innovative displays, eco-friendly paints, and smart labels and sensors. Henceforth, we will briefly review three seminal works in those realms.

High-resolution displays play a critical role in near-eye applications such as VR/AR and 3D displays. These technologies face limitations arising from form factor and additional functionalities, which impose constraints on pixel size. In response to this challenge, a recent study introduced a novel approach utilizing self-assembled nanocavities to create a plasmonic display with consistent, diffuse color regardless of viewing angle and polarization.<sup>545</sup> The integration of this nanostructured optical system into a commercial liquid crystal display (LCD) provided a color display capable of grayscale control and image and video portrayal, Figure 14b. This research represents a significant advancement in the integration of plasmonic nanostructures into display technologies. Although further improvements in color gamut, resonance control, and device integration are suggested by the authors, their work demonstrates the potential for smaller, higher-resolution electrooptic devices and novel display elements facilitated by plasmonic nanostructures.

Addressing the limitations of toxic, fading chemical colorants, recent decades have witnessed the proposal of a myriad of different architectures for structural colors. In particular, recent work has shown how self-assembled plasmonic cavities can be exploited to produce ultralight and vivid optical coloration in large scale with inexpensive materials.<sup>548</sup> The cavities, composed of a self-assembled layer of aluminum nanoislands evaporated onto a thin aluminum oxide film atop an underlying back mirror, selectively absorb specific wavelengths through resonant absorption when illuminated by natural light, while efficiently reflecting nonabsorbed wavelengths. This unique combination results in vivid colors from initially colorless materials, independent of viewing angle and polarization, with the added benefit of adjustability through cavity phase modifications, facilitating diverse color palette creation, Figure 14c. Surpassing the size and substrate limitations typical of many nanostructural architectures and fabrication, the authors developed a self-standing color platform by fabricating their ultralight nanostructures on flakes that can be further mix with a resin to produce an ultralight and eco-friendly paint, that can be transferred to any substrate, demonstrating the commercial potential and bridging the gap between concept and industrial production for large-scale, large-palette, low-cost, and sustainable structural coloration.<sup>548,549</sup>

Beyond high-resolution displays, plasmonic nanostructures also hold promise for sensor applications.<sup>550</sup> Recent research has demonstrated how temperature and humidity sensing functionalities can be achieved through a combination of plasmonic nanocavities and a thermoresponsive polymer, poly(*N*-isopropylacrylamide) (PNIPAM).<sup>551</sup> By strategically incorporating ultrathin PNIPAM layers within the structure, the authors show how colorimetric changes can detect variations in temperature and humidity. This effect arises from the manipulation of plasmonic resonances in metallic nanoparticles, which occur due to changes in the cavity's geometry induced by external stimuli in the polymer layer. The

scalability of fabrication techniques employed, such as spin coating and PVD, suggests promising avenues for real-world sensor deployment beyond laboratory settings at low-cost. Notably, the colorimetric response of these nanosensors could be conveniently read out using a smartphone camera coupled with a dedicated application, enabling user-friendly and *in situ* fast, reliable, and low-cost sensing, Figure 14d.

In summary, plasmonic nanostructures hold immense potential for various applications due to their unique ability to manipulate light. However, conventional nanofabrication techniques limit their real-world impact. Here, PVD based self-assembly emerges as a paradigm breakthrough, offering a scalable and cost-effective approach for creating large-area plasmonic structures that can be commercially employed, paving the path for exciting developments like high-resolution displays with wider viewing angles, eco-friendly and ultralight paints, and user-friendly and power-less sensors. Indeed, by bridging the gap between research and practical applications, large-scale plasmonic nanostructures have the potential to become a 21st century enabling technology. Today, like centuries ago, the crafting of metallic nanostructures to manipulate light continues to inspire awe and yield practical applications.

## 16. SURFACE PATTERNING WITH DNA ORIGAMI

Irina V. Martynenko and Tim Liedl

Despite tremendous advancements in nanophotonic device fabrication through UV- and e-beam lithography or related top-down techniques, several inherent practical limitations remain for such methods. For example, constructing 3D, nanosized and free-standing objects is difficult, especially when different materials are involved. Another remaining challenge is the nanoscale, deterministic positioning of individual, chemically diverse optical components, such as fluorescent (organic) molecules or inorganic nanoparticles.

Structural DNA nanotechnology<sup>552</sup> offers an alternative to circumvent these limitations. By exploiting the programmable recognition of complementary DNA sequences, organic/inorganic hybrid nanostructures of virtually any imaginable shape can be created at a resolution unachievable by top-down fabrication.

DNA origami technology, one of the most prominent branches of DNA nanotechnology,<sup>259,553</sup> has led to the creation of a plethora of DNA nanostructures with nanoscale precision while spanning dimensions from a few nanometers to multiple micrometers.<sup>554,555</sup>

The concept of DNA origami relies on the controlled folding of a long single-stranded DNA (ssDNA) "scaffold", typically derived from M13mp18 phage (~7,000 nucleotides). This scaffold is folded with the help of hundreds of shorter synthetic "staple" strands (Figure 15a), each possessing multiple binding domains.<sup>556</sup> These staples bind to and bring together distant regions of the scaffold through crossover base pairing, effectively knitting the scaffold into a desired shape.<sup>259</sup> The shape design can be programmed by selecting specific strand sequences, which connect designated regions of the scaffold. Upon mixing, heating and slow cooling of the components in a

buffered solution, the staple and scaffold strands self-assemble in a single step, forming trillions of copies of the sequence-programmed DNA origami nanostructure. These structures typically around 100 nm in size, can adopt 2D or 3D shapes as designed with computational tools. Crucially, DNA origami offers exceptional accuracy and precise addressability, enabling site-specific modifications, making it highly valuable for applications in nanophotonics as outlined below. Furthermore, DNA origami can be programmed to form larger architectures assembled from multiple (up to millions and more) individual DNA structures.<sup>554,560</sup>

Compared to other DNA self-assembly techniques, such as tile-based DNA assembly discussed in Section 17, DNA origami generally exhibits higher yield, robustness and the ability to build complex nonperiodic shapes. This advantage partially arises from the highly cooperative nature of the multiple scaffold-staple interactions during the folding process. Prominent advantages of DNA self-assembly include: (i) Cheap and highly parallel production: Self-assembly processes are inherently parallel, affordable<sup>556</sup> and reproducible.<sup>556</sup> In a few microliters, billions of DNA origami structures can simultaneously fold within a few minutes. (ii) Full design freedom in 3D: DNA nanotechnology in general and specifically DNA origami allow to fabricate any desired 3D shape, also those that are particularly difficult to produce by lithographic or 3D printing methods such as overhanging or unsupported structures, shapes with curvatures, sub-10 nm thin features or shapes with cavities or holes. In addition, the hierarchical assembly or polymerization of individual building blocks can result in even more complex 3D DNA and hybrid architectures<sup>557–559</sup> or periodic DNA crystals.<sup>560–567</sup> (iii) Molecular-level resolution: In DNA nanostructures, each strand is made up of a unique sequence and, therefore, allows for distinct spatial addressability within the structure. Coupling diverse subcomponents to the DNA strands yields modular DNA “breadboards” that may carry a wide variety and possibly combinations of optical nanocomponents such as organic dyes,<sup>558,568</sup> metal nanoparticles,<sup>558,568</sup> nitrogen-vacancy centers,<sup>569</sup> carbon nanotubes<sup>570</sup> and semiconductor quantum dots.<sup>571</sup> Subnanometer resolution and orientation control has been demonstrated.<sup>572–574</sup> Indeed, Au nanoparticles have been positioned and detected with a spatial accuracy of 1.20 nm<sup>575</sup> and recently 0.85 nm resolution of positioning individual ssDNA strands separated just by a single base pair on a single-layered sheet of DNA origami has been proven by super-resolving fluorescence blinking of ssDNA-labeled dyes that quickly bind and unbind to the target site.<sup>576,577</sup>

As such, DNA origami has become a state-of-the-art technique for assembling optical nanocomponents including individual molecules or colloidal inorganic nanoparticles in 3D space into well-formed nanophotonic devices with hierarchical complexities. These devices are used in applications such as nanoplasmonics,<sup>578–580</sup> fluorescence imaging,<sup>576</sup> hybrid photonic systems<sup>558,568,581–583</sup> and nanomaterials standardization.<sup>584</sup> More critically, recent advances in large-scale integration of DNA origami on substrates have shifted the focus from individual devices assembled in a buffer solution to arrays of devices on a chip. This development offers an ideal platform for fabricating large-scale, deterministic DNA-programmed arrays of subwavelength optical nanocomponents with complex 2D or 3D architectures. It is therefore consequential that DNA origami-programmed surfaces have

been proposed for applications in optics,<sup>585</sup> photonics,<sup>586</sup> and quantum photonics.<sup>587</sup>

We will briefly summarize the recent progress of DNA origami in nanolithography and multiscale fabrication. Furthermore, we highlight some achievements in DNA-programmed photonics and plasmonics. The general prospects of DNA self-assembly and its application for nanofabrication will conclude this section.

The ability to shape DNA origami into discrete objects or into DNA lattices with nanometer precision can be harnessed to template inorganic nanomaterials of arbitrary shapes with a feature size well below 10 nm. For this, the spatial information stored in the well-defined DNA shapes that are initially folded in a fluid is transferred to other materials in a surface-based process. Two of the commonly reported approaches, DNA coating (Figure 15b-d) or DNA-assisted lithography (Figure 15e-g), result either in hybrid DNA-inorganic or pure inorganic nanostructures, respectively. A third approach relies on patterning substrates with lithography methods followed by depositing DNA origami structures on the patterns and will be discussed below separately.

Via metallization,<sup>588–590</sup> mineralization,<sup>591,592</sup> and atomic layer deposition<sup>560,593</sup> techniques, coatings of DNA origami with noble<sup>588–590</sup> or transition metals,<sup>590,593</sup> SiO<sub>2</sub>,<sup>591,592</sup> or metal oxides,<sup>560,593</sup> have been reported (Figure 15b-d).

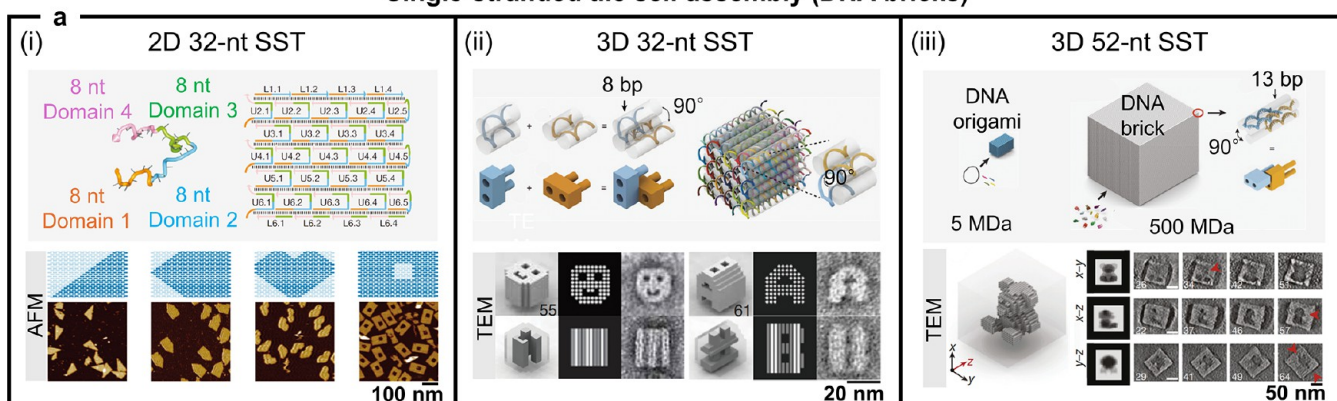
Common to these coating approaches is that DNA structures are exposed to a solution or gaseous phase of the material of interest after folding. Here the DNA then acts as the nucleation site for seeded growth. Often precursors or small nanoparticles are conjugated with the DNA to improve the results or achieve patterns on top of DNA origami sheets or other shapes.<sup>594</sup> Notably, metallization of DNA has been applied early on to create templated nanowires on individual DNA molecules.<sup>595,596</sup>

In a second approach, DNA origami objects or lattices are used as lithographic masks to imprint or transfer their features into inorganic materials on a chip. Figure 15e-g depicts various DNA nanostructures which were used as shadow masks for metal<sup>597</sup> or SiO<sub>2</sub><sup>598,599</sup> deposition and Si,<sup>226,600</sup> SiO<sub>2</sub>,<sup>601,602</sup> or graphene<sup>603</sup> etching. While the resulting structures, composed entirely of inorganic material, have nanoscale features, which can be highly advantageous for many applications, this approach has limited potential for constructing 3D structures.

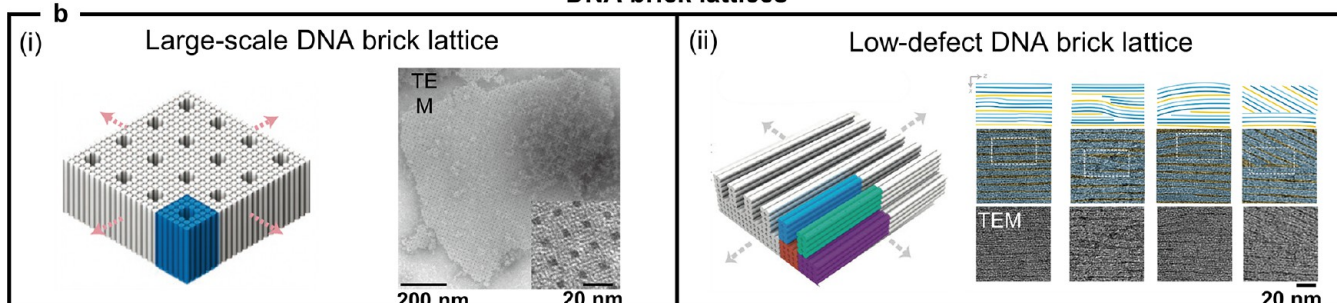
Deterministic integration of the DNA origami assemblies can be achieved via the DNA origami placement (DOP) technology.<sup>604</sup> DOP is based on site- and shape-selective electrostatic immobilization of individual DNA origami objects onto binding sites matching the objects' size and/or shape that have been lithographically defined on desired substrates.<sup>605</sup>

DOP allows one to gain excellent control over the positioning of 2D and 3D DNA origami shapes on a chip surface over macroscopic (millimeters to centimeters) arrays with subwavelength periodicity (Figure 15h, i). This versatile and scalable method relying on self-assembly at ambient temperatures offers the potential to three-dimensionally position any inorganic and organic component compatible with DNA origami nanoarchitecture, demonstrated with gold nanoparticles in Figure 15i. Such near-nanometre-precise spatial positioning of nanoscale building blocks could be crucial for future applications of this method, for example, in optical metamaterials and photonic integrated circuits. Importantly, surface-bound 3D nanostructures can be coated with SiO<sub>2</sub> or other materials to obtain thermal and chemical

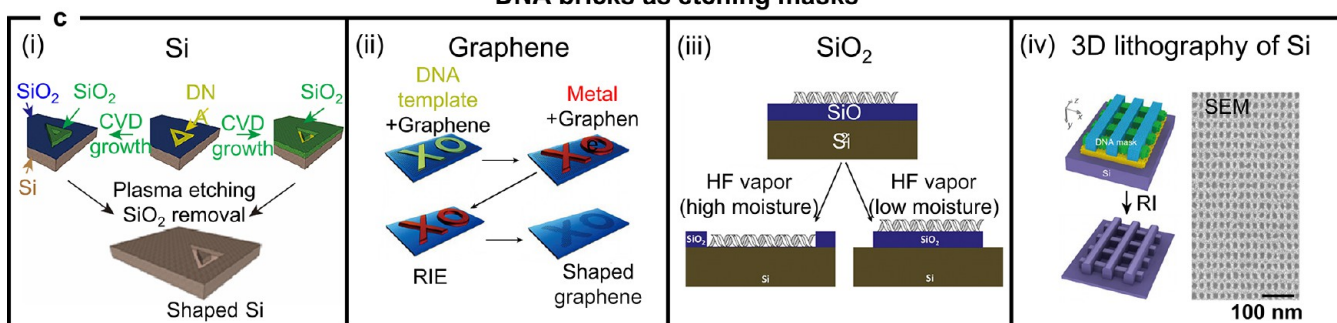
### Single-stranded tile self assembly (DNA bricks)



### DNA brick lattices



### DNA bricks as etching masks



### DNA bricks as material pegboards

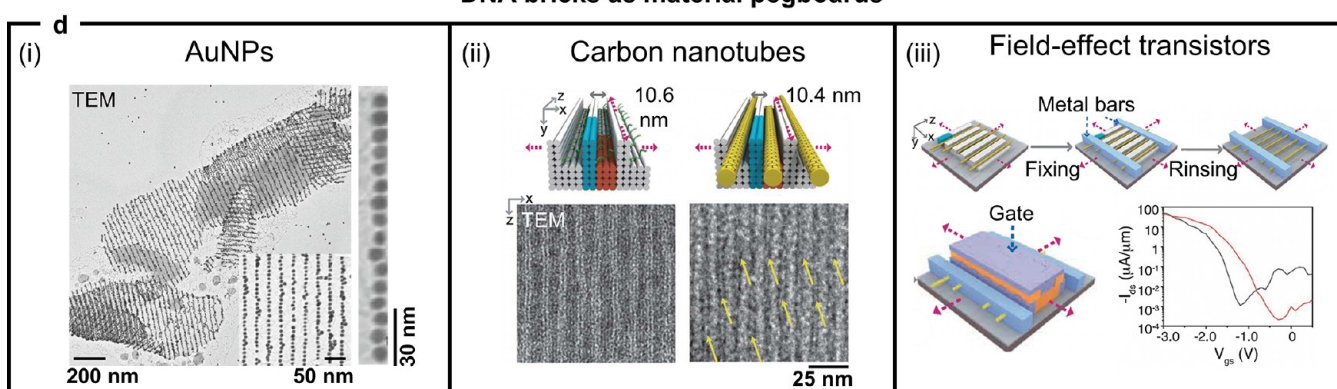


**Figure 16.** Single-stranded tile self-assembly. (a) SST technique for the creation of 2D and 3D DNA nanostructures with complex shapes.<sup>624–626</sup> Adapted with permission from ref 625. Copyright 2012 Springer Nature. Adapted with permission from ref 624. Copyright 2012 AAAS. Adapted with permission from ref 626. Copyright 2017 Springer Nature. (b) Large-scale and low-defect DNA brick crystals with prescribed depths.<sup>627,632</sup> Adapted with permission from ref 627. Copyright 2014 Springer Nature. Adapted with permission under a Creative Common CC BY License from ref 632. Copyright 2021 Springer Nature. (c) DNA structures as etching masks.<sup>226,601,603,633</sup> Adapted with permission under a Creative Common CC BY License from ref 226. Copyright 2021 Springer Nature. Adapted with permission from ref 603. Copyright 2013 Springer Nature. Adapted with permission from ref 601. Copyright 2011 ACS. Adapted with permission from ref 633. Copyright 2013 ACS. (d) DNA structures as material pegboards.<sup>627,634,636</sup> Adapted with permission from ref 627. Copyright 2014 Springer Nature. Adapted with permission from ref 636. Copyright 2020 AAAS. Adapted with permission from ref 634. Copyright 2020 AAAS.

stability.<sup>606</sup> This could help to provide resilience of DNA-based hybrid nanostructures during long-term operation in real-world nanophotonic devices.

UV- and e-beam-lithography have evolved over half a century to a degree of perfection that is hard to rival. Nevertheless, we envision that DNA-assisted lithography and surface-based self-assembly have the potential to outperform the established patterning methods in some aspects such as ease of manufacturing,<sup>607,608</sup> 3D architecting and the possibility of combining materials including the integration of biomolecules, which is crucial for medical applications such as drug or pathogen screening and sequencing. Further applications that might strongly benefit from DNA origami-based fabrication are optical metasurfaces and metamaterials. For example, DNA origami placement can be used to deterministically position DNA-coated metal nanoparticles that resonate with optical wavelengths. A prototypical plasmonic metasurface showing dynamically tunable coloration by DNA origami-directed self-assembly is demonstrated in ref.<sup>609</sup> The polarization-dependent scattering-cross sections of the nanostructures are utilized to create two different red and green images that flip depending on the applied polarization. In another work our group build physical unclonable function labels based on plasmonic coupling of tightly packed randomized nanoparticle assemblies.<sup>610</sup> DNA-assisted self-assembly of colloidal nanoparticles may trigger further research toward the fabrication of nanoengineered metasurfaces.

Despite ongoing advancements in miniaturizing photonic integrating circuits, there is a lack of nanoscale positioning approaches for deterministically integrating single nanoscale emitters such as fluorescent organic molecules or nanoparticles within elements of these circuits.<sup>587</sup> Therefore, additional capabilities enabled by DNA origami and DNA origami placement could prove invaluable. Gopinath, Rothmund, and co-workers demonstrated that DNA origami placement could be used to build chip-based devices with exact numbers of organic dye molecules positioned with high accuracy inside microscopic photonic crystal cavities.<sup>611</sup> In this study, 65,536 independently programmed photonic crystal cavities were fabricated on a single chip, demonstrating the scalability of the DNA-origami-based technique (Figure 15j, k). By exploiting orientational control of a modified DOP approach, this group of authors showed polarization-dependent fluorescence emission of TOTO-3 dyes.<sup>612</sup>

Massively parallel and deterministic placement of individual molecules<sup>611–613</sup> or nanoparticles<sup>614,615</sup> on DNA origami arranged onto large-scale arrays is now within reach. At the same time, the spatial information on discrete DNA origami shapes or DNA lattices positioned on a chip can be transferred readily into inorganic materials. Also, the robustness of silica-coated DNA-origami programmed nanophotonic devices is adequate for long-term operation.<sup>606</sup> Taken together, DNA nanotechnology can bridge the gap between macroscale fabrication and the nanoscale arrangement of individual optical nanocomponents in 3D space.

Future development of strategies to self-assemble even more complex DNA-programmable objects or continuous lattices on lithographically patterned surfaces may open the door for applications in optical metamaterials, photonics and quantum photonics beyond our current expectations. For example, on-surface self-assembly of 3D DNA architectures labeled with noble metal or high-refractive index nanoparticles<sup>616</sup> may boost the development of plasmonic or all-dielectric

metamaterials, respectively. Photonic band gap materials operating in the visible range may be produced by seeded growth of continuous three-dimensional DNA lattices directly on a chip surface. Precise positioning of DNA-embedded quantum emitters<sup>617,618</sup> into designed nanophotonic environments can enable the fabrication of DNA-programmed and chip-integrated single photon sources for quantum communication.

## 17. SURFACE PATTERNING WITH SINGLE-STANDED TILE SELF-ASSEMBLY

Xinxin Jing and Na Liu

In addition to the aforementioned DNA origami technique, complex DNA nanostructures can also be created using scaffold-free DNA tile self-assembly. Different from the DNA origami technique, which imposes limitations on the sizes of DNA structures due to the length of the scaffold strand, this approach enables the construction of larger DNA structures without such constraints. However, a prevalent challenge arises from the formation of ill-formed byproducts due to intertile mismatches, particularly when employing a substantial number of uniquely addressable tiles.<sup>623</sup> To address this challenge, Group Yin introduced another approach utilizing “single-stranded tiles” (SST) as building blocks.<sup>624–626</sup> Each SST consisted of 32/42/52 nucleotides divided into four domains, as illustrated in Figure 16a. Therefore, every SST hybridized with its four neighboring tiles to form a pixel/voxel (up to more than 30,000) on a 2D/3D molecular canvas with a ‘brick-wall’ pattern. Arbitrary-shaped DNA nanostructures could be designed by selecting specific pixels/voxels from such a canvas.

The SST approach offers several distinct advantages. First, the modularity nature allows one to construct a variety of DNA nanostructures using a single canvas. For example, the creation of 107 distinct DNA nanoobjects require only 310 different strands,<sup>625</sup> whereas the creation of one DNA origami object requires about 200 different strands. Second, unlike a multistranded tile scheme, the SST eliminates the need for optimal sequence design and precise stoichiometry control to achieve high assembly yields. Third, it enables the fabrication of low-defect, micrometer-sized 2D crystals with predetermined heights, as depicted in Figure 16b.<sup>627</sup> The fundamental concept involves substituting edge protector strands with connecting strands, resulting in the production of DNA brick crystals instead of discrete DNA nanostructures. Fourthly, DNA brick crystallization does not involve secondary building blocks, allowing for the rearrangement of short SST monomers to eliminate defects. This represents a significant advancement compared to the two-stage hierarchical polymerization process of DNA origami.<sup>628–631</sup> Furthermore, to mitigate crystallographic defects like line dislocations and grain boundaries, Chen et al. employed an orthogonal sequence set. The repeating units contained identical sequences separated by at least 15 nm, ensuring that the rate of line defects could be reduced to less than 1%.<sup>632</sup>

Given its unparalleled high-resolution patterning at the nanoscale and molecular-level programmability, the SST approach opens up new avenues for advanced manufacturing of electronic and photonic devices. Two routes are emerging: DNA structures as etching masks (Figure 16c) and DNA structures as material pegboards (Figure 16d). In the case of the first route, a prerequisite for the masks is that they are robust enough to resist etching. Surwade et al. employed selective CVD growth to deposit a conformal SiO<sub>2</sub> coating on

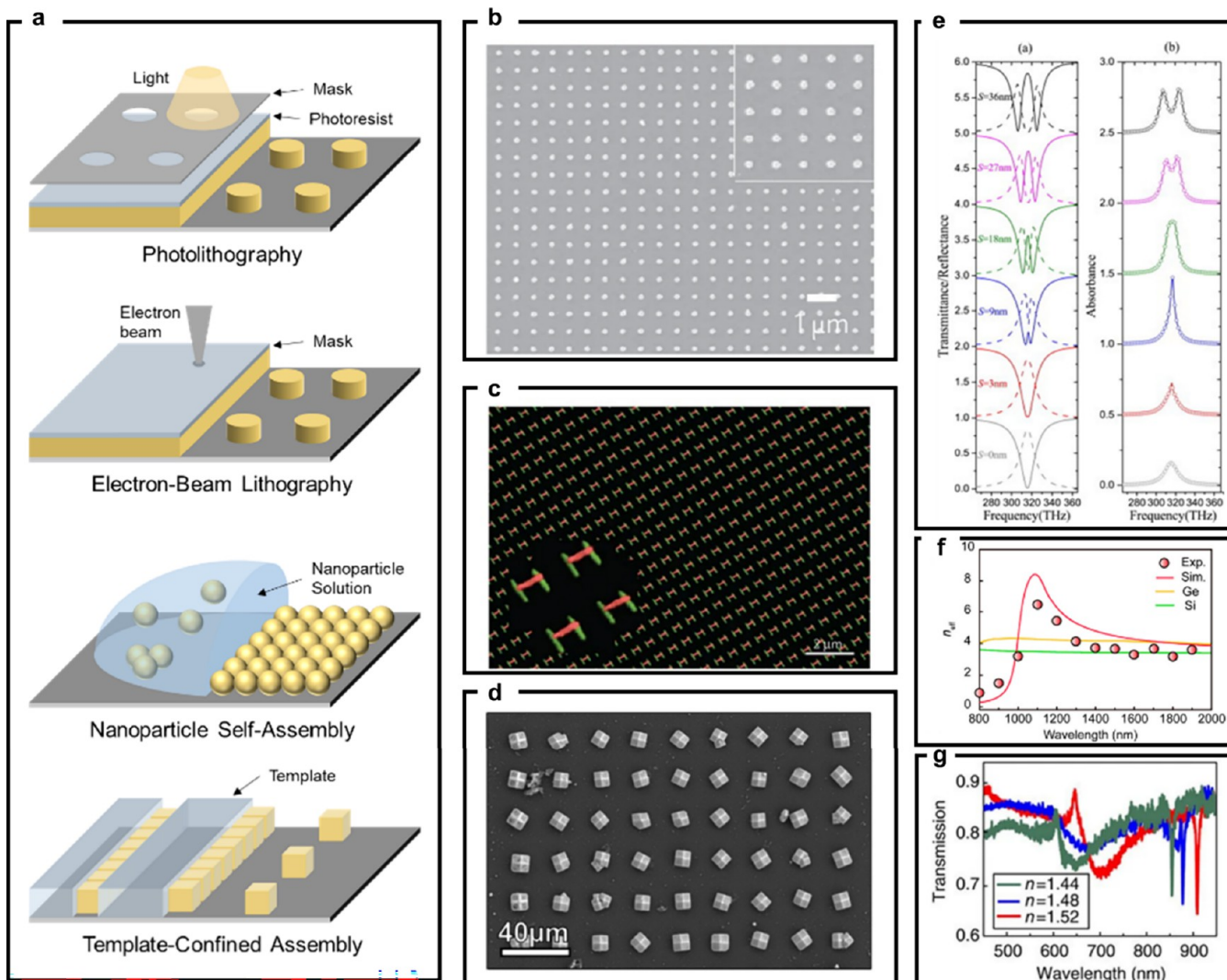


**Figure 17.** Plasmonic nanostructure arrays and assemblies fabricated via nanolithography for photonic applications. (a) Schematics of nanolithographic techniques; from top to bottom: photolithography, electron-beam lithography, nanoparticle self-assembly, template-confined assembly. (b) Ordered Au nanoparticle array made by photolithography.<sup>712</sup> Adapted with permission from ref 712. Copyright 2017 Springer Nature. (c) Array of stacked Au nanobars fashioned by electron-beam lithography.<sup>452</sup> Adapted with permission from ref 452. Copyright 2010 ACS. (d) 3D assembly of Au nanoparticles in photolithographically patterned well.<sup>675</sup> Adapted with permission from ref 675. Copyright 2023 ACS. (e) Plasmon-induced transparency and absorption at different coupling strength.<sup>686</sup> Adapted with permission from ref 686. Copyright 2015 ELSEVIER. (f) Ultrahigh refractive index in plasmonic nanoparticle arrays.<sup>671</sup> Adapted with permission from ref 671. Copyright 2020 ACS. (g) Tunable plasmon lattice resonance in an Au nanoparticle array.<sup>700</sup> Adapted with permission under a Creative Common CC BY License from ref 700. Copyright 2015 Springer Nature.

DNA structures, thereby creating a hard mask for etching the underlying Si substrates.<sup>633</sup> The authors first obtained 26 SiO<sub>2</sub> letters (A to Z) by using corresponding DNA brick letters as templates. Following plasma (SF<sub>6</sub>/O<sub>2</sub>) etching, the patterns were transferred onto Si. Subsequently, the SiO<sub>2</sub> mask was removed using hydrofluoric acid (HF). Similarly, Jin et al. demonstrated the patterning of graphene using metallized DNA nanolithography.<sup>603</sup> After Ar/O<sub>2</sub> plasma RIE and mask removal by sequential soaking in NaCN and formamide, the spatial information on the metallized DNA structures was transferred to graphene, yielding user-defined graphene nanostructures. The metallized DNA mask allowed for plasmonic enhanced Raman spectroscopy of the underlying graphene, providing information on defects, doping and lattice symmetry. However, it is worth noting that both the CVD

oxide growth and metallization steps inevitably compromised the high spatial resolution of the DNA templates.

To further enhance fabrication resolution, a one-step pattern transfer from DNA to an inorganic substrate presents a straightforward solution. However, the direct use of uncoated DNA structures as etching masks demands high chemical and mechanical stability of DNA during etching reactions. To address this challenge, Surwade et al. introduced a novel approach, in which DNA modulated the vapor-phase etching of SiO<sub>2</sub> at the single-molecule level, facilitating a direct pattern transfer from DNA to SiO<sub>2</sub>.<sup>601</sup> The presence of DNA influenced the adsorption of water molecules around it. The disparity between the concentrations of surface-absorbed water on the clean SiO<sub>2</sub> surface and the SiO<sub>2</sub> beneath the DNA was affected by various factors, including the relative humidity of the environment and the substrate temperature. By adjusting

the relative humidity at room temperature, it was possible to alter the relative vapor-phase etching rate, as water could catalyze the etching of  $\text{SiO}_2$  by HF. This modulation led to negative/positive tone pattern transfers from DNA to the  $\text{SiO}_2$  substrate. Building upon previous advancements, Shen et al. introduced a 3D nanolithography technique that utilized DNA brick crystals directly as masks,<sup>226</sup> surpassing the use of monolayer 2D DNA origami or DNA brick nanoobjects. These DNA brick crystals, owing to their significantly greater height, exhibited robustness as etching masks without requiring any inorganic coating. Remarkably, in this study, the line pitch of the etched Si was reduced to as small as 16.2 nm, approximately 50% smaller than values achieved using quadruple patterning or EUV lithography. Furthermore, RIE facilitated the identification of 3D features, such as thickness differences in the DNA brick crystals, resulting in the fabrication of multilayered Si patterns with a vertical critical dimension of 2 nm.

In the context of the second route, DNA brick crystals can serve as ideal platforms for scaffolding various technologically relevant materials, owing to their large-scale, 3D nature, low-defect characteristics, high stability, and rigidity. Ke et al. harnessed DNA brick crystals to assemble densely packed gold nanoparticles within multilayer patterns. The interparticle spacing was as small as 1–2 nm to achieve strong plasmonic coupling.<sup>627</sup> More recently, Sun et al. demonstrated that nanotrenches based on DNA brick crystals could significantly reduce assembly defects, such as crossing, bundling, and irregular pitches of micrometer-sized semiconducting carbon nanotubes (CNTs).<sup>634</sup> This approach resulted in the exclusive parallel alignment of CNTs, facilitating spatially hindered integration of nanotube electronics (SHINE). Notably, the pitch uniformity achieved for CNT arrays via SHINE was 2 orders of magnitude higher than that achieved using thin-film approaches. Moreover, the angular deviation ( $2^\circ$ ) was significantly smaller compared to CNT arrays assembled on flat DNA templates without trenches.

Furthermore, Zhao et al. utilized DNA-templated parallel CNT arrays as model systems to develop a rinsing-after-fixing approach, significantly enhancing key transport performance metrics by more than a factor of 10 compared to other biotemplated field-effect transistors. These DNA-templated transistors demonstrated high on-state performance and fast on-off switching simultaneously.<sup>634,635</sup> Specifically, the rinsing-after-fixing approach allowed for the effective removal of DNA residues without compromising the alignment quality of the CNT arrays. Lithography-defined PMMA cavities were employed to align the assembled CNT arrays on Si substrates on a scale of up to a centimeter.

## 18. NANOLITHOGRAPHY FOR PLASMONIC NANOSTRUCTURE ARRAYS AND ASSEMBLIES

Yuna Kwak and Jwa-Min Nam

Plasmonic nanoparticles, such as those of gold or silver, are known to exhibit unique and useful optical properties due to their localized surface plasmons, the collective oscillation of free electrons upon excitation with light. In their near vicinity, the subwavelength confinement of light generates strongly enhanced electromagnetic fields that can be harnessed for surface-enhanced Raman scattering (SERS)<sup>637,638</sup> and plasmon-enhanced photoluminescence<sup>639–641</sup> applications. In the far field region, they can act as nanoantennas because of their large absorption and extinction cross sections.<sup>642</sup> Interactions

between nanoparticles further enrich their optical behavior: at close distances, plasmon modes couple to form hybrid plasmon modes,<sup>501,643</sup> while in periodic arrays, coupling to diffractive modes creates plasmon lattice resonance modes.<sup>644</sup> The coupling strength is defined not only by the physical characteristics of the individual nanoparticles themselves,<sup>645</sup> but also their relative spatial positioning.<sup>646,647</sup> Therefore, it is crucial to develop methods for manufacturing plasmonic nanostructures with diverse organization at local and long-range scales in a highly controlled manner.

Nanolithography techniques have been extensively employed for constructing plasmonic nanoparticles. Traditional methods include photolithography (Figure 17a, b), in which a photoresist is used to transfer a pattern from a mask to a substrate upon irradiation with light, while in electron-beam lithography, a focused beam of electrons directly patterns the surface (Figure 17a, c). These and similar top-down processes are highly capable of fabricating large-area two-dimensional nanoparticles arrays on planar substrates. The range of plasmonic nanoparticles studied thus far spans simple shapes like nanodiscs<sup>648</sup> and nanorings<sup>649,650</sup> to more complex geometries such as chiral gammadiions.<sup>651</sup> The nanoparticles can be organized in arrays with structural order varying from those with basic repeating units consisting of a single nanoparticle (Figure 17b), to hierarchically ordered configurations where multiple nanoparticles are arranged within each unit cell<sup>452,652,653</sup> (Figure 17c). Furthermore, the spacing between the units can be adjusted from tens to hundreds of nanometers,<sup>654</sup> altering interparticle interactions to tailor their optical properties. Such attributes have driven the design and synthesis of plasmonic nanoparticle arrays demonstrating distinctive optical behaviors.

Despite their advantages, top-down nanolithography faces difficulty in making features smaller than a few nanometers and there is limited control over nanoparticle size, morphology, and uniformity. By contrast, bottom-up methods involve the self-assembly of presynthesized nanoparticles including DNA-tethered metal nanoparticle dimers with ~1 nm gap for single-molecule SERS.<sup>655–657</sup> Through recent advances in colloidal synthesis nanoparticle homogeneity has been greatly improved<sup>452,641</sup> and new nanoparticle designed with intricate morphologies.<sup>658,659</sup> It is even possible to achieve morphologies unattainable by top-down methods, such as nanoparticles with interior nanogaps. These nanogaps can be controlled down to ~1 nm<sup>660</sup> in a variety of configurations such as core-gap-shell,<sup>661–665</sup> dual-gap,<sup>666</sup> and cross-gap structures,<sup>666</sup> with greatly enhanced near field useful SERS applications. Concurrently, various nanoparticle self-assembly techniques have been developed (Figure 17a), including those based on slow-evaporation,<sup>667</sup> capillary forces,<sup>668</sup> and DNA-hybridization.<sup>669</sup> By precisely tuning the interparticle forces involved, we can control particle–particle distance down to the subnanometer scale,<sup>670</sup> which is critical for optical applications as plasmonic interactions at close distances are highly sensitive to their spatial separation. Moreover, the dimensions of the assembled superstructure can readily be modified between one-dimensional chains,<sup>668</sup> two-dimensional arrays<sup>671</sup> and three-dimensional supercrystals with varying crystal packing.<sup>669</sup>

Hybrid approaches that integrate the strengths of both top-down and bottom-up methodologies are also gaining significant attention.<sup>672</sup> Template-confined self-assembly utilizes wells defined via top-down lithography as templates to dictate the locations where nanoparticles assemble on a

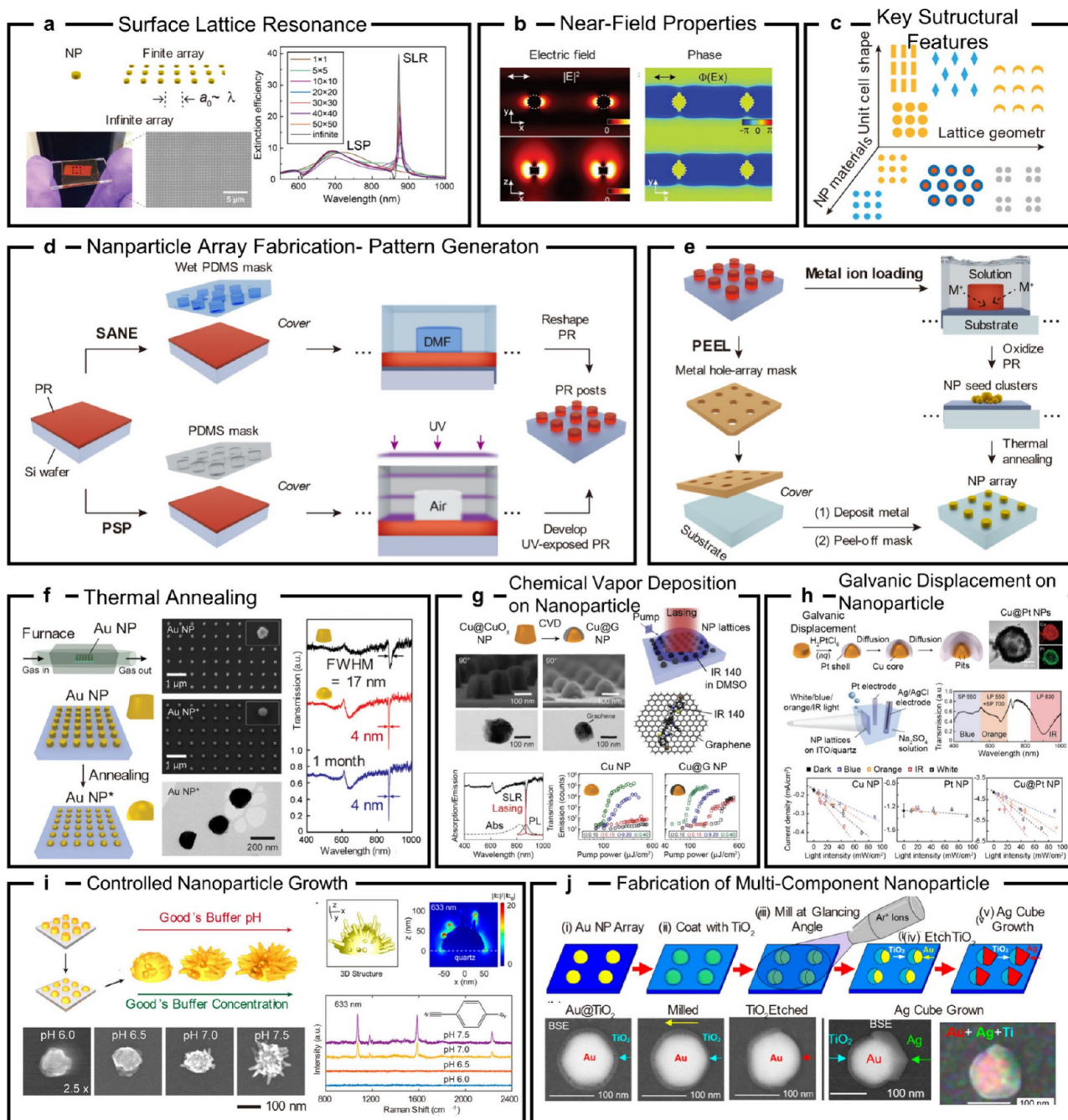


**Figure 18.** Nanofabrication techniques for plasmonic nanoparticle arrays and their postfabrication treatments. (a) Calculated extinction spectra of individual Au nanoparticles and their finite- and infinite arrays. Optical and electron micrograph images were taken from ref 719. Extinction spectra were taken from ref 713. Adapted with permission from ref 713. Copyright 2020 ACS. Adapted with permission from ref 719. Copyright 2019 ACS. (b) Calculated electric near-field and phase distributions of the SLR of an infinite Au nanoparticle array.<sup>714</sup> Adapted with permission from ref 714. Copyright 2023 ELSEVIER. (c) Key structural features of nanoparticle arrays for engineering Surface lattice resonances. SLR: Surface lattice resonance. (d) Schematics of soft lithography techniques, solvent-assisted nanoscale embossing (SANE) and phase-shifting photolithography (PSP), that can pattern PR posts on solid substrates. (e) Schematics of pattern transfer by PEEL (Phase-shift photolithography + Electron-beam deposition + Etching + Lift-off) and metal-ion loading. (f) Thermal annealing treatments of metallic nanoparticle arrays. Scanning- and transmission electron micrographs shown in the middle demonstrate the reshaping of annealed nanoparticles.<sup>698</sup> Adapted with permission under a Creative Common CC BY License from ref 698. Copyright 2015 Academy of Sciences. (g) Graphene formation on Cu nanoparticle arrays via chemical vapor deposition and gain-threshold reduction in their lasing actions.<sup>698</sup> Adapted with permission under a Creative Common CC BY License from ref 698. Copyright 2015 Academy of Sciences. (h) Pt shell formation on Cu nanoparticles on ITO-glass substrates via Galvanic displacement and enhanced photoelectrocatalysis for hydrogen evolution reactions.<sup>738</sup> Adapted with permission from ref 738. Copyright 2021 ACS. (i) Au spike growth on thermally annealed Au nanoparticle arrays and enhanced SERS activity.<sup>741</sup> Adapted with permission from ref 741. Copyright 2023 ACS. (j) Symmetry-broken functionalization of Au NP arrays enabled by combining ALD of  $TiO_2$ , Ar-ion milling, and Ag growth.<sup>744</sup> NP: nanoparticle. Adapted with permission from ref 744. Copyright 2023 ACS.

substrate,<sup>673–676</sup> yielding superstructures with both local and long-range order (Figure 17a, d). In nanoparticle imprint lithography, the pattern of an elastomeric stamp is transferred to nanoparticles dispersed on a substrate.<sup>676,677</sup> Hence the patterning capability of top-down lithography can be combined with colloidal nanoparticles having a sophisticated internal structure with a unique overall architecture. Another innovative technique, substrate-defined growth, involves patterning nanoparticle seeds on a surface, which are subsequently overgrown through wet-chemical synthesis.<sup>678</sup>

Irrespective of the specific method of their fabrication, well-arranged plasmonic nanostructures have been subjects of great interest for the ability to artificially engineer optical properties difficult to achieve with natural materials.<sup>679</sup> Interactions among plasmonic nanoparticles can be categorized into short-range and long-range interactions, and those that arise between a few nanoparticles and many-nanoparticle interactions. At close distances, interactions between nanoparticles are dominated by hybridization between plasmon modes of appropriate energy and symmetry.<sup>642,643,680,681</sup> Up to a few nanometers, the coupling strength increases as nanoparticle separation decreases, corresponding to a red-shift in the resonance peak.<sup>647,682</sup> These hybrid modes can further lead to magnetic induction<sup>683</sup> or be channeled to create a near-perfect absorber<sup>684–686</sup> (Figure 17e). At the other extreme, destructive interference between broadband plasmon modes and subradiant modes as in Fano resonance<sup>687</sup> leads to metamaterials with optical transparency.<sup>653,686,688,689</sup> Extending hybridization beyond a few nanoparticles into large two-dimensional arrays, the capacitive coupling between nanoparticle dipole resonances can be harnessed to create thin films with refractive index higher than values achievable with silicon or germanium<sup>671</sup> (Figure 17f). The large refractive index is due to the large real permittivity of these materials that, upon coupling to a gold film can exhibit a crossover between positive and negative values called the epsilon near-zero condition,<sup>690</sup> which has potential optomechanical applications.<sup>691</sup> Finally, by adding a third dimension to form plasmonic supercrystals with high crystallinity, Mie resonances<sup>692,693</sup> or photonic band gap modes<sup>694</sup> can be engineered.

At longer length scales, periodically ordered nanostructures with interparticle separation on the order of the wavelength of light sustain diffractive surface lattice resonance modes that can couple to plasmon modes to create plasmon lattice resonances<sup>644,695</sup> (Figure 17g). Early lattices had broader line-widths<sup>696</sup> than predicted theoretically<sup>697</sup> due to the large number of lattice defects and high nanoparticle heterogeneity; however, developments in fabrication methods<sup>652</sup> combined with annealing treatment to reduce nanoparticle polycrystallinity and improve shape uniformity<sup>698,699</sup> have led to lattice resonances with ultrahigh quality factors (Q-factors)<sup>13,698,699</sup> and corresponding low losses. The resonance wavelength is determined by the lattice periodicity,<sup>654</sup> the refractive index of the surrounding medium,<sup>700</sup> and the material (aluminum-based lattices can thus support resonances at shorter wavelengths than gold or silver).<sup>654</sup> Furthermore, analysis of their angle-resolved transmission spectra shows their dispersion relations. Though a comparison of lattices of varying symmetry found that there was little effect on the position of the resonance peak,<sup>701</sup> it was discovered that their dispersion relations were widely divergent.<sup>702</sup> Plasmon lattice resonances have received much attention due to their lasing properties upon integration with optical gain materials.<sup>703,704</sup> The

ultranarrow line width combined with the trapping of light at dispersion band-edges<sup>705</sup> provide optimal conditions for low threshold lasing under angle- and polarization-dependent conditions. Utilizing multiple band edges and the higher order modes present in hierarchical arrays at different wavelengths can even generate multimodal, multicolor lasing.<sup>705,706</sup>

In addition to the examples mentioned above, many other collective properties have been demonstrated by plasmonic nanostructures. For instance, chiroptical effects are seen in chiral nanoparticles or achiral nanoparticles with chiral arrangement.<sup>707</sup> These nanostructures can also exhibit plasmon hybridization or coupling to diffractive modes<sup>708</sup> as in the case of their achiral counterparts. Another example is bound-states in the continuum, perfectly confined, nonradiative modes with ultralong lifetimes,<sup>91</sup> which have been studied in plasmonic nanoparticle arrays both theoretically<sup>709,710</sup> and experimentally.<sup>287</sup> A recent work has even shown the ability of plasmonic metamaterials to act as time crystals with periodic oscillations of transmissivity.<sup>181</sup> The incorporation of nanoparticles with intragaps and other complex morphologies, and their organization and patterning into unique superstructures will potentially generate plasmonic nanostructures with heretofore unseen optical properties. This can allow us to explore multiscale interactions, as in the case of strong coupling between gap plasmon modes and lattice modes<sup>711</sup> or open the door to new applications.

## 19. PLASMONIC NANOPARTICLE ARRAY

Sang-Min Park and Teri W. Odom

Arrays of plasmonic nanoparticles with periodicities comparable to the wavelength of light can support surface lattices resonances when their localized surface plasmons couple to diffractive modes.<sup>644,695</sup> At visible wavelengths, surface lattices resonances can exhibit much narrower line widths (2–20 nm) than localized surface plasmons from individual nanoparticles (50–100 nm) because of reduced radiative losses (Figure 18a).<sup>713,714</sup> At resonance, the nanoparticles in the array support electric field oscillations that are in phase, have local near-field intensities 1–2 orders of magnitude higher than that of single nanoparticles, and collectively support an electromagnetic standing wave (Figure 18b).<sup>715</sup> Besides being of interest for these distinct properties, plasmonic nanoparticle arrays are advantageous for use in light-matter interactions in a range of applications. For example, nanoscale lasing and exciton-polariton condensates have been realized by combining plasmonic arrays with different emitters, including organic dyes,<sup>715–717</sup> semiconducting quantum dots,<sup>704</sup> and perovskites nanocrystals.<sup>718</sup> Plasmonic nanoparticle arrays can also show unique radiation profiles by tuning features of the array,<sup>712,719–723</sup> including (i) unit cell shape,<sup>720,721</sup> (ii) lattice geometry,<sup>654,702,712,722,723</sup> and (iii) nanoparticle materials<sup>724</sup> (Figure 18c). In this mega-review section, we will describe methods for scalable nanopatterning of plasmonic nanoparticle arrays and their postfabrication treatment.

To prepare nanoparticle arrays with high-quality surface lattices resonances and desired properties, unit cell shape and lattice geometry should be optimized. Traditionally, serial, direct-write techniques such as electron beam lithography were used because they can pattern nanostructures with arbitrary shapes.<sup>696,725</sup> However, challenges in scaling the patterned array size as well as limited access to these tools have hindered

studies. Parallel nanofabrication methods that combine soft lithography and simple pattern transfer techniques have enabled effective and large-area patterning of nanoparticle arrays over  $10 \text{ cm}^2$ -areas.

Soft lithography can generate large-area patterns made of PR using an elastomeric mask or mold generated by curing PDMS on a master pattern.<sup>726</sup> Figure 18d illustrates two representative techniques: solvent-assisted nanoscale embossing<sup>727</sup> and phase-shifting photolithography.<sup>728</sup> In the solvent-assisted nanoscale embossing process, a PDMS mold is first wet with an organic solvent and then placed into contact with a thin layer of PR on a substrate (usually a Si wafer). The solvent within recessed regions of the mold dissolves the PR, and after an evaporation period with the mold still in contact with the PR, the PR is resolidified to form the same pattern as that on the master. In phase-shifting photolithography, a PDMS mask is placed into conformal contact with a PR-coated substrate, and then UV light exposure followed by development can result in patterned PR. The principle of phase-shifting photolithography takes advantage of the different refractive indices of the air-PDMS mask interface in contact with the PR. When the PDMS (or air) patterns are larger than the diffraction limit, PR features at the edges of the patterns will result after development; when mask patterns have sizes that are subwavelength,<sup>729</sup> then the patterns will be transferred to PR in a 1:1 fashion. One advantage of phase-shifting photolithography over solvent-assisted nanoscale embossing is that multiple exposures with different masks can be used to generate complicated lattice geometries, including moiré lattices.<sup>730</sup> Solvent-assisted nanoscale embossing and phase-shifting photolithography can generate nanoparticle arrays with desirable ranges of periodicities ( $a_0 = 200\text{--}800 \text{ nm}$ ) and post diameters ( $\geq 100 \text{ nm}$ ) in a wide range of lattice geometries. Notably, in contrast to pressure- or heat-driven imprinting techniques,<sup>81,731</sup> the scalable nanofabrication methods do not require sophisticated tools to control PDMS mask position, contact pressure, and substrate temperature.

Starting from PR patterns, plasmonic nanoparticle arrays can be produced by pattern transfer techniques such as PEEL (Phase-shift photolithography + Electron-beam deposition + Etching + Lift-off) (Figure 18e, bottom left).<sup>652</sup> The critical step in PEEL is the generation of a free-standing metal (Au or Cu) hole-array film that can be used either as an etch mask or physical deposition mask; the patterns on the metal mask define features of the nanoparticle array, such as nanoparticle shape, array periodicity, and lattice symmetry.<sup>721</sup> Uniform and large-area nanoparticle arrays can be obtained after deposition of the desired metal through the hole-array mask, which can be easily removed by Scotch tape or chemical etching.

Another pattern transfer method is metal-ion loading, where polymeric posts are used as the sacrificial host materials to form metallic nanoparticles.<sup>699</sup> Poly(4-vinylpyridine) posts incubated in aqueous solutions containing ions of target metals (e.g., Au, Pt, or Pd) can be oxidized with an O<sub>2</sub> plasma, which reduces the metal ions into small nanoparticle seeds (Figure 18e, top right). After thermal annealing, the small nanoparticle seed clusters can merge into ordered and uniform nanoparticles. One distinct advantage of this approach is that nanoparticle arrays can be prepared from various alloyed materials, including AuPd, FePt, or CoPt.

Nanoparticle arrays fabricated by soft lithography followed by pattern transfer can show surface lattice resonances with high quality factors desirable for light-matter interactions.

Recent work has demonstrated that postsynthesis treatments of the nanoparticles offer opportunities to increase the quality factor substantially as well as provide chemical and materials function beneficial for nanophotonic applications. The following subsections review nanofabrication strategies that have expanded the applications of plasmonic nanoparticle arrays for low-threshold nanolasers, photocatalysis, and chemical sensing.

As-fabricated plasmonic nanoparticles produced by physical vapor deposition methods generally exhibit poly crystalline structures, which can result in damping of the plasmon resonances due to electron scattering at nanoscale grain boundaries and lattice defects.<sup>732,733</sup> Also, for more reactive plasmonic metals, such as Ag and Cu, poly crystalline nanoparticles show increased oxidization since reactive species prefer to attack grain boundaries.<sup>734</sup> Therefore, improving the crystallinity of the nanoparticles can improve the quality factor of the surface lattice resonances as well as the chemical stability of the arrays. Thermal annealing of nanoparticle arrays has been shown to be an effective strategy to reshape and to improve nanoparticle crystallinity.<sup>698,735,736</sup> For example, the annealing of Au nanoparticle arrays in an Ar atmosphere at high temperatures (900 °C) can significantly reduce the surface lattice resonance line width (17 to 4 nm), resulting in  $Q > 200$  (Figure 18f); similarly narrow surface lattice resonance line widths were observed from thermally annealed Ag, Al, and Cu nanoparticle arrays, and were stable for months.<sup>698</sup> Such ultranarrow surface lattice resonance modes as cavity modes combined with organic dyes as gain have resulted in lasing action with narrower emission spectra and higher nonlinearity.

Controlling the surface chemistry and functionality of plasmonic nanoparticles can also result in improved optical properties of the arrays. For example, using Cu nanoparticle arrays as catalytic materials, few-layer graphene (G) can be conformally grown on the nanoparticles by chemical vapor deposition in a CH<sub>4</sub> and H<sub>2</sub> atmosphere to produce Cu@G core–shell nanoparticles (Figure 18g).<sup>698,737</sup> Interestingly, the graphene layer not only protects the Cu nanoparticles from oxidation but can also facilitate lasing at lower concentrations of liquid dyes as gain (IR-140 and DCM); this response is attributed to the transient assembly of aromatic dye molecules within the electromagnetic hot spots near the nanoparticle surface because of  $\pi$ – $\pi$  interactions with the graphene.<sup>737</sup> Solution-based chemistry is also an effective approach to impart additional functionality to the nanoparticle arrays. Using galvanic replacement chemistry, Pt shells can be grown with different thicknesses on prepatterned Cu nanoparticle arrays (Figure 18h).<sup>738</sup> Since Pt is catalytic, Cu@Pt core–shell nanoparticle arrays on ITO-substrates could be used as photoelectrocatalysts for hydrogen evolution reactions.<sup>739,740</sup>

Finally, taking advantage of the growth mechanism of colloidal nanoparticles can provide opportunities to modify morphology and composition of surface-patterned nanoparticles.<sup>678</sup> For example, Au spikes have been grown on thermally annealed Au nanoparticle arrays by incubating them in an aqueous growth solution containing Good's buffers and HAuCl<sub>4</sub> (Figure 18i);<sup>741,742</sup> their growth can be precisely controlled via buffer pH and concentration similarly to seed-mediated colloidal synthesis of spiky nanoparticles.<sup>743</sup> The Au spikes can confine the local electric fields at the sharp tips (2–3 nm radius of curvature), which can improve the performance as SERS substrates. Moreover, since relatively large surface-

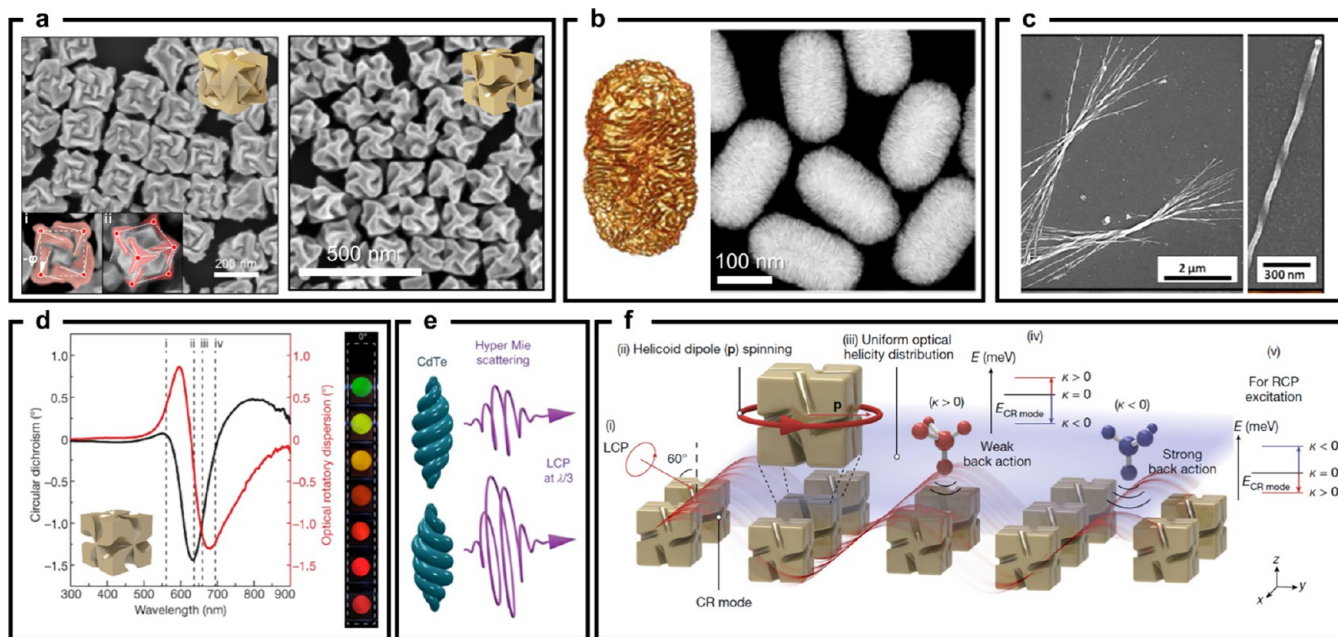


**Figure 19.** 3D chiral morphology shaping in nanoparticles. (a) SEM and schematic images of 432 helicoid I (left) and 432 helicoid III (right) which are synthesized via enantioselective interaction at organic (amino acids and peptides)-inorganic (gold) interface.<sup>658</sup> Adapted with permission from ref 658. Copyright 2018 Springer Nature. (b) Tomography reconstruction (left) and transmission electron microscope (TEM) image (right) of plasmonic gold nanorods with an intricate network of chiral wrinkles, synthesized by chiral template (1,1'-bi(2-naphthol) (BINOL) and its derivative 1,1'-binaphthyl-2,2'-diamine (BINAMINE)) assisted synthesis.<sup>755</sup> Adapted with permission from ref 755. Copyright 2020 AAAS. (c) SEM images of twisted ribbon-shaped semiconductor nanoparticles synthesized through circularly polarized light (CPL).<sup>756</sup> Adapted with permission from ref 756. Copyright 2010 AAAS. (d) Circular dichroism and optical rotatory dispersion response of 432 helicoid III (left) and polarization-resolved color of 432 helicoid III solutions with various resonant wavelengths (right);<sup>658</sup> schematic illustration of 432 helicoid III (inset). Adapted with permission from ref 658. Copyright 2018 Springer Nature, (e) Schematic illustration showing the third-harmonic circular dichroism generation from 3D chiral Cadmium-Telluride (CdTe) dielectric nanoparticles.<sup>770</sup> Adapted with permission from ref 770. Copyright 2022 Springer Nature. (f) Schematic diagram of enantioselective sensing on 2D helicoid crystal. (i) Under CPL illuminations, (ii) the electric dipole ( $p$ ) of each helicoids collectively spins to the direction of CPL, (iii) generating uniform optical helicity ( $h$ ) on 2D helicoid crystal. The introduction of chiral molecules with different handedness on the 2D helicoid crystal distinctively affect the energy levels of 2D helicoid crystal, which excited by (iv) left-handed CPL (LCP) and (v) right-handed CPL (RCP).<sup>708</sup> Adapted with permission from ref 708. Copyright 2022 Springer Nature.

bound nanoparticle arrays can have clean surfaces without needing stabilizing ligands for solubility in solution, nanoparticles with more complex shapes and materials combinations can be created. One example nanomaterial is multi-component nanoparticles as antenna-reactor photocatalysts (Figure 18j) prepared by ALD, FIB, and solution-based nanoparticle growth on annealed Au nanoparticle arrays.<sup>744</sup>

## 20. 3D MORPHOLOGY SHAPING IN NANOPARTICLES

Hye-Eun Lee, Ryeong Myeong Kim, and Ki Tae Nam

Controlling the 3D morphology of optically active inorganic crystals is of significant interest as it allows for new optical modes that 2D patterning using lithography cannot achieve. For example, the 3D chiral morphology can exhibit optical activity from multiple angles, as chirality is controlled in various directions within the 3D structure.<sup>658</sup> Polarization of light and phase can be controlled with 3D morphology controlled nanoparticle. Furthermore, the collective response of arranged 3D chiral particles can lead to a uniformly amplified optical response through interparticle coupling.<sup>708</sup> Given these advantages, shaping 3D morphology at the single nanoparticle level is crucial, especially at the few-nanometer scale, as it enables optical modulation in the visible range and provides desired optical properties. While various shapes of 3D particles (spherical, square, rod, triangle, etc.) can control

polarized light, in this part, we will focus specifically on the emerging field of chiral 3D particles.

Over the past years, various methods for particle control have been developed, including crystallographic, kinetic, ligand-based, and overgrowth techniques.<sup>745,746</sup> Based on these technologies, the inclusion of chirality inducers can transform not only the handedness of single nanoparticles but also their crystal facets, local features, and curvatures in a multidimensional manner. This can result in new chiral morphology diagrams that were previously unattainable. In this section, we will explore three main categories of chiral inducers in 3D morphology control: biomolecule induced enantioselective interactions, ligand self-assembly, and polarized light. We will discuss how these methods contribute to the development of diverse 3D chiral morphologies and examine their optical properties through various examples.

Chirality has long been of interest in scientific fields, driving extensive research into chiral crystals. Early studies focused on crystallographically asymmetric materials like quartz,  $\beta$ -AgSe, and selenium, exploring their chiroptical properties in bulk single crystals. The Markovich group synthesized semiconductor nanocrystals with chiroptical activity, using mercury sulfide, an asymmetric crystal structure, and chiral penicillamine, containing a thiolate group capable of strong enantioselective surface binding.<sup>747</sup> These nanocrystals, approximately 10 nm in size, feature long helices of alternating

mercury and sulfur atoms spiraling around the *c*-axis of the hexagonal unit cell. Extending their research to the Te system, which shares the same chiral space group *P*3<sub>1</sub>21, they used various thiolated chiral biomolecules on Te crystals to synthesize asymmetric nanoparticles characterized by twisted ridges diagonally intersecting between vertices at both ends.<sup>748</sup>

Exposing crystallographically asymmetric surfaces, as demonstrated in previous examples, enhances chirality transfer through enantioselective interactions with asymmetric organic molecules, a critical factor in controlling 3D shapes at the level of individual particles. Interestingly, the chirality of inorganic materials can arise from the asymmetric atomic arrangement on their surfaces, even if the unit cell itself is symmetric (e.g., gold in a face-centered cubic lattice).<sup>749</sup> These enantioselective interaction can be more precisely utilized especially at the interface of high index surface and biomolecules. In bulk single crystal, The Gellman group illustrated on a Au surface that kink atoms can function as asymmetric centers, allowing three crystal surfaces to be oriented either clockwise or counter-clockwise.<sup>750</sup> Depending on the stacking arrangement of Au atoms, these surfaces can exhibit as two distinct chiral forms. Exploiting this surface chirality and its interaction with chiral organic materials- amino acid and peptides, the Nam group successfully synthesized a diverse range of 3D chiral nanostructures known as the 4-, 3-, and 2-fold symmetric helicoid series.<sup>658,751,752</sup> The nanoscale controllability at 3D nanomorphology is unprecedented, resulting uniform chiral nanoparticles.

In their study, the authors structured the growth process into two distinct steps: the initial growth stage involving low-Miller-index-plane-exposed nanoparticles and the subsequent high-Miller-index surface chiral evolution stage. During the chiral evolution stage, cube-shaped seeds with {100} facets underwent a transformation from low-index to high-index surfaces.<sup>658</sup> Concurrently, introduced L-cysteine (L-Cys) molecules selectively adhere to specific chiral faces, facilitating the development of twisted edges that elongate and thicken, eventually forming a chiral morphology exhibiting 432 symmetry, named helicoid I (Figure 19a).

In the same setup, substituting cube seeds with octahedral ones ({111} facets) and introducing glutathione peptide results in the growth of gold surfaces exposing different chiral surfaces which is different from helicoid I. This approach yields 432 helicoid III with pinwheel-like structures on each facet, significantly enhancing the g-factor (anisotropy factor) and showing strong optical responses in the visible range (Figure 19a). By modifying various chemical parameters such as chemical concentrations and seed injection times, subsequent studies explored different intermediate shapes exposing high-index surfaces during gold particle growth,<sup>751</sup> leading to the creation of a chiral plasmonic nanostructure based on a rhombic dodecahedron shape, 432 helicoid IV. Recent advancements include the use of deep learning techniques to identify key motifs for controlling chiral morphology and understanding formation mechanisms, expanding toward diverse chiral inorganic morphogenic processes.<sup>753</sup>

Another method for inducing chirality involves template-guided synthesis using asymmetric assembly of chiral molecules and ligands. Typically, amphiphilic molecules (surfactants) with self-assembled structures are employed as chiral templates. These molecules can incorporate chiral moieties to induce chiral assembly or symmetry-breaking cosurfactants can be introduced to guide chiral structure

formation. For instance, N-miristoyl-L-alanine sodium salt, where an amino acid is attached to the end of an anionic surfactant, forms assemblies that provide chiral channels.<sup>754</sup> By electrostatically binding inorganic precursors using amino-silane, chiral mesoporous silica can be synthesized. Recently, the Liz-Marzan group achieved plasmonic gold nanorods with an intricate network of chiral wrinkles and high anisotropy factors (g-factor ~0.20) using 1,1'-bi(2-naphthol) (BINOL) and its derivative 1,1'-binaphthyl-2,2'-diamine (BINAMINE) as cosurfactants with an achiral cetyltrimethylammonium chloride surfactant (Figure 19b).<sup>755</sup> BINOL molecules, due to their axial chirality, can form worm-like micelles, serving as templates for anisotropic growth. The (R)-BINAMINE-cetyltrimethylammonium chloride covering gold nanorod leads to the formation of chiral wrinkles on the nanorod surface, creating intergrooves tilted at 0° and 45° angles with sizes of 2–3 nm, and exhibiting high anisotropy factors across a broad wavelength range (from 500 to beyond 1350 nm).

Circularly polarized light (CPL) sources are valuable resources for inducing chiral structures due to their ability to provide high enantiopurity and easily adjust resonance wavelengths. The Kotov group reported semiconductor nanoparticles in twisted ribbons forms where handedness varies with the CPL (Figure 19c).<sup>756,757</sup> Light-controlled chiral imprinting relies on the photooxidation of thioglycolic acid stabilizers on CdTe nanoparticles. Initially racemic, these nanoparticles absorb light corresponding to their handedness, activating the photooxidation and transforming them into CdS nanoparticles with fewer ligands. The resulting asymmetrically truncated nanoparticles self-assemble into twisted nanoribbons through cooperative interactions. Through this light-induced self-assembly process, the group synthesized right- (left-)handed twisted nanoribbons with an enantiomeric excess exceeding 30%.<sup>757</sup>

Another intriguing example utilizing CPL involves synthesizing chiral structures using localized electric fields generated when light is absorbed by gold nanoparticles. When CPL is applied to gold nanocuboids, light concentrates at specific corners, creating twisted electric field distributions around plasmonic nanocuboids.<sup>758</sup> Theoretical explanations also suggest that CPL can induce asymmetric excitation of hot carriers in achiral gold structures, facilitating surface chemistry (photogrowth).<sup>759</sup> Experimental evidence shows that applying CPL to nanoprisms concentrates electric fields at their corners, creating blade-like protrusions that grow corners more rapidly, forming spiral patterns.<sup>760</sup>

The development of synthetic procedures for 3D morphology-controlled chiral nanoparticles paves the way for the application of chiral nanostructures across diverse fields, including photonics,<sup>658,755,761–768</sup> spectroscopy,<sup>769–771</sup> optoelectronics,<sup>772–776</sup> sensing,<sup>708,777–783</sup> and biomedical fields.<sup>760,769</sup> These 3D chiral structures exhibit light manipulation capabilities comparable to those of lithography-based 2D chiral nanostructures and demonstrate optical activities absent in perfect 2D chiral configurations.<sup>779,784</sup> For example, the 432 helicoid series,<sup>658,751,752,785,786</sup> with its 432 symmetry representing the most isotropic symmetry in 11 crystallographic point groups at the ~200 nm scale,<sup>787</sup> retain their chirality in three-dimensional space, demonstrating optical activity independent of light propagation direction. Individual 432 helicoid III nanoparticle exhibits a g-factor of approximately 0.8 at single chiral scatterometry,<sup>788</sup> and even in randomly

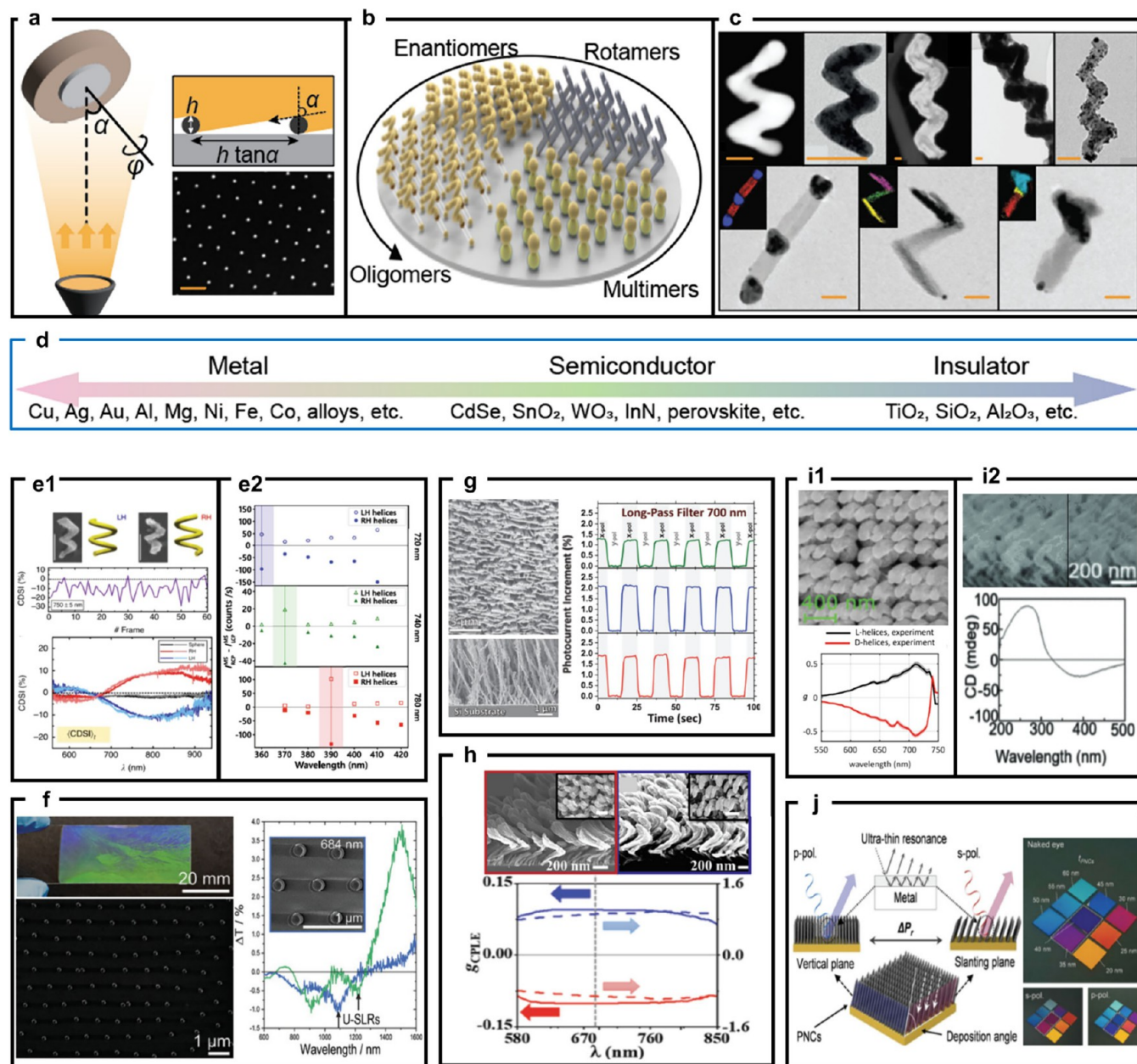


**Figure 20.** Schematics of the glancing angle deposition (GLAD) method and representative applications in nanophotonics. (a) During GLAD fabrication the substrate is tilted at an angle  $\alpha$  with respect to the vapor flux coming from a heated crucible, with optional substrate rotation ( $\varphi$ ) to control the morphology. The setup is in a vacuum chamber and contains electron beam and/or thermal evaporators (not shown). The shadow distance between adjacent seeds is defined by  $h \tan \alpha$ , where  $h$  is the seed height (see image on right). The SEM image below shows an example of a seed layer formed by BCML, where the scale bar is 100 nm. (b) Structural engineering for symmetry. The growth of the structures is away from the surface and the shape is determined by the tilt and rotation angles as well as the flux rate. Representative GLAD-grown structures are schematically shown. These would be grown on separate substrates. (c) A wide spectrum of materials that can be used in GLAD, ranging from metals to semiconductors and insulators. Scale bar: 50 nm.<sup>798,805,811–813</sup> Adapted with permission from ref 798. Copyright 2013 Springer Nature. Adapted with permission under a Creative Common CC BY License from ref 805. Copyright 2023 ACS. Adapted with permission from ref 811. Copyright 2009 Wile-VCH. Adapted with permission from ref 812. Copyright 2014 Springer Nature. Adapted with permission from ref 813. Copyright 2014 Royal Chemical Soceity. (d) TEM images of individual nanohelices made with GLAD from various materials. From left to right the row shows examples, respectively, made from  $\text{Au:Cu}$ ,  $\text{Ag:Cu}$ ,  $\text{Si}$ ,  $\text{WO}_3$ , and  $\text{SiO}_2$ . More rod-like and zig-ag hybrid nanostructures are seen in the bottom row (where the inset shows energy-filtered TEM images). (e1) Chiral nanoparticles and corresponding circular differential scattering intensities of single GLAD-nanohelices spectroscopically observed in solution. (e2) Circular differences in multiphoton scattering intensities for both left-handed and right-handed nanohelix suspensions, excited with 720 nm (top), 740 nm (middle), and 780 nm (bottom) laser light. Each vertical colored line marks the second-harmonic wavelength.<sup>810,822</sup> Adapted with permission under a Creative Common CC BY License from ref 810. Copyright 2020 Springer Nature. Adapted with permission under a Creative Common CC BY License from ref 822. Copyright 2019 American Physical Society. (f) Chiral lattice resonance with metallic nanocrescents.<sup>830</sup> Adapted with permission under a Creative Common CC BY License from ref 830. Copyright 2024 Wiley-VCH. (g) Perovskite nanostructured GLAD film showing optical anisotropy with a polarized light.<sup>841</sup> Adapted with permission from ref 841. Copyright 2022 Wiley-VCH. (h) Polarized light emission with  $\text{CdSe}$  and  $\text{CeO}_2$  nanohelices.<sup>808</sup> Adapted with

Figure 20. continued

permission under a Creative Common CC BY License from ref 808. Copyright 2022 ACS. (i) Arrays of chiral dielectric nanohelices (i: Ge for Mie type, ii: Si for plasmonic resonance).<sup>847,852</sup> Adapted with permission under a Creative Common CC BY License from ref 847. Copyright 2023 Wiley-VCH. Adapted with permission from ref 852. Copyright 2022 Institute of Electrical and Electronics Engineers. (j) Subwavelength film resonance with array of Ge nanorods.<sup>849</sup> Adapted with permission from ref 849. Copyright 2020 Wiley-VCH.

dispersed solutions (i.e., ensemble of nanoparticles), they show a high g-factor of around 0.3.<sup>658,789</sup>

The high polarization controllability of 3D chiral morphology in the visible spectral range facilitates display applications through polarization-resolved color generation.<sup>658</sup> The solution of 432 helicoid III exhibits a strong circular dichroism and optical rotatory dispersion response in the visible range, indicating the optical rotation of incident linearly polarized light (Left, Figure 19d). This optical rotation allows specific wavelengths to display distinct polarization colors through a cross-polarizer. The tunability of 432 helicoid synthesis in size and resonant wavelength further expands its capability for diverse polarization-resolved color generation.

The Kotov group successfully synthesized 3D chiral structures based on dielectric materials (Cadmium-Telluride; CdTe) and observed hyper Mie-scattering of such nanoparticles<sup>769,770</sup> (Right, Figure 19d). Particularly, this nanoparticle exhibits third-harmonic circular dichroism generation, which was successfully applied to chiral spectroscopy for trace-volume sample analysis (Figure 19e).

The exceptional light manipulation capability of plasmonic 3D chiral nanoparticles can be readily extended to coupled plasmonic system such as, 2D plasmonic array and plasmonic-photonic system.<sup>708</sup> Recently, the 2D assembly of helicoid nanoparticles (2D helicoid crystal) successfully hosted the improved chiroptic responses compared to random nanoparticle system through regular nanoparticle coupling. When 432 helicoid III nanoparticles were hexagonally arranged at 400 nm intervals, coupling between nanoparticles and photonic grating modes induced the collective resonance (CR) mode (Figure 19f (i)) and displayed strong circular dichroism in CR mode. Additionally, numerical retrieval of helicoid dipole revealed that the dipoles of individual helicoids exhibit collective spinning behavior following the incident polarization of light, and their collective scattering induced strong optical helicity (*h*), indicating significant interactions between chiral media and circularly polarized light (Figure 19f (ii) and (iii)). The 2D helicoid crystal is successfully leveraged to chiral sensing based on chiral perturbation theory, which describes the effect of molecular chirality parameters (*κ*) on plasmonic resonance (Figure 19f (iv) and (v)).

The unique polarization control exhibited by 3D chiral plasmonic nanoparticles extends beyond the single nanoparticle level to coupled systems of plasmonic-photonic system.<sup>764,766–768,776</sup> For example, the Nam group demonstrated that single helicoid nanoparticles could control the polarization of single photons when coupled with WSe<sub>2</sub> monolayers.<sup>764</sup> Typically, single photons are linearly polarized based on their origination of generation; however, through the coupling with helicoid nanoparticle, a degree of circular polarization (DOCP) of single-photon was achieved to the level of ~0.8.

We explored various strategies for creating 3D chiral morphologies at the nanoparticle level and examined how these 3D chiral nanoparticles can control polarized light for applications in displays, biosensing, and more. By introducing

different chiral inducers, it is possible to achieve asymmetric control at the nanometer scale, while scalable colloidal synthesis methods offer breakthroughs for developing commercially viable large-area plasmonic structures. These advances allow for the large-scale synthesis, assembly, and integration of 3D nanoparticles into devices, opening up possibilities for various industrial and research applications. Furthermore, expanding the core principles of chiral inducers to various materials such as metals, semiconductors, and high-refractive-index nanoparticles, or developing new types of chiral inducers, can open up new opportunities in the fields of nanophotonics and optical metamaterials.

## 21. GLANCING ANGLE DEPOSITION

Hyunah Kwon, Hyeon-Ho Jeong, and Peer Fischer

Light-matter interactions are determined by material and geometric properties. At the nanoscale, where the structure of an optical element is smaller or comparable to the wavelength of visible light, the optical response depends sensitively on both the dielectric function as well as the geometry, which encompasses the shape and/or arrangement of nanostructures. Having tools that can be used to engineer the material composition using pure starting compounds—without the need for stabilizing chemicals, and being able to create shapes that go beyond spherical and rod-like shapes, while ensuring that the nanostructures are uniform, opens up many opportunities for nanophotonics. Physical vapor deposition (PVD) is such a tool, especially, when the material is deposited at an oblique angle (known as shadow growth, when the substrate is not rotated), and when the substrate is in addition manipulated during deposition (known as glancing angle deposition, GLAD).<sup>790</sup> In what follows we will discuss the method itself and describe representative applications in the field of nanophotonics.

The symmetry of nanostructures plays an important role in nanophotonics, both in order to influence the polarization during the light-matter interaction and in order to facilitate the discovery of novel effects that involve material compositions and shapes that one cannot find naturally.<sup>791</sup> GLAD is a simple and efficient technique to achieve control over the symmetry of nanostructures in a parallel manner, permitting the fabrication of hundreds of billions of nanostructures in one growth process and thereby GLAD opens possibilities for exciting nanophotonic applications,<sup>792,793</sup> ranging from single colloidal nanoparticle spectroscopy to wafer-scale functional metasurfaces. GLAD simplifies the lithographic process by tilting the substrate (angle  $\alpha$ ) during PVD,<sup>794,795</sup> as illustrated schematically in Figure 20a, which gives rise to shadowing and permits the simultaneous growth by deposition of many nanostructures with controllable shapes through substrate rotation (angle  $\varphi$ ). The advantage of GLAD is that it eliminates the need for any photolithographic preprocessing with resists or sacrificial materials, thus enhancing efficiency.<sup>794,796</sup> However, the growth of metals at the submicron scale has been challenging as the deposited adatoms tend to move to minimize the surface energy, forming spherical deposits.<sup>797</sup> Extension to the

nanoscale with well-shaped structures for nanophotonics has been achieved by patterning a seed layer of nanoparticles prior to the GLAD deposition.<sup>798,799</sup> The design of the seed layer can be guided by the shadowing effect employing the tangential rule as a guide,<sup>800</sup> as illustrated in the inset of Figure 20a. The shadowed region extends at a tangent of the deposition angle, with a shadow length given by  $h \tan \alpha$ , where  $h$  is the diameter (height) of the seed. Seed patterning facilitates generating separate, uniformly sized nanostructures. An example of creating such a seed layer is through block copolymer micelle nanolithography (BCML),<sup>801</sup> as shown in the SEM images of Figure 20a. Other patterning schemes may also be used.<sup>802</sup>

The GLAD technique permits for the growth of uniform structures on relatively large substrates (typically 2–4") utilizing any material that can be transferred into the gas phase with PVD by electron-beam or thermal heating.<sup>792,798</sup> Spheroidal, rod-like, zigzag, and helical shapes can be grown, as well as symmetric dimer and trimer structures<sup>803</sup> to more complex, low symmetric rotamers<sup>804</sup> and chiral helices as resolved enantiomers (see Figure 20b).<sup>782,805–807</sup> The range of materials is broad and encompasses metals,<sup>782</sup> semiconductors,<sup>808</sup> and insulators (see Figure 20c).<sup>809</sup>

The GLAD-grown substrates are of interest for optical and spectroscopic applications, but it is also possible to form suspensions by detaching the nanostructures and release them from the substrate into a solution via sonication using a commercial ultrasound bath.<sup>798,810</sup>

For applications in optics, particularly plasmonic metals as well as semiconductors, and high- $n$  materials, have been the focus, and these are all excellent materials for GLAD deposition. The top row of Figure 20d shows TEM images of nanohelices grown from five different materials (Au:Cu,<sup>805</sup> Ag:Cu,<sup>798</sup> Si,<sup>811</sup> WO<sub>3</sub>,<sup>812</sup> SiO<sub>2</sub>,<sup>813</sup>). Since the thickness of the deposited layer can be controlled to nm-precision, it is possible to deposit different materials with well-defined interfaces between the different components, as can be seen in the bottom row of Figure 20d.<sup>798</sup> Further, it is possible to utilize codeposition of two, potentially up to many more elements, in order to form alloys and composites. Adding shadow barriers in the deposition chamber also makes it possible to grow surfaces with gradients in material composition and/or shape, which is of interest for high-throughput screening of nanophotonic materials.<sup>814</sup>

Here, we discuss examples where structural engineering in GLAD-grown nanostructures gives rise to intriguing light-matter interactions. In metallic nanostructures (dimension < 100 nm) local surface plasmon resonances can be excited,<sup>815</sup> where the plasmons propagate along the nanostructure, and where GLAD-grown shapes can be used to obtain polarization-resolved coloration effects.<sup>792</sup> Nanorods possess different resonance wavelengths for, respectively, the long and short axes, which can be selectively excited in response to the linearly polarized light.<sup>816</sup> Meanwhile, chiral nanohelices possess dichroic colors, due to differences in the complex refractive indices for left- and right-circularly polarized light, as observed by optical rotatory dispersion and circular dichroism spectroscopy.<sup>813</sup> Metallic nanohelices show very large optical activities, such that even picomolar suspensions give rise to ellipticities on the order of degrees.<sup>798</sup> These chiroptical antennas can be spectrally extended from the NIR, across the whole visible spectrum to the UV, by controlling their material composition, with elements such as Mg (which shows resonances in the

UV),<sup>817</sup> to Al,<sup>818</sup> Ag,<sup>782,819</sup> Cu,<sup>820</sup> and Au,<sup>821</sup> while keeping their overall size below 200 nm. These chiral nanoparticles and their large chiroptical responses have proven useful in nanophotonics, as they allowed a number of new optical effects to be observed (see for instance Figure 20e). For instance, the free diffusion of chiral nanohelices has been spectroscopically tracked at the single particle level, thereby allowing for a background free true chiral observable for a single nanoparticle.<sup>810</sup> Chiral GLAD-grown nanostructures have also been the basis of the first experimental realizations of nonlinear second and third harmonic chiroptical scattering spectroscopies.<sup>822–824</sup> They can also serve as antennas and introduce differential optical near-field enhancements, which can be seen in the Raman scattering signals from achiral molecules nearby.<sup>825</sup> Recently, GLAD has also been used to fabricate nanostructures that mimic the intermediate state of molecular rotamers, where two rods are connected at a programmed dihedral angle.<sup>804</sup> The precise angular control of the nanorotamers enables programmable polarization-resolved coloration, spanning from the IR to visible colors, for both linearly and circularly polarized light. Another interesting aspect of plasmonics is the subwavelength localization of light within nanogaps.<sup>826</sup> Here, GLAD can also be used to form wafer-scale arrays of plasmonic dimers with precise nanogaps between them, generating strong optical near-field enhancements.<sup>803,827</sup> Not only, can plasmonic scatterers be deposited on surfaces, but they can also be embedded within a glass matrix, forming plasmonic superstructures.<sup>828</sup> These permit thickness dependent dichroic color engineering.<sup>829</sup> If plasmonic nanostructures are regularly arranged with a spacing that is a fraction of the wavelength, then far-field optical coupling, known as surface lattice resonance (SLR), showing spectral resonances with a high-Q.<sup>644,695</sup> Arranging half-moon shaped GLAD-grown nanocrescents on a surface can exploit this for 2d-chiroptical, circular polarization-sensitive resonances (see Figure 20f).<sup>830</sup>

Apart from metals, semiconductor nanostructures, which possess a bandgap, are important in nanophotonics due to their ability to excite electron–hole pairs. The latter is important for catalytic processes and energy-related applications.<sup>831,832</sup> Conversely, the recombination of electron–hole pairs results in light emission, which can be exploited in optoelectronic devices. Uniform nanostructured semiconductor thin films can be grown by the GLAD technique on a wide variety of substrates, with the possibility to integrate them with microelectronics-processes and devices, such as in photovoltaics<sup>831</sup> and photodetectors.<sup>833–835</sup> Shape-control with GLAD can be used to enhance quantum confinement,<sup>836</sup> or to provide a large surface-to-volume ratio,<sup>837</sup> and enhanced light scattering effect.<sup>812,838</sup> Specifically, the tilt angle can be tuned to modulate the morphology, phase, and has even been shown to influence the bandgap.<sup>839,840</sup> Chiral GLAD semiconductor structures show strong interaction with polarized light. For example, the GLAD synthesis of perovskite nanostructures has been used to realize highly anisotropic nanowalls.<sup>841</sup> These structures exhibit in-plane optical anisotropy under polarized light, showing a difference in absorption and a wavelength-dependent anisotropic response in photoluminescence (Figure 20g). In another example, a highly efficient circularly polarized-light detector with a significant wavelength selectivity was developed, using TiO<sub>2</sub>–SnO<sub>2</sub> heterochiral thin films.<sup>842</sup> Furthermore, GLAD-fabricated CdSe and CeO<sub>2</sub> nanohelices have been reported to emit

circularly polarized light with amplified optical dissymmetry (Figure 20h), showing their potential for applications in 3D displays, information storage, and biometry.<sup>808</sup>

Lastly, GLAD structures made from dielectrics are also of interest. Bound electrons within dielectrics typically reduce the speed of visible light propagating through the medium (i.e.,  $n > 1$ ) while minimally affecting the light intensity (i.e.,  $k \sim 0$ ). As a result, they are of interest in optical trapping experiments, where they can be manipulated in an optical tweezer as demonstrated with  $\text{Al}_2\text{O}_3$  GLAD-structures.<sup>843,844</sup> When the diameter of the dielectric structures becomes comparable to the wavelength (diameter  $\sim \lambda/n$ ), light can be localized within the structures via size-dependent Mie-type resonances, giving rise to electric- and magnetic-dipolar as well as higher-order multipolar resonances.<sup>845</sup> GLAD-grown dielectric helices correspondingly give rise to chiroptical Mie resonances.<sup>846</sup> Due to their indirect energy bandgap, single-element semiconductors such as Ge and Si can also optically act as dielectrics, and show Mie-type resonances as has been seen in nanohelix arrays (Figure 20i).<sup>847</sup> Subwavelength thin film resonances, coined Gires–Tournois resonances, have also been seen in GLAD nanohelices Figure 20j,<sup>848</sup> with strong structural colors and a reflectance close to unity on resonance. Due to a concomitant sensitivity to any changes in the refractive index of the surrounding medium, they find application in polarization-resolved color displays,<sup>849</sup> colorimetric sensing,<sup>850</sup> and nanophotonic switches.<sup>851</sup> Interestingly, when Si nanostructures are reduced to below 100 nm, the electrons within the Si behave like free electrons under UV light, activating plasmonic resonances.<sup>112</sup> This suggests a new class of GLAD-grown plasmonic materials,<sup>852</sup> which is CMOS-compatible and potentially useful for device applications, e.g. as UV filters and photodetectors. One of the advantages of the GLAD technique is its ability to make nanostructured films with a gradient in material properties by using an additional shadow mask in the deposition setup. For example, a modified GLAD method enabled the fabrication of a spatially graded  $\text{TiO}_2$ – $\text{SiO}_2$  Bragg stack, producing a rainbow-colored photonic bandgap effect through dynamic shadowing.<sup>853</sup>

GLAD-grown nanostructures, especially those with low symmetry, give rise to strong polarization-sensitive differential scattering that can enhance or resolve optical features in linear extinction,<sup>810</sup> vibrational spectroscopies,<sup>825</sup> as well as in nonlinear harmonic scattering.<sup>822,823</sup> Such chiral (plasmonic) nanostructures have been recently used to experimentally observe hyper-Raman optical activity from achiral molecules, which is a physical effect only theoretically predicted in 1979.<sup>854</sup> This effect could deliver additional information on vibrational modes of chiral molecules, although resolving these signals emanating from a few molecules remains challenging.<sup>855</sup> Another promising application of differential scattering is nanostructuring to produce vivid colors as a function of light polarization,<sup>658</sup> which is useful in photonic filters, memory, and anticounterfeiting devices. Recently, these colors have also been shown to be tunable, changing with the structural orientation of chiral particles, such as through magnetic alignment.<sup>856</sup> However, an electrically activated device of active chiral plasmonic structures that gives rise to full color dynamics has not yet been achieved.<sup>857</sup> Furthermore, while GLAD-grown chiral semiconductors have shown the ability to emit photons,<sup>808</sup> their potential for electroluminescence is also unexplored. This opens up possibilities for further develop-

ment in electrically controlled devices made of GLAD-grown nanostructures.<sup>858</sup>

Another advantage of GLAD is the capability to fabricate a diverse range of geometrically complex, multifunctional nanostructures, including alloyed,<sup>782</sup> core@shell,<sup>859</sup> and multi-layered designs,<sup>860–863</sup> providing entire wafers with multifunctional structures for nanophotonics. Once released from the substrate such structures can also be used in suspension. Au–Fe composite nanohelices grown by codeposition,<sup>864</sup> can be manipulated with a magnetic field when released into solution due to the Fe, while the plasmonic Au enhances the optical response, thus enabling magnetically switchable plasmonic signals. Whether such structures form alloys or composites will depend on the respective material phase diagrams.<sup>865,866</sup> Similarly, core@shell nanoparticles can be created, where the core is first grown by GLAD, while the shell is either formed by solution chemistry<sup>867</sup> or by ALD.<sup>859</sup>

For example, conductive polymers can encapsulate GLAD-grown nanostructures, enabling electrical tuning of their optical properties with a low voltage (below 1 V).<sup>851</sup> This opens up possibilities for various nanophotonic devices, where external inputs—such as thermal, acoustic, magnetic, chemical, or mechanical signals—can alter the nanostructure's environment and thereby change its optical response including color.<sup>858,868,869</sup> A particularly promising development in this field is the creation of untethered, externally controlled nanostructures that combine multiple functionalities and thus can be used to for instance position a spectroscopic probe with magnetic, electric or chemical fields in liquid or biological media, thus making for nanophotonic probes attached to nanorobots.

The versatility of the GLAD process also permits the linear growth of stacks, where each layer (and its thickness) gives rise to a desired optical response of a different function.<sup>814,870–874</sup> An example of the latter is a dielectric glass rod with a tip made from Au that shows a plasmonic resonance.<sup>843</sup> The nanorod functions as a handle for the manipulation in an optical tweezer and permits positioning on surface of a biological cell with NIR light. Then, in response to green light, the plasmonic tip is locally heated to several hundred °C and the GLAD-nanorod opens the cell membrane and can thus be inserted into the cell. Recently, such multifunctional GLAD-grown nanostructures have also been controlled magnetically<sup>875</sup> and electrophoretically trapped,<sup>876</sup> enabling highly precise motion control in 3D while using plasmonics for either trapping or sensing near a target object. Thus, structures that are useful in nanophotonics can also be turned into multifunctional nanorobotic systems.

In summary, GLAD is a versatile method for fabricating nanostructured films, particularly suited for nanophotonic applications requiring precise control over material composition and shape. It enables, in combination with nanopatterning techniques, the rapid growth of uniform structures (resolution approaching 10 nm) over large areas (typically up to 10 cm although this does not constitute an upper limit), and allows for a variety of complex nanoshapes, such as chiral helices. In addition, GLAD offers a significant cost advantage over traditional lithography, as it eliminates the need for complex lithographic steps. Defect levels can be significantly lowered by an industrial-level control of vacuum and substrate preparation to enhance reproducibility, making it a potential technique for high-end optics applications that demand defect-free structures. While currently much of the work is lab-scale, the potential of GLAD for integration into next-generation

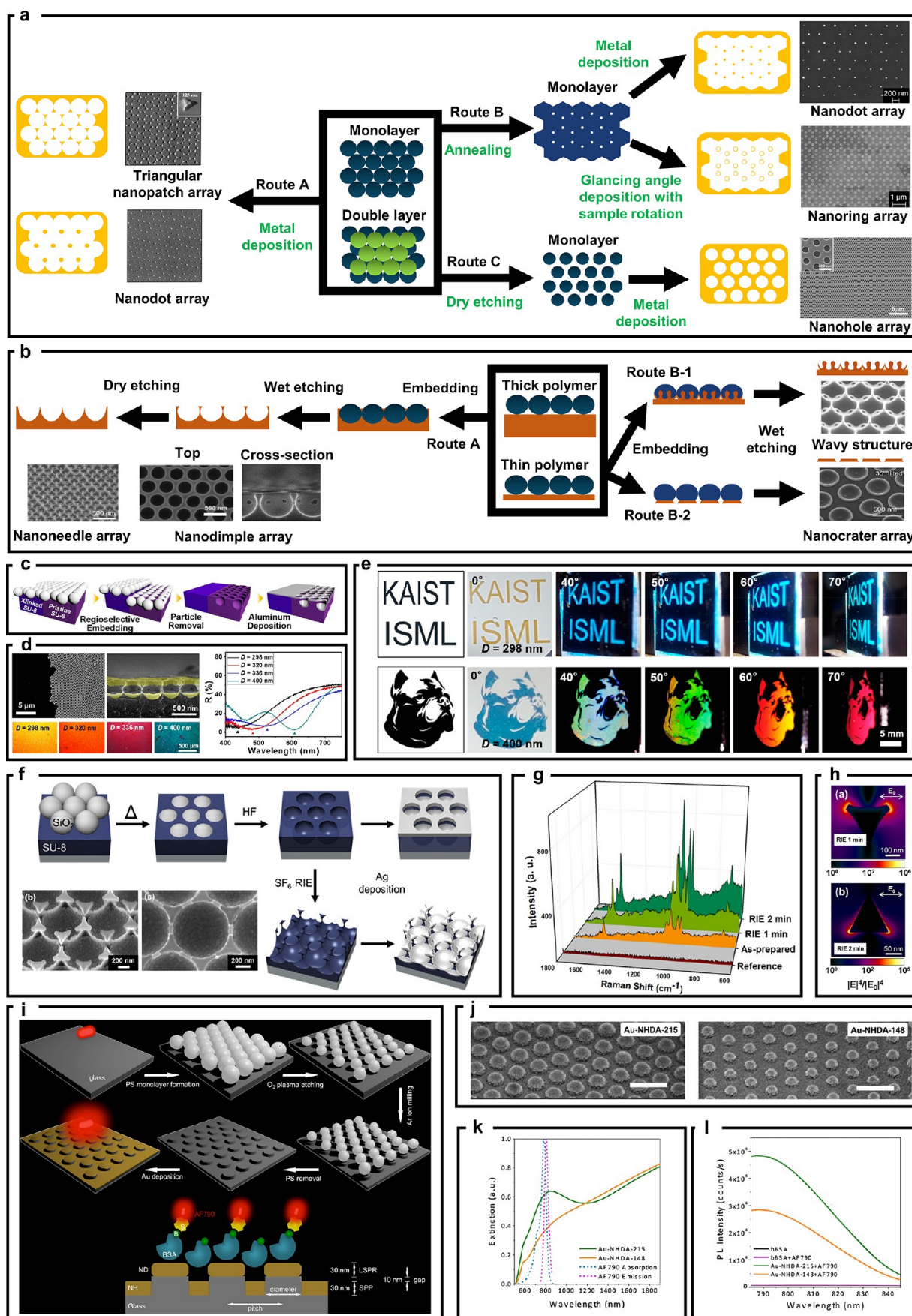


Figure 21. Fabrication process and their applications of CL. (a) Schematic illustration of colloidal arrays used as a mask for metal deposition. Route A shows the formation of triangular nanopatch and nanodot arrays through metal deposition on colloidal monolayer and double layer, respectively.<sup>883</sup> Route B depicts the creation of nanodot and nanoring arrays from colloidal masks deformed by annealing in combination

Figure 21. continued

with vertical metal deposition and glancing angle deposition with sample rotation, respectively.<sup>650</sup> Route C shows the formation of nanohole arrays obtained from nonclose-packed colloidal masks produced by dry etching.<sup>888</sup> Adapted with permission from ref 883. Copyright 2001 ACS. Adapted with permission from ref 650. Copyright 2005 Small press. Adapted with permission from ref 888. Copyright 2009 ACS. (b) Schematics of colloidal array used as a template for creating nanostructures on polymeric film. Route A illustrates the fabrication of nanodimple and nanoneedle arrays designed by embedding colloidal NPs on a thick polymeric film in conjunction with particle removal and dry etching.<sup>893</sup> Routes B-1 and B-2 display the formation of wavy and nanocrater structures depending on the relative thickness of the thin polymeric film to particle radius.<sup>894</sup> Adapted with permission from ref 893. Copyright 2024 Wiley-VCH. Adapted with permission from ref 894. Copyright 2022 Wiley-VCH. (c) Schematic illustration for the production of micropatterned nanodimple arrays by regioselectively embedding silica particle arrays onto a PR film.<sup>896</sup> Adapted with permission from ref 896. Copyright 2022 ACS. (d) SEM images showing a boundary between nanodimple arrays and flat region and the cross section of aluminum-deposited nanodimple arrays (top left panel), optical microscope (OM) images of the nanodimple arrays produced using four different sizes of silica NPs (bottom left panel), and the reflectance spectra of the nanodimple arrays (right panel).<sup>896</sup> Adapted with permission from ref 896. Copyright 2022 ACS. (e) Photographs of the micropatterned nanodimple arrays taken at retroreflection mode for various angles.<sup>896</sup> Adapted with permission from ref 896. Copyright 2022 ACS. (f) Schematics for the production of silver-deposited inverted-triangular nanopost array and SEM images of the nanostructures.<sup>910</sup> Adapted with permission from ref 910. Copyright 2013 ACS. (g) Surface-enhanced Raman scattering (SERS) spectra of benzenethiol obtained from the various nanostructures with different durations of dry etching.<sup>910</sup> Adapted with permission from ref 910. Copyright 2013 ACS. (h) Finite-difference time-domain (FDTD) simulation showing spatial distributions of electric field intensity around silver-deposited inverted-triangular nanopost with two different etching times.<sup>910</sup> Adapted with permission from ref 910. Copyright 2013 ACS. (i) Schematic illustration for production of gold nanohole-disc array by particle etching, glass substrate etching, particle removal, and gold deposition.<sup>916</sup> Adapted with permission under a Creative Common CC BY License from ref 916. Copyright 2019 ACS. (j) SEM images of gold nanohole-disc array for two different disc diameters.<sup>916</sup> Adapted with permission under a Creative Common CC BY License from ref 916. Copyright 2019 ACS. (k) Absorption and emission spectra of AlexaFluor 790 (AF790) (dashed line) and normalized extinction spectra of gold nanohole-disc array for two different disc diameters (solid line).<sup>916</sup> Adapted with permission under a Creative Common CC BY License from ref 916. Copyright 2019 ACS. (l) Photoluminescence (PL) emission spectra of AF790 obtained from biotinylated bovine serum albumin (bBSA)-coated nanostructure-free substrates and two different gold nanohole-disc arrays.<sup>916</sup> Adapted with permission under a Creative Common CC BY License from ref 916. Copyright 2019 ACS.

photronics, nanorobots, and holographic displays is immense, making it powerful tool that has much to offer for nanophotonics.

## 22. COLLOIDAL LITHOGRAPHY

Jiwon Yoon and Shin-Hyun Kim

Colloidal lithography (CL) is a technique for the production of regular nanostructures using self-assembled colloidal arrays as either material deposition masks or sacrificial templates.<sup>877–880</sup> Despite the intrinsic limitations of self-assembly, which usually result in the nanostructures having defects and limited dimensions of single-orientation domains, CL offers rapid and cost-effective means for large-scale nanostructure production. This makes it especially promising for various optical and photonic applications where minor defects or structural misalignments are less critical.

One of the most prominent applications of CL is utilizing it as a metal deposition mask. In this process, hexagonally close-packed arrays of spherical colloidal nanoparticles are typically prepared on target substrates by a simple and fast spin-coating process.<sup>881,882</sup> These colloidal arrays serve directly as a mask for metal deposition. As metal is deposited vertically onto the underlying substrates through interstitial voids among nanoparticles, periodic arrays of triangular patches are created after the removal of the colloidal mask, as illustrated in route A of Figure 21a.<sup>883</sup> When a double layer of hexagonal arrays is used as the deposition mask, small nanodots are created.

The colloidal arrays can undergo various modification to provide a wide range of nanostructures. For example, thermal annealing renders colloidal masks of polymeric nanoparticles, such as polystyrene (PS), to be partially fused, transforming triangular voids into smaller circular voids.<sup>884</sup> Therefore, the use of the modified masks enables the production of nanodots through metal deposition and mask removal, as shown in route B of Figure 21a. Additionally, glancing angle deposition (GLAD) with sample rotation results in the formation of

nanorings.<sup>650</sup> Moreover, the close-packed colloidal arrays can be transformed into nonclose-packed ones by dry etching, such as RIE, which reduces the size of each nanoparticles.<sup>885–887</sup> Consequently, metal deposition followed by mask removal results in the production of nanohole arrays on the metal layer, as illustrated in route C of Figure 21a.<sup>888</sup> It is possible to produce diverse nanobar and nanoantenna arrays through multiple GLAD at various angles relative to the orientation of colloidal masks.<sup>889</sup> Furthermore, when double or multiple layers of colloidal nanoparticles are treated with RIE, nanoparticles in the second or third layers are etched in an anisotropic manner due to the masking effect by nanoparticles in the layer above, which possibly results in more intricate nanopatterns.<sup>890</sup>

Colloidal arrays can be used as sacrificial templates to create 2D or 3D polymeric nanostructures. Colloidal arrays of silica particles prepared on polymeric film are spontaneously embedded into the polymer when the temperature is increased above the glass transition temperature.<sup>891</sup> The embedding is driven by capillary force, which stops when the contact angle on the surface of the particles reaches an equilibrium value. For sufficiently thick polymeric film, more than half of each particle is embedded while maintaining a planar air–polymer interface, which yields nanodimple arrays with flat top surfaces after removal of the particles, as illustrated in route A of Figure 21b. The RIE process can further transform the nanodimple arrays into inverted-triangular nanopost or nanoneedle arrays.<sup>892,893</sup> By contrast, the use of polymeric film thinner than the particle radius results in the formation of wavy interfaces to minimize interfacial energy, as illustrated in route B-1 of Figure 21b. Therefore, periodic 3D wavy structures are created after particle removal, where the degree of waviness varies along with the thickness of the polymer film relative to the size of the particles.<sup>894</sup> When the polymeric film is very thin, it wets the bottom of the particles while being disconnected by dewetting

on the substrate. This leads to the formation of nanocrater arrays, as illustrated in route B-2 of Figure 21b.

Various periodic nanostructures, featured by CL, have been employed as structural motifs for metal deposition to induce surface plasmon resonance (SPR) or localized surface plasmon resonance (LSPR).<sup>895</sup> The metal nanostructures with SPR or LSPR have been used for various applications, including plasmonic coloration, SERS, and plasmon-enhanced fluorescence (PEF). One example of plasmonic coloration uses aluminum-deposited nanodimple arrays.<sup>896</sup> Directional deposition of aluminum creates an aluminum layer with nanohole arrays and an aluminum bowl in each dimple, as illustrated in Figure 21c. It is noteworthy that the use of negative PR as an underlying polymeric layer enables the micropatterning of the nanodimple arrays by photolithography. The combination of nanohole arrays and nanobowls strongly absorbs light in the visible range through coupled SPP and LSPR whose wavelength depends on the diameter of dimples, as shown in Figure 21d. Moreover, the periodic array of nanodimples develops diffraction colors for off-normal observation. Therefore, the aluminum-deposited micropatterned nanodimple arrays display plasmonic color at normal view, while showing iridescent colors at off-normal view by diffraction, as shown in Figure 21e. The production of micropatterned nanodimple arrays is highly reproducible, and these arrays show significant potential for use in optical encoding and anticounterfeiting applications, where minor defects do not substantially impact optical performance. Plasmonic colors are also achievable across various nanostructures of disk, dome and ring, and ring, fabricated by CL including multisteps of RIE and metal deposition on close-packed colloidal arrays.<sup>897</sup> These plasmonic colors are adjustable by controlling geometrical parameters, such as pitch, diameter, and height. Silver nanovolcano arrays are also suggested to display vivid plasmonic colors based on extraordinary optical transmittance (EOT) in the visible range.<sup>898</sup> The interaction of SPRs between the top hole and bottom hole in the nanovolcano structure leads to a sharp transmittance peak, generating distinct transmittance colors, which are tunable by adjusting periodicity. The wavelengths responsible for EOT depend on the *n* of the surroundings. As the *n* of surroundings increases, its color red-shifts with a sensitivity of 314 nm/RIU, possibly applicable as *n* sensors.

Localization of electromagnetic fields near the surface of metal nanostructures can remarkably amplify the Raman signals of molecules in the localized field.<sup>899,900</sup> SERS has been used for the detection of biomolecules, pesticides, and drugs.<sup>901–905</sup> The simple method to prepare SERS substrate based on CL is to deposit metal on a close-packed array of colloidal nanoparticles, which results in a metal film over the nanosphere.<sup>906,907</sup> Also, it is possible to make a gap between nanospheres by RIE to improve the Raman enhancement.<sup>908</sup> Another way to make SERS substrates is to deposit silver on a colloidal array, which is then inverted to create silver nanobowls.<sup>909</sup> Subsequent RIE and silver deposition enable the production of nanocaps and nanotriangles, which exhibit remarkable signal uniformity and high SERS enhancement owing to a high density of hot spots located in gaps between nanotriangles and nanocaps. Arrays of inverted-triangular nanoposts, produced by RIE of nanodimple arrays, are also useful as SERS substrates after silver deposition, as shown in Figure 21f.<sup>910</sup> Controlled duration of RIE results in the inverted-triangular nanoposts with sharp edges, which provides

a high enhancement factor due to the strong localization of the electric field, as shown in Figure 21g and h.

PEF is one of the strategic methods to amplify the fluorescence signals of fluorophores with low quantum yield. It is known that when the LSPR band overlaps with the excitation or emission wavelengths of fluorophores, the fluorescence signal can be remarkably enhanced.<sup>911,912</sup> Therefore, metal nanostructure has been fabricated using CL to achieve high fluorescence intensity.<sup>913</sup> The simplest fabrication method involves silver deposition of metal on a colloidal monolayer.<sup>914</sup> It is observed that overlapping of the LSPR band with excitation wavelength causes more fluorescence enhancement compared to that with emission wavelength. The optimal structure exhibits a 60-fold and 3.4-fold increase in fluorescence enhancement for poly(3-hexylthiophene-2,5-diyl) (P3HT) with low quantum yield and rhodamine B with high quantum yield, respectively. Arrays of triangular patches formed by gold deposition through interstitial voids of a colloidal monolayer mask are employed to achieve high fluorescence enhancement.<sup>915</sup> The optimal substrate shows a fluorescence enhancement of Alex Fluor 790 as high as 70. Gold nanohole-disc arrays are also produced for achieving fluorescence enhancement in the NIR windows.<sup>916</sup> The structure is fabricated by plasma etching of colloidal monolayer, argon ion milling of the underlying glass substrate, removal of particles, and deposition of gold with high reproducibility and low cost, as illustrated in Figure 21i and j. The structure with a nanodisc diameter of 215 nm has an LSPR peak at 848 nm, which is close to the excitation and emission bands of fluorescent dye AF 790, as shown in Figure 21k. The coupling between SPP from gold thin film with nanoholes and LSPR from gold nanodisc induces a strong photoluminescence emission of AF 790, as shown in Figure 21l. The calculated area-averaged fluorescence enhancement factors are found to be 411. As a result, the low quantum yield of NIR/NIR-II fluorophores AF 790, initially at 4%, is remarkably improved to an estimated value of 97%.

## 23. COLLOIDAL LITHOGRAPHY FOR ABSORBER AND Emitter

Sangmin Shim and Dasol Lee

CL uses self-assembled monolayers of particles as lithographic masks to fabricate arrays of nanostructures through directed evaporation and etching processes. This approach enables the fabrication of nanostructures over large areas in a simple, efficient, and parallel manner, eliminating the need for specialized fabrication facilities. CL is suitable for fabricating periodic structure arrays to manipulate the transmission, reflection, and absorption of light in various spectral regions. These features have attracted great interest in applications using nanostructure-light interaction, particularly ranging from perfect absorbers, photovoltaics, and thermal emitters to sensors.<sup>75,879,917–920</sup>

A broadband absorber (BA) is designed to absorb light across a wide range of wavelengths. This characteristic makes it particularly useful in applications requiring efficient light absorption over a broad wavelength region. Various structures, including CL-based patterns, have been proposed. Matsumori et al. have developed a BA from UV to NIR, using a semishell MIM nanostructure. This BA achieved an average absorption of up to 83% in the range of 300 to 1000 nm by using Al as the plasmonic material, which is more cost-effective compared to commonly used noble metals. The broadband absorption is

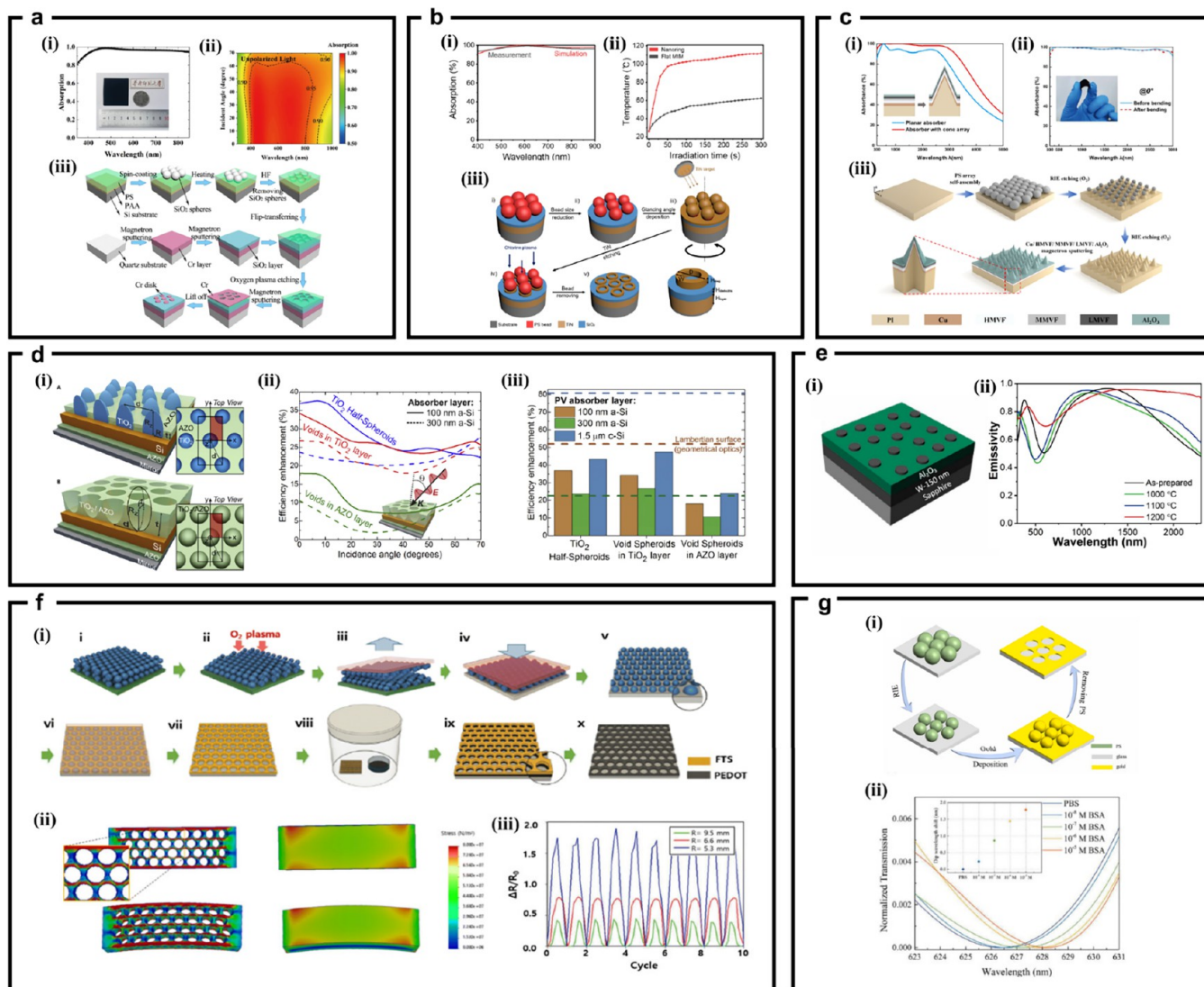


**Figure 22. Colloidal lithography for absorber and emitter.** (a) Absorption spectrum relative to the incident angle on an broadband absorber composed of Cr nanodisk, SiO<sub>2</sub> film, and a Cr substrate subjected to unpolarized light.<sup>918</sup> Adapted with permission under a Creative Common CC BY License from ref 918. Copyright 2023 De Gruyter. (b) Temperature comparison of TiN broadband absorber with nanoring and without nanoring when exposed to an irradiation of 325 mW/cm<sup>2</sup>.<sup>75</sup> Adapted with permission from ref 75. Copyright 2023 ACS. (c) Absorption spectrum of Al<sub>2</sub>O<sub>3</sub> nanocones in broad wavelength despite bending at normal incidence.<sup>920</sup> Adapted with permission under a Creative Common CC BY License from ref 921. Copyright 2022 Optica. (d) Efficiency enhancements of 3 models (TiO<sub>2</sub> half-spheroids, void Spheroids in TiO<sub>2</sub> layer, void spheroids in AZO layer) with different thicknesses of a-Si and c-Si.<sup>943</sup> Adapted with permission under a Creative Common CC BY License from ref 943. Copyright 2018 ELSEVIER. (e) Emissivity spectrum of the W nanodisc emitter after annealing at various temperatures.<sup>945</sup> Adapted with permission under a Creative Common CC BY License from ref 945. Copyright 2023 ELSEVIER. (f) Stress distribution and relative resistance changes of patterned PEDOT film based on bending stress.<sup>951</sup> Adapted with permission from ref 951. Copyright 2023 RSC Publication. (g) Resonance wavelength of Au nanohole arrays for BSA concentration in transmission spectra.<sup>953</sup> Adapted with permission under a Creative Common CC BY License from ref 953. Copyright 2022 De Gruyter.

not sensitive to the incident angle and polarization, which is considered crucial in many studies of BA.<sup>917</sup> In addition to fabricating nanostructures using plasmonic materials such as Al, Au, and silver (Ag), refractory metals, such as chromium (Cr), titanium nitride (TiN), and tungsten (W), also have emerged as new materials for BA. The high melting points of refractory metals make them resistant to external influences, enabling prolonged use in various thermal applications such as photovoltaics (PV) and thermal emitters. Jiang J et al. proposed a perfect BA composed of hexagonal Cr nanodisks, a silicon dioxide (SiO<sub>2</sub>) spacer, and a Cr film through combination of colloidal lithography and magnetic sputtering (Figure 22a.iii). The BA achieved 98.2%, demonstrating over

about 90% absorption for unpolarized light at incident angles up to 70°, as depicted in Figure 22a.i and Figure 22a.ii. This high performance is sustained throughout the entire visible spectrum, facilitated by the spectral overlap between Fabry-Pérot resonance and surface plasmon resonance, which are induced by the surface patterning.<sup>918</sup> Lee et al. employed multiple-patterning CL to create a BA on a large scale. A ring-shaped TiN absorber showed a high absorption of 95% in the visible and NIR regions (400–900 nm). This absorber maintains its optical properties even at elevated temperatures.<sup>879</sup> Go et al. proposed a simplified fabrication method for the ring-shaped absorber. A TiN nanoring BA was fabricated on a large scale using shadow sphere lithography

derived from CL (Figure 22.b.iii). During the deposition step, rotating the substrate at an inclined angle to form a ring shape can omit the etching step. An average absorption of over 95% across the visible to NIR region (300–900 nm), as shown in Figure 22b.i, and photothermal application leading to an increase in temperature was reported. A temperature increase more than 2.3 times higher under light irradiation compared to a flat film was demonstrated as shown in Figure 22b.ii<sup>75</sup>. Guo et al. demonstrated broadband absorption of truncated TiN nanocones from the UV to NIR spectrum regions, achieving an average absorption rate of 96.11% across the wavelength range of 100 to 2500 nm. The absorption rate remained consistently above 80% for all polarizations within the incident angle range of up to 70°.<sup>919</sup> Hou et al. developed a wide-angle and broadband solar absorber composed of Al, Cr, and SiO<sub>2</sub> by using CL. It operated through optical interference of multilayer thin films and magnetic resonance of light-trapping structures, achieving an average absorption rate of over 93% in the range of 300 to 2500 nm for incident angles up to 60°.<sup>921</sup> Yang et al. presented a BA with a nanocone structure composed of copper, ZrO<sub>2</sub>, and aluminum oxide (Al<sub>2</sub>O<sub>3</sub>) using CL (Figure 22c.iii). This absorber has demonstrated an average absorption rate of over 98% across a broad spectrum ranging from 300 to 3000 nm, as shown in Figure 22c.i, and is capable of absorbing light at wide angles. Furthermore, using a flexible polyimide substrate allowed the absorber to resist bending and heating, indicating its potential for various application areas as shown in Figure 22c.ii.<sup>921</sup>

As previously mentioned, the BAs can be utilized for applications in PV and thermal emitters. PV, which converts light into electricity, benefits from materials that absorb light efficiently across a wide spectrum, thus enhancing solar energy system performance, such as solar power generation, large-scale solar farms, and solar panels that can be used in space exploration.<sup>922–926</sup> There are several inefficiencies in PV that BAs may address. First, there is a hindrance in light absorption capacity across the solar spectrum,<sup>927–930</sup> and sunlight is reflected or lost as heat instead of being converted into electricity. Second, the process of charge carrier recombination within the semiconductor reduces energy production. Recombination occurs when charge carriers meet and annihilate each other before they can be converted into electricity.<sup>931–934</sup> Third, power losses arise from sheet resistance, which indicates how easily current can flow through the material.<sup>935–937</sup> These inefficiencies can be addressed by nanostructures, which can absorb a broader range of wavelengths, increase the optical path length, or reduce sheet resistance, thereby enhancing efficiency through light trapping.

Sanchez-Sobrado et al. developed TiO<sub>2</sub> nanostructures using CL and attached these to thin-film solar cells to enhance performance through light trapping that does not contribute to an increase in carrier recombination. These nanostructures act as absorbers, reducing light reflection at shorter wavelengths and promoting light scattering within the absorption layer at longer wavelengths, thereby ultimately increasing the optical path length. A significant enhancement in photocurrent of up to 27.3% compared to conventional antireflective coatings has been reported.<sup>938</sup> In a follow-up study conducted by Sanchez-Sobrado et al., indium zinc oxide (IZO) and aluminum zinc oxide (AZO) were applied to the multilayer configuration that led to strong broadband absorption enhancement for the front contact of solar cells. An efficiency of up to 14.4% was achieved, along with a boost in generated currents of up to

21.5% compared to the flat reference cell.<sup>939</sup> Abdelhameed et al. demonstrated that Schottky junction solar cells based on silicon nanopencils offer superior light-trapping characteristics by exhibiting high external quantum efficiency in the visible and NIR regions, leading to higher short circuit current density compared to flat devices and enhancing the PV conversion efficiency up to 5.6%.<sup>940</sup> Santos et al. have improved the efficiency of crystalline silicon (c-Si) solar cells by adapting TiO<sub>2</sub> nanostructure. This structure provides improved performance through light-trapping, thereby reducing carrier recombination and enhancing absorption by approximately 76% in the visible and NIR regions. Furthermore, when applied to planar interdigitated back-contact solar cells (pIBCSCs), it not only led to remarkable optical photocurrent but also a 30% improvement in efficiency compared to those without the nanocoating.<sup>941</sup> Lee et al. enhanced the power conversion efficiency of organic PV through patterning the indium tin oxide (ITO) layer using CL. The patterning of ITO increases the optical path length and decreases the transport of excited charge carriers, enabling an absorption enhancement of 15–20% compared to an unpatterned system.<sup>942</sup>

Mendes et al. introduced three structures to enhance the optical efficiency of thin-film silicon solar cells: TiO<sub>2</sub> half-spheroids in the transparent conductive oxide (TCO) layer, and spheroidal voids in the TiO<sub>2</sub> and AZO layer on amorphous silicon (a-Si) and crystalline silicon (c-Si), as shown in Figure 22d.i. TiO<sub>2</sub> half-spheroids exploit TiO<sub>2</sub>'s *n* for antireflection and scattering, increasing the optical path length and reducing parasitic absorption, thus enhancing photocurrent by up to 48% through efficient light trapping. Spheroidal voids in the TiO<sub>2</sub> layer also scatter light effectively, improving light absorption and enhancing photocurrent density. While spheroidal voids in the AZO layer may not perform as well as TiO<sub>2</sub>-based structures, they provide a crucial electrical advantage by reducing sheet resistance as shown in Figure 22d.ii,iii.<sup>943</sup> Centeno et al. developed a self-cleaning photonic-enhanced solar cell, which features a hydrophobicity contact angle of up to 165.6° and low adhesion for effective self-cleaning. This surface provides antireflection and light-scattering properties that increase the optical path length, and the nanocrystalline silicon solar cell demonstrated a significant 23.6% increase in short-circuit current density compared to planar reference cells, enabling a 35.2% enhancement in average daily power generation through improved angular response.<sup>944</sup> Thermophotovoltaics (TPV) is a promising method that involves the absorption of light emitted from a thermal emitter by a photovoltaic cell to generate electrical energy. Chirumamilla et al. presented the fabrication of spectrally selective, polarization-independent thermal emitters based on W nanodiscs, aimed at enhancing energy conversion (Figure 22e.i). This method produces W nanodisc spectrally selective emitters, which demonstrate high emissivity below the indium gallium arsenide antimonide (InGaAsSb) PV-cell cutoff wavelength of 2.25 μm despite the high temperature, and a significantly reduced emissivity (down to less than 10%) in the mid-infrared (MIR) region, as shown in Figure 22e.ii.<sup>945</sup>

Contrary to the BA, the fabrication of nanostructures for high absorption or reflection in the narrowband can also be possible through CL. It is widely used in the field of sensors, detecting the resonance shift by the changes in the surrounding environment. Liu et al. introduced a deep-elliptical Ag nanowell array fabricated by combining stretchable imprinting with CL. They noted that the high elasticity of the PDMS

mold allows for easy adjustment of the structure's aspect ratio from 1.7 to 5.0. The highest sensitivity achieved among the structures with different aspect ratios was 1414.1 nm/RIU(*n* unit). It has been used as an immunoassay platform for label-free biosensing and is expected to be applicable as a future refractometric sensor.<sup>453</sup> Dao T et al. introduced a perfect absorber in the MIR region made of Al, combining CL with RIE. This structure achieved nearly perfect absorption, up to 98%, within a narrow bandwidth of 0.75  $\mu\text{m}$ .<sup>946</sup> Using an absorber fabricated similarly to the one mentioned previously, Chen et al. attached 10-carboxydecylphosphonic acid (10-CDPA) to the Al surface through surface functionalization. They successfully detected the characteristic C=O vibration band of molecules using surface-enhanced infrared absorption (SEIRA). The C=O vibration band of the COOH functional groups in 10-CDPA is located at 1680–1710  $\text{cm}^{-1}$  for hydrogen-bonded COOH and at 1735–1760  $\text{cm}^{-1}$  for free nonhydrogen-bonded COOH. Peaks positioned at 1734 and 1767  $\text{cm}^{-1}$  in the absorption spectrum demonstrated effective detection through the Al disks. Additionally, they also detected the physical adsorption of the bovine serum albumin (BSA) protein layer through SEIRA.<sup>947</sup> In a study by Xu et al., large-scale palladium (Pd) nanostructures were created using CL, and their ability to detect hydrogen was investigated. Pd has a distinct chemical interaction with hydrogen, absorbing the gas upon contact to form PdHx. This transformation alters the optical and electrical properties of Pd, allowing for the detection of hydrogen. The Pd nanostructures produced through CL included nanoholes and nanotriangles, with the nanoholes demonstrating superior sensing capabilities.<sup>948</sup> Lay et al. used CL to fabricate a honeycomb structure of Au on quartz crystal microbalance (QCM) electrodes and detected mercury vapor using this structure. The study aimed to determine the optimal pore size for detection performance. The results showed that models with 12 min of plasma etching exhibited a 7.4 times higher response to mercury vapor compared to models without etching. The structure demonstrated high selectivity for Hg vapor in gases containing humidity, ammonia, and volatile organic compounds at an operating temperature of 75 °C.<sup>949</sup> Chul et al. proposed thin films with a hemispherical pore structure to detect gaseous formaldehyde (HCHO) using gravimetric sensing. These films, made through molecularly imprinted polymers (MIPs) and CL, enhance the detection signal for HCHO in QCM sensors. The hemispherical pore structure of the MIP film improved gas molecule adsorption, showing high sensitivity and selectivity toward HCHO.<sup>950</sup> Kim et al. utilized CL and vapor phase polymerization to produce a nanoscale 2D poly(3,4-ethylenedioxythiophene) (PEDOT) films for a transparent and highly sensitive bending sensor, as illustrated in Figure 22f.i. The PEDOT film, with its void structure compared to flat structure, enhanced transparency significantly and demonstrated remarkable electrical sensitivity to bending stress, especially in the narrow-patterned area, as shown in Figure 22f.ii,iii.<sup>951</sup> Šišoláková et al. used CL to uniformly deposit Ni nanocavities on conductive glass, creating a highly sensitive, fast-responding, and selective enzyme-free electrochemical sensor for insulin detection. This sensor demonstrated high sensitivity, a low detection limit, and a broad range for insulin detection. Additionally, it showed excellent selectivity in the presence of various interferents and real blood serum samples.<sup>952</sup> Chen et al. conducted research on a highly sensitive biosensor using Au nanohole arrays (GNAs) by CL,

as shown in Figure 22g.i. GNAs had a maximum *n* sensitivity of 407 nm/RIU. Additionally, they developed a lens-free smartphone-based *n* sensor that does not require a spectrometer. This sensor demonstrated a maximum intensity sensitivity of 137%/RIU and could detect extremely small amounts of BSA molecules in a label-free manner, as shown in Figure 22g.ii.<sup>953</sup>

## 24. COLLOIDAL SELF-ASSEMBLY

Luis A. Pérez, Xiaoyu Qi, and Agustín Mihi

Colloids have emerged as a compelling area of research in recent decades. These nanomaterials offer unique physical properties, such as tunable optical properties and self-assembly behavior while being produced via scalable processes. Additional functionalities can be achieved by using colloids as building blocks of engineered architectures, a rapidly evolving field at the intersection of physics, chemistry, and materials science. This multidisciplinary domain explores the self-organization and manipulation of colloidal nanoparticles with the aim of producing larger constructs with engineered physical properties and high-throughput processability.<sup>954–956</sup>

Colloids exhibit a natural tendency to self-assemble spontaneously into ordered structures without external intervention, seeking minimization of free energy within the system.<sup>957</sup> The self-assembly process is governed by surface chemistry, colloid morphology and environment,<sup>958</sup> all of which have been largely explored in the literature with the aim of producing large crystals with plasmonic, luminescent or mechanical properties.<sup>959</sup> In recent years, higher control over the assembly process has allowed a precise positioning of the colloids on a geometry, thus opening up the number of architectures that can be produced.<sup>960</sup>

Different strategies can be employed to steer the assembly of colloids toward engineered geometries: assembly under electric fields, microfluidics and different templating methods have been employed to hierarchically assemble colloidal particles.<sup>961–965</sup> In the following text we attempt to give a broad overview of some of them.

Certain methodologies exploit the fact that the colloidal stability of most particles dispersed in polar solvents, such as water, primarily relies on their possessing a net surface charge (electrostatic repulsion between particles prevents their agglomeration). This phenomenon is governed by the zeta potential, a key parameter whose value depends, among other factors, on the surface charge of the particles.<sup>966</sup> Charged particles can therefore be directed toward substrates bearing an opposing surface charge. Further control on the assembly process can be gained by applying an external electric field during the assembly (electrophoretic deposition). For instance, Mulvaney's group used a conductive substrate coated with a thin insulating layer featuring an array of holes that, when polarized, caused the charged colloidal particles suspended in the liquid medium to migrate toward the openings in the conductive substrate, filling those voids.<sup>335,967</sup> A similar effect can be achieved on insulating structured substrates by functionalizing with charged molecules (electrostatic assembly).<sup>968</sup> The most widespread example of this process is chemical assembly with DNA, where colloidal particles of interest are functionalized with single-stranded DNA molecules that selectively bind to complementary single-stranded DNA molecules grafted at specific positions on the substrate.<sup>969</sup>

Further examples of colloidal assembly under external fields include the use of optical tweezers to deterministically position

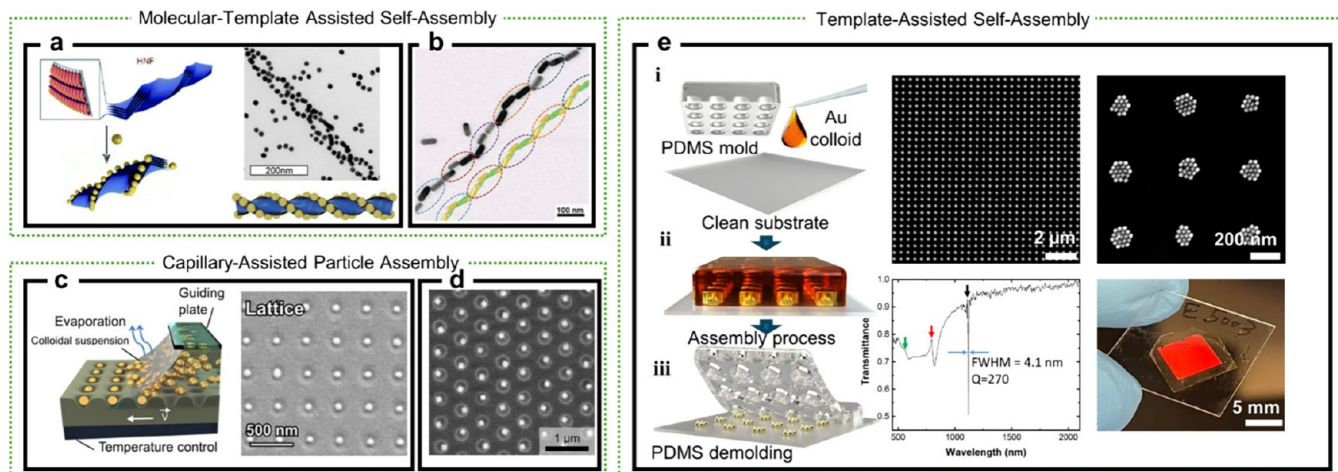


**Figure 23.** Different strategies to assemble colloids using different templates. (a, b) Molecular-template self-assembly of gold nanoparticles and gold nanorods using helical nanofilament (HNF) liquid crystals and amyloid polypeptides.<sup>973,975</sup> Adapted with permission from ref 973. Copyright 2022 Wiley-VCH. Adapted with permission from ref 975. Copyright 2021 AAAS. (c, d) Capillary-assisted particle assembly.<sup>981,983</sup> Adapted with permission under a Creative Common CC BY License from ref 981. Copyright 2019 ACS. Adapted with permission from ref 983. Copyright 2019 ACS. (e) Template-assisted self-assembly.<sup>995</sup> Adapted with permission from ref 995. Copyright 2024 ACS.

plasmonic nanoparticles into ordered arrays, a technique named Optical Printing.<sup>970–972</sup> The particles are “trapped” one by one (or in arrays)<sup>970</sup> in the dispersed medium and deposited on substrates using a focused laser usually at wavelengths close to their LSPR. Within the power gradient, the electromagnetic fields drive them in the radial direction toward the focus. In this way, the trapped particles can be positioned with great precision on various substrates. However, due to thermophoretic effects, it is hard to print particles close to others particles with similar LSPR wavelengths, limiting this technique for submicron features.<sup>971,972</sup>

Besides natural self-assembly, one of the most widespread techniques to assemble colloids is the templated assisted process. Some templates utilized to direct the assembly of nanoparticles are macromolecules and polymers (molecular templates), including DNA, protein fibers, liquid crystals.<sup>568,586,783,973–975</sup> As illustrated in Figure 23a, the helical nanofilament (HNF) phase of a liquid crystal is “decorated” along its edges with gold nanoparticles, thereby creating a helicoidal colloid organization. In this case, the nanoparticles are functionalized with an organic ligand that facilitates the integration into the bent-core molecular structure. Notably, external stimuli such as heat can induce reversible transformations of the structure from ordered to disordered states which opens up venues for tunability of the optical response.<sup>973</sup> The helicoidal arrangement adopted by the gold nanoparticles endows the system with a chiroptical response beyond what can be found in naturally occurring chiral media. Chiral plasmonic structures can also be achieved by using different biomaterials as templates; for example, Lu et al. (Figure 23b) demonstrated that assemblies of nanorods on a human islet amyloid polypeptide fibrils result in a significant boost in the chiral response with potential for biosensing.<sup>975</sup> The synergy between biomolecules and plasmonic particles has been further exploited for attomolar DNA detection with chiral nanorod assemblies<sup>783</sup> and for the detection of early stages of Parkinson disease, when amyloid proteins undergo aggregation into chiral helical nanofibers.<sup>974</sup> Among different macromolecular molds used, DNA stands out for its versatility and programmability, as illustrated by the use of the different

architectures formed by DNA origami as templates for colloidal assembly. Through the ad hoc functionalization of the DNA origami templates at specific locations, precise positioning in the nanometer range of colloids is achieved, enabling studies on spatial dependence of nanoparticle interaction<sup>586</sup> or facilitating a fine control over the fluorophore properties.<sup>568</sup>

Assembling plasmonic colloids into ordered arrays with submicrometric spacings enables the excitation of collective optical resonances over visible wavelengths. These lattice resonances are excited via diffractive modes supported by the grating and can compensate the optical losses of the single metal nanoparticle thus resulting in narrow bandwidths with potential application in sensing or lighting.<sup>644,976</sup> Traditionally 2D ordered arrays are typically fabricated via EBL followed by metal thermal evaporation, an approach that requires specialized equipment and involves a slow, serial process. Consequently, several alternative approaches have been developed for assembling particles on flat or nanostructured substrates.

2D hexagonal arrays of colloids can be directly fabricated by exploiting the formation of colloidal monolayers at liquid/air interfaces. Here, the use of core@shell nanoparticles (e.g., Au or Ag cores encapsulated by poly(*N*-isopropylacrylamide)) is required since the length of the organic shell acts as spacer, determining the lattice periodicity. Different strategies such as using a dip coater, facilitate transferring these monolayers formed at the liquid surface to a solid substrate.<sup>977,978</sup> The natural tendency of the colloids for hexagonal packing restricts mostly the type of 2D lattice achieved, however the large single domains are sufficient to feature remarkable optical properties with surface lattice resonances (SLRs) (plasmonic collective response of the array) with good quality factors ( $Q$ -factors  $\approx \lambda_{SLR}/\Delta\lambda_{SLR}$ , where  $\lambda_{SLR}$  represents the resonance central wavelength and  $\Delta\lambda_{SLR}$  its fwhm.<sup>978</sup>

Utilizing templates to guide a colloidal assembly provides versatility in the choice of pattern geometry. Classical lithography techniques can be employed to fabricate the desired geometries onto a resist, which subsequently serves as a substrate onto which a colloidal dispersion is deposited. In

capillary-force assisted particle assembly (CAPA), the colloidal dispersion is placed between two rigid substrates (one containing the desired pattern, one flat), resembling the directed assembly concept introduced by Xia and co-workers.<sup>979,980</sup> During drying, the capillary forces drive the colloids toward the template voids while dragging away any excess particles with the receding liquid. The CAPA process is controlled by regulating the displacement speed (typically ranging from nm/s to  $\mu\text{m}/\text{s}$ ) and temperature (Figure 23c),<sup>981,982</sup> but additional factors, such as solvent wetting (contact angle) and pattern geometry, can also influence assembly outcomes. Well-designed traps have proven crucial for optimizing yield,<sup>673</sup> the particles are securely confined therein, preventing accumulation on the flat regions of the substrate as extensively demonstrated for both dielectric microparticles and metal colloids in various geometries.<sup>979</sup>

The plasmonic structures produced via CAPA show exceptional optical properties; for instance, Joudénas et al. produced hexagonal arrays of single silver nanocubes (Figure 23d) exhibiting lattice resonances with high quality factors<sup>983</sup> and exciting optomechanical characteristics.<sup>984</sup> Gupta et al. assembled metal colloids onto stretchable substrates, depicting active tuning of the SLR.<sup>981</sup> Other research groups have exploited the precise control over the number of particles trapped in each cavity to go deeper into the near-field plasmonic coupling.<sup>985,986</sup> Furthermore, CAPA offers the capability of sequential depositions, allowing for the creation of assemblies with particles possessing distinct characteristics in the same unit cell, such as PS particles doped with various fluorophores.<sup>987</sup>

An alternative to using rigid patterns as templates is to employ elastomeric prepatterned stamps as the ones used for soft-lithography method (Figure 23e.i).<sup>988</sup> In the template-assisted self-assembly, the flexible and reusable molds containing the desired pattern are placed onto a drop (few microliters) of a highly concentrated colloidal dispersion (typically for Au from 10 to 50 mM Au<sup>0</sup>) placed on a substrate (Figure 23e.ii). As the solvent evaporates, the surfaces gradually approach each other until they make direct contact (Figure 23e.ii). This results in nanoparticles being trapped within the features of the mold while self-assembling, adhering to the flat surface, typically glass (Figure 23e). Metal nanoparticles assembled with this method are typically functionalized with polyethylene glycol via a mercapto groups (PEG-SH) and the dispersion stabilized via additives (CTAC  $\approx$  50  $\mu\text{M}$ ). The surface tension of the aqueous media is further reduced by using water/ethanol mixtures, minimizing coffee ring effects.<sup>989</sup> Templated assisted assembly enables the production of large patterned areas of single crystal arrays, sustaining high quality optical resonances (Figure 23e).

The features within the PDMS molds stem from micrometer sized pyramids,<sup>674</sup> until a few hundred nanometer features.<sup>990</sup> Within each feature, the metal colloids assembled into an ordered face-centered cubic packing.<sup>674</sup> The plasmonic structures assembled via this process have been used shown excellent properties as SERS sensors, particularly for gaseous carbon monoxide detection.<sup>990</sup> Matricardi et al. showcased the tunability of SLR and SERS enhancements across visible and NIR ranges in arrays with different lattice parameters.<sup>991</sup> In general, this technique has been used to produce SERS substrates with large enhancement factors and low standard deviations.<sup>674,992</sup> Furthermore, these plasmonic substrates have led to the development of reusable substrates for on-demand

analyte detection.<sup>993</sup> Additionally, Plou et al. demonstrated label-free detection and imaging of various molecules within extracellular tumor milieu components.<sup>994</sup> The colloidal assembly is not restricted to rigid substrates, the arrays can be either deposited or transfer to diverse substrates.<sup>995,996</sup> On flexible/stretchable (soft-PDMS) substrates, dynamic SLR modulation was observed.<sup>996</sup>

The plasmonic crystals fabricated with soft templates have shown high quality SLRs whose bandwidth can be controlled with the size of the colloids used in each case.<sup>997</sup> Following substrate-superstrate index matching optimization Q factors up to 270 have been shown in these colloidal arrays (Figure 23e).<sup>995</sup> Such sharp resonances can be used for sensing or light emission applications.

It is worth noting that defects such as vacancies, dislocations, and other inhomogeneities decrease the Q factor of the resonance sustained by the nanostructure. However, recent experimental results indicate that the utilization of small sized colloids to build arrays of clustered nanoparticles can significantly reduce the defect density within the structure and offer high quality resonances. Soft molds have been used to assemble gold nanospheres, nanotriangles<sup>992</sup> and nanorods.<sup>999</sup> Beyond plasmonic colloids, this technique has also been used to pattern luminescent nanocrystals, such as CsPbBr<sub>3</sub> perovskite nanocrystals (10 nm in size). The patterned perovskite arrays exhibited ASE in the NIR region under lower optical excitation fluence compared to an equivalent nonstructured perovskite film.<sup>1000</sup> Indeed, the versatility in the patterns that can be obtained is illustrated by using molds engraved with arrays of chiral motifs, therefore endowing chirality to the photoluminescence of conventional perovskite nanocrystals with photoluminescence dissymmetry factors of up to 0.3, surpassing by orders of magnitude the values obtained from unstructured chiral perovskite colloids.<sup>1001</sup>

Looking ahead, the future of colloidal assembly holds promise for even more sophisticated and functional materials. The continued exploration of novel colloidal building blocks, i.e., with asymmetric properties, and novel geometries opens up new avenues for the design of materials with unprecedented functionalities while keeping the scalable processing owed to colloids. Advancements in real-time monitoring and control techniques will further enhance the precision and reproducibility of colloidal assembly processes.

## 25. MODULUS TRANSFER FOR QUANTUM DOT MECHANICAL PATTERNING

Hohyun Keum, Moonsub Shim, and Seok Kim

Colloidal quantum dots (QDs) have attracted immense interest due to their properties that can be tuned by size, composition, surface chemistry, and shape to suit the requirements for various applications, including solar cells, LEDs, lasers, sensors, etc. Advances in synthesis have led to exquisite control over their size, size distribution, and shape for a range of compositions that can be processed through versatile solution chemistry.

To fully exploit the merits of QDs, methods to pattern and arrange them in specific, intended spatial configurations on substrates are needed to coherently integrate these promising materials with other entities of functional devices. However, their soluble nature often makes QDs incompatible with conventional lithographic approaches. Alternative measures to pattern micro/nanoscale features in QD films have included

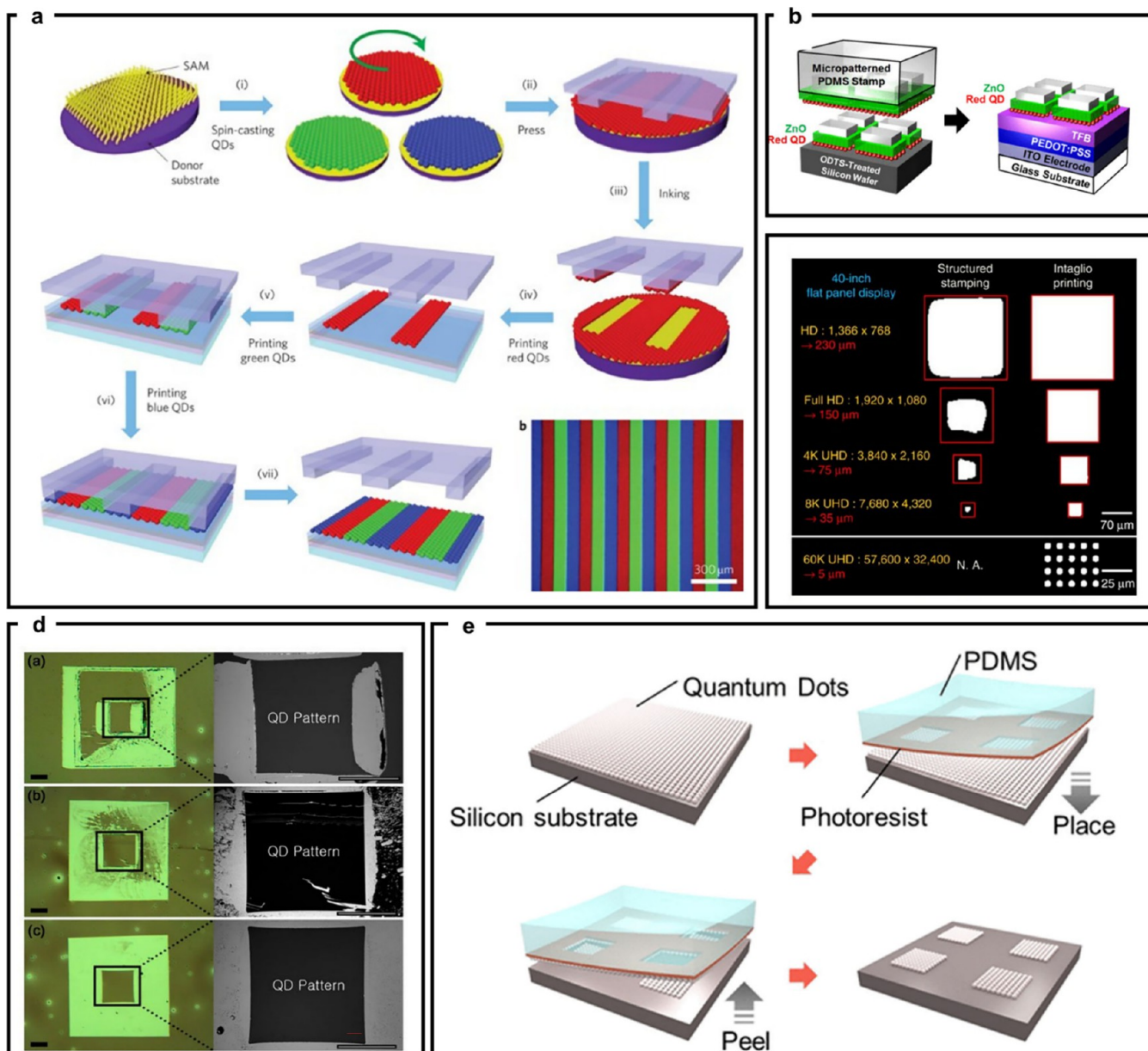


**Figure 24. Modulus transfer for quantum dot mechanical patterning.** (a) Schematic illustration of QD patterning using structured Polydimethylsiloxane (PDMS) elastomer.<sup>1025</sup> Adapted with permission from ref 1025. Copyright 2011 Springer Nature. (b) Schematic illustration of QD composite film patterning.<sup>1017</sup> Adapted with permission from ref 1017. Copyright 2016 ACS. (c) Comparison between elastomeric transfer printing and intaglio transfer printing.<sup>1020</sup> Adapted with permission under a Creative Common CC BY License from ref 1020. Copyright 2015 Nature Publishing Group. (d) QD patterning using SMP and the comparison between three different modes: (top) contacting and separation below  $T_g$ , (middle) contacting and separation above  $T_g$  and (bottom) contacting above  $T_g$  followed by separation after cooling below  $T_g$ .<sup>1022</sup> Adapted with permission from ref 1022. Copyright 2018 MDPI. (e) Schematic illustration of PR contact patterning technique.<sup>1023</sup> Adapted with permission under a Creative Common CC BY License from ref 1023. Copyright 2023 ACS.

Langmuir–Blodgett (LB)/Langmuir–Schaefer (LS) deposition,<sup>1002–1004</sup> Dip-pen nanolithography (DPN),<sup>1005–1008</sup> inkjet printing,<sup>1009,1009–1012</sup> electrophoretic deposition,<sup>1013</sup> template-assisted methods<sup>1014,1015</sup> and microcontact printing ( $\mu$ CP).<sup>1016–1019</sup>

In this section,  $\mu$ CP methods involving various stamp materials to directly pattern QD thin films and/or transfer them onto foreign substrates in predetermined configurations are highlighted. This approach is commonly carried out at relatively low temperature (often at room temperature) in atmospheric pressure while allowing submicron patterns over large areas. Furthermore,  $\mu$ CP merely involves physical

competing cohesive fracture mechanism to pattern and integrate, hence limited environmental impact.

Transfer printing of QDs using elastomers is possibly the most widely practiced method to integrate QD films. Kim and his colleagues have demonstrated transfer printing of discrete patterned QD film from octadecyltrichlorosilane (ODTS) SAM coated Si substrate via structured PDMS.<sup>1016</sup> The ODTS layer displays lower surface energy to facilitate convenient and selective retrieval of QDs within PDMS contacting regions and to allow cohesive fracture of the QD film. The authors have further characterized that this approach requires a high peeling rate (>60 mm/s) and preload (>196 kPa) to achieve close to

100% pick up yield. The applied pressure can improve close packing of QDs, which in turn can be beneficial in device integration as exemplified by higher power efficiency and brightness of QD-LEDs fabricated in this manner (Figure 24a). Structured elastomer stamps can pick-up and print multiple layers to further facilitate construction of functional devices. For example, a micropatterned PDMS elastomer stamp can be exploited to pattern multiple device layers together. (Figure 24b).<sup>1017</sup> Here, ODTs, CdSe/CdS/ZnS core–shell QDs (30 nm), and zinc oxide (ZnO, 25 nm) are successively coated on a Si substrate, followed by shadow mask patterning of Al (100 nm). Upon completion of the composite layer, structured PDMS is brought to contact and remove selected region leaving behind QD, ETL, and Al composite pixel for utilization. Changes in elastic modulus and hardness due to transfer printing have been characterized and transfer printed QD films exhibit higher values (approximately 1.5 times and 3 times, respectively) when compared to pristine QD films on glass substrate.<sup>1019</sup> However, QD films prepared on Si substrates show a higher elastic modulus compared to that of glass substrates, which has been attributed to alkyl chain interaction.

The intaglio transfer printing technique, inspired by the printmaking art technique, is an advanced form of elastomeric  $\mu$ CP process where a thin film of QDs is retrieved using an elastomer from a surface treated substrate followed by negative patterning of the QD film using prepatterned intaglio trench. The remaining desired QD pattern on the elastomer is then transferred onto desired substrates to establish a part of functional devices (Figure 24c).<sup>1020</sup> The incorporation of intaglio trench facilitates patterning of QD films by exploiting higher surface energy (>200 mJ/m<sup>2</sup> for glass/oxide and organic layers compared to 19.8 mJ/m<sup>2</sup> for PDMS) and results in higher patterning resolution, uniformity, and scalability. The performance of the intaglio transfer printing process highly depends on the surface ligands of QDs, where a group of researchers have identified the effects of four different ligand lengths (oleic acid, OA; 1-dodecanethiol, DDT; 1-octanethiol, OT; and tetrabutylammonium iodide, TBAI) attached onto representative CdSe@ZnS QDs.<sup>1021</sup> Through measurement of work of adhesion difference between PDMS-QD and QD-ODTS treated Si, finite element analysis (FEA), and reproducibility experiments, they have shown that OA ligand, which has the longest carbon chain, exhibited better yields compared to the other shorter length ligands (DDT, OT, and TBAI).

Another method of patterning films of QDs is utilizing a thermally activated shape memory polymer (SMP). Thermally activated SMPs are programmed by heating above glass transition temperature ( $T_g$ ) to lower its elastic modulus and deforming it through applied external pressure. Temporary shape is then “locked in” to the SMP at temperatures below  $T_g$ . The material restores its original shape upon heating above  $T_g$  without any external pressure. The utilization of such dual-mode SMPs for patterning QD films is an immense advantage since the adhesion between SMP and QD film can be controlled by the temperature and becomes insensitive to separation velocity. Keum and colleagues have utilized SMP stamps to negatively pattern CdSe/CdS core/shell QDs prepared on ODTs-coated Si substrates (Figure 24d).<sup>1022</sup> The authors have examined and compared three different modes of patterning QDs where the stamp and QDs coated Si substrate are (1) contacted and separated at below  $T_g$ , (2)

contacted and separated above  $T_g$  and (3) contacted at temperature above  $T_g$  and cooled below  $T_g$  prior to separation. All three experiments have been conducted with a fixed preload (~5.5 kPa) and separation rate (~2  $\mu$ m/s), and the results indicate that the first and second modes failed to pattern the QD film efficiently owing to rigid–rigid contact and reduced adhesion of the viscoelastic SMP stamp, respectively, while the third mode have successfully patterned QD films with well-defined features in a clean manner.

PR is a light-sensitive material widely used in micro-manufacturing to transfer patterns onto a diverse class of materials. However, direct PR coating on QD thin films is impractical due to solution spin-casting of PR and the chemical process involved in the development step, which can potentially affect QD film quality and therefore performance. Due to this potential negative effect, PR is first patterned via conventional photolithography and subsequently utilized for negative patterning of QD films. Ensuring conformal contact between patterned PR and the QD film is critical for patterning and replication, which has been successfully demonstrated by employing PDMS elastomer as a substrate for the initial patterning of PR (Figure 24e).<sup>1023</sup> In that work, the PDMS substrate has been coated with SPR 220 PR by spin-coating method and patterned using conventional UV mask aligner. The surface of SPR 220 PR displays higher surface energy compared to PDMS, which allows effortless patterning of QDs upon physical contact and peeling. Furthermore, inspired by detachment lithography where PR is onto different materials, the authors have presented a method of patterning a QD-metal composite inks.<sup>1023,1024</sup> Taking advantage of surface of viscoelastic PDMS, which exhibits diminishing surface free energy with reduced separation velocity and elevated temperature, the authors have transferred patterned PR thin film onto a QD-coated substrate and utilized it as a lift-off mask after PVD of a metallic layer. The transferred PR layer has been removed by pressure-sensitive adhesive (PSA), which removes QDs in contact with PR and leaving the rest of the QD-metal composite ink unaltered for further utilization.

Colloidal QDs are an emerging class of materials with diverse application prospects arising from the merits of their tunable characteristics, scalability, and processability under standard temperature and pressure conditions. However, the solubility of QDs can also limit which existing process measures can be used to fine pattern their thin films to meet specific design requirements. In this section, patterning techniques exploiting mechanical means have been presented. These methods have been carefully designed to fully exploit differences in surface free energies to successfully pattern QD films in a solution-free manner to ensure that properties of pristine QDs are maintained as much as possible.

## 26. NANOTRANSFER PRINTING OF PHOTONIC MATERIALS

Hanhwi Jang and Yeon Sik Jung

Precise and uniform patterning of photonic materials has been extensively studied because the light-matter interaction is highly sensitive to the structural uniformity and periodicity of the photonic structure. In this sense, nanotransfer printing (nTP) has emerged as a promising technique to fabricate highly ordered nanostructures across large areas. This is particularly important in nanophotonics because the light-matter interaction is collectively enhanced by a unit cell of photonic nanostructures. In addition, the ability to fabricate

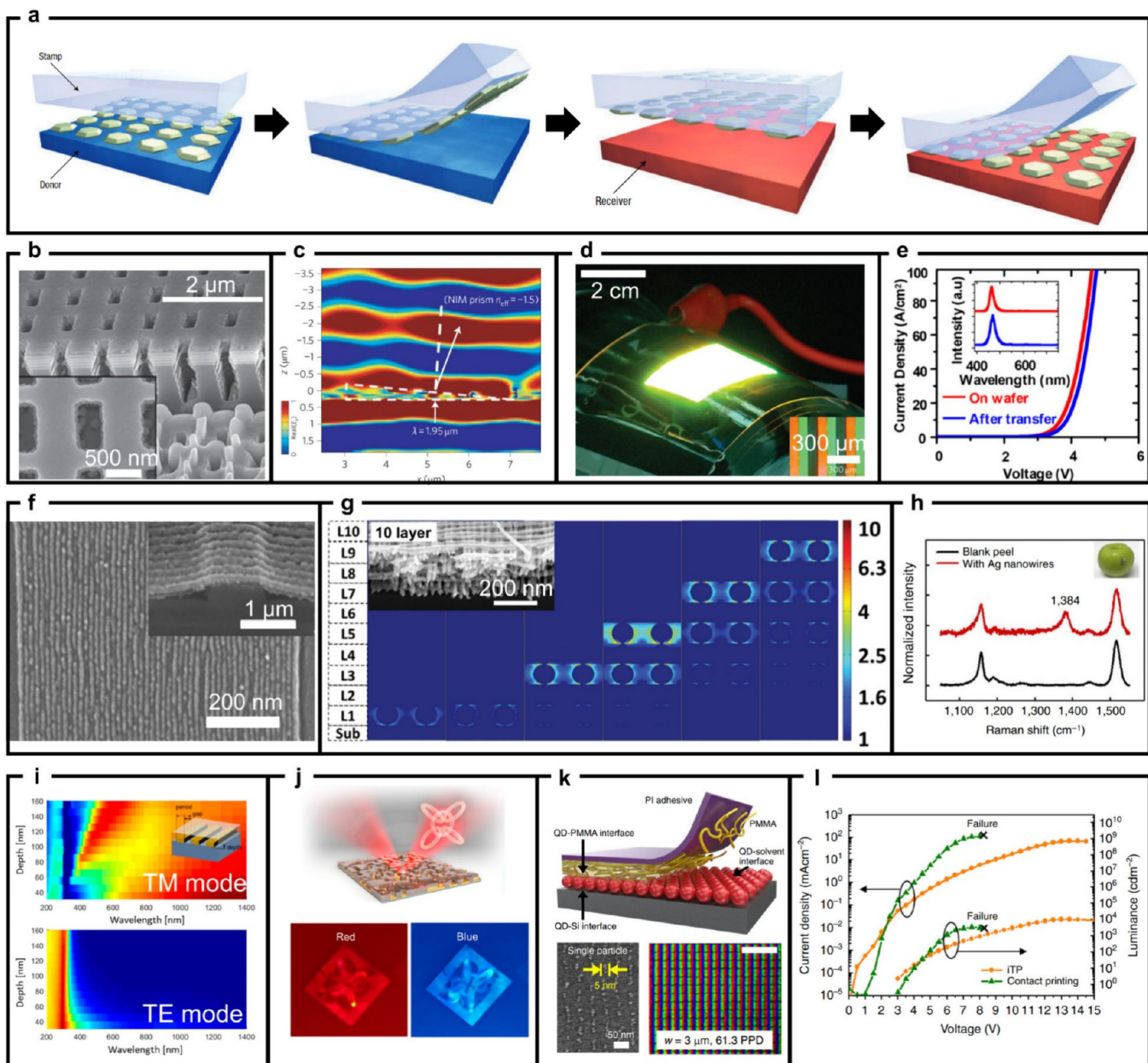


**Figure 25. Nanotransfer printing.** (a) Conventional transfer printing technique by kinetic adhesion control.<sup>1026</sup> Adapted with permission from ref 1026. Copyright 2006 Springer Nature. (b) Tilted view ( $52^\circ$ ) SEM image of Ag/MgF<sub>2</sub> 3D NIM fabricated by nTP technique. Inset is the magnified top view.<sup>523</sup> Adapted with permission from ref 523. Copyright 2011 Nature Publishing Group. (c) FDTD simulation result showing negative phase propagation.<sup>523</sup> Adapted with permission from ref 523. Copyright 2011 Nature Publishing Group. (d) Digital photograph of flexible LED patterned by sequential transfer printing of RGB QDs.<sup>1025</sup> Adapted with permission from ref 1025. Copyright 2011 Nature Publishing Group. (e) Current density–voltage characteristics of the InGaN micro-LED before and after transfer printing. Inset is the emission spectrum.<sup>1032</sup> Adapted with permission under a Creative Common CC BY License from ref 1032. Copyright 2011 National Academy of Science. (f) SEM image of a polymer mold with sub-10 nm line width. Inset is the Au nanowires printed on a patterned Si substrate.<sup>1037</sup> Adapted with permission from ref 1037. Copyright 2014 Nature Publishing Group. (g) FDTD simulation result showing E-field enhancement for 3D stacked Au nanowires. Inset shows 10 layers of orthogonally stacked Au nanowires.<sup>1038</sup> Adapted with permission from ref 1038. Copyright 2016, Wiley-VCH. (h) Raman spectra acquired from the surface of an apple treated with Thiram.<sup>1037</sup> Adapted with permission from ref 1037. Copyright 2014 Nature Publishing Group. (i) FDTD simulation results showing the transmission of TM and TE modes passing Al nanowires.<sup>1049</sup> Adapted with permission from ref 1049. Copyright 2021 ACS. (j) Reflection ring holograms fabricated by the nTP technique. Complex Al patterns are transfer printed on an Al<sub>2</sub>O<sub>3</sub> wafer substrate.<sup>1050</sup> Adapted with permission from ref 1050. Copyright 2023 ACS. (k, l) nTP of QD for LED applications.<sup>1054</sup> (k) iTP of QD patterns using an orthogonal solvent and confocal fluorescence image of the fabricated full-color QD LED. Adapted with permission under a Creative Common CC BY License from ref 1054. Copyright 2023 Springer Nature. (l) Current density–voltage-luminance characteristics of the QD LED device fabricated by iTP and contact printing. Adapted with permission under a Creative Common CC BY License from ref 1054. Copyright 2023 Springer Nature.

complicated nanostructures on various surfaces enables expanded applications in wearable devices, near-eye displays,

and optical sensors. In this section, we will introduce several nTP techniques for fabricating complex photonic structures, their optical properties, and niche applications in photonics.

Essentially, the nTP technique often involves the adhesion switching process for facile transfer of a target material to the receiver substrate. Meitl et al. first proposed the concept of kinetic control of the adhesion force using a PDMS stamp (Figure 25a).<sup>1026</sup> They used the viscoelastic response of the PDMS stamp to adjust the adhesion force during the physical contact of the target material and the PDMS stamp. In other words, once the PDMS stamp is attached to the target material, “picking” or “printing” can be determined by varying the peeling rate of the stamp. For example, the target material adheres strongly to the PDMS stamp when the peeling rate is high (Figure 25a, left), while the target material can be easily transferred to the receiver substrate when the PDMS stamp is gently peeled off (Figure 25a, right). Since the entire process does not require a high temperature process or excessive mechanical pressure, the structural deformation during the transfer process can be minimized. This is particularly important in photonics applications, where even minor damage to the photonic structure can seriously degrade the overall performance.

Subsequently, Chanda et al. have reported the large-area 3D Ag/MgF<sub>2</sub> negative index metamaterial (NIM) fabricated entirely by the nTP process, demonstrating the versatility and applicability of the nTP technique for the photonics applications (Figure 25b).<sup>523</sup> Typically, metasurfaces are prepared by FIB<sup>1027,1028</sup> or EBL<sup>1029–1031</sup> processes to pattern nanoscale features with high precision; however, their size has been limited to the hundreds of μm<sup>2</sup>, which significantly hinders the practical application and commercialization of NIMs. The 3D NIM developed by Chanda et al. can be fabricated to a size of 75 cm<sup>2</sup>, containing more than 10<sup>10</sup> unit cells in the structure consisting of 11 layers of Ag/MgF<sub>2</sub> films. The multilayer structure has been initially formed by sequential electron beam deposition of Ag and MgF<sub>2</sub> on the soft PDMS mold. Then, this structure can be transferred from the mold to the desired receiver substrate, either rigid or flexible, without significant damage to the NIM structure during the transfer process. Optical measurements show that the figure of merit (FOM = Re(n)/Im(n), where Re(n) and Im(n) are the real and imaginary part of the n, respectively) of 8 can be achieved at a wavelength of 1.95 μm with excellent spatial uniformity. FDTD simulation has been performed on the fabricated 3D NIM to visualize the electric field propagation through a 4.48° tilted NIM prism (Figure 25c). Negative phase propagation has been clearly observed inside the NIM prism, causing the outgoing beam to bend in the negative direction.

The application of the nTP technique can also be expanded to the light-emitting devices such as QD LEDs or micro-LEDs. For example, Kim et al. demonstrated a full-color QD LED by the sequential transfer printing of red, green, and blue QDs (Figure 25d).<sup>1025</sup> The QD thin film is first spin-coated on a Si wafer pretreated with SAMs for easy release of QDs in the following steps. Then, the patterned PDMS mold “picks up” the QD films, naturally forming QD line patterns on the mold. Finally, these patterns are transferred to a desired substrate, even on curved and bumpy surfaces, without significantly degrading the optoelectronic properties of the original QD film. Repeating these steps for red, green, and blue QDs results in a full-color QD LED on a flexible PET substrate yet fully functional under normal operating conditions. This method,

called “inking and stamping”, is extensively utilized for patterning QDs for high-resolution and flexible QD LEDs and optoelectronic devices. Similarly, Kim et al. estimated the current density–voltage (J-V) characteristics and emission spectrum before and after the nTP process of InGaN micro-LED (Figure 25e).<sup>1032</sup> Given that QDs and LEDs are highly susceptible to the chemical, thermal, and mechanical damage, the nTP process, which only involves low-temperature processes, are suitable technique to preserve the intrinsic properties of the target material before and after the transfer process. Recent QD nTP processes further improve the pattern quality and the resolution. For example, Choi et al. introduced intaglio process to attain full-color QD LED with resolutions up to 2,460 pixels per inch and exceptional electroluminescence performance of 14,000 cd/m<sup>2</sup> at 7 V.<sup>1020</sup> To meet the resolution requirements for near-eye displays, Meng et al. reported ultrahigh-resolution QD patterning via LB assembly of QD film followed by transfer printing, achieving resolutions up to 25,400 pixels per inch and brightness of up to 262,400 cd/m<sup>2</sup> at 8 V.<sup>1033</sup>

Conventional nTP techniques using the PDMS stamp have provided a venue for scalable fabrication of photonic materials on a flexible substrate. However, the ultimate resolution of the conventional nTP is limited to ~500 nm due to intrinsic limitations of the PDMS stamp itself. For example, mechanical deformation of the PDMS mold (buckling, roof collapse, and sagging) can result in a poor pattern quality.<sup>1034</sup> In addition, the affinity between the target material and the mold should be high enough for successful picking.<sup>1035</sup> This means that nTP of hydrophilic materials may require additional surface treatment of the PDMS mold to overcome the surface energy difference during the picking step. On the other hand, if the adhesion between the mold and the target material is too strong, the transfer yield may be poor.<sup>1036</sup> These drawbacks necessitated the development of an advanced nTP technology capable of producing high-resolution features down to tens of nanometers with improved uniformity and reliability.

In response to this, Jeong et al. proposed a new method to effectively release the target material from the polymer mold by controlling the interfacial adhesion energy.<sup>1037,1038</sup> They first prepared a nanopatterned Si master mold using KrF/ArF photolithography<sup>1039,1040</sup> or directed self-assembly<sup>1041,1042</sup> of block copolymers, and replicated the pattern using the PMMA sacrificial mold. The PMMA mold is separated from the master mold using an adhesive tape, followed by GLAD of a target material using an electron beam evaporation. The shadowing effect of the GLAD process results in a nanowire array composed of the target material on the PMMA mold. For successful transfer of the nanowire array to the receiver substrate, the adhesion between the PMMA mold and the adhesive tape should be weak enough to facilitate the delamination. Here, Jeong et al. has exploited a super-lubrication phenomenon in which the interfacial friction is extremely reduced when the solvent molecules swell the polymer films and prevent interpenetration of the polymer chains. Indeed, the measured peel strength before and after the solvent exposure is 355 and 0.475 N/m, respectively, demonstrating a facile delamination of the polymeric mold from the adhesive tape.<sup>1037</sup> Therefore, after sufficient exposure of the polymeric mold to solvent vapor, mild physical contact of the receiver substrate would promote adhesion switching of the target material and polymeric mold from the adhesive tape to the receiver substrate, while the adhesive tape is easily

peeled off from the mold. Then, the polymeric mold can be easily washed off with organic solvents such as acetone or toluene, leaving only the target material on the substrate. Using the concept called “solvent-injection-assisted nTP” (or S-nTP), Jeong et al. have been able to fabricate metallic nanowires including gold, aluminum, copper, silver, cobalt, and chromium, with sub-10 nm resolution (Figure 25f). These nanoscale metallic nanowires not only act as a plasmonic center for manipulating the optical properties<sup>1043</sup> but also can be used as a template for fabricating complex nanoscale patterns to the diverse substrate. For example, Yim et al. combined sequential nTP and RIE processes to form two layers of orthogonally stacked chromium nanowires on a Si wafer and etch out the area uncovered by the nanowires.<sup>1044</sup> The resulting Si nanowell pattern has been coated with a thin gold layer by vacuum deposition, thereby fabricating sub-20 nm gold nanohole array that exhibits well-defined plasmonic resonance in the visible wavelength range.

Sequential printing of plasmonic structures in orthogonal directions can also be exploited in SERS applications. SERS aims to enhancing the inherently weak scattering intensity of the spectroscopy, which has attracted considerable attention as an advanced chemical sensing platform for nondestructive yet sensitive detection of analytes.<sup>637</sup> In brief, SERS utilizes local electromagnetic field enhancement from nanoscale gaps (called “hot spots”) between plasmonic structures to enhance the signal intensities of Raman scattering. While a single layer of a metallic nanowire array can be used to promote the LSPR effect, Jeong et al. found that stacking these metallic nanowires orthogonally to form woodpile structures generates uniform hot spots with a gap of only a few nanometers between each layer (Figure 25g), leading to the high sensitivity and signal uniformity in SERS applications.<sup>16</sup> While conventional plasmonic SERS structures with high sensitivity required extremely complicated synthesis procedures and signal uniformity issues, the SERS substrate fabricated by sequential nTP of metallic nanowires is still widely used as an highly sensitive but reliable chemical sensing platform for the detection of various analytes including antibiotics,<sup>1045</sup> proteins,<sup>1046,1047</sup> and even gas molecules.<sup>1043</sup> In addition, these SERS structures can be easily transferred to agricultural products to detect residual pesticides or toxic chemicals that may be harmful if ingested (Figure 25h).

Various optical, optoelectronic, and nanophotonic devices can also be fabricated using the nTP technique. For example, ordered metallic nanowires can effectively polarize electromagnetic waves in the UV or visible wavelength region (Figure 25i). An electromagnetic wave consists of transverse electric (TE) and transverse magnetic (TM) modes. The electric field in the TE mode oscillates along the direction of the polarizer, allowing free electrons in the metal to move freely and reflect the light. However, the movement of free electrons through the TM mode is confined by the nanoscale gap, and the light can be transmitted through the polarizer. Using this principle, Oh et al. fabricated aluminum wire-grid polarizers on AlGaN-based UV emitters via S-nTP to achieve a high polarization ratio.<sup>1048</sup> Ko et al. further extended the use of the polarizer to the fabrication of stereographic contact lenses using polarization-based binocular parallax.<sup>1049</sup> Leveraging highly conformal printing capability of the nTP technique, they have been able to fabricate wire-grid polarizers on extremely soft and curved contact lenses, opening up new possibilities for 3D visualization of images with simple processes.

The morphology of the target material is not necessarily limited to the line patterns, and complicated patterns generated by the computer-generated hologram synthesis algorithm can also be transferred onto various substrates using the nTP technique. Ahn et al. demonstrated that aluminum-based reflective ring hologram can be patterned with high transfer yield and process fidelity on Al<sub>2</sub>O<sub>3</sub> wafer (Figure 25j).<sup>1050</sup> They first patterned a Si master mold using conventional photolithography, and the complex pattern has been replicated using a poly(urethane acrylate) (PUA) mold and UV-curable resin. After pattern replication, aluminum was deposited on the PUA mold, followed by plasma etching of the PUA mold for facile delamination of the aluminum pattern. As a result, a centimeter-scale complex ring hologram pattern can be successfully printed on an Al<sub>2</sub>O<sub>3</sub> wafer, demonstrating the broad applicability of nTP to nanophotonic devices. Similarly, Park et al. demonstrated transfer printing of complex nanostructures (e.g., serpentine, hexagons, and ellipsoids) using various materials (e.g., NiO, Pt, WO<sub>3</sub>, Ge<sub>2</sub>Sb<sub>2</sub>Te<sub>5</sub>, and Pd) on an 8-in. wafer with the developed thermally assisted nTP, thus advancing the scalability and versatility of the nTP technique.<sup>1051</sup>

The advancement of nTP has also improved the pattern quality, resolution, and scalability in QD patterning applications. Colloidal QDs have attracted considerable attention as an advanced display material due to their high photoluminescence quantum yield and color purity compared to other luminescent materials.<sup>1007,1052,1053</sup> Since QDs are highly vulnerable to physical or chemical damage such as heat, plasma, or solvent, conventional QD patterning has relied on inking and stamping via a prepatterned PDMS mold or lithographic patterning process consisting of UV exposure and etching steps. However, the inking and stamping process using the PDMS mold hinders the patterning yield, controllability, and reproducibility, while the top-down lithographic patterning inevitably damages the QDs to degrade the superior optoelectronic properties. Therefore, Nam et al. developed a process called “immersion transfer printing (iTTP)” for thermodynamic-driven pressure-free transfer printing of QD patterns (Figure 25k).<sup>1054</sup> Unlike other nTP processes that use a vacuum deposition technique, solution-based colloidal QDs require spin-casting-based techniques. Here, Nam et al. used “one-step programmed self-assembly” of QD patterns instead of conventional lithographic patterning to minimize potential damage from the top-down process. This allows for colloidal QD-based materials to be precisely patterned into the desired morphologies while minimizing the structural damage from the lithography. Briefly, the surface of patterned Si mastermold has been treated with the SAMs, and QDs dispersed in the mixture of solvent and nonsolvent have been spin-coated on the Si mastermold. The presence of nonsolvent spontaneously induces dewetting of the QD patterns and results in the selective wetting of the QD patterns only to the trench, while the mesa region remains uncoated. These self-assembled QD patterns have been picked by PMMA, delaminated with PI tape, and attached to the receiver substrate. Finally, an orthogonal solvent—one that dissolves only the PMMA layer but does not affect the QDs—has been used to gently peel off the PI adhesive from the receiver substrate while preserving the morphology and pattern quality of the QDs. One of the main advantages of iTTP is the ability to modulate the patterning resolution from the entire QD film to the single particle (~5 nm) scale. In addition, QD patterns fabricated by iTTP can be

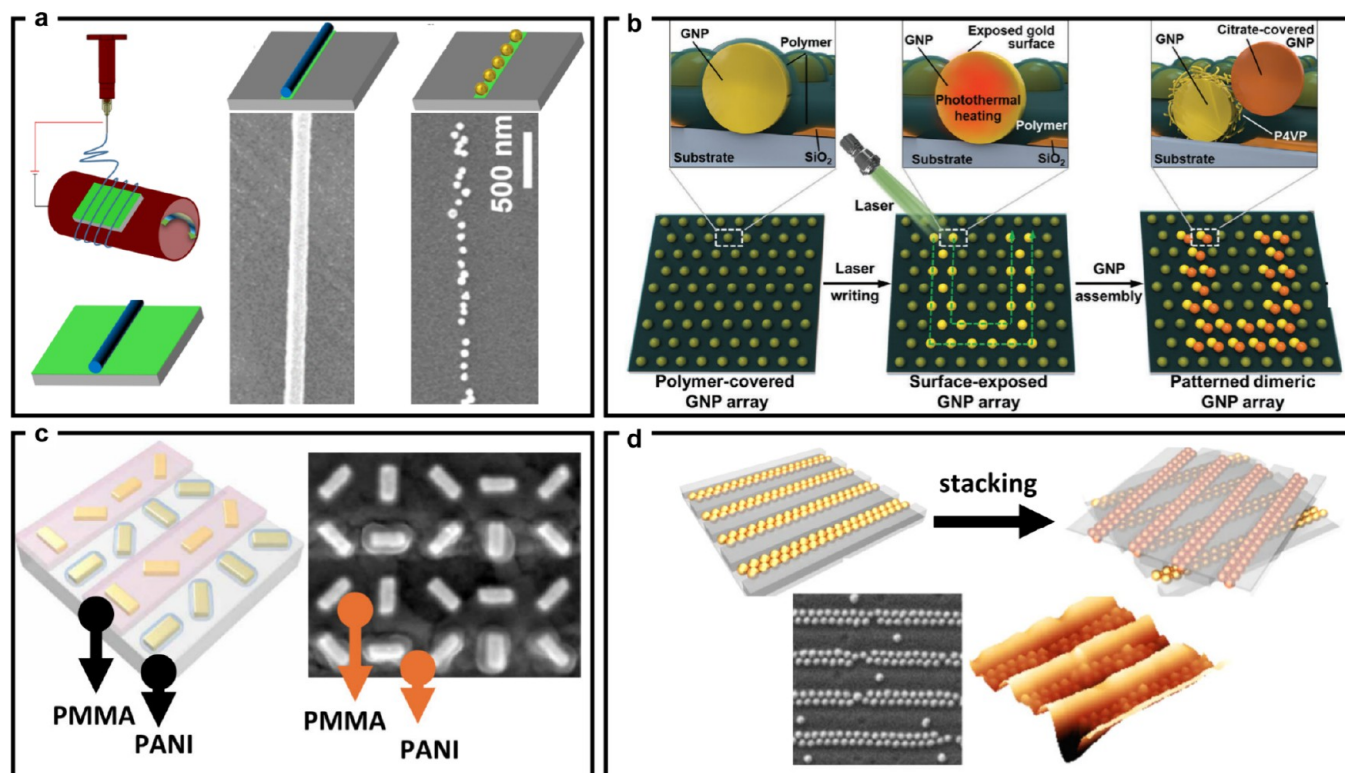


**Figure 26.** Fabrication strategies for hybrid polymer/inorganic self-assembly. (a) A polymer brush pattern is created via an electrospinning mask technique, allowing for selective adsorption of gold nanoparticles.<sup>1064</sup> Adapted with permission from ref 1064. Copyright 2017 ACS. (b) A two-step process involving laser-induced plasmonic heating to remove polymer coatings from gold nanoparticle surfaces, followed by the attachment of a secondary polymer layer that facilitates the precise placement of additional gold nanoparticles.<sup>1069</sup> Adapted with permission from ref 1069. Copyright 2021 Wiley-VCH. (c) Selective and electrochemically guided deposition of conductive polymer (PANI) shells on prealigned gold nanorods, aimed at constructing optical metasurfaces.<sup>1072</sup> Adapted with permission from ref 1072. Copyright 2021 AAAS. (d) Construction of chiral plasmonic systems via the strategic stacking of linear gold nanoparticle arrays, induced by a predetermined tilt angle, where individual nanoparticles are stabilized with achiral poly(ethylene glycol) ligands.<sup>1073</sup> Adapted with permission from ref 1073. Copyright 2021 Springer Nature.

relatively free from structural damage and nonuniform film thickness resulting from the kinetic PDMS printing; therefore, QD LED devices fabricated by iTP showed better stability under high-voltage operation (Figure 25l). As a result, a full-color QD LED with an unprecedented resolution of 368 pixels per degree has been demonstrated, paving the way for future high-resolution near-eye display applications.

## 27. POLYMER/INORGANIC SELF-ASSEMBLY

Christian Rossner, Tobias A.F. König, and Andreas Fery

Polymer/inorganic hybrid nanoparticles combine distinct properties in a single nanosized entity: While the inorganic part can provide specific e.g. plasmonic or excitonic properties, their surface functionalization with polymer ligands can be exploited for bringing in additional functionalities,<sup>1055</sup> to promote energy and charge transfer processes,<sup>1056</sup> and/or to direct the assembly into higher-order structures. At the single-particle level, one obtains modulated plasmonic resonances,<sup>1057</sup> controllable light scattering,<sup>1058</sup> and tunable photoluminescence<sup>1059</sup> resulting from the hybrid nature of these systems. Moving to assemblies of hybrid nanoparticles, coherent coupling can give rise to emergent properties including metamaterial effects.<sup>1060</sup> These possibilities enable applications in many areas, e.g. in messenger materials,<sup>1061</sup> in optoelectronics,<sup>1062</sup> in biosensing<sup>1062</sup> and photocatalysis.<sup>1063</sup> However, despite remarkable progress, studies on how these

hybrid materials can be systematically tailored and utilized for applications in nanophotonics were not reported since only few years ago. In this section, we summarize the current state of the art of nanolithographic techniques and discuss their impact on nanophotonics.

Integrating synthetic polymers into lithography-promoted colloidal self-assembly processes expands the possibilities for scalable structure formation, postassembly modification, and the flexible modulation of emergent properties. For instance, polymer brushes applied to lithographic substrates enable the formation of structured regions for selective nanoparticle adsorption. A recent realization is using electrospun polymer fibers as masks, covering a predefined part of the polymer brush surface. Subsequent oxygen plasma etching delineates nanoscale lines<sup>1064</sup> or islands.<sup>1065</sup> These spatially defined brush-coated regions on the substrates then serve as attachment sites for selective adsorption of (gold) nanoparticles (Figure 26a). Exciting opportunities can be anticipated by incorporating dynamic or even adaptive modulation into the discussed template brush patterns that can thus capture/release different particles under varying external conditions.<sup>1066</sup>

Polymer/inorganic hybrid nanoparticles can serve as basic building blocks for constructing nanophotonic devices. Their inorganic components support collective resonances at the spacing proportional to the LSPR resonance wavelength, known as SLRs.<sup>644</sup> The polymeric component stabilizes the

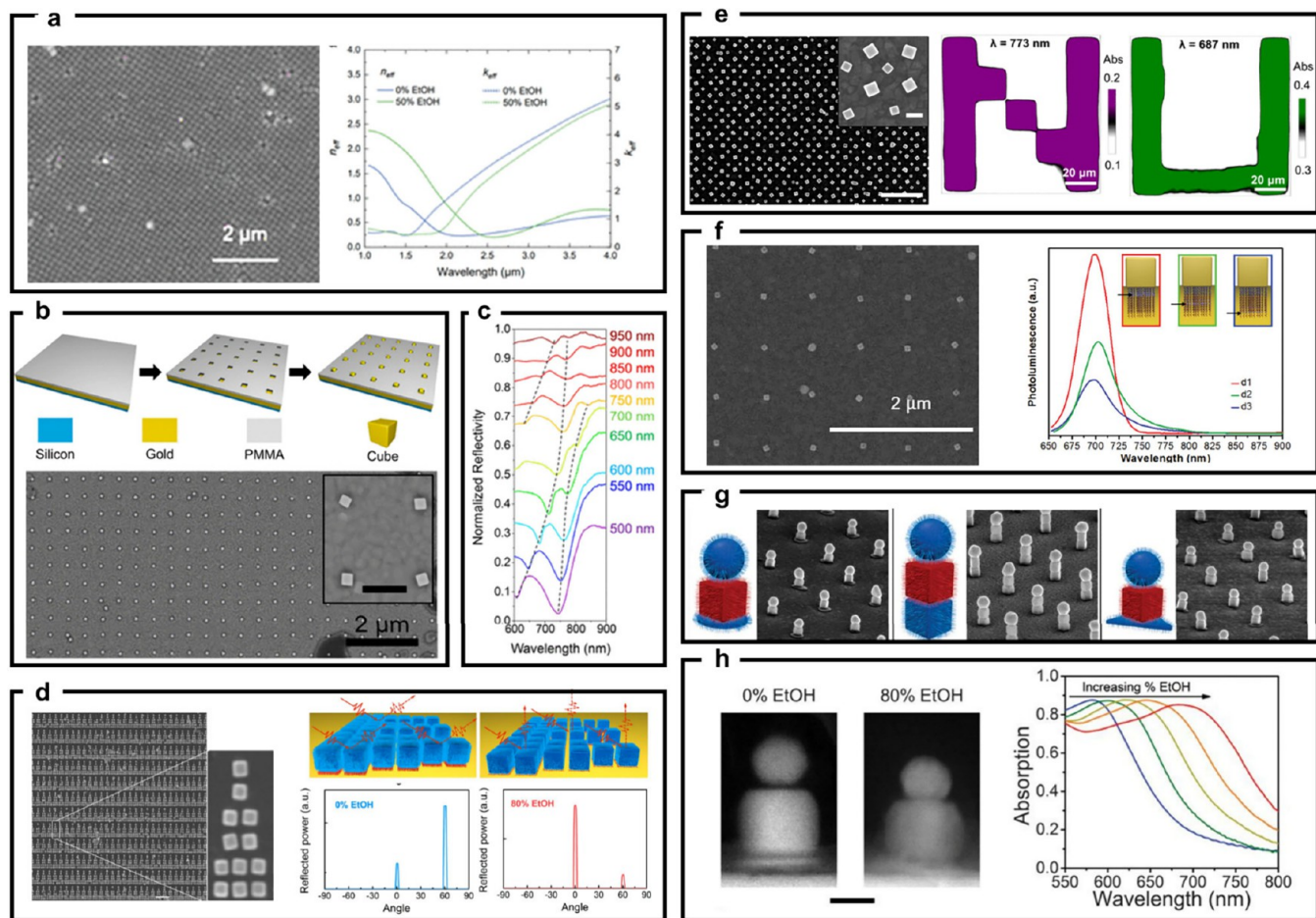


**Figure 27.** (a) SEM image of the metasurfaces made of cubic nanoparticles and measured effective refractive indices at different wavelengths.<sup>690</sup> Adapted with permission from ref 690. Copyright 2021 ACS. (b) Schematic illustration of assembly of individual nanocubes into lithographic wells and the SEM image of a typical cube array.<sup>711</sup> Adapted with permission from ref 711. Copyright 2015 ACS. (c) Reflectivity spectra of cube arrays of different periodicities.<sup>1078</sup> Adapted with permission from ref 1078. Copyright 2018 AAAS. (d) SEM image of a metasurface made of cubic nanoparticles, and experimental reflected power at 670 nm as a function of reflected angle.<sup>1083</sup> Adapted with permission under a Creative Common CC BY License from ref 1083. Copyright 2020 National Academy of Science. (e) SEM image of an array assembled from nanocubes of two different sizes (left panel), and absorption intensity maps of the surface encoders made by lithography.<sup>1084</sup> Adapted with permission from ref 1084. Copyright 2018 ACS. (f) SEM image of an array assembled for cubic nanoparticles, and fluorescence spectra of the array with dyes in different locations.<sup>1077</sup> Adapted with permission from ref 1077. Copyright 2019 Wiley-VCH. (g) SEM images of oriented superlattices assembled in templates made via lithography.<sup>1078</sup> Adapted with permission from ref 1078. Copyright 2018 AAAS. (h) Cross-sectional SEM images (left panel) and experimental optical absorption spectra (right panel) under different volume ratios of ethanol.<sup>1078</sup> Adapted with permission from ref 1078. Copyright 2018 AAAS.

inorganic core and imparts emergent optical properties.<sup>1067</sup> Recent approaches include the selective coating of these hybrid nanoparticles with reactive polymers that can change their optical properties in response to external stimuli such as electrochromic polymers.<sup>1068</sup> Site-selective addition/removal of polymer layers on assembled nanoparticles is another recently established and promising concept for surface patterning. For example, a monolayer of polymer-coated gold nanoparticles can be partially embedded in a spin-coated polymer film, exposing parts of the nanoparticles. Targeted laser-induced plasmonic heating removes surface ligands from these exposed areas, allowing for subsequent functionalization with different polymers like poly(4-vinylpyridine), thus enabling the attachment of diverse nanoparticles to form heterodimer structures (Figure 26b).<sup>1069</sup> This method facilitates information encryption through controlled plasmonic coupling and the alignment of plasmonic dimers as the

substrate is withdrawn from a colloidal solution,<sup>1070</sup> avoiding the need for asymmetric templates.

Polymer/inorganic hybrids offer a promising route to developing advanced metasurfaces with dynamic and programmable properties. Fabricating polymer/inorganic hybrid metasurfaces requires strategic assembly processes in which the nanoparticles act as tunable building blocks. The inorganic components are designed to create the desired plasmonic responses, while the polymeric parts can integrate additional functionalities, e.g., switchable properties or selective binding. For example, a metasurface consisting of hybrid nanoparticles and a thermoresponsive polymer can change its reflectance or transmittance behavior in response to external cues, like electrochemical triggers or pH change.<sup>1071</sup> Further manipulation involves the electrochemical growth of polyaniline (PANI) on gold nanorod arrays with alternating orientations. This process permits *in situ* control over PANI layer thickness, culminating in a metasurface with adjustable optical and

holographic properties (Figure 26c).<sup>1072</sup> Such dynamic behavior extends the usefulness of metasurfaces from static optical elements to active components that can react to environmental stimuli. The uniformity of particle size and shape is crucial for coherent optical behavior, but one can solve this issue with existing synthesis approaches. In addition, the scalability of these fabrication processes is a hurdle that scalable template-assisted self-assembly methods can overcome. Expanding into the 2.5 dimensions, chiral plasmonic properties emerge from assembling achiral poly(ethylene glycol)/gold nanoparticles. The chiral plasmonic metasurface exhibits pronounced circular dichroism at plasmon resonance frequencies (Figure 26d) by stacking these nanoparticle assemblies at specific tilt angles.<sup>1073</sup> Moreover, when constructed on flexible substrates, these materials' chiroplasmonic properties can be mechanically tuned, offering a straightforward approach to modulating their unique optical characteristics.

## 28. COLLOIDAL CRYSTAL ENGINEERING WITH DNA

Zhiwei Li, Koray Aydin, and Chad A. Mirkin

The principles of colloidal crystal engineering with DNA have been utilized to develop design rules for the assembly of fundamental nanoscale building blocks into crystals with programmable structures and properties, including designer photonic characteristics.<sup>1074</sup> Since the introduction of the prototypical building block, the spherical nucleic acid (SNA), in 1996,<sup>563</sup> a nanoconstruct consisting of a spherical nanoparticle core and an oligonucleotide shell, designs rule for the assembly of DNA-functionalized materials with various shapes, sizes, and chemical compositions have been delineated, leading to the realization of new types of programmable matter. These classes of nucleic acid-nanomaterial conjugates have been termed “programmable atom equivalents” (PAEs); their nanoparticle core can be likened to an “atom” and their DNA shell to the electronic “bonds” between atoms. However, unlike atoms, PAEs are unique in that the identity of the nanoparticle “atom” core is decoupled from its DNA “bonding” element.<sup>669,1075</sup> Thus, in many ways, these structures are more versatile and powerful than atomic systems in preparing materials by design. Indeed, driven by chemically well-defined DNA hybridization interactions, PAE assembly can occur on solid substrates or in solution, providing multiple synthetic routes to nanophotonic devices with tunable optical properties.<sup>1076–1078</sup>

Colloidal crystal engineering with DNA on DNA-modified substrates allows for precise control over the spatial arrangement, orientation, and distribution of both the individual particles and superlattices, making it highly useful for synthesizing custom nanophotonic devices.<sup>1079</sup> In a typical experiment, a substrate is modified with DNA strands and complementary PAEs are added to effect hybridization and yield the first layer of the crystal. Layer-by-layer introduction of additional PAEs results in crystal formation and defect minimization (Figure 27a). These highly crystalline two-dimensional (2D) metasurfaces can extend over macroscopic areas and be the basis for device fabrication. In this example, plasmonic nanoparticle building blocks were assembled onto solid substrates to produce photonic metasurfaces with high refractive indices.<sup>690</sup> The real permittivity of such metasurfaces can be tuned across positive and negative values by using ethanol to facilitate DNA expansion or contraction (Figure 27a). Such responsive metasurfaces are particularly interesting

for optical computing, communications, and imaging applications.<sup>387,1080,1081</sup>

Top-down nanolithography can be combined with bottom-up DNA-mediated assembly to provide exquisite control over the position, orientation, and composition of individual nanoparticles or assembled superstructures on solid substrates. Template-confined, DNA-driven assembly leverages customizable templates prepared via lithographic techniques for the programmable assembly of nanoparticles, providing access to many unique photonic devices (Figure 27b).<sup>711,1082,1083</sup> In square lattices made of cubic Au nanoparticles, the nanocubes have efficient surface registration driven by DNA hybridization that occurs at the interface of the nanocubes and the exposed Au substrates (bottom panel in Figure 27b).<sup>711</sup> The ability to systematically change the periodicity gives rise to widely tunable reflection of the square lattices (Figure 27c). This template-confined assembly can be customized to fulfill the design needs of nanophotonic devices, making it possible to design device-quality metasurfaces with interesting optical properties.

Enabled by such a powerful method, an anomalous reflector was developed via the shape-directed assembly of nanocubes into a periodic array (Figure 27d).<sup>1083</sup> In this design, 12 nanocubes form a subcluster in a complex 2D matrix on an Au surface. By matching the template geometry with the shape of the building block, an additional degree of freedom allows control over orientation as well as the relative nanoparticle spatial arrangement with nanometer precision over submillimeter length scales. In addition, the configuration of DNA strands can be reversibly manipulated upon solvent exchange, leading to dynamic lattice expansion-contraction. This methodology permits the realization of responsive photonic metamaterials that display normal or anomalous reflection depending on ethanol concentration (Figure 27d).<sup>1083</sup>

Size matching between nanoparticles is important for obtaining assemblies of high-quality anisotropic nanoparticles on substrates; however, particles with size *mismatches* can be exploited to realize hierarchical superstructures and hybrid crystals that contain nanoparticles with different sizes, shapes, and compositions. This strategy is effective in developing multiplexed photonic devices for surface encoding, color generation, printing, and anticounterfeiting measures. For example, when two sets of pores with different sizes were used as templates, large and small Au nanocubes could be assembled in sequence. The larger nanocubes could be only assembled into the larger pores due to their size mismatch with the smaller pores, leading to highly selective surface registration (Figure 27e).<sup>1084</sup> Using this method, nanocubes of different sizes were assembled into hierarchical superstructures useful for encoding photonic information in solid devices (Figure 27e).<sup>1084</sup> Based on this technique, photonic codes can be written for high-security information encryption and high-resolution color printing.

When plasmonic Au nanocubes are assembled on Au substrates with nanometer-scale precision, highly tunable plasmon coupling occurs between these surfaces, and hotspots are generated. Thus, this system is ideal for studying photonic lattice modes as well as the interplay between dye emission and plasmonic resonance. Dye molecules can be conjugated to specific bases on DNA strands, allowing precise chemical control over the separation between the dyes and the plasmonic entities. In a fundamental study, 80 nm Au nanocubes were assembled into square lattices using the

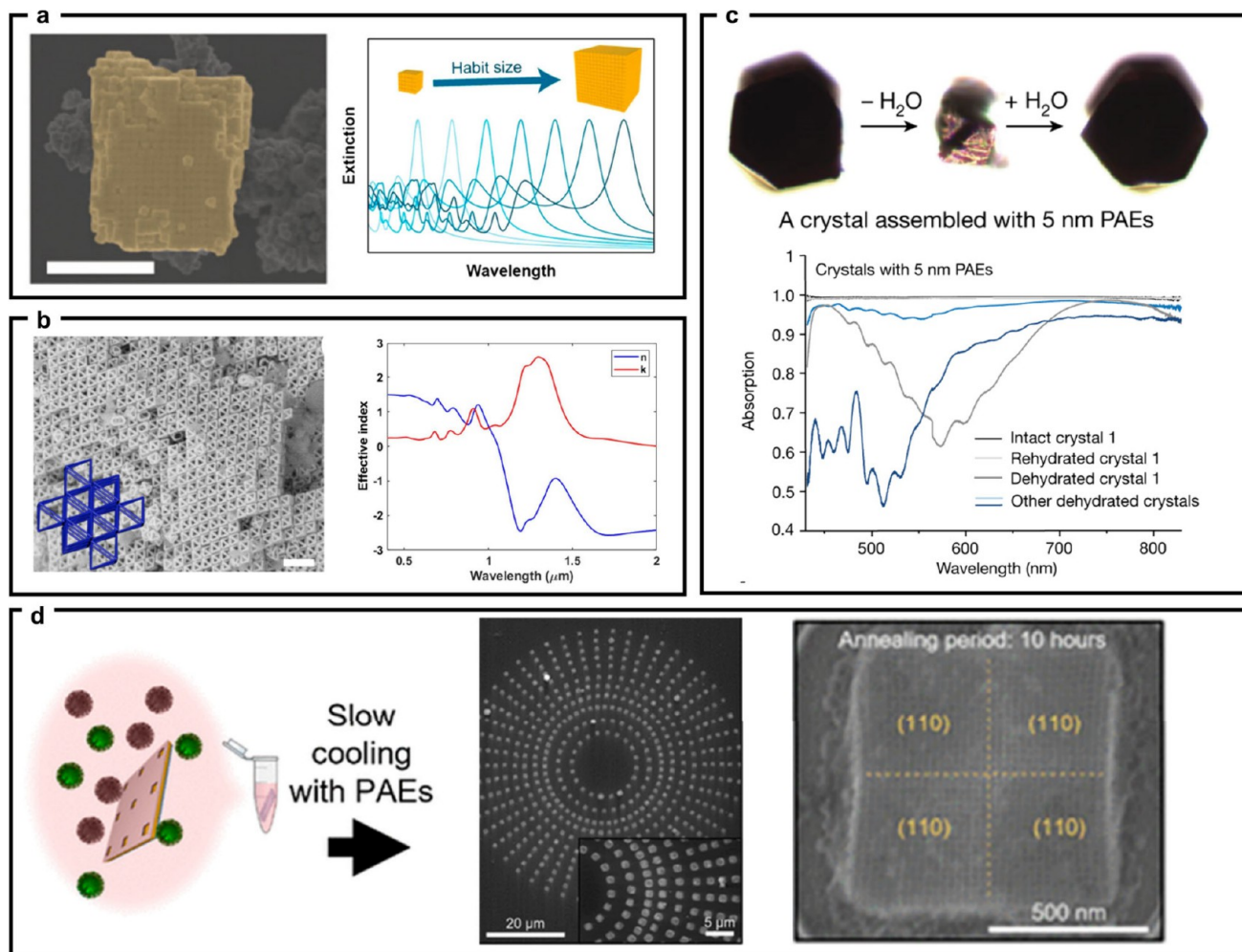


Figure 28. (a) SEM image of superlattices made of nanocubes, and the lattice size-dependent tunability of Mie resonances.<sup>692</sup> Adapted with permission from ref 692. Copyright 2020 ACS. (b) SEM image of open-channel superlattices, and plots of calculated effective refractive index ( $n$ ) and extinction coefficient ( $k$ ).<sup>1076</sup> Adapted with permission from ref 1076. Copyright 2022 Springer Nature. (c) Bright-field optical microscopic images during dehydration-hydration, and the corresponding absorption spectra during the dehydration process.<sup>1085</sup> Adapted with permission from ref 1085. Copyright 2022 Springer Nature. (d) Schematic illustration of the templated assembly of superlattices (left panel), SEM images of the superlattice patterns (middle panel) of one superlattice (right panel) in lithographic patterns.<sup>1086</sup> Adapted with permission from ref 1086. Copyright 2023 ACS.

template-confined assembly strategy.<sup>1077</sup> The nanocubes have a large (over 320 nm) separation such that the plasmon coupling between them is negligible (Figure 27f).<sup>1077</sup> Dye molecules chemically conjugated to DNA at different distances from the particle surface exhibit site-dependent light emission properties, which can be attributed to the electric field intensity within the gaps. That is, an enhanced localized electric field near the nanocube surface leads to stronger fluorescence emission. The optical emission can be modulated by the in-plane structures of the antennas but also actively tuned via choice of solvent. And, because the position of the dye can be tuned with single-base pair precision, this system is a useful platform for the study of structure–property relationships in the plasmon-dye coupled systems. It also encourages the use of template-confined, DNA-mediated colloidal assembly for engineering light-emitting photonic devices.

Three-dimensional superstructures can be prepared using a layer-by-layer assembly strategy.<sup>1078</sup> This multidimensional assembly uses lithographically defined pores as templates and introduces nanoparticles of different shapes (like cubes, plates,

and spheres) as building blocks. Nanoparticles of different shapes are conjugated with complementary DNA strands and coded as different colors (Figure 27g).<sup>1078</sup> Through the layer-by-layer assembly of these nanoparticles in the pores, superstructures can grow along the pores, forming standing structures in an out-of-plane direction (SEM images in Figure 27g). The responses of DNA bonding to solvents also leads to dynamic tuning over the gaps between the nanoparticles within the standing superstructures, which allows active modulation of plasmon coupling between these nanoparticles and hence the peak positions of the extinction spectra (Figure 27h).

Considering current research activities, colloidal crystal engineering with DNA requires additional efforts in discovering fundamental superstructures with emerging optical properties and in optimizing existing materials for real-world devices. The first aspect requires shape-controlled synthesis of building blocks for designated properties. Introducing nanoparticles of diverse shapes also allows us to explore complex colloidal crystals that have interesting photonic properties. In addition, introducing nanoparticles of various chemical compositions would enable designing and realizing functional, hybrid optical

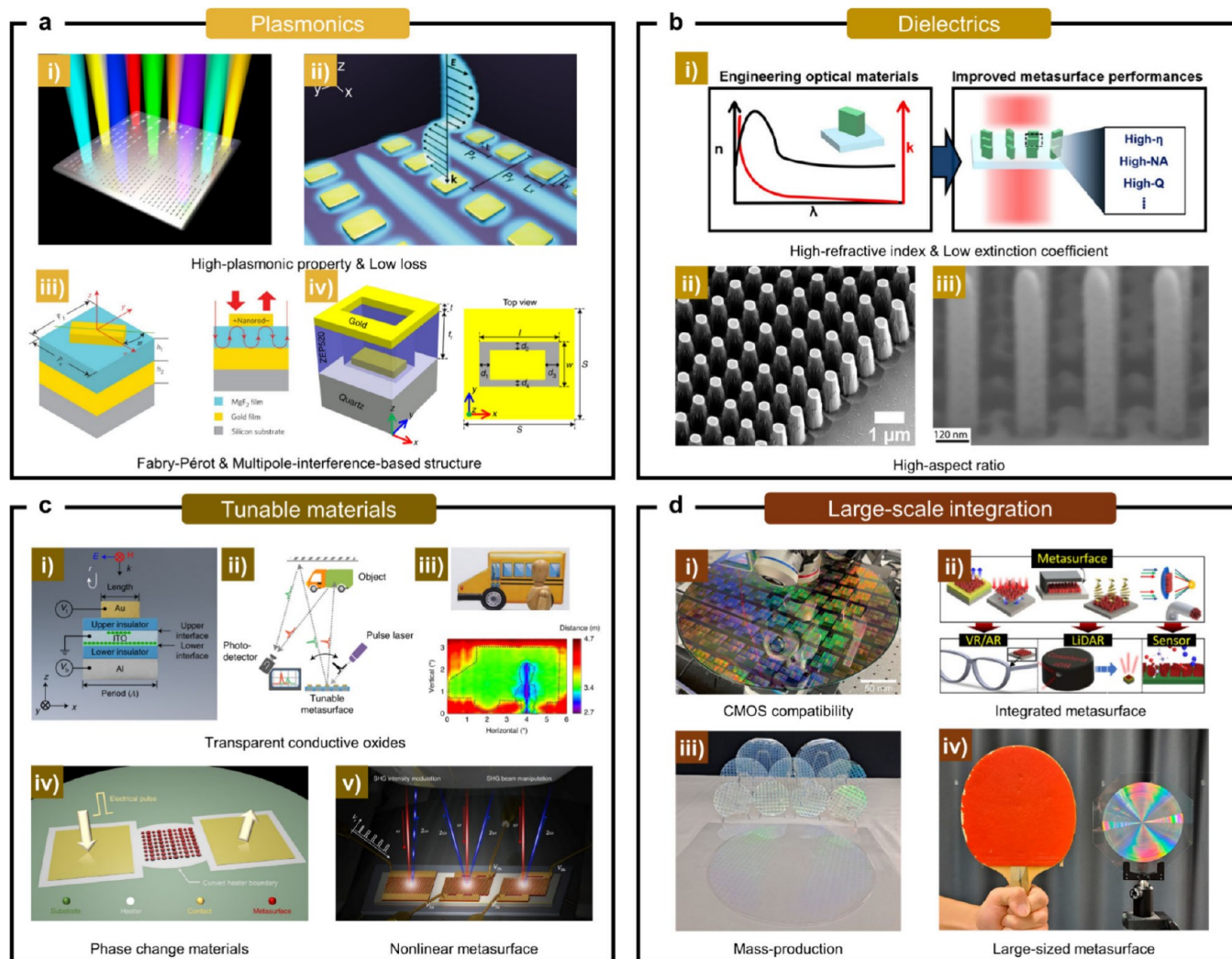


**Figure 29. Materials for optical metasurfaces.** (a) Plasmonic materials. (a.i) Schematic of high color saturation plasmonic metasurface using silver.<sup>14</sup> (a.ii) High-Q factor metasurface nanocavities using gold nanostructures.<sup>13</sup> (a.iii) Unit cell of Fabry-Pérot-based high-efficiency reflective metasurface.<sup>1109</sup> (a.iv) Unit cell of multipole-interference-based high-efficiency transmissive metasurface.<sup>1110</sup> Adapted with permission from ref 14. Copyright 2023 Springer Nature. Adapted with permission under a Creative Common CC BY License from ref 13. Copyright 2021 Springer Nature. Adapted with permission from ref 1109. Copyright 2015 Springer Nature. Adapted with permission under a Creative Common CC BY license from ref 1110. Copyright 2019 Springer Nature. (b) Dielectric materials. (b.i) Effect of optical properties in dielectric metasurfaces. High- $n$  and low extinction coefficient can make high-efficiency, -NA, and -quality factor metasurfaces.<sup>1113</sup> (b.ii) SEM image of all-glass visible metalens.<sup>399</sup> (b.iii) SEM image of high aspect ratio TiO<sub>2</sub> metasurface.<sup>1116</sup> Scale bars in (b.ii) and (b.iii) are 1  $\mu$ m and 100 nm. Adapted with permission from ref 1113. Copyright 2023 ACS. Adapted with permission from ref 399. Copyright 2019 ACS. Adapted with permission under a Creative Common CC BY License from ref 1116. Copyright 2016 National Academy of Science. (c) Tunable materials. (c.i) Schematic of ITO implemented electrically tunable metasurface and (c.ii) and (c.iii) its 3D LiDAR application.<sup>1118</sup> Adapted with permission from ref 1118. Copyright 2021 Springer Nature. (c.iv) Electrically tunable GSST metasurface beam steering metasurface using a micro Joule heater.<sup>1030</sup> Adapted with permission from ref 1030. Copyright 2020 Springer Nature. (c.v) Electrically tunable nonlinear metasurfaces for SHG amplitude shift. (d) Large-scale integration. (d.i) Foundry fabricated metasurfaces on 30 cm wafer using 193 nm DUV lithography.<sup>68</sup> Adapted with permission from ref 68. Copyright 2022 Springer Nature. (d.ii) Schematic of integrated metasurface applied for virtual/augmented reality, LiDAR, and sensors.<sup>1125</sup> Adapted with permission under a Creative Common CC BY License from ref 1125. Copyright 2023 Springer Nature. (d.iii) Hybrid materials for mass-produced and large-aperture metalenses in the visible. One cm diameter metalenses have been fabricated on 4, 6, 8, and 12 in. sized wafers.<sup>81</sup> Adapted with permission from ref 81. Copyright 2023 Springer Nature. (d.iv) A comparison between a table tennis racket and an all-glass metasurface lens with a diameter of 10 cm.<sup>401</sup> Adapted with permission from ref 401. Copyright 2024, ACS.

metamaterials with a wide range of optical functionality and tunability. Quantum dots or semiconductor nanocrystals can be incorporated into colloidal crystal engineering to benefit from the tunability of the quantum effects in colloidal crystals through DNA chemistry. Optimizing exciting photonic colloidal crystals for device-scale engineering and fabrication

would further improve the commercialization capability of these photonic materials. A few challenges in current research include high cost of noble-metal building blocks, complicated assembly processing, as well as the integration between photonic crystal materials with current optical device fabrication methods

In colloidal solutions, DNA-mediated assembly provides an alternative approach to manipulating the photonic properties of superstructures, including Mie-resonant metamaterials,<sup>692</sup> shape-memory colloidal crystals,<sup>1085</sup> negative refractive metamaterials,<sup>1076</sup> and complex architectures.<sup>1086</sup> Important parameters to consider when preparing photonic devices from nanomaterials include crystal periodicity, orientation, symmetry, and habit size, and the building block composition, size, and shape.<sup>1087–1090</sup> For example, three-dimensional simple cubic superlattices can be prepared using Au nanocubes, and the crystal sizes can be tuned (Figure 28a).<sup>692</sup> Multipolar Mie resonances in such metacrystals were observed in the mid-infrared region. As the crystal size increases, the Mie resonances red-shift, demonstrating the size-dependent tunability of the system (Figure 28a).

When porous or hollow nanoparticle building blocks (e.g., nanoframe particles) are used in colloidal crystal engineering with DNA, an edge-to-edge bonding model was identified, and a universal approach was realized that could be used to assemble metallic open-channel superlattices with pores ranging from 10 to 1,000 nm (Figure 28b).<sup>1076</sup> The lattice pore geometry, channel topology, and photonic properties of these crystals can be tuned by controlling the nanoframe particle sizes, shapes, and DNA designs. Interestingly, these new materials have negative refractive indices (Figure 28b).

Colloidal crystal engineering with DNA can be used for synthesizing stimuli-responsive materials, whose optical and mechanical properties can dynamically change in response to external chemical and physical stimuli.<sup>1085</sup> For example, the charges of DNA strands can be reduced using high-concentration metal cations, leading to contraction, and vice versa. Specifically, cation-induced actuation of colloidal crystals engineered with DNA has been performed.<sup>1091</sup> Shape-memory, self-adaptive colloidal crystalline materials were also realized using body-centered cubic colloidal crystals.<sup>1085</sup> These crystals were made of small Au nanospheres bonded by predesigned DNA strands, and high viscoelastic volume fractions were achieved. The crystals deformed into irregular shapes with wrinkles and creases within seconds of dehydration and recovered their original structural integrity after rehydration (Figure 28c).<sup>1085</sup> The hydrated crystals exhibit near-perfect broadband absorption in the ultraviolet–visible region, and the deformed crystals show increased reflection largely as a result of the changes in the effective refractive index of the materials (Figure 28c). Arrays of colloidal crystals for nanophotonic applications can be prepared by combining template confinement with DNA-mediated colloidal crystallization. In this design, colloid crystals are assembled inside pores on solid substrates,<sup>1092</sup> leading to the formation of arrays of colloidal crystals (Figure 28d).<sup>1086</sup> Each pore contains one single- or multicrystalline material with well-defined crystal orientation and uniform crystal habit and size. The combination of DNA-programmable assembly and colloidal crystal engineering with DNA with lithographic fabrication facilitates the development of photonic devices.

## 29. OPTICAL MATERIALS

*Junhwa Seong, Nara Jeon, and Junsuk Rho*

Optical metasurfaces, engineered with subwavelength-scale structures, have garnered significant attention in recent years for their ability to manipulate light in unprecedented ways, enabling various applications ranging from beam steerers, holograms, lenses, structural color filters, sensors, and

more.<sup>29,1093–1105</sup> Their functionalities and performances have been dictated by the design of how the structures are arranged and materials are composed. Advancements in theoretical and computational tools, coupled with significant progress in materials science and experimental techniques, have paved the way for practical applications of metasurfaces.

Plasmonic metasurfaces can direct light at the nanoscale and amplify the local intensity of electromagnetic fields via localized surface plasmon resonances of metallic nanostructures.<sup>679</sup> Effective plasmonic metasurfaces require plasmonic materials with high plasmonic properties and low losses.<sup>1106</sup> Noble metals like silver and gold, meeting these criteria, have been effectively employed to create metasurfaces exhibiting high color saturation in the visible spectrum<sup>1107</sup> and ultrahigh quality (Q) factors in the IR range<sup>1108</sup> (Figure 29a(i), (ii)). However, the efficiency of plasmonic metasurfaces has often been hindered by optical losses arising from the oscillations of free electrons interacting with incident electromagnetic waves. To address this challenge, the Fabry-Pérot structure has been employed to achieve an 80% reflection efficiency at the 800 nm region<sup>1109</sup> and a notable 42.3% transmission efficiency at the 750 nm region through a multipole-interference-based structure<sup>1110</sup> (Figure 29a(iii), (iv)). Nevertheless, there remain constraints on applying plasmonic metasurfaces in the visible spectrum, with optical losses in plasmonic devices significantly constraining their potential to substitute conventional optical elements.

These challenges, discussed regarding plasmonic metasurfaces, can be addressed by substituting metals for dielectrics.<sup>1111</sup> Dielectric metasurfaces rely on the collective scattering of light called Mie scattering, from highly refractive dielectric nanoparticles of similar size to the wavelength of light within the particle. The magnetic response of dielectric scatterers is not connected with significant nonradiative losses.<sup>1112</sup> In addition, the CMOS compatibility of silicon-based materials makes them more accessible to commercial equipment, making them easier to commercialize than plasmonic metasurfaces. These distinctions emphasize the promise of dielectric metasurfaces in advancing optical technologies.

The efficiency of a dielectric metasurface has been significantly constrained by the optical properties of materials, such as  $n$  and extinction coefficient. Materials with relatively high  $n$  can facilitate strong confinement of light modes, while those with low extinction coefficient ( $k$ ) can help minimize optical losses<sup>1113</sup> (Figure 29b(i)). For instance, the deflection efficiencies of beam-steering metasurfaces, within a deflection angle of 70°, 1 μm wavelength range, and 1.8 μm thickness, have been notably enhanced by opting for high  $n$  materials.<sup>1114</sup> Single-crystalline silicon ( $n = 3.4$ ) metasurfaces show four times higher deflection efficiencies compared to silicon dioxide ( $n = 1.44$ ). Additionally, maintaining a high aspect ratio of meta-atoms has proven crucial for achieving high efficiency and complete  $2\pi$  phase control within a single dielectric structure. While all-glass visible metalens based on nanopillars with diameters ranging from 250 nm (AR = 8) to 600 nm (AR = 3.3) and heights of 2.0 μm has been demonstrated, it still falls short of fully covering the entire 0 to  $2\pi$  phase<sup>1115</sup> (Figure 29b(ii)). Furthermore, high aspect ratio TiO<sub>2</sub> metasurfaces have been developed for achieving about 80% efficiency in the visible frequency ( $\lambda = 480, 532, 660$  nm)<sup>1116</sup> (Figure 29b(iii)).

However, both types of metasurfaces mentioned above have been limited to their inability to modify their optical response postfabrication. Tunable metasurfaces using a range of active

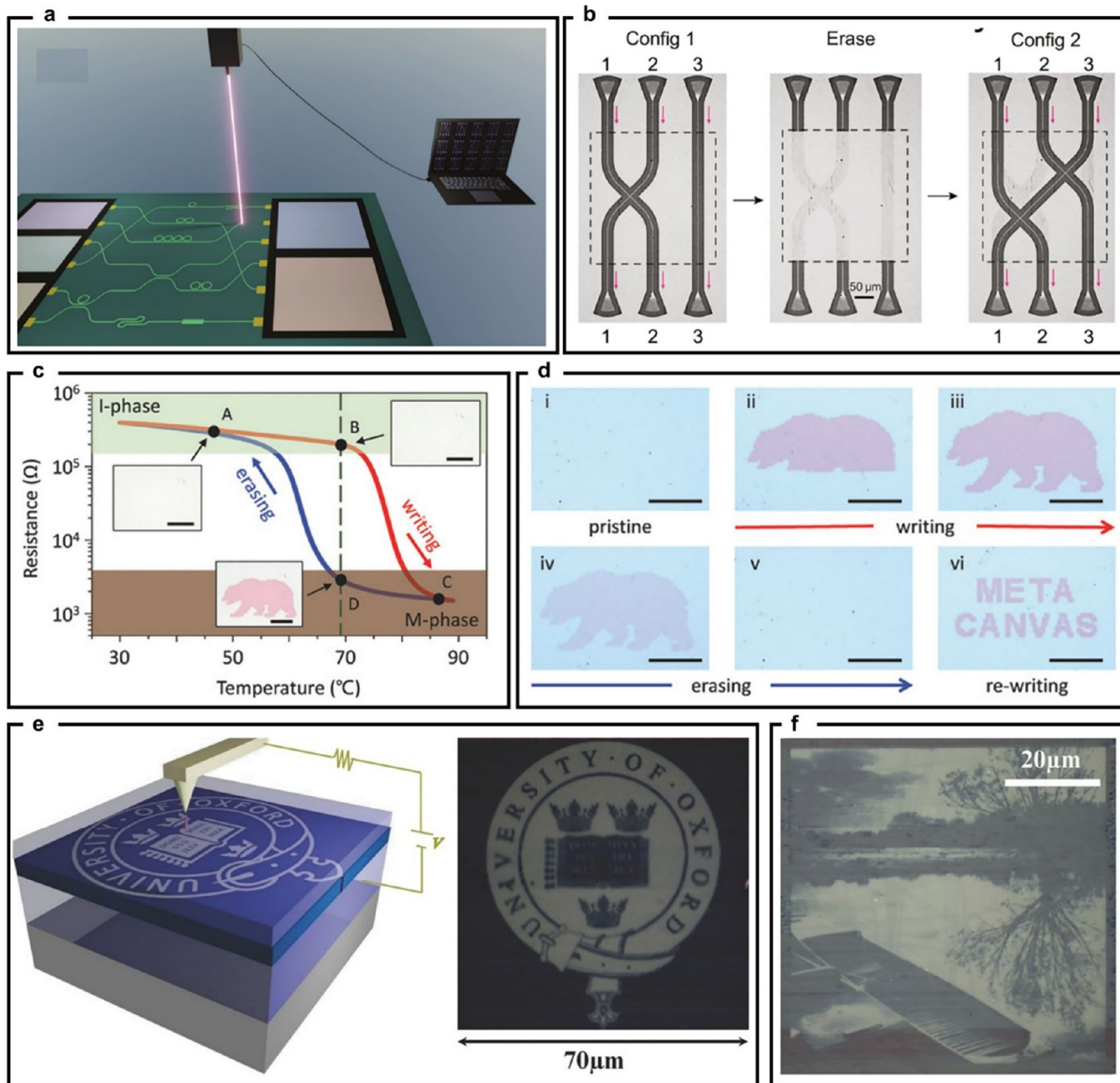


**Figure 30. PCM nanophotonics.** (a) Schematic depicting laser direct writing of photonic circuits in a chalcogenide PCM thin film.<sup>1140</sup> Adapted with permission from ref 1140. Copyright 2024 AAAS. (b) Top-view optical micrographs showing writing, erasure, and rewriting of waveguides connected three pairs of grating couplers. Both the waveguides and couplers correspond to crystallized region in a PCM film patterned using laser writing without etching.<sup>1140</sup> Adapted with permission from ref 1140. Copyright 2024 AAAS. (c) Electrical resistance–temperature hysteresis response of VO<sub>2</sub> during temperature cycling. The vertical line indicates the operation temperature at which a nonvolatile response of VO<sub>2</sub> can be obtained.<sup>1145</sup> Adapted with permission from ref 1145. Copyright 2018 Wiley-VCH. (d) Reversible writing and erasing of a VO<sub>2</sub> based meta-canvas.<sup>1145</sup> Adapted with permission from ref 1145. Copyright 2018 Wiley-VCH. (e) Schematic illustration of nanoscale patterning in chalcogenide PCM using CAFM (left) and a microscale image of Oxford logo patterned using this method.<sup>1147</sup> Adapted with permission under a Creative Common CC BY License from ref 1147. Copyright 2016 Wiley-VCH. (f) A grayscale image in chalcogenide PCM written using CAFM.<sup>1147</sup> Adapted with permission under a Creative Common CC BY License from ref 1147. Copyright 2016 Wiley-VCH.

materials and systems, including electrical, optical, chemical, mechanical, and thermal tuning mechanisms, can suggest promising avenues for overcoming the limitations of conventional metasurfaces.<sup>1117</sup> The primary tunable properties, like operation wavelength and modulation speed, have decided the performance of overall tunable metasurface devices. Considering these options, electrically tunable metasurfaces stand out

for their appeal, as they can smoothly combine with diverse established electronic devices.

Transparent conductive oxides are highly attractive owing to their capability to alter the  $n$  by accumulating or depleting charge carrier concentration, enabling complete phase modulation while maintaining a consistent reflectivity. All-solid-state light detection and ranging (LiDAR) device has

been demonstrated using the manipulation of the carrier concentration profile within ITO layers<sup>1118</sup> (Figure 29c(i), (ii), (iii)). Independent manipulation of the top and bottom regions of the ITO layer has enabled the attainment of two degrees of freedom in independently controlling reflectance and phase shift. Additionally, phase change materials, such as vanadium dioxide,<sup>1119</sup> GeSeTe,<sup>1031</sup> and GeSeSbTe (GSST),<sup>1030</sup> can also offer electrical controllability through the integration of a well-designed micro-Joule heater (Figure 29c(iv)). Although there is an unavoidable reduction in energy efficiency as per thermodynamic principles, it remains intriguing to manipulate materials and operational principles previously beyond our control using electricity. Furthermore, electrically tunable nonlinear metasurface has also been demonstrated using plasmonic nanocavities filled with multiple quantum wells (MQWs)<sup>1120</sup> (Figure 30c(v)). Integrating the nonlinear polarization metasurface with the MQWs' intersubband nonlinear response enables efficient frequency conversion at moderate pumping intensities (tens of kW/cm<sup>2</sup>). However, there exist persistent challenges in achieving widespread adoption, such as the need for device miniaturization, low power consumption, and the attainment of substantial modulation depth.<sup>1121</sup>

Although plasmonic, dielectric, and tunable metasurfaces have successfully shown the innovative concept of harnessing arbitrary control over wavefront manipulation, numerous obstacles hinder the transition of metasurfaces into real-world applications. Large-scale integration should be done with commercially available equipment, products, facilities, etc. to make it easier to reach consumers in the market.<sup>1122</sup> Plasmonics are not suitable for mass production, but titanium nitride and zirconium nitride have recently been exploited for their comparable performance to noble metals and for their low cost and CMOS compatibility.<sup>1123</sup> Despite the difficulty of realizing high aspect ratio nanostructures, silicon-based dielectrics have been actively applied using commercial photolithography techniques. Microcavity arrays with high finesse, fabricated by foundries on 300 mm wafers, have been developed using 193 nm DUV lithography<sup>1124</sup> (Figure 29d(i)). Furthermore, to enhance the utilization of metasurface-based optical systems, harmless and environmentally friendly materials are needed for integrated metasurfaces that can seamlessly integrate with existing devices and function actively<sup>1125</sup> (Figure 29d(ii)). To meet market demands, the latest semiconductor processing equipment and extreme UV and DUV lithography are being used, but the equipment is very expensive and requires the development of new processing methods or materials. A hybrid material, a high-index atomic layer-polymer, has been adapted to enhance the scalability of 1 cm sized metalenses in the visible<sup>81</sup> (Figure 29d(iii)). A batch of 669 metalenses, each measuring 1 cm in size, has been successfully produced through the integration of DUV lithography, wafer-scale nanoimprinting, and ALD. However, these methods rely on a large capacity of design files for the initial reticle design (4× size reticle) and high-speed EBL for reticle fabrication, making it challenging to produce metasurfaces larger than 2 or 3 cm. For larger metasurfaces, multiple reticles and fully developed CMOS-compatible materials can be a viable option. An all-glass metasurface lens with a diameter of 10 cm, containing 18.7 billion nanostructures, has been demonstrated to operate in the visible spectrum, utilizing seven reticles for 248 nm DUV lithography<sup>1126</sup> (Figure 29d(iv)).

It has been demonstrated that metasurfaces provide an efficient and viable means to engineer electromagnetic waves, as the demand grows for compact sizes and highly manipulable light. While some metasurface concepts have moved from lab experiments to practical tools, the material foundations for real-world metasurface applications keep progressing. Despite each material having its limitations in terms of operational range, fabrication methods, and application focus, ongoing advancements and endeavors to materials offer the potential to unlock photonics devices with unparalleled control capabilities, ushering in a transformative epoch in photonics.

### 30. PHASE CHANGE MATERIALS

Zhiyun Xu, Tian Gu, and Juejun Hu

Optical phase change materials (PCMs) broadly refer to materials that exhibit a large optical property contrast when undergoing a solid-state structural transition. In the most general sense, PCMs encompass chalcogenide phase change alloys that switch between amorphous and crystalline phases,<sup>1127,1128</sup> Mott oxides exemplified by VO<sub>2</sub> that undergo metal–insulator transition,<sup>1129,1130</sup> and emerging 2D PCM such as In<sub>2</sub>Se<sub>3</sub>.<sup>6</sup> Owing to their tunable optical responses, they have already been widely adopted in reconfigurable and programmable photonic devices ranging from photonic switches<sup>1131–1133</sup> to active metamaterials.<sup>480,1134,1135</sup>

Nanolithography for photonic device fabrication is a new arena where PCMs are poised to play an important role. Unlike conventional lithographic patterning methods which typically involve subtractive removal of materials to produce device structures, photonic devices in PCMs can be defined by precisely introducing spatially varying structural phases in a PCM film, thereby generating a modulated *n* pattern. Compared to traditional lithographic fabrication, this etch-free patterning scheme features several advantages. First and foremost, this scheme uniquely allows repeated patterning on the same device platform to achieve reconfigurable functions, leveraging reversible structural transitions to “write” and “erase” patterns on-demand. Second, phase transitions in PCMs can be triggered by various physical agents including light,<sup>1136</sup> electron beam,<sup>1137</sup> heat,<sup>1138</sup> ion beam,<sup>1137</sup> and electric field,<sup>1139</sup> enabling a wide array of patterning generation techniques to meet diverse application requirements. Third, the scheme can be readily adapted to create multilevel, gray scale *n* patterns. Lastly, truly “flat” optical devices can be realized leveraging such an approach, which can be advantageous for subsequent integration, for instance 2.5-D device stacking. In the following, we will discuss several examples of PCM enabled nanolithographic fabrication to highlight these unique benefits.

The versatility to directly “write” and “re-write” patterns and functional optical devices was demonstrated in the recent work by Wu et al.<sup>1140</sup> using a nonvolatile low-loss PCM Sb<sub>2</sub>Se<sub>3</sub>.<sup>1141</sup> A commercial laser direct write system (Heidelberg DWL 66+) was used to induce local phase transition in a Sb<sub>2</sub>Se<sub>3</sub> film (Figure 30a). Crystallization and amorphization were achieved on the same system with two sets of laser powers and beam scanning speeds. The large *n* contrast between the amorphous and crystalline phases of Sb<sub>2</sub>Se<sub>3</sub> ( $\Delta n \sim 0.8$ ) enables direct writing of waveguide components with strong optical confinement, such as microring resonators, grating couplers, interferometers, and crossbar arrays, which can also be further erased and rewritten at will to establish different photonic circuit configurations (Figure 30b). In the same vein, reversible

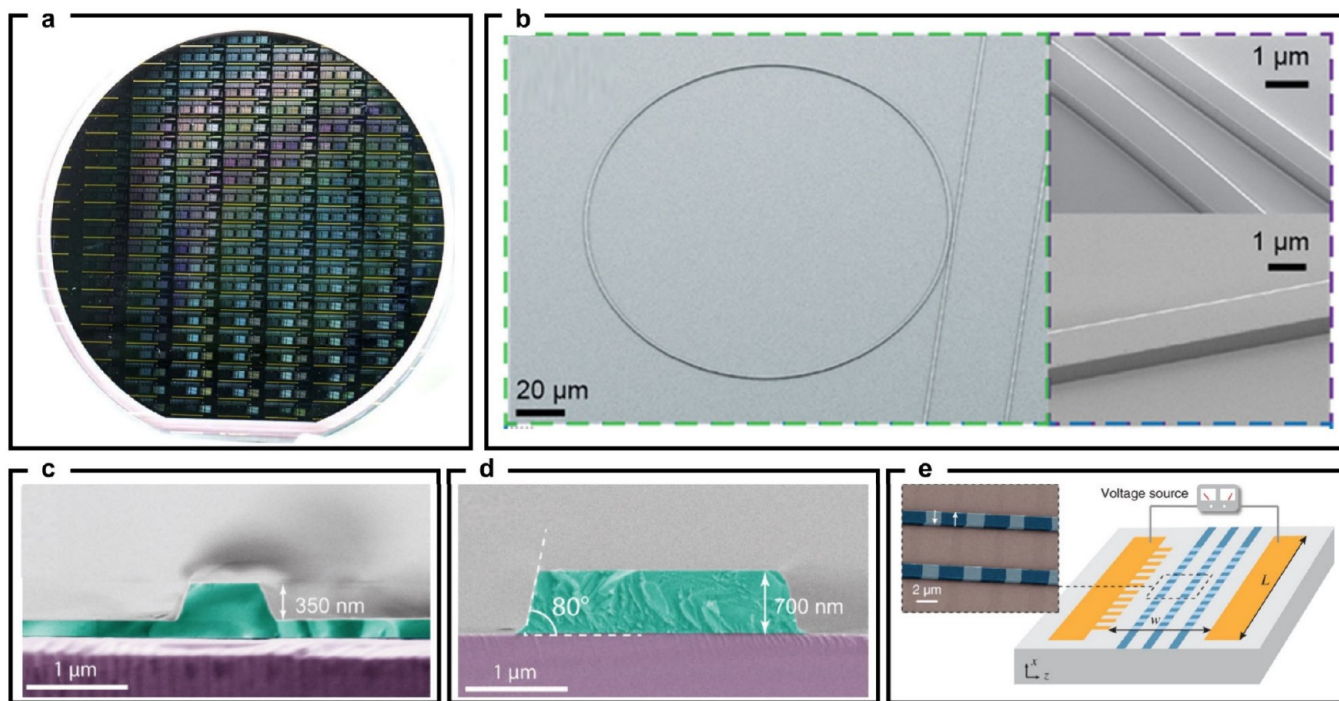


**Figure 31.** Fabrication of TFLN integrated photonic devices (a) Photographs of 6-in. TFLN wafers fabricated using standard nanopatterning process.<sup>1164</sup> Adapted with permission from ref 1164. Copyright 2020 Optica. (b) SEM images of smooth TFLN resonators, with a microring resonator on the left and closeups of smoothly etched waveguides on the right.<sup>1172</sup> Adapted with permission from ref 1172. Copyright 2017 Optica. (c, d) Cross-sectional SEM images of TFLN waveguides. The waveguides are fabricated using soft masks and diamond like carbon as hard masks in (c) and (d), respectively.<sup>1175</sup> Adapted with permission under a Creative Common CC BY License from ref 1175. (e) Schematic illustration of the periodic poling method. Left inset: a close-up SEM image of the periodically poled TFLN waveguides.<sup>1180</sup> Copyright 2015 Springer Nature. Adapted with permission from ref 1180.

laser writing had been employed for patterning of color nanoprints,<sup>110,1142</sup> topologically optimized photonic devices,<sup>1143</sup> optical metasurfaces<sup>1144</sup> and polariton nano-optics in chalcogenide PCMs. In another example by Dong et al., the phase transition oxide VO<sub>2</sub> was used to create a “meta-canvas” which can be repeatedly patterned.<sup>1145</sup> Even though the thermally triggered metal–insulator transition in VO<sub>2</sub> is in general volatile, nonvolatile operation is possible over a limited temperature window (represented by the dotted line in Figure 30c) defined by hysteresis of the transition. Various device structures such as polarizers, holograms, and gratings can be written using a laser beam by heating up the VO<sub>2</sub> film and transforming it locally into the metal (M) state. The device pattern can be readily erased by cooling the entire film to room temperature before the next writing cycle (Figure 30d).

In the two examples above, patterning of device structures in the PCMs was implemented using a scanning laser beam. The ability to induce phase change using alternative stimuli further enables etch-free patterning in PCM with resolution well beyond the optical diffraction limit. Hosseini et al. demonstrated writing of microscale color display patterns in Ge<sub>2</sub>Sb<sub>2</sub>Te<sub>5</sub> (GST-225) and Ag<sub>3</sub>In<sub>4</sub>Sb<sub>76</sub>Te<sub>17</sub> (AIST) using conductive AFM (CAFM, Figure 30e).<sup>1146,1147</sup> Resolution below 50 nm was reported using this approach in a pixel-by-pixel writing mode. In the case of these chalcogenide PCMs, the phase transition is triggered by resistive heating. It is also possible to induce the crystallization phase change in the nanoscale directly using a heated nanoscale tip.<sup>1148,1149</sup> This approach has been recently implemented using commercial thermal scanning probe lithography (TSPL) systems. For instance, Pan et al. showed that crystalline patterns with

resolution down to 100 nm can be formed in Ge<sub>2</sub>Sb<sub>2</sub>Se<sub>4</sub>Te (GSST)<sup>1150</sup> using TSPL.<sup>1151</sup> In VO<sub>2</sub>, it has been shown that electric field applied by a CAFM tip can locally modify the oxygen vacancy concentration, thereby modulating the metal–insulator transition behavior at the nanoscale.<sup>1152</sup>

Yet another advantage of PCM-based nanolithography is the ability to produce nonbinary, continuous grayscale patterns. While this is possible via conventional grayscale lithography, the process is complicated and demands meticulous calibration of the resist dose curve and selectivity during etch pattern transfer.<sup>1153</sup> In chalcogenide PCMs, a continuum of *n* values can be obtained by adjusting the laser/voltage pulse duration and magnitude to control the extent of partial crystallization, an attribute that has already been applied to realizing a wide array of continuously tunable photonic devices.<sup>1030,1154,1155</sup> This presents a facile pathway to achieve multilevel grayscale patterning. As an example, the same CAFM-patterning technique discussed above has also been adapted for generating microscale images with up to 255 grayscale levels (Figure 30f).<sup>1147</sup> The capability to access continuously varying refractive indices may also offer a practical route to realize photonic device architectures derived from continuous density-based topological optimizations without imposing level set.<sup>1156</sup>

Last but not least, PCM-based nanolithography does not involve removal of materials by etching and therefore can form completely flat device structures without surface topology, while still providing sufficient *n* contrast for functional optical devices. This capability eliminates the need for extra planarization steps, which is advantageous for 2.5-D device integration. Another example capitalizing on this feature is the fabrication of gradient index (GRIN) optics in bulk and thin

film Ge–As–Sb–Pb glass ceramics.<sup>1157–1159</sup> The as-prepared Ge–As–Sb–Pb material is a homogeneous glass. Upon laser irradiation followed by heat treatment, precipitation of PbSe nanocrystals can be photothermally induced to modify local  $n$ . This laser-induced vitrification process can be adopted to produce bulk and thin film optical components with on-demand 3-D index distributions and yet a truly flat surface profile.

In summary, optical PCM-enabled nanolithography provides a versatile and yet powerful alternative to traditional lithography and etching based fabrication methods. By precisely introducing a spatially varying microstructure (phase) and modulated  $n$  pattern, optical devices can be defined in PCMs without necessitating subtractive material removal processes. The PCM-based patterning techniques offer full reversibility and reconfigurability, superior resolution beyond the optical diffraction limit, and can create nonbinary, grayscale or gradient  $n$  patterns. Given these unique benefits, we foresee that more exciting applications of PCM-based nanolithography in integrated photonics and metamaterials will continue to unfold in the coming years.

### 31. LITHIUM NIOBATE INTEGRATED PHOTONICS

*Hyounghan Kwon and Hojoong Jung*

Lithium niobate ( $\text{LiNbO}_3$ , LN) is considered as one of the most versatile materials in photonics, possessing exceptional materials properties such as a wide bandgap, second-order optical nonlinearity, piezoelectric, photoelastic, and ferroelectric effects, just to name a few. These advantages enable LN-based efficient optical modulators and frequency converters, which are crucial for high-speed optical communications and nonlinear optical systems. Given its widespread use and the advanced technology of bulk material mass-production, LN is often dubbed the "silicon of (nonlinear) photonics".<sup>1160</sup>

On the other hand, integrated photonics holds great promise for next-generation optical systems, enabling scalability, complexity, and miniaturization. Although materials like silicon, silicon nitride, gallium arsenide, and indium phosphide have shown significant achievements, LN's recent results seem superior for integrated photonics applications. A unique challenge of LN has been wafer-scale production of thin film LN (TFLN) and subsequent nanopatterning. Recent strides in the nanofabrication of TFLN have spurred the development of tightly confined LN integrated photonic devices, marking a significant leap in TFLN photonics. Following the main theme of this mega-review, this section delves into the advancements in nanofabrication of TFLN devices for development of the state-of-the-art photonic applications. In addition, we note that there are many comprehensive review and perspective papers discussing the wide applications of TFLN photonic devices from the perspective of functionality.<sup>1161–1163</sup>

Wafer-scale production of single-crystalline TFLN is a key milestone, enabling the massproduction of the TFLN integrated photonics. Figure 31a shows the photography of the 6-in. wafer-scale TFLN integrated photonic devices which include optical modulators, resonators, and beam splitters.<sup>1164</sup> The production of the TFLN relies on smart-cut technology, using precise ion implantation and wafer bonding followed by thermal annealing, allowing exfoliation of the thin film while preserving LN's unique properties.<sup>1165</sup> To support waveguiding effects, the thin film is cladded with low-index materials such as silicon oxide, sapphire, or air. Commonly,

LN thin films are placed on a silicon oxide layer on a silicon substrate, known as TFLN on insulator platforms. Unlike conventional Ti-diffused lithium niobate waveguides, the large index contrast between TFLN and silicon oxide enables tightly confined waveguides with a mode field diameter below  $1 \mu\text{m}^2$ . The confined TFLN waveguides support high density integration of diverse optical elements with a small bending radius, strong light-matter interactions, and dispersion control, enabling new regimes of nonlinear and quantum optics.<sup>4</sup> In addition to the undoped TFLN layer, MgO-doped TFLN layers are utilized for their high damage threshold and reduced photorefractive effects.<sup>9</sup> Erbium or Ytterbium-doped TFLN is also of great interest for optical amplifier, quantum repeater, and quantum memory.<sup>1166–1169</sup> However, most of the current TFLN layer is not considered stoichiometric due to the ion-implantation step. Development of such stoichiometric materials potentially leads to ultimate limits of the TFLN photonic devices. TFLN on sapphire has been also explored thanks to its MIR transparency and strong mechanical wave confinement.<sup>1170</sup>

Nanopatterning of the TFLN layer involves nanolithography and a subsequent etching process. Deep-UV photolithography can produce wafer-scale, low-loss TFLN photonic devices with low loss of  $0.27 \text{ dB/cm}$ .<sup>1164</sup> Electron-beam lithography, commonly used in academic research of TFLN devices, often employs negative-tone electron beam resists (HSQ) as etching masks to transfer the patterns to the TFLN layers. The etching process is based on argon milling, so physical rather than chemical process. While the seminal work in 2004 has shown the physical etching process of TFLN lithium niobate for the first time,<sup>1171</sup> the high-quality etching method with high optical quality factor of  $10^7$  has been demonstrated in 2017.<sup>1172</sup>

For example, Figure 31b shows the smooth surfaces of the low-loss TFLN waveguides. As shown in Figure 31c, the physical etching often results in the angled sidewalls close to  $50$ – $70$  degree. The angles of the slanted sidewalls depend on the neighboring structures and detailed conditions in the etching process. The current etching process of the TFLN produce residues, thus wet-cleaning of such residues is essential. They are cleaned using solutions like  $\text{H}_2\text{O}_2$  and  $\text{NH}_4\text{OH}$  or KOH. The TFLN waveguides are often cladded by air or PECVD silicon oxide layer. After the nanopatterning and passivation, postannealing is also often performed near  $500$ – $600$  °C in order to improve the optical performance of the TFLN photonic devices.<sup>1173</sup>

Propagation loss of the waveguide is one of the key parameters for the evaluation of nanopatterning process of TFLN integrated photonics. The TFLN integrated photonic devices have shown rapid progress from the aspects of low-loss photonic devices. For example, the intrinsic quality factor of  $2.9 \times 10^7$  has been experimentally demonstrated in 2024.<sup>1174</sup> This high-quality factor indicates the ultralow propagation loss of  $1.3 \text{ dB/m}$ , which approaches measured fundamental limit of  $0.2 \text{ dB/m}$ .<sup>1173</sup> Instead of the soft masks based on the electron beam resist, diamond-like carbon has been recently proposed as a new hard mask for the etching process thanks to its strong hardness and superior etching selectivity.<sup>1175</sup> As shown in Figure 31d, this novel hard mask platform has resulted in the large side-wall angle of  $80$  degree and propagation loss of  $4 \text{ dB/m}$ , showing potentials of dense integrations of TFLN photonic circuits. For the passivation layer, hydrogen-free low-temperature silica is also proposed through inductively coupled

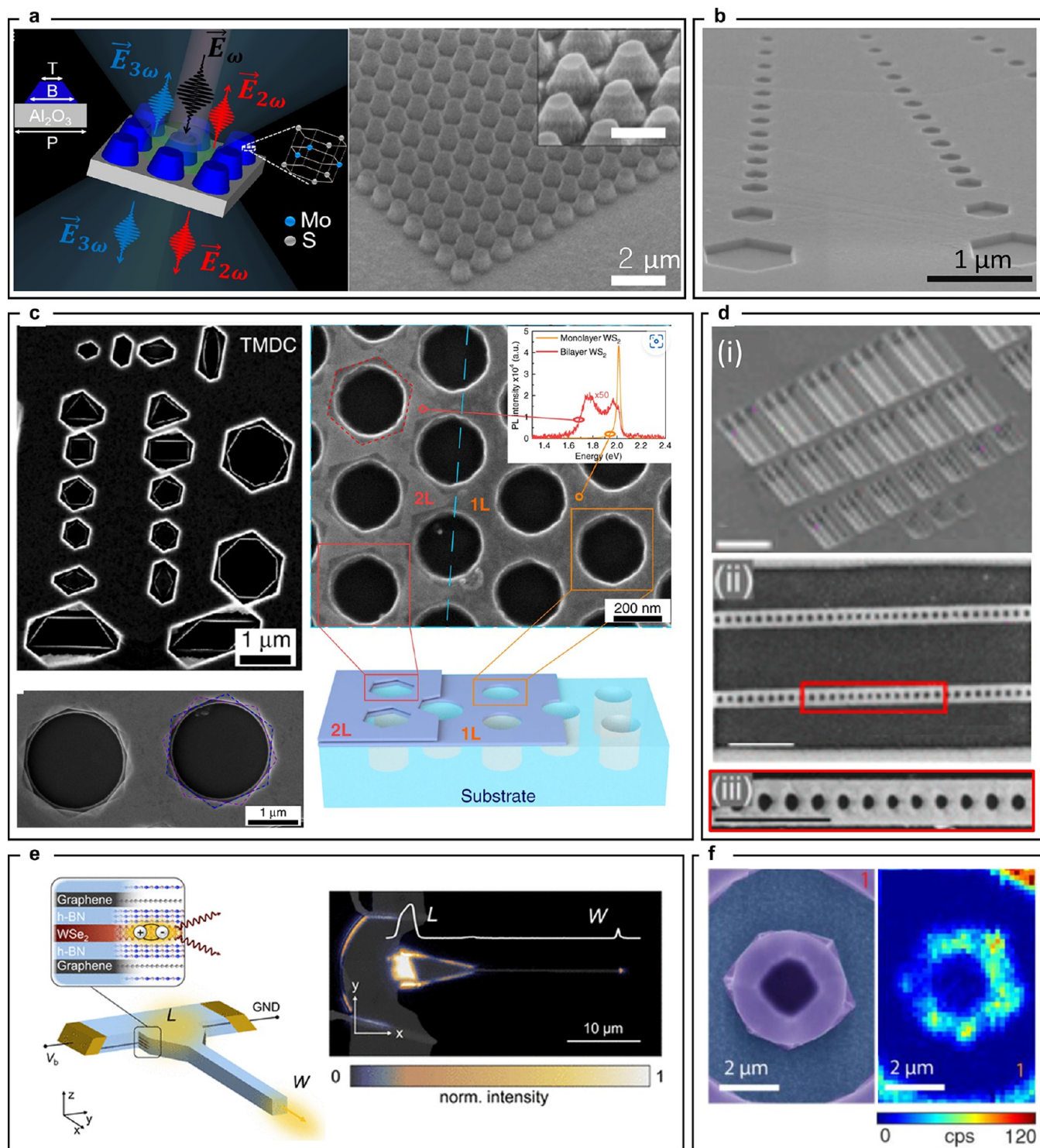


**Figure 32. Nanofabrication with 2D materials.** (a) Left: Schematic of truncated cone-shaped MoS<sub>2</sub> metasurface, top left and bottom right insets show the geometry of the cones and lattice structure of 2H-stacked MoS<sub>2</sub>, respectively; right: the SEM image of the fabricated metasurface with T = 150 nm, B = 240 nm, P = 300 nm and height of 150 nm. <sup>1193</sup> Adapted with permission under a Creative Common CC BY License from ref 1193. Copyright 2021 Springer Nature. (b) SEM image (70° tilted) of anisotropically etched hexagonal holes, with initial circular shapes, in a WS<sub>2</sub> flake on SiO<sub>2</sub>/Si substrate. <sup>1195</sup> Adapted with permission under a Creative Common CC BY License from ref 1195. Copyright 2020 Springer Nature. (c) Top left: SEM image of an anisotropically etched WS<sub>2</sub> flake with initial holes of various shapes. Bottom left: SEM image of etched hexagonal holes in a heterostructure of stacked WS<sub>2</sub> flakes with 30° rotation. Right: schematics (bottom) and the corresponding SEM image (top) of circular holes in monolayer and hexagonal holes in bilayer WS<sub>2</sub> flakes, along with their photoluminescence spectra. Adapted with permission under a Creative Common CC BY License from ref 1195. Copyright 2020 Springer Nature. (d) Coupled cavity-emitter system in hBN, consisting of cavity arrays in silicon substrate (d.i) and suspended photonic crystal cavities in hBN nanobeams (d.ii) and (d.iii). Scale bars in (d.i)-(d.iii) are 10, 1, and 1 μm, respectively. <sup>1201</sup> Adapted with permission from ref 1201. Copyright 2023 ACS. (e) Schematics (top) of a waveguide-coupled LED, consisting of a monolayer WSe<sub>2</sub> between two hBN tunnelling barriers and two monolayer graphene electrodes, and the real-space image (bottom) of its emission ( $V_b = 1.7$  V) overlaid with its shape and intensity distribution.

Figure 32. continued

intensity profile along the central section. L and W denote LED and waveguide, respectively.<sup>1204</sup> Adapted with permission under a Creative Common CC BY License from ref 1204. Copyright 2023 ACS. (f) Confocal (left) and SEM (right) images of a microdisk resonator consisting of a hBN flake covering a silicon nitride ( $\text{Si}_3\text{N}_4$ ) optical cavity.<sup>1208</sup> Adapted with permission under a Creative Common CC BY License from ref 1208. Copyright 2020 De-Gruyter.

plasma-enhanced CVD to overcome TFLN's limits of processing temperature.<sup>1176</sup> Finally, the wet-etching method is also explored for the cost-effective fabrication of smooth surfaces instead of ion-assisted etching. The wet-etching process utilizes mixture of  $\text{H}_2\text{O}_2$  and  $\text{NH}_4\text{OH}$ , and  $\text{H}_2\text{O}$  and results in a quality factor of  $10^7$ .<sup>1177</sup>

Metal electrodes are often integrated into TFLN photonic circuits to exploit the electrooptic, photoelastic, piezoelectric, and ferroelectric effects of LN. While the nanofabrication process for these electrodes is similar to conventional methods, there are some key considerations for developing high-performance TFLN integrated photonic devices. One example is the traveling-wave modulator, capable of achieving modulation speeds exceeding 100 GHz for broadband high-speed electro-optic modulation.<sup>1178</sup> Here, a thick metal layer is crucial for low resistance and minimal microwave signal loss. Additionally, thickness of the bottom oxide layer needs careful selection to match the group velocities of both optical and microwave signals.<sup>1178</sup> Superconducting electrodes have also been explored to further suppress ohmic losses, demonstrating modulators with a half-wavelength voltage as low as 42 mV.<sup>1179</sup> Ferroelectric properties of LN enable poling of TFLN, a process where high voltage pulses change the crystal domains to facilitate nonlinear light interactions through quasi-phase matching, which results in constructive interference in nonlinear interactions despite the inherent phase mismatch of the TFLN waveguide. The most common poling method uses periodic electrodes, resulting in a periodically poled TFLN layer. Figure 31e schematically shows the setup for a periodic poling process. The periodically poled TFLN devices exhibit exceptional nonlinear conversion efficiency for SHG.<sup>1180,1181</sup> With the quasi-phase-matching method, careful dispersion engineering and ultrafast light sources promise to unlock new possibilities in quantum nonlinear optics. However, achieving optimal quasi-phase matching for long waveguides presents a significant challenge.<sup>1184</sup> Highly focused waveguides have considerable dispersion, making the ideal poling period sensitive to geometric parameters like film thickness, etching depth, and waveguide width. The inherent thickness variations caused by the smart-cut process can significantly impact the conversion efficiency. To overcome this hurdle, the concept of adaptive poling has emerged. This approach involves measuring thickness variations and adjusting electrode patterns to achieve optimal quasi-phase matching in long waveguides.<sup>1185</sup>

Additionally, it is worth noting the state of TFLN photonic devices from an industry perspective. Indeed, TFLN nanophotonic devices hold great promise in the market. For example, many startup companies are already shipping diverse products, including different types of TFLN wafers, high-speed electro-optic modulators, and nonlinear photonic products. Like other material platforms in photonic integrated circuits, the foundry services for TFLN devices are also available from several companies. Considering the unique material properties, manufacturing advantages, and various applications across a broad spectrum range TFLN photonic devices have the

potential to show exceptional growth by replacing conventional active and nonlinear optical devices.

This section has discussed the state-of-the-art nanofabrication processes used for TFLN photonic devices. Advancements in nanofabrication have become a key factor in the exceptionally fast growth of TFLN integrated photonics within the field of photonics. We look forward to exciting opportunities for innovations in nanofabrication techniques for TFLN photonic devices. This will lead to the development of disruptive solutions with wide applications in nonlinear optics, quantum photonics, sensing, communications, and analog optical computing.

## 32. 2D MATERIALS

Hossein Alijani and Igor Aharonovich

2D van der Waals materials have emerged as promising candidates for nanophotonics due to their unique excitonic properties, as well as strong and tunable interactions with light.<sup>1186–1189</sup> The wide variety of 2D materials, including graphene, transition-metal dichalcogenides (TMDCs, e.g.,  $\text{WS}_2$ ,  $\text{WSe}_2$ ,  $\text{MoS}_2$ ,  $\text{MoTe}_2$ ), hexagonal boron nitride (hBN), black phosphorus, and MXenes cover the entire electromagnetic spectrum because of their different electronic properties. Benefiting from these optical properties, structural 2D materials have been actively investigated with the development of nanolithography, demonstrating resonant cavities, waveguides, lenses, gratings, and, optical metamaterials and photonic crystals.<sup>1190</sup>

For structural 2D materials, high resolution top-down nanolithography has been extensively used to fabricate micro- and nanoscaled photonic features. The standard nanolithography procedure includes preparing substrates, PR coating, electron-beam exposure using EBL, PR development, and sequent dry or wet etching; optional metal deposition may be added if necessary. These techniques are executed on substrates hosting either CVD-grown or mechanically exfoliated flakes. While the above nanolithography procedure appears standardized, a variety of process parameters, including substrate types, resist (positive or negative), EBL parameters (e.g., electron beam energy and dosage), and etchants (such as gas mixtures), must be carefully selected based on the target 2D material(s) and the desired geometric features.

Specific examples demonstrate that even when creating nanodisk structures to achieve the desired optical responses, the choice of etchant and etching process varies depending on the 2D material(s). For instance, graphene nanodisks, with diameters ranging from 50 to 190 nm, have been fabricated by EBL and oxygen plasma etching to achieve tunability of localized plasmons in graphene.<sup>1191</sup> For the case of  $\text{WS}_2$ , however, nanodisks as high-index dielectric Mie nanoresonators have been patterned with EBL and fabricated using dry-etching with  $\text{CHF}_3$  and Ar.<sup>1192</sup> It was found that the scattering responses of nanodisks could be tuned by changing the radii of the nanodisks.

Top-down nanolithography have been also used for complicated geometries with structural 2D materials, such as

**Table 1.** Summaries of Fabrication Methods for Metaphotonics

	Methods	Advantages	Disadvantages	Applications	Feature size	Related sections
High-resolution nanolithography	Electron beam lithography (EBL)	<ul style="list-style-type: none"> <li>Able to produce photonic structures with various geometries</li> <li>Mask free</li> </ul>	<ul style="list-style-type: none"> <li>Time consuming</li> <li>Low throughput</li> </ul>	Metalens and other nanophotonic structures	Sub 10 nm	2, 4
	Focused ion beam (FIB)	<ul style="list-style-type: none"> <li>Resist free</li> </ul>	<ul style="list-style-type: none"> <li>Time consuming</li> <li>Low throughput</li> </ul>	Nanotip, Nano-Kirigami	Sub 10 nm	5
3D nanofabrication	Electron beam lithography (EBL)	<ul style="list-style-type: none"> <li>Mask free</li> <li>Flexibility to select diverse materials</li> </ul>	<ul style="list-style-type: none"> <li>Feature size limited by the alignment error</li> </ul>	Multiplexed metaholograms, 3D plasmonic ruler	Sub 20 nm	6
	Two-photon lithography	<ul style="list-style-type: none"> <li>Single process</li> <li>Combines high speed and high resolution</li> </ul>	<ul style="list-style-type: none"> <li>Not yet scalable for widespread commercial use</li> </ul>	Chiral metasurfaces, 3D inverse design, waveguides	Sub micron	9
	Aerosol 3D printing	<ul style="list-style-type: none"> <li>Able to fabricate complicated structures</li> </ul>	<ul style="list-style-type: none"> <li>Complicated fabrication</li> </ul>	Plasmonic 3D structures	Sub micron	10
Scalable manufacturing	Glancing angle deposition	<ul style="list-style-type: none"> <li>Able to fabricate complicated structures</li> </ul>	<ul style="list-style-type: none"> <li>Submicron scale structure is challenging</li> </ul>	Chiral nanostructures	~ micron	21
	Origami-inspired nanofabrication	<ul style="list-style-type: none"> <li>Able to fabricate complicated structures</li> </ul>	<ul style="list-style-type: none"> <li>Complicated fabrication</li> </ul>	3D-folded structures	nm-scale	6
	High-speed EBL	<ul style="list-style-type: none"> <li>High-throughput</li> </ul>	<ul style="list-style-type: none"> <li>High cost</li> </ul>	Metalens, Holograms	Sub 10 nm	12
	Nanoimprint lithography (NIL)	<ul style="list-style-type: none"> <li>Does not require secondary operations</li> <li>Low cost</li> </ul>	<ul style="list-style-type: none"> <li>Structures have low refractive index</li> </ul>	Metalens, Holograms	Sub 10 nm	13, 14
	Self-assembly	<ul style="list-style-type: none"> <li>Additional functionalities can be achieved</li> </ul>	<ul style="list-style-type: none"> <li>Structure depends on the template</li> </ul>	Display, Sensing	Sub micro	15–17, 27
	Colloidal lithography (CL)	<ul style="list-style-type: none"> <li>High-throughput</li> </ul>	<ul style="list-style-type: none"> <li>Limited to periodic structures</li> </ul>	Plasmonic color, SERS	Sub 100 nm	22–24
	Direct transfer	<ul style="list-style-type: none"> <li>Easy to fabricate on various substrates</li> <li>Does not require high temperature and pressure</li> </ul>	<ul style="list-style-type: none"> <li>Feature size limited by PDMS stamp</li> </ul>	Wearable device, QLED	~ 500 nm	25, 26
	Atomic layer lithography (ALD)	<ul style="list-style-type: none"> <li>High throughput</li> </ul>	<ul style="list-style-type: none"> <li>Limited to loop shaped structures</li> </ul>	MIM structures	Sub 10 nm	3

truncated cones. For instance, arrays of truncated-cone-shaped nanoresonators have been fabricated out of mechanically exfoliated MoS<sub>2</sub> on a Al<sub>2</sub>O<sub>3</sub> substrate,<sup>1193</sup> Figure 32a (right). These nanoresonators enhance single-beam SHG and third-harmonic generations in a metasurface with high *n*. The fabrication steps include coating the flake with ZEP positive resist and a conductive polymer (for charge dissipation), deposition of an 80 nm-thick Al layer (as the mask for dry-etching), inductive-coupled plasma RIE with SF<sub>6</sub>, CHF<sub>3</sub>, and Ar gas mixture, and removal of the Al layer by a lift-off process.

Using top-down nanolithography, various other structures out of WS<sub>2</sub> have been fabricated, including nanodisks and nanoholes arrays for light harvesting, ring resonators, waveguides, and photonic crystal cavities for low-loss nanophotonics.<sup>1194</sup> We note that achieving uniform coverage of the TMDC flakes on the substrate with PR that has good adhesion presents a primary challenge for fabricating structural 2D materials. To address this challenge, a TI Prime adhesion promoter has been applied before the resist. Alternatively, hexamethyldisilazane (HMDS) can serve as an adhesion promoter; however, it is more susceptible to ambient conditions and might yield less reproducible results.<sup>1194</sup>

Subsequent to EBL and RIE, anisotropic wet etching with a mixture of H<sub>2</sub>O<sub>2</sub> and NH<sub>4</sub>OH in water can be employed to achieve hexagonal nanohole arrays terminated by zigzag edges, applying for metamaterials application in sensing. Figure 32b shows hexagonal holes in a WS<sub>2</sub> flake obtained after 8 min of anisotropically wet etching of circular holes with radii of approximately 1 μm. In wet etching, the initial pattern defines the final structure.<sup>1195</sup> As illustrated in Figure 32c (top left), individual holes with various initial shapes, such as pentagons,

octagons, and ellipsoids, are etched into a WS<sub>2</sub> flake. The same technique has been used to etch a multilayer WS<sub>2</sub> heterostructure consisting of two flakes with 30° relative rotation. Following the rotated flake shapes, the final hexagonal holes are also rotated by 30°, confirming the anisotropic etching even for heterostructures (Figure 32c (bottom left)). Additionally, this method could be used to determine the relative crystallographic orientation of different flakes. Furthermore, dry anisotropic etching with SF<sub>6</sub> has been reported to achieve nm-resolution structures in various 2D materials, such as hexagonal holes/dots and nanowires along the crystallographic orientation of WS<sub>2</sub> and WSe<sub>2</sub>, and arbitrary shapes and orientations in MoS<sub>2</sub> and MoTe<sub>2</sub>.<sup>1196</sup>

The monolayer TMDCs, specifically, have been actively investigated with their interesting excitonic properties and direct bandgap;<sup>1197</sup> however, they might not be as robust as multilayers during nanolithography. Thus, fabrication conditions should be carefully chosen when monolayer TMDCs are used. For the case of monolayer WS<sub>2</sub>, its excitonic properties are preserved during nanolithography processes, specifically during interaction with hydrogen peroxide in wet etching. However, unlike multilayer WS<sub>2</sub>, the circular nanoholes transform into triangular irregularities rather than hexagonal edges, possibly due to substrate surface roughness or different reactivity of monolayer in comparison with multilayer.<sup>1195</sup> Figure 32c (right) shows circular and hexagonal nanoholes in monolayer and bilayer WS<sub>2</sub> flakes, respectively. Both show strong photoluminescence, indicating the preservation of their optical emission during the nanolithography.

hBN is another 2D materials that has unique optical properties, specifically hosting vacancies as quantum sources

for single photon emission in nanophotonics and spin defects used for quantum sensing.<sup>1198,1199</sup> Various nanolithography techniques, including EBL, ion beam etching (IBE), chemically assisted IBE, and RIE have been used to fabricate nanophotonic structures from hBN, such as photonic crystal cavities and bullseye cavities.<sup>1200–1203</sup> Figure 32d shows trench arrays of varying dimensions, on which hBN nanobeam photonic crystal cavities are suspended. This structure gives high quality factors (>2000) across the entire visible spectrum range (from 400 to 850 nm). Dry anisotropic etching with SF<sub>6</sub> can also fabricate arbitrary shapes in hBN with any orientation with less than 5 nm resolution.<sup>1196</sup>

Nanolithography has also been used to fabricate heterostructures of multiple materials. For instance, Figure 32e shows a LED from a monolayer WSe<sub>2</sub> integrated with an hBN waveguide.<sup>1204</sup> This structure was patterned with EBL and etched with SF<sub>6</sub> and Ar.

Another use of nanolithography is to fabricate nanostructures in bulk substrates that are integrated with 2D materials, especially silicon photonic devices.<sup>1205–1207</sup> For example, microdisks from a 112 nm Si<sub>3</sub>N<sub>4</sub> layer on a silicon substrate have been patterned with EBL, and etched by an ICP-RIE recipe using SF<sub>6</sub>, CHF<sub>3</sub> and He, followed by undercutting the silicon substrate with SF<sub>6</sub> to leave the microdisks suspended.<sup>1208</sup> And then, hBN flakes have been transferred onto the microdisks (Figure 32f (left)). Based on the confocal map of the flakes, Figure 32f (right), it was found that strain fields at the folded regions in hBN activated the emitters.

### 33. CONCLUSION

Joohoon Kim and Junsuk Rho

To summarize, this mega-review covers advanced nanofabrication methods for nanophotonics. This review address 5 key trends, elaborated upon through 26 sections: high-resolution nanolithography (Sections 2–6, 19), 3D nanofabrication (Sections 7–11, 20, 21), scalable manufacturing (Sections 12–16, 21–28), and compatible materials (Sections 29–32) for nanophotonics. Table 1 summarizes the overall fabrication methods discussed in this review.

For high-resolution nanolithography, FIB and EBL are introduced. FIB offers high selectivity to nanopattern materials by directly milling through the use of an ion beam, yet its low throughput restricts the patterning area (Section 5). On the other hand, EBL employs electron beams for high-resolution lithography, utilizing a PR as an intermediate medium for patterning nanostructures, which necessitates additional processes like hard mask deposition or etching. Compared to FIB, EBL offers relatively high throughput due to its use of electrons, enabling the fabrication of samples with large areas (Section 2). In addition, methods for achieving single-digit nanometer-scale gaps beyond the resolution of FIB and EBL are also introduced (Sections 3, 4).

Manufacturing 3D nanostructures is more challenging, yet they offer a higher degree of freedom to encompass a wide range of functions (Sections 6–8). For example, freely adjusting the height of each meta-atom on a metasurface enables dispersion engineering<sup>1209</sup> or complex amplitude modulation.<sup>385</sup> To this end, direct laser writing techniques, including two-photon lithography, can be used to fabricate complex 3D structures with submicron resolution (Section 9). However, in this case, the low *n* of the resin poses limitations on confining light when used as the structural material itself. Therefore, aerosol 3D printing, which allows direct printing of

materials, is also utilized to demonstrate 3D nanophotonics devices (Section 10). Moreover, proximity-field nanopatterning and glancing angle deposition allow 3D nanolithography with simple materialization process, large patterning area, and high reproducibility (Sections 11, 21). 3D chiral gold nanoparticles can be synthesized using amino acids and peptides, and utilized for nanophotonics devices (Sections 11, 22).

Scalable manufacturing is essential for the commercialization of nanophotonics devices. Large area, high throughput, and low cost are key property for the scalable nanolithography.<sup>1210–1213</sup> To achieve large area, high-speed electron beam lithography can be used (Section 12). High-speed electron beam lithography maintains similar resolution to conventional electron beam lithography while increasing voltage or current to enhance throughput, enabling the fabrication of centimeter scale metasurfaces. However, direct writing methods still face limitations in scaling up to wafer-scale manufacturing. Therefore, utilizing nanopatterns from high-speed electron beam lithography as photomasks for photolithography enables the repetitive fabrication of the nanopatterns in an array on 8-in. or 12-in. substrates. However, as the resolution increases, the cost also tends to rise. Therefore, in order to replace low-cost conventional optical systems, costs need to decrease significantly. To do so, conventional nanoimprint and roll-to-roll nanoimprint lithography can be used (Sections 13, 14). However, low *n* of printable materials results in low efficiency of nanophotonic devices. To increase effective *n* and device efficiency, nanoparticle-embedded-resin and ALD-based hybrid methods are proposed. It is also possible to directly transfer nanopattern of desired materials through nanotransfer printing (Sections 16, 26, 27). For a consistent nanopatterns with regular periods and structures, CL and self-assembly methods can also be utilized (Sections 15–18, 20–24, 30).

A variety of materials, ranging from metals to dielectrics, have been used as constituent materials in nanophotonics devices (Section 29). Due to differences in optical properties such as permittivity, permeability, and *n* depending on the material, suitable materials are chosen based on the desired wavelength and functionality.<sup>1214,1215</sup> Recently, dielectric materials, including silicon-based ones, are widely used due to their CMOS compatibility and low absorption. In addition to aforementioned materials, there are various intriguing materials available for nanophotonics. Phase change materials, which exhibit changes in optical properties according to stimuli, can be patterned to create active photonics devices (Section 30). Materials with nonlinear characteristics, such as lithium niobate, can be patterned to implement high-speed optical communications or nonlinear optical systems (Section 31). Furthermore, 2D materials with excitonic properties can be patterned to enable photonic lasing or enhance photoluminescence (Section 32).

This mega-review extensively covers the topic of nanolithography for nanophotonics in accordance with five key trends. We aim for our mega-review to inspire curiosity among nanophotonics researchers, encouraging them to blend innovative design with imaginative fabrication techniques. We are genuinely grateful for the contributions made by all authors to this mega-review and hope readers find it enjoyable.

## AUTHOR INFORMATION

### Corresponding Author

**Junsuk Rho** — Department of Mechanical Engineering, Department of Chemical Engineering, and Department of Electrical Engineering, Pohang University of Science and Technology (POSTECH), Pohang 37673, Republic of Korea; POSCO—POSTECH-RIST Convergence Research Center for Flat Optics and Metaphotonics, Pohang 37673, Republic of Korea; [orcid.org/0000-0002-2179-2890](https://orcid.org/0000-0002-2179-2890); Email: [jsrho@postech.ac.kr](mailto:jsrho@postech.ac.kr)

### Authors

**Younghwan Yang** — Department of Mechanical Engineering, Pohang University of Science and Technology (POSTECH), Pohang 37673, Republic of Korea

**Youngsun Jeon** — Department of Mechanical Engineering, Pohang University of Science and Technology (POSTECH), Pohang 37673, Republic of Korea

**Zhaogang Dong** — Institute of Materials Research and Engineering (IMRE), Agency for Science, Technology and Research (A\*STAR), Singapore 138634, Singapore; Department of Materials Science and Engineering, National University of Singapore, Singapore 117575, Singapore; Singapore University of Technology and Design, Singapore 487372, Singapore; [orcid.org/0000-0002-0929-7723](https://orcid.org/0000-0002-0929-7723)

**Joel K. W. Yang** — Singapore University of Technology and Design, Singapore 487372, Singapore; [orcid.org/0000-0003-3301-1040](https://orcid.org/0000-0003-3301-1040)

**Mahsa Haddadi Moghaddam** — Department of Physics, Ulsan National Institute of Science and Technology (UNIST), Ulsan 44919, Republic of Korea

**Dai-Sik Kim** — Department of Physics, Ulsan National Institute of Science and Technology (UNIST), Ulsan 44919, Republic of Korea; [orcid.org/0000-0002-8950-1199](https://orcid.org/0000-0002-8950-1199)

**Dong Kyo Oh** — Department of Mechanical Engineering, Pohang University of Science and Technology (POSTECH), Pohang 37673, Republic of Korea; [orcid.org/0000-0001-7025-6720](https://orcid.org/0000-0001-7025-6720)

**Jihae Lee** — Department of Chemical Engineering, Pohang University of Science and Technology (POSTECH), Pohang 37673, Republic of Korea; [orcid.org/0000-0003-1151-3277](https://orcid.org/0000-0003-1151-3277)

**Mario Hentschel** — fourth Physics Institute and Research Center SCoPE, University of Stuttgart, Stuttgart 70569, Germany

**Harald Giessen** — fourth Physics Institute and Research Center SCoPE, University of Stuttgart, Stuttgart 70569, Germany  
**Dohyun Kang** — Department of Mechanical Engineering, Pohang University of Science and Technology (POSTECH), Pohang 37673, Republic of Korea

**Gyeongtae Kim** — Department of Mechanical Engineering, Pohang University of Science and Technology (POSTECH), Pohang 37673, Republic of Korea

**Takuo Tanaka** — RIKEN Center for Advanced Photonics, Wako 351-0198, Japan; Institute of Post-LED Photonics, Tokushima University, Tokushima 770-8501, Japan; [orcid.org/0000-0001-5714-5401](https://orcid.org/0000-0001-5714-5401)

**Yang Zhao** — Department of Electrical and Computer Engineering, Grainger College of Engineering, University of Illinois Urbana-Champaign, Urbana, Illinois 61801, United States; [orcid.org/0000-0002-0154-3483](https://orcid.org/0000-0002-0154-3483)

**Johannes Bürger** — Chair in Hybrid Nanosystems, NanoInstitute Munich, Ludwig-Maximilians-Universität,

Munich 80539, Germany; [orcid.org/0000-0003-4821-1790](https://orcid.org/0000-0003-4821-1790)

**Stefan A. Maier** — School of Physics and Astronomy, Monash University, Clayton, VIC 3800, Australia; Department of Physics, Imperial College London, London SW72AZ, United Kingdom; [orcid.org/0000-0001-9704-7902](https://orcid.org/0000-0001-9704-7902)

**Haoran Ren** — School of Physics and Astronomy, Monash University, Clayton, VIC 3800, Australia

**Wooik Jung** — Department of Creative Convergence Engineering, Hanbat National University, Daejeon 34158, Republic of Korea

**Mansoo Choi** — Global Frontier Center for Multiscale Energy Systems and Department of Mechanical Engineering, Seoul National University, Seoul 08826, Republic of Korea; [orcid.org/0000-0003-3198-6899](https://orcid.org/0000-0003-3198-6899)

**Gwangmin Bae** — Department of Materials Science and Engineering, Korea University, Seoul 02841, Republic of Korea

**Haomin Chen** — Department of Materials Science and Engineering, Korea University, Seoul 02841, Republic of Korea

**Seokwoo Jeon** — Department of Materials Science and Engineering, Korea University, Seoul 02841, Republic of Korea; [orcid.org/0000-0002-5338-0671](https://orcid.org/0000-0002-5338-0671)

**Jaekyung Kim** — Department of Mechanical Engineering, Pohang University of Science and Technology (POSTECH), Pohang 37673, Republic of Korea

**Eunji Lee** — Department of Chemical Engineering, Pohang University of Science and Technology (POSTECH), Pohang 37673, Republic of Korea

**Hyunjung Kang** — Department of Mechanical Engineering, Pohang University of Science and Technology (POSTECH), Pohang 37673, Republic of Korea

**Yujin Park** — Department of Mechanical Engineering, Pohang University of Science and Technology (POSTECH), Pohang 37673, Republic of Korea

**Dang Du Nguyen** — Department of Biophysics and Department of Intelligent Precision Healthcare Convergence, Sungkyunkwan University, Suwon 16419, Republic of Korea

**Inki Kim** — Department of Biophysics and Department of Intelligent Precision Healthcare Convergence, Sungkyunkwan University, Suwon 16419, Republic of Korea; [orcid.org/0000-0001-8686-6670](https://orcid.org/0000-0001-8686-6670)

**Pablo Cencillo-Abad** — NanoScience Technology Center, University of Central Florida, Florida 32826, United States; [orcid.org/0000-0002-4118-1560](https://orcid.org/0000-0002-4118-1560)

**Debashis Chanda** — NanoScience Technology Center, University of Central Florida, Florida 32826, United States; Department of Physics, University of Central Florida, Florida 32816, United States; The College of Optics and Photonics, University of Central Florida, Orlando, Florida 32816, United States

**Xinxin Jing** — Second Physics Institute, University of Stuttgart, Stuttgart 70569, Germany; Max Planck Institute for Solid State Research, Stuttgart D-70569, Germany

**Na Liu** — Second Physics Institute, University of Stuttgart, Stuttgart 70569, Germany; Max Planck Institute for Solid State Research, Stuttgart D-70569, Germany; [orcid.org/0000-0001-5831-3382](https://orcid.org/0000-0001-5831-3382)

**Irina V. Martynenko** — Faculty of Physics and Center for NanoScience (CeNS) Ludwig-Maximilians-University, Munich 80539, Germany; Skolkovo Institute of Science and

Technology, Moscow 121205, Russia;  [orcid.org/0000-0001-5239-3043](https://orcid.org/0000-0001-5239-3043)

**Tim Liedl** – Faculty of Physics and Center for NanoScience (CeNS) Ludwig-Maximilians-University, Munich 80539, Germany;  [orcid.org/0000-0002-0040-0173](https://orcid.org/0000-0002-0040-0173)

**Yuna Kwak** – Department of Chemistry, Seoul National University, Seoul 08826, Republic of Korea

**Jwa-Min Nam** – Department of Chemistry, Seoul National University, Seoul 08826, Republic of Korea;  [orcid.org/0000-0002-7891-8482](https://orcid.org/0000-0002-7891-8482)

**Sang-Min Park** – Department of Chemistry, Northwestern University, Evanston, Illinois 60208, United States;  [orcid.org/0000-0002-4306-0375](https://orcid.org/0000-0002-4306-0375)

**Teri W. Odom** – Department of Chemistry, Northwestern University, Evanston, Illinois 60208, United States;  [orcid.org/0000-0002-8490-292X](https://orcid.org/0000-0002-8490-292X)

**Hyue-Eun Lee** – Department of Materials Science and Engineering, Seoul National University, Seoul 08826, Republic of Korea

**Ryeong Myeong Kim** – Department of Materials Science and Engineering, Seoul National University, Seoul 08826, Republic of Korea

**Ki Tae Nam** – Department of Materials Science and Engineering, Seoul National University, Seoul 08826, Republic of Korea;  [orcid.org/0000-0001-6353-8877](https://orcid.org/0000-0001-6353-8877)

**Hyunah Kwon** – Max Planck Institute for Medical Research, Heidelberg 69120, Germany; Institute for Molecular Systems Engineering and Advanced Materials, Heidelberg University, Heidelberg 69120, Germany

**Hyeon-Ho Jeong** – School of Electrical Engineering and Computer Science, Gwangju Institute of Science and Technology (GIST), Gwangju 61005, Republic of Korea;  [orcid.org/0000-0002-7029-9592](https://orcid.org/0000-0002-7029-9592)

**Peer Fischer** – Max Planck Institute for Medical Research, Heidelberg 69120, Germany; Institute for Molecular Systems Engineering and Advanced Materials, Heidelberg University, Heidelberg 69120, Germany; Center for Nanomedicine, Institute for Basic Science (IBS), Seoul 03722, Republic of Korea; Department of Nano Biomedical Engineering (NanoBME), Yonsei University, Seoul 03722, Republic of Korea

**Jiwon Yoon** – Department of Chemical and Biomolecular Engineering, Korea Advanced Institute of Science and Technology (KAIST), Daejeon 34141, Republic of Korea

**Shin-Hyun Kim** – Department of Biomedical Engineering, Yonsei University, Wonju 26493, Republic of Korea;  [orcid.org/0000-0003-4095-5779](https://orcid.org/0000-0003-4095-5779)

**Sangmin Shim** – Department of Biomedical Engineering, Yonsei University, Wonju 26493, Republic of Korea

**Dasol Lee** – Department of Biomedical Engineering, Yonsei University, Wonju 26493, Republic of Korea

**Luis A. Pérez** – Institute of Materials Science of Barcelona (ICMAB-CSIC), Bellaterra 08193, Spain;  [orcid.org/0000-0003-2802-4891](https://orcid.org/0000-0003-2802-4891)

**Xiaoyu Qi** – Institute of Materials Science of Barcelona (ICMAB-CSIC), Bellaterra 08193, Spain;  [orcid.org/0009-0008-8677-7879](https://orcid.org/0009-0008-8677-7879)

**Agustin Mihi** – Institute of Materials Science of Barcelona (ICMAB-CSIC), Bellaterra 08193, Spain;  [orcid.org/0000-0003-3821-7881](https://orcid.org/0000-0003-3821-7881)

**Hohyun Keum** – Digital Health Care R&D Department, Korea Institute of Industrial Technology (KITECH),

Cheonan 31056, Republic of Korea;  [orcid.org/0000-0002-7236-7683](https://orcid.org/0000-0002-7236-7683)

**Moonsub Shim** – Department of Materials Science and Engineering, University of Illinois, Urbana-Champaign, Illinois 61801, United States;  [orcid.org/0000-0001-7781-1029](https://orcid.org/0000-0001-7781-1029)

**Seok Kim** – Department of Mechanical Engineering, Pohang University of Science and Technology (POSTECH), Pohang 37673, Republic of Korea;  [orcid.org/0000-0003-3206-8061](https://orcid.org/0000-0003-3206-8061)

**Hanhwi Jang** – Department of Materials Science and Engineering, Korea Advanced Institute of Science and Technology (KAIST), Daejeon 34141, Republic of Korea

**Yeon Sik Jung** – Department of Materials Science and Engineering, Korea Advanced Institute of Science and Technology (KAIST), Daejeon 34141, Republic of Korea;  [orcid.org/0000-0002-7709-8347](https://orcid.org/0000-0002-7709-8347)

**Christian Rossner** – Leibniz-Institut für Polymerforschung Dresden e. V., Dresden 01069, Germany; Faculty of Chemistry and Food Chemistry and Dresden Center for Intelligent Materials (DCIM), Technische Universität Dresden, Dresden 01069, Germany; Department of Polymers, University of Chemistry and Technology Prague, Prague 6 166 28, Czech Republic;  [orcid.org/0000-0002-3428-3542](https://orcid.org/0000-0002-3428-3542)

**Tobias A.F. König** – Leibniz-Institut für Polymerforschung Dresden e. V., Dresden 01069, Germany; Faculty of Chemistry and Food Chemistry, Dresden Center for Intelligent Materials (DCIM), and Center for Advancing Electronics Dresden (cfaed), Technische Universität Dresden, Dresden 01069, Germany;  [orcid.org/0000-0002-8852-8752](https://orcid.org/0000-0002-8852-8752)

**Andreas Fery** – Leibniz-Institut für Polymerforschung Dresden e. V., Dresden 01069, Germany; Center for Advancing Electronics Dresden (cfaed) and Physical Chemistry of Polymeric Materials, Technische Universität Dresden, Dresden 01069, Germany;  [orcid.org/0000-0001-6692-3762](https://orcid.org/0000-0001-6692-3762)

**Zhiwei Li** – Department of Chemistry and International Institute for Nanotechnology, Northwestern University, Evanston, Illinois 60208, United States; Department of Chemistry and Biochemistry, University of Maryland, College Park, Maryland 20742, United States

**Koray Aydin** – International Institute for Nanotechnology and Department of Electrical and Computer Engineering, Northwestern University, Evanston, Illinois 60208, United States;  [orcid.org/0000-0002-3268-2216](https://orcid.org/0000-0002-3268-2216)

**Chad A. Mirkin** – Department of Chemistry, International Institute for Nanotechnology, and Department of Electrical and Computer Engineering, Northwestern University, Evanston, Illinois 60208, United States

**Junhwa Seong** – Department of Mechanical Engineering, Pohang University of Science and Technology (POSTECH), Pohang 37673, Republic of Korea

**Nara Jeon** – Department of Mechanical Engineering, Pohang University of Science and Technology (POSTECH), Pohang 37673, Republic of Korea

**Zhiyun Xu** – Materials Science and Engineering, Massachusetts Institute of Technology, Cambridge, Massachusetts 02139, United States;  [orcid.org/0009-0003-9883-3616](https://orcid.org/0009-0003-9883-3616)

Tian Gu – Materials Science and Engineering, Massachusetts Institute of Technology, Cambridge, Massachusetts 02139, United States;  [orcid.org/0000-0003-3989-6927](https://orcid.org/0000-0003-3989-6927)

Juejun Hu – Materials Science and Engineering, Massachusetts Institute of Technology, Cambridge, Massachusetts 02139, United States;  [orcid.org/0000-0002-7233-3918](https://orcid.org/0000-0002-7233-3918)

Hyounghan Kwon – Center for Quantum Information, Korea Institute of Science and Technology (KIST), Seoul 02792, Republic of Korea; Division of Quantum Information, KIST School, Korea University of Science and Technology, Seoul 02792, Republic of Korea;  [orcid.org/0000-0002-9257-687X](https://orcid.org/0000-0002-9257-687X)

Hojoong Jung – Center for Quantum Information, Korea Institute of Science and Technology (KIST), Seoul 02792, Republic of Korea;  [orcid.org/0000-0001-7059-1713](https://orcid.org/0000-0001-7059-1713)

Hossein Alijani – School of Mathematical and Physical Sciences, Faculty of Science and ARC Centre of Excellence for Transformative Meta-Optical Systems (TMOS), University of Technology Sydney, Ultimo, New South Wales 2007, Australia

Igor Aharonovich – School of Mathematical and Physical Sciences, Faculty of Science and ARC Centre of Excellence for Transformative Meta-Optical Systems (TMOS), University of Technology Sydney, Ultimo, New South Wales 2007, Australia;  [orcid.org/0000-0003-4304-3935](https://orcid.org/0000-0003-4304-3935)

Joohoon Kim – Department of Mechanical Engineering, Pohang University of Science and Technology (POSTECH), Pohang 37673, Republic of Korea;  [orcid.org/0000-0002-0827-1919](https://orcid.org/0000-0002-0827-1919)

Complete contact information is available at:  
<https://pubs.acs.org/10.1021/acsnano.4c10964>

### Author Contributions

J.R. conceived the idea of a mega-review in metasurface fabrications. Y.Y. integrated parts for each section and conducted revision and editing. D.L. and I.K. provided support for the overall manuscript revision, including section structuring and formatting. Section 2: Z.D. and J.K.W.Y. wrote the high-resolution electron beam lithography section. Section 3: M.H.M. and D.S.K. wrote the nanogap lithography section. Section 4: D.K.O., J.L. and J.R. wrote the domino lithography section. Section 5: M.H. and H.G. wrote the high-resolution focused ion beam section. Section 6: G.K., D.K., and J.R. wrote the high-resolution electron beam lithography section. Section 7: T.T. wrote the 3D nano-fabrication section. Section 8: Y.Z. wrote the 3D nano-lithography section. Section 9: J.B., S.A.M., and H.R. wrote the direct laser printing section. Section 10: W.J. and M.C. wrote the aerosol printing section. Section 11: G.B., H.C., and S.J. wrote the proximity-field nanopatterning section. Section 12: J.K., E.L., and J.R. wrote the large-scale electron beam lithography section. Section 13: H.K., Y.P., and J.R. wrote the particle embedded resin section. Section 14: D.D.N. and I.K. wrote the roll-to-roll printing section. Section 15: P.C.-A. and D.C. wrote the physical vapor deposition assisted plasmonic self-assembly section. Section 16: I.V.M. and T.L. wrote the self-assembly section. Section 17: X.J. and N.L. wrote the self-assembly section. Section 18: Y.K. and J.-M. Nam write the nanolithography for plasmonic structure arrays and assemblies section. Section 19: S.-M. P. and T.W.O. wrote the nanolithography for plasmonics section. Section 20: H.-E.L., R.M.K., and K.T.N. wrote the 3D morphology shaping in nanoparticles section. Section 21:

H.K., H.-H. J., and P.F. wrote the glancing angle deposition section. Section 22: J.Y. and S.-H.K. wrote the colloidal lithography section. Section 23: S.S. and D.L. wrote the colloidal lithography for absorber and emitter section. Section 24: L.A.P., X.Q., and A.M. wrote the colloidal self-assembly section. Section 25: H.K., M.S., and S.K. wrote the modulus transfer for quantum dot mechanical patterning section. Section 26: H.J., and Y.S.J. wrote the nanotransfer printing of photonic materials section. Section 27: C.R., T.A.F.K., and A.F. wrote the polymer inorganic self-assembly section. Section 28: Z.L., K.A., and C.A.M. wrote the colloidal crystal engineering with DNA section. Section 29: J.S., N.J., and J.R. wrote the optical materials section. Section 30: Z.X., T.G., and J.H. wrote the phase change materials section. Section 31: H.K. and H.J. wrote the lithium niobite integrated photonics section. Section 32: H.A. and I.A. wrote the 2D materials section. Introduction and Conclusion: J.R., Y.Y., Y.J., and J.K. wrote the introduction, abstract, and conclusion.

### Notes

The authors declare no competing financial interest.

### ACKNOWLEDGMENTS

This work was financially supported by the POSCO–POSTECH-RIST Convergence Research Center program funded by POSCO, the POSTECH-Samsung Semiconductor Research Center (IO201215-08187-01) funded by Samsung Electronics, the National Research Foundation (NRF) grants (RS-2024-00356928, RS-2024-00462912, RS-2024-00416272, RS-2024-00337012, RS-2024-00408286, RS-2024-00440004, RS-2024-00436476, RS-2022-NR066727, RS-2022-NR067559, RS-2022-NR068141, RS-2022-NR068140, RS-2019-NR040065) funded by the Ministry of Science and ICT (MSIT) of the Korean government, and the Korea Planning & Evaluation Institute of Industrial Technology (KEIT) grant (No. 1415179744/20019169, Alchemist project) funded by the Ministry of Trade, Industry and Energy (MOTIE) of the Korean government. Section 2: Z.D. would like to acknowledge the funding support from the Agency for Science, Technology and Research (A\*STAR) under its AME IRG (Project No. A20E5c0093), Career Development Award grant (Project No. C210112019), MTC IRG (Project No. M21K2c0116 and M22K2c0088), the Quantum Engineering Programme 2.0 (Award No. NRF2021-QEP2-03-P09) and DELTA-Q 2.0 (Project No. C230917005). Section 4: D.K.O. acknowledges the NRF Ph.D. fellowship (RS-2024-00414891) funded by the Ministry of Education (MOE) of the Korean government, and the Korea-Switzerland young researchers' exchange program (RS-2024-00445362) funded by the Ministry of Science and ICT (MSIT) of the Korean government. Section 5: This work was supported the Ministerium für Wissenschaft, Forschung und Kunst Baden-Württemberg (RiSC Project "Mie Voids"), Vector Stiftung MINT-Innovationen, and GRK2642 "Towards Graduate Experts in Photonic Quantum Technologies"). Section 6: G.K. acknowledges the Soseon Science fellowship funded by Community Chest of Korea, and the NRF PhD fellowship (RS-2023-00275565) funded by the MOE of the Korean government. Section 9: The authors acknowledge financial support from the Australian Research Council DECRA Fellowship DE220101085 (H.R.) and Australian Research Council Discovery Project DP220102152 (H.R., S.A.M.). S.A.M. additionally acknowledges the Lee-Lucas Chair in

Physics. Section 10: M.C. acknowledges the financial supports from the Nano & Material Technology program (RS-2023-00282896) and Mid-Career Research program (RS-2023-00279529) through the NRF funded by the MSIT of the Korean government. W.J. acknowledges the NRF Sejong Science fellowship (NRF-2022R1C1C2007317) funded by the MSIT of the Korean government, and the NRF Basic Science Research program (NRF-2018R1A6A1A03026005) funded by the MOE of the Korean government. Section 12: E.L. acknowledges the SBS Foundation fellowship, the Presidential Science fellowship funded by the MSIT of the Korean government, and the NRF M.S. fellowship (RS-2024-00464712) funded by the MOE of the Korean government. Section 13: H.K. acknowledges the NRF Ph.D. fellowship (RS-2024-00407755) funded by the MOE of the Korean government. Y.P. acknowledges the Presidential Science fellowships (RS-2024-00460406) funded by the MSIT of the Korean government. Section 15: This work at the University of Central Florida was supported by NSF grant no. ECCS#1920840. Section 17: N.L. acknowledges support from the Max Planck Society (Max Planck Fellow). Section 18: This research was supported by Nano-Material Technology Development Program through the NRF funded by Ministry of Science and ICT (RS-2024-00450828) and the Bio & Medical Technology Development Program of the National Research Foundation (NRF) funded by the Korean government (MSIT) (RS-2024-00440577). Section 18: This research was supported by the NRF grant, funded by Korean government MSIT (NRF-2021R1A2C3010083) and the Bio & Medical Technology Development Program of the NRF funded by the Korean government MSIT (RS-2024-00440577). Section 19: This work was supported by the Office of Naval Research (ONR N00014-21-1-2289). S.-M.P. gratefully acknowledge support from the Ryan Fellowship and the International Institute for Nanotechnology at Northwestern University. Section 20: This research was supported by the Nano & Material Technology Development Program through the National Research Foundation of Korea (NRF) funded by Ministry of Science and ICT (RS-2024-00409405). Section 21: The authors gratefully acknowledge funding from the framework of international cooperation program managed by the National Research Foundation of Korea (NRF-2023K2A9A2A22091303). Section 23: This work was supported by the National Research Foundation of Korea (NRF) grant funded by the Korea government (MSIT) (RS-2025-00556856). Section 27: The authors acknowledge support by GRK 2767 - Projektnummer 451785257 (DFG, German Research Foundation). C.R. acknowledges receipt of a Liebig fellowship (Fonds der Chemischen Industrie). The Volkswagen Foundation financially supported this project through a Freigeist Fellowship to T.K. Section 28: C.A.M. and K.A. acknowledge support from the Air Force Office of Scientific Research under award number FA9550-22-1-0300. Z.L. acknowledges the support from the International Institute for Nanotechnology (IIN) at Northwestern University for the Richard P. Van Duyne Postdoctoral Fellowship. Section 29: N.J. acknowledges the Hyundai Motor Chung Mong-Koo fellowship. Section 32: The authors acknowledge financial support from the Australian Research Council (CE200100010, FT220100053) and the Office of Naval Research Global (N62909-22-1-2028). Conclusion: J.K. acknowledges the Asan Foundation Biomedical Science fellowship, and the Presidential Science fellowship funded by the MSIT of the Korean

government. We acknowledge Doohyuk Han for reviewing and providing comments on the summarized table.

## VOCABULARY

**Electron beam lithography:** A high-resolution nanofabrication technique that uses a focused beam of electrons to directly write patterns on a substrate coated with an electron-sensitive resist.

**Focused ion beam:** A precise fabrication method that employs a focused beam of ions to etch, mill, or deposit materials at the nanoscale for patterning or structural modifications.

**Two-photon lithography:** A 3D nanofabrication technique that uses nonlinear two-photon absorption to polymerize a photoresist at the focal point of a laser beam, enabling complex structures at the nanoscale.

**Nanoimprint:** A lithographic method that mechanically presses a patterned stamp into a resist layer to transfer nanoscale patterns onto a substrate.

**Self-assembly:** A spontaneous process where molecules or nanoparticles organize into ordered structures driven by intermolecular forces and thermodynamics.

**Colloidal lithography:** A patterning technique that uses colloidal particles as masks or templates to create nanostructures through deposition or etching processes.

**Photolithography:** A widely used lithographic process that employs light to transfer geometric patterns from a photomask to a light-sensitive resist on a substrate.

## REFERENCES

- (1) Zhao, H.; Lee, Y.; Han, M.; Sharma, B. K.; Chen, X.; Ahn, J.-H.; Rogers, J. A. Nanofabrication Approaches for Functional Three-Dimensional Architectures. *Nano Today* **2020**, *30*, 100825.
- (2) Sebastian, E. M.; Jain, S. K.; Purohit, R.; Dhakad, S. K.; Rana, R. S. Nanolithography and Its Current Advancements. *Mater. Today Proc.* **2020**, *26*, 2351–2356.
- (3) Oh, D. K.; Kim, Y.; Kim, J.; Kim, I.; Rho, J. Guided Domino Lithography for Uniform Fabrication of Single-Digit-Nanometer Scale Plasmonic Nanoantenna. *Nanophotonics* **2023**, *12* (8), 1435–1441.
- (4) Seong, J.; Jeon, Y.; Yang, Y.; Badloe, T.; Rho, J. Cost-Effective and Environmentally Friendly Mass Manufacturing of Optical Metasurfaces Towards Practical Applications and Commercialization. *Int. J. of Precis. Eng. Manuf.-Green Technol.* **2024**, *11* (2), 685–706.
- (5) Yoon, G.; Tanaka, T.; Zentgraf, T.; Rho, J. Recent Progress on Metasurfaces: Applications and Fabrication. *J. Phys. D Appl. Phys.* **2021**, *54* (38), 383002.
- (6) Koenderink, A. F.; Alù, A.; Polman, A. Nanophotonics: Shrinking Light-Based Technology. *Science* **2015**, *348* (6234), 516–521.
- (7) González-Tudela, A.; Reiserer, A.; García-Ripoll, J. J.; García-Vidal, F. J. Light–Matter Interactions in Quantum Nanophotonic Devices. *Nat. Rev. Phys.* **2024**, *6*, 166–179.
- (8) Pelton, M. Modified Spontaneous Emission in Nanophotonic Structures. *Nat. Photonics* **2015**, *9* (7), 427–435.
- (9) Kim, I.; Martins, R. J.; Jang, J.; Badloe, T.; Khadir, S.; Jung, H.-Y.; Kim, H.; Kim, J.; Genevet, P.; Rho, J. Nanophotonics for Light Detection and Ranging Technology. *Nat. nanotechnol.* **2021**, *16* (5), 508–524.
- (10) Kim, M.; Park, N.; Lee, H. J.; Rho, J. The Latest Trends in Nanophotonics. *Nanophotonics* **2022**, *11* (11), 2389–2392.
- (11) Go, M.; Hong, I.; Lee, D.; Kim, S.; Jang, J.; Kim, K.-W.; Shim, S.; Yong, K.; Rho, J.; Kim, J. K. Ultrabroadband Absorptive Refractory Plasmonics for Photocatalytic Hydrogen Evolution Reactions. *NPG Asia Mater.* **2024**, *16*, 4.
- (12) Kim, W.-G.; Lee, J.-M.; Yang, Y.; Kim, H.; Devaraj, V.; Kim, M.; Jeong, H.; Choi, E.-J.; Yang, J.; Jang, Y.; Badloe, T.; Lee, D.; Rho, J.

- J.; Kim, J. T.; Oh, J.-W. Three-Dimensional Plasmonic Nanocluster-Driven Light–Matter Interaction for Photoluminescence Enhancement and Picomolar-Level Biosensing. *Nano Lett.* **2022**, *22* (12), 4702–4711.
- (13) Bin-Alam, M. S.; Reshef, O.; Mamchur, Y.; Alam, M. Z.; Carlow, G.; Upham, J.; Sullivan, B. T.; Ménard, J.-M.; Huttunen, M. J.; Boyd, R. W.; et al. Ultra-High-Q Resonances in Plasmonic Metasurfaces. *Nat. commun.* **2021**, *12*, 974.
- (14) Song, M.; Feng, L.; Huo, P.; Liu, M.; Huang, C.; Yan, F.; Lu, Y.; Xu, T. Versatile Full-Colour Nanopainting Enabled by a Pixelated Plasmonic Metasurface. *Nat. Nanotechnol.* **2023**, *18*, 71–78.
- (15) Mun, J.; Kim, M.; Yang, Y.; Badloe, T.; Ni, J.; Chen, Y.; Qiu, C.-W.; Rho, J. Electromagnetic Chirality: From Fundamentals to Nontraditional Chiroptical Phenomena. *Light Sci. Appl.* **2020**, *9*, 139.
- (16) Yang, Y.; Kim, M.; Mun, J.; Rho, J. Ultra-Sharp Circular Dichroism Induced by Twisted Layered C4 Oligomers. *Adv. Theory Simul.* **2020**, *3* (3), 1900229.
- (17) Kim, M.; Lee, D.; Kim, T. H.; Yang, Y.; Park, H. J.; Rho, J. Observation of Enhanced Optical Spin Hall Effect in a Vertical Hyperbolic Metamaterial. *ACS Photonics* **2019**, *6* (10), 2530–2536.
- (18) Jung, C.; Yang, Y.; Jang, J.; Badloe, T.; Lee, T.; Mun, J.; Moon, S.-W.; Rho, J. Near-Zero Reflection of All-Dielectric Structural Coloration Enabling Polarization-Sensitive Optical Encryption with Enhanced Switchability. *Nanophotonics* **2020**, *10* (2), 919–926.
- (19) Yang, Y.; Yoon, G.; Park, S.; Namgung, S. D.; Badloe, T.; Nam, K. T.; Rho, J. Revealing Structural Disorder in Hydrogenated Amorphous Silicon for a Low-Loss Photonic Platform at Visible Frequencies. *Adv. Mater.* **2021**, *33* (9), 2005893.
- (20) Wang, Z.; Li, T.; Soman, A.; Mao, D.; Kananen, T.; Gu, T. On-Chip Wavefront Shaping with Dielectric Metasurface. *Nat. commun.* **2019**, *10* (1), 3547.
- (21) Hu, Y.; Li, L.; Wang, Y.; Meng, M.; Jin, L.; Luo, X.; Chen, Y.; Li, X.; Xiao, S.; Wang, H.; Luo, Y.; Qiu, C.-W.; Duan, H. Trichromatic and Tripolarization-Channel Holography with Noninterleaved Dielectric Metasurface. *Nano Lett.* **2020**, *20* (2), 994–1002.
- (22) Ko, B.; Badloe, T.; Yang, Y.; Park, J.; Kim, J.; Jeong, H.; Jung, C.; Rho, J. Tunable Metasurfaces via the Humidity Responsive Swelling of Single-Step Imprinted Polyvinyl Alcohol Nanostructures. *Nat. Commun.* **2022**, *13*, 6256.
- (23) Ko, B.; Kim, J.; Yang, Y.; Badloe, T.; Park, J.; Ko, J. H.; Jeong, M.; Kang, H.; Jung, C.; Song, Y. M.; Rho, J. Humidity-Responsive RGB-Pixels via Swelling of 3D Nanoimprinted Polyvinyl Alcohol. *Adv. Sci.* **2023**, *10* (2), 2204469.
- (24) Ko, B.; Chae, J.-Y.; Badloe, T.; Kim, H.; Kim, S.-J.; Hong, S.-H.; Paik, T.; Rho, J. Multilevel Absorbers via the Integration of Undoped and Tungsten-Doped Multilayered Vanadium Dioxide Thin Films. *ACS Appl. Mater. Interfaces* **2022**, *14* (1), 1404–1412.
- (25) Ren, H.; Fang, X.; Jang, J.; Bürger, J.; Rho, J.; Maier, S. A. Complex-Amplitude Metasurface-Based Orbital Angular Momentum Holography in Momentum Space. *Nat. Nanotechnol.* **2020**, *15* (11), 948–955.
- (26) Zayats, A. V.; Smolyaninov, I. I.; Maradudin, A. A. Nano-Optics of Surface Plasmon Polaritons. *Phys. Rep.* **2005**, *408* (3–4), 131.
- (27) Berini, P.; De Leon, I. Surface Plasmon–Polariton Amplifiers and Lasers. *Nat. photonics* **2012**, *6* (1), 16–24.
- (28) Kim, J.; Seong, J.; Yang, Y.; Moon, S.-W.; Badloe, T.; Rho, J. Tunable Metasurfaces towards Versatile Metalenses and Metaholograms: A Review. *Adv. Photonics* **2022**, *4* (2), 024001–024001.
- (29) Lee, D.; Yang, Y.; Rho, J. Lithography-Free Tailoring of Thin-Film Nanomorphology for Enhanced Real-Time Refractive-Index Sensing with Tunable Resonance Peaks in the Visible Spectrum. *J. Appl. Phys.* **2024**, *135* (9), 093102.
- (30) Jung, C.; Kim, S.-J.; Jang, J.; Ko, J. H.; Kim, D.; Ko, B.; Song, Y. M.; Hong, S.-H.; Rho, J. Disordered-Nanoparticle-Based Etalon for Ultrafast Humidity-Responsive Colorimetric Sensors and Anti-Counterfeiting Displays. *Sci. Adv.* **2022**, *8* (10), eabm8598.
- (31) Badloe, T.; Kim, J.; Kim, I.; Kim, W.-S.; Kim, W. S.; Kim, Y.-K.; Rho, J. Liquid Crystal-Powered Mie Resonators for Electrically Tunable Photorealistic Color Gradients and Dark Blacks. *Light Sci. Appl.* **2022**, *11*, 118.
- (32) Lee, T.; Kim, J.; Koirala, I.; Yang, Y.; Badloe, T.; Jang, J.; Rho, J. Nearly Perfect Transmissive Subtractive Coloration through the Spectral Amplification of Mie Scattering and Lattice Resonance. *ACS Appl. Mater. Interfaces* **2021**, *13* (22), 26299–26307.
- (33) Kim, J.; Kim, Y.; Kim, W.; Oh, D. K.; Kang, D.; Seong, J.; Shin, J. W.; Go, D.; Park, C.; Song, H. 8 "wafer-Scale, Centimeter-Sized, High-Efficiency Metalenses in the Ultraviolet. *Mater. Today* **2024**, *73*, 9.
- (34) Badloe, T.; Kim, Y.; Kim, J.; Park, H.; Barulin, A.; Diep, Y. N.; Cho, H.; Kim, W.-S.; Kim, Y.-K.; Kim, I.; Rho, J. Bright-Field and Edge-Enhanced Imaging Using an Electrically Tunable Dual-Mode Metalens. *ACS Nano* **2023**, *17* (15), 14678–14685.
- (35) Barulin, A.; Kim, Y.; Oh, D. K.; Jang, J.; Park, H.; Rho, J.; Kim, I. Dual-Wavelength Metalens Enables Epi-Fluorescence Detection from Single Molecules. *Nat. Commun.* **2024**, *15*, 26.
- (36) Badloe, T.; Seong, J.; Rho, J. Trichannel Spin-Selective Metalenses. *Nano Lett.* **2023**, *23* (15), 6958–6965.
- (37) Badloe, T.; Kim, I.; Kim, Y.; Kim, J.; Rho, J. Electrically Tunable Bifocal Metalens with Diffraction-Limited Focusing and Imaging at Visible Wavelengths. *Adv. Sci.* **2021**, *8* (21), 2102646.
- (38) Kim, I.; Kim, W.-S.; Kim, K.; Ansari, M. A.; Mehmood, M. Q.; Badloe, T.; Kim, Y.; Gwak, J.; Lee, H.; Kim, Y.-K.; Rho, J. Holographic Metasurface Gas Sensors for Instantaneous Visual Alarms. *Sci. Adv.* **2021**, *7* (15), eabe9943.
- (39) So, S.; Kim, J.; Badloe, T.; Lee, C.; Yang, Y.; Kang, H.; Rho, J. Multicolor and 3D Holography Generated by Inverse-Designed Single-Cell Metasurfaces. *Adv. Mater.* **2023**, *35* (17), 2208520.
- (40) Kim, J.; Jeon, D.; Seong, J.; Badloe, T.; Jeon, N.; Kim, G.; Kim, J.; Baek, S.; Lee, J.-L.; Rho, J. Photonic Encryption Platform via Dual-Band Vectorial Metaholograms in the Ultraviolet and Visible. *ACS Nano* **2022**, *16* (3), 3546–3553.
- (41) Kim, I.; Jang, J.; Kim, G.; Lee, J.; Badloe, T.; Mun, J.; Rho, J. Pixelated Bifunctional Metasurface-Driven Dynamic Vectorial Holographic Color Prints for Photonic Security Platform. *Nat. commun.* **2021**, *12*, 3614.
- (42) Kim, J.; Yang, Y.; Badloe, T.; Kim, I.; Yoon, G.; Rho, J. Geometric and Physical Configurations of Meta-Atoms for Advanced Metasurface Holography. *InfoMat* **2021**, *3* (7), 739–754.
- (43) Kim, J.; Im, J.-H.; So, S.; Choi, Y.; Kang, H.; Lim, B.; Lee, M.; Kim, Y.-K.; Rho, J. Dynamic Hyperspectral Holography Enabled by Inverse-Designed Metasurfaces with Oblique Helicoidal Cholesterics. *Adv. Mater.* **2024**, *36* (24), 2311785.
- (44) Latif, S.; Kim, J.; Khaliq, H. S.; Mahmood, N.; Ansari, M. A.; Chen, X.; Akbar, J.; Badloe, T.; Zubair, M.; Massoud, Y.; Mehmood, M. Q.; Rho, J. Spin-Selective Angular Dispersion Control in Dielectric Metasurfaces for Multichannel Meta-Holographic Displays. *Nano Lett.* **2024**, *24* (2), 708–714.
- (45) Naeem, T.; Kim, J.; Khaliq, H. S.; Seong, J.; Chani, M. T. S.; Tauqueer, T.; Mehmood, M. Q.; Massoud, Y.; Rho, J. Dynamic Chiral Metasurfaces for Broadband Phase-Gradient Holographic Displays. *Adv. Opt. Mater.* **2023**, *11* (5), 2202278.
- (46) Mehmood, M. Q.; Seong, J.; Naveed, M. A.; Kim, J.; Zubair, M.; Riaz, K.; Massoud, Y.; Rho, J. Single-Cell-Driven Tri-Channel Encryption Meta-Displays. *Adv. Sci.* **2022**, *9* (35), 2203962.
- (47) Khaliq, H. S.; Kim, J.; Naeem, T.; Riaz, K.; Badloe, T.; Seong, J.; Akbar, J.; Zubair, M.; Mehmood, M. Q.; Massoud, Y.; Rho, J. Broadband Chiro-Optical Effects for Futuristic Meta-Holographic Displays. *Adv. Opt. Mater.* **2022**, *10* (22), 2201175.
- (48) Javed, I.; Kim, J.; Naveed, M. A.; Oh, D. K.; Jeon, D.; Kim, I.; Zubair, M.; Massoud, Y.; Mehmood, M. Q.; Rho, J. Broad-Band Polarization-Insensitive Metasurface Holography with a Single-Phase Map. *ACS Appl. Mater. Interfaces* **2022**, *14* (31), 36019–36026.
- (49) Naveed, M. A.; Kim, J.; Javed, I.; Ansari, M. A.; Seong, J.; Massoud, Y.; Badloe, T.; Kim, I.; Riaz, K.; Zubair, M.; Mehmood, M. Q.; Rho, J. Novel Spin-Decoupling Strategy in Liquid Crystal-Integrated Metasurfaces for Interactive Metadisplays. *Adv. Opt. Mater.* **2022**, *10* (13), 2200196.

- (50) Lee, C.; Lee, S.; Seong, J.; Park, D. Y.; Rho, J. Inverse-Designed Metasurfaces for Highly Saturated Transmissive Colors. *JOSA B* **2024**, *41* (1), 151–158.
- (51) Jang, J.; Badloe, T.; Yang, Y.; Lee, T.; Mun, J.; Rho, J. Spectral Modulation through the Hybridization of Mie-Scatterers and Quasi-Guided Mode Resonances: Realizing Full and Gradients of Structural Color. *ACS Nano* **2020**, *14* (11), 15317–15326.
- (52) Sun, S.; Zhou, Z.; Zhang, C.; Gao, Y.; Duan, Z.; Xiao, S.; Song, Q. All-Dielectric Full-Color Printing with TiO<sub>2</sub> Metasurfaces. *ACS Nano* **2017**, *11* (5), 4445–4452.
- (53) Kim, I.; Yun, J.; Badloe, T.; Park, H.; Seo, T.; Yang, Y.; Kim, J.; Chung, Y.; Rho, J. Structural Color Switching with a Doped Indium-Gallium-Zinc-Oxide Semiconductor. *Photonics Res.* **2020**, *8* (9), 1409–1415.
- (54) Jeong, H.; Yang, Y.; Cho, H.; Badloe, T.; Kim, I.; Ma, R.-M.; Rho, J. Emerging Advanced Metasurfaces: Alternatives to Conventional Bulk Optical Devices. *Microelectron. Eng.* **2020**, *220*, 111146.
- (55) Jang, J.; Badloe, T.; Sim, Y. C.; Yang, Y.; Mun, J.; Lee, T.; Cho, Y.-H.; Rho, J. Full and Gradient Structural Colouration by Lattice Amplified Gallium Nitride Mie-Resonators. *Nanoscale* **2020**, *12* (41), 21392–21400.
- (56) Kang, H.; Lee, D.; Yang, Y.; Oh, D. K.; Seong, J.; Kim, J.; Jeon, N.; Kang, D.; Rho, J. Emerging Low-Cost, Large-Scale Photonic Platforms with Soft Lithography and Self-Assembly. *Photonics Insights* **2023**, *2* (2), R04.
- (57) Li, Z.; Tian, X.; Qiu, C.-W.; Ho, J. S. Metasurfaces for Bioelectronics and Healthcare. *Nat. Electron.* **2021**, *4* (6), 382–391.
- (58) Shiramanesh, G. K.; Sokhoyan, R.; Wu, P. C.; Atwater, H. A. Electro-Optically Tunable Multifunctional Metasurfaces. *ACS Nano* **2020**, *14* (6), 6912–6920.
- (59) Linh, V. T. N.; Kim, H.; Lee, M.-Y.; Mun, J.; Kim, Y.; Jeong, B.-H.; Park, S.-G.; Kim, D.-H.; Rho, J.; Jung, H. S. 3D Plasmonic Hexaplex Paper Sensor for Label-Free Human Saliva Sensing and Machine Learning-Assisted Early-Stage Lung Cancer Screening. *Biosens. Bioelectron.* **2024**, *244*, 115779.
- (60) Altug, H.; Oh, S.-H.; Maier, S. A.; Homola, J. Advances and Applications of Nanophotonic Biosensors. *Nat. Nanotechnol.* **2022**, *17* (1), 5–16.
- (61) Tseng, M. L.; Jahani, Y.; Leitis, A.; Altug, H. Dielectric Metasurfaces Enabling Advanced Optical Biosensors. *ACS Photonics* **2021**, *8* (1), 47–60.
- (62) Tittl, A.; Leitis, A.; Liu, M.; Yesilkoy, F.; Choi, D.-Y.; Neshev, D. N.; Kivshar, Y. S.; Altug, H. Imaging-Based Molecular Barcoding with Pixelated Dielectric Metasurfaces. *Science* **2018**, *360* (6393), 1105–1109.
- (63) Kim, I.; Kim, H.; Han, S.; Kim, J.; Kim, Y.; Eom, S.; Barulin, A.; Choi, I.; Rho, J.; Lee, L. P. Metasurfaces-Driven Hyperspectral Imaging via Multiplexed Plasmonic Resonance Energy Transfer. *Adv. Mater.* **2023**, *35* (32), 2300229.
- (64) Kim, J.; Kim, H.; Kang, H.; Kim, W.; Chen, Y.; Choi, J.; Lee, H.; Rho, J. A Water-Soluble Label for Food Products Prevents Packaging Waste and Counterfeiting. *Nat. Food* **2024**, *5* (4), 293–300.
- (65) Choi, H.; Kim, J.; Kim, W.; Seong, J.; Park, C.; Choi, M.; Kim, N.; Ha, J.; Qiu, C.-W.; Rho, J.; Lee, H. Realization of High Aspect Ratio Metalenses by Facile Nanoimprint Lithography Using Water-Soluble Stamps. *Photonix* **2023**, *4* (1), 18.
- (66) Kim, W.; Yoon, G.; Kim, J.; Jeong, H.; Kim, Y.; Choi, H.; Badloe, T.; Rho, J.; Lee, H. Thermally-Curable Nanocomposite Printing for the Scalable Manufacturing of Dielectric Metasurfaces. *Microsyst. Nanoeng.* **2022**, *8*, 73.
- (67) Naveed, M. A.; Kim, J.; Ansari, M. A.; Kim, I.; Massoud, Y.; Kim, J.; Oh, D. K.; Badloe, T.; Lee, J.; Kim, Y.; Jeon, D.; Choi, J.; Zubair, M.; Mehmood, M. Q.; Rho, J. Single-Step Fabricable Flexible Metadisplays for Sensitive Chemical/Biomedical Packaging Security and Beyond. *ACS Appl. Mater. Interfaces* **2022**, *14* (27), 31194–31202.
- (68) Panuski, C. L.; Christen, I.; Minkov, M.; Brabec, C. J.; Trajtenberg-Mills, S.; Griffiths, A. D.; McKendry, J. J.; Leake, G. L.; Coleman, D. J.; Tran, C.; et al. A Full Degree-of-Freedom Spatiotemporal Light Modulator. *Nat. Photonics* **2022**, *16* (12), 834–842.
- (69) Chen, Y. Nanofabrication by Electron Beam Lithography and Its Applications: A Review. *Microelectron. Eng.* **2015**, *135*, 57–72.
- (70) Vieu, C.; Carcenac, F.; Pepin, A.; Chen, Y.; Mejias, M.; Lebib, A.; Manin-Ferlazzo, L.; Courraud, L.; Launois, H. Electron Beam Lithography: Resolution Limits and Applications. *Appl. surf. sci.* **2000**, *164* (1–4), 111–117.
- (71) Park, C.; Kim, W.; Kim, Y.; Sung, H.; Park, J.; Song, H.; Kim, J.; Oh, D. K.; Kang, H.; Jeon, N.; Rho, J.; Lee, H. High-Throughput Fabrication of Large-Scale Metaholograms via One-step Printing. *Adv. Opt. Mater.* **2024**, *12*, 2301562.
- (72) Yoon, G.; Kim, K.; Kim, S.-U.; Han, S.; Lee, H.; Rho, J. Printable Nanocomposite Metalens for High-Contrast Near-Infrared Imaging. *ACS Nano* **2021**, *15* (1), 698–706.
- (73) Kim, M.; Oh, D. K.; Kim, J. D.; Jeong, M.; Kim, H.; Jung, C.; Song, J.; Lee, W.; Rho, J.; Ok, J. G. Facile Fabrication of Stretchable Photonic Ag Nanostructures by Soft-Contact Patterning of Ionic Ag Solution Coatings. *Nanophotonics* **2022**, *11* (11), 2693–2700.
- (74) Qiu, T.; Akinoglu, E. M.; Luo, B.; Konarova, M.; Yun, J.; Gentle, I. R.; Wang, L. Nanosphere Lithography: A Versatile Approach to Develop Transparent Conductive Films for Optoelectronic Applications. *Adv. Mater.* **2022**, *34* (19), 2103842.
- (75) Go, M.; Lee, D.; Kim, S.; Jang, J.; Kim, K.-W.; Lee, J.; Shim, S.; Kim, J. K.; Rho, J. Facile Fabrication of Titanium Nitride Nanoring Broad-Band Absorbers in the Visible to Near-Infrared by Shadow Sphere Lithography. *ACS Appl. Mater. Interfaces* **2023**, *15* (2), 3266–3273.
- (76) Mayer, M.; Schnepf, M. J.; König, T. A. F.; Fery, A. Colloidal Self-Assembly Concepts for Plasmonic Metasurfaces. *Adv. Opt. Mater.* **2019**, *7* (1), 1800564.
- (77) Del Pozo, M.; Delaney, C.; Bastiaansen, C. W. M.; Diamond, D.; Schenning, A. P. H. J.; Florea, L. Direct Laser Writing of Four-Dimensional Structural Color Microactuators Using a Photonic Photoresist. *ACS Nano* **2020**, *14* (8), 9832–9839.
- (78) Sakakura, M.; Lei, Y.; Wang, L.; Yu, Y.-H.; Kazansky, P. G. Ultralow-Loss Geometric Phase and Polarization Shaping by Ultrafast Laser Writing in Silica Glass. *Light Sci. Appl.* **2020**, *9*, 15.
- (79) Jung, W.; Jung, Y.-H.; Pikhtsia, P. V.; Feng, J.; Yang, Y.; Kim, M.; Tsai, H.-Y.; Tanaka, T.; Shin, J.; Kim, K.-Y.; et al. Three-Dimensional Nanoprinting via Charged Aerosol Jets. *Nature* **2021**, *592* (7852), 54–59.
- (80) Hines, D. R.; Gu, Y.; Martin, A. A.; Li, P.; Fleischer, J.; Clough-Paez, A.; Stackhouse, G.; Dasgupta, A.; Das, S. Considerations of Aerosol-Jet Printing for the Fabrication of Printed Hybrid Electronic Circuits. *Additive Manufact.* **2021**, *47*, 102325.
- (81) Kim, J.; Seong, J.; Kim, W.; Lee, G.-Y.; Kim, S.; Kim, H.; Moon, S.-W.; Oh, D. K.; Yang, Y.; Park, J.; et al. Scalable Manufacturing of High-Index Atomic Layer–Polymer Hybrid Metasurfaces for Metaphotonics in the Visible. *Nat. Mater.* **2023**, *22* (4), 474–481.
- (82) Moon, S.; Kim, J.; Park, C.; Kim, W.; Yang, Y.; Kim, J.; Lee, S.; Choi, M.; Sung, H.; Park, J.; Song, H.; Lee, H.; Rho, J. Wafer-Scale Manufacturing of Near-Infrared Metalenses. *Laser Photonics Rev.* **2024**, *18*, 2300929.
- (83) Mayer, K. M.; Hafner, J. H. Localized Surface Plasmon Resonance Sensors. *Chem. Rev.* **2011**, *111* (6), 3828–3857.
- (84) Kuznetsov, A. I.; Miroshnichenko, A. E.; Brongersma, M. L.; Kivshar, Y. S.; Luk'yanchuk, B. Optically Resonant Dielectric Nanostructures. *Science* **2016**, *354* (6314), aag2472.
- (85) Miroshnichenko, A. E.; Evlyukhin, A. B.; Yu, Y. F.; Bakker, R. M.; Chipouline, A.; Kuznetsov, A. I.; Luk'yanchuk, B.; Chichkov, B. N.; Kivshar, Y. S. Nonradiating Anapole Modes in Dielectric Nanoparticles. *Nat. Commun.* **2015**, *6* (1), 8069.
- (86) Kaelberer, T.; Fedotov, V. A.; Papasimakis, N.; Tsai, D. P.; Zheludev, N. I. Toroidal Dipolar Response in a Metamaterial. *Science* **2010**, *330* (6010), 1510–1512.
- (87) Jeong, J.; Goldflam, M. D.; Campione, S.; Briscoe, J. L.; Vabishchevich, P. P.; Nogan, J.; Sinclair, M. B.; Luk, T. S.; Brener, I.

- High Quality Factor Toroidal Resonances in Dielectric Metasurfaces. *ACS Photonics* **2020**, *7* (7), 1699–1707.
- (88) Limonov, M. F.; Rybin, M. V.; Poddubny, A. N.; Kivshar, Y. S. Fano Resonances in Photonics. *Nat. Photonics* **2017**, *11* (9), 543–554.
- (89) Dong, Z.; Jin, L.; Rezaei, S. D.; Wang, H.; Chen, Y.; Tjiptoharsono, F.; Ho, J.; Gorelik, S.; Ng, R. J. H.; Ruan, Q.; Qiu, C.-W.; Yang, J. K. W. Schrödinger's Red Pixel by Quasi-Bound-States-in-the-Continuum. *Sci. Adv.* **2022**, *8* (8), eabm4512.
- (90) Ha, S. T.; Fu, Y. H.; Emani, N. K.; Pan, Z.; Bakker, R. M.; Paniagua-Domínguez, R.; Kuznetsov, A. I. Directional Lasing in Resonant Semiconductor Nanoantenna Arrays. *Nat. Nanotechnol.* **2018**, *13* (11), 1042–1047.
- (91) Dong, Z.; Mahfoud, Z.; Paniagua-Domínguez, R.; Wang, H.; Fernández-Domínguez, A. I.; Gorelik, S.; Ha, S. T.; Tjiptoharsono, F.; Kuznetsov, A. I.; Bosman, M.; Yang, J. K. W. Nanoscale Mapping of Optically Inaccessible Bound-States-in-the-Continuum. *Light Sci. Appl.* **2022**, *11*, 20.
- (92) Manfrinato, V. R.; Zhang, L.; Su, D.; Duan, H.; Hobbs, R. G.; Stach, E. A.; Berggren, K. K. Resolution Limits of Electron-Beam Lithography toward the Atomic Scale. *Nano Lett.* **2013**, *13* (4), 1555–1558.
- (93) Yang, J. K. W.; Cord, B.; Duan, H.; Berggren, K. K.; Klingfus, J.; Nam, S.-W.; Kim, K.-B.; Rooks, M. J. Understanding of Hydrogen Silsesquioxane Electron Resist for Sub-5-Nm-Half-Pitch Lithography. *J. Vac. Sci. Technol. B Microelectron. Nanometer Struct.-Process. Meas. Phenom.* **2009**, *27* (6), 2622–2627.
- (94) Hu, W.; Sarveswaran, K.; Lieberman, M.; Bernstein, G. H. Sub-10 nm Electron Beam Lithography Using Cold Development of Poly(Methylmethacrylate). *J. Vac. Sci. Technol. B Microelectron. Nanometer Struct.-Process. Meas. Phenom.* **2004**, *22* (4), 1711–1716.
- (95) Zhang, L.; Dong, Z.; Wang, Y. M.; Liu, Y. J.; Zhang, S.; Yang, J. K. W.; Qiu, C.-W. Dynamically Configurable Hybridization of Plasmon Modes in Nanoring Dimer Arrays. *Nanoscale* **2015**, *7* (28), 12018–12022.
- (96) Yin, T.; Dong, Z.; Jiang, L.; Zhang, L.; Hu, H.; Qiu, C.-W.; Yang, J. K. W.; Shen, Z. X. Anomalous Shift Behaviors in the Photoluminescence of Dolmen-Like Plasmonic Nanostructures. *ACS Photonics* **2016**, *3* (6), 979–984.
- (97) Jiang, L.; Yin, T.; Dong, Z.; Hu, H.; Liao, M.; Allioux, D.; Tan, S. J.; Goh, X. M.; Li, X.; Yang, J. K. W.; Shen, Z. Probing Vertical and Horizontal Plasmonic Resonant States in the Photoluminescence of Gold Nanodisks. *ACS Photonics* **2015**, *2* (8), 1217–1223.
- (98) Jiang, L.; Yin, T.; Dubrovkin, A. M.; Dong, Z.; Chen, Y.; Chen, W.; Yang, J. K. W.; Shen, Z. In-Plane Coherent Control of Plasmon Resonances for Plasmonic Switching and Encoding. *Light Sci. Appl.* **2019**, *8*, 21.
- (99) Ng, R. J. H.; Krishnan, R. V.; Dong, Z.; Ho, J.; Liu, H.; Ruan, Q.; Pey, K. L.; Yang, J. K. W. Micro-Tags for Art: Covert Visible and Infrared Images Using Gap Plasmons in Native Aluminum Oxide. *Opt. Mater. Express* **2019**, *9* (2), 788–801.
- (100) Rezaei, S. D.; Hong Ng, R. J.; Dong, Z.; Ho, J.; Koay, E. H. H.; Ramakrishna, S.; Yang, J. K. W. Wide-Gamut Plasmonic Color Palettes with Constant Subwavelength Resolution. *ACS Nano* **2019**, *13* (3), 3580–3588.
- (101) Sun, S.; Zhou, Z.; Zhang, C.; Gao, Y.; Duan, Z.; Xiao, S.; Song, Q. All-Dielectric Full-Color Printing with TiO<sub>2</sub> Metasurfaces. *ACS Nano* **2017**, *11* (5), 4445–4452.
- (102) Duan, H.; Fernández-Domínguez, A. I.; Bosman, M.; Maier, S. A.; Yang, J. K. W. Nanoplasmonics: Classical down to the Nanometer Scale. *Nano Lett.* **2012**, *12* (3), 1683–1689.
- (103) Lu, L.; Dong, Z.; Tjiptoharsono, F.; Ng, R. J. H.; Wang, H.; Rezaei, S. D.; Wang, Y.; Leong, H. S.; Lim, P. C.; Yang, J. K. W.; Simpson, R. E. Reversible Tuning of Mie Resonances in the Visible Spectrum. *ACS Nano* **2021**, *15* (12), 19722–19732.
- (104) Ho, J.; Fu, Y. H.; Dong, Z.; Paniagua-Domínguez, R.; Koay, E. H. H.; Yu, Y. F.; Valuckas, V.; Kuznetsov, A. I.; Yang, J. K. W. Highly Directive Hybrid Metal–Dielectric Yagi-Uda Nanoantennas. *ACS Nano* **2018**, *12* (8), 8616–8624.
- (105) Jin, L.; Dong, Z.; Mei, S.; Yu, Y. F.; Wei, Z.; Pan, Z.; Rezaei, S. D.; Li, X.; Kuznetsov, A. I.; Kivshar, Y. S.; Yang, J. K. W.; Qiu, C.-W. Noninterleaved Metasurface for (2<sup>0</sup>-1) Spin- and Wavelength-Encoded Holograms. *Nano Lett.* **2018**, *18* (12), 8016–8024.
- (106) Jin, L.; Huang, Y.-W.; Jin, Z.; Devlin, R. C.; Dong, Z.; Mei, S.; Jiang, M.; Chen, W. T.; Wei, Z.; Liu, H.; Teng, J.; Danner, A.; Li, X.; Xiao, S.; Zhang, S.; Yu, C.; Yang, J. K. W.; Capasso, F.; Qiu, C.-W. Dielectric Multi-Momentum Meta-Transformer in the Visible. *Nat. Commun.* **2019**, *10*, 4789.
- (107) Lin, R. J.; Su, V.-C.; Wang, S.; Chen, M. K.; Chung, T. L.; Chen, Y. H.; Kuo, H. Y.; Chen, J.-W.; Chen, J.; Huang, Y.-T.; Wang, J.-H.; Chu, C. H.; Wu, P. C.; Li, T.; Wang, Z.; Zhu, S.; Tsai, D. P. Achromatic Metalens Array for Full-Colour Light-Field Imaging. *Nat. Nanotechnol.* **2019**, *14* (3), 227–231.
- (108) Kruk, S. S.; Wang, L.; Sain, B.; Dong, Z.; Yang, J.; Zentgraf, T.; Kivshar, Y. Asymmetric Parametric Generation of Images with Nonlinear Dielectric Metasurfaces. *Nat. Photonics* **2022**, *16* (8), S61–S65.
- (109) Gu, J.; Liu, Y.; Meng, N.; Sahmuganathan, V.; Tan, S. C.; Sudijono, J.; Tang, J.; Venkatasubramanian, E.; Mallick, A.; Tjiptoharsono, F.; Rezaei, S. D.; Teo, S. L.; Zhu, Q.; Chen, Y.; Lin, M.; Dong, Z.; Loh, K. P. Structural Colors Based on Diamond Metasurface for Information Encryption. *Adv. Opt. Mater.* **2023**, *11* (6), 2202826.
- (110) Liu, H.; Dong, W.; Wang, H.; Lu, L.; Ruan, Q.; Tan, Y. S.; Simpson, R. E.; Yang, J. K. W. Rewritable Color Nanoprints in Antimony Trisulfide Films. *Sci. Adv.* **2020**, *6* (51), eabb7171.
- (111) Abdelraouf, O. A. M.; Anthur, A. P.; Dong, Z.; Liu, H.; Wang, Q.; Krivitsky, L.; Renshaw Wang, X.; Wang, Q. J.; Liu, H. Multistate Tuning of Third Harmonic Generation in Fano-Resonant Hybrid Dielectric Metasurfaces. *Adv. Funct. Mater.* **2021**, *31* (48), 2104627.
- (112) Dong, Z.; Wang, T.; Chi, X.; Ho, J.; Tserkezis, C.; Yap, S. L. K.; Rusydi, A.; Tjiptoharsono, F.; Thian, D.; Mortensen, N. A.; Yang, J. K. W. Ultraviolet Interband Plasmonics With Si Nanostructures. *Nano Lett.* **2019**, *19* (11), 8040–8048.
- (113) Dong, Z.; Ho, J.; Yu, Y. F.; Fu, Y. H.; Paniagua-Domínguez, R.; Wang, S.; Kuznetsov, A. I.; Yang, J. K. W. Printing Beyond sRGB Color Gamut by Mimicking Silicon Nanostructures in Free-Space. *Nano Lett.* **2017**, *17* (12), 7620–7628.
- (114) Paniagua-Domínguez, R.; Yu, Y. F.; Khaidarov, E.; Choi, S.; Leong, V.; Bakker, R. M.; Liang, X.; Fu, Y. H.; Valuckas, V.; Krivitsky, L. A.; Kuznetsov, A. I. A Metalens with a Near-Unity Numerical Aperture. *Nano Lett.* **2018**, *18* (3), 2124–2132.
- (115) Ho, J.; Dong, Z.; Leong, H. S.; Zhang, J.; Tjiptoharsono, F.; Daqiqeh Rezaei, S.; Goh, K. C. H.; Wu, M.; Li, S.; Chee, J.; Wong, C. P. Y.; Kuznetsov, A. I.; Yang, J. K. W. Miniaturizing Color-Sensitive Photodetectors via Hybrid Nanoantennas toward Submicrometer Dimensions. *Sci. Adv.* **2022**, *8* (47), eadd3868.
- (116) Jiang, H.; Fu, J.; Wei, J.; Li, S.; Nie, C.; Sun, F.; Wu, Q. Y. S.; Liu, M.; Dong, Z.; Wei, X.; Gao, W.; Qiu, C.-W. Synergistic-Potential Engineering Enables High-Efficiency Graphene Photodetectors for near- to Mid-Infrared Light. *Nat. Commun.* **2024**, *15*, 1225.
- (117) Rong, K.; Wang, B.; Reuven, A.; Maguid, E.; Cohn, B.; Kleiner, V.; Katzenelson, S.; Koren, E.; Hasman, E. Photonic Rashba Effect from Quantum Emitters Mediated by a Berry-Phase Defective Photonic Crystal. *Nat. Nanotechnol.* **2020**, *15* (11), 927–933.
- (118) Dong, Z.; Gorelik, S.; Paniagua-Domínguez, R.; Yik, J.; Ho, J.; Tjiptoharsono, F.; Lassalle, E.; Rezaei, S. D.; Neo, D. C. J.; Bai, P.; Kuznetsov, A. I.; Yang, J. K. W. Silicon Nanoantenna Mix Arrays for a Trifecta of Quantum Emitter Enhancements. *Nano Lett.* **2021**, *21* (11), 4853–4860.
- (119) Csányi, E.; Liu, Y.; Rezaei, S. D.; Lee, H. Y. L.; Tjiptoharsono, F.; Mahfoud, Z.; Gorelik, S.; Zhao, X.; Lim, L. J.; Zhu, D.; Wu, J.; Goh, K. E. J.; Gao, W.; Tan, Z.-K.; Leggett, G.; Qiu, C.-W.; Dong, Z. Engineering and Controlling Perovskite Emissions via Optical Quasi-Bound-States-in-the-Continuum. *Adv. Funct. Mater.* **2024**, *34* (2), 2309539.
- (120) Zhang, S.; Zhang, J.; Goh, W. P.; Liu, Y.; Tjiptoharsono, F.; Lee, H. Y. L.; Jiang, C.; Ding, J.; Yang, J. K. W.; Dong, Z. Reversible

- Electrical Switching of Nanostructural Color Pixels. *Nanophotonics* **2023**, *12* (8), 1387–1395.
- (121) Duan, H.; Hu, H.; Kumar, K.; Shen, Z.; Yang, J. K. W. Direct and Reliable Patterning of Plasmonic Nanostructures with Sub-10-Nm Gaps. *ACS Nano* **2011**, *5* (9), 7593–7600.
- (122) Duan, H.; Hu, H.; Hui, H. K.; Shen, Z.; Yang, J. K. W. Free-Standing Sub-10 Nm Nanostencils for the Definition of Gaps in Plasmonic Antennas. *Nanotechnology* **2013**, *24* (18), 185301.
- (123) Asbahi, M.; Lim, K. T. P.; Wang, F.; Duan, H.; Thiagarajah, N.; Ng, V.; Yang, J. K. W. Directed Self-Assembly of Densely Packed Gold Nanoparticles. *Langmuir* **2012**, *28* (49), 16782–16787.
- (124) Dong, Z.; Asbahi, M.; Lin, J.; Zhu, D.; Wang, Y. M.; Hippalgaonkar, K.; Chu, H.-S.; Goh, W. P.; Wang, F.; Huang, Z.; Yang, J. K. W. Second-Harmonic Generation from Sub-5 Nm Gaps by Directed Self-Assembly of Nanoparticles onto Template-Stripped Gold Substrates. *Nano Lett.* **2015**, *15* (9), 5976–5981.
- (125) Asbahi, M.; Mahfoud, Z.; Dolmanan, S. B.; Wu, W.; Dong, Z.; Wang, F.; Saifullah, M. S. M.; Tripathy, S.; Chong, K. S. L.; Bosman, M. Ultrasmall Designed Plasmon Resonators by Fused Colloidal Nanopatterning. *ACS Appl. Mater. Interfaces* **2019**, *11* (48), 45207–45213.
- (126) Xu, J.; Dong, Z.; Asbahi, M.; Wu, Y.; Wang, H.; Liang, L.; Ng, R. J. H.; Liu, H.; Vallée, R. A. L.; Yang, J. K. W.; Liu, X. Multiphoton Upconversion Enhanced by Deep Subwavelength Near-Field Confinement. *Nano Lett.* **2021**, *21* (7), 3044–3051.
- (127) Dong, Z.; Bosman, M.; Zhu, D.; Goh, X. M.; Yang, J. K. W. Fabrication of Suspended Metal–Dielectric–Metal Plasmonic Nanostructures. *Nanotechnology* **2014**, *25* (13), 135303.
- (128) Liu, K.; Avouris, Ph.; Buccignano, J.; Martel, R.; Sun, S.; Michl, J. Simple Fabrication Scheme for Sub-10 Nm Electrode Gaps Using Electron-Beam Lithography. *Appl. Phys. Lett.* **2002**, *80* (5), 865–867.
- (129) Lee, H.; Kim, I.; Park, C.; Kang, M.; Choi, J.; Jeong, K.; Mun, J.; Kim, Y.; Park, J.; Raschke, M. B.; Park, H.; Jeong, M. S.; Rho, J.; Park, K. Inducing and Probing Localized Excitons in Atomically Thin Semiconductors via Tip-Enhanced Cavity-Spectroscopy. *Adv. Funct. Mater.* **2021**, *31* (33), 2102893.
- (130) Chen, X.; Park, H.-R.; Pelton, M.; Piao, X.; Lindquist, N. C.; Im, H.; Kim, Y. J.; Ahn, J. S.; Ahn, K. J.; Park, N.; Kim, D.-S.; Oh, S.-H. Atomic Layer Lithography of Wafer-Scale Nanogap Arrays for Extreme Confinement of Electromagnetic Waves. *Nat. Commun.* **2013**, *4*, 2361.
- (131) Du, S.; Yoshida, K.; Zhang, Y.; Hamada, I.; Hirakawa, K. Terahertz Dynamics of Electron–Vibron Coupling in Single Molecules with Tunable Electrostatic Potential. *Nat. Photonics* **2018**, *12* (10), 608–612.
- (132) Das, B.; Yun, H. S.; Park, N.; Jeong, J.; Kim, D.-S. A Transformative Metasurface Based on Zerogap Embedded Template. *Adv. Opt. Mater.* **2021**, *9* (11), 2002164.
- (133) Kim, S.; Das, B.; Ji, K. H.; Moghaddam, M. H.; Chen, C.; Cha, J.; Namgung, S.; Lee, D.; Kim, D.-S. Defining the Zerogap: Cracking along the Photolithographically Defined Au–Cu–Au Lines with Sub-Nanometer Precision. *Nanophotonics* **2023**, *12* (8), 1481–1489.
- (134) Nam, K. H.; Park, I. H.; Ko, S. H. Patterning by Controlled Cracking. *Nature* **2012**, *485* (7397), 221–224.
- (135) Kihm, H. W.; Koo, S. M.; Kim, Q. H.; Bao, K.; Kihm, J. E.; Bak, W. S.; Eah, S. H.; Lienau, C.; Kim, H.; Nordlander, P.; Halas, N. J.; Park, N. K.; Kim, D.-S. Bethe-Hole Polarization Analyser for the Magnetic Vector of Light. *Nat. Commun.* **2011**, *2*, 451.
- (136) Burresi, M.; van Oosten, D.; Kampfrath, T.; Schoenmaker, H.; Heideman, R.; Leinse, A.; Kuipers, L. Probing the Magnetic Field of Light at Optical Frequencies. *Science* **2009**, *326* (5952), 550–553.
- (137) Kalkbrenner, T.; Håkanson, U.; Sandoghdar, V. Tomographic Plasmon Spectroscopy of a Single Gold Nanoparticle. *Nano Lett.* **2004**, *4* (12), 2309–2314.
- (138) Kim, D.; Jeong, J.; Choi, G.; Bahk, Y.-M.; Kang, T.; Lee, D.; Thusa, B.; Kim, D.-S. Giant Field Enhancements in Ultrathin Nanoslots above 1 Terahertz. *ACS Photonics* **2018**, *5* (5), 1885–1890.
- (139) Park, H.-R.; Ahn, K. J.; Han, S.; Bahk, Y.-M.; Park, N.; Kim, D.-S. Colossal Absorption of Molecules Inside Single Terahertz Nanoantennas. *Nano Lett.* **2013**, *13* (4), 1782–1786.
- (140) Park, H.-R.; Namgung, S.; Chen, X.; Lindquist, N. C.; Giannini, V.; Francescato, Y.; Maier, S. A.; Oh, S.-H. Perfect Extinction of Terahertz Waves in Monolayer Graphene over 2-nm-Wide Metallic Apertures. *Adv. Opt. Mater.* **2015**, *3* (5), 667–673.
- (141) Yun, H. S.; Jeong, J.; Kim, D.; Kim, D.-S. Active Thermal Control of 5 nm Gap Terahertz Antennas. *Adv. Opt. Mater.* **2019**, *7* (3), 1800856.
- (142) Lee, K.; Jeong, J.; Bahk, Y.-M.; Rhie, J.; Baek, I.-K.; Lee, B. J.; Kang, Y. H.; Hong, S.; Park, G.-S.; Kim, D.-S. Microwave Funneling through Sub-10 Nm Nanogaps. *ACS Photonics* **2016**, *3* (4), 537–542.
- (143) Bahk, Y.-M.; Kang, B. J.; Kim, Y. S.; Kim, J.-Y.; Kim, W. T.; Kim, T. Y.; Kang, T.; Rhie, J.; Han, S.; Park, C.-H.; Rotermund, F.; Kim, D.-S. Electromagnetic Saturation of Angstrom-Sized Quantum Barriers at Terahertz Frequencies. *Phys. Rev. Lett.* **2015**, *115* (12), 125501.
- (144) Yoo, D.; Nguyen, N.-C.; Martin-Moreno, L.; Mohr, D. A.; Carretero-Palacios, S.; Shaver, J.; Peraire, J.; Ebbesen, T. W.; Oh, S.-H. High-Throughput Fabrication of Resonant Metamaterials with Ultrasmall Coaxial Apertures via Atomic Layer Lithography. *Nano Lett.* **2016**, *16* (3), 2040–2046.
- (145) Beesley, D. J.; Semple, J.; Krishnan Jagadamma, L.; Amassian, A.; McLachlan, M. A.; Anthopoulos, T. D.; deMello, J. C. Sub-15-Nm Patterning of Asymmetric Metal Electrodes and Devices by Adhesion Lithography. *Nat. Commun.* **2014**, *5*, 3933.
- (146) Tripathi, L. N.; Kang, T.; Bahk, Y.-M.; Han, S.; Choi, G.; Rhie, J.; Jeong, J.; Kim, D.-S. Quantum Dots-Nanogap Metamaterials Fabrication by Self-Assembly Lithography and Photoluminescence Studies. *Opt. Express* **2015**, *23* (11), 14937–14945.
- (147) Jeong, J.; Yun, H. S.; Kim, D.; Lee, K. S.; Choi, H.-K.; Kim, Z. H.; Lee, S. W.; Kim, D.-S. High Contrast Detection of Water-Filled Terahertz Nanotrenches. *Adv. Opt. Mater.* **2018**, *6* (21), 1800582.
- (148) Xiang, D.; Jeong, H.; Lee, T.; Mayer, D. Mechanically Controllable Break Junctions for Molecular Electronics. *Adv. Mater.* **2013**, *25* (35), 4845–4867.
- (149) Laible, F.; Braun, K.; Hauler, O.; Eberle, M.; Kern, D. P.; Meixner, A. J.; Fleischer, M. A Flexible Platform for Controlled Optical and Electrical Effects in Tailored Plasmonic Break Junctions. *Nanophotonics* **2020**, *9* (6), 1391–1400.
- (150) Ward, D. R.; Hüser, F.; Pauly, F.; Cuevas, J. C.; Natelson, D. Optical Rectification and Field Enhancement in a Plasmonic Nanogap. *Nat. Nanotechnol.* **2010**, *5* (10), 732–736.
- (151) Kim, D.; Yun, H. S.; Das, B.; Rhie, J.; Vasa, P.; Kim, Y.-I.; Choa, S.-H.; Park, N.; Lee, D.; Bahk, Y.-M.; Kim, D.-S. Topology-Changing Broadband Metamaterials Enabled by Closable Nanotrenches. *Nano Lett.* **2021**, *21* (10), 4202–4208.
- (152) Liu, J.; Guo, H.; Li, M.; Zhang, C.; Chu, Y.; Che, L.; Zhang, Z.; Li, R.; Sun, J.; Lu, Y. Photolithography-Assisted Precise Patterning of Nanocracks for Ultrasensitive Strain Sensors. *J. Mater. Chem. A* **2021**, *9* (7), 4262–4272.
- (153) Moghaddam, M. H.; Dalayoan, D. J. C.; Park, D.; Wang, Z.; Kim, H.; Im, S.; Ji, K.; Kang, D.; Das, B.; Kim, D. S. Lithographically Defined Zerogap Strain Sensors. *ACS Photonics* **2024**, *11* (8), 3239–3249.
- (154) Koh, A. L.; Fernández-Domínguez, A. I.; McComb, D. W.; Maier, S. A.; Yang, J. K. W. High-Resolution Mapping of Electron-Beam-Excited Plasmon Modes in Lithographically Defined Gold Nanostructures. *Nano Lett.* **2011**, *11* (3), 1323–1330.
- (155) Karki, A.; Cincotti, G.; Chen, S.; Stanishev, V.; Darakchieva, V.; Wang, C.; Fahlman, M.; Jonsson, M. P. Electrical Tuning of Plasmonic Conducting Polymer Nanoantennas. *Adv. Mater.* **2022**, *34* (13), 2107172.
- (156) Wang, Q.; Liu, L.; Wang, Y.; Liu, P.; Jiang, H.; Xu, Z.; Ma, Z.; Oren, S.; Chow, E. K. C.; Lu, M.; Dong, L. Tunable Optical Nanoantennas Incorporating Bowtie Nanoantenna Arrays with Stimuli-Responsive Polymer. *Sci. Rep.* **2016**, *5*, 18567.

- (157) Liu, W.; Zou, Q.; Zheng, C.; Jin, C. Metal-Assisted Transfer Strategy for Construction of 2D and 3D Nanostructures on an Elastic Substrate. *ACS Nano* **2019**, *13* (1), 440–448.
- (158) Laible, F.; Gollmer, D. A.; Dickreuter, S.; Kern, D. P.; Fleischer, M. Continuous Reversible Tuning of the Gap Size and Plasmonic Coupling of Bow Tie Nanoantennas on Flexible Substrates. *Nanoscale* **2018**, *10* (31), 14915–14922.
- (159) Liu, F.; Song, B.; Su, G.; Liang, O.; Zhan, P.; Wang, H.; Wu, W.; Xie, Y.; Wang, Z. Sculpting Extreme Electromagnetic Field Enhancement in Free Space for Molecule Sensing. *Small* **2018**, *14* (33), 1801146.
- (160) Song, B.; Yao, Y.; Groenewald, R. E.; Wang, Y.; Liu, H.; Wang, Y.; Li, Y.; Liu, F.; Cronin, S. B.; Schwartzberg, A. M.; Cabrini, S.; Haas, S.; Wu, W. Probing Gap Plasmons Down to Subnanometer Scales Using Collapsible Nanofingers. *ACS Nano* **2017**, *11* (6), 5836–5843.
- (161) Kim, I.; Mun, J.; Hwang, W.; Yang, Y.; Rho, J. Capillary-Force-Induced Collapse Lithography for Controlled Plasmonic Nanogap Structures. *Microsyst. Nanoeng.* **2020**, *6*, 65.
- (162) Kim, I.; Mun, J.; Baek, K. M.; Kim, M.; Hao, C.; Qiu, C.-W.; Jung, Y. S.; Rho, J. Cascade Domino Lithography for Extreme Photon Squeezing. *Mater. Today* **2020**, *39*, 89–97.
- (163) Oh, D. K.; Kim, Y.; Kim, J.; Kim, I.; Rho, J. Guided Domino Lithography for Uniform Fabrication of Single-Digit-Nanometer Scale Plasmonic Nanoantenna. *Nanophotonics* **2023**, *12* (8), 1435–1441.
- (164) Giannuzzi, L. A.; Stevie, F. A. A Review of Focused Ion Beam Milling Techniques for TEM Specimen Preparation. *Micron* **1999**, *30* (3), 197–204.
- (165) Lechner, L.; Biskupek, J.; Kaiser, U. Improved Focused Ion Beam Target Preparation of (S)TEM Specimen—a Method for Obtaining Ultrathin Lamellae. *Microsc. Microanal.* **2012**, *18* (2), 379–384.
- (166) Giannuzzi, L. A., Stevie, F. A. *Introduction to Focused Ion Beams*; Springer, 2004.
- (167) Li, P.; Chen, S.; Dai, H.; Yang, Z.; Chen, Z.; Wang, Y.; Chen, Y.; Peng, W.; Shan, W.; Duan, H. Recent Advances in Focused Ion Beam Nanofabrication for Nanostructures and Devices: Fundamentals and Applications. *Nanoscale* **2021**, *13* (3), 1529–1565.
- (168) Höflich, K.; et al. Roadmap for Focused Ion Beam Technologies. *Applied Physics Reviews* **2023**, *10* (4), No. 041311.
- (169) Moll, P. J. W. Focused Ion Beam Microstructuring of Quantum Matter. *Annu. Rev. Condens. Matter Phys.* **2018**, *9*, 147–162.
- (170) Vesseur, E. J. R.; de Waele, R.; Lezec, H. J.; Atwater, H. A.; García de Abajo, F. J.; Polman, A. Surface Plasmon Polariton Modes in a Single-Crystal Au Nanoresonator Fabricated Using Focused-Ion-Beam Milling. *Appl. Phys. Lett.* **2008**, *92* (8), No. 083110.
- (171) Huang, J.-S.; Callegari, V.; Geisler, P.; Brüning, C.; Kern, J.; Prangsma, J. C.; Wu, X.; Feichtner, T.; Ziegler, J.; Weinmann, P.; Kamp, M.; Forchel, A.; Biagioni, P.; Sennhauser, U.; Hecht, B. Atomically Flat Single-Crystalline Gold Nanostructures for Plasmonic Nanocircuitry. *Nat. Commun.* **2010**, *1*, 150.
- (172) Davis, T. J.; Janoschka, D.; Dreher, P.; Frank, B.; Meyer zu Heringdorf, F.-J.; Giessen, H. Ultrafast Vector Imaging of Plasmonic Skyrmion Dynamics with Deep Subwavelength Resolution. *Science* **2020**, *368* (6489), eaba6415.
- (173) Heath, J.; Taylor, N. *Focused Ion Beam Nanofabrication*; John Wiley & Sons Ltd, Chichester, 2015.
- (174) Farahani, J. N.; Eisler, H.-J.; Pohl, D. W.; Pavius, M.; Flückiger, P.; Gasser, P.; Hecht, B. Bow-Tie Optical Antenna Probes for Single-Emitter Scanning near-Field Optical Microscopy. *Nanotechnology* **2007**, *18* (12), 125506.
- (175) Ropers, C.; Neacsu, C. C.; Elsaesser, T.; Albrecht, M.; Raschke, M. B.; Lienu, C. Grating-Coupling of Surface Plasmons onto Metallic Tips: A Nanoconfined Light Source. *Nano Lett.* **2007**, *7* (9), 2784–2788.
- (176) Li, J.; MacDonald, K. F.; Zheludev, N. I. Optical Control of Nanomechanical Brownian Motion Eigenfrequencies in Metamaterials. *Nano Lett.* **2022**, *22* (11), 4301–4306.
- (177) Karvounis, A.; Gholipour, B.; MacDonald, K. F.; Zheludev, N. I. Giant Electro-Optical Effect through Electrostriction in a Nanomechanical Metamaterial. *Adv. Mater.* **2019**, *31* (1), 1804801.
- (178) Öğüt, B.; Talebi, N.; Vogelgesang, R.; Sigle, W.; Van Aken, P. A. Toroidal Plasmonic Eigenmodes in Oligomer Nanocavities for the Visible. *Nano Lett.* **2012**, *12* (10), 5239–5244.
- (179) Malekian, B.; Xiong, K.; Kang, E. S. H.; Andersson, J.; Emilsson, G.; Rommel, M.; Sannomiya, T.; Jonsson, M. P.; Dahlin, A. Optical Properties of Plasmonic Nanopore Arrays Prepared by Electron Beam and Colloidal Lithography. *Nanoscale Adv.* **2019**, *1* (11), 4282–4289.
- (180) Taleb, M.; Hentschel, M.; Rossnagel, K.; Giessen, H.; Talebi, N. Phase-Locked Photon–Electron Interaction without a Laser. *Nat. Physics* **2023**, *19* (6), 869–876.
- (181) Liu, T.; Ou, J. Y.; MacDonald, K. F.; Zheludev, N. I. Photonic Metamaterial Analogue of a Continuous Time Crystal. *Nat. Physics* **2023**, *19* (7), 986–991.
- (182) Liu, Z.; Du, H.; Li, J.; Lu, L.; Li, Z.-Y.; Fang, N. X. Nano-Kirigami with Giant Optical Chirality. *Sci. Adv.* **2018**, *4* (7), eaat4436.
- (183) Hahn, C.; Hajebifard, A.; Berini, P. Helium Focused Ion Beam Direct Milling of Plasmonic Heptamer-Arranged Nanohole Arrays. *Nanophotonics* **2020**, *9* (2), 393–399.
- (184) Wang, Y.; Abb, M.; Boden, S. a.; Aizpurua, J.; de Groot, C. H.; Muskens, O. L. Ultrafast Nonlinear Control of Progressively Loaded, Single Plasmonic Nanoantennas Fabricated Using Helium Ion Milling. *Nano Lett.* **2013**, *13* (11), 5647–5653.
- (185) Scholder, O.; Jefimovs, K.; Shorubalko, I.; Hafner, C.; Sennhauser, U.; Bona, G. L. Helium Focused Ion Beam Fabricated Plasmonic Antennas with Sub-5 nm Gaps. *Nanotechnology* **2013**, *24*, 395301.
- (186) Kollmann, H.; Piao, X.; Esmann, M.; Becker, S. F.; Hou, D.; Huynh, C.; Kautschor, L. O.; Böske, G.; Vieker, H.; Beyer, A.; Gölzhäuser, A.; Park, N.; Vogelgesang, R.; Silies, M.; Lienau, C. Toward Plasmonics with Nanometer Precision: Nonlinear Optics of Helium-Ion Milled Gold Nanoantennas. *Nano Lett.* **2014**, *14* (8), 4778–4784.
- (187) Deinhart, V.; Kern, L. M.; Kirchhoff, J. N.; Juergensen, S.; Sturm, J.; Krauss, E.; Feichtner, T.; Kovalchuk, S.; Schneider, M.; Enge, D.; Pfau, B.; Hecht, B.; Bolotin, K. I.; Reich, S.; Höflich, K. The Patterning Toolbox FIB-o-Mat: Exploiting the Full Potential of Focused Helium Ions for Nanofabrication. *Beilstein J. Nanotechnol.* **2021**, *12*, 304–318.
- (188) Ristok, S.; Roeder, M.; Thiele, S.; Hentschel, M.; Guenther, T.; Zimmermann, A.; Herkommer, A. M.; Giessen, H. Mass-Producible Micro-Optical Elements by Injection Compression Molding and Focused Ion Beam Structured Titanium Molding Tools. *Opt. Lett.* **2020**, *45* (5), 1184.
- (189) Rajaei, M.; Zeng, J.; Albooyeh, M.; Kamandi, M.; Hanifeh, M.; Capolino, F.; Wickramasinghe, H. K. Giant Circular Dichroism at Visible Frequencies Enabled by Plasmonic Ramp-Shaped Nanostructures. *ACS Photonics* **2019**, *6* (4), 924–931.
- (190) Hentschel, M.; Koshelev, K.; Sterl, F.; Both, S.; Karst, J.; Shamsafar, L.; Weiss, T.; Kivshar, Y.; Giessen, H. Dielectric Mie Voids: Confining Light in Air. *Light Sci. Appl.* **2023**, *12*, 3.
- (191) Horák, M.; Bukvišová, K.; Švarc, V.; Jaskowiec, J.; Křápek, V.; Šíkola, T. Comparative Study of Plasmonic Antennas Fabricated by Electron Beam and Focused Ion Beam Lithography. *Sci. Rep.* **2018**, *8*, 9640.
- (192) Madison, A. C.; Villarrubia, J. S.; Liao, K. T.; Copeland, C. R.; Schumacher, J.; Siebein, K.; Ilic, B. R.; Liddle, J. A.; Stavis, S. M. Unmasking the Resolution–Throughput Tradespace of Focused-Ion-Beam Machining. *Adv. Funct. Mater.* **2022**, *32* (38), 2111840.
- (193) Chen, Y.; Bi, K.; Wang, Q.; Zheng, M.; Liu, Q.; Han, Y.; Yang, J.; Chang, S.; Zhang, G.; Duan, H. Rapid Focused Ion Beam Milling Based Fabrication of Plasmonic Nanoparticles and Assemblies via “Sketch and Peel” Strategy. *ACS Nano* **2016**, *10* (12), 11228–11236.
- (194) Hentschel, M.; Karst, J.; Giessen, H. Tailored Optical Functionality by Combining Electron-Beam and Focused Gold-Ion

- Beam Lithography for Solid and Inverse Coupled Plasmonic Nanostructures. *Adv. Opt. Mater.* **2020**, *8* (19), 2000879.
- (195) Jiang, X.; Gu, Q.; Wang, F.; Lv, J.; Ma, Z.; Si, G. Fabrication of Coaxial Plasmonic Crystals by Focused Ion Beam Milling and Electron-Beam Lithography. *Mater. Lett.* **2013**, *100*, 192–194.
- (196) Dennis, B. S.; Haftel, M. I.; Czaplewski, D. A.; Lopez, D.; Blumberg, G.; Aksyuk, V. A. Compact Nanomechanical Plasmonic Phase Modulators. *Nat. Photonics* **2015**, *9* (4), 267–273.
- (197) She, A.; Zhang, S.; Shian, S.; Clarke, D. R.; Capasso, F. Large Area Metlenses: Design, Characterization, and Mass Manufacturing. *Opt. Express* **2018**, *26* (2), 1573–1585.
- (198) Leitis, A.; Tseng, M. L.; Herpin, A. J.; Kivshar, Y. S.; Altug, H. Wafer-Scale Functional Metasurfaces for Mid-Infrared Photonics and Biosensing. *Adv. Mater.* **2021**, *33* (43), 2102232.
- (199) Wiederrecht, G.; *Handbook of Nanofabrication*, 1st ed.; Academic Press, 2010.
- (200) Groves, T. R.; Pickard, D.; Rafferty, B.; Crosland, N.; Adam, D.; Schubert, G. Maskless Electron Beam Lithography: Prospects, Progress, and Challenges. *Microelectron. Eng.* **2002**, *61*–*62*, 285–293.
- (201) Vieu, C.; Carcenac, F.; Pépin, A.; Chen, Y.; Mejias, M.; Lebib, A.; Manin-Ferlazzo, L.; Couraud, L.; Launois, H. Electron Beam Lithography: Resolution Limits and Applications. *Appl. Surf. Sci.* **2000**, *164* (1–4), 111–117.
- (202) Grigorescu, A. E.; van der Krogt, M. C.; Hagen, C. W.; Kruit, P. 10 Nm Lines and Spaces Written in HSQ<sub>x</sub> Using Electron Beam Lithography. *Microelectron. Eng.* **2007**, *84* (5), 822–824.
- (203) Fischbein, M. D.; Drndić, M. Nanogaps by Direct Lithography for High-Resolution Imaging and Electronic Characterization of Nanostructures. *Appl. Phys. Lett.* **2006**, *88* (6), No. 063116.
- (204) Yoon, G.; Kim, I.; So, S.; Mun, J.; Kim, M.; Rho, J. Fabrication of Three-Dimensional Suspended, Interlayered and Hierarchical Nanostructures by Accuracy-Improved Electron Beam Lithography Overlay. *Sci. Rep.* **2017**, *7*, 6668.
- (205) Liu, N.; Tang, M. L.; Hentschel, M.; Giessen, H.; Alivisatos, A. P. Nanoantenna-Enhanced Gas Sensing in a Single Tailored Nanofocus. *Nat. Mater.* **2011**, *10* (8), 631–636.
- (206) Zhao, R.; Huang, L.; Wang, Y. Recent Advances in Multi-Dimensional Metasurfaces Holographic Technologies. *PhotoniX* **2020**, *1*, 20.
- (207) Kim, I.; Jeong, H.; Kim, J.; Yang, Y.; Lee, D.; Badloe, T.; Kim, G.; Rho, J. Dual-Band Operating Metaholograms with Heterogeneous Meta-Atoms in the Visible and Near-Infrared. *Adv. Opt. Mater.* **2021**, *9* (19), 2100609.
- (208) Kondo, T.; Juodkazis, S.; Mizeikis, V.; Misawa, H.; Matsuo, S. Holographic Lithography of Periodic Two-and Three-Dimensional Microstructures in Photoresist SU-8. *Opt. Express* **2006**, *14* (17), 7943–7953.
- (209) Jang, J.-H.; Ullal, C. K.; Maldovan, M.; Gorishnyy, T.; Kooi, S.; Koh, C.; Thomas, E. L. 3D Micro- and Nanostructures via Interference Lithography. *Adv. Funct. Mater.* **2007**, *17* (16), 3027–3041.
- (210) Ko, B.; Kim, J.; Yang, Y.; Badloe, T.; Park, J.; Ko, J. H.; Jeong, M.; Kang, H.; Jung, C.; Song, Y. M.; Rho, J. Humidity-Responsive RGB-Pixels via Swelling of 3D Nanoimprinted Polyvinyl Alcohol. *Adv. Sci.* **2023**, *10* (2), 2204469.
- (211) Kim, J.; Jeon, D.; Seong, J.; Badloe, T.; Jeon, N.; Kim, G.; Kim, J.; Baek, S.; Lee, J.-L.; Rho, J. Photonic Encryption Platform via Dual-Band Vectorial Metaholograms in the Ultraviolet and Visible. *ACS Nano* **2022**, *16* (3), 3546–3553.
- (212) Liu, N.; Hentschel, M.; Weiss, T.; Alivisatos, A. P.; Giessen, H. Three-Dimensional Plasmon Rulers. *Science* **2011**, *332* (6036), 1407–1410.
- (213) Stolt, T.; Kim, J.; Héron, S.; Vesala, A.; Yang, Y.; Mun, J.; Kim, M.; Huttunen, M. J.; Czaplicki, R.; Kauranen, M.; Rho, J.; Genevet, P. Backward Phase-Matched Second-Harmonic Generation from Stacked Metasurfaces. *Phys. Rev. Lett.* **2021**, *126* (3), No. 033901.
- (214) Chen, S.; Chen, J.; Zhang, X.; Li, Z.-Y.; Li, J. Kirigami/Origami: Unfolding the New Regime of Advanced 3D Micro-fabrication/Nanofabrication with “Folding. *Light Sci. Appl.* **2020**, *9*, 75.
- (215) Cho, J.-H.; Keung, M. D.; Verellen, N.; Lagae, L.; Moshchalkov, V. V.; Van Dorpe, P.; Gracias, D. H. Nanoscale Origami for 3D Optics. *Small* **2011**, *7* (14), 1943–1948.
- (216) Joung, D.; Nemilentsau, A.; Agarwal, K.; Dai, C.; Liu, C.; Su, Q.; Li, J.; Low, T.; Koester, S. J.; Cho, J.-H. Self-Assembled Three-Dimensional Graphene-Based Polyhedrons Inducing Volumetric Light Confinement. *Nano Lett.* **2017**, *17* (3), 1987–1994.
- (217) van Kan, J. A.; Bettoli, A. A.; Watt, F. Three-Dimensional Nanolithography Using Proton Beam Writing. *Appl. Phys. Lett.* **2003**, *83* (8), 1629–1631.
- (218) Burckel, D. B.; Wendt, J. R.; Ten Eyck, G. A.; Ellis, A. R.; Brener, I.; Sinclair, M. B. Fabrication of 3D Metamaterial Resonators Using Self-Aligned Membrane Projection Lithography. *Adv. Mater.* **2010**, *22* (29), 3171–3175.
- (219) Burckel, D. B.; Wendt, J. R.; Ten Eyck, G. A.; Ginn, J. C.; Ellis, A. R.; Brener, I.; Sinclair, M. B. Micrometer-Scale Cubic Unit Cell 3D Metamaterial Layers. *Adv. Mater.* **2010**, *22* (44), 5053–5057.
- (220) Nastaushev, Y. V.; Prinz, V. Y.; Svitashova, S. N. A Technique for Fabricating Au/Ti Micro- and Nanotubes. *Nanotechnol.* **2005**, *16* (6), 908.
- (221) Mei, Y.; Huang, G.; Solovev, A. A.; Ureña, E. B.; Mönch, I.; Ding, F.; Reindl, T.; Fu, R. K. Y.; Chu, P. K.; Schmidt, O. G. Versatile Approach for Integrative and Functionalized Tubes by Strain Engineering of Nanomembranes on Polymers. *Adv. Mater.* **2008**, *20* (21), 4085–4090.
- (222) Chen, C.-C.; Ishikawa, A.; Tang, Y.-H.; Shiao, M.-H.; Tsai, D. P.; Tanaka, T. Uniaxial-Isotropic Metamaterials by Three-Dimensional Split-Ring Resonators. *Adv. Opt. Mater.* **2015**, *3* (1), 44–48.
- (223) Fujikawa, S.; Takaki, R.; Kunitake, T. Fabrication of Arrays of Sub-20-Nm Silica Walls via Photolithography and Solution-Based Molecular Coating. *Langmuir* **2006**, *22* (21), 9057–9061.
- (224) Kubo, W.; Fujikawa, S. Au Double Nanopillars with Nanogap for Plasmonic Sensor. *Nano Lett.* **2011**, *11* (1), 8–15.
- (225) Su, D.-S.; Tsai, D. P.; Yen, T.-J.; Tanaka, T. Ultrasensitive and Selective Gas Sensor Based on a Channel Plasmonic Structure with an Enormous Hot Spot Region. *ACS Sens.* **2019**, *4* (11), 2900–2907.
- (226) Shen, J.; Sun, W.; Liu, D.; Schaus, T.; Yin, P. Three-Dimensional Nanolithography Guided by DNA Modular Epitaxy. *Nat. Mater.* **2021**, *20* (5), 683–690.
- (227) Berganza, E.; Boltynjuk, E.; Mathew, G.; Vallejo, F. F.; Gröger, R.; Scherer, T.; Sekula-Neuner, S.; Hirtz, M. 3D Nanolithography by Means of Lipid Ink Spreading Inhibition. *Small* **2023**, *19* (10), 2205590.
- (228) Yu, X.; Zhang, H.; Oliverio, J. K.; Braun, P. V. Template-Assisted Three-Dimensional Nanolithography via Geometrically Irreversible Processing. *Nano Lett.* **2009**, *9* (12), 4424–4427.
- (229) Zhang, X. A.; Elek, J.; Chang, C.-H. Three-Dimensional Nanolithography Using Light Scattering from Colloidal Particles. *ACS Nano* **2013**, *7* (7), 6212–6218.
- (230) Nagai, H.; Poteet, A.; Zhang, X. A.; Chang, C.-H. Three-Dimensional Colloidal Interference Lithography. *Nanotechnol.* **2017**, *28* (12), 125302.
- (231) Chen, C. C.; Hsiao, C. T.; Sun, S.; Yang, K.-Y.; Wu, P. C.; Chen, W. T.; Tang, Y. H.; Chau, Y.-F.; Plum, E.; Guo, G.-Y.; Zheludev, N. I.; Tsai, D. P. Fabrication of Three Dimensional Split Ring Resonators by Stress-Driven Assembly Method. *Opt. Express* **2012**, *20* (9), 9415–9420.
- (232) Soukoulis, C. M.; Wegener, M. Past Achievements and Future Challenges in the Development of Three-Dimensional Photonic Metamaterials. *Nat. Photonics* **2011**, *5* (9), 523–530.
- (233) Kadic, M.; Milton, G. W.; van Hecke, M.; Wegener, M. 3D Metamaterials. *Nat. Rev. Phys.* **2019**, *1* (3), 198–210.
- (234) Kuznetsov, A. I.; et al. Roadmap for Optical Metasurfaces. *ACS Photonics* **2024**, *11* (3), 816–865.
- (235) Zhao, Y.; Belkin, M. A.; Alù, A. Twisted Optical Metamaterials for Planarized Ultrathin Broadband Circular Polarizers. *Nat. Commun.* **2012**, *3* (1), 870.

- (236) Liu, N.; Guo, H.; Fu, L.; Kaiser, S.; Schweizer, H.; Giessen, H. Three-Dimensional Photonic Metamaterials at Optical Frequencies. *Nat. Mater.* **2008**, *7*, 31–37.
- (237) Kim, A. S.; Goswami, A.; Taghinejad, M.; Cai, W. Phototransformation of Achiral Metasurfaces into Handedness-Selectable Transient Chiral Media. *Proc. Natl. Acad. Sci. U.S.A.* **2024**, *121* (13), e2318713121.
- (238) Zhao, Y.; Shi, J.; Sun, L.; Li, X.; Alù, A. Alignment-Free Three-Dimensional Optical Metamaterials. *Adv. Mater.* **2014**, *26* (9), 1439–1445.
- (239) Saifullah, M. S. M.; Asbahi, M.; Neo, D. C. J.; Mahfoud, Z.; Tan, H. R.; Ha, S. T.; Dwivedi, N.; Dutta, T.; bin Dolmanan, S.; Aabdin, Z.; Bosman, M.; Ganesan, R.; Tripathy, S.; Hasko, D. G.; Valiyaveettil, S. Patterning at the Resolution Limit of Commercial Electron Beam Lithography. *Nano Lett.* **2022**, *22* (18), 7432–7440.
- (240) Zhu, C.; Ekinci, H.; Pan, A.; Cui, B.; Zhu, X. Electron Beam Lithography on Nonplanar and Irregular Surfaces. *Microsyst. Nanoeng.* **2024**, *10*, 1–23.
- (241) Huang, W.; Zhou, J.; Froeter, P. J.; Walsh, K.; Liu, S.; Kraman, M. D.; Li, M.; Michaels, J. A.; Sievers, D. J.; Gong, S.; Li, X. Three-Dimensional Radio-Frequency Transformers Based on a Self-Rolled-up Membrane Platform. *Nat. Electron.* **2018**, *1* (5), 305–313.
- (242) Qin, N.; Qian, Z.-G.; Zhou, C.; Xia, X.-X.; Tao, T. H. 3D Electron-Beam Writing at Sub-15 nm Resolution Using Spider Silk as a Resist. *Nat. Commun.* **2021**, *12*, 5133.
- (243) Wu, S.; Zhao, D.; Qiu, M. 3D Nanoprinting by Electron-Beam with an Ice Resist. *ACS Appl. Mater. Interfaces* **2022**, *14* (1), 1652–1658.
- (244) Tiddi, W.; Elsukova, A.; Le, H. T.; Liu, P.; Beleggia, M.; Han, A. Organic Ice Resists. *Nano Lett.* **2017**, *17* (12), 7886–7891.
- (245) Córdoba, R.; Mailly, D.; Rezaev, R. O.; Smirnova, E. I.; Schmidt, O. G.; Fomin, V. M.; Zeitler, U.; Guillamón, I.; Suderow, H.; De Teresa, J. M. Three-Dimensional Superconducting Nanohelices Grown by He+-Focused-Ion-Beam Direct Writing. *Nano Lett.* **2019**, *19* (12), 8597–8604.
- (246) Klingner, N.; Hlawacek, G.; Mazarov, P.; Pilz, W.; Meyer, F.; Bischoff, L. Imaging and Milling Resolution of Light Ion Beams from Helium Ion Microscopy and FIBs Driven by Liquid Metal Alloy Ion Sources. *Beilstein J. Nanotechnol.* **2020**, *11* (1), 1742–1749.
- (247) He, S.; Tian, R.; Wu, W.; Li, W.-D.; Wang, D. Helium-Ion-Beam Nanofabrication: Extreme Processes and Applications. *Int. J. Extrem. Manuf.* **2021**, *3*, No. 012001.
- (248) Allen, F. I.; Velez, N. R.; Thayer, R. C.; Patel, N. H.; Jones, M. A.; Meyers, G. F.; Minor, A. M. Gallium, Neon and Helium Focused Ion Beam Milling of Thin Films Demonstrated for Polymeric Materials: Study of Implantation Artifacts. *Nanoscale* **2019**, *11* (3), 1403–1409.
- (249) Li, X. Self-Rolled-up Microtube Ring Resonators: A Review of Geometrical and Resonant Properties. *Adv. Opt. Photonics* **2011**, *3* (4), 366–387.
- (250) Jesse, S.; Borisevich, A. Y.; Fowlkes, J. D.; Lupini, A. R.; Rack, P. D.; Unocic, R. R.; Sumpter, B. G.; Kalinin, S. V.; Belianinov, A.; Ovchinnikova, O. S. Directing Matter: Toward Atomic-Scale 3D Nanofabrication. *ACS Nano* **2016**, *10* (6), 5600–5618.
- (251) Utke, I.; Hoffmann, P.; Melngailis, J. Gas-Assisted Focused Electron Beam and Ion Beam Processing and Fabrication. *J. Vac. Sci. Technol. B Microelectron. Nanometer Struct. Process. Meas. Pheno.* **2008**, *26* (4), 1197–1276.
- (252) Lewis, B. B.; Winkler, R.; Sang, X.; Pudasaini, P. R.; Stanford, M. G.; Plank, H.; Unocic, R. R.; Fowlkes, J. D.; Rack, P. D. 3D Nanoprinting via Laser-Assisted Electron Beam Induced Deposition: Growth Kinetics, Enhanced Purity, and Electrical Resistivity. *Beilstein J. Nanotechnol.* **2017**, *8* (1), 801–812.
- (253) Winkler, R.; Fowlkes, J. D.; Rack, P. D.; Plank, H. 3D Nanoprinting via Focused Electron Beams. *J. Appl. Phys.* **2019**, *125* (21), 210901.
- (254) Kawata, S.; Sun, H.-B.; Tanaka, T.; Takada, K. Finer Features for Functional Microdevices. *Nature* **2001**, *412* (6848), 697–698.
- (255) Haske, W.; Chen, V. W.; Hales, J. M.; Dong, W.; Barlow, S.; Marder, S. R.; Perry, J. W. 65 nm Feature Sizes Using Visible Wavelength 3-D Multiphoton Lithography. *Opt. Express* **2007**, *15* (6), 3426–3436.
- (256) Hahn, V.; Messer, T.; Bojanowski, N. M.; Curticean, E. R.; Wacker, I.; Schröder, R. R.; Blasco, E.; Wegener, M. Two-Step Absorption Instead of Two-Photon Absorption in 3D Nanoprinting. *Nat. Photonics* **2021**, *15* (12), 932–938.
- (257) Guan, L.; Cao, C.; Liu, X.; Liu, Q.; Qiu, Y.; Wang, X.; Yang, Z.; Lai, H.; Sun, Q.; Ding, C.; Zhu, D.; Kuang, C.; Liu, X. Light and Matter Co-Confining Multi-Photon Lithography. *Nat. Commun.* **2024**, *15*, 2387.
- (258) Chen, Y.-S.; Tal, A.; Torrance, D. B.; Kuebler, S. M. Fabrication and Characterization of Three-Dimensional Silver-Coated Polymeric Microstructures. *Adv. Funct. Mater.* **2006**, *16* (13), 1739–1744.
- (259) Rothemund, P. W. K. Folding DNA to Create Nanoscale Shapes and Patterns. *Nature* **2006**, *440* (7082), 297–302.
- (260) Xin, L.; Duan, X.; Liu, N. Dimerization and Oligomerization of DNA-Assembled Building Blocks for Controlled Multi-Motion in High-Order Architectures. *Nat. Commun.* **2021**, *12*, 3207.
- (261) Maruo, S.; Nakamura, O.; Kawata, S. Three-Dimensional Microfabrication with Two-Photon-Absorbed Photopolymerization. *Opt. Lett.* **1997**, *22* (2), 132–134.
- (262) Marschner, D. E.; Pagliano, S.; Huang, P.-H.; Niklaus, F. A Methodology for Two-Photon Polymerization Micro 3D Printing of Objects with Long Overhanging Structures. *Additive Manufact.* **2023**, *66*, 103474.
- (263) Hermatschweiler, M. Nanoscribe whitepapers: Gain a deeper understanding of microfabrication technologies. <https://www.nanoscribe.com/en/whitepaper/> (accessed 2024-05-24).
- (264) Mayer, F.; Richter, S.; Westhauser, J.; Blasco, E.; Barber-Kowollik, C.; Wegener, M. Multimaterial 3D Laser Microprinting Using an Integrated Microfluidic System. *Sci. Adv.* **2019**, *5* (2), eaau9160.
- (265) LaFratta, C. N.; Fourkas, J. T.; Baldacchini, T.; Farrer, R. A. Multiphoton Fabrication. *Angew. Chem. Inter. Ed.* **2007**, *46* (33), 6238–6258.
- (266) Tan, D.; Li, Y.; Qi, F.; Yang, H.; Gong, Q.; Dong, X.; Duan, X. Reduction in Feature Size of Two-Photon Polymerization Using SCR500. *Appl. Phys. Lett.* **2007**, *90* (7), No. 071106.
- (267) Fischer, J.; Wegener, M. Three-Dimensional Optical Laser Lithography beyond the Diffraction Limit. *Laser Photonics Rev.* **2013**, *7* (1), 22–44.
- (268) NanoGuide. <https://support.nanoscribe.com/hc/en-gb> (accessed 2024-05-24).
- (269) Hahn, V.; Mayer, F.; Thiel, M.; Wegener, M. 3-D Laser Nanoprinting. *Opt. Photonics News* **2019**, *30* (10), 28–35.
- (270) Fischer, J.; Wegener, M. Three-Dimensional Direct Laser Writing Inspired by Stimulated-Emission-Depletion Microscopy [Invited]. *Opt. Mater. Express* **2011**, *1* (4), 614–624.
- (271) Liu, Y.; Wang, H.; Ho, J.; Ng, R. C.; Ng, R. J. H.; Hall-Chen, V. H.; Koay, E. H. H.; Dong, Z.; Liu, H.; Qiu, C.-W.; Greer, J. R.; Yang, J. K. W. Structural Color Three-Dimensional Printing by Shrinking Photonic Crystals. *Nat. Commun.* **2019**, *10* (1), 4340.
- (272) Kiefer, P.; Hahn, V.; Kalt, S.; Sun, Q.; Eggeler, Y. M.; Wegener, M. A Multi-Photon ( $7 \times 7$ )-Focus 3D Laser Printer Based on a 3D-Printed Diffractive Optical Element and a 3D-Printed Multi-Lens Array. *Light Adv. Manufact.* **2024**, *4* (1), 28–41.
- (273) Purtov, J.; Rogin, P.; Verch, A.; Johansen, V. E.; Hensel, R. Nanopillar Diffraction Gratings by Two-Photon Lithography. *Nanomaterials* **2019**, *9* (10), 1495.
- (274) Gao, H.; Chen, G. F. R.; Xing, P.; Choi, J. W.; Low, H. Y.; Tan, D. T. H. High-Resolution 3D Printed Photonic Waveguide Devices. *Adv. Opt. Mater.* **2020**, *8* (18), 2000613.
- (275) Gansel, J. K.; Thiel, M.; Rill, M. S.; Decker, M.; Bade, K.; Saile, V.; von Freymann, G.; Linden, S.; Wegener, M. Gold Helix Photonic Metamaterial as Broadband Circular Polarizer. *Science* **2009**, *325* (5947), 1513–1515.

- (276) Plum, E.; Fedotov, V. A.; Zheludev, N. I. Extrinsic Electromagnetic Chirality in Metamaterials. *J. Opt. A: Pure Appl. Opt.* **2009**, *11* (7), No. 074009.
- (277) Frenzel, T.; Kadic, M.; Wegener, M. Three-Dimensional Mechanical Metamaterials with a Twist. *Science* **2017**, *358* (6366), 1072–1074.
- (278) Wang, C.; Wang, C. Chirality-Reversed Bidirectional High-Efficiency Dichroic Metalens Based on Hybrid Helical Surfaces. *Laser Photonics Rev.* **2022**, *16* (12), 2200346.
- (279) Zöttl, A.; Tesser, F.; Matsunaga, D.; Laurent, J.; du Roure, O.; Lindner, A. Asymmetric Bistability of Chiral Particle Orientation in Viscous Shear Flows. *Proc. Natl. Acad. Sci. U.S.A.* **2023**, *120* (45), e2310939120.
- (280) von Freymann, G.; Ledermann, A.; Thiel, M.; Staude, I.; Essig, S.; Busch, K.; Wegener, M. Three-Dimensional Nanostructures for Photonics. *Adv. Funct. Mater.* **2010**, *20* (7), 1038–1052.
- (281) Deubel, M.; von Freymann, G.; Wegener, M.; Pereira, S.; Busch, K.; Soukoulis, C. M. Direct Laser Writing of Three-Dimensional Photonic-Crystal Templates for Telecommunications. *Nat. Mater.* **2004**, *3* (7), 444–447.
- (282) Melnikov, A.; Köble, S.; Schweiger, S.; Chiang, Y. K.; Marburg, S.; Powell, D. A. Microacoustic Metagratings at Ultra-High Frequencies Fabricated by Two-Photon Lithography. *Adv. Sci.* **2022**, *9* (20), 2200990.
- (283) Kühner, L.; Wendisch, F. J.; Antonov, A. A.; Bürger, J.; Hüttenhofer, L.; de S. Menezes, L.; Maier, S. A.; Gorkunov, M. V.; Kivshar, Y.; Tittl, A. Unlocking the Out-of-Plane Dimension for Photonic Bound States in the Continuum to Achieve Maximum Optical Chirality. *Light Sci. Appl.* **2023**, *12*, 250.
- (284) Balli, F.; Sultan, M. A.; Ozdemir, A.; Hastings, J. T. An Ultrabroadband 3D Achromatic Metalens. *Nanophotonics* **2021**, *10* (4), 1259–1264.
- (285) Sun, T.; Yang, X.; Xu, F.; Wang, C. Single Chip Simultaneous Chiral and Achiral Imaging Based on High Efficiency 3D Plasmonic Metalens. *Nanophotonics* **2023**, *12* (16), 3243–3255.
- (286) Li, C.; Wieduwilt, T.; Wendisch, F. J.; Márquez, A.; Menezes, L. de S.; Maier, S. A.; Schmidt, M. A.; Ren, H. Metafiber Transforming Arbitrarily Structured Light. *Nat. Commun.* **2023**, *14*, 7222.
- (287) Aigner, A.; Tittl, A.; Wang, J.; Weber, T.; Kivshar, Y.; Maier, S. A.; Ren, H. Plasmonic Bound States in the Continuum to Tailor Light-Matter Coupling. *Sci. Adv.* **2022**, *8* (49), eadd4816.
- (288) Roberts, G.; Ballew, C.; Zheng, T.; Garcia, J. C.; Camayd-Muñoz, S.; Hon, P. W. C.; Faraon, A. 3D-Patterned Inverse-Designed Mid-Infrared Metaoptics. *Nat. Commun.* **2023**, *14*, 2768.
- (289) Dinc, N. U.; Lim, J.; Kakkava, E.; Moser, C.; Psaltis, D. Computer Generated Optical Volume Elements by Additive Manufacturing. *Nanophotonics* **2020**, *9* (13), 4173–4181.
- (290) Hadibrata, W.; Wei, H.; Krishnaswamy, S.; Aydin, K. Inverse Design and 3D Printing of a Metalens on an Optical Fiber Tip for Direct Laser Lithography. *Nano Lett.* **2021**, *21* (6), 2422–2428.
- (291) Gissibl, T.; Thiele, S.; Herkommer, A.; Giessen, H. Two-Photon Direct Laser Writing of Ultracompat Multi-Lens Objectives. *Nat. Photonics* **2016**, *10* (8), 554–560.
- (292) Balli, F.; Sultan, M.; Lami, S. K.; Hastings, J. T. A Hybrid Achromatic Metalens. *Nat. Commun.* **2020**, *11*, 3892.
- (293) Liang, H.; Lin, Q.; Xie, X.; Sun, Q.; Wang, Y.; Zhou, L.; Liu, L.; Yu, X.; Zhou, J.; Krauss, T. F.; Li, J. Ultrahigh Numerical Aperture Metalens at Visible Wavelengths. *Nano Lett.* **2018**, *18* (7), 4460–4466.
- (294) Dinc, N. U.; Psaltis, D.; Brunner, D. Optical neural networks: The 3D connection. *Photoniques* **2020**, *104*, 34–38.
- (295) McMahon, P. L. The Physics of Optical Computing. *Nat. Rev. Phys.* **2023**, *5* (12), 717–734.
- (296) Grabulosa, A.; Moughames, J.; Porte, X.; Kadic, M.; Brunner, D. Additive 3D Photonic Integration That Is CMOS Compatible. *Nanotechnology* **2023**, *34* (32), 322002.
- (297) Goi, E.; Schoenhardt, S.; Gu, M. Direct Retrieval of Zernike-Based Pupil Functions Using Integrated Diffractive Deep Neural Networks. *Nat. Commun.* **2022**, *13*, 7531.
- (298) Bürger, J.; Kim, J.; Jang, B.; Gargiulo, J.; Schmidt, M. A.; Maier, S. A. Ultrahigh-Aspect-Ratio Light Cages: Fabrication Limits and Tolerances of Free-Standing 3D Nanoprinted Waveguides. *Opt. Mater. Express* **2021**, *11* (4), 1046–1057.
- (299) Bürger, J.; Schalles, V.; Kim, J.; Jang, B.; Zeisberger, M.; Gargiulo, J.; de S. Menezes, L.; Schmidt, M. A.; Maier, S. A. 3D-Nanoprinted Antiresonant Hollow-Core Microgap Waveguide: An on-Chip Platform for Integrated Photonic Devices and Sensors. *ACS Photonics* **2022**, *9* (9), 3012–3024.
- (300) Kim, J.; Bürger, J.; Jang, B.; Zeisberger, M.; Gargiulo, J.; Menezes, L. de S.; Maier, S. A.; Schmidt, M. A. 3D-Nanoprinted on-Chip Antiresonant Waveguide with Hollow Core and Microgaps for Integrated Optofluidic Spectroscopy. *Opt. Express* **2023**, *31* (2), 2833–2845.
- (301) Bürger, J.; Kim, J.; Weiss, T.; Maier, S. A.; Schmidt, M. A. On-Chip Twisted Hollow-Core Light Cages: Enhancing Planar Photonics with 3D Nanoprinting. *arXiv*, **2024**, 2409.07602. DOI: 10.48550/arXiv.2409.07602 (accessed Sep 11, 2025).
- (302) Roth, P.; Chen, Y.; Günecli, M. C.; Beravat, R.; Edavalath, N. N.; Frozs, M. H.; Ahmed, G.; Wong, G. K. L.; Russell, P. S. J. Strong Circular Dichroism for the HE<sub>11</sub> Mode in Twisted Single-Ring Hollow-Core Photonic Crystal Fiber. *Optica* **2018**, *5* (10), 1315–1321.
- (303) Fendler, C.; Denker, C.; Harberts, J.; Bayat, P.; Zierold, R.; Loers, G.; Münzenberg, M.; Blick, R. H. Microcaffolds by Direct Laser Writing for Neurite Guidance Leading to Tailor-Made Neuronal Networks. *Adv. Biosys.* **2019**, *3* (5), 1800329.
- (304) Jayne, R. K.; Karakan, M. Ç.; Zhang, K.; Pierce, N.; Michas, C.; Bishop, D. J.; Chen, C. S.; Ekinci, K. L.; White, A. E. Direct Laser Writing for Cardiac Tissue Engineering: A Microfluidic Heart on a Chip with Integrated Transducers. *Lab Chip* **2021**, *21* (9), 1724–1737.
- (305) Balmert, S. C.; Carey, C. D.; Falo, G. D.; Sethi, S. K.; Erdos, G.; Korkmaz, E.; Falo, L. D. Dissolving Undercut Microneedle Arrays for Multicomponent Cutaneous Vaccination. *J. Controlled Release* **2020**, *317*, 336–346.
- (306) Plidschun, M.; Zeisberger, M.; Kim, J.; Wieduwilt, T.; Schmidt, M. A. Fiber-Based 3D Nano-Printed Holography with Individually Phase-Engineered Remote Points. *Sci. Rep.* **2022**, *12*, 20920.
- (307) Gissibl, T.; Thiele, S.; Herkommer, A.; Giessen, H. Sub-Micrometre Accurate Free-Form Optics by Three-Dimensional Printing on Single-Mode Fibres. *Nat. Commun.* **2016**, *7*, 11763.
- (308) Li, J.; Fejes, P.; Lorenser, D.; Quirk, B. C.; Noble, P. B.; Kirk, R. W.; Orth, A.; Wood, F. M.; Gibson, B. C.; Sampson, D. D.; McLaughlin, R. A. Two-Photon Polymerisation 3D Printed Freeform Micro-Optics for Optical Coherence Tomography Fibre Probes. *Sci. Rep.* **2018**, *8*, 14789.
- (309) Blaicher, M.; Billah, M. R.; Kemal, J.; Hoose, T.; Marin-Palomo, P.; Hofmann, A.; Kutuvantavida, Y.; Kieninger, C.; Dietrich, P.-I.; Lauermann, M.; Wolf, S.; Troppenz, U.; Moehrle, M.; Merget, F.; Skacel, S.; Witzenz, J.; Randel, S.; Freude, W.; Koos, C. Hybrid Multi-Chip Assembly of Optical Communication Engines by in Situ 3D Nano-Lithography. *Light Sci. Appl.* **2020**, *9*, 71.
- (310) Lindenmann, N.; Balthasar, G.; Hillerkuss, D.; Schmogrow, R.; Jordan, M.; Leuthold, J.; Freude, W.; Koos, C. Photonic Wire Bonding: A Novel Concept for Chip-Scale Interconnects. *Opt. Express* **2012**, *20* (16), 17667–17677.
- (311) Schumann, M.; Bückmann, T.; Gruhler, N.; Wegener, M.; Pernice, W. Hybrid 2D–3D Optical Devices for Integrated Optics by Direct Laser Writing. *Light Sci. Appl.* **2014**, *3* (6), e175–e175.
- (312) Guo, R.; Xiao, S.; Zhai, X.; Li, J.; Xia, A.; Huang, W. Micro Lens Fabrication by Means of Femtosecond Two Photon Photopolymerization. *Opt. Express* **2006**, *14* (2), 810–816.
- (313) Skarda, J.; Trivedi, R.; Su, L.; Ahmad-Stein, D.; Kwon, H.; Han, S.; Fan, S.; Vučković, J. Low-Overhead Distribution Strategy for

- Simulation and Optimization of Large-Area Metasurfaces. *NPJ Comput. Mater.* **2022**, *8*, 78.
- (314) Chandra, D.; Yang, S. Capillary-Force-Induced Clustering of Micropillar Arrays: Is It Caused by Isolated Capillary Bridges or by the Lateral Capillary Meniscus Interaction Force? *Langmuir* **2009**, *25* (18), 10430–10434.
- (315) Purtov, J.; Verch, A.; Rogin, P.; Hensel, R. Improved Development Procedure to Enhance the Stability of Microstructures Created by Two-Photon Polymerization. *Microelectron. Eng.* **2018**, *194*, 45–50.
- (316) Ouyang, W.; Xu, X.; Lu, W.; Zhao, N.; Han, F.; Chen, S.-C. Ultrafast 3D Nanofabrication via Digital Holography. *Nat. Commun.* **2023**, *14*, 1716.
- (317) Hahn, V.; Rietz, P.; Hermann, F.; Müller, P.; Barner-Kowollik, C.; Schlöder, T.; Wenzel, W.; Blasco, E.; Wegener, M. Light-Sheet 3D Microprinting via Two-Colour Two-Step Absorption. *Nat. Photonics* **2022**, *16* (11), 784–791.
- (318) Gan, Z.; Cao, Y.; Evans, R. A.; Gu, M. Three-Dimensional Deep Sub-Diffraction Optical Beam Lithography with 9 nm Feature Size. *Nat. Commun.* **2013**, *4*, 2061.
- (319) Thiel, M.; Ott, J.; Radke, A.; Kaschke, J.; Wegener, M. Dip-in Depletion Optical Lithography of Three-Dimensional Chiral Polarizers. *Opt. Lett.* **2013**, *38* (20), 4252–4255.
- (320) Li, X.; Cao, Y.; Gu, M. Superresolution-Focal-Volume Induced 3.0 Tbytes/Disk Capacity by Focusing a Radially Polarized Beam. *Opt. Lett.* **2011**, *36* (13), 2510–2512.
- (321) Moughames, J.; Porte, X.; Thiel, M.; Ulliac, G.; Larger, L.; Jacquot, M.; Kadic, M.; Brunner, D. Three-Dimensional Waveguide Interconnects for Scalable Integration of Photonic Neural Networks. *Optica* **2020**, *7* (6), 640–646.
- (322) Lin, X.; Rivenson, Y.; Yardimci, N. T.; Veli, M.; Luo, Y.; Jarrahi, M.; Ozcan, A. All-Optical Machine Learning Using Diffractive Deep Neural Networks. *Science* **2018**, *361* (6406), 1004–1008.
- (323) Kim, H.; Kim, J.; Yang, H.; Suh, J.; Kim, T.; Han, B.; Kim, S.; Kim, D. S.; Pikhitsa, P. V.; Choi, M. Parallel Patterning of Nanoparticles via Electrodynamic Focusing of Charged Aerosols. *Nat. Nanotechnol.* **2006**, *1* (2), 117–121.
- (324) Jung, W.; Pikhitsa, P. V.; Jung, Y.-H.; Shin, J.; Han, M.; Choi, M. 3D Nanoprinting with Charged Aerosol Particles—An Overview. *Acc. Mater. Res.* **2021**, *2* (11), 1117–1128.
- (325) Hinds, W. C.; Zhu, Y.; *Aerosol Technology: Properties, Behavior, and Measurement of Airborne Particles*, 3rd ed.; Wiley, 2022.
- (326) You, S.; Han, K.; Kim, H.; Lee, H.; Woo, C. G.; Jeong, C.; Nam, W.; Choi, M. High-Resolution, Parallel Patterning of Nanoparticles via an Ion-Induced Focusing Mask. *Small* **2010**, *6* (19), 2146–2152.
- (327) Woo, C. G.; Shin, H.; Jeong, C.; Jun, K.; Lee, J.; Lee, J.-R.; Lee, H.; You, S.; Son, Y.; Choi, M. Selective Nanopatterning of Protein via Ion-Induced Focusing and Its Application to Metal-Enhanced Fluorescence. *Small* **2011**, *7* (13), 1790–1794.
- (328) Han, K.; Kim, W.; Yu, J.; Lee, J.; Lee, H.; Gyu Woo, C.; Choi, M. A Study of Pin-to-Plate Type Spark Discharge Generator for Producing Unagglomerated Nanoaerosols. *J. Aerosol Sci.* **2012**, *52*, 80–88.
- (329) Chae, S.; Lee, D.; Kim, M.-C.; Kim, D. S.; Choi, M. Wire-in-Hole-Type Spark Discharge Generator for Long-Time Consistent Generation of Unagglomerated Nanoparticles. *Aerosol Sci. Technol.* **2015**, *49* (7), 463–471.
- (330) Tabrizi, N. S.; Ullmann, M.; Vons, V. A.; Lafont, U.; Schmidt-Ott, A. Generation of Nanoparticles by Spark Discharge. *J. Nanopart. Res.* **2009**, *11* (2), 315–332.
- (331) Lee, H.; You, S.; Pikhitsa, P. V.; Kim, J.; Kwon, S.; Woo, C. G.; Choi, M. Three-Dimensional Assembly of Nanoparticles from Charged Aerosols. *Nano Lett.* **2011**, *11* (1), 119–124.
- (332) Jung, K.; Hahn, J.; In, S.; Bae, Y.; Lee, H.; Pikhitsa, P. V.; Ahn, K.; Ha, K.; Lee, J.-K.; Park, N.; Choi, M. Hotspot-Engineered 3D Multipetal Flower Assemblies for Surface-Enhanced Raman Spectroscopy. *Adv. Mater.* **2014**, *26* (34), 5924–5929.
- (333) Bae, Y.; Pikhitsa, P. V.; Cho, H.; Choi, M. Multifurcation Assembly of Charged Aerosols and Its Application to 3D Structured Gas Sensors. *Adv. Mater.* **2017**, *29* (2), 1604159.
- (334) Yang, Y.; Jung, W.; Hur, C.; Kim, H.; Shin, J.; Choi, M.; Rho, J. Angle-Resolved Polarimetry with Quasi-Bound States in the Continuum Plasmonic Metamaterials via 3D Aerosol Nanoprinting. *ACS Nano* **2024**, *18* (20), 12771–12780.
- (335) Zhang, H.; Cadusch, J.; Kinnear, C.; James, T.; Roberts, A.; Mulvaney, P. Direct Assembly of Large Area Nanoparticle Arrays. *ACS Nano* **2018**, *12* (8), 7529–7537.
- (336) Lee, K.; Choi, H.; Kim, D. S.; Jang, M. S.; Choi, M. Vertical Stacking of Three-Dimensional Nanostructures via an Aerosol Lithography for Advanced Optical Applications. *Nanotechnology* **2017**, *28* (47), 475302.
- (337) Choi, H.; Kang, S.; Jung, W.; Jung, Y.; Park, S. J.; Kim, D. S.; Choi, M. Controlled Electrostatic Focusing of Charged Aerosol Nanoparticles via an Electrified Mask. *J. Aerosol Sci.* **2015**, *88*, 90–97.
- (338) Jung, W.; Jung, Y.-H.; Pikhitsa, P. V.; Feng, J.; Yang, Y.; Kim, M.; Tsai, H.-Y.; Tanaka, T.; Shin, J.; Kim, K.-Y.; Choi, H.; Rho, J.; Choi, M. Three-Dimensional Nanoprinting via Charged Aerosol Jets. *Nature* **2021**, *592* (7852), 54–59.
- (339) Wu, P. C.; Sun, G.; Chen, W. T.; Yang, K.-Y.; Huang, Y.-W.; Chen, Y.-H.; Huang, H. L.; Hsu, W.-L.; Chiang, H. P.; Tsai, D. P. Vertical Split-Ring Resonator Based Nanoplasmonic Sensor. *Appl. Phys. Lett.* **2014**, *105* (3), No. 033105.
- (340) Shin, J.; Jung, Y.-H.; Pikhitsa, P. V.; Hur, C.; Cho, W.; Jung, W.; Choi, M. Three-Dimensional Nanoprinting with Charged Aerosol Focusing via an Electrified Mask. *Additive Manufact.* **2022**, *60*, 103206.
- (341) Zhou, J.; Koschny, Th.; Kafesaki, M.; Economou, E. N.; Pendry, J. B.; Soukoulis, C. M. Saturation of the Magnetic Response of Split-Ring Resonators at Optical Frequencies. *Phys. Rev. Lett.* **2005**, *95* (22), 223902.
- (342) Chen, H.-T.; Taylor, A. J.; Yu, N. A Review of Metasurfaces: Physics and Applications. *Rep. Prog. Phys.* **2016**, *79* (7), No. 076401.
- (343) Jeon, S.; Park, J.-U.; Cirelli, R.; Yang, S.; Heitzman, C. E.; Braun, P. V.; Kenis, P. J. A.; Rogers, J. A. Fabricating Complex Three-Dimensional Nanostructures with High-Resolution Conformable Phase Masks. *Proc. Natl. Acad. Sci. U.S.A.* **2004**, *101* (34), 12428–12433.
- (344) Maria, J.; Jeon, S.; Rogers, J. A. Nanopatterning with Conformable Phase Masks. *J. Photochem. Photobiol. A Chem.* **2004**, *166* (1–3), 149–154.
- (345) Jeon, S.; Malyarchuk, V.; Rogers, J. A.; Wiederrecht, G. P. Fabricating Three Dimensional Nanostructures Using Two Photon Lithography in a Single Exposure Step. *Opt. Express* **2006**, *14* (6), 2300–2308.
- (346) Nam, S.-H.; Hyun, G.; Cho, D.; Han, S.; Bae, G.; Chen, H.; Kim, K.; Ham, Y.; Park, J.; Jeon, S. Fundamental Principles and Development of Proximity-Field Nanopatterning toward Advanced 3D Nanofabrication. *Nano Res.* **2021**, *14* (9), 2965–2980.
- (347) Shir, D. J.; Jeon, S.; Liao, H.; Highland, M.; Cahill, D. G.; Su, M. F.; El-Kady, I. F.; Christodoulou, C. G.; Bogart, G. R.; Hamza, A. V.; Rogers, J. A. Three-Dimensional Nanofabrication with Elastomeric Phase Masks. *J. Phys. Chem. B* **2007**, *111* (45), 12945–12958.
- (348) Hsia, K. J.; Huang, Y.; Menard, E.; Park, J.-U.; Zhou, W.; Rogers, J.; Fulton, J. M. Collapse of Stamps for Soft Lithography Due to Interfacial Adhesion. *Appl. Phys. Lett.* **2005**, *86* (15), 154106.
- (349) Jeon, S.; Malyarchuk, V.; White, J. O.; Rogers, J. A. Optically Fabricated Three Dimensional Nanofluidic Mixers for Microfluidic Devices. *Nano Lett.* **2005**, *5* (7), 1351–1356.
- (350) Jeon, S.; Nam, Y.-S.; Shir, D. J.-L.; Rogers, J. A.; Hamza, A. Three Dimensional Nanoporous Density Graded Materials Formed by Optical Exposures through Conformable Phase Masks. *Appl. Phys. Lett.* **2006**, *89* (25), 253101.
- (351) Wen, J.; Zhang, Y.; Xiao, M. The Talbot Effect: Recent Advances in Classical Optics, Nonlinear Optics, and Quantum Optics. *Adv. Opt. Photonics* **2013**, *5* (1), 83–130.

- (352) Hyun, J. K.; Park, J.; Kim, E.; Lauhon, L. J.; Jeon, S. Rational Control of Diffraction and Interference from Conformal Phase Gratings: Toward High-Resolution 3D Nanopatterning. *Adv. Opt. Mater.* **2014**, *2* (12), 1213–1220.
- (353) Shir, D.; Liao, H.; Jeon, S.; Xiao, D.; Johnson, H. T.; Bogart, G. R.; Bogart, K. H. A.; Rogers, J. A. Three-Dimensional Nanostructures Formed by Single Step, Two-Photon Exposures through Elastomeric Penrose Quasicrystal Phase Masks. *Nano Lett.* **2008**, *8* (8), 2236–2244.
- (354) Nam, S.-H.; Park, J.; Jeon, S. Rapid and Large-Scale Fabrication of Full Color Woodpile Photonic Crystals via Interference from a Conformal Multilevel Phase Mask. *Adv. Funct. Mater.* **2019**, *29* (44), 1904971.
- (355) Nam, S.-H.; Kim, M.; Kim, N.; Cho, D.; Choi, M.; Park, J. H.; Shin, J.; Jeon, S. Photolithographic Realization of Target Nanostructures in 3D Space by Inverse Design of Phase Modulation. *Sci. Adv.* **2022**, *8* (21), eabm6310.
- (356) Park, J.; Kim, K.-I.; Kim, K.; Kim, D.-C.; Cho, D.; Lee, J. H.; Jeon, S. Rapid, High-Resolution 3D Interference Printing of Multilevel Ultralong Nanochannel Arrays for High-Throughput Nanofluidic Transport. *Adv. Mater.* **2015**, *27* (48), 8000–8006.
- (357) Hyun, G.; Cao, S.; Ham, Y.; Youn, D.-Y.; Kim, I.-D.; Chen, X.; Jeon, S. Three-Dimensional, Submicron Porous Electrode with a Density Gradient to Enhance Charge Carrier Transport. *ACS Nano* **2022**, *16* (6), 9762–9771.
- (358) Cho, D.; Suh, J. M.; Nam, S.-H.; Park, S. Y.; Park, M.; Lee, T. H.; Choi, K. S.; Lee, J.; Ahn, C.; Jang, H. W.; Shim, Y.-S.; Jeon, S. Optically Activated 3D Thin-Shell TiO<sub>2</sub> for Super-Sensitive Chemo-resistive Responses: Toward Visible Light Activation. *Adv. Sci.* **2021**, *8* (3), 2001883.
- (359) Lee, J.; Cho, D.; Chen, H.; Shim, Y.-S.; Park, J.; Jeon, S. Proximity-Field Nanopatterning for High-Performance Chemical and Mechanical Sensor Applications Based on 3D Nanostructures. *Appl. Phys. Rev.* **2022**, *9* (1), No. 011322.
- (360) Park, J.; Seo, J.; Jung, H. K.; Hyun, G.; Park, S. Y.; Jeon, S. Direct Optical Fabrication of Fluorescent, Multilevel 3D Nanostructures for Highly Efficient Chemosensing Platforms. *Adv. Funct. Mater.* **2016**, *26* (39), 7170–7177.
- (361) Suh, J. M.; Cho, D.; Lee, S.; Lee, T. H.; Jung, J.-W.; Lee, J.; Cho, S. H.; Eom, T. H.; Hong, J.-W.; Shim, Y.-S.; Jeon, S.; Jang, H. W. Rationally Designed TiO<sub>2</sub> Nanostructures of Continuous Pore Network for Fast-Responding and Highly Sensitive Acetone Sensor. *Small Methods* **2021**, *5* (12), 2100941.
- (362) Ahn, C.; Park, J.; Cho, D.; Hyun, G.; Ham, Y.; Kim, K.; Nam, S.-H.; Bae, G.; Lee, K.; Shim, Y.-S.; Ang, J. N. S.; Jeon, S. High-Performance Functional Nanocomposites Using 3D Ordered and Continuous Nanostructures Generated from Proximity-Field Nanopatterning. *Funct. Compos. Struct.* **2019**, *1* (3), No. 032002.
- (363) Choi, M.; An, J.; Lee, H.; Jang, H.; Park, J. H.; Cho, D.; Song, J. Y.; Kim, S. M.; Oh, M.-W.; Shin, H.; Jeon, S. High Figure-of-Merit for ZnO Nanostructures by Interfacing Lowly-Oxidized Graphene Quantum Dots. *Nat. Commun.* **2024**, *15*, 1996.
- (364) Ham, Y.; Fritz, N. J.; Hyun, G.; Lee, Y. B.; Nam, J. S.; Kim, I.-D.; Braun, P. V.; Jeon, S. 3D Periodic Polyimide Nano-Networks for Ultrahigh-Rate and Sustainable Energy Storage. *Energy Environ. Sci.* **2021**, *14* (11), 5894–5902.
- (365) Hyun, G.; Cho, S.-H.; Park, J.; Kim, K.; Ahn, C.; Tiwari, A. P.; Kim, I.-D.; Jeon, S. 3D Ordered Carbon/SnO<sub>2</sub> Hybrid Nanostructures for Energy Storage Applications. *Electrochim. Acta* **2018**, *288*, 108–114.
- (366) Kim, H.; Yun, S.; Kim, K.; Kim, W.; Ryu, J.; Nam, H. G.; Han, S. M.; Jeon, S.; Hong, S. Breaking the Elastic Limit of Piezoelectric Ceramics Using Nanostructures: A Case Study Using ZnO. *Nano Energy* **2020**, *78*, 105259.
- (367) Kuk, S. K.; Ham, Y.; Gopinath, K.; Boonmongkolras, P.; Lee, Y.; Lee, Y. W.; Kondaveeti, S.; Ahn, C.; Shin, B.; Lee, J.-K.; Jeon, S.; Park, C. B. Continuous 3D Titanium Nitride Nanoshell Structure for Solar-Driven Unbiased Biocatalytic CO<sub>2</sub> Reduction. *Adv. Energy Mater.* **2019**, *9* (25), 1900029.
- (368) Rhee, R.; Kim, T. G.; Jang, G. Y.; Bae, G.; Lee, J. H.; Lee, S.; Kim, S.; Jeon, S.; Park, J. H. Unassisted Overall Water Splitting with a Solar-to-Hydrogen Efficiency of over 10% by Coupled Lead Halide Perovskite Photoelectrodes. *Carbon Energy* **2023**, *5* (1), e232.
- (369) Ahn, C.; Kim, S.-M.; Jung, J.-W.; Park, J.; Kim, T.; Lee, S. E.; Jang, D.; Hong, J.-W.; Han, S. M.; Jeon, S. Multifunctional Polymer Nanocomposites Reinforced by 3D Continuous Ceramic Nanofillers. *ACS Nano* **2018**, *12* (9), 9126–9133.
- (370) Ahn, C.; Park, J.; Kim, D.; Jeon, S. Monolithic 3D Titania with Ultrathin Nanoshell Structures for Enhanced Photocatalytic Activity and Recyclability. *Nanoscale* **2013**, *5* (21), 10384–10389.
- (371) Bae, G.; Choi, G.-M.; Ahn, C.; Kim, S.-M.; Kim, W.; Choi, Y.; Park, D.; Jang, D.; Hong, J.-W.; Han, S. M.; Bae, B.-S.; Jeon, S. Flexible Protective Film: Ultrahard, Yet Flexible Hybrid Nanocomposite Reinforced by 3D Inorganic Nanoshell Structures. *Adv. Funct. Mater.* **2021**, *31* (18), 2010254.
- (372) Bae, G.; Jang, D.; Jeon, S. Scalable Fabrication of High-Performance Thin-Shell Oxide Nanoarchitected Materials via Proximity-Field Nanopatterning. *ACS Nano* **2021**, *15* (3), 3960–3970.
- (373) Na, Y.; Shin, D.; Kim, K.; Ahn, C.; Jeon, S.; Jang, D. Emergence of New Density–Strength Scaling Law in 3D Hollow Ceramic Nanoarchitectures. *Small* **2018**, *14* (44), 1802239.
- (374) Park, J.; Wang, S.; Li, M.; Ahn, C.; Hyun, J. K.; Kim, D. S.; Kim, D. K.; Rogers, J. A.; Huang, Y.; Jeon, S. Three-Dimensional Nanonetworks for Giant Stretchability in Dielectrics and Conductors. *Nat. Commun.* **2012**, *3*, 916.
- (375) Hyun, G.; Ham, Y.; Harding, J.; Jeon, S. Towards Optimal 3D Battery Electrode Architecture: Integrating Structural Engineering with AI-Driven Optimization. *Energy Storage Mater.* **2024**, *69*, 103395.
- (376) Cho, D.; Chen, H.; Shin, J.; Jeon, S. Mechanoresponsive Scatterers for High-Contrast Optical Modulation. *Nanophotonics* **2022**, *11* (11), 2737–2762.
- (377) Cho, D.; Park, J.; Kim, T.; Jeon, S. Recent Advances in Lithographic Fabrication of Micro-/Nanostructured Polydimethylsiloxanes and Their Soft Electronic Applications. *J. Semicond.* **2019**, *40* (11), 111605.
- (378) Cho, D.; Shim, Y.-S.; Jung, J.-W.; Nam, S.-H.; Min, S.; Lee, S.-E.; Ham, Y.; Lee, K.; Park, J.; Shin, J.; Hong, J.-W.; Jeon, S. High-Contrast Optical Modulation from Strain-Induced Nanogaps at 3D Heterogeneous Interfaces. *Adv. Sci.* **2020**, *7* (11), 1903708.
- (379) Chen, H.; Cho, D.; Ko, K.; Qin, C.; Kim, M. P.; Zhang, H.; Lee, J.-H.; Kim, E.; Park, D.; Shen, X.; Yang, J.; Ko, H.; Hong, J.-W.; Kim, J.-K.; Jeon, S. Interdigitated Three-Dimensional Heterogeneous Nanocomposites for High-Performance Mechanochromic Smart Membranes. *ACS Nano* **2022**, *16* (1), 68–77.
- (380) Kwon, Y. W.; Park, J.; Kim, T.; Kang, S. H.; Kim, H.; Shin, J.; Jeon, S.; Hong, S. W. Flexible Near-Field Nanopatterning with Ultrathin, Conformal Phase Masks on Nonplanar Substrates for Biomimetic Hierarchical Photonic Structures. *ACS Nano* **2016**, *10* (4), 4609–4617.
- (381) Chang, H.; Kwon, S.; Bae, G.; Jeon, S. Rational Design of Arbitrary Topology in Three-Dimensional Space via Inverse Calculation of Phase Modulation. *Nanophotonics* **2024**, *13* (7), 971–982.
- (382) Phan, T.; Sell, D.; Wang, E. W.; Doshay, S.; Eddee, K.; Yang, J.; Fan, J. A. High-Efficiency, Large-Area, Topology-Optimized Metasurfaces. *Light Sci. Appl.* **2019**, *8*, 48.
- (383) Chung, H.; Miller, O. D. High-NA Achromatic Metalenses by Inverse Design. *Opt. Express* **2020**, *28* (5), 6945–6965.
- (384) Jung, C.; Kim, G.; Jeong, M.; Jang, J.; Dong, Z.; Badloe, T.; Yang, J. K. W.; Rho, J. Metasurface-Driven Optically Variable Devices. *Chem. Rev.* **2021**, *121* (21), 13013–13050.
- (385) Ren, H.; Fang, X.; Jang, J.; Bürger, J.; Rho, J.; Maier, S. A. Complex-Amplitude Metasurface-Based Orbital Angular Momentum Holography in Momentum Space. *Nat. Nanotechnol.* **2020**, *15* (11), 948–955.
- (386) Lawrence, M.; Barton, D. R.; Dixon, J.; Song, J.-H.; van de Groep, J.; Brongersma, M. L.; Dionne, J. A. High Quality Factor

- Phase Gradient Metasurfaces. *Nat. Nanotechnol.* **2020**, *15* (11), 956–961.
- (387) Tanriover, I.; Dereshgi, S. A.; Aydin, K. Metasurface Enabled Broadband All Optical Edge Detection in Visible Frequencies. *Nat. Commun.* **2023**, *14*, 6484.
- (388) Al Hasan, M.; Ullah, Z.; Nawi, I.; Ben Mabrouk, I. Fabrication of a Large Scale Metasurface with High Resolution and Enhanced Absorption. *Opt. Mater. Express* **2023**, *13* (1), 130–141.
- (389) Sin Tan, Y.; Wang, H.; Wang, H.; Pan, C.; Yang, J. K. W. High-Throughput Fabrication of Large-Scale Metasurfaces Using Electron-Beam Lithography with SU-8 Gratings for Multilevel Security Printing. *Photonics Res.* **2023**, *11* (3), B103–B110.
- (390) Zeitner, U. D.; Banasch, M.; Trost, M. Potential of E-Beam Lithography for Micro- and Nano-Optics Fabrication on Large Areas. *J. Micro/Nanopatterning Mater. Metrology* **2023**, *22* (4), No. 041405.
- (391) Li, Z.; Lin, P.; Huang, Y.-W.; Park, J.-S.; Chen, W. T.; Shi, Z.; Qiu, C.-W.; Cheng, J.-X.; Capasso, F. Meta-Optics Achieves RGB-Achromatic Focusing for Virtual Reality. *Sci. Adv.* **2021**, *7* (5), eabe4458.
- (392) Li, Z.; Pestourie, R.; Park, J.-S.; Huang, Y.-W.; Johnson, S. G.; Capasso, F. Inverse Design Enables Large-Scale High-Performance Meta-Optics Reshaping Virtual Reality. *Nat. Commun.* **2022**, *13*, 2409.
- (393) Greve, M. M.; Holst, B. Optimization of an Electron Beam Lithography Instrument for Fast, Large Area Writing at 10 kV Acceleration Voltage. *J. Vac. Sci. Technol. B* **2013**, *31* (4), No. 043202.
- (394) Åstrand, M.; Frisk, T.; Ohlin, H.; Vogt, U. Understanding Dose Correction for High-Resolution 50 kV Electron-Beam Lithography on Thick Resist Layers. *Micro Nano Eng.* **2022**, *16*, 100141.
- (395) Li, K.; Li, J.; Reardon, C.; Schuster, C. S.; Wang, Y.; Triggs, G. J.; Damnik, N.; Müenchenberger, J.; Wang, X.; Martins, E. R.; Krauss, T. F. High Speed E-Beam Writing for Large Area Photonic Nanostructures — a Choice of Parameters. *Sci. Rep.* **2016**, *6*, 32945.
- (396) TAKAHASHI, N.; KIKUCHI, H. Rayleigh Criterion. *Ann. Bus. Adm. Sci.* **2017**, *16* (5), 203–213.
- (397) Leitis, A.; Tseng, M. L.; John-Herpin, A.; Kivshar, Y. S.; Altug, H. Wafer-Scale Functional Metasurfaces for Mid-Infrared Photonics and Biosensing. *Adv. Mater.* **2021**, *33* (43), 2102232.
- (398) Hu, T.; Zhong, Q.; Li, N.; Dong, Y.; Xu, Z.; Fu, Y. H.; Li, D.; Bliznetsov, V.; Zhou, Y.; Lai, K. H.; Lin, Q.; Zhu, S.; Singh, N. CMOS-Compatible a-Si Metalenses on a 12-Inch Glass Wafer for Fingerprint Imaging. *Nanophotonics* **2020**, *9* (4), 823–830.
- (399) Park, J.-S.; Zhang, S.; She, A.; Chen, W. T.; Lin, P.; Yousef, K. M. A.; Cheng, J.-X.; Capasso, F. All-Glass, Large Metalens at Visible Wavelength Using Deep-Ultraviolet Projection Lithography. *Nano Lett.* **2019**, *19* (12), 8673–8682.
- (400) Moon, S.-W.; Kim, J.; Park, C.; Kim, W.; Yang, Y.; Kim, J.; Lee, S.; Choi, M.; Sung, H.; Park, J.; Song, H.; Lee, H.; Rho, J. Wafer-Scale Manufacturing of Near-Infrared Metalenses. *Laser Photonics Rev.* **2024**, *18* (4), 2300929.
- (401) Park, J.-S.; Lim, S. W. D.; Amirzhan, A.; Kang, H.; Karrfalt, K.; Kim, D.; Leger, J.; Urbas, A.; Ossiander, M.; Li, Z.; Capasso, F. All-Glass 100 Mm Diameter Visible Metalens for Imaging the Cosmos. *ACS Nano* **2024**, *18* (4), 3187–3198.
- (402) Zhang, L.; Chang, S.; Chen, X.; Ding, Y.; Rahman, M. T.; Duan, Y.; Stephen, M.; Ni, X. High-Efficiency, 80 mm Aperture Metalens Telescope. *Nano Lett.* **2023**, *23* (1), 51–57.
- (403) Tao, J.; You, Q.; Li, Z.; Luo, M.; Liu, Z.; Qiu, Y.; Yang, Y.; Zeng, Y.; He, Z.; Xiao, X.; Zheng, G.; Yu, S. Mass-Manufactured Beam-Steering Metasurfaces for High-Speed Full-Duplex Optical Wireless-Broadcasting Communications. *Adv. Mater.* **2022**, *34* (6), 2106080.
- (404) Gwyn, C. W.; Stulen, R.; Sweeney, D.; Attwood, D. Extreme Ultraviolet Lithography. *J. Vac. Sci. Technol. B Microelectron. Nanometer Struct. Process. Meas. Phenom.* **1998**, *16* (6), 3142–3149.
- (405) Ahn, S. H.; Guo, L. J. Large-Area Roll-to-Roll and Roll-to-Plate Nanoimprint Lithography: A Step toward High-Throughput Application of Continuous Nanoimprinting. *ACS Nano* **2009**, *3* (8), 2304–2310.
- (406) Gong, J.; Xiong, L.; Pu, M.; Li, X.; Ma, X.; Luo, X. Visible Meta-Displays for Anti-Counterfeiting with Printable Dielectric Metasurfaces. *Adv. Sci.* **2024**, *11* (17), 2308687.
- (407) Einck, V. J.; Torfeh, M.; McClung, A.; Jung, D. E.; Mansouree, M.; Arbabi, A.; Watkins, J. J. Scalable Nanoimprint Lithography Process for Manufacturing Visible Metasurfaces Composed of High Aspect Ratio TiO<sub>2</sub>Meta-Atoms. *ACS Photonics* **2021**, *8* (8), 2400–2409.
- (408) Choi, J.-H.; Jo, H.-B.; Choi, H.-J.; Lee, H. Fabrication of TiO<sub>2</sub> Nano-to-Microscale Structures Using UV Nanoimprint Lithography. *Nanotechnology* **2013**, *24* (19), 195301.
- (409) Jo, H.-B.; Byeon, K.-J.; Lee, H.; Kwon, M.-H.; Choi, K.-W. Fabrication of ZnO Nano-Structures Using UV Nanoimprint Lithography of a ZnO Nano-Particle Dispersion Resin. *J. Mater. Chem.* **2012**, *22* (38), 20742–20746.
- (410) Yoon, G.; Kim, K.; Huh, D.; Lee, H.; Rho, J. Single-Step Manufacturing of Hierarchical Dielectric Metalens in the Visible. *Nat. Commun.* **2020**, *11*, 2268.
- (411) Kim, J.; Oh, D. K.; Kim, H.; Yoon, G.; Jung, C.; Kim, J.; Badloe, T.; Kang, H.; Kim, S.; Yang, Y.; Lee, J.; Ko, B.; Ok, J. G.; Rho, J. Metasurface Holography Reaching the Highest Efficiency Limit in the Visible via One-Step Nanoparticle-Embedded-Resin Printing. *Laser Photonics Rev.* **2022**, *16* (8), 2200098.
- (412) Zhang, C.; Nie, X.; Liu, Z.; Chen, Z.; Ma, C.; Yue, F.; Wang, L.; He, Z. High Resolution UV Spectral Imaging and Bio-Detection with Magnetic Dipole Quasi-BIC Resonant Dielectric Metasurfaces. *Opt. Commun.* **2023**, *530*, 129173.
- (413) Deng, Y.; Wang, X.; Gong, Z.; Dong, K.; Lou, S.; Pégard, N.; Tom, K. B.; Yang, F.; You, Z.; Waller, L.; Yao, J. All-Silicon Broadband Ultraviolet Metasurfaces. *Adv. Mater.* **2018**, *30* (38), 1802632.
- (414) Tseng, M. L.; Semmlinger, M.; Zhang, M.; Arndt, C.; Huang, T.-T.; Yang, J.; Kuo, H. Y.; Su, V.-C.; Chen, M. K.; Chu, C. H.; Cerjan, B.; Tsai, D. P.; Nordlander, P.; Halas, N. J. Vacuum Ultraviolet Nonlinear Metalens. *Sci. Adv.* **2022**, *8* (16), eabn5644.
- (415) Li, K.; Martins, A.; Bohora, S.; Dhakal, A.; Martins, E. R.; Krauss, T. F. Hybrid Metalens for Miniaturised Ultraviolet Fluorescence Detection. *Adv. Opt. Mater.* **2023**, *11* (22), 2300852.
- (416) Zhang, C.; Chen, L.; Lin, Z.; Song, J.; Wang, D.; Li, M.; Koksal, O.; Wang, Z.; Spektor, G.; Carlson, D.; Lezec, H. J.; Zhu, W.; Papp, S.; Agrawal, A. Tantalum Pentoxide: A New Material Platform for High-Performance Dielectric Metasurface Optics in the Ultraviolet and Visible Region. *Light Sci. Appl.* **2024**, *13*, 23.
- (417) Zhang, C.; Divitt, S.; Fan, Q.; Zhu, W.; Agrawal, A.; Lu, Y.; Xu, T.; Lezec, H. J. Low-Loss Metasurface Optics down to the Deep Ultraviolet Region. *Light Sci. Appl.* **2020**, *9*, 55.
- (418) Huang, K.; Deng, J.; Leong, H. S.; Yap, S. L. K.; Yang, R. B.; Teng, J.; Liu, H. Ultraviolet Metasurfaces of ≈80% Efficiency with Antiferromagnetic Resonances for Optical Vectorial Anti-Counterfeiting. *Laser Photonics Rev.* **2019**, *13* (5), 1800289.
- (419) Kim, J.; Kim, W.; Oh, D. K.; Kang, H.; Kim, H.; Badloe, T.; Kim, S.; Park, C.; Choi, H.; Lee, H. One-Step Printable Platform for High-Efficiency Metasurfaces down to the Deep-Ultraviolet Region. *Light Sci. Appl.* **2023**, *12*, 68.
- (420) Kang, H.; Oh, D.; Jeon, N.; Kim, J.; Kim, H.; Badloe, T.; Rho, J. Tailoring High-Refractive-Index Nanocomposites for Manufacturing of Ultraviolet Metasurfaces. *Microsyst. Nanoeng.* **2024**, *10*, 53.
- (421) Chen, W. T.; Zhu, A. Y.; Sanjeev, V.; Khorasaninejad, M.; Shi, Z.; Lee, E.; Capasso, F. A Broadband Achromatic Metalens for Focusing and Imaging in the Visible. *Nat. Nanotechnol.* **2018**, *13* (3), 220–226.
- (422) Yang, W.; Xiao, S.; Song, Q.; Liu, Y.; Wu, Y.; Wang, S.; Yu, J.; Han, J.; Tsai, D.-P. All-Dielectric Metasurface for High-Performance Structural Color. *Nat. Commun.* **2020**, *11*, 1864.
- (423) Jang, J.; Badloe, T.; Yang, Y.; Lee, T.; Mun, J.; Rho, J. Spectral Modulation through the Hybridization of Mie-Scatterers and Quasi-Guided Mode Resonances: Realizing Full and Gradients of Structural Color. *ACS Nano* **2020**, *14* (11), 15317–15326.

- (424) Song, Q.; Baroni, A.; Sawant, R.; Ni, P.; Brandli, V.; Chenot, S.; Vézian, S.; Damilano, B.; de Mierry, P.; Khadir, S.; Ferrand, P.; Genevet, P. Ptychography Retrieval of Fully Polarized Holograms from Geometric-Phase Metasurfaces. *Nat. Commun.* **2020**, *11*, 2651.
- (425) Song, Q.; Baroni, A.; Wu, P. C.; Chenot, S.; Brandli, V.; Vézian, S.; Damilano, B.; de Mierry, P.; Khadir, S.; Ferrand, P.; Genevet, P. Broadband Decoupling of Intensity and Polarization with Vectorial Fourier Metasurfaces. *Nat. Commun.* **2021**, *12*, 3631.
- (426) Kim, G.; Kim, Y.; Yun, J.; Moon, S.-W.; Kim, S.; Kim, J.; Park, J.; Badloe, T.; Kim, I.; Rho, J. Metasurface-Driven Full-Space Structured Light for Three-Dimensional Imaging. *Nat. Commun.* **2022**, *13*, 5920.
- (427) Zhang, L.; Ding, J.; Zheng, H.; An, S.; Lin, H.; Zheng, B.; Du, Q.; Yin, G.; Michon, J.; Zhang, Y.; Fang, Z.; Shalaginov, M. Y.; Deng, L.; Gu, T.; Zhang, H.; Hu, J. Ultra-Thin High-Efficiency Mid-Infrared Transmissive Huygens Meta-Optics. *Nat. Commun.* **2018**, *9*, 1481.
- (428) John-Herpin, A.; Kavungal, D.; von Mücke, L.; Altug, H. Infrared Metasurface Augmented by Deep Learning for Monitoring Dynamics between All Major Classes of Biomolecules. *Adv. Mater.* **2021**, *33* (14), 2006054.
- (429) Zhu, Y.; Li, Z.; Hao, Z.; DiMarco, C.; Maturavongsadit, P.; Hao, Y.; Lu, M.; Stein, A.; Wang, Q.; Hone, J.; Yu, N.; Lin, Q. Optical Conductivity-Based Ultrasensitive Mid-Infrared Biosensing on a Hybrid Metasurface. *Light Sci. Appl.* **2018**, *7*, 67.
- (430) Wang, L.; Kruk, S.; Tang, H.; Li, T.; Kravchenko, I.; Neshev, D. N.; Kivshar, Y. S. Grayscale Transparent Metasurface Holograms. *Optica* **2016**, *3* (12), 1504–1505.
- (431) Zhou, Z.-X.; Ye, M.-J.; Yu, M.-W.; Yang, J.-H.; Su, K.-L.; Yang, C.-C.; Lin, C.-Y.; Babicheva, V. E.; Timofeev, I. V.; Chen, K.-P. Germanium Metasurfaces with Lattice Kerker Effect in Near-Infrared Photodetectors. *ACS Nano* **2022**, *16* (4), 5994–6001.
- (432) Tian, J.; Luo, H.; Li, Q.; Pei, X.; Du, K.; Qiu, M. Near-Infrared Super-Absorbing All-Dielectric Metasurface Based on Single-Layer Germanium Nanostructures. *Laser & Photonics Reviews* **2018**, *12* (9), 1800076.
- (433) Lewi, T.; Evans, H. A.; Butakov, N. A.; Schuller, J. A. Ultrawide Thermo-Optic Tuning of PbTe Meta-Atoms. *Nano Lett.* **2017**, *17* (6), 3940–3945.
- (434) Cui, T.; Bai, B.; Sun, H.-B. Tunable Metasurfaces Based on Active Materials. *Adv. Funct. Mater.* **2019**, *29* (10), 1806692.
- (435) Barho, F. B.; Gonzalez-Posada, F.; Bomers, M.; Mezy, A.; Cerutti, L.; Taliercio, T. Surface-Enhanced Thermal Emission Spectroscopy with Perfect Absorber Metasurfaces. *ACS Photonics* **2019**, *6* (6), 1506–1514.
- (436) Barho, F. B.; Gonzalez-Posada, F.; Cerutti, L.; Taliercio, T. Heavily Doped Semiconductor Metamaterials for Mid-Infrared Multispectral Perfect Absorption and Thermal Emission. *Adv. Opt. Mater.* **2020**, *8* (6), 1901502.
- (437) Yoon, G.; Kim, K.; Kim, S.-U.; Han, S.; Lee, H.; Rho, J. Printable Nanocomposite Metalens for High-Contrast Near-Infrared Imaging. *ACS Nano* **2021**, *15* (1), 698–706.
- (438) Ahn, S. H.; Guo, L. J. Large-Area Roll-to-Roll and Roll-to-Plate Nanoimprint Lithography: A Step toward High-Throughput Application of Continuous Nanoimprinting. *ACS Nano* **2009**, *3* (8), 2304–2310.
- (439) Kooy, N.; Mohamed, K.; Pin, L. T.; Guan, O. S. A Review of Roll-to-Roll Nanoimprint Lithography. *Nanoscale Res. Lett.* **2014**, *9*, 320.
- (440) Lee, T.; Lee, C.; Oh, D. K.; Badloe, T.; Ok, J. G.; Rho, J. Scalable and High-Throughput Top-down Manufacturing of Optical Metasurfaces. *Sensors* **2020**, *20* (15), 4108.
- (441) Oh, D. K.; Lee, T.; Ko, B.; Badloe, T.; Ok, J. G.; Rho, J. Nanoimprint Lithography for High-Throughput Fabrication of Metasurfaces. *Front. Optoelectron.* **2021**, *14* (2), 229–251.
- (442) Shneidman, A. V.; Becker, K. P.; Lukas, M. A.; Torgerson, N.; Wang, C.; Reshef, O.; Burek, M. J.; Paul, K.; McLellan, J.; Lončar, M. All-Polymer Integrated Optical Resonators by Roll-to-Roll Nanoimprint Lithography. *ACS Photonics* **2018**, *5* (5), 1839–1845.
- (443) Karioja, P.; Hiltunen, J.; Aikio, S. M.; Alajoki, T.; Tuominen, J.; Hiltunen, M.; Siitonens, S.; Kontturi, V.; Böhnen, K.; Hauser, R. Toward Large-Area Roll-to-Roll Printed Nanophotonic Sensors. In *Optical Sensing and Detection III*; SPIE, 2014; Vol. 9141, pp 68–79. DOI: [DOI: 10.1117/12.2052496](https://doi.org/10.1117/12.2052496).
- (444) Ok, J. G.; Kwak, M. K.; Huard, C. M.; Youn, H. S.; Guo, L. J. Photo-Roll Lithography (PRL) for Continuous and Scalable Patterning with Application in Flexible Electronics. *Adv. Mater.* **2013**, *25* (45), 6554–6561.
- (445) Leung, S.-F.; Gu, L.; Zhang, Q.; Tsui, K.-H.; Shieh, J.-M.; Shen, C.-H.; Hsiao, T.-H.; Hsu, C.-H.; Lu, L.; Li, D.; et al. Roll-to-Roll Fabrication of Large Scale and Regular Arrays of Three-Dimensional Nanospikes for High Efficiency and Flexible Photovoltaics. *Sci. Rep.* **2014**, *4*, 4243.
- (446) Ahn, S. H.; Guo, L. J. High-Speed Roll-to-Roll Nanoimprint Lithography on Flexible Plastic Substrates. *Adv. Mater.* **2008**, *20* (11), 2044–2049.
- (447) Lan, H.; Liu, H. UV-Nanoimprint Lithography: Structure, Materials and Fabrication of Flexible Molds. *J. Nanosci. Nanotechnol.* **2013**, *13* (S), 3145–3172.
- (448) Vogler, M.; Wiedenberg, S.; Mühlberger, M.; Bergmair, I.; Glinsner, T.; Schmidt, H.; Kley, E.-B.; Grützner, G. Development of a Novel, Low-Viscosity UV-Curable Polymer System for UV-Nanoimprint Lithography. *Microelectron. Eng.* **2007**, *84* (S–8), 984–988.
- (449) Lee, J.; Park, S.; Choi, K.; Kim, G. Nano-Scale Patterning Using the Roll Typed UV-Nanoimprint Lithography Tool. *Microelectron. Eng.* **2008**, *85* (5–6), 861–865.
- (450) Unno, N.; Mäkelä, T. Thermal Nanoimprint Lithography—a Review of the Process, Mold Fabrication, and Material. *Nanomaterials* **2023**, *13* (14), 2031.
- (451) Hao, J.; Wang, J.; Liu, X.; Padilla, W. J.; Zhou, L.; Qiu, M. High Performance Optical Absorber Based on a Plasmonic Metamaterial. *Appl. Phys. Lett.* **2010**, *96* (25), 251104.
- (452) Liu, N.; Langguth, L.; Weiss, T.; Kastel, J.; Fleischhauer, M.; Pfau, T.; Giessen, H. Plasma Analogue of Electromagnetically Induced Transparency at the Drude Damping Limit. *Nat. Mater.* **2009**, *8*, 758–762.
- (453) Liu, X.; Liu, W.; Yang, B. Deep-Elliptical-Silver-Nanowell Array (d-EAgNWAs) Fabricated by Stretchable Imprinting Combining Colloidal Lithography: A Highly Sensitive Plasmonic Sensing Platform. *Nano Res.* **2019**, *12*, 845–853.
- (454) Ok, J. G.; Seok Youn, H.; Kyu Kwak, M.; Lee, K.-T.; Jae Shin, Y.; Jay Guo, L.; Greenwald, A.; Liu, Y. Continuous and Scalable Fabrication of Flexible Metamaterial Films via Roll-to-Roll Nanoimprint Process for Broadband Plasmonic Infrared Filters. *Appl. Phys. Lett.* **2012**, *101* (22), 223102.
- (455) Pina-Hernandez, C.; Guo, L. J.; Fu, P.-F. High-Resolution Functional Epoxysilsesquioxane-Based Patterning Layers for Large-Area Nanoimprinting. *ACS Nano* **2010**, *4* (8), 4776–4784.
- (456) Murthy, S.; Pranov, H.; Feidenhans, N. A.; Madsen, J. S.; Hansen, P. E.; Pedersen, H. C.; Taborsky, R. Plasmonic Color Metasurfaces Fabricated by a High Speed Roll-to-Roll Method. *Nanoscale* **2017**, *9* (37), 14280–14287.
- (457) Hao, J.; Lheurette, É.; Burgnies, L.; Okada, É.; Lippens, D. Bandwidth Enhancement in Disordered Metamaterial Absorbers. *Appl. Phys. Lett.* **2014**, *105*, 223102.
- (458) Zhai, Y.; Ma, Y.; David, S. N.; Zhao, D.; Lou, R.; Tan, G.; Yang, R.; Yin, X. Scalable-Manufactured Randomized Glass-Polymer Hybrid Metamaterial for Daytime Radiative Cooling. *Science* **2017**, *355* (6329), 1062–1066.
- (459) Rephaeli, E.; Raman, A.; Fan, S. Ultrabroadband Photonic Structures To Achieve High-Performance Daytime Radiative Cooling. *Nano Lett.* **2013**, *13* (4), 1457–1461.
- (460) Hossain, M. M.; Jia, B.; Gu, M. A Metamaterial Emitter for Highly Efficient Radiative Cooling. *Adv. Opt. Mater.* **2015**, *3* (8), 1047–1051.
- (461) Lin, K.-T.; Nian, X.; Li, K.; Han, J.; Zheng, N.; Lu, X.; Guo, C.; Lin, H.; Jia, B. Highly Efficient Flexible Structured Metasurface by

- Roll-to-Roll Printing for Diurnal Radiative Cooling. *eLight* **2023**, *3*, 22.
- (462) Lin, K.-T.; Nian, X.; Li, K.; Han, J.; Zheng, N.; Lu, X.; Guo, C.; Lin, H.; Jia, B. Highly Efficient Flexible Structured Metasurface by Roll-to-Roll Printing for Diurnal Radiative Cooling. *eLight* **2023**, *3*, 22.
- (463) Guo, L. J. Nanoimprint Lithography: Methods and Material Requirements. *Adv. Mater.* **2007**, *19* (4), 495–513.
- (464) Park, S.; Choi, K.; Kim, G.; Lee, J. Nanoscale Patterning with the Double-Layered Soft Cylindrical Stamps by Means of UV-Nanoimprint Lithography. *Microelectron. Eng.* **2009**, *86* (4–6), 604–607.
- (465) Ye, X.; Liu, H.; Ding, Y.; Li, H.; Lu, B. Research on the Cast Molding Process for High Quality PDMS Molds. *Microelectron. Eng.* **2009**, *86* (3), 310–313.
- (466) Leitgeb, M.; Nees, D.; Ruttloff, S.; Palfinger, U.; Götz, J.; Liska, R.; Belegratis, M. R.; Stadlober, B. Multilength Scale Patterning of Functional Layers by Roll-to-Roll Ultraviolet-Light-Assisted Nanoimprint Lithography. *ACS Nano* **2016**, *10* (5), 4926–4941.
- (467) Kotz, F.; Schneider, N.; Striegel, A.; Wolfschläger, A.; Keller, N.; Worgull, M.; Bauer, W.; Schild, D.; Milich, M.; Greiner, C.; Helmer, D.; Rapp, B. E. Glassomer—Processing Fused Silica Glass Like a Polymer. *Adv. Mater.* **2018**, *30* (22), 1707100.
- (468) Lee, J. H.; Na, M.; Kim, J.; Yoo, K.; Park, J.; Kim, J. D.; Oh, D. K.; Lee, S.; Youn, H.; Kwak, M. K.; Ok, J. G. Rapid and Conformal Coating of Polymer Resins by Airbrushing for Continuous and High-Speed Roll-to-Roll Nanopatterning: Parametric Quality Controls and Extended Applications. *Nano Converg.* **2017**, *4*, 11.
- (469) Donie, Y. J.; Ramamurthy, M.; Chakraborty, R. D.; Francis, L. F.; Frisbie, C. D.; Ferry, V. E. Roll-to-Roll Compatible Topochemical Wetting Control for Metamaterial Printing. *Adv. Opt. Mater.* **2024**, *12*, 2302785.
- (470) Badloe, T.; Kim, J.; Kim, I.; Kim, W.-S.; Kim, W. S.; Kim, Y.-K.; Rho, J. Liquid Crystal-Powered Mie Resonators for Electrically Tunable Photorealistic Color Gradients and Dark Blacks. *Light Sci. Appl.* **2022**, *11*, 118.
- (471) Kim, I.; Jang, J.; Kim, G.; Lee, J.; Badloe, T.; Mun, J.; Rho, J. Pixelated Bifunctional Metasurface-Driven Dynamic Vectorial Holographic Color Prints for Photonic Security Platform. *Nat. Commun.* **2021**, *12*, 3614.
- (472) Ansari, M. A.; Kim, I.; Lee, D.; Waseem, M. H.; Zubair, M.; Mahmood, N.; Badloe, T.; Yerci, S.; Tauqueer, T.; Mehmood, M. Q.; Rho, J. A Spin-Encoded All-Dielectric Metahologram for Visible Light. *Laser Photonics Rev.* **2019**, *13* (5), 1900065.
- (473) Tittl, A.; Leitis, A.; Liu, M.; Yesilkoy, F.; Choi, D.-Y.; Neshev, D. N.; Kivshar, Y. S.; Altug, H. Imaging-Based Molecular Barcoding with Pixelated Dielectric Metasurfaces. *Science* **2018**, *360* (6393), 1105–1109.
- (474) Yesilkoy, F.; Arvelo, E. R.; Jahani, Y.; Liu, M.; Tittl, A.; Cevher, V.; Kivshar, Y.; Altug, H. Ultrasensitive Hyperspectral Imaging and Biodetection Enabled by Dielectric Metasurfaces. *Nat. Photonics* **2019**, *13* (6), 390–396.
- (475) Jahani, Y.; Arvelo, E. R.; Yesilkoy, F.; Koshelev, K.; Cianciaruso, C.; De Palma, M.; Kivshar, Y.; Altug, H. Imaging-Based Spectrometer-Less Optofluidic Biosensors Based on Dielectric Metasurfaces for Detecting Extracellular Vesicles. *Nat. Commun.* **2021**, *12*, 3246.
- (476) Nguyen, D. D.; Lee, S.; Kim, I. Recent Advances in Metaphotonic Biosensors. *Biosensors* **2023**, *13* (6), 631.
- (477) Barulin, A.; Nguyen, D. D.; Kim, Y.; Ko, C.; Kim, I. Metasurfaces for Quantitative Biosciences of Molecules, Cells, and Tissues: Sensing and Diagnostics. *ACS Photonics* **2024**, *11* (3), 904–916.
- (478) Kim, K.; Yoon, G.; Baek, S.; Rho, J.; Lee, H. Facile Nanocasting of Dielectric Metasurfaces with Sub-100 nm Resolution. *ACS Appl. Mater. Interfaces* **2019**, *11* (29), 26109–26115.
- (479) Barulin, A.; Kim, Y.; Oh, D. K.; Jang, J.; Park, H.; Rho, J.; Kim, I. Dual-Wavelength Metalens Enables Epi-Fluorescence Detection from Single Molecules. *Nat. Commun.* **2024**, *15*, 26.
- (480) Shalaginov, M. Y.; An, S.; Zhang, Y.; Yang, F.; Su, P.; Liberman, V.; Chou, J. B.; Roberts, C. M.; Kang, M.; Rios, C.; et al. Reconfigurable All-Dielectric Metalens with Diffraction-Limited Performance. *Nat. commun.* **2021**, *12*, 1225.
- (481) Yin, X.; Park, J.-S.; Stensvad, K. K.; Brott, R. L.; Rubin, N.; Wolk, M. B.; Capasso, F. Roll-to-Roll Dielectric Metasurfaces. In *Metamaterials, Metadevices, and Metasystems 2020*; SPIE, 2020; Vol. 11460, p 114600S DOI: 10.1117/12.2576210.
- (482) Kim, I.; Martins, R. J.; Jang, J.; Badloe, T.; Khadir, S.; Jung, H.-Y.; Kim, H.; Kim, J.; Genet, P.; Rho, J. Nanophotonics for Light Detection and Ranging Technology. *Nat. nanotechnol.* **2021**, *16* (5), 508–524.
- (483) Ruchhoeft, P.; Colburn, M.; Choi, B.; Nounou, H.; Johnson, S.; Bailey, T.; Damle, S.; Stewart, M.; Ekerdt, J.; Sreenivasan, S. V.; et al. Patterning Curved Surfaces: Template Generation by Ion Beam Proximity Lithography and Relief Transfer by Step and Flash Imprint Lithography. *J. Vac. Sci. Technol. B Microelectron. Nanometer Struct. Proc., Meas. Phenom.* **1999**, *17* (6), 2965–2969.
- (484) Dauksher, W. J.; Nordquist, K. J.; Mancini, D. P.; Resnick, D. J.; Baker, J. H.; Hooper, A. E.; Talin, A. A.; Bailey, T. C.; Lemonds, A. M.; Sreenivasan, S. V.; et al. Characterization of and Imprint Results Using Indium Tin Oxide-Based Step and Flash Imprint Lithography Templates. *J. Vac. Sci. Technol. B Microelectron. Nanometer Struct. Proc. Meas. Phenom.* **2002**, *20* (6), 2857–2861.
- (485) Le, N. V.; Dauksher, W. J.; Gehoski, K. A.; Nordquist, K. J.; Ainley, E.; Mangat, P. Direct Pattern Transfer for Sub-45 nm Features Using Nanoimprint Lithography. *Microelectron. Eng.* **2006**, *83* (4–9), 839–842.
- (486) Perret, C.; Gourgon, C.; Lazzarino, F.; Tallal, J.; Landis, S.; Pelzer, R. Characterization of 8-in. Wafers Printed by Nanoimprint Lithography. *Microelectron. Eng.* **2004**, *73*, 172–177.
- (487) Hiroshima, H.; Komuro, M. Control of Bubble Defects in UV Nanoimprint. *Japanese J. appl. phys.* **2007**, *46* (9S), 6391.
- (488) Hiroshima, H. Quick Cavity Filling in UV Nanoimprint Using Pentafluoropropane. *Japanese J. Appl. phys.* **2008**, *47* (6S), S151.
- (489) Hiroshima, H.; Atobe, H.; Wang, Q.; Youn, S.-W. UV Nanoimprint in Pentafluoropropane at a Minimal Imprint Pressure. *Japanese J. appl. phys.* **2010**, *49* (6S), No. 06GL01.
- (490) Colburn, M.; Bailey, T.; Choi, B. J.; Ekerdt, J. G.; Sreenivasan, S. V.; Willson, C. G. Development and Advantages of Step-and-Flash Lithography. *Sol. State Technol.* **2001**, *44* (7), 67–80.
- (491) Bessonov, A.; Cho, Y.; Jung, S.-J.; Park, E.-A.; Hwang, E.-S.; Lee, J.-W.; Shin, M.; Lee, S. Nanoimprint Patterning for Tunable Light Trapping in Large-Area Silicon Solar Cells. *Sol. Energy Mater. Sol. Cells* **2011**, *95* (10), 2886–2892.
- (492) Choi, C.-G.; Kee, C.-S.; Shift, H. Fabrication of Polymer Photonic Crystal Slabs Using Nanoimprint Lithography. *Current Appl. Phys.* **2006**, *6*, e8–e11.
- (493) Kim, G. E.; Kim, H.; Woo, K.; Kang, Y.; Lee, S.-H.; Jeon, Y.; Lee, M. G.; Kwon, S. Uniform Pressing Mechanism in Large-Area Roll-to-Roll Nanoimprint Lithography Process. *Appl. Sci.* **2021**, *11* (20), 9571.
- (494) Snieder, J.; Dielen, M.; van Ostden, R. A. Simulating the Residual Layer Thickness in Roll-to-Plate Nanoimprinting with Tensioned Webs. *Micromachines* **2022**, *13* (3), 461.
- (495) Jain, A.; Bonnecaze, R. T. Fluid Management in Roll-to-Roll Nanoimprint Lithography. *J. Appl. Phys.* **2013**, *113* (23), 234511.
- (496) Tahir, U.; Kim, J. I.; Javeed, S.; Khaliq, A.; Kim, J.-H.; Kim, D.-I.; Jeong, M. Y. Process Optimization for Manufacturing Functional Nanosurfaces by Roll-to-Roll Nanoimprint Lithography. *Nanomaterials* **2022**, *12* (3), 480.
- (497) Jacobo-Martín, A.; Jost, N.; Hernández, J. J.; Domínguez, C.; Vallerotto, G.; Askins, S.; Antón, I.; Rodríguez, I. Roll-to-Roll Nanoimprint Lithography of High Efficiency Fresnel Lenses for Micro-Concentrator Photovoltaics. *Opt. Express* **2021**, *29* (21), 34135–34149.
- (498) Tanner, N. P.; In *Decrees of the Ecumenical Councils: Vol. 1: Nicaea I to Lateran V*; Georgetown University Press, 2016.

- (499) Pérez-Villar, S.; Rubio, J.; Oteo, J. L. Study of Color and Structural Changes in Silver Painted Medieval Glasses. *J. Non-Cryst. Solids* **2008**, *354* (17), 1833–1844.
- (500) Maier, S. A. *Plasmonics: Fundamentals and Applications*; Springer, 2007.
- (501) Wang, H.; Brandl, D. W.; Nordlander, P.; Halas, N. J. Plasmonic Nanostructures: Artificial Molecules. *Acc. Chem. Res.* **2007**, *40* (1), 53–62.
- (502) Maier, S. A.; Atwater, H. A. Plasmonics: Localization and Guiding of Electromagnetic Energy in Metal/Dielectric Structures. *J. Appl. Phys.* **2005**, *98* (1), No. 011101.
- (503) Barnes, W. L.; Dereux, A.; Ebbesen, T. W. Surface Plasmon Subwavelength Optics. *Nature* **2003**, *424* (6950), 824–830.
- (504) Murray, W. A.; Barnes, W. L. Plasmonic Materials. *Adv. Mater.* **2007**, *19* (22), 3771–3782.
- (505) Ozbay, E. Plasmonics: Merging Photonics and Electronics at Nanoscale Dimensions. *Science* **2006**, *311* (5758), 189–193.
- (506) Hutter, E.; Fendler, J. H. Exploitation of Localized Surface Plasmon Resonance. *Adv. Mater.* **2004**, *16* (19), 1685–1706.
- (507) Schuller, J. A.; Barnard, E. S.; Cai, W.; Jun, Y. C.; White, J. S.; Brongersma, M. L. Plasmonics for Extreme Light Concentration and Manipulation. *Nat. Mater.* **2010**, *9* (3), 193–204.
- (508) Stewart, M. E.; Anderton, C. R.; Thompson, L. B.; Maria, J.; Gray, S. K.; Rogers, J. A.; Nuzzo, R. G. Nanostructured Plasmonic Sensors. *Chem. Rev.* **2008**, *108* (2), 494–521.
- (509) Li, M.; Cushing, S. K.; Wu, N. Plasmon-Enhanced Optical Sensors: A Review. *Analyst* **2015**, *140* (2), 386–406.
- (510) Shrivastav, A. M.; Cvelbar, U.; Abdulhalim, I. A Comprehensive Review on Plasmonic-Based Biosensors Used in Viral Diagnostics. *Commun. Biol.* **2021**, *4*, 70.
- (511) Butt, M. A.; Kazanskiy, N. L.; Khonina, S. N.; Voronkov, G. S.; Grakhova, E. P.; Kutlyarov, R. V. A Review on Photonic Sensing Technologies: Status and Outlook. *Biosensors* **2023**, *13* (5), 568.
- (512) Biswas, A.; Cencillo-Abad, P.; Shabbir, M. W.; Karmakar, M.; Chanda, D. Tunable Plasmonic Superchiral Light for Ultrasensitive Detection of Chiral Molecules. *Sci. Adv.* **2024**, *10* (8), eadk2560.
- (513) Wang, Y.; Sun, T.; Paudel, T.; Zhang, Y.; Ren, Z.; Kempa, K. Metamaterial-Plasmonic Absorber Structure for High Efficiency Amorphous Silicon Solar Cells. *Nano Lett.* **2012**, *12* (1), 440–445.
- (514) Cui, Y.; He, Y.; Jin, Y.; Ding, F.; Yang, L.; Ye, Y.; Zhong, S.; Lin, Y.; He, S. Plasmonic and Metamaterial Structures as Electromagnetic Absorbers. *Laser Photonics Rev.* **2014**, *8* (4), 495–520.
- (515) Fei Guo, C.; Sun, T.; Cao, F.; Liu, Q.; Ren, Z. Metallic Nanostructures for Light Trapping in Energy-Harvesting Devices. *Light Sci. Appl.* **2014**, *3* (4), e161–e161.
- (516) Green, M. A.; Pillai, S. Harnessing Plasmonics for Solar Cells. *Nat. Photonics* **2012**, *6* (3), 130–132.
- (517) Guo, T.; Dasgupta, A.; Chandra, S.; Ballav, S.; Cencillo-Abad, P.; Mukherjee, S.; Biswas, A.; Shabbir, M. W.; Chanda, D. Frequency Modulation Based Long-Wave Infrared Detection and Imaging at Room Temperature. *Adv. Funct. Mater.* **2024**, *34* (4), 2309298.
- (518) Catchpole, K. R.; Polman, A. Plasmonic Solar Cells. *Opt. Express* **2008**, *16* (26), 21793–21800.
- (519) Ferry, V. E.; Verschuren, M. A.; Li, H. B. T.; Verhagen, E.; Walters, R. J.; Schropp, R. E. I.; Atwater, H. A.; Polman, A. Light Trapping in Ultrathin Plasmonic Solar Cells. *Opt. Express* **2010**, *18* (102), A237–A245.
- (520) Safaei, A.; Chandra, S.; Vázquez-Guardado, A.; Calderon, J.; Franklin, D.; Tetard, L.; Zhai, L.; Leuenberger, M. N.; Chanda, D. Dynamically Tunable Extraordinary Light Absorption in Monolayer Graphene. *Phys. Rev. B* **2017**, *96* (16), 165431.
- (521) Vázquez-Guardado, A.; Safaei, A.; Modak, S.; Franklin, D.; Chanda, D. Hybrid Coupling Mechanism in a System Supporting High Order Diffraction, Plasmonic, and Cavity Resonances. *Phys. Rev. Lett.* **2014**, *113*, 263902.
- (522) Pendry, J. B. Negative Refraction Makes a Perfect Lens. *Phys. Rev. Lett.* **2000**, *85* (18), 3966–3969.
- (523) Chanda, D.; Shigeta, K.; Gupta, S.; Cain, T.; Carlson, A.; Mihi, A.; Baca, A. J.; Bogart, G. R.; Braun, P.; Rogers, J. A. Large-Area Flexible 3D Optical Negative Index Metamaterial Formed by Nanotransfer Printing. *Nat. Nanotechnol.* **2011**, *6* (7), 402–407.
- (524) Gao, L.; Kim, Y.; Vazquez-Guardado, A.; Shigeta, K.; Hartanto, S.; Franklin, D.; Progler, C. J.; Bogart, G. R.; Rogers, J. A.; Chanda, D. Materials Selections and Growth Conditions for Large-Area, Multilayered, Visible Negative Index Metamaterials Formed by Nanotransfer Printing. *Adv. Opt. Mater.* **2014**, *2* (3), 256–261.
- (525) Gao, L.; Shigeta, K.; Vazquez-Guardado, A.; Progler, C. J.; Bogart, G. R.; Rogers, J. A.; Chanda, D. Nanoimprinting Techniques for Large-Area Three-Dimensional Negative Index Metamaterials with Operation in the Visible and Telecom Bands. *ACS Nano* **2014**, *8* (6), 5535–5542.
- (526) Schurig, D.; Mock, J. J.; Justice, B. J.; Cummer, S. A.; Pendry, J. B.; Starr, A. F.; Smith, D. R. Metamaterial Electromagnetic Cloak at Microwave Frequencies. *Science* **2006**, *314* (5801), 977–980.
- (527) Engheta, N.; Ziolkowski, R. W. *Metamaterials: Physics and Engineering Explorations*; John Wiley & Sons, 2006.
- (528) Cencillo-Abad, P.; Zheludev, N. I.; Plum, E. Metadevice for Intensity Modulation with Sub-Wavelength Spatial Resolution. *Sci. Rep.* **2016**, *6* (1), 37109.
- (529) Cencillo-Abad, P.; Plum, E.; Rogers, E. T. F.; Zheludev, N. I. Spatial Optical Phase-Modulating Metadevice with Subwavelength Pixelation. *Opt. Express* **2016**, *24* (16), 18790–18798.
- (530) Franklin, D.; Frank, R.; Wu, S.-T.; Chanda, D. Actively Addressed Single Pixel Full-Colour Plasmonic Display. *Nat. Commun.* **2017**, *8*, 15209.
- (531) Cai, X.; Zhang, L.; Ou, J.-Y.; Wang, Q.; Cencillo-Abad, P. Tunable Angle-Selective Optical Transparency Induced by Photonic Topological Transition in Dirac Semimetals-Based Hyperbolic Metamaterials. *Opt. Express* **2022**, *30* (13), 23102–23114.
- (532) Zhang, L.; Liu, W.; Cencillo-Abad, P.; Wang, Q.; Huang, X.; Leng, Y. A Tunable Broadband Polarization-Independent Metamaterial Terahertz Absorber Based on VO<sub>2</sub> and Dirac Semimetal. *Opt. Commun.* **2023**, *542*, 129602.
- (533) Zheludev, N. I.; Kivshar, Y. S. From Metamaterials to Metadevices. *Nat. Mater.* **2012**, *11* (11), 917–924.
- (534) Maier, S. A.; Brongersma, M. L.; Kik, P. G.; Meltzer, S.; Requicha, A. a. G.; Atwater, H. A. Plasmonics—A Route to Nanoscale Optical Devices. *Adv. Mater.* **2001**, *13* (19), 1501–1505.
- (535) Mattox, D. M. *Handbook of Physical Vapor Deposition (PVD) Processing*; William Andrew, 2010.
- (536) Cao, G. *Nanostructures & Nanomaterials: Synthesis, Properties & Applications*; Imperial College Press, 2004.
- (537) Ohring, M. *Materials Science of Thin Films: Deposition and Structure*; Elsevier, 2001.
- (538) Biswas, A.; Bayer, I. S.; Biris, A. S.; Wang, T.; Dervishi, E.; Faupel, F. Advances in Top-down and Bottom-up Surface Nanofabrication: Techniques, Applications & Future Prospects. *Adv. Colloid Interface Sci.* **2012**, *170* (1), 2–27.
- (539) Gates, B. D.; Xu, Q.; Stewart, M.; Ryan, D.; Willson, C. G.; Whitesides, G. M. New Approaches to Nanofabrication: Molding, Printing, and Other Techniques. *Chem. Rev.* **2005**, *105* (4), 1171–1196.
- (540) Ariga, K.; Hill, J. P.; Ji, Q. Layer-by-Layer Assembly as a Versatile Bottom-up Nanofabrication Technique for Exploratory Research and Realistic Application. *Phys. Chem. Chem. Phys.* **2007**, *9* (19), 2319–2340.
- (541) Chen, Y.; Pépin, A. Nanofabrication: Conventional and Nonconventional Methods. *Electrophor.* **2001**, *22* (2), 187–207.
- (542) Tan, S. J.; Campolongo, M. J.; Luo, D.; Cheng, W. Building Plasmonic Nanostructures with DNA. *Nat. Nanotechnol.* **2011**, *6* (5), 268–276.
- (543) Kim, S.-H.; Lee, S. Y.; Yang, S.-M.; Yi, G.-R. Self-Assembled Colloidal Structures for Photonics. *NPG Asia Mater.* **2011**, *3*, 25–33.
- (544) Hawkeye, M. M.; Brett, M. J. Glancing Angle Deposition: Fabrication, Properties, and Applications of Micro- and Nanostructured Thin Films. *J. Vac. Sci. Technol. A* **2007**, *25* (5), 1317–1335.

- (545) Franklin, D.; He, Z.; Mastranzo Ortega, P.; Safaei, A.; Cencillo-Abad, P.; Wu, S.-T.; Chanda, D. Self-Assembled Plasmonics for Angle-Independent Structural Color Displays with Actively Addressed Black States. *Proc. Natl. Acad. Sci. U.S.A.* **2020**, *117* (24), 13350–13358.
- (546) Daqiqeh Rezaei, S.; Dong, Z.; You En Chan, J.; Trisno, J.; Ng, R. J. H.; Ruan, Q.; Qiu, C. W.; Mortensen, N. A.; Yang, J. K. W. Nanophotonic Structural Colors. *ACS Photonics* **2021**, *8* (1), 18–33.
- (547) Cencillo-Abad, P.; McCormack, S.; Guo, T.; Biswas, A.; Chanda, D. Angle- and Polarization-Independent Structural Color Based on Controlled Phase and Gain Margins in Ultrathin Transparent Dielectrics. *ACS Photonics* **2023**, *10* (8), 2909–2917.
- (548) Cencillo-Abad, P.; Franklin, D.; Mastranzo-Ortega, P.; Sanchez-Mondragon, J.; Chanda, D. Ultralight Plasmonic Structural Color Paint. *Sci. Adv.* **2023**, *9* (10), eadf7207.
- (549) Moscatelli, A. Plasmonic Structural Colour Paint Gets Commercial Attention. *Nat. Nanotechnol.* **2023**, *18* (7), 703–703.
- (550) Brolo, A. G. Plasmonics for Future Biosensors. *Nat. Photonics* **2012**, *6* (11), 709–713.
- (551) Cencillo-Abad, P.; Mastranzo-Ortega, P.; Appavoo, D.; Guo, T.; Zhai, L.; Sanchez-Mondragon, J.; Chanda, D. Reusable Structural Colored Nanostructure for Powerless Temperature and Humidity Sensing. *Adv. Opt. Mater.* **2023**, *11* (16), 2300300.
- (552) Seeman, N. C. DNA in a Material World. *Nature* **2003**, *421* (6921), 427–431.
- (553) Douglas, S. M.; Dietz, H.; Liedl, T.; Höglberg, B.; Graf, F.; Shih, W. M. Self-Assembly of DNA into Nanoscale Three-Dimensional Shapes. *Nature* **2009**, *459* (7245), 414–418.
- (554) Wintersinger, C. M.; Minev, D.; Ershova, A.; Sasaki, H. M.; Gowri, G.; Berengut, J. F.; Corea-Dilbert, F. E.; Yin, P.; Shih, W. M. Multi-Micron Crisscross Structures Grown from DNA-Origami Slats. *Nat. Nanotechnol.* **2023**, *18* (3), 281–289.
- (555) Seeman, N. C.; Sleiman, H. F. DNA Nanotechnology. *Nat. Rev. Mater.* **2018**, *3*, 17068.
- (556) Wagenbauer, K. F.; Engelhardt, F. A. S.; Stahl, E.; Hecht, V. K.; Stömmer, P.; Seebacher, F.; Meregalli, L.; Ketterer, P.; Gerling, T.; Dietz, H. How We Make DNA Origami. *ChemBioChem.* **2017**, *18* (19), 1873–1885.
- (557) Wagenbauer, K. F.; Sigl, C.; Dietz, H. Gigadalton-Scale Shape-Programmable DNA Assemblies. *Nature* **2017**, *552* (7683), 78–83.
- (558) Schreiber, R.; Do, J.; Roller, E.-M.; Zhang, T.; Schüller, V. J.; Nickels, P. C.; Feldmann, J.; Liedl, T. Hierarchical Assembly of Metal Nanoparticles, Quantum Dots and Organic Dyes Using DNA Origami Scaffolds. *Nat. Nanotechnol.* **2014**, *9*, 74–78.
- (559) Sun, W.; Boulais, E.; Hakobyan, Y.; Wang, W. L.; Guan, A.; Bathe, M.; Yin, P. Casting Inorganic Structures with DNA Molds. *Science* **2014**, *346* (6210), 1258361.
- (560) Posnjak, G.; Yin, X.; Butler, P.; Bienek, O.; Dass, M.; Lee, S.; Sharp, I. D.; Liedl, T. Diamond-Lattice Photonic Crystals Assembled from DNA Origami. *Science* **2024**, *384* (6697), 781–785.
- (561) Liu, H.; Matthies, M.; Russo, J.; Rovigatti, L.; Narayanan, R. P.; Diep, T.; McKeen, D.; Gang, O.; Stephanopoulos, N.; Sciortino, F.; Yan, H.; Romano, F.; Sulc, P. Inverse Design of a Pyrochlore Lattice of DNA Origami through Model-Driven Experiments. *Science* **2024**, *384* (6697), 776–781.
- (562) Winfree, E.; Liu, F.; Wenzler, L. A.; Seeman, N. C. Design and Self-Assembly of Two-Dimensional DNA Crystals. *Nature* **1998**, *394* (6693), 539–544.
- (563) Mirkin, C. A.; Letsinger, R. L.; Mucic, R. C.; Storhoff, J. J. A DNA-Based Method for Rationally Assembling Nanoparticles into Macroscopic Materials. *Nature* **1996**, *382* (6592), 607–609.
- (564) Zheng, J.; Birktoft, J. J.; Chen, Y.; Wang, T.; Sha, R.; Constantiou, P. E.; Ginell, S. L.; Mao, C.; Seeman, N. C. From Molecular to Macroscopic via the Rational Design of a Self-Assembled 3D DNA Crystal. *Nature* **2009**, *461* (7260), 74–77.
- (565) Tian, Y.; Zhang, Y.; Wang, T.; Xin, H. L.; Li, H.; Gang, O. Lattice Engineering through Nanoparticle-DNA Frameworks. *Nat. Mater.* **2016**, *15* (6), 654–661.
- (566) Zhang, T.; Hartl, C.; Frank, K.; Heuer-Jungemann, A.; Fischer, S.; Nickels, P. C.; Nickel, B.; Liedl, T. 3D DNA Origami Crystals. *Adv. Mater.* **2018**, *30* (28), 1800273.
- (567) Zhang, C.; Macfarlane, R. J.; Young, K. L.; Choi, C. H. J.; Hao, L.; Auyeung, E.; Liu, G.; Zhou, X.; Mirkin, C. A. A General Approach to DNA-Programmable Atom Equivalents. *Nat. Mater.* **2013**, *12* (8), 741–746.
- (568) Acuna, G. P.; Möller, F. M.; Holzmeister, P.; Beater, S.; Lalkens, B.; Tinnefeld, P. Fluorescence Enhancement at Docking Sites of DNA-Directed Self-Assembled Nanoantennas. *Science* **2012**, *338* (6106), 506–510.
- (569) Gür, F. N.; McPolin, C. P. T.; Raza, S.; Mayer, M.; Roth, D. J.; Steiner, A. M.; Löffler, M.; Fery, A.; Brongersma, M. L.; Zayats, A. V.; König, T. A. F.; Schmidt, T. L. DNA-Assembled Plasmonic Waveguides for Nanoscale Light Propagation to a Fluorescent Nanodiamond. *Nano Lett.* **2018**, *18* (11), 7323–7329.
- (570) Maune, H. T.; Han, S.-p.; Barish, R. D.; Bockrath, M.; Goddard, W. A., III; Rothenmund, P. W. K.; Winfree, E. Self-Assembly of Carbon Nanotubes into Two-Dimensional Geometries Using DNA Origami Templates. *Nat. Nanotechnol.* **2010**, *5*, 61–66.
- (571) Bui, H.; Onodera, C.; Kidwell, C.; Tan, Y.; Graugnard, E.; Kuang, W.; Lee, J.; Knowlton, W. B.; Yurke, B.; Hughes, W. L. Programmable Periodicity of Quantum Dot Arrays with DNA Origami Nanotubes. *Nano Lett.* **2010**, *10* (9), 3367–3372.
- (572) Funke, J. J.; Dietz, H. Placing Molecules with Bohr Radius Resolution Using DNA Origami. *Nat. Nanotechnol.* **2016**, *11*, 47–52.
- (573) Fischer, S.; Hartl, C.; Frank, K.; Rädler, J. O.; Liedl, T.; Nickel, B. Shape and Interhelical Spacing of DNA Origami Nanostructures Studied by Small-Angle X-Ray Scattering. *Nano Lett.* **2016**, *16* (7), 4282–4287.
- (574) Adamczyk, A. K.; Huijben, T. A. P. M.; Sison, M.; Di Luca, A.; Chiarelli, G.; Vanni, S.; Brasselet, S.; Mortensen, K. I.; Stefani, F. D.; Pilo-Pais, M.; Acuna, G. P. DNA Self-Assembly of Single Molecules with Deterministic Position and Orientation. *ACS Nano* **2022**, *16* (10), 16924–16931.
- (575) Hartl, C.; Frank, K.; Amenitsch, H.; Fischer, S.; Liedl, T.; Nickel, B. Position Accuracy of Gold Nanoparticles on DNA Origami Structures Studied with Small-Angle X-Ray Scattering. *Nano Lett.* **2018**, *18* (4), 2609–2615.
- (576) Reinhardt, S. C. M.; Masullo, L. A.; Baudrexel, I.; Steen, P. R.; Kowalewski, R.; Eklund, A. S.; Strauss, S.; Unterauer, E. M.; Schlichthaerle, T.; Strauss, M. T.; Klein, C.; Jungmann, R. Ångström-Resolution Fluorescence Microscopy. *Nature* **2023**, *617* (7962), 711–716.
- (577) Jungmann, R.; Steinhauer, C.; Scheible, M.; Kuzyk, A.; Tinnefeld, P.; Simmel, F. C. Single-Molecule Kinetics and Super-Resolution Microscopy by Fluorescence Imaging of Transient Binding on DNA Origami. *Nano Lett.* **2010**, *10* (11), 4756–4761.
- (578) Liu, N.; Liedl, T. DNA-Assembled Advanced Plasmonic Architectures. *Chem. Rev.* **2018**, *118* (6), 3032–3053.
- (579) Kuzyk, A.; Schreiber, R.; Fan, Z.; Pardatscher, G.; Roller, E.-M.; Högele, A.; Simmel, F. C.; Govorov, A. O.; Liedl, T. DNA-Based Self-Assembly of Chiral Plasmonic Nanostructures with Tailored Optical Response. *Nature* **2012**, *483* (7389), 311–314.
- (580) Roller, E.-M.; Besteiro, L. V.; Pupp, C.; Khorashad, L. K.; Govorov, A. O.; Liedl, T. Hotspot-Mediated Non-Dissipative and Ultrafast Plasmon Passage. *Nat. Phys.* **2017**, *13* (8), 761–765.
- (581) Acuna, G. P.; Bucher, M.; Stein, I. H.; Steinhauer, C.; Kuzyk, A.; Holzmeister, P.; Schreiber, R.; Moroz, A.; Stefani, F. D.; Liedl, T.; Simmel, F. C.; Tinnefeld, P. Distance Dependence of Single-Fluorophore Quenching by Gold Nanoparticles Studied on DNA Origami. *ACS Nano* **2012**, *6* (4), 3189–3195.
- (582) Nickels, P. C.; Wünsch, B.; Holzmeister, P.; Bae, W.; Kneer, L. M.; Grohmann, D.; Tinnefeld, P.; Liedl, T. Molecular Force Spectroscopy with a DNA Origami-Based Nanoscopic Force Clamp. *Science* **2016**, *354* (6310), 305–307.
- (583) Curto, A. G.; Volpe, G.; Tamini, T. H.; Kreuzer, M. P.; Quidant, R.; van Hulst, N. F. Unidirectional Emission of a Quantum Dot Coupled to a Nanoantenna. *Science* **2010**, *329* (5994), 930–933.

- (584) Kolbeck, P. J.; Dass, M.; Martynenko, I. V.; van Dijk-Moes, R. J. A.; Brouwer, K. J. H.; van Blaaderen, A.; Vanderlinde, W.; Liedl, T.; Lipfert, J. DNA Origami Fiducial for Accurate 3D Atomic Force Microscopy Imaging. *Nano Lett.* **2023**, *23* (4), 1236–1243.
- (585) Pilo-Pais, M.; Acuna, G. P.; Tinnefeld, P.; Liedl, T. Sculpting Light by Arranging Optical Components with DNA Nanostructures. *MRS Bull.* **2017**, *42* (12), 936–942.
- (586) Kuzyk, A.; Jungmann, R.; Acuna, G. P.; Liu, N. DNA Origami Route for Nanophotonics. *ACS Photonics* **2018**, *5* (4), 1151–1163.
- (587) Cho, Y.; Park, S. H.; Huh, J.-H.; Gopinath, A.; Lee, S. DNA as Grabbers and Steerers of Quantum Emitters. *Nanophotonics* **2023**, *12* (3), 399–412.
- (588) Liu, J.; Geng, Y.; Pound, E.; Gyawali, S.; Ashton, J. R.; Hickey, J.; Woolley, A. T.; Harb, J. N. Metallization of Branched DNA Origami for Nanoelectronic Circuit Fabrication. *ACS Nano* **2011**, *5* (3), 2240–2247.
- (589) Schreiber, R.; Kempfer, S.; Holler, S.; Schüller, V.; Schiffels, D.; Simmel, S. S.; Nickels, P. C.; Liedl, T. DNA Origami-Templated Growth of Arbitrarily Shaped Metal Nanoparticles. *Small* **2011**, *7* (13), 1795–1799.
- (590) Shani, L.; Michelson, A. N.; Minevich, B.; Fleger, Y.; Stern, M.; Shaulov, A.; Yesheurun, Y.; Gang, O. DNA-Assembled Superconducting 3D Nanoscale Architectures. *Nat. Commun.* **2020**, *11*, 5697.
- (591) Liu, X.; Zhang, F.; Jing, X.; Pan, M.; Liu, P.; Li, W.; Zhu, B.; Li, J.; Chen, H.; Wang, L.; Lin, J.; Liu, Y.; Zhao, D.; Yan, H.; Fan, C. Complex Silica Composite Nanomaterials Templated with DNA Origami. *Nature* **2018**, *559* (7715), 593–598.
- (592) Nguyen, L.; Döblinger, M.; Liedl, T.; Heuer-Jungemann, A. DNA-Origami-Templated Silica Growth by Sol–Gel Chemistry. *Angew. Chem. Inter. Ed.* **2019**, *58* (3), 912–916.
- (593) Michelson, A.; Subramanian, A.; Kisslinger, K.; Tiwale, N.; Xiang, S.; Shen, E.; Kahn, J. S.; Nykypanchuk, D.; Yan, H.; Nam, C.-Y.; Gang, O. Three-Dimensional Nanoscale Metal, Metal Oxide, and Semiconductor Frameworks through DNA-Programmable Assembly and Templating. *Sci. Adv.* **2024**, *10* (2), eadl0604.
- (594) Jia, S.; Wang, J.; Xie, M.; Sun, J.; Liu, H.; Zhang, Y.; Chao, J.; Li, J.; Wang, L.; Lin, J.; Gothelf, K. V.; Fan, C. Programming DNA Origami Patterning with Non-Canonical DNA-Based Metallization Reactions. *Nat. Commun.* **2019**, *10*, 5597.
- (595) Braun, E.; Eichen, Y.; Sivan, U.; Ben-Yoseph, G. DNA-Templated Assembly and Electrode Attachment of a Conducting Silver Wire. *Nature* **1998**, *391* (6669), 775–778.
- (596) Keren, K.; Krueger, M.; Gilad, R.; Ben-Yoseph, G.; Sivan, U.; Braun, E. Sequence-Specific Molecular Lithography on Single DNA Molecules. *Science* **2002**, *297* (5578), 72–75.
- (597) Deng, Z.; Mao, C. Molecular Lithography with DNA Nanostructures. *Angew. Chem. Inter. Ed.* **2004**, *43* (31), 4068–4070.
- (598) Shen, B.; Linko, V.; Tapiola, K.; Pikker, S.; Lemma, T.; Gopinath, A.; Gothelf, K. V.; Kostiainen, M. A.; Toppari, J. J. Plasmonic Nanostructures through DNA-Assisted Lithography. *Sci. Adv.* **2018**, *4* (2), eaap8978.
- (599) Piskunen, P.; Shen, B.; Keller, A.; Toppari, J. J.; Kostiainen, M. A.; Linko, V. Biotemplated Lithography of Inorganic Nanostructures (BLIN) for Versatile Patterning of Functional Materials. *ACS Appl. Nano Mater.* **2021**, *4* (1), 529–538.
- (600) Thomas, G.; Diagne, C. T.; Baillin, X.; Chevolleau, T.; Charvolin, T.; Tiron, R. DNA Origami for Silicon Patterning. *ACS Appl. Mater. Interfaces* **2020**, *12* (32), 36799–36809.
- (601) Surwade, S. P.; Zhao, S.; Liu, H. Molecular Lithography through DNA-Mediated Etching and Masking of SiO<sub>2</sub>. *J. Am. Chem. Soc.* **2011**, *133* (31), 11868–11871.
- (602) Diagne, C. T.; Brun, C.; Gasparutto, D.; Baillin, X.; Tiron, R. DNA Origami Mask for Sub-Ten-Nanometer Lithography. *ACS Nano* **2016**, *10* (7), 6458–6463.
- (603) Jin, Z.; Sun, W.; Ke, Y.; Shih, C.-J.; Paulus, G. L. C.; Hua Wang, Q.; Mu, B.; Yin, P.; Strano, M. S. Metallized DNA Nanolithography for Encoding and Transferring Spatial Information for Graphene Patterning. *Nat. Commun.* **2013**, *4*, 1663.
- (604) Kershner, R. J.; Bozano, L. D.; Micheel, C. M.; Hung, A. M.; Fornof, A. R.; Cha, J. N.; Rettner, C. T.; Bersani, M.; Frommer, J.; Rothemund, P. W. K.; Wallraff, G. M. Placement and Orientation of Individual DNA Shapes on Lithographically Patterned Surfaces. *Nat. Nanotechnol.* **2009**, *4* (9), 557–561.
- (605) Gopinath, A.; Rothemund, P. W. K. Optimized Assembly and Covalent Coupling of Single-Molecule DNA Origami Nanoarrays. *ACS Nano* **2014**, *8* (12), 12030–12040.
- (606) Martynenko, I. V.; Erber, E.; Ruider, V.; Dass, M.; Posnjak, G.; Yin, X.; Altpeter, P.; Liedl, T. Site-Directed Placement of Three-Dimensional DNA Origami. *Nat. Nanotechnol.* **2023**, *18* (12), 1456–1462.
- (607) Shetty, R. M.; Brady, S. R.; Rothemund, P. W. K.; Hariadi, R. F.; Gopinath, A. Bench-Top Fabrication of Single-Molecule Nanoarrays by DNA Origami Placement. *ACS Nano* **2021**, *15* (7), 11441–11450.
- (608) Martynenko, I. V.; Ruider, V.; Dass, M.; Liedl, T.; Nickels, P. C. DNA Origami Meets Bottom-Up Nanopatterning. *ACS Nano* **2021**, *15* (7), 10769–10774.
- (609) Sikeler, C.; Haslinger, F.; Martynenko, I. V.; Liedl, T. DNA Origami-Directed Self-Assembly of Gold Nanospheres for Plasmonic Metasurfaces. *Adv. Funct. Mater.* **2024**, *34* (42), 2404766.
- (610) Dass, M.; Raab, L.; Pauer, C.; Sikeler, C.; Heinze, L.; Tavacoli, J.; Martynenko, I. V.; Rührmair, U.; Posnjak, G.; Liedl, T. Self-Assembled Physical Unclonable Function Labels Based on Plasmonic Coupling. *arXiv*, **2023**, 2310.19587. (accessed Oct. 30, 2023).
- (611) Gopinath, A.; Miyazono, E.; Faraon, A.; Rothemund, P. W. K. Engineering and Mapping Nanocavity Emission via Precision Placement of DNA Origami. *Nature* **2016**, *535* (7612), 401–405.
- (612) Gopinath, A.; Thachuk, C.; Mitskovets, A.; Atwater, H. A.; Kirkpatrick, D.; Rothemund, P. W. K. Absolute and Arbitrary Orientation of Single-Molecule Shapes. *Science* **2021**, *371* (6531), eabd6179.
- (613) Pibiri, E.; Holzmeister, P.; Lalkens, B.; Acuna, G. P.; Tinnefeld, P. Single-Molecule Positioning in Zeremode Waveguides by DNA Origami Nanoadapters. *Nano Lett.* **2014**, *14* (6), 3499–3503.
- (614) Hung, A. M.; Micheel, C. M.; Bozano, L. D.; Osterbur, L. W.; Wallraff, G. M.; Cha, J. N. Large-Area Spatially Ordered Arrays of Gold Nanoparticles Directed by Lithographically Confined DNA Origami. *Nat. Nanotechnol.* **2010**, *5* (2), 121–126.
- (615) Huang, D.; Freeley, M.; Palma, M. DNA-Mediated Patterning of Single Quantum Dot Nanoarrays: A Reusable Platform for Single-Molecule Control. *Sci. Rep.* **2017**, *7* (1), 45591.
- (616) Siegel, N.; Hasebe, H.; Chiarelli, G.; Garoli, D.; Sugimoto, H.; Fujii, M.; Acuna, G. P.; Kołataj, K. Universal Click-Chemistry Approach for the DNA Functionalization of Nanoparticles. *J. Am. Chem. Soc.* **2024**, *146* (25), 17250–17260.
- (617) Wang, Y.; Yu, Z.; Smith, C. S.; Caneva, S. Site-Specific Integration of Hexagonal Boron Nitride Quantum Emitters on 2D DNA Origami Nanopores. *Nano Lett.* **2024**, *24* (28), 8510–8517.
- (618) Yeşilyurt, A. T. M.; Sanz-Paz, M.; Zhu, F.; Wu, X.; Sunil, K. S.; Acuna, G. P.; Huang, J.-S. Unidirectional Meta-Emitters Based on the Kerker Condition Assembled by DNA Origami. *ACS Nano* **2023**, *17* (19), 19189–19196.
- (619) Douglas, S. M.; Marblestone, A. H.; Teerapittayanon, S.; Vazquez, A.; Church, G. M.; Shih, W. M. Rapid Prototyping of 3D DNA-Origami Shapes with caDNAno. *Nucleic Acids Res.* **2009**, *37* (15), 5001–5006.
- (620) Kim, D.-N.; Kilchherr, F.; Dietz, H.; Bathe, M. Quantitative Prediction of 3D Solution Shape and Flexibility of Nucleic Acid Nanostructures. *Nucleic Acids Res.* **2012**, *40* (7), 2862–2868.
- (621) Poppletton, E.; Romero, R.; Mallya, A.; Rovigatti, L.; Šulc, P. OxDNA.Org: A Public Webserver for Coarse-Grained Simulations of DNA and RNA Nanostructures. *Nucleic Acids Res.* **2021**, *49* (W1), W491–W498.
- (622) Glaser, M.; Deb, S.; Seier, F.; Agrawal, A.; Liedl, T.; Douglas, S.; Gupta, M. K.; Smith, D. M. The Art of Designing DNA Nanostructures with CAD Software. *Molecules* **2021**, *26* (8), 2287.

- (623) Evans, C. G.; Winfree, E. Physical Principles for DNA Tile Self-Assembly. *Chem. Soc. Rev.* **2017**, *46* (12), 3808–3829.
- (624) Ke, Y.; Ong, L. L.; Shih, W. M.; Yin, P. Three-Dimensional Structures Self-Assembled from DNA Bricks. *Science* **2012**, *338* (6111), 1177–1183.
- (625) Wei, B.; Dai, M.; Yin, P. Complex Shapes Self-Assembled from Single-Stranded DNA Tiles. *Nature* **2012**, *485* (7400), 623–626.
- (626) Ong, L. L.; Hanikel, N.; Yaghi, O. K.; Grun, C.; Strauss, M. T.; Bron, P.; Lai-Kee-Him, J.; Schueider, F.; Wang, B.; Wang, P.; Kishi, J. Y.; Myhrvold, C.; Zhu, A.; Jungmann, R.; Bellot, G.; Ke, Y.; Yin, P. Programmable Self-Assembly of Three-Dimensional Nanostructures from 10,000 Unique Components. *Nature* **2017**, *552* (7683), 72–77.
- (627) Ke, Y.; Ong, L. L.; Sun, W.; Song, J.; Dong, M.; Shih, W. M.; Yin, P. DNA Brick Crystals with Prescribed Depths. *Nat. Chem.* **2014**, *6* (11), 994–1002.
- (628) Liu, W.; Zhong, H.; Wang, R.; Seeman, N. C. Crystalline Two-Dimensional DNA-Origami Arrays. *Angew. Chem. Inter. Ed.* **2011**, *50* (1), 264–267.
- (629) Wang, P.; Gaitanaros, S.; Lee, S.; Bathe, M.; Shih, W. M.; Ke, Y. Programming Self-Assembly of DNA Origami Honeycomb Two-Dimensional Lattices and Plasmonic Metamaterials. *J. Am. Chem. Soc.* **2016**, *138* (24), 7733–7740.
- (630) Tikhomirov, G.; Petersen, P.; Qian, L. Triangular DNA Origami Tilings. *J. Am. Chem. Soc.* **2018**, *140* (50), 17361–17364.
- (631) Wang, Y.; Dai, L.; Ding, Z.; Ji, M.; Liu, J.; Xing, H.; Liu, X.; Ke, Y.; Fan, C.; Wang, P.; Tian, Y. DNA Origami Single Crystals with Wulff Shapes. *Nat. Commun.* **2021**, *12*, 3011.
- (632) Chen, Y.; Yang, C.; Zhu, Z.; Sun, W. Suppressing High-Dimensional Crystallographic Defects for Ultra-Scaled DNA Arrays. *Nat. Commun.* **2022**, *13*, 2707.
- (633) Surwade, S. P.; Zhou, F.; Wei, B.; Sun, W.; Powell, A.; O'Donnell, C.; Yin, P.; Liu, H. Nanoscale Growth and Patterning of Inorganic Oxides Using DNA Nanostructure Templates. *J. Am. Chem. Soc.* **2013**, *135* (18), 6778–6781.
- (634) Zhao, M.; Chen, Y.; Wang, K.; Zhang, Z.; Streit, J. K.; Fagan, J. A.; Tang, J.; Zheng, M.; Yang, C.; Zhu, Z.; Sun, W. DNA-Directed Nanofabrication of High-Performance Carbon Nanotube Field-Effect Transistors. *Science* **2020**, *368* (6493), 878–881.
- (635) Chen, Y.; Zhao, M.; Ouyang, Y.; Zhang, S.; Liu, Z.; Wang, K.; Zhang, Z.; Liu, Y.; Yang, C.; Sun, W.; Shen, J.; Zhu, Z. Biотemplated Precise Assembly Approach toward Ultra-Scaled High-Performance Electronics. *Nat. Protoc.* **2023**, *18* (10), 2975–2997.
- (636) Sun, W.; Shen, J.; Zhao, Z.; Arellano, N.; Rettner, C.; Tang, J.; Cao, T.; Zhou, Z.; Ta, T.; Streit, J. K.; Fagan, J. A.; Schaus, T.; Zheng, M.; Han, S.-J.; Shih, W. M.; Maune, H. T.; Yin, P. Precise Pitch-Scaling of Carbon Nanotube Arrays within Three-Dimensional DNA Nanotrenches. *Science* **2020**, *368* (6493), 874–877.
- (637) Langer, J.; et al. Present and Future of Surface-Enhanced Raman Scattering. *ACS Nano* **2020**, *14* (1), 28–117.
- (638) Son, J.; Kim, G.-H.; Lee, Y.; Lee, C.; Cha, S.; Nam, J.-M. Toward Quantitative Surface-Enhanced Raman Scattering with Plasmonic Nanoparticles: Multiscale View on Heterogeneities in Particle Morphology, Surface Modification, Interface, and Analytical Protocols. *J. Am. Chem. Soc.* **2022**, *144* (49), 22337–22351.
- (639) Park, W.; Lu, D.; Ahn, S. Plasmon Enhancement of Luminescence Upconversion. *Chem. Soc. Rev.* **2015**, *44* (10), 2940–2962.
- (640) Huang, J.; Akselrod, G. M.; Ming, T.; Kong, J.; Mikkelsen, M. H. Tailored Emission Spectrum of 2D Semiconductors Using Plasmonic Nanocavities. *ACS Photonics* **2018**, *5* (2), 552–558.
- (641) Jung, Y.; Kim, Y.; Lee, Y.; Son, J.; Lim, M.; Nam, J.-M. Selective Flocculation and H<sub>2</sub>O<sub>2</sub>-Free Oxidative Etching-Based Synthesis of Highly Monodisperse Ag Nanospheres for Uniform Quantum Dot Photoluminescence-Enhancing Plasmonic Cavity Applications. *J. Am. Chem. Soc.* **2024**, *146* (15), 10591.
- (642) Giannini, V.; Fernández-Dominguez, A. I.; Heck, S. C.; Maier, S. A. Plasmonic Nanoantennas: Fundamentals and Their Use in Controlling the Radiative Properties of Nanoemitters. *Chem. Rev.* **2011**, *111* (6), 3888–3912.
- (643) Prodan, E.; Radloff, C.; Halas, N. J.; Nordlander, P. A Hybridization Model for the Plasmon Response of Complex Nanostructures. *Science* **2003**, *302* (5644), 419–422.
- (644) Kravets, V. G.; Kabashin, A. V.; Barnes, W. L.; Grigorenko, A. N. Plasmonic Surface Lattice Resonances: A Review of Properties and Applications. *Chem. Rev.* **2018**, *118* (12), 5912–5951.
- (645) Lu, X.; Rycenga, M.; Skrabalak, S. E.; Wiley, B.; Xia, Y. Chemical Synthesis of Novel Plasmonic Nanoparticles. *Annu. Rev. Phys. Chem.* **2009**, *60*, 167–192.
- (646) Lee, H.; Kim, G.-H.; Lee, J.-H.; Kim, N. H.; Nam, J.-M.; Suh, Y. D. Quantitative Plasmon Mode and Surface-Enhanced Raman Scattering Analyses of Strongly Coupled Plasmonic Nanotrimers with Diverse Geometries. *Nano Lett.* **2015**, *15* (7), 4628–4636.
- (647) Mock, J. J.; Hill, R. T.; Degiron, A.; Zauscher, S.; Chilkoti, A.; Smith, D. R. Distance-Dependent Plasmon Resonant Coupling between a Gold Nanoparticle and Gold Film. *Nano Lett.* **2008**, *8* (8), 2245–2252.
- (648) Fredriksson, H.; Alaverdyan, Y.; Dmitriev, A.; Langhammer, C.; Sutherland, D. S.; Zäch, M.; Kasemo, B. Hole-Mask Colloidal Lithography. *Adv. Mater.* **2007**, *19* (23), 4297–4302.
- (649) Bouanane, I.; Bedu, F.; Ozerov, I.; Sciacca, B.; Santinacci, L.; Duché, D.; Berginc, G.; Escoubas, L.; Margeat, O.; Le Rouzo, J. Design of Infrared Optical Absorber Using Silver Nanorings Array Made by a Top-down Process. *Sci. Rep.* **2023**, *13*, 7770.
- (650) Kosiorek, A.; Kandulski, W.; Glaczynska, H.; Giersig, M. Fabrication of Nanoscale Rings, Dots, and Rods by Combining Shadow Nanosphere Lithography and Annealed Polystyrene Nanosphere Masks. *Small* **2005**, *1* (4), 439–444.
- (651) Decker, M.; Klein, M. W.; Wegener, M.; Linden, S. Circular Dichroism of Planar Chiral Magnetic Metamaterials. *Opt. Lett.* **2007**, *32* (7), 856–858.
- (652) Henzie, J.; Lee, M. H.; Odom, T. W. Multiscale Patterning of Plasmonic Metamaterials. *Nat. Nanotechnol.* **2007**, *2* (9), 549–554.
- (653) Liu, N.; Mukherjee, S.; Bao, K.; Brown, L. V.; Dorfmüller, J.; Nordlander, P.; Halas, N. J. Magnetic Plasmon Formation and Propagation in Artificial Aromatic Molecules. *Nano Lett.* **2012**, *12* (1), 364–369.
- (654) Yang, A.; Hryny, A. J.; Bourgeois, M. R.; Lee, W.-K.; Hu, J.; Schatz, G. C.; Odom, T. W. Programmable and Reversible Plasmon Mode Engineering. *Proc. Natl. Acad. Sci. U.S.A.* **2016**, *113* (50), 14201–14206.
- (655) Lim, D.-K.; Jeon, K.-S.; Kim, H. M.; Nam, J.-M.; Suh, Y. D. Nanogap-Engineerable Raman-Active Nanodumbbells for Single-Molecule Detection. *Nat. Mater.* **2010**, *9*, 60–67.
- (656) Lee, J.-H.; Nam, J.-M.; Jeon, K.-S.; Lim, D.-K.; Kim, H.; Kwon, S.; Lee, H.; Suh, Y. D. Tuning and Maximizing the Single-Molecule Surface-Enhanced Raman Scattering from DNA-Tethered Nanodumbbells. *ACS Nano* **2012**, *6* (11), 9574–9584.
- (657) Lee, H.; Lee, J.-H.; Jin, S. M.; Suh, Y. D.; Nam, J.-M. Single-Molecule and Single-Particle-Based Correlation Studies between Localized Surface Plasmons of Dimeric Nanostructures with ~1 nm Gap and Surface-Enhanced Raman Scattering. *Nano Lett.* **2013**, *13* (12), 6113–6121.
- (658) Lee, H. E.; Ahn, H. Y.; Mun, J.; Lee, Y. Y.; Kim, M.; Cho, N. H.; Chang, K.; Kim, W. S.; Rho, J.; Nam, K. T. Amino-Acid- A Nd Peptide-Directed Synthesis of Chiral Plasmonic Gold Nanoparticles. *Nature* **2018**, *556* (7701), 360–364.
- (659) Kim, J.-M.; Kim, J.; Choi, K.; Nam, J.-M. Plasmonic Dual-Gap Nanodumbbells for Label-Free On-Particle Raman DNA Assays. *Adv. Mater.* **2023**, *35* (15), 2208250.
- (660) Nam, J.-M.; Oh, J.-W.; Lee, H.; Suh, Y. D. Plasmonic Nanogap-Enhanced Raman Scattering with Nanoparticles. *Acc. Chem. Res.* **2016**, *49* (12), 2746–2755.
- (661) Lim, D.-K.; Jeon, K.-S.; Hwang, J.-H.; Kim, H.; Kwon, S.; Suh, Y. D.; Nam, J.-M. Highly Uniform and Reproducible Surface-Enhanced Raman Scattering from DNA-Tailorable Nanoparticles with 1-nm Interior Gap. *Nat. Nanotechnol.* **2011**, *6* (7), 452–460.
- (662) Kim, J.-M.; Kim, J.; Ha, M.; Nam, J.-M. Cyclodextrin-Based Synthesis and Host–Guest Chemistry of Plasmonic Nanogap

- Particles with Strong, Quantitative, and Highly Multiplexable Surface-Enhanced Raman Scattering Signals. *J. Phys. Chem. Lett.* **2020**, *11* (19), 8358–8364.
- (663) Kim, M.; Ko, S. M.; Kim, J.-M.; Son, J.; Lee, C.; Rhim, W.-K.; Nam, J.-M. Dealloyed Intra-Nanogap Particles with Highly Robust, Quantifiable Surface-Enhanced Raman Scattering Signals for Biosensing and Bioimaging Applications. *ACS Cent. Sci.* **2018**, *4* (2), 277–287.
- (664) Oh, J.-W.; Lim, D.-K.; Kim, G.-H.; Suh, Y. D.; Nam, J.-M. Thiolated DNA-Based Chemistry and Control in the Structure and Optical Properties of Plasmonic Nanoparticles with Ultrasmall Interior Nanogap. *J. Am. Chem. Soc.* **2014**, *136* (40), 14052–14059.
- (665) Park, J.-E.; Kim, S.; Son, J.; Lee, Y.; Nam, J.-M. Highly Controlled Synthesis and Super-Radiant Photoluminescence of Plasmonic Cube-in-Cube Nanoparticles. *Nano Lett.* **2016**, *16* (12), 7962–7967.
- (666) Kim, J.; Kim, J.-M.; Choi, K.; Park, J.-E.; Nam, J.-M. Open Cross-Gap Gold Nanocubes with Strong, Large-Area, Symmetric Electromagnetic Field Enhancement for On-Particle Molecular-Fingerprint Raman Bioassays. *J. Am. Chem. Soc.* **2024**, *146* (20), 14012–14021.
- (667) Schulz, F.; Pavelka, O.; Lehmkühler, F.; Westermeier, F.; Okamura, Y.; Mueller, N. S.; Reich, S.; Lange, H. Structural Order in Plasmonic Superlattices. *Nat. Commun.* **2020**, *11*, 3821.
- (668) Kim, P. Y.; Oh, J.-W.; Nam, J.-M. Controlled Co-Assembly of Nanoparticles and Polymer into Ultralong and Continuous One-Dimensional Nanochains. *J. Am. Chem. Soc.* **2015**, *137* (25), 8030–8033.
- (669) Samanta, D.; Zhou, W.; Ebrahimi, S. B.; Petrosko, S. H.; Mirkin, C. A. Programmable Matter: The Nanoparticle Atom and DNA Bond. *Adv. Mater.* **2022**, *34* (12), 2107875.
- (670) Arul, R.; Grys, D.-B.; Chikkaraddy, R.; Mueller, N. S.; Xomalis, A.; Miele, E.; Euser, T. G.; Baumberg, J. J. Giant Mid-IR Resonant Coupling to Molecular Vibrations in Sub-Nm Gaps of Plasmonic Multilayer Metafilms. *Light Sci. Appl.* **2022**, *11*, 281.
- (671) Huh, J.-H.; Lee, J.; Lee, S. Soft Plasmonic Assemblies Exhibiting Unnaturally High Refractive Index. *Nano Lett.* **2020**, *20* (7), 4768–4774.
- (672) Isaacoff, B. P.; Brown, K. A. Progress in Top-Down Control of Bottom-Up Assembly. *Nano Lett.* **2017**, *17* (11), 6508–6510.
- (673) Flauraud, V.; Mastrangeli, M.; Bernasconi, G. D.; Butet, J.; Alexander, D. T. L.; Shahrami, E.; Martin, O. J. F.; Brugger, J. Nanoscale Topographical Control of Capillary Assembly of Nanoparticles. *Nat. Nanotechnol.* **2017**, *12*, 73–80.
- (674) Hanske, C.; González-Rubio, G.; Hamon, C.; Formentín, P.; Modin, E.; Chuvalin, A.; Guerrero-Martínez, A.; Marsal, L. F.; Liz-Marzán, L. M. Large-Scale Plasmonic Pyramidal Supercrystals via Templated Self-Assembly of Monodisperse Gold Nanospheres. *J. Phys. Chem. C* **2017**, *121* (20), 10899–10906.
- (675) Hueckel, T.; Lewis, D. J.; Mertiri, A.; Carter, D. J. D.; Macfarlane, R. J. Controlling Colloidal Crystal Nucleation and Growth with Photolithographically Defined Templates. *ACS Nano* **2023**, *17* (21), 22121–22128.
- (676) Liang, C.-C.; Liao, M.-Y.; Chen, W.-Y.; Cheng, T.-C.; Chang, W.-H.; Lin, C.-H. Plasmonic Metallic Nanostructures by Direct Nanoimprinting of Gold Nanoparticles. *Opt. Express* **2011**, *19* (5), 4768–4776.
- (677) Agrawal, H.; Garnett, E. C. Nanocube Imprint Lithography. *ACS Nano* **2020**, *14* (9), 11009–11016.
- (678) Vinnicombe-Willson, G. A.; Conti, Y.; Stefanču, A.; Weiss, P. S.; Cortés, E.; Scarabelli, L. Direct Bottom-Up In Situ Growth: A Paradigm Shift for Studies in Wet-Chemical Synthesis of Gold Nanoparticles. *Chem. Rev.* **2023**, *123* (13), 8488–8529.
- (679) Meinzer, N.; Barnes, W. L.; Hooper, I. R. Plasmonic Meta-Atoms and Metasurfaces. *Nat. Photonics* **2014**, *8* (12), 889–898.
- (680) Park, T.-H.; Nordlander, P. On the Nature of the Bonding and Antibonding Metallic Film and Nanoshell Plasmons. *Chem. Phys. Lett.* **2009**, *472* (4), 228–231.
- (681) Chikkaraddy, R.; Zheng, X.; Benz, F.; Brooks, L. J.; de Nijs, B.; Carnegie, C.; Kleemann, M.-E.; Mertens, J.; Bowman, R. W.; Vandenbergbosch, G. A. E.; Moshchalkov, V. V.; Baumberg, J. J. How Ultranarrow Gap Symmetries Control Plasmonic Nanocavity Modes: From Cubes to Spheres in the Nanoparticle-on-Mirror. *ACS Photonics* **2017**, *4* (3), 469–475.
- (682) Chen, T.; Pourmand, M.; Feizpour, A.; Cushman, B.; Reinhard, B. M. Tailoring Plasmon Coupling in Self-Assembled One-Dimensional Au Nanoparticle Chains through Simultaneous Control of Size and Gap Separation. *J. Phys. Chem. Lett.* **2013**, *4* (13), 2147–2152.
- (683) Moreau, A.; Ciraci, C.; Mock, J. J.; Hill, R. T.; Wang, Q.; Wiley, B. J.; Chilkoti, A.; Smith, D. R. Controlled-Reflectance Surfaces with Film-Coupled Colloidal Nanoantennas. *Nature* **2012**, *492* (7427), 86–89.
- (684) Chen, K.; Adato, R.; Altug, H. Dual-Band Perfect Absorber for Multispectral Plasmon-Enhanced Infrared Spectroscopy. *ACS Nano* **2012**, *6* (9), 7998–8006.
- (685) Ng, C.; Wesemann, L.; Panchenko, E.; Song, J.; Davis, T. J.; Roberts, A.; Gómez, D. E. Plasmonic Near-Complete Optical Absorption and Its Applications. *Adv. Opt. Mater.* **2019**, *7* (14), 1801660.
- (686) Wan, M.; He, J.; Song, Y.; Zhou, F. Electromagnetically Induced Transparency and Absorption in Plasmonic Metasurfaces Based on Near-Field Coupling. *Phys. Lett. A* **2015**, *379* (30), 1791–1795.
- (687) Luk'yanchuk, B.; Zheludev, N. I.; Maier, S. A.; Halas, N. J.; Nordlander, P.; Giessen, H.; Chong, C. T. The Fano Resonance in Plasmonic Nanostructures and Metamaterials. *Nat. Mater.* **2010**, *9* (9), 707–715.
- (688) Zhang, S.; Genov, D. A.; Wang, Y.; Liu, M.; Zhang, X. Plasmon-Induced Transparency in Metamaterials. *Phys. Rev. Lett.* **2008**, *101* (4), No. 047401.
- (689) Farhadi, S.; Miri, M.; Farmani, A. Plasmon-Induced Transparency Sensor for Detection of Minuscule Refractive Index Changes in Ultra-Low Index Materials. *Sci. Rep.* **2021**, *11*, 21692.
- (690) Zheng, C. Y.; Hadibrata, W.; Kim, S.; Schatz, G. C.; Aydin, K.; Mirkin, C. A. Large-Area, Highly Crystalline DNA-Assembled Metasurfaces Exhibiting Widely Tunable Epsilon-Near-Zero Behavior. *ACS Nano* **2021**, *15* (11), 18289–18296.
- (691) Kiasat, Y.; Donato, M. G.; Hinczewski, M.; ElKabbash, M.; Letsou, T.; Saija, R.; Maragò, O. M.; Strangi, G.; Engheta, N. Epsilon-near-Zero (ENZ)-Based Optomechanics. *Commun. Phys.* **2023**, *6*, 69.
- (692) Kim, S.; Zheng, C. Y.; Schatz, G. C.; Aydin, K.; Kim, K.-H.; Mirkin, C. A. Mie-Resonant Three-Dimensional Metacrystals. *Nano Lett.* **2020**, *20* (11), 8096–8101.
- (693) Singh, H. J.; Misatiou, D.; Wheeler, C.; Buendía, Á.; Giannini, V.; Sánchez-Gil, J. A.; Werts, M. H. V.; Brown, T.; El-Sagheer, A. H.; Kanaras, A. G.; Muskens, O. L. Optical Mie Scattering by DNA-Assembled Three-Dimensional Gold Nanoparticle Superlattice Crystals. *ACS Appl. Opt. Mater.* **2023**, *1* (1), 69–77.
- (694) Sun, L.; Lin, H.; Kohlstedt, K. L.; Schatz, G. C.; Mirkin, C. A. Design Principles for Photonic Crystals Based on Plasmonic Nanoparticle Superlattices. *Proc. Natl. Acad. Sci. U.S.A.* **2018**, *115* (28), 7242–7247.
- (695) Cherqui, C.; Bourgeois, M. R.; Wang, D.; Schatz, G. C. Plasmonic Surface Lattice Resonances: Theory and Computation. *Acc. Chem. Res.* **2019**, *52* (9), 2548–2558.
- (696) Kravets, V. G.; Schedin, F.; Grigorenko, A. N. Extremely Narrow Plasmon Resonances Based on Diffraction Coupling of Localized Plasmons in Arrays of Metallic Nanoparticles. *Phys. Rev. Lett.* **2008**, *101* (8), No. 087403.
- (697) Zou, S.; Schatz, G. C. Narrow Plasmonic/Photonic Extinction and Scattering Line Shapes for One and Two Dimensional Silver Nanoparticle Arrays. *J. Chem. Phys.* **2004**, *121* (24), 12606–12612.
- (698) Deng, S.; Li, R.; Park, J.-E.; Guan, J.; Choo, P.; Hu, J.; Smeets, P. J. M.; Odom, T. W. Ultranarrow Plasmon Resonances from Annealed Nanoparticle Lattices. *Proc. Natl. Acad. Sci. U.S.A.* **2020**, *117* (38), 23380–23384.

- (699) Yang, F.; Chen, Q.; Wang, J.; Chang, J. J.; Dong, W.; Cao, W.; Ye, S.; Shi, L.; Nie, Z. Fabrication of Centimeter-Scale Plasmonic Nanoparticle Arrays with Ultrnarrow Surface Lattice Resonances. *ACS Nano* **2023**, *17* (1), 725–734.
- (700) Yang, A.; Hoang, T. B.; Dridi, M.; Deeb, C.; Mikkelsen, M. H.; Schatz, G. C.; Odom, T. W. Real-Time Tunable Lasing from Plasmonic Nanocavity Arrays. *Nat. Commun.* **2015**, *6*, 6939.
- (701) Humphrey, A. D.; Barnes, W. L. Plasmonic Surface Lattice Resonances on Arrays of Different Lattice Symmetry. *Phys. Rev. B* **2014**, *90* (7), No. 075404.
- (702) Guo, R.; Hakala, T. K.; Törmä, P. Geometry Dependence of Surface Lattice Resonances in Plasmonic Nanoparticle Arrays. *Phys. Rev. B* **2017**, *95* (15), 155423.
- (703) Hakala, T. K.; Rekola, H. T.; Väkeväinen, A. I.; Martikainen, J.-P.; Nečada, M.; Moilanen, A. J.; Törmä, P. Lasing in Dark and Bright Modes of a Finite-Sized Plasmonic Lattice. *Nat. Commun.* **2017**, *8*, 13687.
- (704) Guan, J.; Sagar, L. K.; Li, R.; Wang, D.; Bappi, G.; Wang, W.; Watkins, N.; Bourgeois, M. R.; Levina, L.; Fan, F.; Hoogland, S.; Voznyy, O.; de Pina, J. M.; Schaller, R. D.; Schatz, G. C.; Sargent, E. H.; Odom, T. W. Quantum Dot-Plasmon Lasing with Controlled Polarization Patterns. *ACS Nano* **2020**, *14* (3), 3426–3433.
- (705) Schokker, A. H.; Koenderink, A. F. Lasing at the Band Edges of Plasmonic Lattices. *Phys. Rev. B* **2014**, *90* (15), 155452.
- (706) Heilmann, R.; Arjas, K.; Hakala, T. K.; Törmä, Päivi Multimode Lasing in Supercell Plasmonic Nanoparticle Arrays. *ACS Photonics* **2023**, *10* (11), 3955–3962.
- (707) Ogier, R.; Fang, Y.; Svedendahl, M.; Johansson, P.; Käll, M. Macroscopic Layers of Chiral Plasmonic Nanoparticle Oligomers from Colloidal Lithography. *ACS Photonics* **2014**, *1* (10), 1074–1081.
- (708) Kim, R. M.; Huh, J.-H.; Yoo, S.; Kim, T. G.; Kim, C.; Kim, H.; Han, J. H.; Cho, N. H.; Lim, Y.-C.; Im, S. W.; Im, E.; Jeong, J. R.; Lee, M. H.; Yoon, T.-Y.; Lee, H.-Y.; Park, Q.-H.; Lee, S.; Nam, K. T. Enantioselective Sensing by Collective Circular Dichroism. *Nature* **2022**, *612* (7940), 470–476.
- (709) Trinh, Q. T.; Nguyen, S. K.; Nguyen, D. H.; Tran, G. K.; Le, V. H.; Nguyen, H.-S.; Le-Van, Q. Coexistence of Surface Lattice Resonances and Bound States in the Continuum in a Plasmonic Lattice. *Opt. Lett.* **2022**, *47* (6), 1510–1513.
- (710) Azzam, S. I.; Shalaev, V. M.; Boltasseva, A.; Kildishev, A. V. Formation of Bound States in the Continuum in Hybrid Plasmonic-Photonic Systems. *Phys. Rev. Lett.* **2018**, *121* (25), 253901.
- (711) Lin, Q.-Y.; Li, Z.; Brown, K. A.; O'Brien, M. N.; Ross, M. B.; Zhou, Y.; Butun, S.; Chen, P.-C.; Schatz, G. C.; Dravid, V. P.; Aydin, K.; Mirkin, C. A. Strong Coupling between Plasmonic Gap Modes and Photonic Lattice Modes in DNA-Assembled Gold Nanocube Arrays. *Nano Lett.* **2015**, *15* (7), 4699–4703.
- (712) Wang, D.; Yang, A.; Wang, W.; Hua, Y.; Schaller, R. D.; Schatz, G. C.; Odom, T. W. Band-Edge Engineering for Controlled Multi-Modal Nanolasing in Plasmonic Superlattices. *Nat. Nanotechnol.* **2017**, *12* (9), 889–894.
- (713) Wang, D.; Bourgeois, M. R.; Guan, J.; Fumani, A. K.; Schatz, G. C.; Odom, T. W. Lasing from Finite Plasmonic Nanoparticle Lattices. *ACS Photonics* **2020**, *7* (3), 630–636.
- (714) Wang, W.; Ramezani, M.; Väkeväinen, A. I.; Törmä, P.; Rivas, J. G.; Odom, T. W. The Rich Photonic World of Plasmonic Nanoparticle Arrays. *Mater. Today* **2018**, *21* (3), 303–314.
- (715) Zhou, W.; Dridi, M.; Suh, J. Y.; Kim, C. H.; Co, D. T.; Wasielewski, M. R.; Schatz, G. C.; Odom, T. W. Lasing Action in Strongly Coupled Plasmonic Nanocavity Arrays. *Nat. Nanotechnol.* **2013**, *8* (7), 506–511.
- (716) Väkeväinen, A. I.; Moilanen, A. J.; Nečada, M.; Hakala, T. K.; Daskalakis, K. S.; Törmä, P. Sub-Picosecond Thermalization Dynamics in Condensation of Strongly Coupled Lattice Plasmons. *Nat. Commun.* **2020**, *11* (1), 3139.
- (717) Ramezani, M.; Halpin, A.; Fernández-Domínguez, A. I.; Feist, J.; Rodriguez, S. R.-K.; Garcia-Vidal, F. J.; Rivas, J. G. Plasmon-Exciton-Polariton Lasing. *Optica* **2017**, *4* (1), 31–37.
- (718) Tan, M. J. H.; Park, J.-E.; Freire-Fernández, F.; Guan, J.; Juarez, X. G.; Odom, T. W. Lasing Action from Quasi-Propagating Modes. *Adv. Mater.* **2022**, *34* (34), 2203999.
- (719) Wang, D.; Guan, J.; Hu, J.; Bourgeois, M. R.; Odom, T. W. Manipulating Light–Matter Interactions in Plasmonic Nanoparticle Lattices. *Acc. Chem. Res.* **2019**, *52* (11), 2997–3007.
- (720) Lin, Y.; Wang, D.; Hu, J.; Liu, J.; Wang, W.; Guan, J.; Schaller, R. D.; Odom, T. W. Engineering Symmetry-Breaking Nanocrescent Arrays for Nanolasering. *Adv. Funct. Mater.* **2019**, *29* (42), 1904157.
- (721) Knudson, M. P.; Li, R.; Wang, D.; Wang, W.; Schaller, R. D.; Odom, T. W. Polarization-Dependent Lasing Behavior from Low-Symmetry Nanocavity Arrays. *ACS Nano* **2019**, *13* (7), 7435–7441.
- (722) Wang, D.; Bourgeois, M. R.; Lee, W.-K.; Li, R.; Trivedi, D.; Knudson, M. P.; Wang, W.; Schatz, G. C.; Odom, T. W. Stretchable Nanolasing from Hybrid Quadrupole Plasmons. *Nano Lett.* **2018**, *18* (7), 4549–4555.
- (723) Salerno, G.; Heilmann, R.; Arjas, K.; Aronen, K.; Martikainen, J.-P.; Törmä, P. Loss-Driven Topological Transitions in Lasing. *Phys. Rev. Lett.* **2022**, *129* (17), 173901.
- (724) Freire-Fernández, F.; Reese, T.; Rhee, D.; Guan, J.; Li, R.; Schaller, R. D.; Schatz, G. C.; Odom, T. W. Quasi-Random Multimetalllic Nanoparticle Arrays. *ACS Nano* **2023**, *17* (21), 21905–21911.
- (725) Hicks, E. M.; Zou, S.; Schatz, G. C.; Spears, K. G.; Van Duyne, R. P.; Gunnarsson, L.; Rindzevicius, T.; Kasemo, B.; Käll, M. Controlling Plasmon Line Shapes through Diffractive Coupling in Linear Arrays of Cylindrical Nanoparticles Fabricated by Electron Beam Lithography. *Nano Lett.* **2005**, *5* (6), 1065–1070.
- (726) Qin, D.; Xia, Y.; Whitesides, G. M. Soft Lithography for Micro- and Nanoscale Patterning. *Nat. Protoc.* **2010**, *5* (3), 491–502.
- (727) Lee, M. H.; Huntington, M. D.; Zhou, W.; Yang, J.-C.; Odom, T. W. Programmable Soft Lithography: Solvent-Assisted Nanoscale Embossing. *Nano Lett.* **2011**, *11* (2), 311–315.
- (728) Huntington, M. D.; Odom, T. W. A Portable, Benchtop Photolithography System Based on a Solid-State Light Source. *Small* **2011**, *7* (22), 3144–3147.
- (729) Odom, T. W.; Love, J. C.; Wolfe, D. B.; Paul, K. E.; Whitesides, G. M. Improved Pattern Transfer in Soft Lithography Using Composite Stamps. *Langmuir* **2002**, *18* (13), 5314–5320.
- (730) Lubin, S. M.; Zhou, W.; Hryn, A. J.; Huntington, M. D.; Odom, T. W. High-Rotational Symmetry Lattices Fabricated by Moiré Nanolithography. *Nano Lett.* **2012**, *12* (9), 4948–4952.
- (731) Verschueren, M. A.; Knight, M. W.; Megens, M.; Polman, A. Nanoscale Spatial Limitations of Large-Area Substrate Conformal Imprint Lithography. *Nanotechnology* **2019**, *30* (34), 345301.
- (732) Chen, K.-P.; Drachev, V. P.; Borneman, J. D.; Kildishev, A. V.; Shalaev, V. M. Drude Relaxation Rate in Grained Gold Nanoantennas. *Nano Lett.* **2010**, *10* (3), 916–922.
- (733) Lee, H. S.; Awada, C.; Boutami, S.; Charra, F.; Douillard, L.; Lemaestre, R. E. de Loss Mechanisms of Surface Plasmon Polaritons Propagating on a Smooth Polycrystalline Cu Surface. *Opt. Express* **2012**, *20* (8), 8974–8981.
- (734) Novikov, S. M.; Popok, V. N.; Evlyukhin, A. B.; Hanif, M.; Morgen, P.; Fiutowski, J.; Beermann, J.; Rubahn, H.-G.; Bozhevolnyi, S. I. Highly Stable Monocrystalline Silver Clusters for Plasmonic Applications. *Langmuir* **2017**, *33* (24), 6062–6070.
- (735) Oikawa, S.; Minamimoto, H.; Murakoshi, K. Low-Temperature Annealing of Plasmonic Metal Arrays for Improved Light Confinement. *J. Phys. Chem. C* **2022**, *126* (2), 1188–1195.
- (736) Zhang, F.; Proust, J.; Gérard, D.; Plain, J.; Martin, J. Reduction of Plasmon Damping in Aluminum Nanoparticles with Rapid Thermal Annealing. *J. Phys. Chem. C* **2017**, *121* (13), 7429–7434.
- (737) Deng, S.; Park, J.-E.; Kang, G.; Guan, J.; Li, R.; Schatz, G. C.; Odom, T. W. Interfacial Engineering of Plasmonic Nanoparticle Metasurfaces. *Proc. Natl. Acad. Sci. U.S.A.* **2022**, *119* (22), e2202621119.
- (738) Deng, S.; Zhang, B.; Choo, P.; Smeets, P. J. M.; Odom, T. W. Plasmonic Photoelectrocatalysis in Copper–Platinum Core–Shell Nanoparticle Lattices. *Nano Lett.* **2021**, *21* (3), 1523–1529.

- (739) Zheng, Z.; Tachikawa, T.; Majima, T. Single-Particle Study of Pt-Modified Au Nanorods for Plasmon-Enhanced Hydrogen Generation in Visible to Near-Infrared Region. *J. Am. Chem. Soc.* **2014**, *136* (19), 6870–6873.
- (740) Zhu, J.; Hu, L.; Zhao, P.; Lee, L. Y. S.; Wong, K.-Y. Recent Advances in Electrocatalytic Hydrogen Evolution Using Nanoparticles. *Chem. Rev.* **2020**, *120* (2), 851–918.
- (741) Jia, J.; Metzkow, N.; Park, S.-M.; Wu, Y. L.; Sample, A. D.; Diloknawarit, B.; Jung, I.; Odom, T. W. Spike Growth on Patterned Gold Nanoparticle Scaffolds. *Nano Lett.* **2023**, *23* (23), 11260–11265.
- (742) Demille, T. B.; Hughes, R. A.; Dominique, N.; Olson, J. E.; Rouvimov, S.; Camden, J. P.; Neretina, S. Large-Area Periodic Arrays of Gold Nanostars Derived from HEPES-, DMF-, and Ascorbic-Acid-Driven Syntheses. *Nanoscale* **2020**, *12* (31), 16489–16500.
- (743) M. Pallares, R.; Stilson, T.; Choo, P.; Hu, J.; Odom, T. W. Using Good's Buffers To Control the Anisotropic Structure and Optical Properties of Spiky Gold Nanoparticles for Refractive Index Sensing. *ACS Appl. Nano Mater.* **2019**, *2* (8), 5266–5271.
- (744) Tuff, W. J.; Hughes, R. A.; Golze, S. D.; Neretina, S. Ion Beam Milling as a Symmetry-Breaking Control in the Synthesis of Periodic Arrays of Identically Aligned Bimetallic Janus Nanocrystals. *ACS Nano* **2023**, *17* (4), 4050–4061.
- (745) Grzelczak, M.; Pérez-Juste, J.; Mulvaney, P.; Liz-Marzán, L. M. Shape Control in Gold Nanoparticle Synthesis. *Chem. Soc. Rev.* **2008**, *37* (9), 1783–1791.
- (746) Langille, M. R.; Personick, M. L.; Zhang, J.; Mirkin, C. A. Defining Rules for the Shape Evolution of Gold Nanoparticles. *J. Am. Chem. Soc.* **2012**, *134* (35), 14542–14554.
- (747) Ben-Moshe, A.; Govorov, A. O.; Markovich, G. Enantioselective Synthesis of Intrinsically Chiral Mercury Sulfide Nanocrystals. *Angew. Chem. Inter. Ed.* **2013**, *52* (4), 1275–1279.
- (748) Ben-Moshe, A.; Wolf, S. G.; Sadan, M. B.; Houben, L.; Fan, Z.; Govorov, A. O.; Markovich, G. Enantioselective Control of Lattice and Shape Chirality in Inorganic Nanostructures Using Chiral Biomolecules. *Nat. Commun.* **2014**, *5* (1), 4302.
- (749) Shukla, N.; Gellman, A. J. Chiral Metal Surfaces for Enantioselective Processes. *Nat. Mater.* **2020**, *19* (9), 939–945.
- (750) McFadden, C. F.; Cremer, P. S.; Gellman, A. J. Adsorption of Chiral Alcohols on “Chiral” Metal Surfaces. *Langmuir* **1996**, *12* (10), 2483–2487.
- (751) Lee, H.-E.; Kim, R. M.; Ahn, H.-Y.; Lee, Y. Y.; Byun, G. H.; Im, S. W.; Mun, J.; Rho, J.; Nam, K. T. Cysteine-Encoded Chirality Evolution in Plasmonic Rhombic Dodecahedral Gold Nanoparticles. *Nat. Commun.* **2020**, *11* (1), 263.
- (752) Kim, H.; Im, S. W.; Cho, N. H.; Seo, D. H.; Kim, R. M.; Lim, Y.-C.; Lee, H.-E.; Ahn, H.-Y.; Nam, K. T.  $\gamma$ -Glutamylcysteine- and Cysteinylglycine-Directed Growth of Chiral Gold Nanoparticles and Their Crystallographic Analysis. *Angew. Chem. Inter. Ed.* **2020**, *59* (31), 12976–12983.
- (753) Im, S. W.; Zhang, D.; Han, J. H.; Kim, R. M.; Choi, C.; Kim, Y. M.; Nam, K. T. Investigating Chiral Morphogenesis of Gold Using Generative Cellular Automata. *Nat. Mater.* **2024**, *23* (7), 977–983.
- (754) Che, S.; Liu, Z.; Ohsuna, T.; Sakamoto, K.; Terasaki, O.; Tatsumi, T. Synthesis and Characterization of Chiral Mesoporous Silica. *Nature* **2004**, *429* (6989), 281–284.
- (755) González-Rubio, G.; Mosquera, J.; Kumar, V.; Pedrazo-Tardajos, A.; Llombart, P.; Solís, D. M.; Lobato, I.; Noya, E. G.; Guerrero-Martínez, A.; Taboada, J. M.; Obelleiro, F.; MacDowell, L. G.; Bals, S.; Liz-Marzán, L. M. Micelle-Directed Chiral Seeded Growth on Anisotropic Gold Nanocrystals. *Science* **2020**, *368* (6498), 1472–1477.
- (756) Srivastava, S.; Santos, A.; Critchley, K.; Kim, K.-S.; Podsiadlo, P.; Sun, K.; Lee, J.; Xu, C.; Lilly, G. D.; Glotzer, S. C.; Kotov, N. A. Light-Controlled Self-Assembly of Semiconductor Nanoparticles into Twisted Ribbons. *Science* **2010**, *327* (5971), 1355–1359.
- (757) Yeom, J.; Yeom, B.; Chan, H.; Smith, K. W.; Dominguez-Medina, S.; Bahng, J. H.; Zhao, G.; Chang, W.-S.; Chang, S.-J.; Chuvilin, A.; Melnikau, D.; Rogach, A. L.; Zhang, P.; Link, S.; Král, P.; Kotov, N. A. Chiral Templating of Self-Assembling Nanostructures by Circularly Polarized Light. *Nat. Mater.* **2015**, *14* (1), 66–72.
- (758) Saito, K.; Tatsuma, T. Chiral Plasmonic Nanostructures Fabricated by Circularly Polarized Light. *Nano Lett.* **2018**, *18* (5), 3209–3212.
- (759) Besteiro, L. V.; Movsesyan, A.; Ávalos-Ovando, O.; Lee, S.; Cortés, E.; Correa-Duarte, M. A.; Wang, Z. M.; Govorov, A. O. Local Growth Mediated by Plasmonic Hot Carriers: Chirality from Achiral Nanocrystals Using Circularly Polarized Light. *Nano Lett.* **2021**, *21* (24), 10315–10324.
- (760) Xu, L.; Wang, X.; Wang, W.; Sun, M.; Choi, W. J.; Kim, J.-Y.; Hao, C.; Li, S.; Qu, A.; Lu, M.; Wu, X.; Colombari, F. M.; Gomes, W. R.; Blanco, A. L.; de Moura, A. F.; Guo, X.; Kuang, H.; Kotov, N. A.; Xu, C. Enantiomer-Dependent Immunological Response to Chiral Nanoparticles. *Nature* **2022**, *601* (7893), 366–373.
- (761) Ayuso, D.; Neufeld, O.; Ordóñez, A. F.; Declava, P.; Lerner, G.; Cohen, O.; Ivanov, M.; Smirnova, O. Synthetic Chiral Light for Efficient Control of Chiral Light–Matter Interaction. *Nat. Photonics* **2019**, *13* (12), 866–871.
- (762) Spreyer, F.; Mun, J.; Kim, H.; Kim, R. M.; Nam, K. T.; Rho, J.; Zentgraf, T. Second Harmonic Optical Circular Dichroism of Plasmonic Chiral Helicoid-III Nanoparticles. *ACS Photonics* **2022**, *9* (3), 784–792.
- (763) Ahn, H.-Y.; Le, K. Q.; Narushima, T.; Yamanishi, J.; Kim, R. M.; Nam, K. T.; Okamoto, H. Highly Chiral Light Emission Using Plasmonic Helicoid Nanoparticles. *Adv. Opt. Mater.* **2024**, *12* (22), 2400699.
- (764) Lee, S.-J.; So, J.-P.; Kim, R. M.; Kim, K.-H.; Rha, H.-H.; Na, G.; Han, J. H.; Jeong, K.-Y.; Nam, K. T.; Park, H.-G. Spin Angular Momentum–Encoded Single-Photon Emitters in a Chiral Nanoparticle–Coupled WSe<sub>2</sub> Monolayer. *Sci. Adv.* **2024**, *10* (21), eadn7210.
- (765) Kim, H.; Im, E.; Kim, R. M.; Cho, N. H.; Han, J. H.; Ahn, H.-Y.; Huh, J.-H.; Yoo, S.; Lee, S.; Nam, K. T. Capacitive Enhancements of the Chiroptical Response in Plasmonic Helicoids. *Adv. Opt. Mater.* **2023**, *11* (16), 2300205.
- (766) Kim, J. W.; Cho, N. H.; Kim, R. M.; Han, J. H.; Choi, S.; Namgung, S. D.; Kim, H.; Nam, K. T. Magnetic Control of the Plasmonic Chirality in Gold Helicoids. *Nano Lett.* **2022**, *22* (20), 8181–8188.
- (767) Lee, S.; Lim, Y.-C.; Kim, H.; Seo, D. H.; Na, J.; Kim, H.; Nam, K. T.; Jeong, Y. Random Lasing with a High Degree of Circular Dichroism by Chiral Plasmonic Gold Nanoparticles. *ACS Photonics* **2022**, *9* (2), 613–620.
- (768) Kim, S.; Lim, Y.-C.; Kim, R. M.; Frölich, J. E.; Tran, T. N.; Nam, K. T.; Aharonovich, I. A Single Chiral Nanoparticle Induced Valley Polarization Enhancement. *Small* **2020**, *16* (37), 2003005.
- (769) Yan, J.; Feng, W.; Kim, J.-Y.; Lu, J.; Kumar, P.; Mu, Z.; Wu, X.; Mao, X.; Kotov, N. A. Self-Assembly of Chiral Nanoparticles into Semiconductor Helices with Tunable near-Infrared Optical Activity. *Chem. Mater.* **2020**, *32* (1), 476–488.
- (770) Ohnoutek, L.; Kim, J.-Y.; Lu, J.; Olohan, B. J.; Răsădean, D. M.; Dan Păntoș, G.; Kotov, N. A.; Valev, V. K. Third-Harmonic Mie Scattering from Semiconductor Nanohelices. *Nat. Photonics* **2022**, *16* (2), 126–133.
- (771) Ohnoutek, L.; Cho, N. H.; Allen Murphy, A. W.; Kim, H.; Răsădean, D. M.; Păntoș, G. D.; Nam, K. T.; Valev, V. K. Single Nanoparticle Chiroptics in a Liquid: Optical Activity in Hyper-Rayleigh Scattering from Au Helicoids. *Nano Lett.* **2020**, *20* (8), 5792–5798.
- (772) Namgung, S. D.; Kim, R. M.; Han, J. H.; Nam, K. T. Circular Polarization Sensitive Opto-Neuromorphic Operation at Plasmonic Hot Electron Transistor Using Chiral Gold Nanoparticles. *Nanotechnology* **2024**, *35* (24), 245201.
- (773) Li, W.; Coppens, Z. J.; Besteiro, L. V.; Wang, W.; Govorov, A. O.; Valentine, J. Circularly Polarized Light Detection with Hot Electrons in Chiral Plasmonic Metamaterials. *Nat. Commun.* **2015**, *6*, 8379.

- (774) Liu, T.; Besteiro, L. V.; Liedl, T.; Correa-Duarte, M. A.; Wang, Z.; Govorov, A. O. Chiral Plasmonic Nanocrystals for Generation of Hot Electrons: Toward Polarization-Sensitive Photochemistry. *Nano Lett.* **2019**, *19* (2), 1395–1407.
- (775) Lee, S.; Fan, C.; Movsesyan, A.; Bürger, J.; Wendisch, F. J.; De S. Menezes, L.; Maier, S. A.; Ren, H.; Liedl, T.; Besteiro, L. V.; Govorov, A. O.; Cortés, E. Unraveling the Chirality Transfer from Circularly Polarized Light to Single Plasmonic Nanoparticles. *Angew. Chem. Inter. Ed.* **2024**, *63* (11), e202319920.
- (776) Kim, H.; Kim, R. M.; Namgung, S. D.; Cho, N. H.; Son, J. B.; Bang, K.; Choi, M.; Kim, S. K.; Nam, K. T.; Lee, J. W.; Oh, J. H. Ultrasensitive Near-Infrared Circularly Polarized Light Detection Using 3D Perovskite Embedded with Chiral Plasmonic Nanoparticles. *Adv. Sci.* **2022**, *9* (5), 2104598.
- (777) Song, L.; Wang, S.; Kotov, N. A.; Xia, Y. Nonexclusive Fluorescent Sensing for l/d Enantiomers Enabled by Dynamic Nanoparticle-Nanorod Assemblies. *Anal. Chem.* **2012**, *84* (17), 7330–7335.
- (778) Tang, L.; Li, S.; Xu, L.; Ma, W.; Kuang, H.; Wang, L.; Xu, C. Chirality-Based Au@Ag Nanorod Dimers Sensor for Ultrasensitive PSA Detection. *ACS Appl. Mater. Interfaces* **2015**, *7* (23), 12708–12712.
- (779) Kim, R. M.; Han, J. H.; Lee, S. M.; Kim, H.; Lim, Y.-C.; Lee, H.-E.; Ahn, H.-Y.; Lee, Y. H.; Ha, I. H.; Nam, K. T. Chiral Plasmonic Sensing: From the Perspective of Light–Matter Interaction. *J. Chem. Phys.* **2024**, *160* (6), No. 061001.
- (780) Han, J. H.; Lim, Y.-C.; Kim, R. M.; Lv, J.; Cho, N. H.; Kim, H.; Namgung, S. D.; Im, S. W.; Nam, K. T. Neural-Network-Enabled Design of a Chiral Plasmonic Nanodimer for Target-Specific Chirality Sensing. *ACS Nano* **2023**, *17* (3), 2306–2317.
- (781) Lee, Y. Y.; Kim, R. M.; Im, S. W.; Balamurugan, M.; Nam, K. T. Plasmonic Metamaterials for Chiral Sensing Applications. *Nanoscale* **2020**, *12*, 58–66.
- (782) Jeong, H.-H.; Mark, A. G.; Alarcón-Correia, M.; Kim, I.; Oswald, P.; Lee, T.-C.; Fischer, P. Dispersion and Shape Engineered Plasmonic Nanosensors. *Nat. Commun.* **2016**, *7*, 11331.
- (783) Ma, W.; Kuang, H.; Xu, L.; Ding, L.; Xu, C.; Wang, L.; Kotov, N. A. Attomolar DNA Detection with Chiral Nanorod Assemblies. *Nat. Commun.* **2013**, *4*, 2689.
- (784) Arteaga, O.; Sancho-Parramon, J.; Nichols, S.; Maoz, B. M.; Canillas, A.; Bosch, S.; Markovich, G.; Kahr, B. Relation between 2D/3D Chirality and the Appearance of Chiroptical Effects in Real Nanostructures. *Opt. Express* **2016**, *24* (3), 2242–2252.
- (785) Cho, N. H.; Kim, Y. B.; Lee, Y. Y.; Im, S. W.; Kim, R. M.; Kim, J. W.; Namgung, S. D.; Lee, H.-E.; Kim, H.; Han, J. H.; Chung, H. W.; Lee, Y. H.; Han, J. W.; Nam, K. T. Adenine Oligomer Directed Synthesis of Chiral Gold Nanoparticles. *Nat. Commun.* **2022**, *13*, 3831.
- (786) Im, S. W.; Jo, E.; Kim, R. M.; Han, J. H.; Nam, K. T. 32-Symmetric Chiral Gold Nanoplates with Near-Infrared Circular Dichroism. *Adv. Opt. Mater.* **2023**, *11* (18), 2300037.
- (787) Im, S. W.; Ahn, H.-Y.; Kim, R. M.; Cho, N. H.; Kim, H.; Lim, Y.-C.; Lee, H.-E.; Nam, K. T. Chiral Surface and Geometry of Metal Nanocrystals. *Adv. Mater.* **2020**, *32* (41), 1905758.
- (788) Karst, J.; Cho, N. H.; Kim, H.; Lee, H.-E.; Nam, K. T.; Giessen, H.; Hentschel, M. Chiral Scatterometry on Chemically Synthesized Single Plasmonic Nanoparticles. *ACS Nano* **2019**, *13* (8), 8659–8668.
- (789) Cho, N. H.; Byun, G. H.; Lim, Y.-C.; Im, S. W.; Kim, H.; Lee, H.-E.; Ahn, H.-Y.; Nam, K. T. Uniform Chiral Gap Synthesis for High Dissymmetry Factor in Single Plasmonic Gold Nanoparticle. *ACS Nano* **2020**, *14* (3), 3595–3602.
- (790) Robbie, K.; Friedrich, L. J.; Dew, S. K.; Smy, T.; Brett, M. J. Fabrication of Thin Films with Highly Porous Microstructures. *J. Vac. Sci. Technol. A* **1995**, *13* (3), 1032–1035.
- (791) Krasnok, A.; Alù, A. Low-Symmetry Nanophotonics. *ACS Photonics* **2022**, *9* (1), 2–24.
- (792) Han, J.-H.; Kim, D.; Kim, J.; Kim, G.; Fischer, P.; Jeong, H.-H. Plasmonic Nanostructure Engineering with Shadow Growth. *Adv. Mater.* **2023**, *35* (34), 2107917.
- (793) Abdulhalim, I. Plasmonic Sensing Using Metallic Nano-Sculptured Thin Films. *Small* **2014**, *10* (17), 3499–3514.
- (794) Hawkeye, M. M.; Brett, M. J. Glancing Angle Deposition: Fabrication, Properties, and Applications of Micro- and Nanostructured Thin Films. *J. Vac. Sci. Technol. A* **2007**, *25* (5), 1317–1335.
- (795) Ai, B.; Zhao, Y. Glancing Angle Deposition Meets Colloidal Lithography: A New Evolution in the Design of Nanostructures. *Nanophotonics* **2018**, *8* (1), 1–26.
- (796) Huang, Z.; Bai, F. Wafer-Scale, Three-Dimensional Helical Porous Thin Films Deposited at a Glancing Angle. *Nanoscale* **2014**, *6* (16), 9401–9409.
- (797) Gallas, B.; Guth, N.; Rivory, J.; Arwin, H.; Magnusson, R.; Guida, G.; Yang, J.; Robbie, K. Nanostructured Chiral Silver Thin Films: A Route to Metamaterials at Optical Frequencies. *Thin Sol. Films* **2011**, *519* (9), 2650–2654.
- (798) Mark, A. G.; Gibbs, J. G.; Lee, T.-C.; Fischer, P. Hybrid Nanocolloids with Programmed Three-Dimensional Shape and Material Composition. *Nat. Mater.* **2013**, *12*, 802–807.
- (799) Jeong, H.-H.; Mark, A. G.; Gibbs, J. G.; Reindl, T.; Waizmann, U.; Weis, J.; Fischer, P. Shape Control in Wafer-Based Aperiodic 3D Nanostructures. *Nanotechnology* **2014**, *25* (23), 235302.
- (800) Barranco, A.; Borras, A.; Gonzalez-Elipe, A. R.; Palmero, A. Perspectives on Oblique Angle Deposition of Thin Films: From Fundamentals to Devices. *Prog. Mater. Sci.* **2016**, *76*, 59–153.
- (801) Glass, R.; Möller, M.; Spatz, J. P. Block Copolymer Micelle Nanolithography. *Nanotechnology* **2003**, *14* (10), 1153–1160.
- (802) Barad, H.-N.; Kwon, H.; Alarcón-Correia, M.; Fischer, P. Large Area Patterning of Nanoparticles and Nanostructures: Current Status and Future Prospects. *ACS Nano* **2021**, *15* (4), 5861–5875.
- (803) Jeong, H. H.; Adams, M. C.; Günther, J. P.; Alarcón-Correia, M.; Kim, I.; Choi, E.; Miksch, C.; Mark, A. F. A. G.; Mark, A. F. A. G.; Fischer, P. Arrays of Plasmonic Nanoparticle Dimers with Defined Nanogap Spacers. *ACS Nano* **2019**, *13* (10), 11453–11459.
- (804) Kim, J.; Han, J.-H.; Kim, H. M.; Lee, T.-C.; Jeong, H.-H. Plasmonic Nano-Rotamers with Programmable Polarization-Resolved Coloration. *Adv. Opt. Mater.* **2024**, *12* (2), 2301730.
- (805) Lingstädter, R.; Davoodi, F.; Elibol, K.; Taleb, M.; Kwon, H.; Fischer, P.; Talebi, N.; van Aken, P. A. Electron Beam Induced Circularly Polarized Light Emission of Chiral Gold Nanohelices. *ACS Nano* **2023**, *17* (24), 25496–25506.
- (806) Matuschek, M.; Singh, D. P.; Jeong, H.-H.; Nesterov, M.; Weiss, T.; Fischer, P.; Neubrech, F.; Liu, N. Chiral Plasmonic Hydrogen Sensors. *Small* **2018**, *14* (7), 1702990.
- (807) Huang, Z.; Liu, J. Chiroptically Active Metallic Nanohelices with Helical Anisotropy. *Small* **2017**, *13* (43), 1701883.
- (808) Ni, Z.; Qin, P.; Liu, H.; Chen, J.; Cai, S.; Tang, W.; Xiao, H.; Wang, C.; Qu, G.; Lin, C.; Fan, Z.; Xu, Z.-X.; Li, G.; Huang, Z. Significant Enhancement of Circular Polarization in Light Emission through Controlling Helical Pitches of Semiconductor Nanohelices. *ACS Nano* **2023**, *17* (20), 20611–20620.
- (809) Xi, J.-Q.; Schubert, M. F.; Kim, J. K.; Schubert, E. F.; Chen, M.; Lin, S.-Y.; Liu, W.; Smart, J. A. Optical Thin-Film Materials with Low Refractive Index for Broadband Elimination of Fresnel Reflection. *Nat. Photonics* **2007**, *1* (3), 176–179.
- (810) Sachs, J.; Günther, J.-P.; Mark, A. G.; Fischer, P. Chiroptical Spectroscopy of a Freely Diffusing Single Nanoparticle. *Nat. Commun.* **2020**, *11*, 4513.
- (811) Huang, Z.; Harris, K. D.; Brett, M. J. Morphology Control of Nanotube Arrays. *Adv. Mater.* **2009**, *21* (29), 2983–2987.
- (812) Shi, X.; Choi, I. Y.; Zhang, K.; Kwon, J.; Kim, D. Y.; Lee, J. K.; Oh, S. H.; Kim, J. K.; Park, J. H. Efficient Photoelectrochemical Hydrogen Production from Bismuth Vanadate-Decorated Tungsten Trioxide Helix Nanostructures. *Nat. Commun.* **2014**, *5*, 4775.

- (813) Gibbs, J. G.; Mark, A. G.; Lee, T.-C.; Eslami, S.; Schamel, D.; Fischer, P. Nanohelices by Shadow Growth. *Nanoscale* **2014**, *6* (16), 9457–9466.
- (814) Barad, H.-N.; Alarcón-Correa, M.; Salinas, G.; Oren, E.; Peter, F.; Kuhn, A.; Fischer, P. Combinatorial Growth of Multinary Nanostructured Thin Functional Films. *Mater. Today* **2021**, *50*, 89–99.
- (815) Mayer, K. M.; Hafner, J. H. Localized Surface Plasmon Resonance Sensors. *Chem. Rev.* **2011**, *111* (6), 3828–3857.
- (816) Zhao, Y.; Kumar, A.; Yang, Y. Unveiling Practical Considerations for Reliable and Standardized SERS Measurements: Lessons from a Comprehensive Review of Oblique Angle Deposition-Fabricated Silver Nanorod Array Substrates. *Chem. Soc. Rev.* **2024**, *53* (2), 1004–1057.
- (817) Jeong, H.-H.; Mark, A. G.; Fischer, P. Magnesium Plasmonics for UV Applications and Chiral Sensing. *Chem. Commun.* **2016**, *52* (82), 12179–12182.
- (818) Liu, J.; Yang, L.; Zhang, H.; Wang, J.; Huang, Z. Ultraviolet-Visible Chiroptical Activity of Aluminum Nanostructures. *Small* **2017**, *13* (39), 1701112.
- (819) Garcia-Santiago, X.; Hammerschmidt, M.; Sachs, J.; Burger, S.; Kwon, H.; Knöller, M.; Arens, T.; Fischer, P.; Fernandez-Corbaton, I.; Rockstuhl, C. Toward Maximally Electromagnetically Chiral Scatterers at Optical Frequencies. *ACS Photonics* **2022**, *9* (6), 1954–1964.
- (820) Gibbs, J. G.; Mark, A. G.; Eslami, S.; Fischer, P. Plasmonic Nanohelix Metamaterials with Tailorable Giant Circular Dichroism. *Appl. Phys. Lett.* **2013**, *103* (21), 213101.
- (821) Hooper, D. C.; Mark, A. G.; Kuppe, C.; Collins, J. T.; Fischer, P.; Valev, V. K. Strong Rotational Anisotropies Affect Nonlinear Chiral Metamaterials. *Adv. Mater.* **2017**, *29* (13), 1605110.
- (822) Collins, J. T. T.; Rusimova, K. R. R.; Hooper, D. C. C.; Jeong, H.-H.; Ohnoutek, L.; Pradaux-Caggiano, F.; Verbiest, T.; Carbery, D. R. R.; Fischer, P.; Valev, V. K. K. First Observation of Optical Activity in Hyper-Rayleigh Scattering. *Phys. Rev. X* **2019**, *9*, No. 011024.
- (823) Ohnoutek, L.; Jeong, H.-H.; Jones, R. R.; Sachs, J.; Olohan, B. J.; Răsădean, D.-M.; Pantoș, G. D.; Andrews, D. L.; Fischer, P.; Valev, V. K. Optical Activity in Third-Harmonic Rayleigh Scattering: A New Route for Measuring Chirality. *Laser Photonics Rev.* **2021**, *15* (11), 2100235.
- (824) Ohnoutek, L.; Olohan, B. J.; Jones, R. R.; Zheng, X.; Jeong, H.-H.; Valev, V. K. Second Harmonic Rayleigh Scattering Optical Activity of Single Ag Nanohelices in a Liquid. *Nanoscale* **2022**, *14* (10), 3888–3898.
- (825) Jones, R. R.; Miksch, C.; Kwon, H.; Pothoven, C.; Rusimova, K. R.; Kamp, M.; Gong, K.; Zhang, L.; Batten, T.; Smith, B.; Silhanek, A. V.; Fischer, P.; Wolverson, D.; Valev, V. K. Dense Arrays of Nanohelices: Raman Scattering from Achiral Molecules Reveals the Near-Field Enhancements at Chiral Metasurfaces. *Adv. Mater.* **2023**, *35* (34), 2209282.
- (826) Baumberg, J. J.; Aizpurua, J.; Mikkelsen, M. H.; Smith, D. R. Extreme Nanophotonics from Ultrathin Metallic Gaps. *Nat. Mater.* **2019**, *18*, 668–678.
- (827) Paria, D.; Roy, K.; Singh, H. J.; Kumar, S.; Raghavan, S.; Ghosh, A.; Ghosh, A. Ultrahigh Field Enhancement and Photoresponse in Atomically Separated Arrays of Plasmonic Dimers. *Adv. Mater.* **2015**, *27* (10), 1751–1758.
- (828) Haechler, I.; Ferru, N.; Schnoering, G.; Mitridis, E.; Schutzius, T. M.; Poulikakos, D. Transparent Sunlight-Activated Antifogging Metamaterials. *Nat. Nanotechnol.* **2023**, *18* (2), 137–144.
- (829) Han, J.-H.; Kim, J.; Kim, G.; Jo, Y.-R.; Kim, D.; Kim, H. M.; Lee, S.-Y.; Jeong, H.-H. Dichroic Engineering from Invisible to Full Colors Using Plasmonics. *Adv. Funct. Mater.* **2024**, *34* (28), 2314434.
- (830) Goerlitzer, E. S. A.; Mohammadi, R.; Nechayev, S.; Volk, K.; Rey, M.; Banzer, P.; Karg, M.; Vogel, N. Chiral Surface Lattice Resonances. *Adv. Mater.* **2020**, *32* (22), 2001330.
- (831) Gohri, S.; Madan, J.; Pandey, R. Enhancing the Efficiency of SnS-Based Solar Cells Using a GLAD Technique and CZTSSe Layer. *Sol. State Commun.* **2024**, *377*, 115380.
- (832) Kim, J. H.; Choi, I. Y.; Kim, J. H.; Kim, J.; Kim, Y. K.; Kim, J. K.; Lee, J. S. ZnFe<sub>2</sub>O<sub>4</sub> Dendrite/SnO<sub>2</sub> Helix 3D Hetero-Structure Photoanodes for Enhanced Photoelectrochemical Water Splitting: Triple Functions of SnO<sub>2</sub> Nanohelix. *Small* **2021**, *17* (47), 2103861.
- (833) Dhar Dwivedi, S. M. M.; Dalal, A.; Ghosh, A.; Murkute, P.; Ghadi, H.; Ghosh, C.; Chakrabarti, S.; Bhunia, S.; Mondal, A. InN Nanowires Based Near-Infrared Broadband Optical Detector. *IEEE Photonics Technol. Lett.* **2019**, *31* (18), 1526–1529.
- (834) Tetseo, M.; Deb, P.; Daimary, S.; Dhar, J. C. CuO Nanowire-Based Metal Semiconductor Metal Infrared Photodetector. *Appl. Phys. A: Mater. Sci. Process.* **2021**, *127* (5), 380.
- (835) Lahiri, R.; Ghosh, A.; Choudhuri, B.; Mondal, A. Investigation on Improved Performance of Erbium Doped TiO<sub>2</sub> Nanowire Based UV Detector. *Mater. Res. Bull.* **2018**, *103*, 259–267.
- (836) Chinnamuthu, P.; Mondal, A.; Singh, N. K.; Dhar, J. C.; Chattopadhyay, K. K.; Bhattacharya, S. Band Gap Enhancement of Glancing Angle Deposited TiO<sub>2</sub> Nanowire Array. *J. Appl. Phys.* **2012**, *112* (5), 54315.
- (837) Kwon, H.; Ham, J.; Kim, D. Y.; Oh, S. J.; Lee, S.; Oh, S. H.; Schubert, E. F.; Lim, K.-G.; Lee, T.-W.; Kim, S.; Lee, J.-L.; Kim, J. K. Three-Dimensional Nanostructured Indium-Tin-Oxide Electrodes for Enhanced Performance of Bulk Heterojunction Organic Solar Cells. *Adv. Energy Mater.* **2014**, *4* (7), 1301566.
- (838) Lee, S. H.; Kwon, J.; Kim, D. Y.; Song, K.; Oh, S. H.; Cho, J.; Schubert, E. F.; Park, J. H.; Kim, J. K. Enhanced Power Conversion Efficiency of Dye-Sensitized Solar Cells with Multifunctional Photoanodes Based on a Three-Dimensional TiO<sub>2</sub> Nanohelix Array. *Sol. Energy Mater. Sol. Cells* **2015**, *132*, 47–55.
- (839) Sazideh, M. R.; Dizaji, H. R.; Ehsani, M. H.; Moghadam, R. Z. Modification of the Morphology and Optical Properties of SnS Films Using Glancing Angle Deposition Technique. *Appl. Surf. Sci.* **2017**, *405*, 514–520.
- (840) Kim, K.; Park, J. H.; Kim, H.; Kim, J. K.; Fred Schubert, E.; Cho, J. Energy Bandgap Variation in Oblique Angle-Deposited Indium Tin Oxide. *Appl. Phys. Lett.* **2016**, *108* (4), 41910.
- (841) Castillo-Seoane, J.; Contreras-Bernal, L.; Obrero-Perez, J. M.; García-Casas, X.; Lorenzo-Lázaro, F.; Aparicio, F. J.; Lopez-Santos, C.; Rojas, T. C.; Anta, J. A.; Borrás, A.; Barranco, A.; Sanchez-Valencia, J. R. Highly Anisotropic Organometal Halide Perovskite Nanowalls Grown by Glancing-Angle Deposition. *Adv. Mater.* **2022**, *34* (18), 2107739.
- (842) Lee, S. H.; Singh, D. P.; Sung, J. H.; Jo, M.-H.; Kwon, K. C.; Kim, S. Y.; Jang, H. W.; Kim, J. K. Highly Photoresponsive and Wavelength-Selective Circularly-Polarized-Light Detector Based on Metal-Oxides Hetero-Chiral Thin Film. *Sci. Rep.* **2016**, *6*, 19580.
- (843) Maier, C. M.; Huergo, M. A.; Milosevic, S.; Pernpeintner, C.; Li, M.; Singh, D. P.; Walker, D.; Fischer, P.; Feldmann, J.; Lohmueller, T. Optical and Thermophoretic Control of Janus Nanoparticle Injection into Living Cells. *Nano Lett.* **2018**, *18* (12), 7935–794118.
- (844) Ghosh, S.; Ghosh, A. All Optical Dynamic Nanomanipulation with Active Colloidal Tweezers. *Nat. Commun.* **2019**, *10*, 4191.
- (845) Singh, H. J.; Ghosh, A. Harnessing Magnetic Dipole Resonance in Novel Dielectric Nanomaterials. *Nanoscale* **2018**, *10* (34), 16102–16106.
- (846) Singh, H. J.; Ghosh, A. Chiro-Optical Response in Helically Arranged Achiral Dielectric Nanoparticles. *J. Mater. Chem. C* **2018**, *6* (10), 2430–2434.
- (847) Ellrott, G.; Beck, P.; Sultanov, V.; Rothau, S.; Lindlein, N.; Chekhova, M.; Krstić, V. Collectively Enhanced Giant Circular Dichroism of Germanium Nanohelix Square Lattice Arrays. *Adv. Photonics Res.* **2023**, *4* (10), 2300159.
- (848) Yoo, Y. J.; Ko, J. H.; Lee, G. J.; Kang, J.; Kim, M. S.; Stanciu, S. G.; Jeong, H.-H.; Kim, D.-H.; Song, Y. M. Gires–Tournois Immunoassay Platform for Label-Free Bright-Field Imaging and Facile Quantification of Bioparticles. *Adv. Mater.* **2022**, *34* (21), 2110003.
- (849) Ko, J. H.; Yoo, Y. J.; Kim, Y. J.; Lee, S.-S.; Song, Y. M. Flexible, Large-Area Covert Polarization Display Based on Ultrathin Lossy

- Nanocolumns on a Metal Film. *Adv. Funct. Mater.* **2020**, *30* (11), 1908592.
- (850) Yoo, Y. J.; Kim, W.-G.; Ko, J. H.; Kim, Y. J.; Lee, Y.; Stanciu, S. G.; Lee, J.-M.; Kim, S.; Oh, J.-W.; Song, Y. M. Large-Area Virus Coated Ultrathin Colorimetric Sensors with a Highly Lossy Resonant Promoter for Enhanced Chromaticity. *Adv. Sci.* **2020**, *7* (18), 2000978.
- (851) Ko, J. H.; Seo, D. H.; Jeong, H.-H.; Kim, S.; Song, Y. M. Sub-1-V Electrically Programmable Optical Modulator Based on Active Tamm Plasmon. *Adv. Mater.* **2024**, *36* (15), 2310556.
- (852) Kim, J.; Han, J.-H.; Kim, G.; Kim, H. M.; Jeong, H.-H. Three-Dimensionally Shaped Silicon Nanostructures for Ultraviolet Plasmonics. In *2022 IEEE Research and Applications of Photonics in Defense Conference (RAPID)*; 2022; pp 1–2. <http://10.1109/RAPID54472.2022.9911563>.
- (853) Singh, D. P.; Lee, S. H.; Choi, I. Y.; Kim, J. K. Spatially Graded TiO<sub>2</sub>-SiO<sub>2</sub> Bragg Reflector with Rainbow-Colored Photonic Band Gap. *Opt. Express* **2015**, *23* (13), 17568–17575.
- (854) Jones, R. R.; Kerr, J. F.; Kwon, H.; Clowes, S. R.; Ji, R.; Petronijevic, E.; Zhang, L.; Dan Pantoš, G.; Smith, B.; Batten, T.; Fischer, P.; Wolverson, D.; Andrews, D. L.; Valev, V. K. Chirality Conferral Enables the Observation of Hyper-Raman Optical Activity. *Nat. Photonics* **2024**, *18* (9), 982–989.
- (855) Parchański, V.; Kapitán, J.; Bour, P. Inspecting Chiral Molecules by Raman Optical Activity Spectroscopy. *RSC Adv.* **2014**, *4* (100), 57125–57136.
- (856) Li, Z.; Fan, Q.; Ye, Z.; Wu, C.; Wang, Z.; Yin, Y. A Magnetic Assembly Approach to Chiral Superstructures. *Science* **2023**, *380* (6652), 1384–1390.
- (857) Lin, H.; Mitomo, H.; Yonamine, Y.; Guo, Z.; Ijiro, K. Core-Gap–Shell Nanoparticles@Polyaniline with Tunable Plasmonic Chiroptical Activities by pH and Electric Potential Dual Modulation. *Chem. Mater.* **2022**, *34* (9), 4062–4072.
- (858) Han, J.-H.; Kim, D.; Kim, J.; Kim, G.; Kim, J. T.; Jeong, H.-H. Responsive Photonic Nanopixels with Hybrid Scatterers. *2022*, *11* (9), 1863–1886.
- (859) Jeong, H.-H.; Alarcón-Correa, M.; Mark, A. G.; Son, K.; Lee, T.-C.; Fischer, P. Corrosion-Protected Hybrid Nanoparticles. *Adv. Sci.* **2017**, *4* (12), 1700234.
- (860) Jeong, H.-H.; Mark, A. G.; Lee, T.-C.; Son, K.; Chen, W.; Alarcón-Correa, M.; Kim, I.; Schütz, G.; Fischer, P. Selectable Nanopattern Arrays for Nanolithographic Imprint and Etch-Mask Applications. *Adv. Sci.* **2015**, *2* (7), 1500016.
- (861) Walker, D.; Kübler, M.; Morozov, K. I.; Fischer, P.; Leshansky, A. M. Optimal Length of Low Reynolds Number Nanopropellers. *Nano Lett.* **2015**, *15* (7), 4412–4416.
- (862) Singh, D. P.; Choudhury, U.; Fischer, P.; Mark, A. G. Non-Equilibrium Assembly of Light-Activated Colloidal Mixtures. *Adv. Mater.* **2017**, *29* (32), 1701328.
- (863) Singh, D. P.; Uspal, W. E.; Popescu, M. N.; Wilson, L. G.; Fischer, P. Photogravitactic Microswimmers. *Adv. Funct. Mater.* **2018**, *28* (25), 1706660.
- (864) Jeong, H.-H.; Mark, A. G.; Lee, T.-C.; Alarcón-Correa, M. A.; Eslami, S.; Qiu, T.; Gibbs, J. G.; Fischer, P. Active Nanorheology with Plasmonics. *Nano Lett.* **2016**, *16* (8), 4887–4894.
- (865) Chen, P. C.; Liu, X.; Hedrick, J. L.; Xie, Z.; Wang, S.; Lin, Q. Y.; Hersam, M. C.; Dravid, V. P.; Mirkin, C. A. Polyelemental Nanoparticle Libraries. *Science* **2016**, *352* (6293), 1565–1569.
- (866) Du, J. S.; Cherqui, C.; Ueltschi, T. W.; Wahl, C. B.; Bourgeois, M.; Van Duyne, R. P.; Schatz, G. C.; Dravid, V. P.; Mirkin, C. A. Discovering Polyelemental Nanostructures with Redistributed Plasmonic Modes through Combinatorial Synthesis. *Sci. Adv.* **2023**, *9* (51), eadj6129.
- (867) Wu, Z.; Troll, J.; Jeong, H. H.; Wei, Q.; Stang, M.; Ziemssen, F.; Wang, Z.; Dong, M.; Schnichels, S.; Qiu, T.; Fischer, P. A Swarm of Slippery Micropropellers Penetrates the Vitreous Body of the Eye. *Sci. Adv.* **2018**, *4* (11), eaat4388.
- (868) Ko, J. H.; Yoo, Y. J.; Lee, Y.; Jeong, H.-H.; Song, Y. M. A Review of Tunable Photonics: Optically Active Materials and Applications from Visible to Terahertz. *iScience* **2022**, *25* (8), 104727.
- (869) Jiang, N.; Zhuo, X.; Wang, J. Active Plasmonics: Principles, Structures, and Applications. *Chem. Rev.* **2018**, *118*, 3054–3099.
- (870) Walker, D.; Käsdorf, B. T.; Jeong, H.-H. H.; Lieleg, O.; Fischer, P. Enzymatically Active Biomimetic Micropropellers for the Penetration of Mucin Gels. *Sci. Adv.* **2015**, *1* (11), e1500501.
- (871) Kim, J. T.; Choudhury, U.; Jeong, H.-H.; Fischer, P. Nanodiamonds That Swim. *Adv. Mater.* **2017**, *29* (30), 1701024.
- (872) Kadiri, V. M.; Bussi, C.; Holle, A. W.; Son, K.; Kwon, H.; Schütz, G.; Gutierrez, M. G.; Fischer, P. Biocompatible Magnetic Micro- and Nanodevices: Fabrication of FePt Nanopropellers and Cell Transfection. *Adv. Mater.* **2020**, *32* (25), 2001114.
- (873) Hou, Y.; Leung, H. M.; Chan, C. T.; Du, J.; Chan, H. L.-W.; Lei, D. Y. Ultrabroadband Optical Superchirality in a 3D Stacked-Patch Plasmonic Metamaterial Designed by Two-Step Glancing Angle Deposition. *Adv. Funct. Mater.* **2016**, *26* (43), 7807–7816.
- (874) Yang, X.; Huang, S.; Chikkaraddy, R.; Goerlitzer, E. S. A.; Chen, F.; Du, J.; Vogel, N.; Weiss, T.; Baumberg, J. J.; Hou, Y. Chiral Plasmonic Shells: High-Performance Metamaterials for Sensitive Chiral Biomolecule Detection. *ACS Appl. Mater. Interfaces* **2022**, *14* (47), 53183–53192.
- (875) Ghosh, S.; Ghosh, A. Mobile Nanotweezers for Active Colloidal Manipulation. *Sci. Robotics* **2018**, *3* (14), eaao0076.
- (876) Li, H.; Teal, D.; Liang, Z.; Kwon, H.; Huo, D.; Jin, A.; Fischer, P.; Fan, D. E. Precise ElectrokINETIC Position and Three-Dimensional Orientation Control of a Nanowire Bioprobe in Solution. *Nat. Nanotechnol.* **2023**, *18* (10), 1213–1221.
- (877) Hulteen, J. C.; Van Duyne, R. P. Nanosphere Lithography: A Materials General Fabrication Process for Periodic Particle Array Surfaces. *J. Vac. Sci. Technol. A* **1995**, *13* (3), 1553–1558.
- (878) Ai, B.; Möhwald, H.; Wang, D.; Zhang, G. Advanced Colloidal Lithography Beyond Surface Patterning. *Adv. Mater. Interfaces* **2017**, *4* (1), 1600271.
- (879) Lee, D.; Go, M.; Kim, M.; Jang, J.; Choi, C.; Kim, J. K.; Rho, J. Multiple-Patterning Colloidal Lithography-Implemented Scalable Manufacturing of Heat-Tolerant Titanium Nitride Broadband Absorbers in the Visible to near-Infrared. *Microsyst. Nanoeng.* **2021**, *7*, 14.
- (880) Wang, J.; Duan, G.; Li, Y.; Liu, G.; Cai, W. Wet Etching-Assisted Colloidal Lithography: A General Strategy toward Nanodisk and Nanohole Arrays on Arbitrary Substrates. *ACS Appl. Mater. Interfaces* **2014**, *6* (12), 9207–9213.
- (881) Chen, J.; Dong, P.; Di, D.; Wang, C.; Wang, H.; Wang, J.; Wu, X. Controllable Fabrication of 2D Colloidal-Crystal Films with Polystyrene Nanospheres of Various Diameters by Spin-Coating. *Appl. Surf. Sci.* **2013**, *270*, 6–15.
- (882) Colson, P.; Cloots, R.; Henrist, C. Experimental Design Applied to Spin Coating of 2D Colloidal Crystal Masks: A Relevant Method? *Langmuir* **2011**, *27* (21), 12800–12806.
- (883) Haynes, C. L.; Van Duyne, R. P. Nanosphere Lithography: A Versatile Nanofabrication Tool for Studies of Size-Dependent Nanoparticle Optics. *J. Phys. Chem. B* **2001**, *105* (24), 5599–5611.
- (884) Geng, C.; Zheng, L.; Yu, J.; Yan, Q.; Wei, T.; Wang, X.; Shen, D. Thermal Annealing of Colloidal Monolayer at the Air/Water Interface: A Facile Approach to Transferrable Colloidal Masks with Tunable Interstice Size for Nanosphere Lithography. *J. Mater. Chem.* **2012**, *22* (42), 22678–22685.
- (885) Tan, B. J.-Y.; Sow, C.-H.; Lim, K.-Y.; Cheong, F.-C.; Chong, G.-L.; Wee, A. T.-S.; Ong, C.-K. Fabrication of a Two-Dimensional Periodic Non-Close-Packed Array of Polystyrene Particles. *J. Phys. Chem. B* **2004**, *108* (48), 18575–18579.
- (886) Zhou, Z.; Yu, Y.; Sun, N.; Möhwald, H.; Gu, P.; Wang, L.; Zhang, W.; König, T. A. F.; Fery, A.; Zhang, G. Broad-Range Electrically Tunable Plasmonic Resonances of a Multilayer Coaxial Nanohole Array with an Electroactive Polymer Wrapper. *ACS Appl. Mater. Interfaces* **2017**, *9* (40), 35244–35252.

- (887) Plett, A.; Enderle, F.; Saitner, M.; Manzke, A.; Pfahler, C.; Wiedemann, S.; Zieman, P. Non-Close-Packed Crystals from Self-Assembled Polystyrene Spheres by Isotropic Plasma Etching: Adding Flexibility to Colloid Lithography. *Adv. Funct. Mater.* **2009**, *19* (20), 3279–3284.
- (888) Lee, S. H.; Bantz, K. C.; Lindquist, N. C.; Oh, S.-H.; Haynes, C. L. Self-Assembled Plasmonic Nanohole Arrays. *Langmuir* **2009**, *25* (23), 13685–13693.
- (889) Nemirovski, A.; Gonidec, M.; Fox, J. M.; Jean-Remy, P.; Turnage, E.; Whitesides, G. M. Engineering Shadows to Fabricate Optical Metasurfaces. *ACS Nano* **2014**, *8* (11), 11061–11070.
- (890) Choi, D.-G.; Yu, H. K.; Jang, S. G.; Yang, S.-M. Colloidal Lithographic Nanopatterning via Reactive Ion Etching. *J. Am. Chem. Soc.* **2004**, *126* (22), 7019–7025.
- (891) Lee, J.-S.; Je, K.; Kim, S.-H. Designing Multicolored Photonic Micropatterns through the Regioselective Thermal Compression of Inverse Opals. *Adv. Funct. Mater.* **2016**, *26* (25), 4587–4594.
- (892) Kang, H.; Heo, Y. J.; Kim, D. J.; Kim, J. H.; Jeon, T. Y.; Cho, S.; So, H.-M.; Chang, W. S.; Kim, S.-H. Droplet-Guiding Superhydrophobic Arrays of Plasmonic Microposts for Molecular Concentration and Detection. *ACS Appl. Mater. Interfaces* **2017**, *9* (42), 37201–37209.
- (893) Park, S.; Kim, S.-H. Regioselective Growth of Colloidal Crystals Induced by Depletion Attraction. *Adv. Mater.* **2024**, *36* (4), 2309938.
- (894) Lee, H. J.; Park, S.; Kim, J. B.; Kim, S.-H. Designing 3D Polymeric Structures through Capillary Wetting on Colloidal Monolayer. *Adv. Funct. Mater.* **2023**, *33* (1), 2208402.
- (895) Tabatabaei, M.; Sangar, A.; Kazemi-Zanjani, N.; Torchio, P.; Merlen, A.; Lagugné-Labarthet, F. Optical Properties of Silver and Gold Tetrahedral Nanopyramid Arrays Prepared by Nanosphere Lithography. *J. Phys. Chem. C* **2013**, *117* (28), 14778–14786.
- (896) Lee, S. Y.; Yoon, J.; Kim, S.-H. Metallic Nanodimple Arrays for Wide-Angle Coloration via Plasmonic and Structural Resonances. *Chem. Mater.* **2021**, *33* (12), 4628–4637.
- (897) Wang, L.; Ng, R. J. H.; Safari Dinachali, S.; Jalali, M.; Yu, Y.; Yang, J. K. W. Large Area Plasmonic Color Palettes with Expanded Gamut Using Colloidal Self-Assembly. *ACS Photonics* **2016**, *3* (4), 627–633.
- (898) Ai, B.; Yu, Y.; Möhwald, H.; Zhang, G. Responsive Monochromatic Color Display Based on Nanovolcano Arrays. *Adv. Opt. Mater.* **2013**, *1* (10), 724–731.
- (899) Zhang, X.; Xiao, X.; Dai, Z.; Wu, W.; Zhang, X.; Fu, L.; Jiang, C. Ultrasensitive SERS performance in 3D “sunflower-like” nanoarrays decorated with Ag nanoparticles. *Nanoscale* **2017**, *9*, 3114–3120.
- (900) Lin, D.; Wu, Z.; Li, S.; Zhao, W.; Ma, C.; Wang, J.; Jiang, Z.; Zhong, Z.; Zheng, Y.; Yang, X. Large-Area Au-Nanoparticle-Functionalized Si Nanorod Arrays for Spatially Uniform Surface-Enhanced Raman Spectroscopy. *ACS Nano* **2017**, *11* (2), 1478–1487.
- (901) Fazio, B.; D’Andrea, C.; Foti, A.; Messina, E.; Irrera, A.; Donato, M. G.; Villari, V.; Micali, N.; Maragò, O. M.; Guccardi, P. G. SERS Detection of Biomolecules at Physiological pH via Aggregation of Gold Nanorods Mediated by Optical Forces and Plasmonic Heating. *Sci. Rep.* **2016**, *6*, 26952.
- (902) Koh, E. H.; Lee, W.-C.; Choi, Y.-J.; Moon, J.-I.; Jang, J.; Park, S.-G.; Choo, J.; Kim, D.-H.; Jung, H. S. A Wearable Surface-Enhanced Raman Scattering Sensor for Label-Free Molecular Detection. *ACS Appl. Mater. Interfaces* **2021**, *13* (2), 3024–3032.
- (903) Kim, D. J.; Jeon, T. Y.; Park, S.-G.; Han, H. J.; Im, S. H.; Kim, D.-H.; Kim, S.-H. Uniform Microgels Containing Agglomerates of Silver Nanocubes for Molecular Size-Selectivity and High SERS Activity. *Small* **2017**, *13* (23), 1604048.
- (904) Koh, E. H.; Mun, C.; Kim, C.; Park, S.-G.; Choi, E. J.; Kim, S. H.; Dang, J.; Choo, J.; Oh, J.-W.; Kim, D.-H.; Jung, H. S. M13 Bacteriophage/Silver Nanowire Surface-Enhanced Raman Scattering Sensor for Sensitive and Selective Pesticide Detection. *ACS Appl. Mater. Interfaces* **2018**, *10* (12), 10388–10397.
- (905) Kim, Y. H.; Kim, D. J.; Lee, S.; Kim, D.-H.; Park, S.-G.; Kim, S.-H. Microfluidic Designing Microgels Containing Highly Concentrated Gold Nanoparticles for SERS Analysis of Complex Fluids. *Small* **2019**, *15* (52), 1905076.
- (906) Greeneltch, N. G.; Blaber, M. G.; Henry, A.-I.; Schatz, G. C.; Van Duyne, R. P. Immobilized Nanorod Assemblies: Fabrication and Understanding of Large Area Surface-Enhanced Raman Spectroscopy Substrates. *Anal. Chem.* **2013**, *85* (4), 2297–2303.
- (907) Fu, C. Y.; Kho, K. W.; Dinish, U. S.; Koh, Z. Y.; Malini, O. Enhancement in SERS Intensity with Hierarchical Nanostructures by Bimetallic Deposition Approach. *J. Raman Spectrosc.* **2012**, *43* (8), 977–985.
- (908) Wang, Z.; Yang, H.; Wang, M.; Petti, L.; Jiang, T.; Jia, Z.; Xie, S.; Zhou, J. SERS-Based Multiplex Immunoassay of Tumor Markers Using Double  $\text{SiO}_2/\text{Ag}$  Immune Probes and Gold-Film Hemisphere Array Immune Substrate. *Coll. Surf. A* **2018**, *546*, 48–58.
- (909) Zhao, X.; Wen, J.; Zhang, M.; Wang, D.; Wang, Y.; Chen, L.; Zhang, Y.; Yang, J.; Du, Y. Design of Hybrid Nanostructural Arrays to Manipulate SERS-Active Substrates by Nanosphere Lithography. *ACS Appl. Mater. Interfaces* **2017**, *9* (8), 7710–7716.
- (910) Jeon, T. Y.; Park, S.-G.; Lee, S. Y.; Jeon, H. C.; Yang, S.-M. Shape Control of Ag Nanostructures for Practical SERS Substrates. *ACS Appl. Mater. Interfaces* **2013**, *5* (2), 243–248.
- (911) Gao, Y.; Wang, J.; Wang, W.; Zhao, T.; Cui, Y.; Liu, P.; Xu, S.; Luo, X. More Symmetrical “Hot Spots” Ensure Stronger Plasmon-Enhanced Fluorescence: From Au Nanorods to Nanostars. *Anal. Chem.* **2021**, *93* (4), 2480–2489.
- (912) Liu, S.-Y.; Huang, L.; Li, J.-F.; Wang, C.; Li, Q.; Xu, H.-X.; Guo, H.-L.; Meng, Z.-M.; Shi, Z.; Li, Z.-Y. Simultaneous Excitation and Emission Enhancement of Fluorescence Assisted by Double Plasmon Modes of Gold Nanorods. *J. Phys. Chem. C* **2013**, *117* (20), 10636–10642.
- (913) Theodorou, I. G.; Jawad, Z. a. R.; Qin, H.; Aboagye, E. O.; Porter, A. E.; Ryan, M. P.; Xie, F. Significant Metal Enhanced Fluorescence of  $\text{Ag}_2\text{S}$  Quantum Dots in the Second Near-Infrared Window. *Nanoscale* **2016**, *8* (26), 12869–12873.
- (914) Hong, W.; Zhang, Y.; Gan, L.; Chen, X.; Zhang, M. Control of plasmonic fluorescence enhancement on self-assembled 2-D colloidal crystals. *J. Mater. Chem. C* **2015**, *3*, 6185–6191.
- (915) Xie, F.; Centeno, A.; Ryan, M. R.; Riley, D. J.; Alford, N. M. Au Nanostructures by Colloidal Lithography: From Quenching to Extensive Fluorescence Enhancement. *J. Mater. Chem. B* **2013**, *1* (4), 536–543.
- (916) Pang, J. S.; Theodorou, I. G.; Centeno, A.; Petrov, P. K.; Alford, N. M.; Ryan, M. P.; Xie, F. Tunable Three-Dimensional Plasmonic Arrays for Large Near-Infrared Fluorescence Enhancement. *ACS Appl. Mater. Interfaces* **2019**, *11* (26), 23083–23092.
- (917) Matsumori, K.; Fujimura, R. Broadband Light Absorption of an Al Semishell-MIM Nanostructure in the UV to near-Infrared Regions. *Opt. Lett.* **2018**, *43* (12), 2981–2984.
- (918) Jiang, J.; Cao, Y.; Zhou, X.; Xu, H.; Ning, K.; Xiao, X.; Lu, Y.; Ding, C.; Chen, Y.; Dong, J. Colloidal Self-Assembly Based Ultrathin Metasurface for Perfect Absorption across the Entire Visible Spectrum. *Nanophotonics* **2023**, *12* (8), 1581–1590.
- (919) Guo, Z.; Liu, X.; Li, C.; Li, J.; Cai, H.; Fu, M.; He, D.; Wang, Y. Near-Perfect Broadband Metamaterial Absorbers of Truncated Nanocones Using Colloidal Lithography. *Opt. Mater.* **2021**, *119*, 111352.
- (920) Hou, W.; Yang, F.; Chen, Z.; Dong, J.; Jiang, S. Wide-Angle and Broadband Solar Absorber Made Using Highly Efficient Large-Area Fabrication Strategy. *Opt. Express* **2022**, *30* (3), 4424–4433.
- (921) Yang, F.; Li, R.-H.; Tan, S.-L.; Dong, J.-W.; Jiang, S.-J. Visible-Mid Infrared Ultra-Broadband and Wide-Angle Metamaterial Perfect Absorber Based on Cermet Films with Nano-Cone Structure. *Nanophotonics* **2023**, *12* (13), 2451–2460.
- (922) Lazaroiu, A. C.; Gmal Osman, M.; Strejoiu, C.-V.; Lazaroiu, G. A Comprehensive Overview of Photovoltaic Technologies and Their Efficiency for Climate Neutrality. *Sustainability* **2023**, *15* (23), 16297.

- (923) Nayak, P. K.; Mahesh, S.; Snaith, H. J.; Cahen, D. Photovoltaic Solar Cell Technologies: Analysing the State of the Art. *Nat. Rev. Mater.* **2019**, *4* (4), 269–285.
- (924) Ali, A.; El-Mellouhi, F.; Mitra, A.; Aïssa, B. Research Progress of Plasmonic Nanostructure-Enhanced Photovoltaic Solar Cells. *Nanomaterials* **2022**, *12* (5), 788.
- (925) Atwater, H. A.; Polman, A. Plasmonics for Improved Photovoltaic Devices. *Nat. Mater.* **2010**, *9* (3), 205–213.
- (926) Dambare, M. V.; Butey, B.; Moharil, S. V. Solar Photovoltaic Technology: A Review of Different Types of Solar Cells and Its Future Trends. *J. Phys. Conf. Ser.* **2021**, *1913* (1), No. 012053.
- (927) Elsarrag, E.; Pernau, H.; Heuer, J.; Roshan, N.; Alhor, Y.; Bartholomé, K. Spectrum Splitting for Efficient Utilization of Solar Radiation: A Novel Photovoltaic-Thermoelectric Power Generation System. *Renewables: Wind, Water, and Solar* **2015**, *2*, 16.
- (928) Qiao, F.; Xie, Y.; He, G.; Chu, H.; Liu, W.; Chen, Z. Light Trapping Structures and Plasmons Synergistically Enhance the Photovoltaic Performance of Full-Spectrum Solar Cells. *Nanoscale* **2020**, *12* (3), 1269–1280.
- (929) He, Z.; Tian, Y. Design and Analysis of Comprehensive Solar Utilization System Based on Photovoltaic Concentration and Spectral Splitting. *Processes* **2023**, *11* (7), 1944.
- (930) Bierman, D. M.; Lenert, A.; Wang, E. N. Spectral Splitting Optimization for High-Efficiency Solar Photovoltaic and Thermal Power Generation. *Appl. Phys. Lett.* **2016**, *109* (24), 243904.
- (931) Kuik, M.; Wetzel, G.-J. A. H.; Nicolai, H. T.; Craciun, N. I.; De Leeuw, D. M.; Blom, P. W. M. 25th Anniversary Article: Charge Transport and Recombination in Polymer Light-Emitting Diodes. *Adv. Mater.* **2014**, *26* (4), 512–531.
- (932) Ye, L.; Zhang, S.; Huo, L.; Zhang, M.; Hou, J. Molecular Design toward Highly Efficient Photovoltaic Polymers Based on Two-Dimensional Conjugated Benzodithiophene. *Acc. Chem. Res.* **2014**, *47* (5), 1595–1603.
- (933) Blom, P. W. M.; Mihailetti, V. D.; Koster, L. J. A.; Markov, D. E. Device Physics of Polymer:Fullerene Bulk Heterojunction Solar Cells. *Adv. Mater.* **2007**, *19* (12), 1551–1566.
- (934) Riquelme, A.; Bennett, L. J.; Courtier, N. E.; Wolf, M. J.; Contreras-Bernal, L.; Walker, A. B.; Richardson, G.; Anta, J. A. Identification of Recombination Losses and Charge Collection Efficiency in a Perovskite Solar Cell by Comparing Impedance Response to a Drift-Diffusion Model. *Nanoscale* **2020**, *12* (33), 17385–17398.
- (935) Muchuweni, E.; Mombeshora, E. T.; Martincigh, B. S.; Nyamori, V. O. Recent Applications of Carbon Nanotubes in Organic Solar Cells. *Front. Chem.* **2022**, *9*, 733552.
- (936) Cui, N.; Song, Y.; Tan, C.-H.; Zhang, K.; Yang, X.; Dong, S.; Xie, B.; Huang, F. Stretchable Transparent Electrodes for Conformable Wearable Organic Photovoltaic Devices. *npj Flex Electron* **2021**, *5*, 31.
- (937) Zhu, J.; et al. Changes of Solar Cell Parameters during Damp-Heat Exposure. *Prog. Photovolt. Res. Appl.* **2016**, *24* (10), 1346–1358.
- (938) Sanchez-Sobrado, O.; Mendes, M. J.; Haque, S.; Mateus, T.; Araujo, A.; Aguas, H.; Fortunato, E.; Martins, R. Colloidal-Lithographed TiO<sub>2</sub> Photonic Nanostructures for Solar Cell Light Trapping. *J. Mater. Chem. C* **2017**, *5* (27), 6852–6861.
- (939) Sanchez-Sobrado, O.; Mendes, M. J.; Haque, S.; Mateus, T.; Aguas, H.; Fortunato, E.; Martins, R. Lightwave Trapping in Thin Film Solar Cells with Improved Photonic-Structured Front Contacts. *J. Mater. Chem. C* **2019**, *7* (21), 6456–6464.
- (940) Abdelhameed, M.; Abdelbar, M. F.; El Basaty, A. B.; Jevasuhan, W.; Dai, K.; Shinotsuka, K.; Hatta, Y.; Fukata, N. Current Transport Characterization and Photovoltaic Performance of Si Nanopencil-Based Schottky Junction Assisted with VO<sub>x</sub> as a Hole-Injection Layer. *Micro Nanostructures* **2023**, *176*, 207519.
- (941) Santos, I. M.; Alexandre, M.; Mihailetti, V. D.; Silva, J. A.; Mateus, T.; Mouquinho, A.; Boane, J.; Vicente, A. T.; Nunes, D.; Menda, U. D.; Aguas, H.; Fortunato, E.; Martins, R.; Mendes, M. J. Optically-Boosted Planar IBC Solar Cells with Electrically-Harmless Photonic Nanocoatings. *Adv. Opt. Mater.* **2023**, *11* (15), 2300276.
- (942) Lee, J.-S.; Yu, J.-H.; Hwang, K.-H.; Nam, S.-H.; Boo, J.-H.; Yun, S. H. Patterning ITO by Template-Assisted Colloidal-Lithography for Enhancing Power Conversion Efficiency in Organic Photovoltaic. *J. Nanosci Nanotechnol.* **2016**, *16* (5), 5024–5028.
- (943) Mendes, M. J.; Haque, S.; Sanchez-Sobrado, O.; Araújo, A.; Águas, H.; Fortunato, E.; Martins, R. Optimal-Enhanced Solar Cell Ultra-Thinning with Broadband Nanophotonic Light Capture. *iScience* **2018**, *3*, 238–254.
- (944) Centeno, P.; Alexandre, M. F.; Chapa, M.; Pinto, J. V.; Deuermeier, J.; Mateus, T.; Fortunato, E.; Martins, R.; Águas, H.; Mendes, M. J. Self-Cleaned Photonic-Enhanced Solar Cells with Nanostructured Parylene-C. *Adv. Mater. Interfaces* **2020**, *7* (15), 2000264.
- (945) Chirumamilla, A.; Ding, F.; Yang, Y.; Mani Rajan, M. S.; Bozhevskyi, S. I.; Sutherland, D. S.; Pedersen, K.; Chirumamilla, M. Tungsten Nanodisc-Based Spectrally-Selective Polarization-Independent Thermal Emitters. *Sol. Energy Mater. Sol. Cells* **2023**, *259*, 112449.
- (946) Dao, T. D.; Chen, K.; Ishii, S.; Ohi, A.; Nabatame, T.; Kitajima, M.; Nagao, T. Infrared Perfect Absorbers Fabricated by Colloidal Mask Etching of Al-Al<sub>2</sub>O<sub>3</sub>-Al Trilayers. *ACS Photonics* **2015**, *2* (7), 964–970.
- (947) Chen, K.; Dao, T. D.; Ishii, S.; Aono, M.; Nagao, T. Infrared Aluminum Metamaterial Perfect Absorbers for Plasmon-Enhanced Infrared Spectroscopy. *Adv. Funct. Mater.* **2015**, *25* (42), 6637–6643.
- (948) Xu, F.; Zhang, Z.; Ma, J.; Ma, C.; Guan, B.-O.; Chen, K. Large-Area Ordered Palladium Nanostructures by Colloidal Lithography for Hydrogen Sensing. *Molecules* **2022**, *27* (18), 6100.
- (949) Lay, B.; Kandjani, A. E.; Kabir, K. M. M.; Hartley, P.; Sabri, Y. M.; Bhargava, S. K. Gas Sensing Performance Enhancement: Determining the Role of Active Sites through Colloidal Lithography. *Sensors Actuat. Chem.* **2018**, *273*, 1376–1384.
- (950) Chul Yang, J.; Won Hong, S.; Jeon, S.; Il Park, W.; Byun, M.; Park, J. Molecular Imprinting of Hemispherical Pore-Structured Thin Films via Colloidal Lithography for Gaseous Formaldehyde Gravimetric Sensing. *Appl. Surf. Sci.* **2021**, *570*, 151161.
- (951) Kim, D. H.; Lee, H. J.; Park, D.; Yim, J.-H.; Choi, H. K. Fabrication of a Nanoscale 2D PEDOT Pattern via the Combination of Colloidal Lithography and Vapor Phase Polymerization for Application in Transparent, Highly Sensitive Bending Sensors. *Nanoscale* **2023**, *15* (9), 4620–4627.
- (952) Sišláková, I.; Petruš, O.; Shepa, J.; Farka, Z.; Oriňák, A.; Oriňáková, R. Colloidal Lithography as a Novel Approach for the Development of Ni-Nanocavity Insulin Sensor. *Sci. Rep.* **2022**, *12*, 11020.
- (953) Zhang, Z.; Zhao, F.; Gao, R.; Jao, C.-Y.; Ma, C.; Li, J.; Li, X.; Guan, B.-O.; Cetin, A. E.; Chen, K. Rayleigh Anomaly-Enabled Mode Hybridization in Gold Nanohole Arrays by Scalable Colloidal Lithography for Highly-Sensitive Biosensing. *Nanophotonics* **2022**, *11* (3), 507–517.
- (954) Li, F.; Josephson, D. P.; Stein, A. Colloidal Assembly: The Road from Particles to Colloidal Molecules and Crystals. *Angew. Chem. Inter. Ed.* **2011**, *50* (2), 360–388.
- (955) Whitesides, G. M.; Grzybowski, B. Self-Assembly at All Scales. *Science* **2002**, *295* (5564), 2418–2421.
- (956) Whitesides, G. M.; Boncheva, M. Beyond Molecules: Self-Assembly of Mesoscopic and Macroscopic Components. *Proc. Natl. Acad. Sci. U.S.A.* **2002**, *99* (8), 4769–4774.
- (957) Boles, M. A.; Engel, M.; Talapin, D. V. Self-Assembly of Colloidal Nanocrystals: From Intricate Structures to Functional Materials. *Chem. Rev.* **2016**, *116* (18), 11220–11289.
- (958) Gómez-Graña, S.; Fernández-López, C.; Polavarapu, L.; Salmon, J.-B.; Leng, J.; Pastoriza-Santos, I.; Pérez-Juste, J. Gold Nanoctahedra with Tunable Size and Microfluidic-Induced 3D Assembly for Highly Uniform SERS-Active Supercrystals. *Chem. Mater.* **2015**, *27* (24), 8310–8317.
- (959) Schulz, F.; Lange, H. Optimizing Interparticle Gaps in Large-Scale Gold Nanoparticle Supercrystals for Flexible Light-Matter Coupling. *Adv. Opt. Mater.* **2022**, *10* (24), 2202064.

- (960) Cheng, W.; Campolongo, M. J.; Cha, J. J.; Tan, S. J.; Umbach, C. C.; Muller, D. A.; Luo, D. Free-Standing Nanoparticle Superlattice Sheets Controlled by DNA. *Nat. Mater.* **2009**, *8* (6), 519–525.
- (961) Xia, Y.; Whitesides, G. M. Soft Lithography. *Angew. Chem. Inter. Ed.* **1998**, *37* (5), 550–575.
- (962) Tien, J.; Terfert, A.; Whitesides, G. M. Microfabrication through Electrostatic Self-Assembly. *Langmuir* **1997**, *13* (20), 5349–5355.
- (963) Angly, J.; Iazzolino, A.; Salmon, J.-B.; Leng, J.; Chandran, S. P.; Ponsinet, V.; Dézert, A.; Le Beulze, A.; Mornet, S.; Tréguer-Delapierre, M.; Correa-Duarte, M. A. Microfluidic-Induced Growth and Shape-Up of Three-Dimensional Extended Arrays of Densely Packed Nanoparticles. *ACS Nano* **2013**, *7* (8), 6465–6477.
- (964) Si, K. J.; Sikdar, D.; Chen, Y.; Eftekhari, F.; Xu, Z.; Tang, Y.; Xiong, W.; Guo, P.; Zhang, S.; Lu, Y.; Bao, Q.; Zhu, W.; Premaratne, M.; Cheng, W. Giant Plasmene Nanosheets, Nanoribbons, and Origami. *ACS Nano* **2014**, *8* (11), 11086–11093.
- (965) Si, K. J.; Dong, D.; Shi, Q.; Zhu, W.; Premaratne, M.; Cheng, W. Ultrathin Fresnel Lens Based on Plasmene Nanosheets. *Mater. Today* **2019**, *23*, 9–15.
- (966) Hunter, R. J.; Ottewill, R. H.; Rowell, R. L. *Charge and potential distribution at interfaces*; Academic Press: New York, 1981.
- (967) Zhang, H.; Liu, Y.; Shahidan, M. F. S.; Kinnear, C.; Maasoumi, F.; Cadusch, J.; Akinoglu, E. M.; James, T. D.; Widmer-Cooper, A.; Roberts, A.; Mulvaney, P. Direct Assembly of Vertically Oriented, Gold Nanorod Arrays. *Adv. Funct. Mater.* **2021**, *31* (6), 2006753.
- (968) Kinnear, C.; Cadusch, J.; Zhang, H.; Lu, J.; James, T. D.; Roberts, A.; Mulvaney, P. Directed Chemical Assembly of Single and Clustered Nanoparticles with Silanized Templates. *Langmuir* **2018**, *34* (25), 7355–7363.
- (969) Myers, B. D.; Palacios, E.; Myers, D. I.; Butun, S.; Aydin, K.; Dravid, V. P. Stimuli-Responsive DNA-Linked Nanoparticle Arrays as Programmable Surfaces. *Nano Lett.* **2019**, *19* (7), 4535–4542.
- (970) Nedev, S.; Urban, A. S.; Lutich, A. A.; Feldmann, J. Optical Force Stamping Lithography. *Nano Lett.* **2011**, *11* (11), 5066–5070.
- (971) Gargiulo, J.; Cerrota, S.; Cortés, E.; Violi, I. L.; Stefani, F. D. Connecting Metallic Nanoparticles by Optical Printing. *Nano Lett.* **2016**, *16* (2), 1224–1229.
- (972) Gargiulo, J.; Violi, I. L.; Cerrota, S.; Chvátal, L.; Cortés, E.; Perassi, E. M.; Diaz, F.; Zemánek, P.; Stefani, F. D. Accuracy and Mechanistic Details of Optical Printing of Single Au and Ag Nanoparticles. *ACS Nano* **2017**, *11* (10), 9678–9688.
- (973) Grzelak, D.; Tupikowska, M.; Vila-Liarte, D.; Beutel, D.; Bagiński, M.; Parzyszek, S.; Góra, M.; Rockstuhl, C.; Liz-Marzáñ, L. M.; Lewandowski, W. Liquid Crystal Templatated Chiral Plasmonic Films with Dynamic Tunability and Moldability. *Adv. Funct. Mater.* **2022**, *32* (16), 2111280.
- (974) Kumar, J.; Eraña, H.; López-Martínez, E.; Claes, N.; Martín, V. F.; Solís, D. M.; Bals, S.; Cortajarena, A. L.; Castilla, J.; Liz-Marzáñ, L. M. Detection of Amyloid Fibrils in Parkinson's Disease Using Plasmonic Chirality. *Proc. Natl. Acad. Sci. U.S.A.* **2018**, *115* (13), 3225–3230.
- (975) Lu, J.; Xue, Y.; Bernardino, K.; Zhang, N.-N.; Gomes, W. R.; Ramesar, N. S.; Liu, S.; Hu, Z.; Sun, T.; de Moura, A. F.; Kotov, N. A.; Liu, K. Enhanced Optical Asymmetry in Supramolecular Chiroplasmonic Assemblies with Long-Range Order. *Science* **2021**, *371* (6536), 1368–1374.
- (976) Kasani, S.; Curtin, K.; Wu, N. A Review of 2D and 3D Plasmonic Nanostructure Array Patterns: Fabrication, Light Management and Sensing Applications. *Nanophotonics* **2019**, *8* (12), 2065–2089.
- (977) Volk, K.; Fitzgerald, J. P. S.; Karg, M. In-Plane Surface Lattice and Higher Order Resonances in Self-Assembled Plasmonic Monolayers: From Substrate-Supported to Free-Standing Thin Films. *ACS Appl. Mater. Interfaces* **2019**, *11* (17), 16096–16106.
- (978) Ponomareva, E.; Volk, K.; Mulvaney, P.; Karg, M. Surface Lattice Resonances in Self-Assembled Gold Nanoparticle Arrays: Impact of Lattice Period, Structural Disorder, and Refractive Index on Resonance Quality. *Langmuir* **2020**, *36* (45), 13601–13612.
- (979) Rycenga, M.; Camargo, P. H. C.; Xia, Y. Template-Assisted Self-Assembly: A Versatile Approach to Complex Micro- and Nanostructures. *Soft Matter* **2009**, *5* (6), 1129–1136.
- (980) Yin, Y.; Lu, Y.; Xia, Y. A Self-Assembly Approach to the Formation of Asymmetric Dimers from Monodispersed Spherical Colloids. *J. Am. Chem. Soc.* **2001**, *123* (4), 771–772.
- (981) Gupta, V.; Probst, P. T.; Goßler, F. R.; Steiner, A. M.; Schubert, J.; Brasse, Y.; König, T. A. F.; Fery, A. Mechanotunable Surface Lattice Resonances in the Visible Optical Range by Soft Lithography Templates and Directed Self-Assembly. *ACS Appl. Mater. Interfaces* **2019**, *11* (31), 28189–28196.
- (982) Malaquin, L.; Kraus, T.; Schmid, H.; Delamarche, E.; Wolf, H. Controlled Particle Placement through Convective and Capillary Assembly. *Langmuir* **2007**, *23* (23), 11513–11521.
- (983) Juodénas, M.; Tamulevičius, T.; Henzie, J.; Erts, D.; Tamulevičius, S. Surface Lattice Resonances in Self-Assembled Arrays of Monodisperse Ag Cuboctahedra. *ACS Nano* **2019**, *13* (8), 9038–9047.
- (984) Juodénas, M.; Peckus, D.; Tamulevičius, T.; Yamauchi, Y.; Tamulevičius, S.; Henzie, J. Effect of Ag Nanocube Optomechanical Modes on Plasmonic Surface Lattice Resonances. *ACS Photonics* **2020**, *7* (11), 3130–3140.
- (985) Greybush, N. J.; Liberal, I.; Malassis, L.; Kikkawa, J. M.; Engheta, N.; Murray, C. B.; Kagan, C. R. Plasmon Resonances in Self-Assembled Two-Dimensional Au Nanocrystal Metamolecules. *ACS Nano* **2017**, *11* (3), 2917–2927.
- (986) Fan, J. A.; Bao, K.; Sun, L.; Bao, J.; Manoharan, V. N.; Nordlander, P.; Capasso, F. Plasmonic Mode Engineering with Templated Self-Assembled Nanoclusters. *Nano Lett.* **2012**, *12* (10), 5318–5324.
- (987) Pioli, R.; Fernandez-Rodriguez, M. A.; Grillo, F.; Alvarez, L.; Stocker, R.; Isa, L.; Secchi, E. Sequential Capillarity-Assisted Particle Assembly in a Microfluidic Channel. *Lab Chip* **2021**, *21* (5), 888–895.
- (988) Cheng, W.; Park, N.; Walter, M. T.; Hartman, M. R.; Luo, D. Nanopatterning Self-Assembled Nanoparticle Superlattices by Moulding Microdroplets. *Nat. Nanotechnol.* **2008**, *3* (11), 682–690.
- (989) Scarabelli, L.; Vila-Liarte, D.; Mihi, A.; Liz-Marzáñ, L. M. Templated Colloidal Self-Assembly for Lattice Plasmon Engineering. *Acc. Mater. Res.* **2021**, *2* (9), 816–827.
- (990) Alba, M.; Pazos-Perez, N.; Vaz, B.; Formentin, P.; Tebbe, M.; Correa-Duarte, M. A.; Granero, P.; Ferré-Borrull, J.; Alvarez, R.; Pallares, J.; Fery, A.; de Lera, A. R.; Marsal, L. F.; Alvarez-Puebla, R. A. Macroscale Plasmonic Substrates for Highly Sensitive Surface-Enhanced Raman Scattering. *Angew. Chem. Inter. Ed.* **2013**, *52* (25), 6459–6463.
- (991) Matricardi, C.; Hanske, C.; Garcia-Pomar, J. L.; Langer, J.; Mihi, A.; Liz-Marzáñ, L. M. Gold Nanoparticle Plasmonic Superlattices as Surface-Enhanced Raman Spectroscopy Substrates. *ACS Nano* **2018**, *12* (8), 8531–8539.
- (992) Charconnet, M.; Korsa, M. T.; Petersen, S.; Plou, J.; Hanske, C.; Adam, J.; Seifert, A. Generalization of Self-Assembly Toward Differently Shaped Colloidal Nanoparticles for Plasmonic Superlattices. *Small Methods* **2023**, *7* (4), 2201546.
- (993) Plou, J.; Charconnet, M.; García, I.; Calvo, J.; Liz-Marzáñ, L. M. Preventing Memory Effects in Surface-Enhanced Raman Scattering Substrates by Polymer Coating and Laser-Activated Deprotection. *ACS Nano* **2021**, *15* (5), 8984–8995.
- (994) Plou, J.; García, I.; Charconnet, M.; Astobiza, I.; García-Astrain, C.; Matricardi, C.; Mihi, A.; Carracedo, A.; Liz-Marzáñ, L. M. Multiplex SERS Detection of Metabolic Alterations in Tumor Extracellular Media. *Adv. Funct. Mater.* **2020**, *30* (17), 1910335.
- (995) Qi, X.; Pérez, L. A.; Alonso, M. I.; Mihi, A. High Q-Factor Plasmonic Surface Lattice Resonances in Colloidal Nanoparticle Arrays. *ACS Appl. Mater. Interfaces* **2024**, *16* (1), 1259–1267.
- (996) Charconnet, M.; Kuttner, C.; Plou, J.; García-Pomar, J. L.; Mihi, A.; Liz-Marzáñ, L. M.; Seifert, A. Mechanically Tunable Lattice-Plasmon Resonances by Templated Self-Assembled Superlattices for

- Multi-Wavelength Surface-Enhanced Raman Spectroscopy. *Small Methods* **2021**, *5* (10), 2100453.
- (997) Molet, P.; Passarelli, N.; Pérez, L. A.; Scarabelli, L.; Mihi, A. Engineering Plasmonic Colloidal Meta-Molecules for Tunable Photonic Supercrystals. *Adv. Opt. Mater.* **2021**, *9* (20), 2100761.
- (998) Conti, Y.; Passarelli, N.; Mendoza-Carreño, J.; Scarabelli, L.; Mihi, A. Colloidal Silver Nanoparticle Plasmonic Arrays for Versatile Lasing Architectures via Template-Assisted Self-Assembly. *Adv. Opt. Mater.* **2023**, *11* (23), 2300983.
- (999) Hanske, C.; Hill, E. H.; Vila-Liarte, D.; González-Rubio, G.; Matricardi, C.; Mihi, A.; Liz-Marzán, L. M. Solvent-Assisted Self-Assembly of Gold Nanorods into Hierarchically Organized Plasmonic Mesostructures. *ACS Appl. Mater. Interfaces* **2019**, *11* (12), 11763–11771.
- (1000) Vila-Liarte, D.; Feil, M. W.; Manzi, A.; Garcia-Pomar, J. L.; Huang, H.; Döblinger, M.; Liz-Marzán, L. M.; Feldmann, J.; Polavarapu, L.; Mihi, A. Templated-Assembly of CsPbBr<sub>3</sub> Perovskite Nanocrystals into 2D Photonic Supercrystals with Amplified Spontaneous Emission. *Angew. Chem. Inter. Ed.* **2020**, *59* (40), 17750–17756.
- (1001) Mendoza-Carreño, J.; Molet, P.; Otero-Martínez, C.; Alonso, M. I.; Polavarapu, L.; Mihi, A. Nanoimprinted 2D-Chiral Perovskite Nanocrystal Metasurfaces for Circularly Polarized Photoluminescence. *Adv. Mater.* **2023**, *35* (15), 2210477.
- (1002) Lambert, K.; Moreels, I.; Thourhout, D. V.; Hens, Z. Quantum Dot Micropatterning on Si. *Langmuir* **2008**, *24* (11), 5961–5966.
- (1003) Achermann, M.; Petruska, M. A.; Crooker, S. A.; Klimov, V. I. Picosecond Energy Transfer in Quantum Dot Langmuir–Blodgett Nanoassemblies. *J. Phys. Chem. B* **2003**, *107* (50), 13782–13787.
- (1004) Crawford, N. F.; Leblanc, R. M. CdSe and CdSe(ZnS) Quantum Dots in 2D: A Langmuir Monolayer Approach. *Coord. Chem. Rev.* **2014**, *263*–264, 13–24.
- (1005) Biswas, S.; Brinkmann, F.; Hirtz, M.; Fuchs, H. Patterning of Quantum Dots by Dip-Pen and Polymer Pen Nanolithography. *Nanofabrication* **2015**, *2* (1), 19–26.
- (1006) Taylor, Z. R.; Sanchez, E. S.; Keay, J. C.; Johnson, M. B.; Schmidke, D. W. Patterning of Quantum Dot Bioconjugates via Particle Lithography. *Langmuir* **2010**, *26* (24), 18938–18944.
- (1007) Nam, T. W.; Choi, M.-J.; Jung, Y. S. Ultrahigh-Resolution Quantum Dot Patterning for Advanced Optoelectronic Devices. *Chem. Commun.* **2023**, *59* (19), 2697–2710.
- (1008) Li, Z.-Q.; Guo, P.; Zhou, Y.-G. Dip-Pen Nanolithography Enabled Functional Nanomaterials and Their Applications. *Adv. Mater. Technol.* **2021**, *6* (4), 2000897.
- (1009) Liu, Y.; Li, F.; Xu, Z.; Zheng, C.; Guo, T.; Xie, X.; Qian, L.; Fu, D.; Yan, X. Efficient All-Solution Processed Quantum Dot Light Emitting Diodes Based on Inkjet Printing Technique. *ACS Appl. Mater. Interfaces* **2017**, *9* (30), 25506–25512.
- (1010) Haverinen, H. M.; Myllylä, R. A.; Jabbour, G. E. Inkjet Printing of Light Emitting Quantum Dots. *Appl. Phys. Lett.* **2009**, *94* (7), No. 073108.
- (1011) Jiang, C.; Zhong, Z.; Liu, B.; He, Z.; Zou, J.; Wang, L.; Wang, J.; Peng, J.; Cao, Y. Coffee-Ring-Free Quantum Dot Thin Film Using Inkjet Printing from a Mixed-Solvent System on Modified ZnO Transport Layer for Light-Emitting Devices. *ACS Appl. Mater. Interfaces* **2016**, *8* (39), 26162–26168.
- (1012) Han, J.; Ko, D.; Park, M.; Roh, J.; Jung, H.; Lee, Y.; Kwon, Y.; Sohn, J.; Bae, W. K.; Chin, B. D.; Lee, C. Toward High-Resolution, Inkjet-Printed, Quantum Dot Light-Emitting Diodes for next-Generation Displays. *J. Soc. Inf. Display* **2016**, *24* (9), 545–551.
- (1013) Stanisavljevic, M.; Vaculovicova, M.; Kizek, R.; Adam, V. Capillary Electrophoresis of Quantum Dots: Minireview. *Electrophor.* **2014**, *35* (14), 1929–1937.
- (1014) Aftenieva, O.; Sudzius, M.; Prudnikau, A.; Adnan, M.; Sarkar, S.; Lesnyak, V.; Leo, K.; Fery, A.; König, T. A. F. Lasing by Template-Assisted Self-Assembled Quantum Dots. *Adv. Opt. Mater.* **2023**, *11* (6), 2202226.
- (1015) Hu, X.; Lu, C.; Wang, Q.; Xu, J.; Cui, Y. A High-Precision, Template-Assisted, Anisotropic Wet Etching Method for Fabricating Perovskite Microstructure Arrays. *RSC Adv.* **2020**, *10* (63), 38220–38226.
- (1016) Bao, Y.; Yu, Y.; Xu, H.; Guo, C.; Li, J.; Sun, S.; Zhou, Z.-K.; Qiu, C.-W.; Wang, X.-H. Full-Colour Nanoprint-Hologram Synchronous Metasurface with Arbitrary Hue-Saturation-Brightness Control. *Light Sci. Appl.* **2019**, *8* (1), 95.
- (1017) Kim, B. H.; Nam, S.; Oh, N.; Cho, S.-Y.; Yu, K. J.; Lee, C. H.; Zhang, J.; Deshpande, K.; Trefonas, P.; Kim, J.-H.; Lee, J.; Shin, J. H.; Yu, Y.; Lim, J. B.; Won, S. M.; Cho, Y. K.; Kim, N. H.; Seo, K. J.; Lee, H.; Kim, T.; Shim, M.; Rogers, J. A. Multilayer Transfer Printing for Pixelated, Multicolor Quantum Dot Light-Emitting Diodes. *ACS Nano* **2016**, *10* (5), 4920–4925.
- (1018) Mahmoud, N.; Walravens, W.; Kuhs, J.; Detavernier, C.; Hens, Z.; Roelkens, G. Micro-Transfer-Printing of Al<sub>2</sub>O<sub>3</sub>-Capped Short-Wave-Infrared PbS Quantum Dot Photoconductors. *ACS Appl. Nano Mater.* **2019**, *2* (1), 299–306.
- (1019) Lee, S.; Yoon, D.; Choi, D.; Kim, T.-H. Mechanical Characterizations of High-Quality Quantum Dot Arrays via Transfer Printing. *Nanotechnology* **2013**, *24* (2), No. 025702.
- (1020) Choi, M. K.; Yang, J.; Kang, K.; Kim, D. C.; Choi, C.; Park, C.; Kim, S. J.; Chae, S. I.; Kim, T.-H.; Kim, J. H.; Hyeon, T.; Kim, D.-H. Wearable Red–Green–Blue Quantum Dot Light-Emitting Diode Array Using High-Resolution Intaglio Transfer Printing. *Nat. Commun.* **2015**, *6*, 7149.
- (1021) Kim, S. Y.; Kwon, J. I.; Song, H. H.; Lee, G. H.; Yu, W. S.; Li, S.; Choi, M. K.; Yang, J. Effects of the Surface Ligands of Quantum Dots on the Intaglio Transfer Printing Process. *Appl. Surf. Sci.* **2023**, *610*, 155579.
- (1022) Keum, H.; Jiang, Y.; Park, J. K.; Flanagan, J. C.; Shim, M.; Kim, S. Solvent-Free Patterning of Colloidal Quantum Dot Films Utilizing Shape Memory Polymers. *Micromachines* **2017**, *8* (1), 18.
- (1023) Keum, H.; Jiang, Y.; Park, J. K.; Flanagan, J. C.; Shim, M.; Kim, S. Photoresist Contact Patterning of Quantum Dot Films. *ACS Nano* **2018**, *12* (10), 10024–10031.
- (1024) Yeom, J.; Shannon, M. A. Detachment Lithography of Photosensitive Polymers: A Route to Fabricating Three-Dimensional Structures. *Adv. Funct. Mater.* **2010**, *20* (2), 289–295.
- (1025) Kim, T.-H.; Cho, K.-S.; Lee, E. K.; Lee, S. J.; Chae, J.; Kim, J. W.; Kim, D. H.; Kwon, J.-Y.; Amarantunga, G.; Lee, S. Y.; Choi, B. L.; Kuk, Y.; Kim, J. M.; Kim, K. Full-Colour Quantum Dot Displays Fabricated by Transfer Printing. *Nat. Photonics* **2011**, *5* (3), 176–182.
- (1026) Meitl, M. A.; Zhu, Z.-T.; Kumar, V.; Lee, K. J.; Feng, X.; Huang, Y. Y.; Adesida, I.; Nuzzo, R. G.; Rogers, J. A. Transfer Printing by Kinetic Control of Adhesion to an Elastomeric Stamp. *Nat. Mater.* **2006**, *5*, 33–38.
- (1027) Valentine, J.; Zhang, S.; Zentgraf, T.; Ulin-Avila, E.; Genov, D. A.; Bartal, G.; Zhang, X. Three-Dimensional Optical Metamaterial with a Negative Refractive Index. *Nature* **2008**, *455* (7211), 376–379.
- (1028) Semple, M.; Hryciw, A. C.; Li, P.; Flaim, E.; Iyer, A. K. Patterning of Complex, Nanometer-Scale Features in Wide-Area Gold Nanoplasmonic Structures Using Helium Focused Ion Beam Milling. *ACS Appl. Mater. Interfaces* **2021**, *13* (36), 43209–43220.
- (1029) Groever, B.; Chen, W. T.; Capasso, F. Meta-Lens Doublet in the Visible Region. *Nano Lett.* **2017**, *17* (8), 4902–4907.
- (1030) Zhang, Y.; Fowler, C.; Liang, J.; Azhar, B.; Shalaginov, M. Y.; Deckoff-Jones, S.; An, S.; Chou, J. B.; Roberts, C. M.; Liberman, V.; Kang, M.; Ríos, C.; Richardson, K. A.; Rivero-Baleine, C.; Gu, T.; Zhang, H.; Hu, J. Electrically Reconfigurable Non-Volatile Metasurface Using Low-Loss Optical Phase-Change Material. *Nat. Nanotechnol.* **2021**, *16* (6), 661–666.
- (1031) Wang, Y.; Landreman, P.; Schoen, D.; Okabe, K.; Marshall, A.; Celano, U.; Wong, H.-S. P.; Park, J.; Brongersma, M. L. Electrical Tuning of Phase-Change Antennas and Metasurfaces. *Nat. Nanotechnol.* **2021**, *16* (6), 667–672.
- (1032) Kim, H.; Brueckner, E.; Song, J.; Li, Y.; Kim, S.; Lu, C.; Sulkin, J.; Choquette, K.; Huang, Y.; Nuzzo, R. G.; Rogers, J. A. Unusual Strategies for Using Indium Gallium Nitride Grown on

- Silicon (111) for Solid-State Lighting. *Proc. Natl. Acad. Sci. U.S.A.* **2011**, *108* (25), 10072–10077.
- (1033) Meng, T.; Zheng, Y.; Zhao, D.; Hu, H.; Zhu, Y.; Xu, Z.; Ju, S.; Jing, J.; Chen, X.; Gao, H.; Yang, K.; Guo, T.; Li, F.; Fan, J.; Qian, L. Ultrahigh-Resolution Quantum-Dot Light-Emitting Diodes. *Nat. Photonics* **2022**, *16* (4), 297–303.
- (1034) Finn, A.; Lu, B.; Kirchner, R.; Thrun, X.; Richter, K.; Fischer, W.-J. High Aspect Ratio Pattern Collapse of Polymeric UV-Nano-Imprint Molds Due to Cleaning. *Microelectron. Eng.* **2013**, *110*, 112–118.
- (1035) Perl, A.; Reinhoudt, D. N.; Huskens, J. Microcontact Printing: Limitations and Achievements. *Adv. Mater.* **2009**, *21* (22), 2257–2268.
- (1036) Ahn, J.; Jang, H.; Jeong, Y.; Choi, S.; Ko, J.; Hwang, S. H.; Jeong, J.-H.; Jung, Y. S.; Park, I. Illuminating Recent Progress in Nanotransfer Printing: Core Principles, Emerging Applications, and Future Perspectives. *Adv. Sci.* **2024**, *11* (1), 2303704.
- (1037) Jeong, J. W.; Yang, S. R.; Hur, Y. H.; Kim, S. W.; Baek, K. M.; Yim, S.; Jang, H.-I.; Park, J. H.; Lee, S. Y.; Park, C.-O.; Jung, Y. S. High-Resolution Nanotransfer Printing Applicable to Diverse Surfaces via Interface-Targeted Adhesion Switching. *Nat. Commun.* **2014**, *5*, 5387.
- (1038) Jeong, J. W.; Arnob, M. M. P.; Baek, K.-M.; Lee, S. Y.; Shih, W.-C.; Jung, Y. S. 3D Cross-Point Plasmonic Nanoarchitectures Containing Dense and Regular Hot Spots for Surface-Enhanced Raman Spectroscopy Analysis. *Adv. Mater.* **2016**, *28* (39), 8695–8704.
- (1039) Gao, M.; Zhao, Y.-B.; Zhao, Z.-J.; Qiu, G.; Tao, Y.; Bao, G.; Du, Y.; Spillmann, M.; Tang, J.; Hwang, S.; Jeong, J.-H.; Wang, J. Wafer-Scale Gold Nanomesh via Nanotransfer Printing toward a Cost-Efficient Multiplex Sensing Platform. *Adv. Mater. Technol.* **2023**, *8* (9), 2201758.
- (1040) Zhao, Z.-J.; Shin, S.-H.; Lee, S. Y.; Son, B.; Liao, Y.; Hwang, S.; Jeon, S.; Kang, H.; Kim, M.; Jeong, J.-H. Direct Chemisorption-Assisted Nanotransfer Printing with Wafer-Scale Uniformity and Controllability. *ACS Nano* **2022**, *16* (1), 378–385.
- (1041) Bita, I.; Yang, J. K. W.; Jung, Y. S.; Ross, C. A.; Thomas, E. L.; Berggren, K. K. Graphoepitaxy of Self-Assembled Block Copolymers on Two-Dimensional Periodic Patterned Templates. *Science* **2008**, *321* (5891), 939–943.
- (1042) Jeong, J. W.; Park, W. I.; Do, L.-M.; Park, J.-H.; Kim, T.-H.; Chae, G.; Jung, Y. S. Nanotransfer Printing with Sub-10 nm Resolution Realized Using Directed Self-Assembly. *Adv. Mater.* **2012**, *24* (26), 3526–3531.
- (1043) Han, H. J.; Cho, S. H.; Han, S.; Jang, J.-S.; Lee, G. R.; Cho, E. N.; Kim, S.-J.; Kim, I.-D.; Jang, M. S.; Tuller, H. L.; Cha, J. J.; Jung, Y. S. Synergistic Integration of Chemo-Resistive and SERS Sensing for Label-Free Multiplex Gas Detection. *Adv. Mater.* **2021**, *33* (44), 2105199.
- (1044) Yim, S.; Jeon, S.; Kim, J. M.; Baek, K. M.; Lee, G. H.; Kim, H.; Shin, J.; Jung, Y. S. Transferrable Plasmonic Au Thin Film Containing Sub-20 nm Nanohole Array Constructed via High-Resolution Polymer Self-Assembly and Nanotransfer Printing. *ACS Appl. Mater. Interfaces* **2018**, *10* (3), 2216–2223.
- (1045) Cho, S. H.; Baek, K. M.; Han, H. J.; Kim, M.; Park, H.; Jung, Y. S. Selective, Quantitative, and Multiplexed Surface-Enhanced Raman Spectroscopy Using Aptamer-Functionalized Monolithic Plasmonic Nanogrids Derived from Cross-Point Nano-Welding. *Adv. Funct. Mater.* **2020**, *30* (19), 2000612.
- (1046) Kim, M.; Huh, S.; Park, H. J.; Cho, S. H.; Lee, M.-Y.; Jo, S.; Jung, Y. S. Surface-Functionalized SERS Platform for Deep Learning-Assisted Diagnosis of Alzheimer's Disease. *Biosens. Bioelectron.* **2024**, *251*, 116128.
- (1047) Park, H. J.; Cho, S.; Kim, M.; Jung, Y. S. Carboxylic Acid-Functionalized, Graphitic Layer-Coated Three-Dimensional SERS Substrate for Label-Free Analysis of Alzheimer's Disease Biomarkers. *Nano Lett.* **2020**, *20* (4), 2576–2584.
- (1048) Oh, S.; Lee, J. H.; Lee, H.-J.; Kim, Y. S.; Cho, J.; Park, J. H.; Kim, K.-K.; Jung, Y. S.; Park, S.-J. Polarized Ultraviolet Emitters with Al Wire-Grid Polarizers Fabricated by Solvent-Assisted Nanotransfer Process. *Nanotechnology* **2020**, *31* (4), No. 045304.
- (1049) Ko, J.; Kang, H. J.; Ahn, J.; Zhao, Z.-J.; Jeong, Y.; Hwang, S. H.; Bok, M.; Jeon, S.; Gu, J.; Ha, J.-H.; Rho, J.; Jeong, J.-H.; Park, I. Biocompatible Nanotransfer Printing Based on Water Bridge Formation in Hyaluronic Acid and Its Application to Smart Contact Lenses. *ACS Appl. Mater. Interfaces* **2021**, *13* (29), 35069–35078.
- (1050) Ahn, J.; Gu, J.; Jeong, Y.; Ha, J.-H.; Ko, J.; Kang, B.; Hwang, S. H.; Park, J.; Jeon, S.; Kim, H.; Jeong, J.-H.; Park, I. Nanotransfer-on-Things: From Rigid to Stretchable Nanophotonic Devices. *ACS Nano* **2023**, *17* (6), 5935–5942.
- (1051) Park, T. W.; Byun, M.; Jung, H.; Lee, G. R.; Park, J. H.; Jang, H.-I.; Lee, J. W.; Kwon, S. H.; Hong, S.; Lee, J.-H.; Jung, Y. S.; Kim, K. H.; Park, W. I. Thermally Assisted Nanotransfer Printing with Sub-20-Nm Resolution and 8-Inch Wafer Scalability. *Sci. Adv.* **2020**, *6* (31), eabb6462.
- (1052) Pradhan, S.; Di Stasio, F.; Bi, Y.; Gupta, S.; Christodoulou, S.; Stavrinadis, A.; Konstantatos, G. High-Efficiency Colloidal Quantum Dot Infrared Light-Emitting Diodes via Engineering at the Supra-Nanocrystalline Level. *Nat. Nanotechnol.* **2019**, *14*, 72–79.
- (1053) Choi, M.-J.; Kim, Y.; Lim, H.; Alarousu, E.; Adhikari, A.; Shaheen, B. S.; Kim, Y. H.; Mohammed, O. F.; Sargent, E. H.; Kim, J. Y.; Jung, Y. S. Tuning Solute-Redistribution Dynamics for Scalable Fabrication of Colloidal Quantum-Dot Optoelectronics. *Adv. Mater.* **2019**, *31* (32), 1805886.
- (1054) Nam, T. W.; Kim, M.; Wang, Y.; Kim, G. Y.; Choi, W.; Lim, H.; Song, K. M.; Choi, M.-J.; Jeon, D. Y.; Grossman, J. C.; Jung, Y. S. Thermodynamic-Driven Polychromatic Quantum Dot Patterning for Light-Emitting Diodes beyond Eye-Limiting Resolution. *Nat. Commun.* **2020**, *11*, 3040.
- (1055) Rossner, C.; König, T. A. F.; Fery, A. Hairy Plasmonic Nanoparticles. In *Hairy Nanoparticles - From Synthesis to Applications*; Wiley-VCH, 2023; pp 351–374.
- (1056) Steiner, A. M.; Lissel, F.; Fery, A.; Lauth, J.; Scheele, M. Prospects of Coupled Organic–Inorganic Nanostructures for Charge and Energy Transfer Applications. *Angew. Chem. Inter. Ed.* **2021**, *60* (3), 1152–1175.
- (1057) Lee, J.; Bae, C.; Ou, Z.; Park, S.; Kim, J.; Kim, J. Nanoscopic Morphological Effect on the Optical Properties of Polymer-Grafted Gold Polyhedra. *Nanoscale Adv.* **2021**, *3*, 1927–1933.
- (1058) Jain, P. K.; Lee, K. S.; El-Sayed, I. H.; El-Sayed, M. A. Calculated Absorption and Scattering Properties of Gold Nanoparticles of Different Size, Shape, and Composition: Applications in Biological Imaging and Biomedicine. *J. Phys. Chem. B* **2006**, *110* (14), 7238–7248.
- (1059) Cepraga, C.; Favier, A.; Lerouge, F.; Alcouffe, P.; Chamignon, C.; Lanoë, P. H.; Monnereau, C.; Marotte, S.; Ben Daoud, E.; Marvel, J.; Leverrier, Y.; Andraud, C.; Parola, S.; Charreyre, M. T. Fluorescent Gold Nanoparticles with Chain-End Grafted RAFT Copolymers: Influence of the Polymer Molecular Weight and Type of Chromophore. *Polymer Chem.* **2016**, *7* (44), 6812–6825.
- (1060) Rossner, C.; König, T. A. F.; Fery, A. Plasmonic Properties of Colloidal Assemblies. *Adv. Opt. Mater.* **2021**, *9*, 73413.
- (1061) Jancke, S.; Liu, C.; Wang, R.; Sarkar, S.; Besford, Q. A.; König, T. A. F.; Popp, J.; Cialla-May, D.; Rossner, C. Turning on Hotspots: Supracolloidal SERS Probes Made Brilliant by an External Activation Mechanism. *Nanoscale* **2023**, *15* (46), 18687–18695.
- (1062) Minopoli, A.; Della Ventura, B.; Lenyk, B.; Gentile, F.; Tanner, J. A.; Offenhausser, A.; Mayer, D.; Velotta, R. Ultrasensitive Antibody-Aptamer Plasmonic Biosensor for Malaria Biomarker Detection in Whole Blood. *Nat. Commun.* **2020**, *11*, 6134.
- (1063) Linic, S.; Christopher, P.; Ingram, D. B. Plasmonic-Metal Nanostructures for Efficient Conversion of Solar to Chemical Energy. *Nat. Mater.* **2011**, *10* (12), 911–921.
- (1064) Kiremitler, N. B.; Pekdemir, S.; Patarroyo, J.; Karabel, S.; Torun, I.; Puntes, V. F.; Onses, M. S. Assembly of Plasmonic Nanoparticles on Nanopatterns of Polymer Brushes Fabricated by Electrospin Nanolithography. *ACS Macro Lett.* **2017**, *6* (6), 603–608.

- (1065) Pekdemir, S.; Torun, I.; Sakir, M.; Ruzi, M.; Rogers, J. A.; Onses, M. S. Chemical Funneling of Colloidal Gold Nanoparticles on Printed Arrays of End-Grafted Polymers for Plasmonic Applications. *ACS Nano* **2020**, *14* (7), 8276–8286.
- (1066) Yu, Y.; et al. Pick up, Move and Release of Nanoparticles Utilizing Co-Non-Solvency of PNIPAM Brushes. *Nanoscale* **2017**, *9*, 1670.
- (1067) Volk, K.; Fitzgerald, J. P. S.; Ruckdeschel, P.; Retsch, M.; König, T. A. F.; Karg, M. Reversible Tuning of Visible Wavelength Surface Lattice Resonances in Self-Assembled Hybrid Monolayers. *Adv. Opt. Mater.* **2017**, *5* (9), No. 1600971.
- (1068) König, T. A. F.; Ledin, P. A.; Kerszulis, J.; Mahmoud, M. A.; El-Sayed, M. A.; Reynolds, J. R.; Tsukruk, V. V. Electrically Tunable Plasmonic Behavior of Nanocube-Polymer Nanomaterials Induced by a Redox-Active Electrochromic Polymer. *ACS Nano* **2014**, *8* (6), 6182–6192.
- (1069) Yang, F.; Ye, S.; Dong, W.; Zheng, D.; Xia, Y.; Yi, C.; Tao, J.; Sun, C.; Zhang, L.; Wang, L.; Chen, Q. Y.; Wang, Y.; Nie, Z. Laser-Scanning-Guided Assembly of Quasi-3D Patterned Arrays of Plasmonic Dimers for Information Encryption. *Adv. Mater.* **2021**, *33* (24), 2100325.
- (1070) Ye, S.; Zha, H.; Xia, Y.; Dong, W.; Yang, F.; Yi, C.; Tao, J.; Shen, X.; Yang, D.; Nie, Z. Centimeter-Scale Superlattices of Three-Dimensionally Orientated Plasmonic Dimers with Highly Tunable Collective Properties. *ACS Nano* **2022**, *16* (3), 4609–4618.
- (1071) Brasse, Y.; Ng, C.; Magnozzi, M.; Zhang, H.; Mulvaney, P.; Fery, A.; Gómez, D. E. A Tunable Polymer–Metal Based Anti-Reflective Metasurface. *Macromol. Rapid Commun.* **2020**, *41* (1), 1900415.
- (1072) Kaissner, R.; Li, J.; Lu, W.; Li, X.; Neubrech, F.; Wang, J.; Liu, N. Electrochemically Controlled Metasurfaces with High-Contrast Switching at Visible Frequencies. *Sci. Adv.* **2021**, *7* (19), eabd9450.
- (1073) Probst, P. T.; Mayer, M.; Gupta, V.; Steiner, A. M.; Zhou, Z.; Auernhammer, G. K.; König, T. A. F.; Fery, A. Mechano-Tunable Chiral Metasurfaces via Colloidal Assembly. *Nat. Mater.* **2021**, *20*, 1024–1028.
- (1074) Laramy, C. R.; O'Brien, M. N.; Mirkin, C. A. Crystal Engineering with DNA. *Nat. Rev. Mater.* **2019**, *4* (3), 201–224.
- (1075) Mirkin, C. A.; Petrosko, S. H. Inspired Beyond Nature: Three Decades of Spherical Nucleic Acids and Colloidal Crystal Engineering with DNA. *ACS Nano* **2023**, *17* (17), 16291–16307.
- (1076) Li, Y.; Zhou, W.; Tanriover, I.; Hadibrata, W.; Partridge, B. E.; Lin, H.; Hu, X.; Lee, B.; Liu, J.; Dravid, V. P.; Aydin, K.; Mirkin, C. A. Open-Channel Metal Particle Superlattices. *Nature* **2022**, *611* (7937), 695–701.
- (1077) Zheng, C. Y.; Palacios, E.; Zhou, W.; Hadibrata, W.; Sun, L.; Huang, Z.; Schatz, G. C.; Aydin, K.; Mirkin, C. A. Tunable Fluorescence from Dye-Modified DNA-Assembled Plasmonic Nanocube Arrays. *Adv. Mater.* **2019**, *31* (41), 1904448.
- (1078) Lin, Q.-Y.; Mason, J. A.; Li, Z.; Zhou, W.; O'Brien, M. N.; Brown, K. A.; Jones, M. R.; Butun, S.; Lee, B.; Dravid, V. P.; Aydin, K.; Mirkin, C. A. Building Superlattices from Individual Nanoparticles via Template-Confining DNA-Mediated Assembly. *Science* **2018**, *359* (6376), 669–672.
- (1079) Cai, Z.; Li, Z.; Ravaine, S.; He, M.; Song, Y.; Yin, Y.; Zheng, H.; Teng, J.; Zhang, A. From Colloidal Particles to Photonic Crystals: Advances in Self-Assembly and Their Emerging Applications. *Chem. Soc. Rev.* **2021**, *50* (10), 5898–5951.
- (1080) Aydin, K.; Ferry, V. E.; Briggs, R. M.; Atwater, H. A. Broadband Polarization-Independent Resonant Light Absorption Using Ultrathin Plasmonic Super Absorbers. *Nat. Commun.* **2011**, *2*, 517.
- (1081) Kaplan, G.; Aydin, K.; Scheuer, J. Dynamically Controlled Plasmonic Nano-Antenna Phased Array Utilizing Vanadium Dioxide [Invited]. *Opt. Mater. Express* **2015**, *5* (11), 2513–2524.
- (1082) Li, Z.; Fan, Q.; Yin, Y. Colloidal Self-Assembly Approaches to Smart Nanostructured Materials. *Chem. Rev.* **2022**, *122* (5), 4976–5067.
- (1083) Zhou, W.; Liu, Z.; Huang, Z.; Lin, H.; Samanta, D.; Lin, Q.-Y.; Aydin, K.; Mirkin, C. A. Device-Quality, Reconfigurable Metamaterials from Shape-Directed Nanocrystal Assembly. *Proc. Natl. Acad. Sci. U.S.A.* **2020**, *117* (35), 21052–21057.
- (1084) Lin, Q.-Y.; Palacios, E.; Zhou, W.; Li, Z.; Mason, J. A.; Liu, Z.; Lin, H.; Chen, P.-C.; Dravid, V. P.; Aydin, K.; Mirkin, C. A. DNA-Mediated Size-Selective Nanoparticle Assembly for Multiplexed Surface Encoding. *Nano Lett.* **2018**, *18* (4), 2645–2649.
- (1085) Lee, S.; Calcaterra, H. A.; Lee, S.; Hadibrata, W.; Lee, B.; Oh, E.; Aydin, K.; Glotzer, S. C.; Mirkin, C. A. Shape Memory in Self-Adapting Colloidal Crystals. *Nature* **2022**, *610* (7933), 674–679.
- (1086) Wong, A. M.; Je, K.; Zheng, C. Y.; Jibril, L.; Miao, Z.; Glotzer, S. C.; Mirkin, C. A. Arrays of Colloidal Single Crystals Engineered with DNA in Lithographically Defined Microwells. *Nano Lett.* **2023**, *23* (1), 116–123.
- (1087) Li, Z.; Yin, Y. Stimuli-Responsive Optical Nanomaterials. *Adv. Mater.* **2019**, *31* (15), 1807061.
- (1088) Li, Z.; Wang, M.; Zhang, X.; Wang, D.; Xu, W.; Yin, Y. Magnetic Assembly of Nanocubes for Orientation-Dependent Photonic Responses. *Nano Lett.* **2019**, *19* (9), 6673–6680.
- (1089) Park, D. J.; Zhang, C.; Ku, J. C.; Zhou, Y.; Schatz, G. C.; Mirkin, C. A. Plasmonic Photonic Crystals Realized through DNA-Programmable Assembly. *Proc. Natl. Acad. Sci. U.S.A.* **2015**, *112* (4), 977–981.
- (1090) Hensley, A.; Jacobs, W. M.; Rogers, W. B. Self-Assembly of Photonic Crystals by Controlling the Nucleation and Growth of DNA-Coated Colloids. *Proc. Natl. Acad. Sci. U.S.A.* **2022**, *119* (1), e2114050118.
- (1091) Samanta, D.; Iscen, A.; Laramy, C. R.; Ebrahimi, S. B.; Bujold, K. E.; Schatz, G. C.; Mirkin, C. A. Multivalent Cation-Induced Actuation of DNA-Mediated Colloidal Superlattices. *J. Am. Chem. Soc.* **2019**, *141* (51), 19973–19977.
- (1092) Zheng, C. Y.; Yao, Y.; Deng, J.; Seifert, S.; Wong, A. M.; Lee, B.; Mirkin, C. A. Confined Growth of DNA-Assembled Superlattice Films. *ACS Nano* **2022**, *16* (3), 4813–4822.
- (1093) Yu, N.; Capasso, F. Flat Optics with Designer Metasurfaces. *Nat. Mater.* **2014**, *13* (2), 139–150.
- (1094) Chen, W. T.; Zhu, A. Y.; Capasso, F. Flat Optics with Dispersion-Engineered Metasurfaces. *Nat. Rev. Mater.* **2020**, *5* (8), 604–620.
- (1095) Lee, D.; Yang, Y.; Yoon, G.; Kim, M.; Rho, J. Resolution Enhancement of Fluorescence Microscopy Using Encoded Patterns from All-Dielectric Metasurfaces. *Appl. Phys. Lett.* **2019**, *115* (10), 101102.
- (1096) Kim, M.; Yang, Y.; Lee, D.; Kim, Y.; Kim, H.; Rho, J. Spin Hall Effect of Light: From Fundamentals To Recent Advancements. *Laser Photonics Rev.* **2023**, *17* (1), 2200046.
- (1097) Yang, Y.; Kim, H.; Badloe, T.; Rho, J. Gap-Plasmon-Driven Spin Angular Momentum Selection of Chiral Metasurfaces for Intensity-Tunable Metaholography Working at Visible Frequencies. *Nanophotonics* **2022**, *11* (17), 4123–4133.
- (1098) Kim, M.; Lee, D.; Yang, Y.; Kim, Y.; Rho, J. Reaching the Highest Efficiency of Spin Hall Effect of Light in the Near-Infrared Using All-Dielectric Metasurfaces. *Nat. Commun.* **2022**, *13*, 2036.
- (1099) Moon, S.-W.; Lee, C.; Yang, Y.; Kim, J.; Badloe, T.; Jung, C.; Yoon, G.; Rho, J. Tutorial on Metalenses for Advanced Flat Optics: Design, Fabrication, and Critical Considerations. *J. Appl. Phys.* **2022**, *131* (9), No. 091101.
- (1100) So, S.; Yang, Y.; Son, S.; Lee, D.; Chae, D.; Lee, H.; Rho, J. Highly Suppressed Solar Absorption in a Daytime Radiative Cooler Designed by Genetic Algorithm. *Nanophotonics* **2022**, *11* (9), 2107–2115.
- (1101) Kim, M.; Lee, D.; Son, S.; Yang, Y.; Lee, H.; Rho, J. Visibly Transparent Radiative Cooler under Direct Sunlight. *Adv. Opt. Mater.* **2021**, *9* (13), 2002226.
- (1102) Cho, H.; Yang, Y.; Lee, D.; So, S.; Rho, J. Experimental Demonstration of Broadband Negative Refraction at Visible Frequencies by Critical Layer Thickness Analysis in a Vertical Hyperbolic Metamaterial. *Nanophotonics* **2021**, *10* (15), 3871–3877.

- (1103) Lee, C.; Chang, G.; Kim, J.; Hyun, G.; Bae, G.; So, S.; Yun, J.; Seong, J.; Yang, Y.; Park, D. Y.; Jeon, S.; Rho, J. Concurrent Optimization of Diffraction Fields from Binary Phase Mask for Three-Dimensional Nanopatterning. *ACS Photonics* **2022**, *10* (4), 919–927.
- (1104) Kang, D.; Heo, H.; Yang, Y.; Seong, J.; Kim, H.; Kim, J.; Rho, J. Liquid Crystal-Integrated Metasurfaces for an Active Photonic Platform. *Opto-Electron. Adv.* **2024**, *7*, 230216–230225.
- (1105) Tang, P.; Kim, Y.; Badloe, T.; Xiao, L.; Yang, Y.; Kim, M.; Rho, J.; Li, G. Polarization-Independent Edge Detection Based on the Spin–Orbit Interaction of Light. *Opt. Express* **2024**, *32* (10), 17560–17570.
- (1106) Choudhury, S. M.; Wang, D.; Chaudhuri, K.; DeVault, C.; Kildishev, A. V.; Boltasseva, A.; Shalaev, V. M. Material Platforms for Optical Metasurfaces. *Nanophotonics* **2018**, *7* (6), 959–987.
- (1107) Song, M.; Feng, L.; Huo, P.; Liu, M.; Huang, C.; Yan, F.; Lu, Y.; Xu, T. Versatile Full-Colour Nanopainting Enabled by a Pixelated Plasmonic Metasurface. *Nat. Nanotechnol.* **2023**, *18*, 71–78.
- (1108) Bin-Alam, M. S.; Reshef, O.; Mamchur, Y.; Alam, M. Z.; Carlow, G.; Upham, J.; Sullivan, B. T.; Ménard, J.-M.; Huttunen, M. J.; Boyd, R. W.; Dolgaleva, K. Ultra-High-Q Resonances in Plasmonic Metasurfaces. *Nat. Commun.* **2021**, *12*, 974.
- (1109) Zheng, G.; Mühlenernd, H.; Kenney, M.; Li, G.; Zentgraf, T.; Zhang, S. Metasurface Holograms Reaching 80% Efficiency. *Nat. Nanotechnol.* **2015**, *10* (4), 308–312.
- (1110) Zhang, J.; ElKabbash, M.; Wei, R.; Singh, S. C.; Lam, B.; Guo, C. Plasmonic Metasurfaces with 42.3% Transmission Efficiency in the Visible. *Light Sci. Appl.* **2019**, *8*, 53.
- (1111) Kamali, S. M.; Arbabi, E.; Arbabi, A.; Faraon, A. A Review of Dielectric Optical Metasurfaces for Wavefront Control. *Nanophotonics* **2018**, *7* (6), 1041–1068.
- (1112) Genevet, P.; Capasso, F.; Aieta, F.; Khorasaninejad, M.; Devlin, R. Recent Advances in Planar Optics: From Plasmonic to Dielectric Metasurfaces. *Optica* **2017**, *4* (1), 139–152.
- (1113) Yang, Y.; Kang, H.; Jung, C.; Seong, J.; Jeon, N.; Kim, J.; Oh, D. K.; Park, J.; Kim, H.; Rho, J. Revisiting Optical Material Platforms for Efficient Linear and Nonlinear Dielectric Metasurfaces in the Ultraviolet, Visible, and Infrared. *ACS Photonics* **2023**, *10* (2), 307–321.
- (1114) Yang, J.; Fan, J. A. Analysis of Material Selection on Dielectric Metasurface Performance. *Opt. Express* **2017**, *25* (20), 23899–23909.
- (1115) Park, J.-S.; Zhang, S.; She, A.; Chen, W. T.; Lin, P.; Yousef, K. M. A.; Cheng, J.-X.; Capasso, F. All-Glass, Large Metalens at Visible Wavelength Using Deep-Ultraviolet Projection Lithography. *Nano Lett.* **2019**, *19* (12), 8673–8682.
- (1116) Devlin, R. C.; Khorasaninejad, M.; Chen, W. T.; Oh, J.; Capasso, F. Broadband High-Efficiency Dielectric Metasurfaces for the Visible Spectrum. *Proc. Natl. Acad. Sci. U.S.A.* **2016**, *113* (38), 10473–10478.
- (1117) Abdelraouf, O. A. M.; Wang, Z.; Liu, H.; Dong, Z.; Wang, Q.; Ye, M.; Wang, X. R.; Wang, Q. J.; Liu, H. Recent Advances in Tunable Metasurfaces: Materials, Design, and Applications. *ACS Nano* **2022**, *16* (9), 13339–13369.
- (1118) Park, J.; Jeong, B. G.; Kim, S. I.; Lee, D.; Kim, J.; Shin, C.; Lee, C. B.; Otsuka, T.; Kyoung, J.; Kim, S.; Yang, K.-Y.; Park, Y.-Y.; Lee, J.; Hwang, I.; Jang, J.; Song, S. H.; Brongersma, M. L.; Ha, K.; Hwang, S.-W.; Choo, H.; Choi, B. L. All-Solid-State Spatial Light Modulator with Independent Phase and Amplitude Control for Three-Dimensional LiDAR Applications. *Nat. Nanotechnol.* **2021**, *16*, 69–76.
- (1119) Shu, F.; Wang, J.; Peng, R.; Xiong, B.; Fan, R.; Gao, Y.; Liu, Y.; Qi, D.; Wang, M. Electrically Driven Tunable Broadband Polarization States via Active Metasurfaces Based on Joule-Heat-Induced Phase Transition of Vanadium Dioxide. *Laser Photonics Rev.* **2021**, *15* (10), 2100155.
- (1120) Yu, J.; Park, S.; Hwang, I.; Kim, D.; Demmerle, F.; Boehm, G.; Amann, M.-C.; Belkin, M. A.; Lee, J. Electrically Tunable Nonlinear Polaritonic Metasurface. *Nat. Photonics* **2022**, *16*, 72–78.
- (1121) Gu, T.; Kim, H. J.; Rivero-Baleine, C.; Hu, J. Reconfigurable Metasurfaces towards Commercial Success. *Nat. Photonics* **2023**, *17*, 48–58.
- (1122) Seong, J.; Jeon, Y.; Yang, Y.; Badloe, T.; Rho, J. Cost-Effective and Environmentally Friendly Mass Manufacturing of Optical Metasurfaces Towards Practical Applications and Commercialization. *Inter. J. Precision Eng. Manufact. Green Technology* **2024**, *11* (2), 685–706.
- (1123) Shah, D.; Kudyshev, Z. A.; Saha, S.; Shalaev, V. M.; Boltasseva, A. Transdimensional Material Platforms for Tunable Metasurface Design. *MRS Bull.* **2020**, *45* (3), 188–195.
- (1124) Panuski, C. L.; Christen, I.; Minkov, M.; Brabec, C. J.; Trajtenberg-Mills, S.; Griffiths, A. D.; McKendry, J. J. D.; Leake, G. L.; Coleman, D. J.; Tran, C.; St Louis, J.; Mucci, J.; Horvath, C.; Westwood-Bachman, J. N.; Preble, S. F.; Dawson, M. D.; Strain, M. J.; Fanto, M. L.; Englund, D. R. A Full Degree-of-Freedom Spatiotemporal Light Modulator. *Nat. Photonics* **2022**, *16* (12), 834–842.
- (1125) Yang, Y.; Seong, J.; Choi, M.; Park, J.; Kim, G.; Kim, H.; Jeong, J.; Jung, C.; Kim, J.; Jeon, G.; Lee, K.; Yoon, D. H.; Rho, J. Integrated Metasurfaces for Re-Envisioning a near-Future Disruptive Optical Platform. *Light Sci. Appl.* **2023**, *12*, 152.
- (1126) Park, J.-S.; Lim, S. W. D.; Amirzhan, A.; Kang, H.; Karrfalt, K.; Kim, D.; Leger, J.; Urbas, A.; Ossiander, M.; Li, Z.; Capasso, F. All-Glass 100 mm Diameter Visible Metalens for Imaging the Cosmos. *ACS Nano* **2024**, *18* (4), 3187–3198.
- (1127) Wuttig, M.; Bhaskaran, H.; Taubner, T. Phase-Change Materials for Non-Volatile Photonic Applications. *Nat. Photonics* **2017**, *11* (8), 465–476.
- (1128) Abdollahramezani, S.; Hemmatyar, O.; Taghinejad, H.; Krasnok, A.; Kiarashinejad, Y.; Zandehshahvar, M.; Alù, A.; Adibi, A. Tunable Nanophotonics Enabled by Chalcogenide Phase-Change Materials. *Nanophotonics* **2020**, *9* (5), 1189–1241.
- (1129) Ko, B.; Badloe, T.; Rho, J. Vanadium Dioxide for Dynamically Tunable Photonics. *ChemNanoMat* **2021**, *7* (7), 713–727.
- (1130) Cueff, S.; John, J.; Zhang, Z.; Parra, J.; Sun, J.; Orobctchouk, R.; Ramanathan, S.; Sanchis, P. VO<sub>2</sub> Nanophotonics. *APL Photonics* **2020**, *5* (11), 110901.
- (1131) Gholipour, B.; Zhang, J.; MacDonald, K. F.; Hewak, D. W.; Zheludev, N. I. An All-Optical, Non-Volatile, Bidirectional, Phase-Change Meta-Switch. *Adv. Mater.* **2013**, *25* (22), 3050–3054.
- (1132) Xu, P.; Zheng, J.; Doylend, J. K.; Majumdar, A. Low-Loss and Broadband Nonvolatile Phase-Change Directional Coupler Switches. *ACS Photonics* **2019**, *6* (2), 553–557.
- (1133) Zhang, H.; Zhou, L.; Lu, L.; Xu, J.; Wang, N.; Hu, H.; Rahman, B. M. A.; Zhou, Z.; Chen, J. Miniature Multilevel Optical Memristive Switch Using Phase Change Material. *ACS Photonics* **2019**, *6* (9), 2205–2212.
- (1134) Yang, F.; Lin, H.-I.; Shalaginov, M. Y.; Stoll, K.; An, S.; Rivero-Baleine, C.; Kang, M.; Agarwal, A.; Richardson, K.; Zhang, H.; Hu, J.; Gu, T. Reconfigurable Parfocal Zoom Metalens. *Adv. Opt. Mater.* **2022**, *10* (17), 2200721.
- (1135) Ding, F.; Yang, Y.; Bozhevolnyi, S. I. Dynamic Metasurfaces Using Phase-Change Chalcogenides. *Adv. Opt. Mater.* **2019**, *7* (14), 1801709.
- (1136) Ríos, C.; Stegmaier, M.; Hosseini, P.; Wang, D.; Scherer, T.; Wright, C. D.; Bhaskaran, H.; Pernice, W. H. P. Integrated All-Photonic Non-Volatile Multi-Level Memory. *Nat. Photonics* **2015**, *9* (11), 725–732.
- (1137) Jiang, T.-T.; Wang, J.-J.; Lu, L.; Ma, C.-S.; Zhang, D.-L.; Rao, F.; Jia, C.-L.; Zhang, W. Progressive Amorphization of GeSbTe Phase-Change Material under Electron Beam Irradiation. *APL Mater.* **2019**, *7* (8), No. 081121.
- (1138) Popescu, C.-C.; Dao, K. P.; Ranno, L.; Mills, B.; Martin-Monier, L.; Zhang, Y.; Bono, D.; Neltner, B.; Gu, T.; Hu, J.; Aryana, K.; Humphreys, W. M.; Kim, H. J.; Vitale, S.; Miller, P.; Roberts, C.; Geiger, S.; Callahan, D.; Moebius, M.; Kang, M.; Richardson, K. A.; Ríos Ocampo, C. A. An Open-Source Multifunctional Testing

- Platform for Optical Phase Change Materials. *Small Sci.* **2023**, *3* (12), 2300098.
- (1139) Rathi, S.; Park, J.-H.; Lee, I.; Baik, J. M.; Yi, K. S.; Kim, G.-H. Unravelling the Switching Mechanisms in Electric Field Induced Insulator–Metal Transitions in VO<sub>2</sub> Nanobeams. *J. Phys. D: Appl. Phys.* **2014**, *47* (29), 295101.
- (1140) Wu, C.; Deng, H.; Huang, Y.-S.; Yu, H.; Takeuchi, I.; Ríos Ocampo, C. A.; Li, M. Freeform Direct-Write and Rewritable Photonic Integrated Circuits in Phase-Change Thin Films. *Sci. Adv.* **2024**, *10* (1), eadk1361.
- (1141) Delaney, M.; Zeimpekis, I.; Lawson, D.; Hewak, D. W.; Muskens, O. L. A New Family of Ultralow Loss Reversible Phase-Change Materials for Photonic Integrated Circuits: Sb<sub>2</sub>S<sub>3</sub> and Sb<sub>2</sub>Se<sub>3</sub>. *Adv. Funct. Mater.* **2020**, *30* (36), 2002447.
- (1142) Wang, Q.; Maddock, J.; Rogers, E. T. F.; Roy, T.; Craig, C.; Macdonald, K. F.; Hewak, D. W.; Zheludev, N. I. 1.7 Gbit/in.2 Gray-Scale Continuous-Phase-Change Femtosecond Image Storage. *Appl. Phys. Lett.* **2014**, *104* (12), 121105.
- (1143) Delaney, M.; Zeimpekis, I.; Du, H.; Yan, X.; Banakar, M.; Thomson, D. J.; Hewak, D. W.; Muskens, O. L. Nonvolatile Programmable Silicon Photonics Using an Ultralow-Loss Sb<sub>2</sub>Se<sub>3</sub> Phase Change Material. *Sci. Adv.* **2021**, *7* (25), eabg3500.
- (1144) Wang, Q.; Rogers, E. T. F.; Gholipour, B.; Wang, C.-M.; Yuan, G.; Teng, J.; Zheludev, N. I. Optically Reconfigurable Metasurfaces and Photonic Devices Based on Phase Change Materials. *Nat. Photonics* **2016**, *10*, 60–65.
- (1145) Dong, K.; Hong, S.; Deng, Y.; Ma, H.; Li, J.; Wang, X.; Yeo, J.; Wang, L.; Lou, S.; Tom, K. B.; You, Z.; Wei, Y.; Grigoropoulos, C. P.; Yao, J.; Wu, J. A Lithography-Free and Field-Programmable Photonic Metacanvers. *Adv. Mater.* **2018**, *30* (5), 1703878.
- (1146) Hosseini, P.; Wright, C. D.; Bhaskaran, H. An Optoelectronic Framework Enabled by Low-Dimensional Phase-Change Films. *Nature* **2014**, *511* (7508), 206–211.
- (1147) Ríos, C.; Hosseini, P.; Taylor, R. A.; Bhaskaran, H. Color Depth Modulation and Resolution in Phase-Change Material Nanodisplays. *Adv. Mater.* **2016**, *28* (23), 4720–4726.
- (1148) Bichet, O.; Wright, C. D.; Samson, Y.; Gidon, S. Local Characterization and Transformation of Phase-Change Media by Scanning Thermal Probes. *J. Appl. Phys.* **2004**, *95* (5), 2360–2364.
- (1149) Hamann, H. F.; O’Boyle, M.; Martin, Y. C.; Rooks, M.; Wickramasinghe, H. K. Ultra-High-Density Phase-Change Storage and Memory. *Nat. Mater.* **2006**, *5* (5), 383–387.
- (1150) Zhang, Y.; Chou, J. B.; Li, J.; Li, H.; Du, Q.; Yadav, A.; Zhou, S.; Shalaginov, M. Y.; Fang, Z.; Zhong, H.; Roberts, C.; Robinson, P.; Bohlin, B.; Ríos, C.; Lin, H.; Kang, M.; Gu, T.; Warner, J.; Liberman, V.; Richardson, K.; Hu, J. Broadband Transparent Optical Phase Change Materials for High-Performance Nonvolatile Photonics. *Nat. Commun.* **2019**, *10*, 4279.
- (1151) Schwarz, C. M.; Kuebler, S. M.; Rivero-Baleine, C.; Triplett, B.; Kang, M.; Altemose, Q.; Blanco, C.; Richardson, K. A.; Du, Q.; Deckoff-Jones, S.; Hu, J.; Zhang, Y.; Pan, Y.; Ríos, C. Structurally and Morphologically Engineered Chalcogenide Materials for Optical and Photonic Devices. *J. Opt. Microsys.* **2021**, *1* (1), No. 013502.
- (1152) Sharma, Y.; Balachandran, J.; Sohn, C.; Krogel, J. T.; Ganesh, P.; Collins, L.; Ivlev, A. V.; Li, Q.; Gao, X.; Balke, N.; Ovchinnikova, O. S.; Kalinin, S. V.; Heinonen, O.; Lee, H. N. Nanoscale Control of Oxygen Defects and Metal–Insulator Transition in Epitaxial Vanadium Dioxides. *ACS Nano* **2018**, *12* (7), 7159–7166.
- (1153) Dillon, T.; Zablocki, M.; Murakowski, J.; Prather, D. Processing and Modeling Optimization for Grayscale Lithography. In *Advances in Resist Materials and Processing Technology XXV*; SPIE, 2008; Vol. 6923, pp 1039–1051. DOI: [10.1117/12.773213](https://doi.org/10.1117/12.773213).
- (1154) Li, X.; Youngblood, N.; Ríos, C.; Cheng, Z.; Wright, C. D.; Pernice, W. H.; Bhaskaran, H. Fast and Reliable Storage Using a 5 Bit, Nonvolatile Photonic Memory Cell. *Optica* **2019**, *6* (1), 1–6.
- (1155) Chen, R.; Fang, Z.; Perez, C.; Miller, F.; Kumari, K.; Saxena, A.; Zheng, J.; Geiger, S. J.; Goodson, K. E.; Majumdar, A. Non-Volatile Electrically Programmable Integrated Photonics with a 5-Bit Operation. *Nat. Commun.* **2023**, *14* (1), 3465.
- (1156) Piggott, A. Y.; Lu, J.; Lagoudakis, K. G.; Petykiewicz, J.; Babinec, T. M.; Vučković, J. Inverse Design and Demonstration of a Compact and Broadband On-Chip Wavelength Demultiplexer. *Nat. Photonics* **2015**, *9* (6), 374–377.
- (1157) Kang, M.; Swisher, A. M.; Pogrebnyakov, A. V.; Liu, L.; Kirk, A.; Aiken, S.; Sisken, L.; Lonergan, C.; Cook, J.; Malendevych, T.; Kompan, F.; Divlansky, I.; Glebov, L. B.; Richardson, M. C.; Rivero-Baleine, C.; Pantano, C. G.; Mayer, T. S.; Richardson, K. Ultralow Dispersion Multicomponent Thin-Film Chalcogenide Glass for Broadband Gradient-Index Optics. *Adv. Mater.* **2018**, *30* (39), 1803628.
- (1158) Kang, M.; Sisken, L.; Cook, J.; Blanco, C.; Richardson, M. C.; Mingareev, I.; Richardson, K. Refractive Index Patterning of Infrared Glass Ceramics through Laser-Induced Vitrification [Invited]. *Opt. Mater. Express* **2018**, *8* (9), 2722–2733.
- (1159) Mingareev, I.; Kang, M.; Truman, M.; Qin, J.; Yin, G.; Hu, J.; Schwarz, C. M.; Murray, I. B.; Richardson, M. C.; Richardson, K. A. Spatial Tailoring of the Refractive Index in Infrared Glass-Ceramic Films Enabled by Direct Laser Writing. *Optics Laser Technol.* **2020**, *126*, 106058.
- (1160) Di Bartolo, B.; Collins, J. *Nano-Optics for Enhancing Light-Matter Interactions on a Molecular Scale: Plasmonics, Photonic Materials and Sub-Wavelength Resolution*; NATO Science for Peace and Security Series B: Physics and Biophysics; Springer Netherlands: Dordrecht, 2013.
- (1161) Boes, A.; Chang, L.; Langrock, C.; Yu, M.; Zhang, M.; Lin, Q.; Lončar, M.; Fejer, M.; Bowers, J.; Mitchell, A. Lithium Niobate Photonics: Unlocking the Electromagnetic Spectrum. *Science* **2023**, *379* (6627), eabj4396.
- (1162) Saravi, S.; Pertsch, T.; Setzpfandt, F. Lithium Niobate on Insulator: An Emerging Platform for Integrated Quantum Photonics. *Adv. Opt. Mater.* **2021**, *9* (22), 2100789.
- (1163) Zhu, D.; Shao, L.; Yu, M.; Cheng, R.; Desiatov, B.; Xin, C. J.; Hu, Y.; Holzgrafe, J.; Ghosh, S.; Shams-Ansari, A.; Puma, E.; Sinclair, N.; Reimer, C.; Zhang, M.; Lončar, M. Integrated Photonics on Thin-Film Lithium Niobate. *Adv. Opt. Photonics* **2021**, *13* (2), 242–352.
- (1164) Luke, K.; Kharel, P.; Reimer, C.; He, L.; Loncar, M.; Zhang, M. Wafer-Scale Low-Loss Lithium Niobate Photonic Integrated Circuits. *Opt. Express* **2020**, *28* (17), 24452–24458.
- (1165) Levy, M.; Osgood, R. M., Jr.; Liu, R.; Cross, L. E.; Cargill, G. S., III; Kumar, A.; Bakru, H. Fabrication of Single-Crystal Lithium Niobate Films by Crystal Ion Slicing. *Appl. Phys. Lett.* **1998**, *73* (16), 2293–2295.
- (1166) McKenna, T. P.; Stokowski, H. S.; Ansari, V.; Mishra, J.; Jankowski, M.; Sarabalis, C. J.; Herrmann, J. F.; Langrock, C.; Fejer, M. M.; Safavi-Naeini, A. H. Ultra-Low-Power Second-Order Nonlinear Optics on a Chip. *Nat. Commun.* **2022**, *13*, 4532.
- (1167) Zhou, J.; Liang, Y.; Liu, Z.; Chu, W.; Zhang, H.; Yin, D.; Fang, Z.; Wu, R.; Zhang, J.; Chen, W.; Wang, Z.; Zhou, Y.; Wang, M.; Cheng, Y. On-Chip Integrated Waveguide Amplifiers on Erbium-Doped Thin-Film Lithium Niobate on Insulator. *Laser Photonics Rev.* **2021**, *15* (8), 2100030.
- (1168) Pak, D.; An, H.; Nandi, A.; Jiang, X.; Xuan, Y.; Hosseini, M. Ytterbium-Implanted Photonic Resonators Based on Thin Film Lithium Niobate. *J. Appl. Phys.* **2020**, *128* (8), No. 084302.
- (1169) Yang, L.; Wang, S.; Tang, H. X. Toward Radiative-Limited Coherence of Erbium Dopants in a Nanophotonic Resonator. *Appl. Phys. Lett.* **2023**, *123* (12), 124001.
- (1170) Sarabalis, C. J.; McKenna, T. P.; Patel, R. N.; Van Laer, R.; Safavi-Naeini, A. H. Acousto-Optic Modulation in Lithium Niobate on Sapphire. *APL Photonics* **2020**, *5* (8), No. 086104.
- (1171) Rabiei, P.; Gunter, P. Optical and Electro-Optical Properties of Submicrometer Lithium Niobate Slab Waveguides Prepared by Crystal Ion Slicing and Wafer Bonding. *Appl. Phys. Lett.* **2004**, *85*, 4603–4605.
- (1172) Zhang, M.; Wang, C.; Cheng, R.; Shams-Ansari, A.; Lončar, M. Monolithic Ultra-High-Q Lithium Niobate Microring Resonator. *Optica* **2017**, *4* (12), 1536–1537.

- (1173) Shams-Ansari, A.; Huang, G.; He, L.; Li, Z.; Holzgrafe, J.; Jankowski, M.; Churaev, M.; Kharel, P.; Cheng, R.; Zhu, D.; Sinclair, N.; Desiatov, B.; Zhang, M.; Kippenberg, T. J.; Lončar, M. Reduced Material Loss in Thin-Film Lithium Niobate Waveguides. *APL Photonics* **2022**, *7* (8), No. 081301.
- (1174) Zhu, X.; Hu, Y.; Lu, S.; Warner, H. K.; Li, X.; Song, Y.; Magalhaes, L.; Shams-Ansari, A.; Sinclair, N.; Loncar, M. Twenty-Nine Million Intrinsic Q-Factor Monolithic Microresonators on Thin Film Lithium Niobate. *Photonics Res.* **2024**, *12* (8), A63–A68.
- (1175) Li, Z.; Wang, R. N.; Lihachev, G.; Zhang, J.; Tan, Z.; Churaev, M.; Kuznetsov, N.; Siddharth, A.; Bereyhi, M. J.; Riemensberger, J.; Kippenberg, T. J. High Density Lithium Niobate Photonic Integrated Circuits. *Nat. Commun.* **2023**, *14*, 4856.
- (1176) Qiu, Z.; Li, Z.; Wang, R. N.; Ji, X.; Divall, M.; Siddharth, A.; Kippenberg, T. J. Hydrogen-Free Low-Temperature Silica for next Generation Integrated Photonics. *arXiv*, **2024**, 2312.07203. DOI: 10.48550/arXiv.2312.07203 (accessed Dec. 12, 2023).
- (1177) Zhuang, R.; He, J.; Qi, Y.; Li, Y. High-Q Thin-Film Lithium Niobate Microrings Fabricated with Wet Etching. *Adv. Mater.* **2023**, *35* (3), 2208113.
- (1178) Wang, C.; Zhang, M.; Chen, X.; Bertrand, M.; Shams-Ansari, A.; Chandrasekhar, S.; Winzer, P.; Lončar, M. Integrated Lithium Niobate Electro-Optic Modulators Operating at CMOS-Compatible Voltages. *Nature* **2018**, *562* (7725), 101–104.
- (1179) Shen, M.; Xie, J.; Xu, Y.; Wang, S.; Cheng, R.; Fu, W.; Zhou, Y.; Tang, H. X. Photonic Link from Single-Flux-Quantum Circuits to Room Temperature. *Nat. Photonics* **2024**, *18* (4), 371–378.
- (1180) Wang, C.; Langrock, C.; Marandi, A.; Jankowski, M.; Zhang, M.; Desiatov, B.; Fejer, M. M.; Lončar, M. Ultrahigh-Efficiency Wavelength Conversion in Nanophotonic Periodically Poled Lithium Niobate Waveguides. *Optica* **2018**, *5* (11), 1438–1441.
- (1181) Lu, J.; Li, M.; Zou, C.-L.; Sayem, A. A.; Tang, H. X. Toward 1% Single-Photon Anharmonicity with Periodically Poled Lithium Niobate Microring Resonators. *Optica* **2020**, *7* (12), 1654–1659.
- (1182) Yanagimoto, R.; Ng, E.; Jankowski, M.; Nehra, R.; McKenna, T. P.; Onodera, T.; Wright, L. G.; Hamerly, R.; Marandi, A.; Fejer, M. M.; Mabuchi, H. Mesoscopic Ultrafast Nonlinear Optics - The Emergence of Multimode Quantum Non-Gaussian Physics. *Optica* **2024**, *11* (7), 896–918.
- (1183) Jankowski, M.; Mishra, J.; Fejer, M. M. Dispersion-Engineered  $\chi^2$  Nanophotonics: A Flexible Tool for Nonclassical Light. *J. Phys. Photonics* **2021**, *3* (4), No. 042005.
- (1184) Zhao, J.; Li, X.; Hu, T.-C.; Sayem, A. A.; Li, H.; Tate, A.; Kim, K.; Kopf, R.; Sanjari, P.; Earnshaw, M.; Fontaine, N. K.; Wang, C.; Blanco-Redondo, A. Unveiling the Origins of Quasi-Phase Matching Spectral Imperfections in Thin-Film Lithium Niobate Frequency Doublers. *APL Photonics* **2023**, *8* (12), 126106.
- (1185) Chen, P.-K.; Briggs, I.; Cui, C.; Zhang, L.; Shah, M.; Fan, L. Adapted Poling to Break the Nonlinear Efficiency Limit in Nanophotonic Lithium Niobate Waveguides. *Nat. Nanotechnol.* **2024**, *19*, 44–50.
- (1186) Xia, F.; Wang, H.; Xiao, D.; Dubey, M.; Ramasubramaniam, A. Two-Dimensional Material Nanophotonics. *Nat. Photonics* **2014**, *8* (12), 899–907.
- (1187) Tan, T.; Jiang, X.; Wang, C.; Yao, B.; Zhang, H. 2D Material Optoelectronics for Information Functional Device Applications: Status and Challenges. *Adv. Sci.* **2020**, *7* (11), 2000058.
- (1188) Novoselov, K. S.; Geim, A. K.; Morozov, S. V.; Jiang, D.; Katsnelson, M. I.; Grigorieva, I. V.; Dubonos, S. V.; Firsov, A. A. Two-Dimensional Gas of Massless Dirac Fermions in Graphene. *Nature* **2005**, *438*, 197–200.
- (1189) Splendiani, A.; Sun, L.; Zhang, Y.; Li, T.; Kim, J.; Chim, C.-Y.; Galli, G.; Wang, F. Emerging Photoluminescence in Monolayer MoS<sub>2</sub>. *Nano Lett.* **2010**, *10* (4), 1271–1275.
- (1190) Yang, J.; Wang, Z.; Wang, F.; Xu, R.; Tao, J.; Zhang, S.; Qin, Q.; Luther-Davies, B.; Jagadish, C.; Yu, Z.; Lu, Y. Atomically Thin Optical Lenses and Gratings. *Light Sci. Appl.* **2016**, *5* (3), e16046–e16046.
- (1191) Fang, Z.; Thongrattanasiri, S.; Schlather, A.; Liu, Z.; Ma, L.; Wang, Y.; Ajayan, P. M.; Nordlander, P.; Halas, N. J.; García de Abajo, F. J. Gated Tunability and Hybridization of Localized Plasmons in Nanostructured Graphene. *ACS Nano* **2013**, *7* (3), 2388–2395.
- (1192) Verre, R.; Baranov, D. G.; Munkhbat, B.; Cuadra, J.; Käll, M.; Shegai, T. Transition Metal Dichalcogenide Nanodisks as High-Index Dielectric Mie Nanoresonators. *Nat. Nanotechnol.* **2019**, *14* (7), 679–683.
- (1193) Nauman, M.; Yan, J.; de Ceglia, D.; Rahmani, M.; Zangeneh Kamali, K.; De Angelis, C.; Miroshnichenko, A. E.; Lu, Y.; Neshev, D. N. Tunable Unidirectional Nonlinear Emission from Transition-Metal-Dichalcogenide Metasurfaces. *Nat. Commun.* **2021**, *12*, 5597.
- (1194) Munkhbat, B.; Küçüköz, B.; Baranov, D. G.; Antosiewicz, T. J.; Shegai, T. O. Nanostructured Transition Metal Dichalcogenide Multilayers for Advanced Nanophotonics. *Laser Photonics Rev.* **2023**, *17* (1), 2200057.
- (1195) Munkhbat, B.; Yankovich, A. B.; Baranov, D. G.; Verre, R.; Olsson, E.; Shegai, T. O. Transition Metal Dichalcogenide Metamaterials with Atomic Precision. *Nat. Commun.* **2020**, *11*, 4604.
- (1196) Danielsen, D. R.; Lyksborg-Andersen, A.; Nielsen, K. E. S.; Jessen, B. S.; Booth, T. J.; Doan, M.-H.; Zhou, Y.; Bøggild, P.; Gammelgaard, L. Super-Resolution Nanolithography of Two-Dimensional Materials by Anisotropic Etching. *ACS Appl. Mater. Interfaces* **2021**, *13* (35), 41886–41894.
- (1197) Yang, X.; Li, B. Monolayer MoS<sub>2</sub> for Nanoscale Photonics. *Nanophotonics* **2020**, *9* (7), 1557–1577.
- (1198) Vaidya, S.; Gao, X.; Dikshit, S.; Aharonovich, I.; Li, T. Quantum Sensing and Imaging with Spin Defects in Hexagonal Boron Nitride. *Adv. Physics X* **2023**, *8* (1), 2206049.
- (1199) Aharonovich, I.; Tetienne, J.-P.; Toth, M. Quantum Emitters in Hexagonal Boron Nitride. *Nano Lett.* **2022**, *22* (23), 9227–9235.
- (1200) Spencer, L.; Horder, J.; Kim, S.; Toth, M.; Aharonovich, I. Monolithic Integration of Single Quantum Emitters in hBN Bullseye Cavities. *ACS Photonics* **2023**, *10* (12), 4417–4424.
- (1201) Nonahal, M.; Horder, J.; Gale, A.; Ding, L.; Li, C.; Hennessey, M.; Ha, S. T.; Toth, M.; Aharonovich, I. Deterministic Fabrication of a Coupled Cavity–Emitter System in Hexagonal Boron Nitride. *Nano Lett.* **2023**, *23* (14), 6645–6650.
- (1202) Fröch, J. E.; Hwang, Y.; Kim, S.; Aharonovich, I.; Toth, M. Photonic Nanostructures from Hexagonal Boron Nitride. *Adv. Opt. Mater.* **2019**, *7* (4), 1801344.
- (1203) Kim, S.; Fröch, J. E.; Christian, J.; Straw, M.; Bishop, J.; Totonjian, D.; Watanabe, K.; Taniguchi, T.; Toth, M.; Aharonovich, I. Photonic Crystal Cavities from Hexagonal Boron Nitride. *Nat. Commun.* **2018**, *9*, 2623.
- (1204) Khelifa, R.; Shan, S.; Moilanen, A. J.; Taniguchi, T.; Watanabe, K.; Novotny, L. WSe<sub>2</sub> Light-Emitting Device Coupled to an h-BN Waveguide. *ACS Photonics* **2023**, *10* (5), 1328–1333.
- (1205) Gherabli, R.; Indukuri, S. R. K. C.; Zektzer, R.; Frydendahl, C.; Levy, U. MoSe<sub>2</sub>/WS<sub>2</sub> Heterojunction Photodiode Integrated with a Silicon Nitride Waveguide for near Infrared Light Detection with High Responsivity. *Light Sci. Appl.* **2023**, *12*, 60.
- (1206) Wang, Y.; Peligrin, V.; Gyger, S.; Uddin, G. M.; Bai, X.; Lafforgue, C.; Vivien, L.; Jöns, K. D.; Cassan, E.; Sun, Z. Enhancing Si3N4 Waveguide Nonlinearity with Heterogeneous Integration of Few-Layer WS<sub>2</sub>. *ACS Photonics* **2021**, *8* (9), 2713–2721.
- (1207) Yao, B.; Huang, S.-W.; Liu, Y.; Vinod, A. K.; Choi, C.; Hoff, M.; Li, Y.; Yu, M.; Feng, Z.; Kwong, D.-L.; Huang, Y.; Rao, Y.; Duan, X.; Wong, C. W. Gate-Tunable Frequency Combs in Graphene–Nitride Microresonators. *Nature* **2018**, *558* (7710), 410–414.
- (1208) Proscia, N. V.; Jayakumar, H.; Ge, X.; Lopez-Morales, G.; Shotan, Z.; Zhou, W.; Meriles, C. A.; Menon, V. M. Microcavity-Coupled Emitters in Hexagonal Boron Nitride. *Nanophotonics* **2020**, *9* (9), 2937–2944.
- (1209) Ren, H.; Jang, J.; Li, C.; Aigner, A.; Plidschun, M.; Kim, J.; Rho, J.; Schmidt, M. A.; Miaer, S. A. An achromatic metafiber for focusing and imaging across the entire telecommunication range. *Nat. Commun.* **2022**, *13*, 4183.

(1210) Choi, M.; Kim, J.; Moon, S.; et al. Roll-to-plate printable RGB achromatic metalens for wide-field-of-view holographic near-eye displays. *Nat. Mater.* **2025**. DOI: 10.1038/s41563-025-02121-0

(1211) Kim, J.; An, J.; Kim, W.; Seong, J.; Park, Y.; Lee, E.; Kim, S.; Moon, S.; Lee, C.-K.; Lee, H.; Rho, J. Large-Area Floating Display with Wafer-Scale Manufactured Metalens Arrays. *Laser Photonics Rev.* **2025**, 19, 2401425.

(1212) Kim, H.; Yun, H.; Jeong, S.; Lee, S.; Cho, E.; Rho, J. Optical Metasurfaces for Biomedical Imaging and Sensing. *ACS Nano* **2025**, 19, 3085–3114.

(1213) Yang, Y.; Lee, E.; Park, Y.; Seong, J.; Kim, H.; Kang, H.; Kang, D.; Han, D.; Rho, J. The Road to Commercializing Optical Metasurfaces: Current Challenges and Future Directions. *ACS Nano* **2025**, 19, 3008–3018.

(1214) Kang, H.; Kim, H.; Kim, K.; Rho, J. Printable Spin-Multiplexed Metasurfaces for Ultraviolet Holographic Displays. *ACS Nano* **2024**, 18, 21504–21511.

(1215) Park, Y.; Kim, J.; Yang, Y.; Oh, D. K.; Kang, H.; Kim, H.; Rho, J. Tape-Assisted Residual Layer-Free One-Step Nanoimprinting of High-Index Hybrid Polymer for Optical Loss-Suppressed Metasurfaces. *Adv. Sci.* **2025**, 12, 2409371.